Creep and anelasticity of conventional and ODS steels

Thesis

The Open University

Faculty of Mathematics, Computing & Technology

Department of Engineering & Innovation

Materials Engineering Group

Creep and Anelasticity of Conventional and ODS Steels

By

José Rodolpho de Oliveira Leo

December 2015

A THESIS SUBMITTED TO THE DEPARTMENT OF ENGINEERING & INNOVATION OF THE OPEN UNIVERSITY FOR THE DEGREE OF DOCTOR OF PHILOSOPHY

DATE of SUBMISSION : 23 DECEMBER 2015

DATE of AWARD : 5 NOVEMBER 2016

PREFACE

This thesis is submitted for the degree of Doctor of Philosophy of The Open University, United Kingdom. The work herein described was carried out in the Department of Engineering & Innovation, Faculty of Mathematics, Computing and Technology, between January 2012 and December 2015, under the supervision of Prof. Michael Fitzpatrick, Dr. Amir Shirzadi and Mr. Jan Kowal.

This work is original, to the best of my knowledge, except where reference is made to the work of others. This work has not been and is not in process of submission, in whole or part, for any other degree at any other university.

José Rodolpho de Oliveira Leo

December 2015

ABSTRACT

Materials for the components of advanced nuclear reactors are expected to undergo harsh operational conditions, in which high temperature levels (of the order of 650°C or higher) and severe mechanical stresses provide conditions for creep deformation to be significant as to become a key factor limiting the lifetime of the material. At the same time, components in nuclear power plants are subject to cycles of start-up and shut-down, due to operations of maintenance, refuelling, variations in demand and emergency stops. These conditions, characterized by removal of mechanical loads only or both mechanical loads and temperature, trigger a time-dependent recovery of the plastic strain accumulated during creep deformation, known as anelasticity.

The studies herein presented were aimed at investigations on the creep performance and on the impact of stress transients on the creep behaviour of the materials, due to the anelastic response. These transient tests, carried out by imposing stages of load removal, were concentrated at simulating the in-service conditions. Specific goals were set for each material. For the 316H, the anelastic response under partial unloading conditions was investigated, in an effort to determine the magnitude of the back stress, which is the driving force for anelastic recovery, stemming from basic physical mechanisms within the crystalline domains. The Oxide Dispersion Strengthened (ODS) 316L steel had its mechanical properties characterised, with particular focus on the creep response, analysed under the scope of performance requirements established by structural integrity code for materials in nuclear applications. And, finally, the behaviour in full load removal transients was characterised for the MA956 ferritic ODS steel, in order to study its anelastic response.

It was observed that, for the 316H, partial unloading stages produce the same recovery effect on the microstructure, provided that the drop in stress is accompanied by change in the dominant creep mechanism from dislocation-based to diffusion-controlled.

Moreover, the heterogeneous dislocation arrangement model of back stress was successfully applied for calculating the intragranular stresses and, along with neutron diffraction measurements of intergranular stresses, found good correspondence with the anelastic behaviour of the material. As for the ODS 316L, creep properties at 650°C were found to comply with the RCC MR code for the stress levels tested, but its creep performance fell short of a conventional 316L. HRTEM surveys on the oxides and a pilot diffusion-bonding study showed the effects of particle growth and how they influence the mechanical response of this alloy. And, in the case of the MA956, the investigations suggested that anelasticity is absent in this ODS steel. Although a more detailed approach is required, all the results obtained provided evidence that most of the grains in this material are resisting creep deformation.

The outcomes of the investigations are the deepening of the understanding of the potential for recovery of steels subject to creep deformation, in terms of the basic microstructural features, and how they influence the creep response. From these studies, better materials assessment procedures may be envisaged.

ACKNOWLEDGEMENTS

First of all, I would like to express my deepest gratitude to Prof. Mike Fitzpatrick, this talented academic and, most important, fantastic human being, with whom I had the honour to work along the last four years. Mike's guidance, support in every aspect of this doctoral degree programme and friendly approach in dealing with his students is a rarity that must be praised and acknowledged.

I also would like to extend this gratitude to my internal supervisors, Dr. Amir Shirzadi, for the collaboration, hints, involvement, good will and useful discussions; and to Mr. Jan Kowal, for his interest the research, support and assistance. The funding provided by the EPSRC is greatly and deeply appreciated, along with the opportunity to develop the degree in such an interesting topic.

There are a number of people without which the work conducted would have never been possible and to whom my earnest thanks are due. Mr. Peter Ledgard and Mr. Damian Flack, from the workshop, you are not technicians, you are true artisans. Thank your for all the beautiful specimens that came out of your machines and hands. Mr. Stan Hiller, I thank you for the lessons on how to make the working environment a better place! And know that most of the mechanical tests were accomplished thanks to your skills and guidance. I could not forget Mr. Gordon Imlach, for his assistance with the SEM, the TEM sample preparation and the zeal for good laboratory practices; and Mrs. Heather Davies, for the kindness and patience in the TEM training, as well as for the useful discussions. Also, I am extremely grateful to Dr. Hon Tong Pang, from the Department of Materials Science and Metallurgy, University of Cambridge, for kindly conducting a creep test on my behalf.

I am very grateful to all my PhD friends and colleagues, who shared with me, along these years, the joys and pains of being a PhD student. My salutation to those who conquered their degrees while I was still treading the terrains of my journey! In particular, my salutation to Dr. David Githinji, for his friendship and help with TEM theory and practices! A cheerful greeting to Dr. Yuki Sakanashi for her example of dedication! I

revere Dr. Yéli Traoré, Dr. Abdul Khadar Syed, Dr. Bilal Ahmad and Dr. Jino Mathew, invaluable friends and talented researchers with whom I shared fruitful discussions and chats, and rekindled my strength in the many hard moments. A special hail to Dr. Shanmukha Moturu, for his outstanding victory, for his help with the EBSD and his constant friendship (and also for being a priceless housemate)! My gratitude and best wishes for those who are walking their paths (Abdullah, Avishek, Beverly, Gerardo, Jeferson, Paheli and Rahul). Particular thanks for great comradeship and friendship are addressed to Ellies Muyupa, Yadu Das, Anas Achouri and, in special, for his kind personality and strong commitment to elevated ideals, Shah Karim.

A big thank you to the Materials Engineering staff as a whole, for the warm welcome I received; to Dr. Richard Moat, for the funny moments of chatting, for the deep discussions and for the Journal Club meetings; to Dr. Soraia Barroso, for sharing the word about this PhD opportunity five years ago; to my family and friends, here and in Brazil, who supported me throughout my journey so far. The highest gratitude is owed to my mother, my greatest sponsor and supporter, to whom I dedicate this thesis! And, above all, thank God, for the miracles of everyday!

José Rodolpho de Oliveira Leo

December 2015

TABLE OF CONTENTS

LIST OF SYMBOLS AND ABBREVIATIONS

A – a constant associated with the material in Norton's power law
APD – anti-phase domain
ASTM – American Standard for Testing and Materials
a_0 – lattice parameter
b – Burger's vector
bcc – body centred cubic crystal structure
bct – body centred tetragon crystal structure
b_e – Edge component of a Burger's vector
b_p – Burger's vector of partial dislocations
BSE – Backscattered electrons
C – material-dependent constant for Larsson-Miller Parameter calculation
c – speed of light
CBED – convergent beam electron diffraction
d – interplanar spacing
DBTT – ductile-to-brittle transition temperature
d_{eq} – equilibrium separation of partial dislocations
D_{gb} – grain boundary self-diffusion coefficient
D_L – lattice self-diffusion coefficient
d_l – average length of the diagonals of the indentation produced on a sample (HV)
DSA – dynamic strain ageing
D_V – bulk diffusion coefficient
d_0 – stress-free interplanar spacing
d_l – resolution of a microscope
E – Young's modulus
EBSD – Electron Backscatter Diffraction
EDM – electric discharge machining
EDS – x-ray energy dispersive spectroscopy
EELS – electron energy loss spectroscopy
f – frequency
fcc – face centred cubic crystal structure
FEG – Field Emission Gun
f_f – fundamental flexural frequency (mechano-acoustic technique)
FFT – Fast Fourier Transform
f_G – fraction (percentage) of grains with heterogeneous dislocation structures
f_w – fraction of "hard zones" inside grains
G – shear modulus
$\boldsymbol{g}$ – diffraction vectors in the reciprocal lattice space (TEM)
GBS – grain boundary sliding
G_M – free energy of mixing
h – Planck's constant
hcp – hexagonal close-packed crystal structure
HIP – hot isostatic pressing
HRTEM – high-resolution transmission electron microscopy
HV – Vickers hardness
k – relaxation parameter in Rôsler and Arzt's model of detachment
k_B – Boltzmann's constant
K_1 – constant in Nabarro-Herring creep regime
K_2 – constant in Coble creep regime
L – length (of a sample)
LMP – Larsson-Miller Parameter
L_t – total length of line drawn in the MLI technique

LVDT – linear variable displacement transducer
M – Taylor orientation factor (related to the crystal structure and associated with an average of the effects of the resolved shear stress in different slip systems)
m – mass (of a sample)
MLI – Mean line intercept value
N – total number of intersections between dislocations and the drawn lines
n – stress-sensitivity exponent
ODS – oxide-dispersion strengthened
P – applied load in a Vickers hardness measurement
p – linear momentum of a photon
Q_C – activation energy for diffusion
$\boldsymbol{R}$ – displacement field of atoms in a crystal
R – universal gas constant
RAF/M – reduced-activation ferritic/martensitic steel
r_p – particle radius
SADP – selected area diffraction pattern
SANS – small angle neutron scattering
SEM – Scanning Electron Microscope
SFE – stacking fault energy
STEM – scanning transmission electron microscopy
T – absolute temperature
t – thickness of a TEM foil
TEM – transmission electron microscopy
T_m – absolute melting point of a material
TMLS – tempered martensite lath structure
TMT – thermomechanical treatment
t_r – time to rupture
t_t – thickness (of a sample)
t_τ – time
T_1 – ASTM C1259 correction factor for the calculation of the flexural mode of vibration
u – dislocation line unit vector
U_s – strain energy of a dislocation in a crystal
USE – upper shelf energy (Charpy impact test)
v – velocity of a neutron
w – length of a projected defect (TEM imaging)
x – mole fraction of a powder component in a blend
X_{intra} – intragranular component of back stress
XRD – x-ray diffraction

Greek letters

α – constant depending on the type of elastic interactions of dislocations
α_1, α_2 – constants related to stress and temperature (time-dependent plastic deformation)
γ – angle between the plane of the defect and the zone axis
δ – tilt angle of an observed high-contrast TEM image
ð – grain size of a polycrystalline material
□ – a factor representing the fraction of a grain boundary intersected by a plane of unit area
ε – strain
ε_0 – instantaneous strain on loading (time-dependent plastic deformation)
ε_{tot} – total strain (time-dependent plastic deformation)
$\dot{\varepsilon}$ – secondary (steady state) creep rate
θ – incidence angle
λ – wavelength of the incident neutron beam

λ_{fp} – average free path between particles in a crystal matrix
μ – shear modulus of the 316H steel
μ_i^0 – molar energy of powder component "i" in a mixture
ν – Poisson's ratio
ξ – angle of the indenter's facets in a Vickers hardness test
ρ – dislocation density (in m^{-2})
ρ_c – "channel" (free matrix) dislocation density
ρ_w – hard zones dislocation density
Σ – flow stress of a material
σ – applied stress
σ_0 – shear stress needed to overcome the lattice resistance to dislocation motion (in the absence of other dislocations
σ_{std} – standard deviation of an experimental data average
ψ – a material-dependent constant in the Hall-Petch equation
Ω – volume of a vacancy

LIST OF FIGURES

LIST OF TABLES

So, my son, be admonished: to the crafting of books there is no end, and too much dedication to them is weariness of the body.

Ecclesiastes 12:12

Chapter 1 – Introduction

1.1 Background and aim

The on-going march of modern societies towards progress is characterised by the harnessing of Nature's means and phenomena for their benefit, aligned with concerns about the sustainability of these explorations for the near and distant futures. Everywhere on the planet, nations have to find balance between usage of natural resources and management of a livable environment, in order to make their economy sustainable in the long-term. In this scenario, energy plays a major role, and its relevance is such that this subject is deemed strategic in every government's agenda and discussions about the energy market are of worldwide concern, since demands, sources and technology change over time.

The likelihood of depletion of hydrocarbons and the attempts to curb the emissions of greenhouse gases are prompting the world to lean towards more environmentally friendly technologies, acting upon safer and cleaner energy options relying either on technologies currently under development, such as hydrogen fuel cell engines, or on the improvement of established technologies, whose impacts on the environment are being targeted, in order to improve their reliability and decrease their harmful effects. This scenario suggests promising opportunities for broadening the use of nuclear energy from both modalities, fusion and fission [1].

The possibilities of achievement of a breeding cycle, in the case of fission nuclear reactors, which would modify an exhaustible source of energy supply into a virtually limitless source, associated with large-scale electricity supply without severe impacts to the environment and generation of huge amounts of heat as by-product, and which could be redirected to hydrogen production and harvesting technologies, provide good enough reasons to justify investments in a new generation of nuclear power plants and their permanence in a country's energy mix. Moreover, the most significant environmental asset

resides on the fact that nuclear electricity generation does not emit greenhouse gases or pollution [1–3], meeting the requirements for clean technologies committed to the future of the planet. As shown in Figure 1.1, among all the options of electricity generation, nuclear energy presents the smallest relative amounts of CO_2 emitted, either in construction of the plant or when the facility is operational.

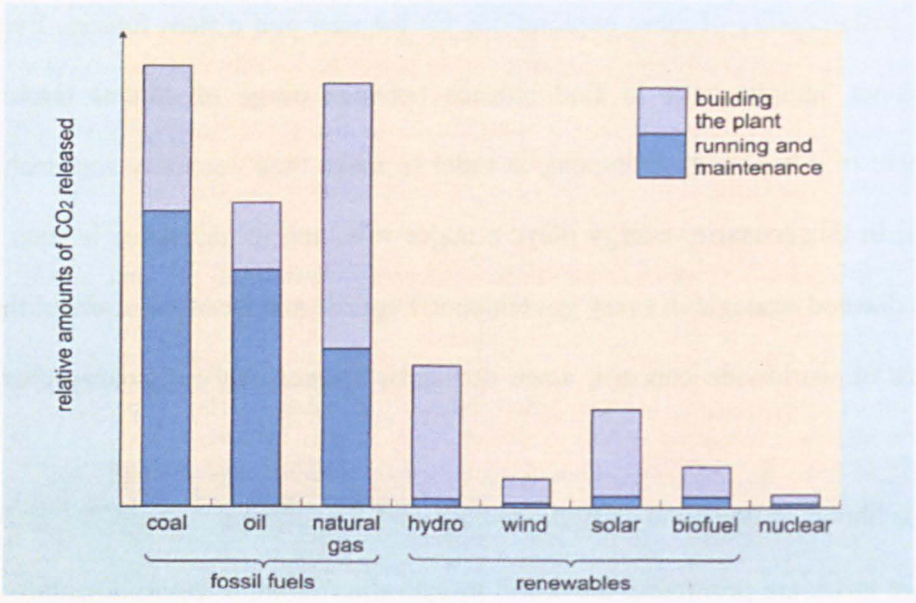

Figure 1.1- Relative amounts of CO_2 according to the source of energy generation [1].

However, if the rewards are high, the challenges are also immense, with many obstacles to overcome and improvements to be made. This is particularly true for the correct deployment of materials in GEN IV advanced nuclear reactor components and structures. During operation, these reactor components will be subjected to relatively high temperatures, massive doses of neutron radiation, corrosive environments and severe thermal and mechanical stresses [4–7]. These factors may greatly affect the microstructure of materials, leading to degradation and, subsequently, impairing the goals of improving reliability and lifetime. Moreover, there is possibility for a combined intensified influence exerted upon the material, driven by synergistic interactions between the thermo-mechanical loads and the radiation damage [5]. Since an increase in reactor lifetime is pursued, a very careful assessment of the effects of all these factors must be conducted in

order to understand the behaviour of materials and make the proper choice for reactor components.

There is a range of properties that materials must fulfil in order to be successfully deployed in high temperature nuclear power plants. These include dimensional stability under irradiation, whether the component is stressed (resistance to irradiation creep) or not (resistance to swelling); the ability to resist changes in their properties arising from the corrosive action of reactor coolant or process fluid; and acceptable mechanical properties after exposure to the effects of the nuclear environment [8]. As high temperatures and stress levels are involved, it is expected that creep will occur, sometimes at very significant levels. Furthermore, maintenance stops and variations in energy demands from operational reactors may give rise to transient regimes of loading, which may trigger anelastic recovery effects on materials. These anelastic processes, in turn, affect the creep properties, such as creep ductility and rupture life.

Given these considerations as the background, the objectives of this research are defined as follows:

- To investigate the anelastic response of 316H austenitic stainless steel subjected to transients of stress characterized by partial load removal during creep deformation, in terms of the material basic crystal lattice entities and their kinetics, assessing both intergranular and intragranular mechanisms. This material is largely deployed in the nuclear industry, due to the desirable mechanical properties at high temperatures, and may yet play a role on key components such as steam headers and piping systems.
- To characterize the mechanical behaviour of an austenitic version of Oxide Dispersion-Strenghthened (ODS) steel, the ODS 316L, studying its room and high temperature tensile properties, as well as its creep response, comparing its performance with conventional 316L. Its properties are also investigated with regards to microstructural features.

- To investigate whether anelasticity is extensively observed in a highly textured grade of a ferritic ODS steel, MA956, known to have a characteristic microstructure, comprised of columnar-like elongated grains in the extrusion direction and a fine distribution of yttria; and to what extent the anelastic behaviour depends on intragranular and intergranular phenomena, given the reduced number of grain interfaces consequent to the fibrous texture.

1.2 Project information

The work carried out along this PhD course was part of the EPSRC-based PROMINENT programme, led by Prof. Michael Fitzpatrick. This research consortium, whose name is the acronym for "Performance and Reliability of Metallic Materials for Nuclear Fission Power Generation", was aimed at addressing the main challenges expected for candidate materials to be used in structures and components of advanced nuclear fission power plants, grouped in III+ and IV generations. The consortium involved a multi-technique approach across several UK universities, including The Open University, where several experimental research programmes looked into the effects of long-term exposure of different alloy systems to complex loading conditions, marked by transients of load and temperature, expected to occur in power plants due to variations in demand, refuelling operation and maintenance stops. It is in this specific niche of experimental investigation that the activities here reported were developed. It is hoped that the findings herein described help in understanding the basic phenomena involved in a material's high temperature deformation and recovery, thus improving assessment methods for predictions on its structural integrity in long-term operational conditions.

1.3 Thesis outline

This document reports on the multi-technique work carried out on the three alloy systems mentioned in section 1.1, the conventional austenitic steel 316H and the ODS

alloys 316L (austenitic) and MA956 (ferritic), in an effort to characterize their creep properties and anelastic response caused by conditions triggered in transients of load.

While this chapter is dedicated to the presentation of the scientific context of the research, chapter 2 provides a review on the main physical, mechanical and metallurgical aspects of the stainless steels tested along the PhD programme.

Chapter 3 describes the experimental techniques and tests deployed in the investigations. Here, tensile, creep and creep transient tests are described, as well as techniques for characterization and assessment of microstructural features, such as optical and electron microscopy. The chapter deals, yet, with a brief explanation on the use of neutron diffraction for measurement of intergranular internal stresses.

Chapter 4 is concerned with description of the whole investigative approach on the 316H material. Emphasis is given to the role of neutron diffraction in computing intergranular stresses, and of Transmission Electron Microscopy (TEM) on the evolution of intragranular dislocation arrangements and the resulting intragranular back stresses.

In chapter 5, detailed characterization of an austenitic ODS steel is provided. Focus is changed to the investigation of mechanical properties, with emphasis on creep-rupture life and overall performance of the austenitic ODS 316L steel. Again, microscopy provides useful insights to the baseline creep investigations of this steel, whose behaviour is investigated using methods for prediction and analysis of creep response. Also, this chapter briefly describes a pilot study of diffusion bonding carried out on the ODS austenitic steel, for the purpose of increasing the availability of test specimens.

Chapter 6 is dedicated to the studies on the correlation between microstructure and mechanical properties of the MA956, especially on its anelastic response during creep with load transients. Similarly to what is reported in chapter 4, the full experimental work plan is covered.

Interpretation of the results from previous chapters is provided in chapter 7, to deepen the discussions of the findings in comparison with state-of-the-art works, models and different points of view on certain phenomena.

Finally, chapter 8 contains the overall conclusions and suggestions of possible future lines of investigation that may stem from the current work.

1.4 References

[1] S. Smidt, J. Kowal, and J. James, "Inside Nuclear Energy," *Science Short Module*. The Open University, p. 226, 2011.

[2] "Nuclear Fusion Power." [Online]. Available: http://www.world-nuclear.org/info/inf66.html. [Accessed: 18-Apr-2012].

[3] O. ITER, "Fusion Fuels," 2012. [Online]. Available: http://www.iter.org/sci/fusionfuels. [Accessed: 12-Jun-2012].

[4] Y. Li, T. Nagasaka, and T. Muroga, "Long-Term Thermal Stability of Ferritic and Martensitic Steels as Structural Materials of Fusion Blanket," *Plasma Fusion Res. Artic.*, vol. 5, no. S1036, pp. 1–5, 2010.

[5] R. J. Kurtz, A. Alamo, E. Lucon, Q. Huang, S. Jitsukawa, A. Kimura, R. L. Klueh, G. R. Odette, C. Petersen, M. A. Sokolov, P. Spätig, and J. W. Rensman, "Recent progress toward development of reduced activation ferritic/martensitic steels for fusion structural applications," *J. Nucl. Mater.*, vol. 386–388, pp. 411–417, 2009.

[6] R. L. Klueh and D. R. Harries, *High-Chromium Ferritic and Martensitic Steels for Nuclear Applications*. American Society for Testing and Materials, 2001.

[7] W. C. Patterson, *Nuclear Power with a New Postscript*. Pelican Books, 1978.

[8] P. Yvon and F. Carré, "Structural Materials Challenges for Advanced Reactor Systems," *J. Nucl. Mater.*, vol. 385, pp. 217–222, 2009.

Chapter 2 – Literature Review

2.1 Introduction

The purpose of the work developed through the PhD course was to characterize the high-temperature plastic strain behaviour of conventional and ODS steels for advanced nuclear power plant applications. This chapter, then, explores the needs of the nuclear industry in terms of the challenges imposed on materials, and presents the most relevant microstructural and metallurgical concepts related to their mechanisms of deformation, which are necessary for understanding the basic phenomena involved in creep-rupture and creep transient responses as well as the explanations provided for the observed behaviours.

2.2 Materials for advanced nuclear applications

While the feasibility of energy production from fusion nuclear reactors at commercial scale is still under investigation, through extensive research carried out worldwide, the challenge for nuclear fission lies on improvements to current technologies, in order to achieve economic competitiveness, and enhanced safety and sustainability (by minimization and management of radioactive wastes). These objectives are guiding the development of the Fourth Generation nuclear power plants, comprised by six designs of reactors: Sodium-cooled Fast Reactors (SFR), Gas-cooled Fast Reactors (GFR), Lead-cooled Fast Reactors (LFR), Very High Temperature Reactors (VHTR), Supercritical Water Reactor (SCWR) and Molten Salt Reactor (MSR) [1]. The common feature they share amongst each other and with fusion reactors are the high levels of demands for materials performance. Apart from the operational requirements mentioned earlier, costs of fabrication, ease of assembly and possibility of composition optimization in order to secure low-activation features for safe maintenance and disposal are criteria currently sought to be met, under normal operation as well as in extraordinary circumstances. Although similar in nature to the requirements for the current commercial reactors, these criteria for future

power plants are much more demanding, due to the operational specifications of the new systems [2, 3]. This can be easily inferred from **Error! Reference source not found.**, comparing the temperatures and correspondent displacement per atom (dpa) dose levels, which measures the number of times an atom in the crystalline structure is expected to be displaced from its site due to interactions with neutrons, for fusion, generation IV fission and existing operational reactors, which belong to Generation II:

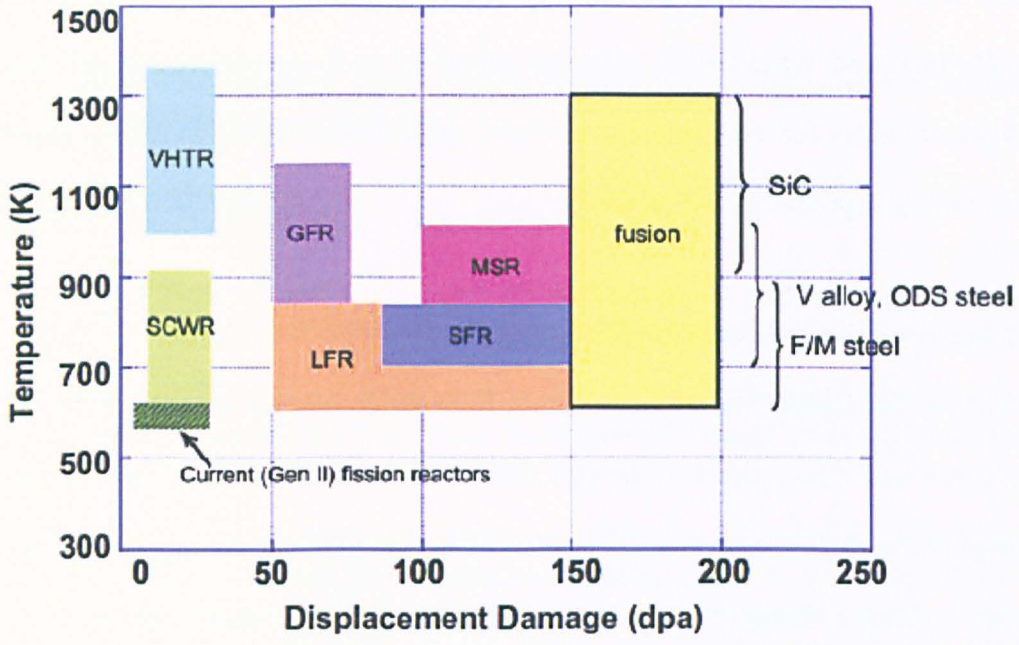

Figure 2.1- Temperatures and displacement doses according to the reactor system [3].

With reliability being a key goal for the future nuclear reactors, materials are expected to withstand the rigorous conditions for around 60 years or more of operation, another arduous requirement to be met [4].

In the case of fusion reactors, structural components are expected to be subject to mechanical and thermal loads, these latter potentially adding up to 10 MW/m² [5]; high-energy neutron irradiation (14.1 MeV) producing displacement of atoms in the crystalline structure; helium and hydrogen accumulation; thermal creep deformation [6] and radiation-induced hardening and embrittlement [7]. Even for the cases of components that do not have plasma-facing surfaces, mechanical strength and creep resistance at temperatures in

the range 600°C – 700°C [8, 9], as well as compatibility with aqueous or liquid metal coolants are desirable properties for candidate materials.

For the case of fission technology, the nuclear fission reactors are being prepared for a leap in terms of innovations, as previous generations of power plants are gradually replaced by Generation III+ and the prototypes, currently under development, of the Generation IV of nuclear power plants. Figure 2.2 illustrates the evolution of each generation, along with its features and examples.

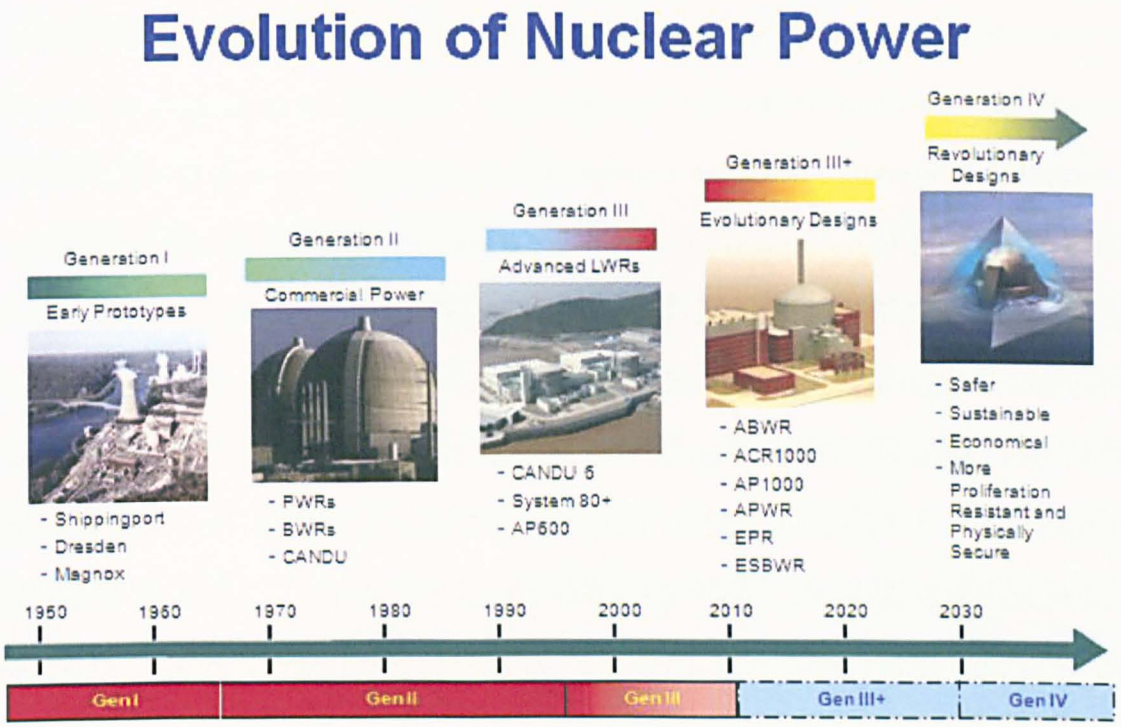

Figure 2.2- Nuclear Fission Reactor generations and their evolution [10].

The advanced reactors and the prototypes of the IV generation impose much more intense demands, in terms of performance, on materials for its components. The higher temperatures of operation (expected to range from 650°C up to almost 1000°C, being considerably higher than the current 300°C of light water reactors) are justified by the purposes of the reactors: from the six prototypes of the GEN IV, one is dedicated to the generation of huge amounts of heat for hydrogen production and three are fast reactors,

aiming to increase the efficiency of uranium usage as a fuel [11] and to burn the minor actinides generated during the fission process. These innovations are introduced in order to minimize long-lived radioactive wastes, reducing their post-service radioactive period from some millennia to only a few centuries, making nuclear fission a more sustainable option [2, 3]. As a consequence, materials used in the construction of some vital structures as the fuel-pin assemblies and breeding blankets will be directly exposed to a severe environment. Apart from the elevated temperatures, which may reach 920 K at fuel claddings and wrappers, displacements per atom doses of up to 150 dpa and increased pressure of coolant inside the fuel cladding, expected to reach 25 MPa [3, 12], will be present upon the components of fast reactors. Again, materials for these applications must be capable of operating under the imposed loading conditions for long periods, besides having the ability to resist peaks of temperature at hot spots approaching 980 K and retain dimensional stability under neutron and irradiation effects [13]. In particular, good mechanical properties such as ductility, to avoid premature failure under stresses arising from interactions between fuel and clad or stresses caused by release of gaseous fission products [9, 14], fracture toughness and creep resistance are sought when considering fission reactor components. Figure 2.3 shows a simplified sketch of a fuel-pin assembly, where the fuel pellets are stacked end-to-end and encased in the cladding, which is the tube whose material will be heavily demanded.

Figure 2.3- Simplified sketch of a fuel-pin rod and assembly [10].

Through many decades, many materials were investigated and considered for crucial applications in nuclear power plants, by means of extensive programs of research aimed at the development of new materials or optimization of existing alloys [1, 15]. As the most important structural materials for all industries, given their wide range of properties, steels have found potential applications in nuclear power reactors. From traditional alloys like stainless steel to non-commercial composites of metallic matrix with nanodispersoids, several steels are being regarded for deployment in fusion and fission power plants. Some of them are presented hereafter, along with their basic microstructural features of interest behind the mechanics of deformation.

2.3 Stainless steels

The stainless steels comprise a range of alloys that are highly resistant to corrosion (oxidation) in sundry environments, including those under high temperatures and ambient atmosphere. Their success resides in the alloying elements, of which chromium is the predominant. High Cr contents lead to the formation of a passivation layer, an impervious chromium oxide protective scale on the surface. Other elements that help in improving the properties of these steels are nickel and molybdenum. Depending on the amount of these and other alloying elements, the stainless steels can be classified in three major groups, according to the predominant phase in their microstructure: the ferritic, martensitic and austenitic steels.

Ferritic steels present the body centred cube (*bcc*) ferrite as the crystal structure. The alloying elements added are those encouraging the formation of the δ- and α-iron, thus maximizing the range of temperatures in the equilibrium diagram where ferrite prevails [16]. This steel is a Fe-Cr alloy and, usually, has the highest chromium contents among all stainless steels, ranging from 12% to 30%. However, ferritic steels for high temperature applications tend to have a lower percentage of Cr, to avoid the formation of sigma (σ) phase during prolonged heating up to 400-500°C. This intermetallic compound causes loss

of ductility and toughness in this range of temperature, a phenomenon commonly dubbed "embrittlement at 475°C" [17]. A high concentration of impurities or appreciable contents of molybdenum also favour the formation of σ-phase.

The martensitic steels have lower chromium content than the ferritic ones. Although it is usual practice to consider "stainless" steels as those Fe-Cr alloys with at least 10.5 % wt. of Cr, martensitic steels usually have lower chromium content, since they need to be austenitised, although there are some steels with Cr contents of up to 12%. Because high contents of Cr cause the austenite field of the phase diagram of the steel to be reduced (or even supressed), the composition is tailored so that, upon heating, the steel reaches the austenitising temperature, which is high enough to dissolve carbides. The alloy, then, is quickly cooled, in order to prevent the diffusion of carbon. As a result, the austenite does not transform into ferrite, but into a distorted and metastable body-centred tetragonal (*bct*) structure, which is the martensite. Of the several microstructures that may be produced for a steel, martensite is the hardest, the strongest and, in addition, the most brittle. In the as-quenched state, martensitic steel is so hard and brittle that it is not suitable for the majority of applications. This is why a complementary heat treatment, the tempering, is carried out by heating the steel up to a temperature level below the eutectoid point, so that diffusional processes can convert the *bct* structure into tempered martensite, which is formed by α-iron (ferrite) and Fe_3C phases, thus restoring some of the toughness and ductility to the steel, but still preserving the hardness.

The class of austenitic stainless steels is the largest of the three main groups, in terms of number of alloy systems, and represents most stainless steels with major industrial applications. In terms of composition, the difference between this class of steel and its counterparts is that austenitic steels are Fe-Cr-Ni alloys. While chromium is an α-forming element, contributing to the stabilization of bcc iron, high contents of nickel, a γ-forming element, expand the field for stable austenite in the equilibrium diagram over a wider range of composition and temperature. Because the expansion in the γ-iron field means

contraction of the bcc ferrite fields (the α and δ), enough additions of nickel as well as other γ-stabilizer elements, such as manganese or cobalt, allow *fcc* austenite to replace ferrite down to room temperature. Further effects of alloying elements on the microstructure of stainless steels are discussed later. Figure 2.4 shows the possible phase diagram of iron alloys, according to the composition:

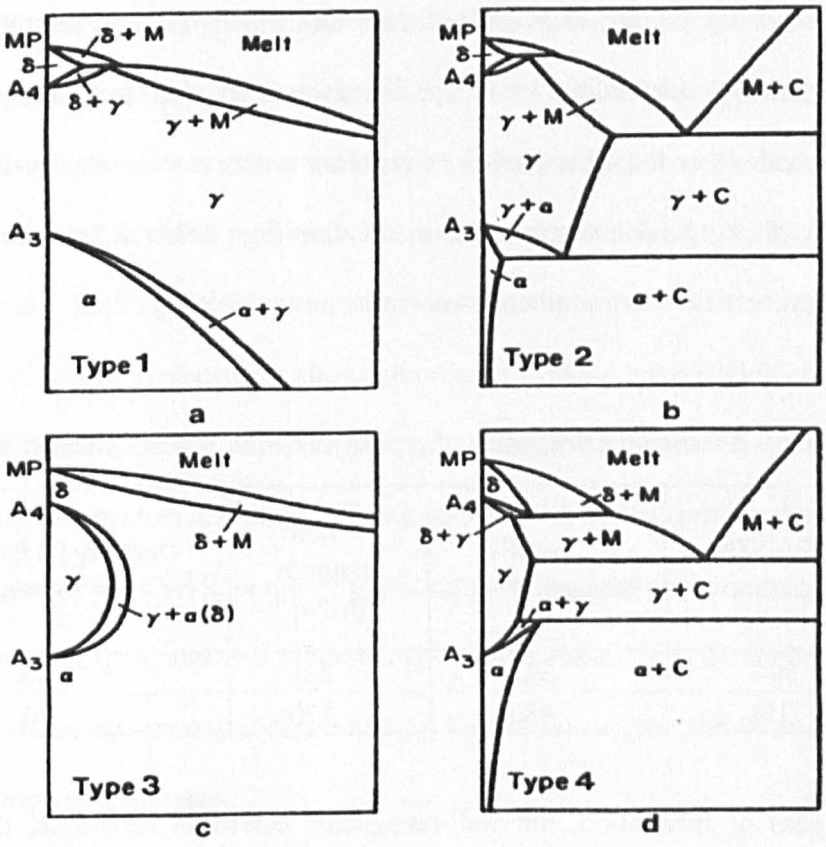

Figure 2.4- Possible Fe-C alloy phase diagrams; (a) open γ-field; (b) expanded γ-field; (c) closed γ-field and (d) contracted γ-field [18].

Within the class of stainless steels, there are also duplex stainless steels, which present a mixed microstructure of austenite and ferrite, being particularly resistant to localized corrosion processes, such as pitting and stress-corrosion cracking; and precipitation hardened steels, which are subjected to ageing heat treatments for the development of fine precipitates, responsible for imparting to the matrix a high mechanical strength [16], easily

exceeding 1500 MPa. The microstructure of these latter, rich in precipitates, is achieved with additions of alloying elements such as niobium, titanium, copper, among others [19].

2.3.1 Austenitic stainless steels

The austenitic stainless steels present a very desirable combination of properties: apart from being the most resistant to corrosion, due to the high chromium and nickel contents, some of them bring together elevated ultimate tensile strength and relatively moderate yield strength (thus demanding lower applied stresses in manufacturing processes), in comparison with other the other classes of stainless steels, along with excellent ductility, which make them good materials for metal forming. Table 2.2 summarizes some mechanical properties of two of the most common austenitic alloys:

Table 2.1- Mechanical properties of typical austenitic steels - adapted from [16].

AISI/ASTM designation	Tensile Strength [MPa]	Yield Strength [MPa]	Ductility [% Elongation in 50 mm]
304	515	205	40
316L	485	170	40

Due to ease of fabrication, the well-recognized corrosion resistance, the ability to preserve mechanical integrity at high temperatures and good weldability, austenitic stainless steels play a lead role in many specialized applications. In the nuclear power scenario, the 316 austenitic stainless steels, in both high and low carbon grades, commonly referred to as Type 316, are deployed successfully in various components. The history of the usage of the 316 steels is noteworthy, since it stems from the understanding of its behaviour from the basic microstructural features.

2.3.2 Use of Type 316 steel in nuclear power plants

The long-term successful deployment of 316 stainless steels in industry led to their adoption for several critical components in the first generations of fission reactors, such as steam headers and welded structures. Furthermore, until 1974, 316H was the undisputed choice for structural components in advanced liquid metal-cooled breeder reactor prototypes and started being considered for fusion applications [15]. However, observations in early stages of operation showed the susceptibility of this steel to the development of cavities during neutron irradiation. This form of damage, associated with the naturally high thermal expansion coefficient of the material, was observed to lead to high rates of swelling, causing prohibitive dimensional instabilities [1, 9, 15, 20]. As this deficiency could limit the life span of in-core components, efforts started to be concentrated on finding replacement alloys, in order to achieve optimization of operational stability and extended life for advanced reactors. Although 316 was rejected for in-core structures in fission reactors and plasma facing components in fusion units, their properties make them suitable for a wide range of applications in nuclear power plants, like piping systems, heat exchangers and many others. This is the reason why a number of studies [21–24] have been continuously conducted to further investigate the behaviour of 316 Type steel at high temperatures.

2.3.3 Alloying elements and precipitation in 316H steel

The 316 austenitic steels are multicomponent alloy systems, in whose compositions several alloying elements figure in different conditions: in the free state, forming an intermetallic compound with Fe (or with each other); in the form of oxides, nitrides, sulphides or any other non-metallic particles; as part of carbides, or, finally, as solid solution in the iron matrix [18]. It is usual practice to divide the alloying elements in two groups, namely, those who do not form stable carbides in steel and those who do.

Elements such as nickel, silicon, cobalt, aluminium, copper and nitrogen belong to the first group. By not forming chemical compounds with iron or carbon, almost all of them are found chiefly as solid solutions in the matrix. However, each of these elements can be added for specific purposes.

Silicon is a common element to all stainless steels, usually added at the very end of steel melting process, in order to act as a deoxidizer [25, 26]. The higher affinity with oxygen causes removal of this element from the iron matrix, with the subsequent formation of silicon oxides. However, amounts must be carefully introduced in austenitic stainless steels, since this element acts an α-stabilizer and forms brittle silicides with iron, when present in more than 1% weight.

Aluminium is another element with higher oxygen affinity than iron, and exactly for this reason is also used as deoxidizer. Again, care must be taken when adding it to austenitic stainless steels, since large contents of aluminium also tend to promote ferrite at the expense of the austenite field [26].

Cobalt, just like nickel, widens the range of temperatures in which austenite is stable. In sufficient amounts, these elements can completely supress the α-iron phase field, making it possible to replace the ferrite with austenite at room temperature, thus creating phase diagrams with aspect similar to the one shown in Figure 2.4a.

One of the most important alloying elements in austenitic stainless steels, nitrogen provides numerous benefits to the microstructure. It is known for increasing tensile, fatigue and creep strength of the material [27], and has the additional advantage of expanding the γ-phase field, thus stabilizing the austenite phase, although this effect is cut short, in comparison to nickel (or cobalt) due to the tendency of forming nitrides [28]. An austenitic steel rich in this element would present a phase diagram as shown in Fig. 2.4b. Nitrogen is considered the most effective solid solution strengthener in austenite, remarkably increasing creep strength (and decreasing minimum creep rate), with this improvement connected to the creation of short-range ordered zones, as pointed out by Shankar et al.

[29] with pairs of dislocations associated with precipitated Cr_2N phase observed in an 316LN steel, to a reduction in the stacking fault energy of the material, as well as to Dynamic Strain Aging [27]. Nitrogen is also reported to increase intergranular stress corrosion cracking resistance and pitting corrosion resistance [29].

Among the elements that form stable carbides, chromium, manganese and molybdenum are some of the most relevant, along with carbon. This latter exists as interstitial solid solution in steels and, just like nitrogen, is a promoter of austenite stability, leading to a phase diagram similar to the one of Fig. 2.4b. At high temperatures, though, carbon combines with other elements and forms compounds, the carbides, which tend to precipitate, given that alloying elements commonly exist in a supersaturated state within the austenitic matrix, so that when exposed to elevated temperatures, solute atom diffusion mechanisms assure precipitation. It is the amount of carbon that dictates the difference between 316H and 316L, the "L" being indicative of low carbon content (< 0.03% wt.), while, in 316H, carbon contents range from 0.04% wt. to 0.10% wt. [16].

Manganese is added to practically all grades of steel, also stabilising austenite, although its effect is more significant when nickel is part of the composition. The most recognized contributions manganese provides to steels are improvement of workability, especially at high temperatures, by preventing hot cracking, and increase of the solubility of nitrogen in the austenitic phase [30].

Molybdenum acts as an α-stabilizer, but its effects are dependent on the grade of steel in which the element is introduced. In austenitic steels, it is known for improving high temperature strength and producing secondary hardening by the formation of carbides. However, its content is kept low, in order to avoid adverse effects, such as decrease in hot workability and the formation of σ-phase and intermetallic Laves phase, which arise with long-term ageing of the material [32, 33].

The role of precipitates in creep and anelastic response of 316H steel is of fundamental relevance and it changes the microstructure and, as a consequence, the properties of the

steel. Although several elements are present in the steel and different compounds (carbides, nitrides, sulphides, carbonitrides) can be formed, the most common stable precipitate found in stainless steel is the $M_{23}C_6$ carbide, where "M" denotes metals like Fe, Cr, Mo and Mn. High thermodynamic affinity is found between carbon and these elements [30]. Because precipitation requires diffusion, the extent to which it happens will depend on temperature and time. Therefore, as temperature increases, diffusion rates of solute inside the matrix also increase, while the driving force for precipitation is reduced. By lowering the temperatures, the solubility decreases, leading to supersaturation of free solute [82]. Thermodynamically driven precipitation, then, occurs, in such a way as to minimise the interfaces and, therefore, lower the surface energy. This process, at first, will take place in discontinuity regions, that is, along grain boundaries, as illustrated in Figure 2.5. This is due to the high surface energy of high-angle grain boundaries, which makes them preferential sites for diffusion, precipitation and other solid-state reactions [33]. Other sites include incoherent and coherent twin boundaries. Only then, intragranular precipitation proceeds. It is reported that finer precipitates are produced when particles nucleate on dislocations of the matrix [25]. These processes have opposing effects on the 316H properties: while the precipitates formed increase creep strength, the creation of chromium-depleted zones reduces the corrosion and oxidation resistance of the steel, making it prone to sensitization. It is important to mention that these precipitates are formed over a wide range of temperatures, usually above 500°C. Also, an increase in temperature will promote the formation of other compounds, such as M_6C, when temperatures rise to 600°C and above (being "M" the general representation for Mo, Ti, Nb, V and Fe); and intermetallic Laves phase, like Fe_2W, Fe_2Mo or Fe_2Ti, which precipitates intragranularly (and, occasionally, on grain boundaries) in steels exposed to temperatures around 600°C for sufficiently long periods of time [25].

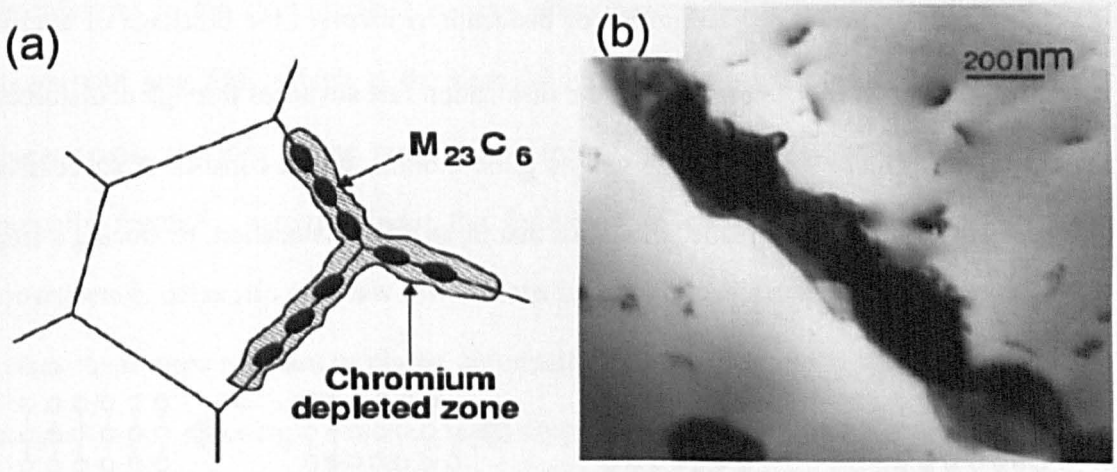

Figure 2.5- Sketch of precipitates along grain boundaries of (a) and a TEM micrograph showing precipitates on boundary as well as intragranular carbides.

2.3.4 Plastic deformation of 316H steel

Austenitic stainless steels present an *fcc* crystal structure. Therefore, the most likely slip systems to be active at the onset of plastic deformation are defined by the close-packed {111} atomic planes and, within these planes, the close-packed <110> directions. Since there are four {111} planes, each containing three <110> directions, there are 12 possible crystallographic systems along which the motion of dislocations can readily occur [33]. There are two basic types of dislocations, the edge dislocation and the screw dislocation. The first type glides or slips in a direction perpendicular to its length, while the screw dislocation moves in a direction parallel to its line. Since the Burgers vector represents motion of a dislocation from one atomic position to the next, the dislocation line is perpendicular to its Burgers vector, in an edge dislocation, and parallel to it in a screw dislocation. In real crystals, though, these defects are not straight lines and rarely lie in a single plane. Dislocations, in general, present screw segments and edge segments [34]. Irrespective of the type, the basic Burgers vector of the *fcc* crystal is $(a_0/2)[110]$, equivalent to the displacement from one atom at a cube corner to the atom at the centre of a cube face. Plastic deformation takes place, at room temperature, by the glide of dislocations along the active slip system, under the effect of a critical resolved shear stress, τ_c, when the material

is deformed under stress, σ. The motion of dislocations involves the breakage of atomic bonds and establishment of new ones, as the dislocation line advances through undisturbed crystal regions. Figure 2.6 shows the simple glide motion, which consists of successive displacements of extra "half-plane" of atoms, that is, an edge dislocation, producing a step at the free surface of the crystal:

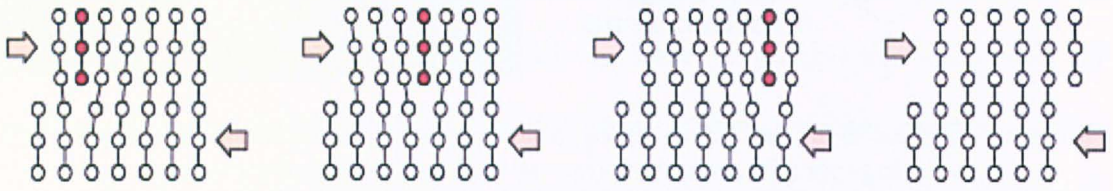

Figure 2.6- Motion of an edge dislocation through the crystal lattice. The arrows indicate the directions of the shear stress – adapted from [16].

However, considerations of the atomic arrangements in an *fcc* lattice suggest that glide does not take place so directly. The strain energy of a dislocation is proportional to the square of the magnitude of the Burgers vector:

$$U_s = Gb^2/2 \qquad \text{(Eq. 2.1)}$$

Therefore, it may be more energetically favourable for the shear displacement in the crystal to be accomplished by the decomposition of a dislocation into two partials, with lower Burger's vectors, that is, minimized strain energy. However, because these partials do not produce complete lattice translations, the region delimited by them presents different crystallographic orientation than the *fcc* crystal and characterises a planar defect called a stacking fault. The Burger's vectors of the partial dislocations on a stacking fault form an angle of 60° and, due to that, they tend to repel each other [33]. The repulsion is counterbalanced by the surface tension of the stacking fault, which is provided by a characteristic energy of the material, the stacking fault energy, SFE [34]. This parameter is influenced by the chemical composition of the alloy and dictates its deformation behaviour: *fcc* materials with high SFE, such as aluminium (SFE ~ 140 – 200 mJ/m²) [34, 36], present narrow stacking faults, so that the recombination of the partials into

constrictions in the stacking fault is easy, allowing cross slip to occur readily; whereas alloys with low SFE, which is the case of austenitic stainless steels, reported to have characteristic energies in the range 18-40 mJ/m^2, wide stacking fault regions between mutually repulsive partials hinder the formation of constrictions [34, 37, 38]. As a consequence, cross slip of screw dislocations in these alloys demands more energy, which makes them more resistant to plastic deformation and more prone to strain hardening. An external input of energy, such as high temperature or high straining levels, provides conditions for cross slip to occur over long atomic domains, since the formation of constrictions can be assisted by thermal activation and by strain compatibility requirements within grains, this latter arising from the necessity of cohesion between crystals in an anisotropic polycrystalline material, achieved by stabilizing intergranular stresses [40]. It is timely to conceptualize cross slip as the process by means of which a screw segment of dislocations moves from one slip plane to another, provided that the initial slip plane and the one to which motion has occurred share a common slip direction [25, 33, 34].

Another mechanism by which deformation occurs is twinning, resulting from a portion of the crystal assuming a definite and symmetrically related orientation with regards to the unaffected lattice. Twinning also occurs on specific planes, such as {111}, and atoms are displaced by less than an atomic distance. Twins can be produced by mechanical deformation, which is less common for austenitic steels, happening only at very low temperatures or under rapid rate of loading; or by annealing after plastic strain, in which case the result is called annealing twins [38]. It is convenient to notice, though, that twinning is not a dominant deformation mechanism in alloys with many slip systems, being favoured just when active slip systems are restricted or when the stress for twinning becomes lower than the stress for slip [33].

The most important consequence of the plastic deformation mechanisms in austenitic steels like 316H, especially those related to generation and motion of dislocations, is strain hardening and its subsequent effect of microstructural strengthening. Along their motion

through the crystal lattice, dislocations will interact with other dislocations, grain boundaries, solute atoms and precipitates. Each of these interactions plays a part on strengthening, which is more pronounced at room temperature, but also takes place at high temperature deformation, as will be further explained in section 2.5.

Dislocations gliding in an active slip system will suffer resistance from long-range stress fields of surrounding dislocations, as well as from short-range interactions with forest dislocations cutting through the glide plane [39]. The more strain hardening the material experiences, the more likely these interactions become, given the increase of dislocation density that ensues. Interactions between dislocations hinder their motion and give rise to dislocation structures inside the grains, which will, in turn, contribute to the strain hardening effect [35, 41]. One such structure happens when dislocations on an active slip system pile up at obstacles such as grain boundaries, precipitates or other dislocations with unfavourable Burgers vector for gliding (sessile dislocations). The pile-up generates a back stress acting in opposition to the applied stress and hindering the motion of additional dislocations along the slip plane. Other interactions involve the formation of jogs, which restrict the glide motion of the segmented line. In order to slip across new positions, these dislocations become dependent on nonconservative processes, such as climb, and, thus, motion is impeded at temperatures where diffusion does not occur appreciably [33]. Changes in the material's flow stress (Σ) due to microstructural features are generally represented by equations of the Taylor hardening form [34, 42]:

$$\Sigma = \sigma_0 + M\alpha Gb\sqrt{\rho} \qquad \text{(Eq. 2.2)}$$

where σ_0 is the shear stress needed to overcome lattice resistance to dislocation motion in the absence of other dislocations, M is the Taylor orientation factor, dependent on the crystal structure, since it represents the effect of the resolved shear stress in different slip systems combined [33], and taken as 3.06 for *fcc* structure [42]; α is a constant depending on elastic interactions of dislocations, G is the shear modulus, b is the magnitude of the Burger's vector and ρ is the dislocation density [34, 41].

In polycrystalline materials, grain boundaries represent interfacial regions between crystals with different orientations and, as such, act as obstacles to dislocation motion. The presence of a boundary forces the dislocations to change their direction of slip from one grain to the adjacent. Moreover, the less ordered atomic structure (with regards to a crystal) within the boundary creates discontinuity of slip planes in the grains involved [16], so that the motion is indirectly imparted between grains: when pile-ups at grain boundaries contain many dislocations, the stress on the leading dislocation in the pile-up can approach the shear stress of the crystal. This stress can either promote yielding on the other side of the boundary, by producing shear stress on a potentially active slip system of that grain, or nucleate a crack. Because the stress at the head of a dislocation pile-up increases with the grain size, coarse grains are more effective at transmitting plastic deformation across the boundary than fine grains, from where it is easy to infer that a fine-grained material is more resistant and harder than a coarse-grained one. For many crystalline materials, there's a relation between the yield strength (Σ) and the grain size ($\eth$), expressed by the Hall-Petch equation:

$$\Sigma = \sigma_0 + \psi \eth^{-1/2} \qquad \text{(Eq. 2.3)}$$

in which ψ is a constant for a particular material [33] and σ_0 has the same meaning as in equation 2.2.

The constitution of alloys invariably involves the addition of elements whose difference, in size, from that of the atoms of the base metal causes distortion of the lattice. Depending on its size, the solute atom can be substitutional, if it occupies sites of the crystal lattice, or interstitial, when interstitial positions of the solvent lattice are occupied. Solute atoms of approximately the same size as the parent solvent atoms form substitutional solid solutions and promote less strengthening effect than the interstitial atoms, even though the size of these latter is smaller [43]. Carbon, nitrogen, oxygen and boron are well-known interstitial solid solution elements in 316H steel.

The interaction between solute atoms and dislocations may take place by short-range or long-range mechanisms. The difference between them is based not only on the extent of atomic distances of their effects, but also on the relative insensitivity to temperature, which is higher for the long-range interactions [33]. These comprise the elastic interaction, the modulus interaction and the long-range ordering. Elastic interactions arise from the mutual interactions between dislocations and the stress fields around misfit solute atoms. Modulus interaction takes place when a solute atom, even if identical in size and valence to the atoms of the matrix, is introduced, as it locally alters the modulus of the crystal and this will affect dislocation motion, given that dislocations are attracted to solutes with lower shear modulus than the matrix and repelled by those elastically stiffer [34, 40].

Long-range ordering is a typical interaction of fully ordered lattices (superlattices), where periodic arrangements of dissimilar atoms can be found. When a dislocation moves through these arrangements, a configuration opposed to that of the ordered lattice is created, as the atoms of the slip plane move out of phase with respect to the superlattice structure, giving origin to an anti-phase domain (APD). However, the disorder can be minimized by the dissociation of a superdislocation in a pair of ordinary dislocations separated by a ribbon of the anti-phase domain [39]. As slip proceeds, more APDs are produced, increasing the rate of strain hardening of the ordered material.

Among the mechanisms of short-range interactions, the short-range ordering, the electrical interaction and the stacking fault interaction are counted. Short-range ordering occurs when solute atoms tend to form arrangements in which they have more than the equilibrium number of dissimilar neighbours. The motion of dislocations through a short-range ordered zone locally disrupts the order, increasing the energy barrier against further motion. In order to sustain the motion in an energetically unfavourable condition, extra energy needs to be provided. The effects of short-range order are less pronounced than those for long-range ordering, particularly on creep resistance [44], but discernible and relevant. It was reported by Shankar et al. [29] as the main strengthening mechanism for a

316L steel alloyed with nitrogen, termed 316LN, in terms of flow stress and increase on fatigue life, due to the presence of ordered Cr-N zones.

When the rearrangements of electrons around the dislocation core are such that leave them with a dipole or a shortage of electrons, attraction between dislocations and solute atoms of different valences promotes the electric interaction. Although its strengthening effect is considered secondary to elastic interaction, becoming relevant only when the valence difference between matrix and solute is large and the elastic misfit is small [45], some authors attribute to the electrical interaction the observed improvement in creep strength of the 316LN: the core of dislocations bears positive charge, that is, there's a shortage of free electrons associated with this region, which attracts nitrogen atoms, since these exist in austenitic stainless steels as negatively charged atoms [28, 47]. The resulting electrostatic interaction is enhanced by the increase of nitrogen content in the steel, which contributes to the strengthening of the alloy.

As seen before, plastic deformation of austenitic stainless steels involves the creation of stacking faults, regions of different crystallographic orientation (which are *hcp* arrangements) in the *fcc* crystal lattice, limited by two partial dislocations. Due to its own nature, the cohesive energy between atoms of a stacking fault differs from that of the lattice atoms. This becomes a driving force for segregation of solute atoms to the stacking faults, resulting in a difference of equilibrium concentration between the matrix and the stacking faults [40, 48]. Also known as chemical or Suzuki interaction, the increase of solute atom concentration in the stacking fault reduces the SFE, enlarging the separation between the partial dislocations. As a result, extra work needs to be done in order to create constriction in the partials, so dislocation motion is hindered. This interaction seems to play a relevant part on the creep transient behaviour of 316H steel, as suggested in Chapter 4.

Finally, in practically all of the significant alloys for industrial use (or potential use), second-phase particles constitute a very effective strengthening mechanism. In 316H,

particles result from precipitation hardening (or age hardening), which is achieved by subjecting the alloy to solution heat treatment at high temperature, followed by quenching and ageing at a lower temperature [16]. The hardening associated with precipitates scattered throughout the matrix (intragranular particles) stems from the fact that additional stress is required for dislocations to cut through a coherent precipitate. Coherency is a key concept in second-phase strengthening, indicating an atomic matching between the lattices of the precipitates and of the matrix. It is usual for a particle to experience loss of coherency when growth exceeds a critical size, with continued ageing time. When this happens, dislocations can no longer cut through precipitates, so that strain hardening starts to be determined by the shear stress required for bowing a pinned dislocation line and ensuring its motion past the particle [48].

The degree of strengthening achieved with precipitates is dependent on the distribution of particles in the matrix [33]. Therefore, besides morphology, second-phase particles can be described in terms of volume fraction, average diameter (or size) and mean interparticle spacing, these factors being interconnected; that is, for the same volume fraction, for example, a reduction in the particle size decreases the interparticle spacing. It is usual practice to subject alloys to thermomechanical treatments in order to achieve a fine dispersion of precipitates and grow them to the peak hardness condition, in which they become incoherent. For this case, the strengthening mechanism is associated with the shear stress required to bow a dislocation between particles separated by a distance λ. As shown in Figure 2.7, when impeded from cutting through the precipitates, a dislocation line starts to bow in order to bypass them, leaving behind a loop around each particle. The original dislocation line, then, is free to resume its motion through the crystal [34]. Each dislocation gliding in the considered slip plane adds one loop to the particles, and these loops produce a back stress on the sources of dislocation, thus promoting a hardening effect known as Orowan bowing mechanism. This interaction, as it will be seen in section 2.5.2, is also

present when the strengthening particles are dispersoids introduced in the matrix by powder metallurgy techniques, although more complex phenomena act simultaneously.

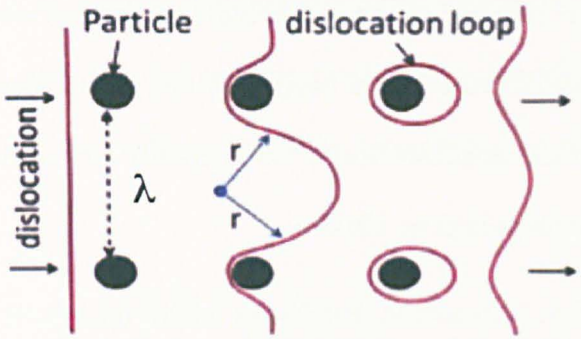

Figure 2.7 – Schematic drawing of a dislocation interaction with particles [33].

2.4 Reduced-activation Ferritic/Martensitic Steels

The verification of unsuitability of the 316 Type came to a definite appraisal only after some attempts of overcoming the swelling problem, like application of cold working and stabilization of austenitic alloys with titanium, resulted in delay of the onset of this phenomenon instead of eliminating it. A wide range of materials started to be investigated, which included ferritic, martensitic and precipitation strengthened alloys, nickel-based alloys, molybdenum alloys, among others.

The suitability of ferritic and martensitic steels became more evident after observation of severe post-irradiation embrittlement in precipitation-hardened alloys [49]. In the fusion technology scenario, after preliminary simplified calculations showed that the interaction between the strong magnetic fields created by the plasma confinement system (tokamak) and a ferromagnetic material resulted in stresses of acceptable magnitudes that would have to be incorporated in the stress analysis of fusion reactor designs [50], ferritic and martensitic steels started to be strongly considered, especially because first insights showed that these ferromagnetic materials would behave paramagnetically under the intense magnetic fields [51].

The requirements for swelling resistance and adequate toughness and strength at elevated temperatures found in these ferritic and martensitic steels very promising candidate materials for fuel cladding in advanced fast neutron reactors. As Figure 2.8 illustrates for dimensional changes in the hoop direction, ferritic/martensitic steels exhibit much lower swelling than austenitic steels, conventional and reinforced with titanium, even at displacement doses as high as 150 dpa.

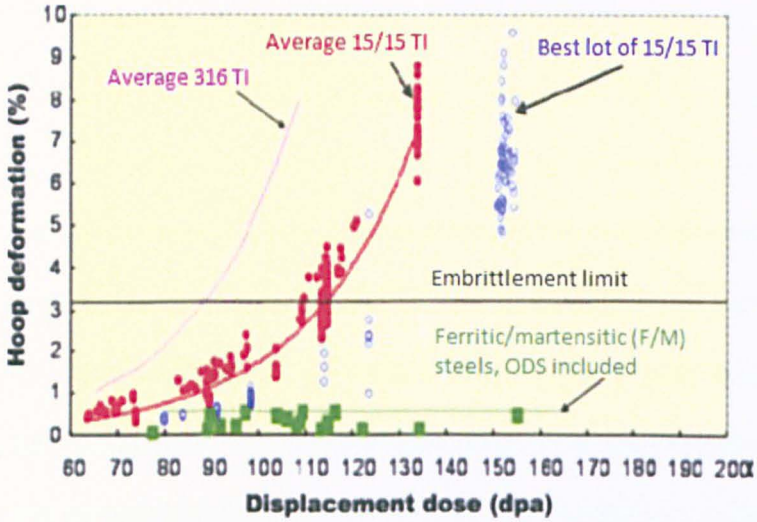

Figure 2.8 - Maximum hoop deformation for some grades of austenitic and ferritic/martensitic steels tested at temperatures between 675 and 825 K – adapted from [3].

Demands for proper decommission of nuclear power plants and disposal of radioactive wastes, aiming at minimizing the environmental impact, motivated the enhancement of these ferritic/martensitic alloys with regards to the decay of induced radioactivity. Programs were started in Japan, Europe and United States in the mid-1980s to adjust the chemical composition of the steels in order to exclude or minimize elements which pose long-lived radioactivity (thousands of years), such as Ni, Co, Mo, Cu and N [2, 15, 20]. This marked the introduction of the concept "reduced-activation" ferritic/martensitic alloys (RAF/M). Replacement of the aforementioned elements by W, V and Ta are being encouraged, in order to produce materials with accelerated decay rates (a few centuries,

instead of thousands for years), acceptable for recycling or shallow land burial after its service life span. The importance of progress in this initiative is reflected on economy and safety principles: costs associated with deep geological containers for radioactive wastes would not be needed. Besides, maintenance practices for operating power plants could make use of more direct interventions, instead of being based on rather expensive remote programmes.

The RAF/M steels evolved from the same batch of chemical compositions as the steels for fossil fuel power plants, as Figure 2.9 tracks, based on the criterion of creep strength behaviour. Chromium contents vary between 7 and 12% for martensitic steels, with 9%Cr as an optimal point, not only for the martensitic transformation, but also from the point of view of the creep response:

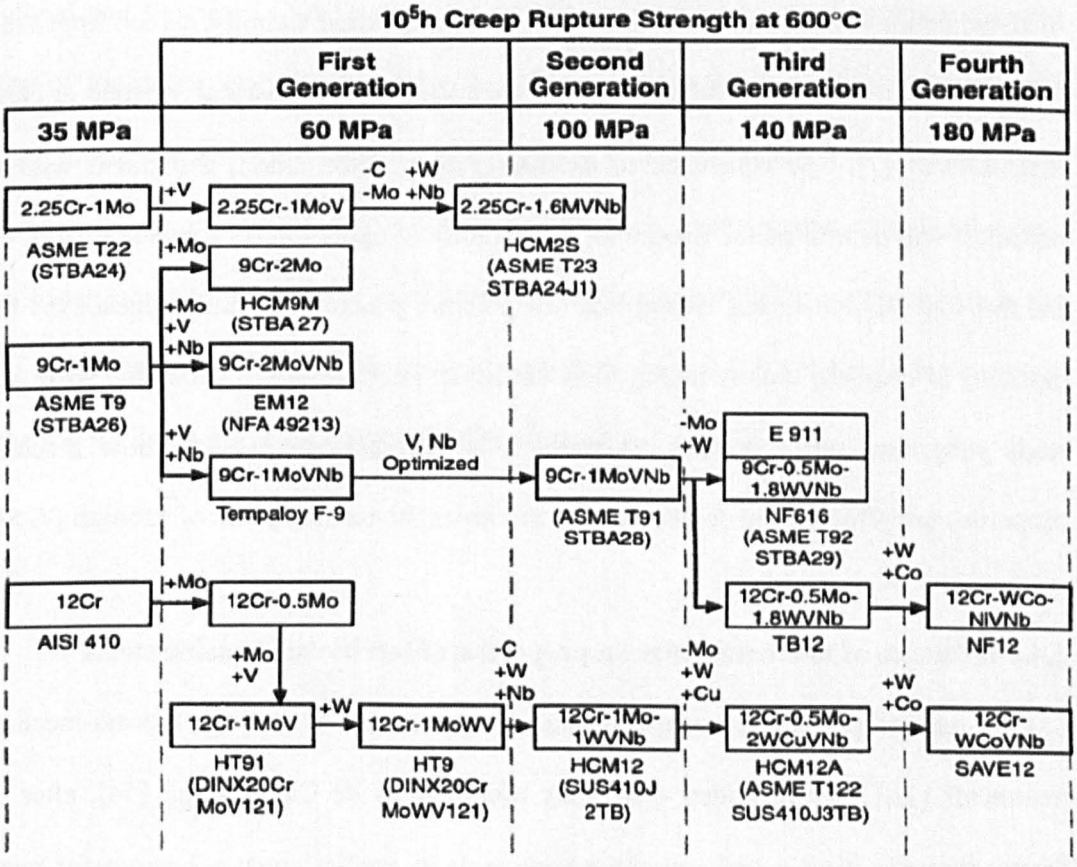

Figure 2.9 - Evolution of ferritic and martensitic steels for high temperature strength [2].

The RAF/M steels are amongst the most suitable structural materials for modern nuclear power plants. Assessment of desirable properties in these alloys were the object of extensive researches in the past few years, especially after confirmation that ferritic/martensitic steels have better corrosion behaviour, when facing liquid Pb-alloys, than austenitic steels [3]. However, these same researches revealed the limitations and shortcomings of these steels.

As mentioned earlier, a very important feature for materials considered for deployment in nuclear reactors is high-temperature strength. In metals and alloys, this is achieved by building obstacles to dislocation motion into the metallic matrix. Similarly to the case of austenitic steels, for RAF/M steels, precipitates of some types and sizes provide these obstacles: larger $M_{23}C_6$ particles (60-200 nm) and located mainly on lath boundaries or grain boundaries; and fine MX precipitates, 20-80 nm, inside the matrix. The effectiveness of these precipitates as obstacles is related to their thermal stability, which improves the microstructural stability of the steel and, subsequently, its mechanical strength at elevated temperatures [7]. The resistance to extensive creep deformation, associated with these particles, will determine the maximum temperature of operation for a material [52]. Given the fact that thermal ageing during high temperature plastic deformation causes the $M_{23}C_6$ particles to coarsen, thus reducing their ability to interfere with dislocation motion, and leads subgrains, when present, to grow, it is necessary to evaluate how mechanical properties are affected and devise ways to minimize the resulting loss of strength [7, 54].

2.4.1 Influence of microstructure on properties of ferritic/martensitic steels

One way of producing creep-resistant microstructures is through thermo-mechanical treatments (TMT's). This idea was firstly proposed by de Carlan et al. [54], after using thermodynamic, kinetic and neural network tools to predict creep behaviour for possible compositions of a martensitic steel Fe-9CrWV. Klueh et al. [55], while working with a series of commercial and experimental martensitic 9-12%Cr steels, sought to develop a

thermo-mechanical treatment aimed at the maximization of MX precipitates, based on the idea that most of the strengthening effect in these steels is due to the fine nitrides or carbonitride particles in the matrix [56]. By performing computational thermodynamics calculations, they determined proper concentrations of nitrogen, niobium and vanadium in order to achieve high number densities of nanometric MX through the TMT, which consisted of dissolving existing solutes in an austenitising temperature range between 1050°C and 1300°C, followed by hot working (700-1000°C), applied to introduce a high density of dislocations that provide sites for nucleation of a fine distribution of precipitates; annealing to grow the particles to optimal size for hardening and, finally, air cooling to form martensite from austenite. Although the authors have found significantly improved strength properties, as Figures 2.10 (a) and (b) depict for 0.2% yield stress and creep-rupture life, which was found to be 80 times greater than that of the conventional normalized and tempered (N&T) steel, the validity of the results are conditioned to the stability of the precipitates produced by the TMT, since methods of extrapolation were used. Although the steels are allowed to be used at 650-700°C, which is a considerable improvement over the limit of 550-600°C for its N&T counterparts, the nitrides and carbonitrides won't be as stable as incoherent dispersoids in a metallic matrix, which is the case of oxides in an ODS steel. The great advantage of these TMT's is the reduced cost in comparison with expensive processes of ODS alloys [9].

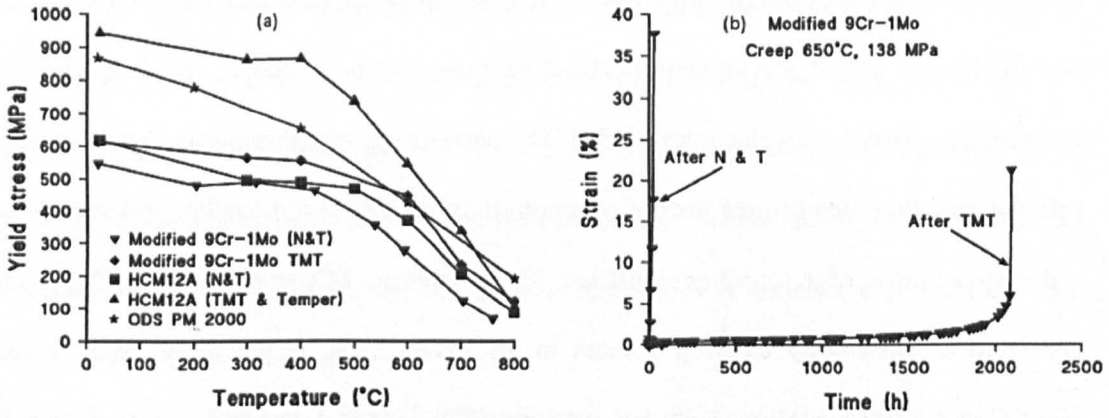

Figure 2.10 (a) comparison of yield stress as a function of temperature for two martensitic steels in their N&T condition, the same steels after the novel TMT and an ODS steel; and (b) creep curves for a 9% Cr steel tested at 138 MPa and 650°C in N&T and TMT conditions [55].

The development of the above TMT's motivated further research on RAFM steels, in order to assess microstructural changes during creep, their causes and effects on the performance at high temperature. Dudova et al. [57] investigated a 9%Cr-2%W martensitic steel, known as P-92, modified with 3% cobalt, in an attempt to understand the role of second-phase particles (MX, $M_{23}C_6$, Laves) and the new element, Co, on the stability of the tempered martensite lath structure (TMLS) during creep at 650°C. The superior creep properties of such martensitic steels are attributed to this TMLS, which is stabilized by nanoparticles precipitated during the tempering treatment and during creep [59, 60]. It was found out that, although the $M_{23}C_6$ particles tend to coarsen much more than the MX, they play the major role in the stabilization of the TMLS, due to [57, 60]:

- Zener pinning pressure on the lath boundaries
- Interruption of knitting reactions, between subgrain boundaries and free dislocations in the matrix, which are responsible for the lath/subgrain growth

Similar behaviour was found for Laves, an intermetallic Fe_2W phase formed during creep, although their influence on the lath stability is not as prominent as the effects of the $M_{23}C_6$ carbides. Given the observed size of Laves particles when they appear at the

boundaries, which is around 245 nm, the results disagree with the idea that this phase gives significant additional contribution to precipitation strengthening on its early stages of formation, as suggested by Klueh and Harries [2].

Figures 2.11 show TEM images registering the microstructural evolution of this martensitic steel during creep tests at 650°C under a stress of 140 MPa, for different levels of deformation. The prolonged exposure to the high temperature causes the coarsening of the carbides and the Laves phase at boundaries, thus decreasing the Zener pinning pressure upon the martensite laths, which become unstable and grow into subgrains. The loss of resistance to creep deformation is attributed to this growth of subgrains at the expenses of the TMLS.

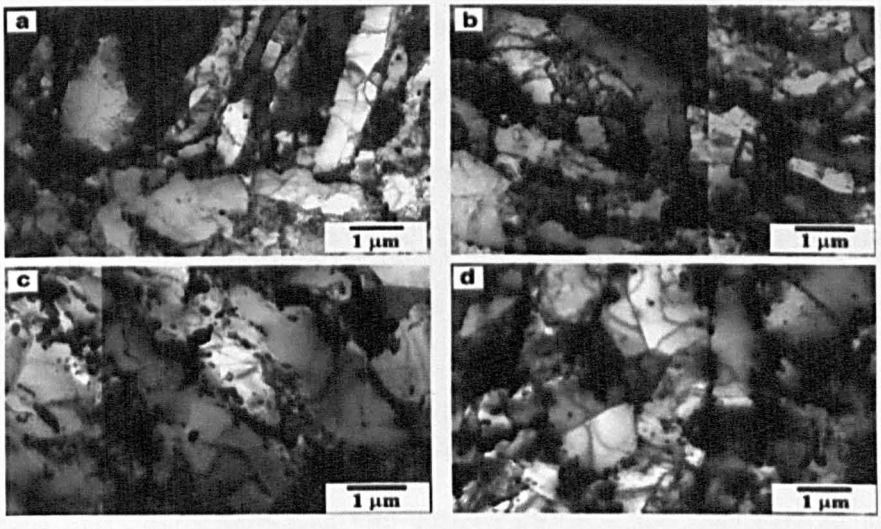

Figure 2.11 - Changes in the microstructure of P-92 steel during creep at 650°C and 140 MPa at different strain levels: (a) 1% strain, small precipitates at the boundaries of the laths; (b) 4%, particles starting to grow; (c) 5.5%, large particles and subgrains; (d) 12% strain; ruptured [57].

Similar results were achieved by Kipelova et al. [60], for another cobalt-modified martensitic steel, termed P911, investigated under creep conditions at 600-650°C and 120-200 MPa. They also observed progressive replacement of martensite laths and blocks by a subgrain structure, followed by a decrease in dislocation density during the process. Although the Co contents need to be minimized in steels for nuclear applications, the martensitic P911 and P92 are currently being investigated for advanced fossil fuel power

plants. However, their properties at high temperature are reference for the expected behaviour of the reduced-activation martensitic alloys for nuclear reactors.

With the limitations on high temperature performance of these steels being pointed out by the investigations, the efforts to reinforce the microstructure of a material against creep started to focus on the introduction of fine dispersoids as obstacles for dislocation motion, from which the oxide-dispersion strengthened (ODS) steels started to be considered.

2.5 Oxide-Dispersion Strengthened (ODS) steels

As the role of second phase precipitates on the creep behaviour of RAF/M steels started to be understood, it became clear that these particles would coarsen under thermal ageing at the elevated temperatures envisaged for advanced nuclear power plants. Given the resulting loss of resistance, alternative strengthening mechanisms, based on more stable particles, led to investigations on composites with a metallic matrix, where the reinforcements are provided by nanometric particles of oxides, among which titanium oxide (titania), aluminium oxide (alumina) and, mainly, yttrium oxide, Y_2O_3, also known as yttria.

The idea of the ODS alloy consists in incorporating yttria particles into the steel matrix by means of complex and sophisticated powder metallurgy routines. These routines involve a sequence of powder production, characterization, consolidation techniques and complementary treatments for full development of the material. These steels first started to be developed during the 1960's and 70's as structural materials for piping systems of secondary heat exchangers in fast breeder reactors [61].

ODS steels are produced by the dispersion of very fine oxide particles, presenting less than 100 nm in size, in the matrix of the steel, which is also called the base alloy for the production of the ODS. It is usual practice to directly introduce previously prepared oxides, such as yttria, for mixing with the matrix powder during mechanical alloying. However, Wolski et al. [62] described *in situ* oxidation of prealloyed FeAl powders as

another possible (and even preferable, in this case) operation, to produce iron aluminides as homogeneously distributed nanometric oxide particles, which would result from subsequent sintering.

In these steels, strengthening is associated with the dispersion size [63, 64], so that the nature of the oxide is not of essential concern. Oxides are chosen for their stability, but also for being insoluble in the matrix at temperatures that are near the melting point of the base alloy [65, 66]. Steels chosen for the base alloy are diverse in nature, ranging from austenitic grades to the RAF/M steels earlier mentioned, so that mechanical properties at high temperatures such as resistance to creep and recrystallization are improved, without loss of the advantages of the underlying austenitic, ferritic or martensitic microstructures, especially, in the case of the two latter, the resistance to void swelling [67, 68].

Powders are prepared by several different techniques, divided in three categories: physical methods, chemical methods and mechanical methods. The most important physical method is known as "atomization" and consists of driving a stream of liquid, usually water, or gas, against a stream of the molten base alloy in order to break it into droplets, which solidify as powder particles. Important properties of the powder include average particle size, particle size distribution, and shape, as they will affect the grain size distribution in the microstructure of the material [68]. Chemical methods are those involving reduction reactions on chemical compounds of the desired metal, as in the case of the production of iron powder from decomposition of iron oxide with carbon monoxide. Mechanical methods are used only in special cases for powder mixtures with brittle materials.

The merging of the yttria nanoparticles with the steel powder occurs through a powder metallurgy route known as mechanical alloying (MA). The MA processes use equipment such as an attritor or ball milling to promote homogenization of the blend of yttria powder with the steel powder under the protection of hydrogen or an inert gas such as argon. Details of the mechanical events the powders are subject to during mechanical alloying are

described in subsection 2.5.1 for the production of a ferritic grade of ODS steels known as MA956. The alloy is degassed before the application of a consolidation step. Figure 2.12 depicts a sequence of powder metallurgy routines through which a 9Cr-ODS steel was produced [69]:

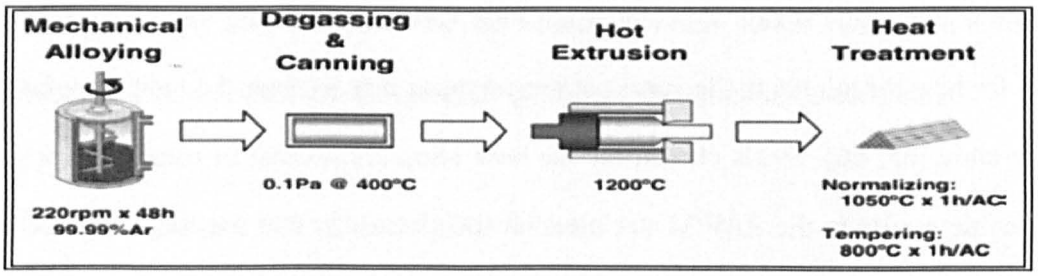

Figure 2.12 - A process procedure for fabrication of 9Cr-ODS RAF/M steel [69].

Further to hot extrusion, consolidation process can be performed by hot forging, hot pressing in rigid dies; or hot isostatic pressing (HIP), where the alloyed powder is confined in flexible envelopes made of sheets of steel and subjected to gas pressure at high temperatures. Whatever the case, the consolidated product is often called a "green compact" and presents a lower density and much higher porosity than the cast or wrought product of the same material. The complementary heat or thermomechanical treatments aim at eliminating the porosity and improve some mechanical properties of the final product.

In terms of performance, mechanical properties are expected to present a desirable combination of strength under a variety of imposed loads. Besides resistance to deformation, sought in superior high temperature mechanical properties, the ability to resist catastrophic cleavage failure is a very relevant factor for structural integrity. In this scenario, Charpy properties and ductile-to-brittle transition temperature (DBTT) are routinely investigated. Early experiments on ODS Eurofer 97 showed degradation of the impact behaviour of the steel, relative to the non-ODS Eurofer, and this behaviour was attributed to the mechanical alloying routes, even though the HIP process, which is deemed

the most promising route for advanced nuclear components due to the fact that no anisotropy is induced, was used [71].

The previous result on impact properties is of major concern for RAF/M ODS steels, especially those presenting higher chromium contents (Cr > 12%). From one side, these alloys present a well-recognized ability to trap radiation-induced point defects and helium bubbles, due to the evenly distributed nanosized yttria particles, as recent testing at the High Flux Isotope Reactor (HFIR) under similar conditions to those expected for a fusion reactor confirmed, after observation that yttrium and titanium oxide clusters effectively prevented the bubbles from reaching grain boundaries [72]. In addition, the *bcc* structure provides high resistance to swelling and irradiation creep [62, 73], likely due to the high rates of recombination of interstitials and voids, as well as the absence of a close-packed slipping system. From the other side, recent studies are indicating that ODS steels may present poor mechanical and physical properties, such as low upper shelf energy (USE) in impact and high DBTT temperature. To some extent these results can be associated with porosity, impurities, texture, distribution of grain size and particles at interfaces, which are common features of these steels, as shown in figure 2.13 for a 9Cr-ODS steel:

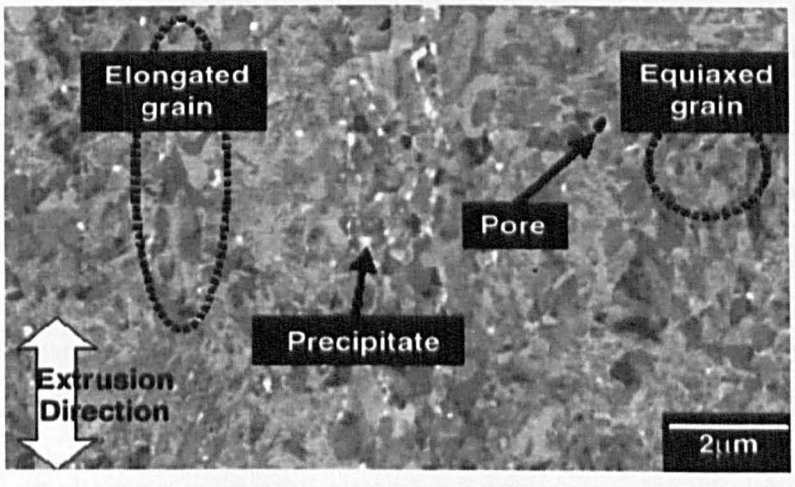

Figure 2.13 - Typical ODS microstructure for RAF/M ODS steels after powder metallurgy processing [69].

Recent studies have engaged in investigating the effect of thermomechanical treatments (TMT's) on the ODS alloys microstructure and mechanical properties. Oksiuta et al. [14]

investigated the role of two different TMT's on the properties of a ferritic 14%Cr ODS steel and concluded that TMT's yield considerable improvement on its impact behaviour. However, the TMT's improvements were only relative, and the material still presented unsatisfying impact properties, as shown in Table 2.2 for the steel with and without complementary TMT:

Table 2.2- Properties of a 14%Cr ODS steel before (HIP+HT) and after TMT [14].

Material	$\mu HV_{0.1}$	Mean grain size, μm	CV	USE, J	DBTT, °C
HIP + HT	414 ± 24	2.8 ± 2.1	0.71	2.7	130
HIP + HP + HT	430 ± 19	1.5 ± 0.6	0.41	4.5	65
HIP + HR + HT	478 ± 13	0.5 ± 0.3	0.60	2.9	55

Following the same trend, Wang et al. [74] reported improvement of ductility of an austenitic 310 ODS steel after applying a complementary TMT to the as-HIPped alloy. They attributed the observed improvement to the reduction of porosity associated with entrapped gas from the protective atmosphere used during milling, and reduction of voids. Although plastic deformations imposed by the TMT's are relatively effective at closing some pores and improve the microstructure, their reach is limited, for they fail to eliminate these defects, which remain a common flaw of the ODS microstructures [75].

Many studies [54, 62, 76] reported several factors of influence on impact properties of ODS steels, such as:

- Shape of extrusion; rod-shaped materials present better impact behaviour than plates.
- Sample orientation regarding the extrusion direction; generally the impact energy of rolled sheet metals depends strongly on the fracture plane orientation regarding the elongated grains.
- Chromium contents; comparison between a 9% Cr (recrystallized ferritic) with a 14%Cr (ferritic) showed that, overall, the 14%Cr presents better properties, since

the USE, which means the maximum energy absorbed, was much higher than that of a 9%Cr, even though the DBTT was shifted by almost 50°C towards higher temperatures, as seen in figure 2.14:

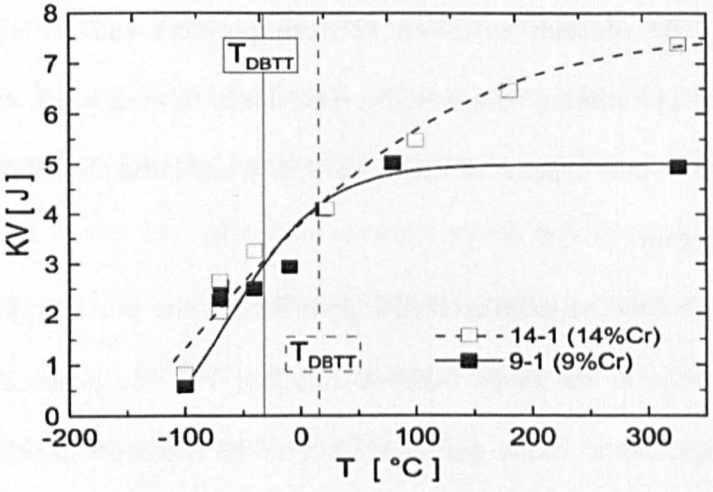

Figure 2.14 - Effect of Cr content on impact energy properties of ODS steels [61].

- Yttria contents; increasing it improves slightly the tensile properties, but decreases the USE of the steel.
- Tungsten contents; W causes the same effect as chromium.

Two features of the ODS steels are considered the most important among the mechanical properties. One is the highly anisotropic behaviour, noted in practically all studies performed so far and which affects also the creep response [77]; the other is the excellent creep strength achieved, over a range of very high temperatures considered, as explained further ahead in section 2.6. This latter property is regarded to be dependent on the oxide particle size, which is a paramount microstructural feature of these steels, for it plays a key role on the mechanisms involved in plasticity, and is considered in the next section.

2.5.1 Effect of oxide size

In ODS steels, the strengthening agents are second-phase particles resulting from dispersion hardening, that is, the particles, in the form of a powder, are mixed with the

base alloy powder and consolidated by powder metallurgy processes. During mechanical alloying (milling), these powders undergo significant deformation, with true strains of the order of 9 (equivalent to an engineering strain of about 8000) being imparted to the particles [78]. The constant collisions between powders and milling balls press the particles together, promoting cold-welding. The flakes formed, again subjected to further collisions with the balls, experience fracture [79, 80], and these processes go on throughout the whole milling time.

While this explains the submicrometric grain size of the as-milled base metal powder, which usually falls in the range 300-500 nm [69, 79], the phenomena involving the formation of nanometric oxide particles seem to be more complex. There have been numerous studies aimed at understanding the mechanisms of formation of the dispersed nanoclusters. Recent investigations by Saber et al. [81] showed that nanometric oxide dispersion is achieved during milling, regardless of whether the initial yttria powder is nanometric or micron size. Their work was motivated by the need of providing visual evidence of the phenomena leading to nanocluster formation. By using Scanning Transmission Electron Microscopy (STEM) techniques, they sought to provide the basis for the idea of dissolution of the primary yttrium oxide into the matrix. For a 10% wt. yttria containing steel, they reported an absence of micron size oxide particles and of crystalline Y_2O_3 after milling, while the selected area diffraction pattern indicated the presence of an amorphous undissolved yttria phase.

When it comes to details on the mechanisms related to the formation of nano-size oxides, two scenarios are suggested: one states that the mechanical alloying process does not cause dissolution of the oxides, but, instead, drives the yttria into the base alloy powder by continuously fragmenting it into finer particles. This is the line of argument adopted by Dai et al. [82], who studied the evolution of size and structure of yttria during the powder metallurgy routine of fabrication of a ferritic 9Cr-ODS steel with 15 wt.% yttria. They used chemical extraction to sample nanocrystals from the as-milled and as-milled/annealed

powders and examined them with TEM and high-resolution TEM (HRTEM), where fragmented, irregularly shaped nanocrystals of Y_2O_3 were observed, as shown in figure 2.15a. Based on comparison between the as-milled and milled/annealed nanocrystals and their correspondent Selected Area Diffraction Patterns (SADP's), they proposed that mechanical milling does not break the bonds between yttrium and oxygen. Instead, the severe plastic deformation imposed by the ball-powder-ball collisions promotes gradual fracture of the brittle oxides into nanoscale crystals, which will grow during subsequent annealing (in the range 773K – 1023K) due to Ostwald ripening, that is, a decrease of the total energy of the system by elimination of interfaces, as growth takes place at the expenses of the volume fractions of smaller particles [83].

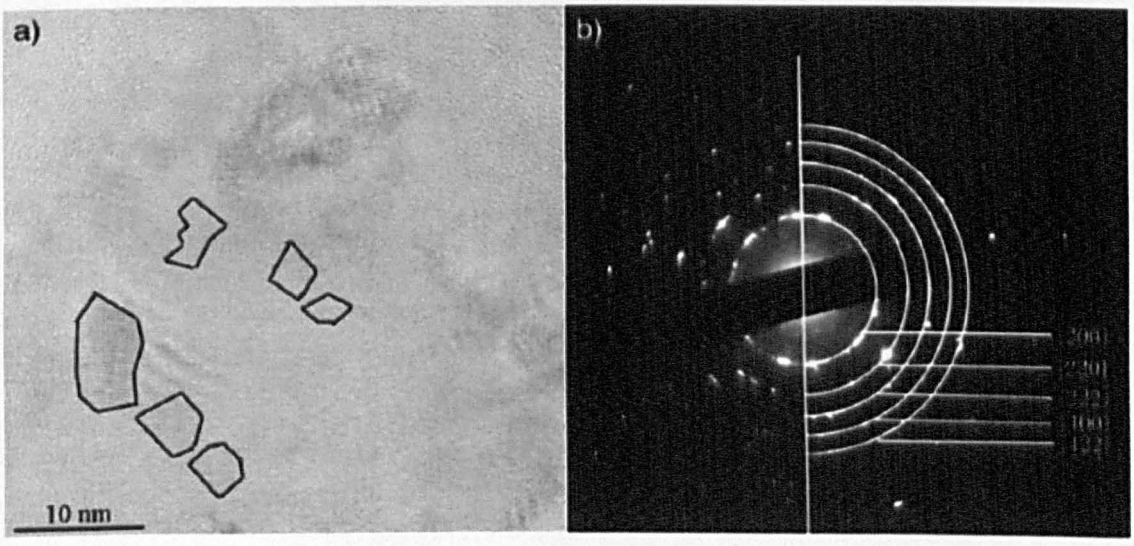

Figure 2.15 - HRTEM image of as-milled (100 h) Y_2O_3 nanocrystals, marked by the black contour lines (a) and correspondent diffraction pattern (b) – adapted from [82].

This idea is also shared by Bhadeshia [78], who claims, from his studies on thermodynamics of recrystallization of iron-based and nickel-based ODS alloys, that most of the yttria remains intact during milling and consolidation stages, but reacts with aluminium (or titanium) and oxygen to produce different complex oxides. It also finds support in previous works [83, 84], such as the one developed by Schaffer and colleagues [84], who reported no change in the dispersoids after hot rolling, while subsequent zone annealing was observed to markedly change the Y-Al-O oxide phases comprising the

dispersoids. They also attributed to Ostwald ripening the growth detected after heat treatment at 1100°C.

The alternative scenario claims that mechanical dissolution of the oxides into the matrix effectively occurs during the milling process, with re-precipitation following in subsequent heat treatments [81] or consolidation stages [85]. This suggestion seems to have gained wider acceptance among the ODS community, with a number of studies [85–88] employing different techniques to provide evidence of the dissolution, such as Small Angle Neutron Scattering (SANS), TEM, and neutron and X-ray diffraction. According to this theory, the severe strains imparted to the powders during mechanical alloying will dissociate the Y_2O_3 into elementary oxygen and yttrium, which will go into solid solution in the steel matrix, provided that the amount of yttria content initially mixed is within the limit of solubility in the base alloy lattice. Toualbi et al. [88] used neutron diffraction on a ferritic 9%Cr ODS steel bearing 10%wt. Y_2O_3 (a composition deliberately designed so that any changes with the oxides along the fabrication routine could be easily detected), in order to track the evolution of the yttria along the fabrication processes. Their findings are well summarized in figure 2.16; following completion of the milling stage, the neutron diffraction peaks corresponding to Y_2O_3 disappear, only to start reappearing after later heat treatment at 1100°C for 1 hour.

Their results found good agreement with the TEM investigations carried out by Saber et al. [81], who also worked with a 10 wt.% yttria ODS material and reported the presence of an amorphous-like ring in their SADP along with elemental map distributions showing regions with portions of uniformly distributed yttrium, which they interpreted as indications of dissolution of a small part of the 10 wt.% yttria into the matrix, while the largest part of the primary oxides is fractured to amorphous nanoscale fragments.

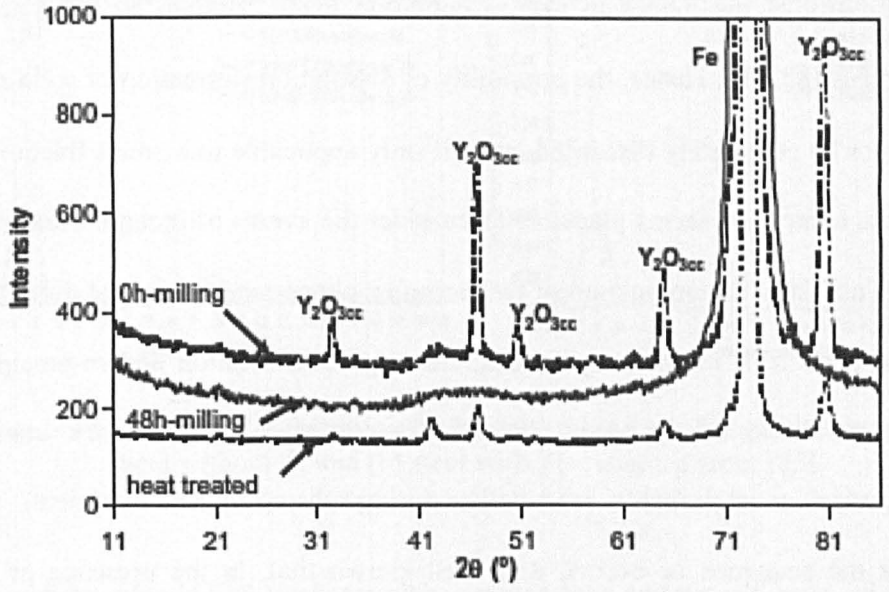

Figure 2.16 - Neutron diffraction pattern for the ODS steel before milling, after completion (48 h milling) and after subsequent heat treatment [88].

However, despite the agreement between both results and the support the dissolution theory receives, the discussion seems to find measure of agreement somewhere in between the two scenarios, as Toualbi and co-workers themselves acknowledged that disappearance of the peaks does not provide compelling evidence that the oxides were effectively dissociated and the constituents, Y and O, went into solid solution, based on results of neutron diffraction measurements of the Fe matrix lattice parameter [88]. While this was expected to vary due to the yttrium and oxygen atoms entering solid solution, their investigation showed a practically constant value along the same material processing procedures. This point of view is shared by Hilger and co-authors [89], who, in recent work, also measured the lattice parameter of the α-Fe matrix from their 5 wt.% Y_2O_3 steel using X-ray diffraction (XRD) and, likewise, concluded that no significant shift in the lattice parameter could be detected; therefore, significant dissolution of yttria was deemed unlikely for the milling conditions deployed.

ODS steels with potential applications for energy industry bear much lower yttria contents (between 0.25 wt.% and 0.5 wt.%), however, even these amounts are above the

limit of solubility of the oxides in iron, a condition made possible by the mechanical alloying process [88, 90]. Hence, the possibility of dissolution (formation of solid solution in iron) cannot be completely discarded, even if only applicable to a small fraction of the primary oxide content. It seems plausible to consider the events of incorporation of yttria into the steel matrix as a combination of two complex phenomena: chemical dissolution of a very small portion of the primary oxides, entering solid solution and re-precipitating, and, for the remainder of the yttria contents, fragmentation to nanometric amorphous compounds, which, most probably, recrystallize during subsequent heat treatment.

Whatever the sequence of events, it is well known that, in the presence of certain alloying elements, the re-precipitation of oxides does not restore the original Y_2O_3. Instead, complex oxides are formed with the added element. Given that yttria particle size increases during the fabrication stages following re-precipitation (consolidation and heat treatments), some elements are added in order to refine the dispersion. This is the case for titanium and aluminium [91]. While encouraging the formation of finer oxides than the primary Y_2O_3, these elements still preserve their desired stability. However, it seems titanium and aluminium promote opposite effects, when associated with yttria for the formation of complex oxides.

The influence of titanium was extensively studied in recent years by a variety of techniques, which include SANS, Atom Probe Tomography (APT) and TEM [85, 87]. These investigations showed that titanium plays a major role on the stabilization of the oxides, producing phases which are much more resistant to coarsening than the yttria nanocrystals without it. Ratti and colleagues [85], using SANS, observed much finer distribution of oxide size for their ODS steel with Ti subjected to isochronal (1 hour) heat treatments ranging from 850°C to 1300°C than for the counterpart steel in which that element was absent, as shown in figure 2.17, where *h(R)* denotes the ratio between the number of particles with a radius R and the total number of particles.

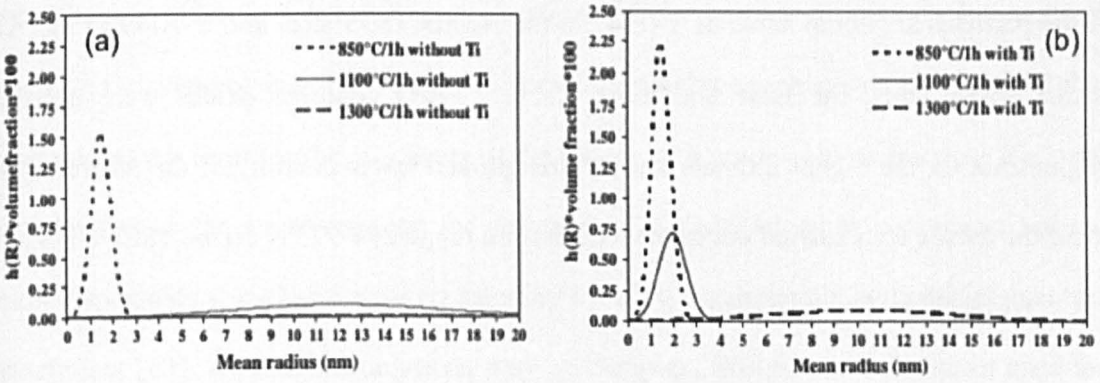

Figure 2.17 - Particle size distribution after milling and various heat treatments for (a) steel without Ti and (b) steel with Ti – adapted from [85].

Aluminium-added ODS steels are also very common and the influence of this element on the size distribution of the dispersoids has, previously, been investigated also. While it is acknowledged that the complex oxides formed by Y, Al and O are finer than the primary yttria (provided that elements such as titanium are absent from the composition), refinement is not so significant and heat treatments at high temperatures (above 1100°C) render the complex Y-Al-O oxides coarser than those obtained with Ti, as evidenced in the work carried out by Kasada and co-workers [91], who reported much higher tensile strength for their ODS ferritic steel that did not contain aluminium, in comparison to the same material in which this element was present. They attributed the observed difference in behaviour to the difference in the size of nanoparticles in their steels. These results match the recent findings of Lee [92]. He applied TEM and X-ray Energy Dispersive Spectroscopy (EDS) to study the distribution of oxide particles, in terms of density, size and mean interparticle spacing, as well as the chemical composition of the oxides in, once more, two versions of his ferritic Fe-18Cr-0.2Ti-0.35Y_2O_3 ODS steel, one bearing 5 wt.% aluminium and the other, without this element. He reported an increase in the mean oxide particle diameter and in the interparticle spacing, accompanied by a reduction in the number density, for the Al-added material. These microstructural effects are known to degrade the strength of the ODS steel. Moreover, the EDS investigations revealed that the

oxide particles are compounds of Y-Ti-O in the Al-free ODS steel and Y-Al-O in the Al-added alloy. Thus, the finer and more stable Y-Ti-O complex oxides were deemed responsible for the higher ultimate tensile strength and lower ductility of the Al-free steel in all the tensile tests carried out in the temperature range 298-973 K on the 18Cr-ODS and 18Cr5Al-ODS, as shown in Figure 2.18:

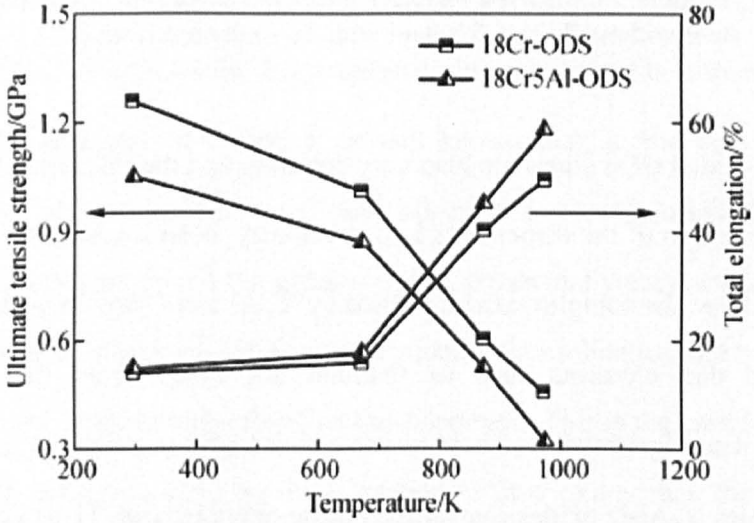

Figure 2.18 - Tensile strength and total elongation of the ODS steels tested over the range of temperatures 298-973 K [92].

Although titanium and aluminium are the most common additions to ODS steels, recent results provide evidence that they are not the only ones potentially promoting refinement of the oxide particles. Oka et al. [93] investigated the effect of the presence of hafnium and zirconium on a batch of austenitic ODS steel, claiming that these elements improved the distribution of oxides in the matrix. The observed increment in number density of oxides and the simultaneous decrease in its diameter were attributed to these minor elements. In a complementary work, the same authors identified the complex oxides formed as $Y_2Hf_2O_7$, predominantly, when Hf was added [94], although $Y_2Zr_2O_7$ is also formed.

Regardless of the element added in order to promote refinement of the oxide particles, one observation is timely. While it is desirable to achieve reduced particle sizes so that the

strengthening effect is increased, considerations of the particle-dislocation interactions, based on Orowan bowing and attractive interaction pinning mechanisms [95], predict that there might be a limit for the efficiency of the oxides, at a given volume fraction: too large particles reduce the stress required for detachment of dislocations to take place, but too small dispersoids would also weaken the alloy by allowing thermally activated dislocation detachment [63]. Although estimations may be complex, Wolski and colleagues used the aforementioned considerations along with thermal stability requirements to suggest the optimal dispersion size as of the order of 50 nm [62]. For as much as this number may seem above considerations of some of the previous works engaged on manufacturing of the ODS steels and tensile test results, for example [85], [92], [93], the size suggested by Wolski and co-workers seems more in line with considerations stemming from creep studies of these nanostructured alloys, which are discussed later. Besides, in final shape ODS steels, obtained after consolidation, complementary heat treatments or even thermo-mechanical treatments (TMT's), it is not unusual to find a broader distribution of sizes. And, finally, some elements, such as aluminium, may even be intentionally introduced in significant amounts for purposes of improving oxidation resistance, as in the case of the MA956 steel, having the additional effect of preventing too small oxides in the matrix.

2.5.2 MA956 ferritic ODS steel

Incoloy alloy MA956 denotes an ODS steel with a ferritic matrix, considered to be established commercially, given the reproducibility of its microstructural features, and, therefore, its properties [78]. It is a well-acknowledged fact that variations in processing conditions can significantly change the final state of the ODS material [72, 96], so, the alloys which present variations within reasonable statistical limits, such as MA956, MA957 and PM2000, among others, are deemed of commercial significance.

MA956 has nominal chemical composition Fe-20Cr-5Al-0.5Y_2O_3, a composition aimed at excellent oxidation resistance, by virtue of the large Cr and Al amounts. Indeed, the high

content of aluminium in the matrix causes the formation of an adherent, slow growing alumina scale that provides superior resistance to aggressive environments and high temperature oxidation [97]. On top of that, the alloy is reputed to exhibit outstanding strength at temperatures as high as 1000°C and above, due to the fine dispersoids resulting from the formation of complex Y-Al-O oxides, scattered through the matrix in a relatively homogeneous way [98]. These iron-based alloys belonging to the category of commercial grades are designed to present superior creep strength, in comparison to equivalent cast alloys.

This steel, although primarily intended to be deployed in gas turbines, could easily be regarded for components of advanced nuclear plants, given the suitability to high temperature applications and the microstructural features that impart to the MA956 the ability to withstand harsh operational environments, notably, the dispersoids, which are much less susceptible to coarsening than precipitates and remain effective at temperatures near the melting point of the base alloy [98].

The well-established fabrication routine the MA956 undergoes is responsible for its very distinctive microstructure. It starts with the usual mechanical alloying of the powders, previously described, promoting their mixture and intense mechanical deformation. The benefit of this process lies on the fact that mechanical mixture permits the limits of solid solubility to be exceeded [78, 90], in addition to ensuring uniform introduction of the dispersoids into the bulk material. Consolidation of the as-milled powders takes place by hot extrusion. In the as-extruded condition, the alloy is too hard and brittle for any use. Therefore, heat treatment is applied, either isothermal or in temperature gradient, in order to induce recrystallization. As a result, the grain morphology evolves towards the development of a columnar structure, characterized by grains elongated in the extrusion direction, reaching millimetre size, often exceeding 300 mm length. It is common to observe aspect ratios (that is, the ratio between grain length and diameter) higher than 30:1 [97], sometimes reaching 100:1, as reported by Dubiel and colleagues [98]. On top of that,

very pronounced texture is reported for these microstructures, with crystallographic components of {001}<110> and {111}<110>, that is, the so-called α and γ fibres, respectively, as the most pronounced [78, 99]. An optical micrograph of MA956 depicting the grains in the elongated direction is provided in figure 2.19:

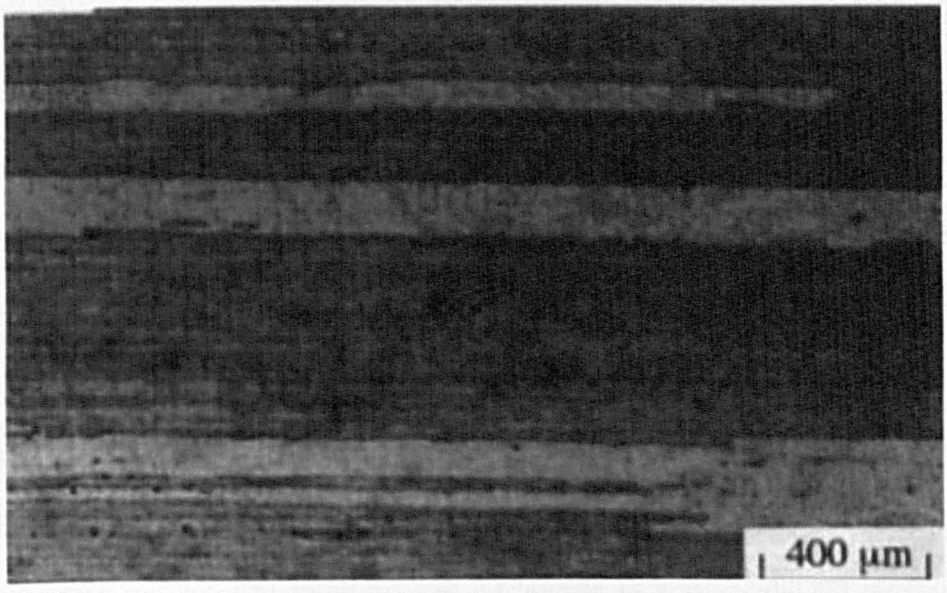

Figure 2.19 - Coarse recrystallized grains, elongated in the working direction, as typical microstructure of the MA956 steel – adapted from [99].

Another interesting aspect pertaining to the microstructure is the fact that although reduced in number, the grain boundaries have interesting serrated interfaces, which enable a strong degree of interlocking between adjacent grains [98]. In order to understand the development this morphology from a microstructural point of view, some considerations in thermodynamics and recrystallization of ODS alloys are timely.

2.5.2.1 Thermodynamics of mechanical alloying

Thermodynamic theory of solid solution formation begins with the mixture of component atoms and dictates that this mixture is considered a solution, rather than a compound, when a single homogeneous phase is obtained, preserving the crystal structure of the solvent [25]. A solution that is homogeneous, nevertheless, exhibits concentration differences of increasing magnitudes as the domain of investigation is gradually decreased

towards atomic level. There are fluctuations that increase the randomness of atom distribution, obeying the laws of stochastic processes.

In the case of mechanical mixtures, homogeneity is achieved by intense mechanical deformation, which forces atoms into positions they would not prefer to occupy at equilibrium [78]. This observation does not mean that solutions are thermodynamically ideal, but that mechanical alloying forces a state of randomness in the dispersion of atoms. In other words, alloys fabricated according to these processes are in a mechanically homogenized non-equilibrium condition and it would be reasonable, then, to expect deviation from randomness, given enough time of exposure to annealing conditions, as observed in Fe-Cr alloys, in which clustering of chromium atoms occurs, eventually leading to the formation of Cr-rich α' phase [100].

From these considerations, it is possible, then, to infer that the mechanical alloying process allows for introduction of dispersoids beyond limits of solubility, since the high-energy deformations will ensure randomness of atomic distribution. A question that arises, then, concerns at what point, in terms of size scale considered, mechanical mixtures start to exhibit the behaviour of a solution [78]. Thermodynamics, once again, provides tools to investigate this, based on free energy of mixing, enthalpy and configurational entropy. It is not unreasonable to consider that starting powders have large enough size not to be affected by interatomic forces between unlike atoms. Also, the number of ways in which the mixture can be arranged is not significantly different than one. With these considerations obeyed, a blend of powders A and B will have free energy described by equation 2.4:

$$G_M = (1 - x)\mu_A^0 + x\mu_B^0 \qquad \text{(Eq. 2.4)}$$

where G_M is the free energy of mixing, x is the mole fraction of powder B and μ_A^0 and μ_B^0 are the molar free energies of components A and B, respectively [64]. In words, the equation means that the blend has a free energy that is the weighted mean of the energies of the components.

Unlike a mechanical mixture, the concept of solution involves smaller entities, such as atoms and molecules, so that a change in enthalpy associated with a change in neighbour bonds exists. The total number of ways the particles in the mixture can arrange themselves is very high, leading to increased configuration entropy, and this causes a reduction in the free energy of the solution. The difference in free energy between these two conditions corresponds to the free energy of mixing, an essential thermodynamic term for solution models, and is shown in figure 2.20:

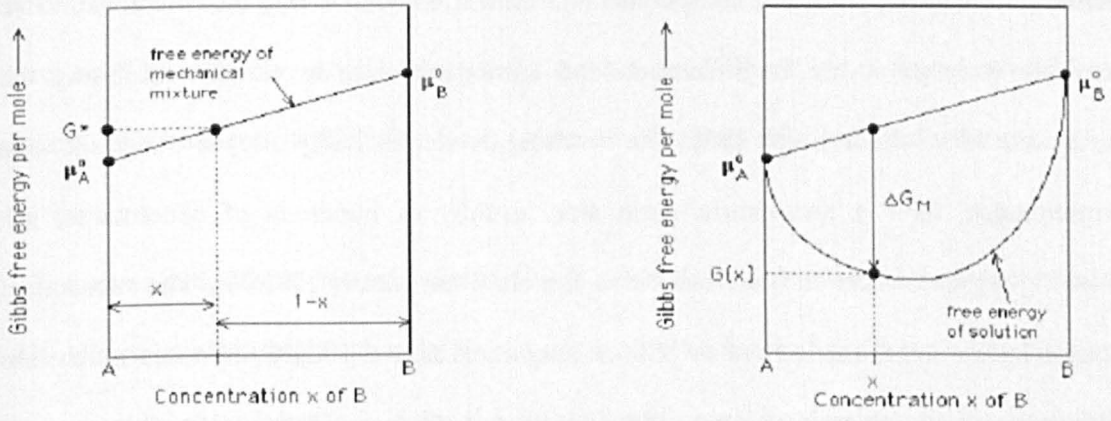

Figure 2.20 - Comparison between the free energy of a mechanical mixture and that of a solution [78].

It is, then, natural to expect the largest reduction in free energy to occur when the particle sizes are atomic. As previously discussed, starting powders produced by powder metallurgy present a typical size of some tens of μm, so that, at the starting of the milling, the entropy of mixing can be completely neglected. As the process goes on, the constant fracture, cold welding and attrition to which the particles are subjected gradually reduce the free energy of the mixture, causing a gradual change in its character. Bhadeshia [78] studied commercially relevant binary powders, such as Fe-Cr and Ni-Cr, which are the basic mixtures for iron-based and nickel-based ODS steels, and affirmed that solution-like behaviour occurs for particle size of the order of 10^2 atoms, in a mixture where all the particles have uniform size and homogeneous composition. This suggests a basis for

increasing the milling time, in order to maximise the homogeneity of the resulting particle, as observed by Oka and colleagues [93], although an optimum range of 24 to 72 hours is suggested in their work, in order to avoid contamination of the mixture. In order to understand the development of the microstructure along the subsequent fabrication steps, recrystallization is studied from the MA956 microstructural point of view.

2.5.2.2 Recrystallization of Fe-based ODS steels

As previously described, the mechanical alloying process imparts high-energy deformations to the powders, compounds and oxides, in such a way that the constitutive particles undergo severe fragmentation and homogenisation, eventually exhibiting the behaviour of a solid solution [96]. The resulting as-mechanically alloyed materials, as a consequence, have a nanometric grain size, usually of hundreds of nanometres, but showing regions where the size can be as fine as 2 nm locally [78, 96]. The subsequent consolidation stage, carried out at bulk temperatures above 1000°C, imposes much less deformation to the material, but provides conditions for dynamic recrystallization to occur. It is accepted that, along with heating up and consolidation itself, which is hot extrusion for the case of the MA956, recrystallization happens several times, leading to the development of a sub-micrometric grain structure, probably the finest achieved in bulk materials, bearing large relative misorientations [78, 99, 102].

An interesting feature of the Fe-based ODS alloys rests on its microstructure immediately after consolidation, comprised of ultra-fine grains elongated in the extrusion direction and containing features of a cold-worked alloy, such as high dislocation densities, reported to be of the order of $10^{15}\ m^{-2}$ (a high value, yet below those found in conventional martensitic steels), strong texture and, as a consequence, anisotropy in its mechanical properties and a high degree of brittleness [78, 101]. Hence, the need for further heat treatment to be applied, which will induce "directional" recrystallization, that is, the

growth of grains into a very coarse, column-shaped structure, irrespective of whether the material is isothermally or zone annealing treated [99].

While heat treatment certainly alleviates the brittleness and the dislocation density, making the alloy suitable for intended applications, its most notable feature is the abnormally high recrystallization temperature (about $0.9T_m$, where T_m denotes the melting point of the steel), along with its fast recrystallization kinetics [96, 102]. Generally, recrystallization takes place when cold-worked alloys are heated up to temperature levels that allow movement of high-energy grain boundaries, which are swept through the lattice, replacing deformed grains by new ones, with defects of less energy and an equiaxed structure. However, the powder metallurgy routine for ODS alloys is an unconventional process, in which recrystallization leads to the development of a highly anisotropic grain structure.

The as-extruded MA956, and, similarly, all other Fe-based and Ni-based commercial ODS alloys, exhibits high values of stored energy in the form of grain boundaries, given the high number of interfaces in the fine grains, and, to a lesser extent, dislocations and other high-entropy defects of the crystal arrangement (such as vacancies) [78]. Several studies on the microstructure development of the MA956 have investigated the sources of these high-entropy defects, and particularly, if the yttria particles would fit in this category. Chou and Bhadeshia [99] used Differential Scanning Calorimetry (DSC) to measure the stored energy released by the recrystallization of MA956 and MA957 ferritic steels and noticed a surprising result, according to which the stored energy of the MA957 steel (an alloy with 14%Cr and 0.25%Y_2O_3 wt.) was found to be significantly higher than that of the MA956. Nevertheless, the recrystallization temperature of the MA957 was also found to be approximately 100°C higher, as Table 2.3 summarizes:

Table 2.3 – Data for recrystallization and microstructure of mechanically alloyed steels MA956 and MA957 [99].

Alloy	Stored energy ($J\,g^{-1}$)	T_s[a] (°C)	T_f[a] (°C)	Texture	Recrystallized grain structure
As-received MA956	0.40	1273	1334	⟨110⟩ fibre with stronger {001}⟨110⟩, {111}⟨110⟩ components	Elongated grains, high grain aspect ratio
As-received MA957	1.00	1429	1447	Very weak ⟨110⟩ fibre	Coarse grains, low grain aspect ratio
Preannealed MA957	0.70	1362	1382	⟨110⟩ fibre with sharpened {111}⟨110⟩ component	Equiaxed fine grain

[a] T_s and T_f are the start and finish temperatures for recrystallization respectively, measured by DSC at 20 K min^{-1}.

By means of the analysis of the above data, they concluded that yttria could not be considered a high-entropy defect, since the MA956 has a higher content than the MA957. It turns out, then, that the yttria particles are not the cause of the high recrystallization temperatures observed. Moreover, it is normally expected that an increase in stored energy accelerates recrystallization, lowering its temperature of occurrence.

Chou [102] investigated the factors affecting recrystallization behaviour of the MA956 steel, among which he accounted for driving forces, aiding the onset of the recrystallization process, and drag forces, hindering grain boundary motion. He estimated, based on the properties of the material, contributions from driving pressure to boundary migration arising from stored energies associated with dislocations and with grain boundaries, finding this latter effect one order of magnitude higher than that associated with dislocations. Also, he considered the experimental observation that consolidation processes like extrusion and rolling promote alignment of dispersoids along the working direction [78], as shown in figure 2.21, and determined the energy associated with the Zener pinning effect caused by the particles on migrating boundaries, thus imposing difficulties to the recrystallization. The value found was substantially lower than the driving forces, what prompted the conclusion that, although the dispersoids' alignment plays a role in the development of the recrystallized columnar grain structure, by exerting a less pronounced Zener pinning pressure on boundaries parallel to the extrusion direction and, thus, making

this the favourable path for grain growth, it does not dominate the onset of recrystallization.

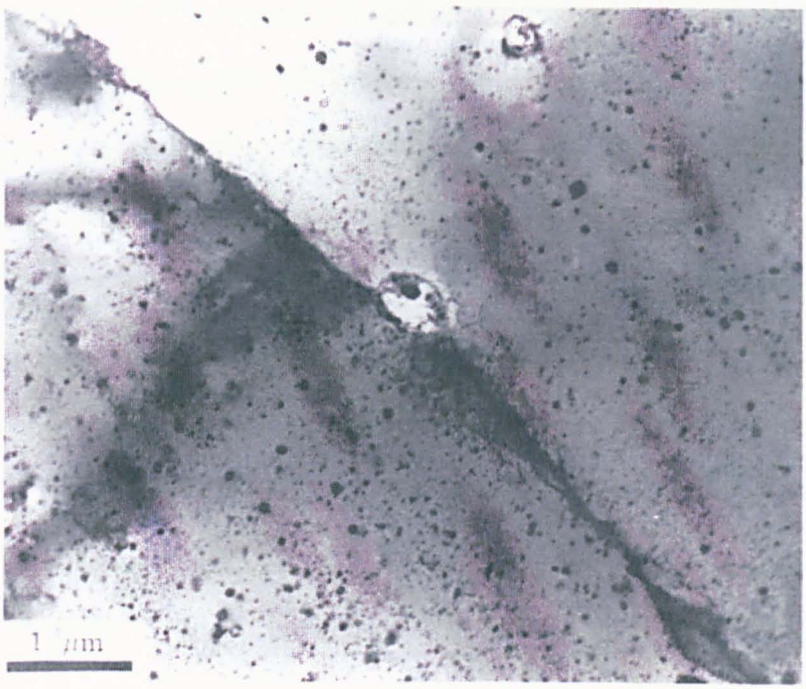

Figure 2. 21 - TEM micrograph of MA956 depicting the alignment of oxides in a direction indicated by the grain boundary [78].

Given that recrystallization of these ODS alloys occurs very rapidly in isothermal heat treatments or over a narrow range of temperatures during continuous heating, explanations for the remarkably high temperatures for these materials to recrystallize concentrate around the concept of large activation energy. However, large values of this parameter seem unlikely to be associated with grain boundary motion, for which an activation energy magnitude not much different than that for lattice self-diffusion is expected.

This difficulty started to be overcome with the theoretical approach considering nucleation of recrystallized grains in detail [96]. It is largely accepted that nucleation of recrystallization takes place by the bowing of grain boundaries, a quite straightforward process for conventional steels, since the distance between grain boundary junctions is larger than that of other pinning points, so the pinning forces imposed are easily overcome. But when the grain size becomes sufficiently small, individual grains can no longer be

considered topologically independent. This being the case for mechanically alloyed materials, grain boundary junctions provide a much stronger pinning effect, thus preventing recrystallization nucleation, than that of dispersoids. Figure 2.22 is a schematic illustrating the difference in pinning between grains of conventional steels and those of an ODS alloy. With the submicrometric grains acting as severe pinning lines for gran boundary bulging, geometrical considerations of the bulging motion of an initially flat boundary show that a huge activation energy is needed, due to an increase in the interface energy as the interfacial area increases [96, 102].

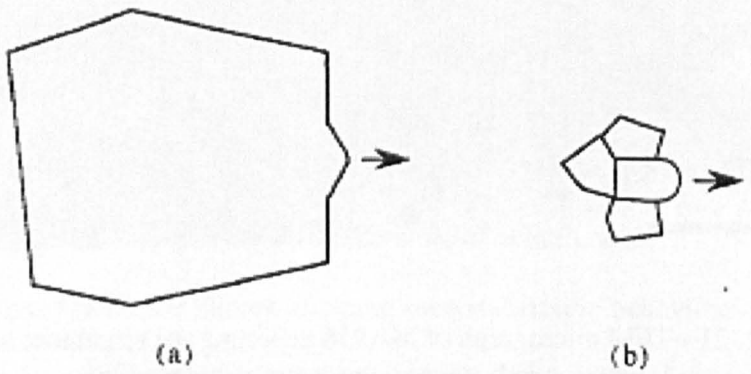

Figure 2.22 - Schematics of grain-boundary bulging and pinning for (a) conventional materials and (b) ODS alloys [96].

This model has the merit of addressing the main difficulty associated with the recrystallization of mechanically alloyed materials, by explaining the elevated temperatures for this event, irrespective of the alloy system. Moreover, it has a remarkable consequence of predicting that recrystallization temperature should decrease if a pre-annealing treatment, carried out at lower temperature, is applied so that the stored energy is reduced as a consequence of uniform coarsening of the submicrometric grain structure. This has been experimentally verified in several works [17, 96, 99], among which it is noteworthy mentioning the contribution given by the studies of Chou and Bhadeshia [99], who acknowledged the effects of texture on the recrystallization of the ODS steels by a series of investigations on MA956 and MA957. Data on the correlation between the

presence of texture and recrystallization indicate that certain texture components naturally develop faster growing rates at the expenses of the others. The process is similar to directional solidification and leads to the predominance of a particular orientation in the final microstructure. This is the case for the {111} texture component in cold-deformed ferritic steels and a reasonable explanation is that the mobility of grain boundaries contributing to its development is relatively high. It follows, then, that, for a given amount of stored energy, a microstructure with pronounced {111} texture recrystallizes more easily. The aforementioned authors experimentally verified this when they applied a pre-annealing treatment on the MA957, which, originally, bore a nearly random texture, in order to intensify the {111} component and, as a consequence, observed an expressive reduction on the recrystallization temperature of the material, as an inspection of the two bottom lines of Table 2.3 on page 54 shows.

Regardless of processing details, it can be seen that the very high recrystallization temperatures make these alloys suitable for elevated temperature applications, given that their grain morphologies have the potential to remain stable, even when creep is expected to occur and to induce changes in the microstructure, which is the reason why a review on this topic is next provided.

2.6 Creep

In simple words, creep can be conceptualized as merely the time-dependent plastic strain observed in materials subjected to high temperatures. However, like all immediate definitions, this one lacks complete information and, although it's useful to establish the main feature of creep, it requires further explanations to characterize the phenomenon in a more proper way. Firstly, the idea of high temperature is not essential. Rather, it's specific to each material, depending on its absolute melting point. And then, because, in order to understand the behaviour at high temperatures under different loading regimes, the behaviour of materials at room temperature provides good means for comparison.

At temperatures relatively low (below approximately $0.3T_m$, where T_m is the absolute melting point of the material), where diffusion processes can be neglected, if a load is applied to a ductile metal (or an alloy), being high enough to cause stresses exceeding the elastic limit, but not high enough to cause immediate fracture, there will be a virtually instantaneous strain, comprised of both elastic and plastic components, which can be readily determined from the stress-strain curve for the imposed test conditions [39]. If this stress is maintained, the material will continue its deformation in a time-dependent regime. The total strain, then, is the sum of the instantaneous strain on loading and the subsequent time-dependent strain, which accumulates in accordance with a logarithmic expression, as shown by equation 2.5 below [39]:

$$\varepsilon_{tot} = \varepsilon_0 + \alpha_1 \ln(\alpha_2 t_\tau + 1) \qquad \text{(Eq. 2.5)}$$

where α_1 and α_2 are constants related to stress and temperature, ε_0 is the instantaneous strain on loading and t_τ is the time. The deformation processes undergone by the material in these conditions are characterized by strain hardening due to generation and displacement of dislocations, as the specimen is extended, until the flow stress becomes equal to the applied stress. At this point, further movements of any dislocation are opposed by long-range events, manifested as stress fields of neighbour dislocations, and also by short-range obstacles, such as net dislocations intersecting the plane of gliding and resistance imposed by jogs, which are sharp breaks on the moving dislocation line, taking it out of the glide plane [33]. Since diffusion is quite limited at these lower temperatures, only short-range obstacles are overcome. Once these events requiring a minimal thermal energy take place in short time, the strain rate will decrease continuously, with time, towards zero. Equation 2.6, representing the deformation rate associated with the strain accumulation in equation 2.5, corroborates this statement, as the strain rate tends to zero with increasing time:

$$\dot{\varepsilon}_{tot} = (\alpha_1 \alpha_2)/(\alpha_2 t + 1) \qquad \text{(Eq. 2.6)}$$

Under these circumstances, generally very low plastic strains can be found, being insufficient to lead to eventual fracture [103]. However, as temperatures approach about $0.4T_m$ and above, diffusion processes become gradually more relevant. The increase in diffusion rates causes the motion of defects, such as vacancies and dislocations, to be more appreciable, giving opportunity for the reorganization of these defects in structures of lower energy. In the case of dislocation motion, for example, recovery processes like climb and cross slip lead to the occurrence of reorganisation and annihilation of dislocations. As for vacancies, the rearrangement of these defects according to the concentration gradient between sources and sinks is enhanced as temperature increases.

From the above statements, it can be easily inferred that the thermal fluctuations allowing the applied stress to take further in time the movement of dislocations and vacancies have, as a consequence, a continued deformation, termed creep. Under these circumstances, the total strains can be large and, eventually, lead the material to failure. Creep, then, is a thermally activated phenomenon by means of which the strain rate decays more gradually, not towards zero, as for lower temperatures, but to a constant rate, that represents the steady-state condition achieved through the interplay of generation and movement of dislocations and the recovery processes [48]. A typical creep curve exhibits three well-defined portions, each corresponding to a creep stage:

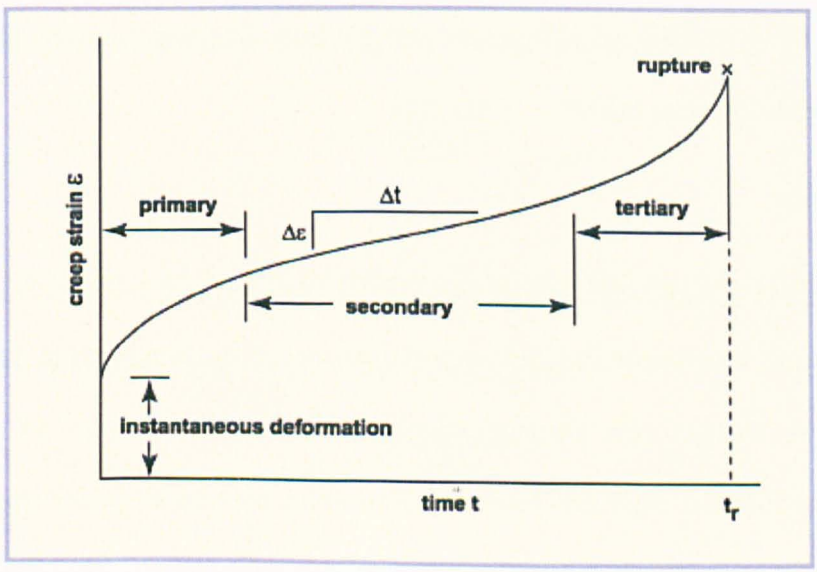

Figure 2.23 - Typical creep curve and its stages [104].

As observed, after the instantaneous strain on loading, the material starts to deform in a time-dependent manner, becoming progressively more resistant to creep as it strain hardens. This characterizes the first or primary creep stage. The creep rate decreases continuously, until the minimal or steady-state rate creep rate is achieved, which defines the secondary creep stage. In most applications, including structural components for nuclear reactors, where in-service failure is not an option, the steady-state creep rate is a major parameter of analysis, and this stage is often intended to be maximized. There are several factors that can disrupt this steady-state condition and cause the creep rate to grow, during the tertiary stage, until fracture [2, 40]:

- Mechanical instabilities, such as reduction of effective cross sectional area due to development of a neck under tensile load or internal cavities;
- Development of cracks as a result of damage build-up;
- Metallurgical processes like recrystallization, grain growth and, in the case of age-hardening materials, coarsening of secondary hardening precipitates.

The actual shape of a creep curve will vary from one material to another, regarding the time span and the amount of strain for each stage, and for different stress-temperature conditions [33]. Also, the mechanisms by means of which the secondary creep stage takes place are affected by the microstructure and properties of the material and by the stress-temperature range considered. Thus, one of the following mechanisms of creep may prevail on the steady-state regime:

Diffusion creep

At stress levels that are too low for dislocation motion to be significant ($\sigma/E < 10^{-4}$), high-temperature time-dependent deformation can occur by stress-driven vacancy flow. Applied stress changes the vacancy concentration on the surfaces of grains in a polycrystalline material such that vacancies flow from boundaries under tensile stress to

those under compressive stress. This means a counterflow of atoms in the opposite direction, which stretches the crystal. Diffusional creep may occur through the crystal lattice, then being termed Nabarro-Herring creep; or through the grain boundaries, when it is called Coble creep. Since the activation energy for lattice self-diffusion is higher [39], Nabarro-Herring creep predominates at higher temperatures. Coble creep is dominant at lower temperatures, since free energy at grain boundaries can provide part of the necessary activation for the process [103]:

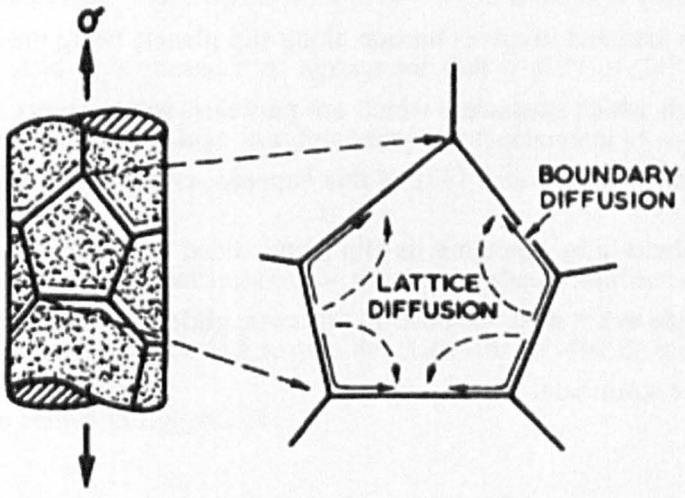

Figure 2.24 - Representation of vacancy flow in Nabarro-Herring creep (dashed arrows) and in Coble creep (solid arrow) [105].

Both mechanisms of diffusional creep are grain size dependent (ð), as it can be inferred from the semi-empirical expressions for steady-state creep rate of pure metals presented below for the lattice self-diffusion creep regime (Nabarro-Herring) [39]:

$$\dot{\varepsilon}_s = \frac{K_1 D_L \Omega \sigma}{RT ð^2}$$

(Eq. 2.7)

where K_1 is a constant of the order of 10, D_L is the lattice self-diffusion coefficient and Ω is the volume of a vacancy; and for the Coble creep regime:

$$\dot{\varepsilon}_s = \frac{K_2 D_{gb} ƀ \Omega \sigma}{RT ð^3}$$

(Eq. 2.8)

in which case the constant K_2 assumes a value of around 40, D_{gb} is the grain boundary self-diffusion coefficient and δ represents the grain boundary "width", that is, the factor ð/ð represents the area of a grain boundary intersected by a plane of unit area [48]. An interesting aspect of these theoretical expressions is that the secondary creep rate is directly proportional to the applied stress.

Dislocation creep

At higher stresses, deformation results from dislocation motion, such as glide, which is activated under load and involves motion along slip planes, being the creep rate dependent on the ease with which obstacles, which are particles, solute atoms or other dislocations impede the gliding dislocations [33]. If this happens, climb may permit the dislocation to surmount the obstacle by changing its slip plane, aided by the diffusion of vacancies, and continue the glide to the next obstacle. In this case, glide produces the strain, but the climb step controls the strain rate.

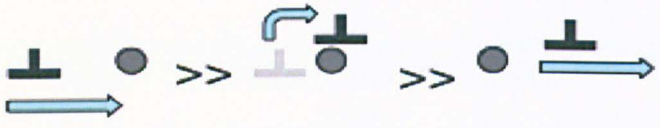

Figure 2.25 - Schematic of a dislocation-based creep process, showing the glide to an obstacle and the climb step.

More than one creep mechanism may be active for a given stress/temperature condition. When two or more mechanisms are operating simultaneously, which means, independently of each other, the fastest will dominate the creep rate. A well-accepted way to describe changes in the governing process is provided by fitting a power law expression, known as Norton's power law, which relates the strain rate to the applied stress:

$$\dot{\varepsilon}_s = A\sigma^n \exp\left(-Q_c/_{RT}\right) \qquad \text{(Eq. 2.9)}$$

In the above equation, the exponential term is the Arrhenius model, representing the dependence of creep rate on temperature [39], with Q_C being the activation energy for lattice or grain boundary diffusion, n is called the stress-sensitivity exponent and A is a constant associated with the properties of the material, but it is also used to express the grain size dependence of diffusional creep rate, which contributes more to the overall deformation process at smaller grain sizes. This expression is general, being used to correlate secondary creep rate with applied stress, regardless of the dominant regime, from which it can be inferred that, when diffusional creep is the dominant process, the stress exponent is unitary. And it is measure of agreement that a shift of "n" from the unit towards higher values indicates change in rate-controlling mechanism to dislocation creep processes [34, 39, 48, 103].

These considerations allow identification of the predominant mechanism for a given stress/temperature condition, which led to the development of deformation mechanism maps, such as the one shown in figure 2.26:

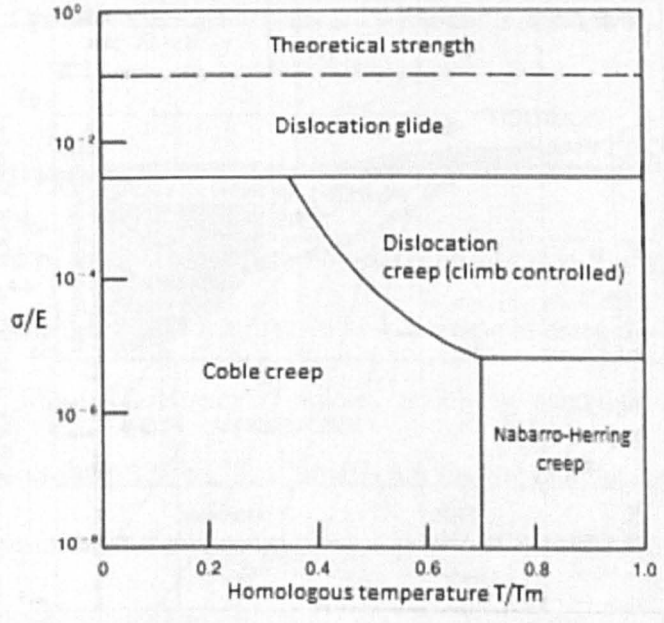

Figure 2.26- Qualitative deformation mechanism map – adapted from [33].

Because creep deformation mechanisms are essentially stress and temperature dependent, the deformation mechanism map, built having the horizontal axis defined by temperatures normalized by the absolute melting point and the vertical axis defined by stress normalized by the Young's modulus (or shear modulus) allows prediction of the dominant mechanism at given operational conditions. The contours between adjacent regions in the map represent points in which two deformation mechanisms equally contribute to the creep rate.

Although the qualitative deformation mechanism map illustrates well its purpose, it is worthy mentioning that, usually, the map is prepared for each material, with a specific grain size, and superimposed by contours of constant strain rate calculated as averages from the constitutive equations of all mechanisms contributing to each point of its points. The mechanism map built for the 316 austenitic stainless steel provided in Figure 2.27, illustrates the details considered:

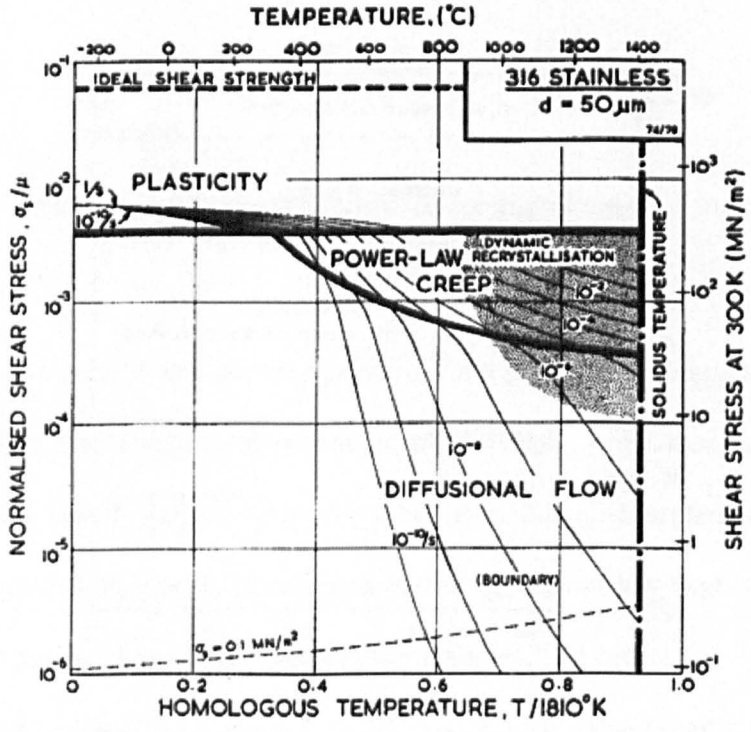

Figure 2.27 - Detailed deformation map for the 316 stainless steel [105].

When predominant in creep deformation regimes, dislocation-based processes in single metals and simple alloys usually present a stress exponent n in the range 3-7. But for fine-dispersion strengthened alloys, this value may be markedly higher, as shown later.

Some other mechanisms exist which involve vacancy diffusion through dislocations, instead of grain boundaries. This is termed pipe-diffusion and a change in activation energy to a value around half the one expected for lattice self-diffusion when dislocation creep is predominant ($n > 3$) is regarded as evidence of predominance of this regime [39].

However, grain boundary sliding (GBS) becomes an important mechanism of creep deformation at high temperatures or reduced creep rates [48], therefore, this mechanism can be active in conditions of diffusional creep. GBS takes place by subjecting regions near boundaries to plastic deformation by shear, due to sliding along the grain boundary. This mechanism is discontinuous in time and the shear displacement is not uniform along the boundary [33]. Its importance lies in the fact that it can initiate wedge cracking, as well as cause stress concentration on hard particles at grain boundaries, increasing the possibility of decohesion [103]. GBS tends to be minimized as grain size is increased, due to the reduction of grain boundary surface.

2.6.2 Creep in ODS steels

The trump card of the ODS particles is their ability to effectively anchor dislocations, thus enhancing creep resistance, manifested as a decrease in creep ductility and an increase in creep-rupture life [61]. However, studies trying to establish the upper operating temperature limit for these steels [73, 106, 107] are finding that the creep behaviour is very sensitive to composition and microstructure, as previous considerations attested, based on the chemical composition, stability of oxides and microstructure.

Klueh et al. [107] performed creep tests on two 12%Cr ODS ferritic steels of similar compositions, one being enriched with 0.35% titanium and 2.5% tungsten, designated 12YWT, while the other, without these elements, was called 12Y1; both prepared under

the same mechanical alloying and TMT routes. In agreement with the works concentrated on the fabrication of the ODS alloy and effects of oxide particle size, discussed in section 2.5.1, preliminary microscopic examination, illustrated in Fig. 2.28a and b, revealed much finer and regular distribution of nanoparticles in Y-Ti-O clusters for the 12YWT steel, which was reflected on its outstanding creep resistance: as Fig. 2.28c shows, after 5000 hr of test at 138 MPa and 800°C, this material appeared to be still in the secondary creep stage, being superior to many other alloys, including the 12Y1, MA957 (a 14%Cr ODS steel) and a vanadium alloy, also tested at 800°C but at a much lower stress, which is also a candidate for fusion applications:

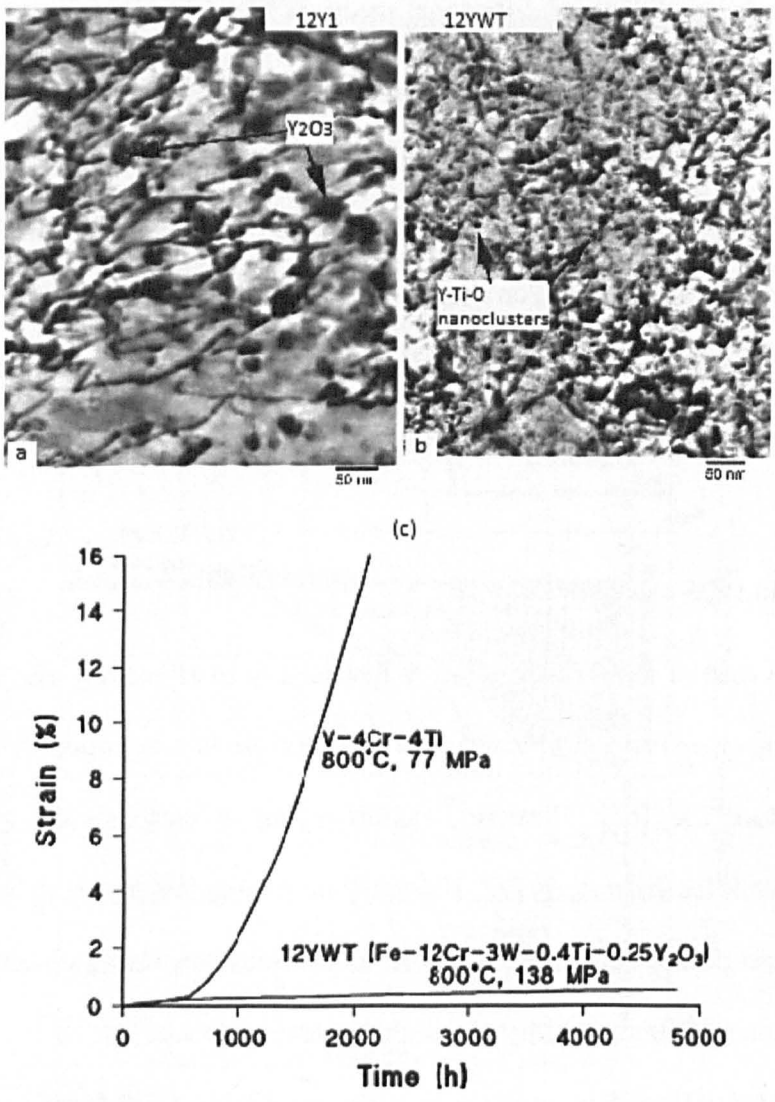

Figure 2.28 - TEM images of (a) 12Y1 and (b) 12YWT, showing one order of magnitude more dislocations pinned by nanoparticles; and (c) a comparison of creep response of the ODS 12YWT steel and V-4Cr-4Ti alloy - [107].

Alamo and co-workers [73] studied the creep performance of MA957, a ferritic ODS steel with nominal composition Fe-14Cr-1Ti-0.3Mo-0.25Y_2O_3, in two different conditions, one with fine elongated grains (0.5 μm mean diameter and length/diameter ratio of 10-20), and the other, recrystallized, presenting grain sizes of 10-50 μm diameter and minimum texture, both with the same oxide particle size distribution. They found that recrystallized specimens are less creep-resistant than the fine grain samples for short rupture (high stress) tests, but for long rupture tests, which means, lower stresses, their behaviour at 650°C becomes comparable. This seems to suggest that diffusion mechanisms can play a significant role, since the bigger grain size of the recrystallized material influenced the creep response at high temperatures. But, due to strong crystallographic texture of the fine grain samples, lower creep strength is expected in the radial direction, while nearly isotropic creep properties are envisaged for the recrystallized material.

Evans et al. [108] emphasized the necessity for two-stage heat treatment, comprised by annealing and ageing, as a way to avoid, by means of deposition of intermetallic chi-phase ($Fe_{36}Cr_{12}Ti_7Mo_3$) particles at grain boundaries of a 13%Cr ferritic steel, an anomalous instability, manifested by two inflexion points in the primary stage portion of the creep curve. This was suggested to be associated with grain boundary migration providing free sites for dislocation multiplication.

Many researchers found a different unexpected creep response, characterized by little or no tertiary stage. This behaviour was reported for a dual-phase 9%Cr-ODS steel [70], for MA957 [109] and for the 14WYT [110] among others. Although, at first, it was believed to be associated to the fine oxide dispersion, later research reported a normal shape for creep curves [13, 108]. It can be speculated that this trend may be associated with brittleness or excess porosity. Yet, with regards to the 14WYT, a 14%Cr ODS steel developed at the Oak Ridge National Laboratory, very similar creep rates were observed for samples presenting vastly different grain structures, in terms of size and morphology,

each resulting from an annealing treatment at 1000°C and time intervals ranging from 1 hour up to 11 days. These results suggested insensitivity of the secondary creep rates to the microstructure [110], a behaviour noted solely for this particular ODS steel.

Regardless of the shape of the curve, or peculiar response of the steel, the most remarkable feature of the ODS materials is the high strain-rate sensitivity to the applied stress, characterized by much greater stress exponent n than the values of 3-5 commonly found for pure metals and conventional alloys under Norton's power law scope. Zakine et al. [111] found n ranging from 11 to 13 for a 13%Cr ODS steel reinforced with titanium oxide (material termed DT) and n values between 17 and 25 for the same steel strengthened with titanium and yttrium oxides (termed DY). Alamo and colleagues [73] reported n around 50 for the MA957, and exponents of 45, 23 and 200 were reported by Rösler and Arzt [112] for dispersion-strengthened tungsten, nickel and aluminium alloys, respectively. This particular creep behaviour was firstly addressed by considering a threshold stress, σ_{th}, below which the creep rate given in Norton's law becomes negligible. This concept is useful to the extent that it allows results to be expressed by a single master curve, as a function of the applied stress corrected by the threshold stress [111].

The physical origin of σ_{th} is not well known, but it was thought to be related to an attractive interaction between dislocations and particles due to local relaxation of the stress field, by slipping and quick diffusion, at the matrix/particle interface, as proposed by Srolovitz et al. [113]. This attractive interaction, according to Rösler and Arzt [112], activates a new strengthening mechanism: detachment of dislocations from the departure side of dispersoids over which these same dislocations have climbed. Studies with ODS steels [110, 112, 113, 115] presented TEM observations revealing strong pinning of dislocations to the departure side of oxide particles, giving support to the idea of attractive interaction, as Fig. 2.29 illustrates:

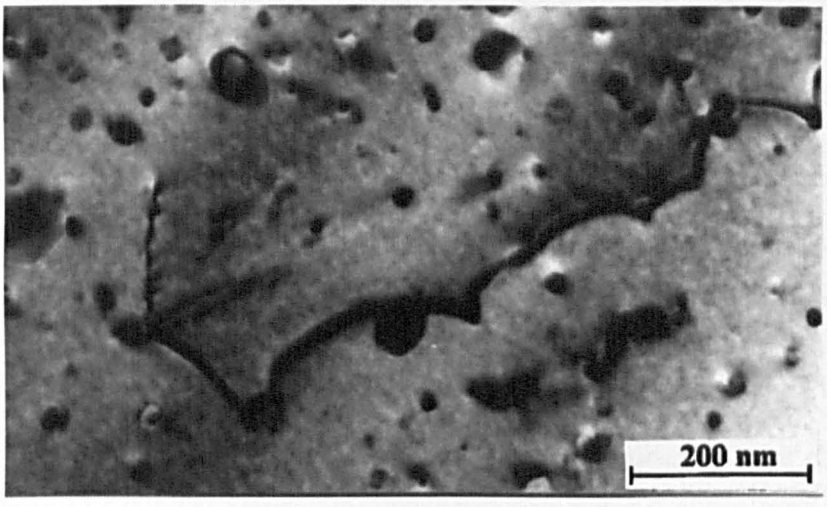

Figure 2.29 - Pinning of dislocations at the particle/matrix interface, on the departure side of the oxides [114].

Based on the detachment energy analysis proposed by Arzt and Wilkinson [95], Rösler and Arzt derived a stress-strain rate equation for dispersion strengthened materials when detachment is the rate controlling process:

$$\frac{\dot{\varepsilon}}{D_v} = \frac{6 \cdot \lambda_{fp} \cdot \rho}{b} exp\left(\frac{-Gb^2 r_p \left[(1-k)\left(1-\frac{\sigma}{\sigma_d}\right)\right]^{3/2}}{k_B T}\right)$$

(Eq. 2.10)

where $\dot{\varepsilon}/D_v$ is the creep rate normalized by the bulk diffusion coefficient; $2\lambda_{fp}$ is the average free path between obstacles; ρ is the dislocation density; b, the Burgers vector; G, the shear modulus of the matrix; r, the particle radius; k_B is the Boltzmann's constant; T, the absolute temperature; $k = T_P/T_M$ is the relaxation parameter defined as the ratio of dislocation line energy at the particle to that in the matrix. For $k = 1$, no attraction exists between particle and dislocation, while for $k < 1$, attractive interaction arises, becoming stronger as k diminishes. Finally, applied stress σ is normalized by the athermal detachment stress, σ_d, which is the stress required for detachment in the absence of thermal activation. σ_d relates to the Orowan stress, σ_{Or}, as $\sigma_d = \sigma_{Or}(1-k^2)^{1/2}$.

This model is preferable to the threshold stress, given the dependence of this latter on temperature and, often, applied stress. Zakine et al. [111] found this model satisfactory to describe coarse-grained ODS alloys (a few mm size). However, no significant agreement was found between Eq. 2.10 and experimental data for the intermediate grain size DT and DY alloys, being the most reasonable agreed result achieved for k around 0.97. According to Arzt and Wilkinson [95], the critical value of k for detachment-controlled creep is 0.94, which led to the conclusion that a second creep mechanism, such as Coble creep, acts in parallel for the control of the strain rate. This would explain the intermediate values found for the DT and DY alloys (in the range 11-25), as diffusional processes prevent higher stress sensitivities.

Although not accurate for many ODS materials, these models are providing insight to phenomena taking place between dislocations and particles, in attempts to find the basic mechanisms behind high temperature plastic deformation processes, which are required for understanding creep and anelastic response of materials. The model describes quite well the deformation behaviour of MA956 steel, as reported by Wasilowska and colleagues [114], even though its predictions were in good agreement with the creep test results only when these were carried out at stresses close to the critical (threshold) value, discussed above.

2.7 Anelasticity

Variations in demand of operational reactors as well as periodic programmed stops for maintenance are expected, which may impose regimes of partial or total load removal or load and temperature transients. Under these circumstances, time-dependent strain recovery after unloading a material, during creep deformation, will be present. As figure 2.30 shows for a creep test, after sudden removal of the load, the material undergoes an immediate elastic drop, followed by a time-dependent decay in strain, which is the anelasticity, until the specimen is reloaded [23, 34].

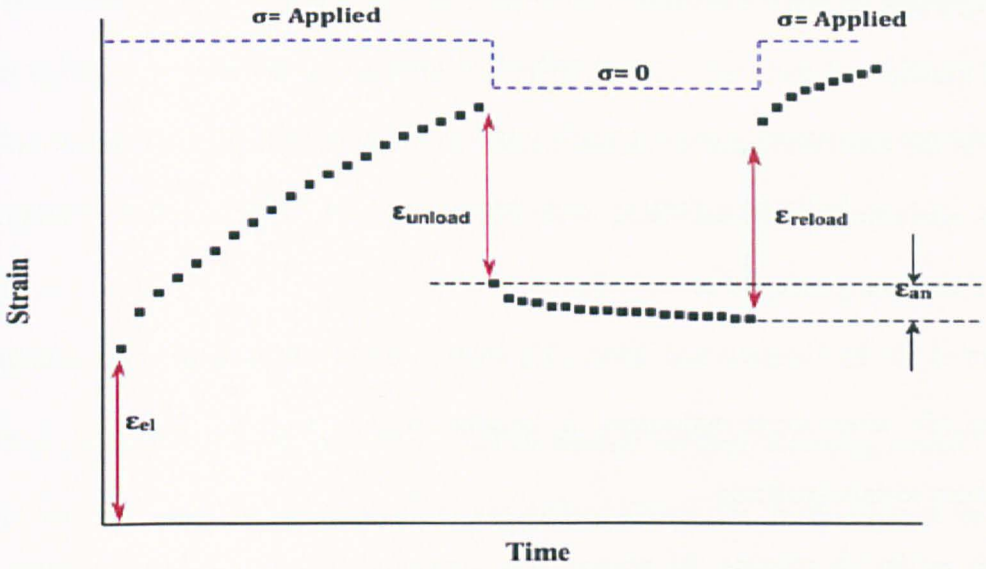

Figure 2.30 - Anelastic strain recovery, ε_{an}, after unloading a creep specimen [115].

Through recent investigations on 316H stainless steel subjected to creep with low-cycle partial unloading tests, simulating the expected mechanical conditions in advanced nuclear reactors, anelasticity was found to affect creep response of the material, by decreasing the ductility and, subsequently, causing an increase in creep-rupture life [115]. These effects are maximized when both temperature and load are removed. Therefore, it becomes of great importance to understand the phenomena involved in creep transients, in order to avoid premature withdrawal of a component from operation, as well as to improve assessment of the evolution of materials properties for long-term demands.

It naturally followed, then, to study the anelastic response of a material by means of transient tests. The latter may result from changes in stress, temperature, strain-rate, or a combination of these variables, as well as any other parameter influencing the microstructure. However, as observed by Biberger and Gibeling [116], instantaneous temperature change experiments were found to be extremely difficult to reproduce with good resolution, and, besides, represent not very realistic conditions expected from the majority of applications. Strain-rate tests are feasible, but more demanding in terms of analysis, chiefly due to the impossibility of controlling solely the plastic strain, rather than the total strain. Thus, stress-dip tests became largely deployed for studying transients.

Investigations on creep transients following stress changes work in line with the most essential principle of materials science, trying to correlate the mechanical response of a material to the observed state of microstructure. Early investigations were based on the idea that anelasticity was associated with dislocation motion in a constant subgrain structure, commonly referred to as "constant structure creep" [116, 117]. However, after work carried out by Hausselt and Blum [35] showed that changes in the microstructure occur quickly after stress reduction, it became widely accepted that only a few substructures remain unaltered.

Further evidences refuting the constant structure model were found in a number of subsequent works adopting a totally different approach, based on the magnitude of the anelastic response since drop, following suggestion from Ahlquist and Nix [118] that this variable could be used to measure internal stress developed during creep. The central idea behind the suggestion of internal stresses associated with anelastic response was the observation that creep response after stress reduction can be positive, zero or negative, depending on the magnitude of the drop in stress. It is speculated, then, that unloading a sample to a level higher than the internal (back) stress would result in creep, with a reduced steady-state rate, while stress removal below the back stress would trigger anelastic recovery and a stress drop to the back stress level would result in the zero rate. A number of works based on these ideas try to correlate the shape of the creep curve after unloading with the inherent microstructural mechanisms responsible for it, in several types of conventional and ODS stainless steels [110, 112, 119, 120]. While some of these authors associated the back stresses to the presence of dislocation cells, described as inhomogeneous structures formed by soft and hard areas coupled by requirements of stress balance, others ascribed the generation of back stresses to free dislocations in the matrix bowing out while interacting with precipitates, particles and other obstacles, when no cell structure is observed. Although the contribution of free dislocations under Orowan bowing interactions is acknowledged, it seems unrealistic to attribute the back stresses to

individual dislocation interactions and neglect the inhomogeneous arrangements of these defects throughout the matrix, forming the hard areas.

In order to properly understand the concepts related to key parameters associated with the investigation of anelasticity, a brief introduction to them is provided.

2.7.1 Residual Stresses

The classical definition states that residual stresses are self-balancing stresses existing in a material when no external loads are acting. Generally, these stresses arise from incompatibilities between deforming regions of a material (or component) due to inhomogeneous plastic strain, thermal expansion or volume change [121].

The relevance of the residual stresses lies in the fact that they may be beneficial to the material, when they act as to minimize the effect of an external stress, as in the case of compressive residual stresses induced by peening on the surface of a component expected to be loaded in tension, or they may be superimposed to in-service stresses and intensify the deleterious effects, causing premature failure [115].

Another relevant aspect is related to the domains over which the residual stresses are analysed, defined by the length scale considered. In this regard, residual stresses are divided in types I, II and III [122]. Type I residual stresses are self-equilibrated over a length scale comparable to the bulk of the material. They are also termed macrostresses and can be described by approaches based on continuum mechanics. Their origins are associated with mechanical and thermomechanical processes, such as welding, machining and shot peening. Type II stresses are considered over the grain scale of the material, acting within long-range crystal domains. They are related to the inhomogeneity of deformation at the grain scale, caused by differences in elastic behaviour between grains, as well as by differences in slip systems from one grain to another. These stresses arise from fabrication processes involving extensive deformation, such as rolling, forging, among others, and from phase transformations. Finally, type III residual stresses occur on a

finer scale, inside grains, extending over domains of the atomic length, being associated with dislocations, point defects, solute atoms and their interactions.

Although this separation according to the length scale is usual practice, the total residual stress acting at any given point of a material corresponds to the superposition of the three stress types. Residual stresses of the second order (type II), along with those of the third order (type III) are collectively known as microstresses [122] or internal stresses [23]. Since the analysis of the anelastic response of a polycrystalline material relies on the basic physical features responsible for plastic deformation, attention is focused onto these microstresses and how they are developed through the course of deformation.

2.7.2 Generation of internal stresses

When a polycrystalline material is subjected to external stress, the applied load is not homogeneously distributed, considering the grain scale and below. In fact, differences in elastic properties from one grain to another, or between different phases, will promote redistribution of the load amongst the different crystals [22]. As a consequence, some grains will start deforming plastically, while others will still present only elastic strains. These differences in behaviour, causing different rates of hardening in adjacent grains, lead to plastic strain mismatches between crystals, with the consequent development of internal stresses between grains and in their interiors. Since these stresses remain after removal of the external load, they correspond to the type II and type III stresses previously presented, playing a role in the anelastic response of a material, as suggested by Ahlquist and Nix [118]. Thus, the development of internal stresses is a consequence of the natural anisotropy in mechanical properties shown by polycrystalline materials at grain scale, which occurs in both regimes of deformation, elastic and plastic.

Elastic anisotropy stems from the fact that the elastic stiffness of a crystal depends on its orientation with regards to the direction of the applied load [115]. Therefore, differently oriented grains bear different fractions of the external load and this is reflected in the

lattice strains of each crystallographic plane considered. Plastic anisotropy, in its turn, relates to the fact that the slip motion of dislocations occurs in certain preferential planes and directions. Thus, plastic strains lead to further intensification of the mismatches that generate the internal stresses.

2.7.3 Back stresses and effective stresses

From the considerations discussed above, it can be seen that anelasticity, that is, the time-dependent plastic strain recovery of previous deformation suffered, depends on an inhomogeneous distribution of strain within the material. In a recent work, Rao et al. [23] looked at the evolution of stresses between differently oriented grain families via neutron diffraction on a 316H sample subjected to creep with full unloading stages at 650°C, providing evidence of anisotropy in creep deformation at the grain scale, as seen below in Fig. 2.31:

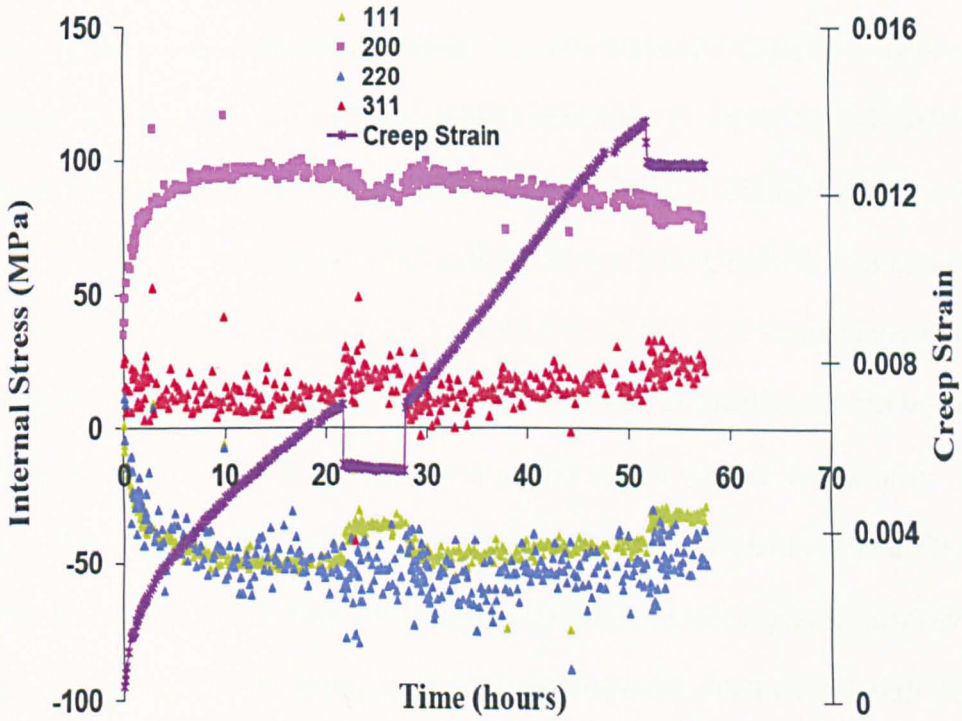

Figure 2.31 - Evolution of internal stresses for some crystallographic families along creep deformation with full unloading transients. The orientations of the grain families are measured with regards to the loading direction [115].

These stresses are the intergranular long-range internal stresses, related to plastic mismatches between grains of different orientation with regards to the loading direction and from events of dislocation generation, emission and passage across grain boundaries [123]. However, the basic mechanisms behind plastic deformation and recovery are strongly dependent on events taking place inside grains. Thus, at a scale smaller than the grain, long-range stresses arising from local straining processes involving mobile dislocation interactions are responsible for the intragranular back stresses.

It has become usual practice to describe polycrystalline materials as a partition between grain boundary zones and grains [38, 123, 124], each set giving a particular contribution to deformation, depending on the loading conditions and plastic strain level (or creep regime). This procedure seems to be valid for any deformation process imposed, such as tension, cyclic loading and creep. A very good description of the internal stresses associated with dislocations structures developed inside grains was developed by Mughrabi [125] and successfully applied by Feaugas [40] to explain the origin of tensile flow stress in 316L stainless steel at room temperature. Feaugas proposed the long-range internal (back) stresses developed in tensile straining to result from the same intergranular and intragranular levels of incompatibility explained previously. The intergranular component is associated with the crystal structure as well as with events of plastic strain incompatibility between grains, that is, in grain boundaries. The intragranular back stress component originates from the heterogeneity of the spatial dislocation distribution inside grains and can be evaluated in terms of dislocation arrangements and structures, and areas of free dislocations. Further details on the determination of back stresses are provided in chapter 4, along with the mathematical model used.

Given that creep causes the material to deform and anelasticity promotes recovery, the effective stress becomes a convenient means of quantification of softening or hardening of the material, in terms of its basic defects responsible for plasticity, that is, the dislocations. It correlates the density of free dislocations in the matrix with the stress level required for

them to become mobile, as expressed in Equation 2.2. Feaugas [40] stated that the effective stress is equal to the yield stress at the onset of plastic strain, given that, at this stage, α, which accounts for different types of elastic dislocation interactions acting in plasticity [123], is very small ($\alpha = 0.025$), due to only one active slip system. The effective stress is useful to estimate how easy it is for free dislocations to move across the matrix. A small value of effective stress corresponds to a high degree of mobility and vice-versa. While not a material's property, the effective stress provides an indication of the flow stress variation and, if added to the back stress, it equals the applied stress. Therefore, changes in the materials internal state and, consequently, in its mechanical properties, are readily quantified by this parameter.

2.8 Summary

Materials for advanced nuclear power plant applications are expected to perform under harsh operational conditions, characterised by elevated temperatures, reaching 650°C (or higher), increased mechanical loads and irradiation effects. It is demanded from them the ability to withstand the rigorous conditions for 60 years or more, for which good mechanical properties, such as ductility, fracture toughness and superior creep resistance; as well as corrosion resistance and dimensional stability under irradiation are fundamental.

Austenitic stainless steels, particularly the 316 grades, are well-established materials for a wide range of applications in nuclear power plant components, such as piping systems, heat exchangers and others, but their susceptibility to swelling under irradiation makes them unsuitable for in-core applications.

Oxide Dispersion-Strengthened steels have great potential for use in the next generations of nuclear power plants, due to the presence of a fine dispersion of oxides presenting higher stability, in comparison with conventional precipitation strengthened alloys. Owing to this, ODS steels can be used at higher temperatures than conventional high-Cr steels and have improved resistance to creep, recrystallization and void swelling.

The size distribution of the oxides is the parameter of primary concern, over the nature of the oxides, for the strengthening effects.

The ferritic ODS steel MA956 is a potentially strong candidate for advanced nuclear applications, given its superior corrosion resistance (due to the content of Al), stable recrystallized microstructure, comprised by coarse column-like grains, with high aspect ratio, and a fine distribution of oxides.

Creep, a time-dependent plastic deformation at high temperatures, is a major life-limiting phenomenon in the conditions expected, so that the study of creep properties is fundamental for investigating the suitability of the steels for the advanced nuclear reactors.

Creep-transient behaviour is, likewise, very important, given that the anelastic recovery triggered by the removal of the applied stress alters the properties of the materials. A study of anelasticity of the 316H steel in partial unloading conditions has not been addressed. A model for internal (back) stresses becomes a convenient way to describe the creep-transient behaviour in terms of the material internal state. A comprehensive study of creep transient behaviour of ODS steels has not yet been conducted.

2.9 References

[1] A. Hishinuma, A. Kohyama, R. L. Klueh, D. S. Gelles, W. Dietz, and K. Ehrlich, "Current status and future R&D for reduced-activation ferritic/martensitic steels," *J. Nucl. Mater.*, vol. 258–263, P, no. 0, pp. 193–204, 1998.

[2] R. L. Klueh and D. R. Harries, *High-Chromium Ferritic and Martensitic Steels for Nuclear Applications*. American Society for Testing and Materials, 2001.

[3] P. Yvon and F. Carré, "Structural Materials Challenges for Advanced Reactor Systems," *J. Nucl. Mater.*, vol. 385, pp. 217–222, 2009.

[4] W. R. Corwin, "U.S. Generation IV Reactors Integrated Materials Technology," *Nucl. Eng. Technol.*, vol. 38, no. 7, pp. 591–618, 2006.

[5] G. Pintsuk, Z. Oksiuta, J. Linke, and N. Baluc, "High heat flux testing of 12-14Cr ODS ferritic steels," *J. Nucl. Mater.*, vol. 396, pp. 20–25, 2010.

[6] Y. Li, T. Nagasaka, and T. Muroga, "Long-Term Thermal Stability of Reduced Activation Ferritic/Martensitic Steels as Structural Materials of Fusion Blanket," *Plasma Fusion Res.*, vol. 5, pp. S1036–S1036, 2010.

[7] R. J. Kurtz, A. Alamo, E. Lucon, Q. Huang, S. Jitsukawa, A. Kimura, R. L. Klueh, G. R. Odette, C. Petersen, M. A. Sokolov, P. Spätig, and J. W. Rensman, "Recent progress toward development of reduced activation ferritic/martensitic steels for fusion structural applications," *J. Nucl. Mater.*, vol. 386–388, pp. 411–417, 2009.

[8] Y. de Carlan, M. Murugananth, T. Sourmail, and H. K. D. . Bhadeshia, "Design of new Fe–9CrWV reduced-activation martensitic steels for creep properties at 650 °C," *J. Nucl. Mater.*, vol. 329–333, no. 2004, pp. 238–242, Aug. 2004.

[9] R. L. Klueh, N. Hashimoto, R. F. Buck, and M. A. Sokolov, "A potential new ferritic/martensitic steel for fusion applications," *J. Nucl. Mater.*, vol. 283–287, P, no. 0, pp. 697–701, 2000.

[10] "TalkNuclear," 2012. [Online]. Available: http://talknuclear.ca/2012/04/the-evolution-of-nuclear-power/. [Accessed: 19-Mar-2015].

[11] W. C. Patterson, *Nuclear Power with a New Postscript*. Pelican Books, 1978.

[12] V. V Sagaradze, V. I. Shalaev, V. L. Arbuzov, B. N. Goshchitskii, Y. Tian, W. Qun, and S. Jiguang, "Radiation resistance and thermal creep of ODS ferritic steels," *J. Nucl. Mater.*, vol. 295, no. 2–3, pp. 265–272, 2001.

[13] R. W. Evans, J. A. Preston, B. Wilshire, and E. A. Little, "Creep and creep fracture of an oxide-dispersion-strengthened 13% chromium ferritic steel," *Mater. Sci. Eng. A*, vol. A167, pp. 65–72, 1993.

[14] Z. Oksiuta, P. Mueller, P. Spätig, and N. Baluc, "Effect of thermo-mechanical treatments on the microstructure and mechanical properties of an ODS ferritic steel," *J. Nucl. Mater.*, vol. 412, no. 2, pp. 221–226, 2011.

[15] D. S. Gelles, "Development of Martensitic Steels for High Neutron Damage Applications," *J. Nucl. Mater.*, vol. 239, pp. 99–106, 1996.

[16] W. D. Callister, *Materials Science and Engineering: An Introduction*, 5th Editio. John Wiley & Sons, 2000.

[17] J. Chao, J. L. González-Carrasco, and C. Capdevilla, "Influence of Annealing at 1100°C and 475°C on the Mechanical Properties at Room Temperature of an Iron Base ODS Alloy," *ISIJ Int.*, vol. 47, pp. 1214–1220, 2007.

[18] M. Maalekian, "The Effects of Alloying Elements on Steels," vol. I. Christian Doppler Laboratory for Early Stages of Precipitation, Technische Universität Graz, on-line publishing, 2007.

[19] E. C. Bain, *Alloying Elements is Steels*. ASM, 1939.

[20] A. Kohyama, A. Hishinuma, D. S. Gelles, R. L. Klueh, W. Dietz, and K. Ehrlich, "Low-activation ferritic and martensitic steels for fusion application," *J. Nucl. Mater.*, vol. 233–237, pp. 138–147, 1996.

[21] D. G. Morris, "Creep in Type 316 Stainless Steel," *Acta Metall.*, vol. 26, pp. 1143–1151, 1978.

[22] M. R. Daymond and P. J. Bouchard, "Elastoplastic Deformation of 316 Stainless Steel Under Tensile Loading at Elevated Temperatures," *Metall. Mater. Trans. A*, vol. 37, no. June, pp. 1863–1873, 2006.

[23] A. Rao, P. John Bouchard, S. M. Northover, and M. E. Fitzpatrick, "Anelasticity in austenitic stainless steel," *Acta Mater.*, vol. 60, no. 19, pp. 6851–6861, Nov. 2012.

[24] D. G. Morris and D. R. Harries, "The cyclic creep behaviour of Type 316 stainless steel," *J. Mater. Sci.*, vol. 13, pp. 985–996, 1978.

[25] H. K. D. H. Bhadeshia and R. W. K. Honeycombe, *Steels: Microstructure and Properties*, Third. Elsevier, 2006.

[26] L. Zhang, W. Pluschkell, and B. G. Thomas, "Nucleation and growth of alumina inclusions during steel deoxidation," in *85th Steelmaking Conference*, 2002, vol. 85, pp. 463–476.

[27] M. D. Mathew, K. Laha, and V. Ganesan, "Improving creep strength of 316L stainless steel by alloying with nitrogen," *Mater. Sci. Eng. A*, vol. 535, pp. 76–83, 2012.

[28] P. Shankar, "Cr2N Precipitation stages in 316LN Austenitic Stainless Steels," *Scr. Metall. Mater.*, vol. 31, no. 5, pp. 589–593, 1994.

[29] P. Shankar, H. Shaikh, S. Sivakumar, S. Venugopal, D. Sundararaman, and H. S. Khatak, "Effect of thermal aging on the room temperature tensile properties of AISI type 316LN stainless steel," *J. Nucl. Mater.*, vol. 264, no. 1–2, pp. 29–34, 1999.

[30] M. F. McGuire, *Stainless steels for design engineers*, 1st editio. ASM International, 2008.

[31] R. L. Klueh, N. Hashimoto, and P. J. Maziasz, "New nano-particle-strengthened ferritic/martensitic steels by conventional thermo-mechanical treatment," *J. Nucl. Mater.*, vol. 367–370, pp. 48–53, 2007.

[32] Y. Yamamoto, M. L. Santella, M. P. Brady, H. Bei, and P. J. Maziasz, "Effect of Alloying Additions on Phase Equilibria and Creep Resistance of Alumina-Forming Austenitic Stainless Steels," *Metall. Mater. Trans. A*, vol. 40, no. 8, pp. 1868–1880, Jun. 2009.

[33] G. E. Dieter, *Mechanical Metallurgy*. McGraw-Hill, 1986.

[34] D. Hull and D. J. Bacon, *Introduction to dislocations*, 5th Editio. Butterworth-Heinemann, 2007.

[35] J. Hausselt and W. Blum, "Dynamic recovery during and after steady state deformation of Al-11wt%Zn," *Acta Metall.*, vol. 24, no. 11, pp. 1027–1039, Nov. 1976.

[36] D. G. Morris, "Anelasticity and creep transients in an austenitic steel," *J. Mater. Sci.*, vol. 13, pp. 1849–1854, 1978.

[37] P. Lee and R. Raj, "Colossal anelasticity in polycrystals deforming under conditions of diffusional creep," *Acta Mater.*, vol. 58, no. 2, pp. 702–708, Jan. 2010.

[38] P. J. Szabo, "Effect of partial recrystallization on the grain size and grain boundary structure of austenitic steel," *Mater. Charact.*, vol. 66, pp. 99–103, Apr. 2012.

[39] R. W. Evans and B. Wilshire, *Creep of Metals and Alloys*. The Institute of Metals, 1985.

[40] X. Feaugas, "On the origin of the tensile flow stress in the stainless steel AISI 316L at 300 K: back stress and effective stress," *Acta Mater.*, vol. 47, no. 13, pp. 3617–3632, Oct. 1999.

[41] U. Kocks, "Laws for work-hardening and low temperature creep," *J. Eng. Mater. Technol.*, vol. 98, pp. 76–85, 1976.

[42] L.-E. Lindgren, K. Domkin, and S. Hansson, "Dislocations, vacancies and solute diffusion in physical based plasticity for AISI 316L," *Mech. Mater.*, vol. 40, pp. 907–919, 2008.

[43] R. L. Fleischer, "Solid Solution Hardening," in *The Strengthening of Metals*, D. Peckner, Ed. Reinhold Publishing Corporation, 1964.

[44] T. Sourmail, "Precipitates in creep-resistant austenitic stainless steel," *Mater. Sci.& Technol.*, vol. 17(1), pp. 1–14, 2001.

[45] I. Kovács and L. Zsoldos, *Dislocations and Plastic Deformations (Monographs in Natural Philosophy)*, First Edit. Pergamon Press, 1973.

[46] V. G. Gavriljuk and H. Berns, *High Nitrogen Steels*. Springer, 1999.

[47] T. Whittaker, M. Evans, and B. Wilshire, "Long-term creep data prediction for type 316H stainless steel," *Mater. Sci. Eng. A*, vol. 552, pp. 145–150, Aug. 2012.

[48] J. Bressers, *Creep and Fatigue in High Temperature Alloys*. Applied Science Publishers, 1981.

[49] W. J. S. Yang, D. S. Gelles, J. L. Straalsund, and R. Bajaj, "Post-irradiation ductility loss of Fe-15%Ni-base precipitation hardenable alloys," *J. Nucl. Mater.*, vol. 132, no. 3, pp. 249–265, 1985.

[50] J. Rawls, W. Chen, E. Chung, J. Dalessandro, P. Miller, S. Rosenwasser, and L. Thompson, "Assessment of Martensitic Steels as Structural Materials in Magnetic Fusion Devices," 1980.

[51] H. Attaya, G. L. Kulcinski, and W. G. Wolfer, "Analysis of forces on ferromagnetic components used in magnetic fusion reactors," *J. Nucl. Mater.*, vol. 122, no. 1–3, pp. 96–100, 1984.

[52] Y. Li, T. Nagasaka, and T. Muroga, "Long-Term Thermal Stability of Ferritic and Martensitic Steels as Structural Materials of Fusion Blanket," *Plasma Fusion Res. Artic.*, vol. 5, no. S1036, pp. 1–5, 2010.

[53] D. Preininger, "Modelling of the effect of precipitates on work-hardening, ductility and impact behaviour of ferritic-martensitic Cr steels," *J. Nucl. Mater.*, vol. 307–311, pp. 514–520, 2002.

[54] Y. de Carlan, M. Murugananth, T. Sourmail, and H. K. D. H. Bhadeshia, "Design of new Fe–9CrWV reduced-activation martensitic steels for creep properties at 650 °C," *J. Nucl. Mater.*, vol. 329–333, P, no. 0, pp. 238–242, 2004.

[55] R. L. Klueh, N. Hashimoto, and P. J. Maziasz, "New nano-particle-strengthened ferritic/martensitic steels by conventional thermo-mechanical treatment," *J. Nucl. Mater.*, vol. 367–370, no. 2007, pp. 48–53, Aug. 2007.

[56] L. Lundin, S. Fallman, and H.-O. Andrén, "Microstructure and mechanical properties of a 10% chromium steel with improved creep resistance at 600°C," *Mater. Sci. Technol.* , vol. 13, no. 3, pp. 233–242, 1997.

[57] N. Dudova, A. Plotnikova, D. Molodov, A. Belyakov, and R. Kaibyshev, "Structural changes of tempered martensitic 9%Cr–2%W–3%Co steel during creep at 650 °C," *Mater. Sci. Eng. A*, vol. 534, no. 0, pp. 632–639, 2011.

[58] F. Abe, T. Horiuchi, M. Taneike, and K. Sawada, "Stabilization of martensitic microstructure in advanced 9Cr steel during creep at high temperature," *Mater. Sci. Eng. A*, vol. 378, no. 1–2, pp. 299–303, 2004.

[59] R. Agamennone, W. Blum, C. Gupta, and J. K. Chakravartty, "Evolution of microstructure and deformation resistance in creep of tempered martensitic 9–12%Cr–2%W–5%Co steels," *Acta Mater.*, vol. 54, no. 11, pp. 3003–3014, 2006.

[60] A. Kipelova, R. Kaibyshev, A. Belyakov, and D. Molodov, "Microstructure evolution in a 3%Co modified P911 heat resistant steel under tempering and creep conditions," *Mater. Sci. Eng. A*, vol. 528, no. 3, pp. 1280–1286, 2011.

[61] H. Hadraba, B. Fournier, L. Stratil, J. Malaplate, A. L. Rouffié, P. Wident, L. Ziolek, and J. L. Béchade, "Influence of microstructure on impact properties of 9–18%Cr ODS steels for fusion/fission applications," *J. Nucl. Mater.*, vol. 411, no. 1–3, pp. 112–118, 2011.

[62] K. Wolski, F. Thévenot, and J. Le Coze, "Effect of nanometric oxide dispersion on creep resistance of ODS-FeAl prepared by mechanical alloying," *Intermet. A*, vol. 4, pp. 299–307, 1996.

[63] E. Arzt, "Creep of Oxide-dispersion Strengthened Alloys," *Encyclopedia of Materials: Science and Technology*. Elsevier, pp. 1800–1806, 2001.

[64] F. V Lenel, *Powder Metallurgy Principles and Applications*. Metal Powder Industries Federation, 1980.

[65] J. Chen, P. Jung, M. A. Pouchon, T. Rebac, and W. Hoffelner, "Irradiation creep and precipitation in a ferritic ODS steel under helium implantation," *J. Nucl. Mater.*, vol. 373, no. 1–3, pp. 22–27, 2008.

[66] M. B. Toloczko, D. S. Gelles, F. A. Garner, R. J. Kurtz, and K. Abe, "Irradiation creep and swelling from 400 to 600 °C of the oxide dispersion strengthened ferritic alloy MA957," *J. Nucl. Mater.*, vol. 329–333, P, no. 0, pp. 352–355, 2004.

[67] H. Kishimoto, K. Yutani, R. Kasada, O. Hashitomi, and A. Kimura, "Heavy-ion irradiation effects on the morphology of complex oxide particles in oxide dispersion strengthened ferritic steels," *J. Nucl. Mater.*, vol. 367–370, P, no. 0, pp. 179–184, 2007.

[68] H. Kishimoto, M. J. Alinger, G. R. Odette, and T. Yamamoto, "TEM examination of microstructural evolution during processing of 14CrYWTi nanostructured ferritic alloys," *J. Nucl. Mater.*, vol. 329–333, P, no. 0, pp. 369–371, 2004.

[69] H. Sakasegawa, S. Ohtsuka, S. Ukai, H. Tanigawa, M. Fujiwara, H. Ogiwara, and A. Kohyama, "Microstructural evolution during creep of 9Cr-ODS steels," *Fusion Eng. Des.*, vol. 81, no. 8–14, pp. 1013–1018, 2006.

[70] H. Sakasegawa, S. Ukai, M. Tamura, S. Ohtsuka, H. Tanigawa, H. Ogiwara, A. Kohyama, and M. Fujiwara, "Creep constitutive equation of dual phase 9Cr-ODS steel," *J. Nucl. Mater.*, vol. 373, no. 1–3, pp. 82–89, 2008.

[71] R. Lindau, A. Möslang, M. Schirra, P. Schlossmacher, and M. Klimenkov, "Mechanical and microstructural properties of a hipped RAFM ODS-steel," *J. Nucl. Mater.*, vol. 307–311, P, no. 0, pp. 769–772, 2002.

[72] J. Pearce, "Fusion Materials Development at ORNL," *ASTM Standardization News*, 2010. [Online]. Available: http://www.astm.org/SNEWS/JF_2010/pearce_jf10.html.

[73] A. Alamo, V. Lambard, X. Averty, and M. H. Mathon, "Assessment of ODS-14%Cr ferritic alloy for high temperature applications," *J. Nucl. Mater.*, vol. 329–333, pp. 333–337, 2004.

[74] M. Wang, Z. Zhou, H. Sun, H. Hu, and S. Li, "Effects of plastic deformations on microstructure and mechanical properties of ODS-310 austenitic steel," *J. Nucl. Mater.*, vol. 430, no. 1–3, pp. 259–263, Nov. 2012.

[75] C. Capdevila, M. K. Miller, I. Toda, and J. Chao, "Influence of the α–α′ phase separation on the tensile properties of Fe-base ODS PM 2000 alloy," *Mater. Sci. Eng. A*, vol. 527, no. 29–30, pp. 7931–7938, Nov. 2010.

[76] P. Olier, A. Bougault, A. Alamo, and Y. de Carlan, "Effects of the forming processes and Y2O3 content on ODS-Eurofer mechanical properties," *J. Nucl. Mater.*, vol. 386–388, no. 0, pp. 561–563, 2009.

[77] A. Steckmeyer, V. H. Rodrigo, J. M. Gentzbittel, V. Rabeau, and B. Fournier, "Tensile anisotropy and creep properties of a Fe–14CrWTi ODS ferritic steel," *J. Nucl. Mater.*, vol. 426, no. 1–3, pp. 182–188, 2012.

[78] H. K. D. H. Bhadeshia, "Recrystallization of practical mechanically alloyed Iron-base and Nickel-base Superalloys," *Mater. Sci. Eng. A*, vol. 223, pp. 64–77, 1997.

[79] J. Hoffmann, M. Klimenkov, R. Lindau, and M. Rieth, "TEM study of mechanically alloyed ODS steel powder," *J. Nucl. Mater.*, vol. 428, no. 1–3, pp. 165–169, Sep. 2012.

[80] M. Wang, Z. Zhou, H. Sun, H. Hu, and S. Li, "Microstructural observation and tensile properties of ODS-304 austenitic steel," *Mater. Sci. Eng. A*, vol. 559, pp. 287–292, Jan. 2013.

[81] M. Saber, W. Xu, L. Li, Y. Zhu, C. C. Koch, and R. O. Scattergood, "Size effect of primary Y2O3 additions on the characteristics of the nanostructured ferritic ODS alloys: Comparing as-milled and as-milled/annealed alloys using S/TEM," *J. Nucl. Mater.*, vol. 452, no. 1–3, pp. 223–229, Sep. 2014.

[82] L. Dai, Y. Liu, and Z. Dong, "Size and structure evolution of yttria in ODS ferritic alloy powder during mechanical milling and subsequent annealing," *Powder Technol.*, vol. 217, pp. 281–287, Feb. 2012.

[83] P. Krautwasser, A. Czyrska-Filemonowicz, M. Widera, and F. Carsughi, "Thermal stability of dispersoids in ferritic oxide-dispersion-strengthened alloys," *Mater. Sci. Eng. A*, vol. 177, no. 1–2, pp. 199–208, Apr. 1994.

[84] G. B. Schaffer, M. H. Loretto, R. E. Smallman, and J. W. Brooks, "The stability of the oxide dispersion in INCONEL alloy MA6000," *Acta Metall.*, vol. 37, no. 9, pp. 2551–2558, Sep. 1989.

[85] M. Ratti, D. Leuvrey, M. H. Mathon, and Y. de Carlan, "Influence of titanium on nano-cluster (Y, Ti, O) stability in ODS ferritic materials," *J. Nucl. Mater.*, vol. 386–388, pp. 540–543, 2009.

[86] S. Ohtsuka, T. Kaito, S. Kim, M. Inoue, T. Asayama, M. Ohnuma, and J. Suzuki, "Effect of Nano-Size Oxide Particle Dispersion and δ-Ferrite Proportion on Creep Strength of 9Cr-ODS Steel," *Mater. Trans.*, vol. 50, no. 7, pp. 1778–1784, 2009.

[87] H. Kishimoto, R. Kasada, O. Hashitomi, and A. Kimura, "Stability of Y–Ti complex oxides in Fe–16Cr–0.1Ti ODS ferritic steel before and after heavy-ion irradiation," *J. Nucl. Mater.*, vol. 386–388, pp. 533–536, 2009.

[88] L. Toualbi, M. Ratti, G. André, F. Onimus, and Y. de Carlan, "Use of neutron and X-ray diffraction to study the precipitation mechanisms of oxides in ODS materials," *J. Nucl. Mater.*, vol. 417, no. 1–3, pp. 225–228, 2011.

[89] I. Hilger, M. Tegel, M. J. Gorley, P. S. Grant, T. Weißgärber, and B. Kieback, "The structural changes of Y2O3 in ferritic ODS alloys during milling," *J. Nucl. Mater.*, vol. 447, no. 1–3, pp. 242–247, Apr. 2014.

[90] A. P. Backhouse, S. S. Babu, K. Mino, and H. K. D. H. Bhadeshia, "Project Report - Part II," 1991.

[91] R. Kasada, N. Toda, K. Yutani, H. S. Cho, H. Kishimoto, and A. Kimura, "Pre- and post-deformation microstructures of oxide dispersion strengthened ferritic steels," *J. Nucl. Mater.*, vol. 367–370, pp. 222–228, Aug. 2007.

[92] J. H. Lee, "Development of oxide dispersion strengthened ferritic steels with and without aluminum," *Front. Energy*, vol. 6, no. 1, pp. 29–34, Mar. 2012.

[93] H. Oka, M. Watanabe, S. Ohnuki, N. Hashimoto, S. Yamashita, and S. Ohtsuka, "Effects of milling process and alloying additions on oxide particle dispersion in austenitic stainless steel," *J. Nucl. Mater.*, vol. 447, pp. 248–253, 2014.

[94] H. Oka, M. Watanabe, N. Hashimoto, S. Ohnuki, S. Yamashita, and S. Ohtsuka, "Morphology of oxide particles in ODS austenitic stainless steel," *J. Nucl. Mater.*, vol. 442, no. 1–3, pp. S164–S168, Nov. 2013.

[95] E. Arzt and D. S. Wilkinson, "Threshold stresses for dislocation climb over hard particles: The effect of an attractive interaction," *Acta Metall.*, vol. 34, no. 10, pp. 1893–1898, 1986.

[96] W. Sha and H. K. D. H. Bhadeshia, "Modelling of recrystallisation in mechanically alloyed materials," *Mater. Sci. Eng. A*, vol. 223, no. 1–2, pp. 91–98, Feb. 1997.

[97] A. Czyrska-Filemonowicz, "Microscopy (AFM, TEM, SEM) studies of oxide scale formation on FeCrAl based ODS alloys," *Solid State Ionics*, vol. 117, no. 1–2, pp. 13–20, Feb. 1999.

[98] B. Dubiel, W. Osuch, M. Wróbel, P. J. Ennis, and A. Czyrska-Filemonowicz, "Correlation of the Microstructure and the Tensile Deformation of Incoloy MA956," *J. Mater. Process. Technol.*, vol. 53, pp. 121–130, 1995.

[99] T. S. Chou and H. K. D. H. Bhadeshia, "Recrystallization temperatures in mechanically alloyed oxide-dispersion-strengthened MA956 and MA957 steels," *Mater. Sci. Eng. A*, vol. 189, no. 1–2, pp. 229–233, Dec. 1994.

[100] W. Betz, R. Brunetaud, D. Coutsouradis, H. Fischmeister, T. B. Gibbons, I. Kvernes, Y. Lindblom, J. B. Marriott, and D. B. Meadowcroft, Eds., *High Temperature Alloys for Gas Turbines and Other Applications*. D. Reidel Publishing Company, 1986.

[101] J. R. O. Leo (2014) *Heat Treatment of ferritic ODS steel MA956.* Unpublished research, The Open University

[102] T. S. Chou, "Recrystallisation behaviour and grain structure in mechanically alloyed oxide dispersion strengthened MA956 steel," *Mater. Sci. Eng. A*, vol. 223, no. 1–2, pp. 78–90, Feb. 1997.

[103] M. E. Kassner and M. T. Pérez-Prado, *Fundamentals Of Creep In Metals and Alloys*, Second Edi. Elsevier, 2009.

[104] M. Tarr, "Stress and its effect on materials." [Online]. Available: http://www.ami.ac.uk/courses/topics/0124_seom/index.html.

[105] H. J. Frost and M. F. Ashby, *Deformation-Mechanism Maps: The Plasticity and Creep of Metals and Ceramics*. Pergamon Press, 1982.

[106] M. Tamura, H. Sakasegawa, A. Kohyama, H. Esaka, and K. Shinozuka, "Creep deformation of iron strengthened by MX type particles," *J. Nucl. Mater.*, vol. 329–333, P, no. 0, pp. 328–332, 2004.

[107] R. L. Klueh, P. J. Maziasz, I. S. Kim, L. Heatherly, D. T. Hoelzer, N. Hashimoto, E. A. Kenik, and K. Miyahara, "Tensile and Creep Properties of an Oxide Dispersion-Strengthened Ferritic Steel," *J. Nucl. Mater.*, vol. 307–311, pp. 773–777, 2002.

[108] R. W. Evans, J. Preston, B. Wilshire, and E. A. Little, "Creep transients in a nuclear-grade ODS ferritic steel," *J. Nucl. Mater.*, vol. 195, pp. 24–28, 1992.

[109] J. Malaplate, F. Mompiou, J. L. Béchade, T. Van Den Berghe, and M. Ratti, "Creep behavior of ODS materials: A study of dislocations/precipitates interactions," *J. Nucl. Mater.*, vol. 417, no. 1–3, pp. 205–208, 2011.

[110] T. Hayashi, P. M. Sarosi, J. H. Schneibel, and M. J. Mills, "Creep response and deformation processes in nanocluster-strengthened ferritic steels," *Acta Mater.*, vol. 56, no. 7, pp. 1407–1416, Apr. 2008.

[111] C. Zakine, C. Prioul, and D. François, "Creep behaviour of ODS steels," *Mater. Sci. Eng. A*, vol. 219, no. 1–2, pp. 102–108, 1996.

[112] J. Rösler and E. Arzt, "A new model-based creep equation for dispersion strengthened materials," *Acta Metall. Mater.*, vol. 38, no. 4, pp. 671–683, 1990.

[113] D. J. Srolovitz, M. J. Luton, R. Petkovic-Luton, D. M. Barnett, and W. D. Nix, "Diffusionally modified dislocation-particle elastic interactions," *Acta Metall.*, vol. 32, no. 7, pp. 1079–1088, 1984.

[114] A. Wasilkowska, M. Bartsch, U. Messerschmidt, R. Herzog, and A. Czyrska-Filemonowicz, "Creep mechanisms of ferritic oxide dispersion strengthened alloys," *J. Mater. Process. Technol.*, vol. 133, no. 1–2, pp. 218–224, Feb. 2003.

[115] A. Rao, "Creep and Anelastic Deformation in Austenitic Steels," The Open University, 2010.

[116] M. Biberger and J. C. Gibeling, "Analysis of creep transients in pure metals following stress changes," *Acta Metall. Mater.*, vol. 43, no. 9, pp. 3427–3260, 1995.

[117] J. C. Gibeling and W. D. Nix, "Observations of anelastic backflow following stress reductions during creep of pure metals," *Acta Metall.*, vol. 29, no. 10, pp. 1769–1784, 1981.

[118] C. N. Ahlquist and W. D. Nix, "The measurement of internal stresses during creep of al and Al-Mg alloys," *Acta Metall.*, vol. 19, no. 4, pp. 373–385, Apr. 1971.

[119] M. Pahutová, J. Čadek, and V. Černý, "Transients in the creep of a 16Cr-12Ni-2.5Mo austenitic steel II: Structure," *Mater. Sci. Eng.*, vol. 62, no. 1, pp. 33–40, Jan. 1984.

[120] K. Sawada, K. Kimura, and F. Abe, "Mechanical response of 9% Cr heat-resistant martensitic steels to abrupt stress loading at high temperature," *Mater. Sci. Eng. A*, vol. 358, no. 1–2, pp. 52–58, Oct. 2003.

[121] R. A. Winholtz, "Analysis of residual stress by diffraction using neutron and synchrotron radiation," *Characterization of Macrostresses*. Taylor & Francis, London, pp. 60–77, 2003.

[122] A. Lodini, "Calculation of residual stress from measured strain," in *Analysis of Residual Stress by Diffraction using Neutron and Synchrotron Radiation*, M. E. Fitzpatrick and A. Lodini, Eds. Taylor & Francis, 2003, pp. 47–59.

[123] C. Gaudin and X. Feaugas, "Cyclic creep process in AISI 316L stainless steel in terms of dislocation patterns and internal stresses," *Acta Mater.*, vol. 52, no. 10, pp. 3097–3110, Jun. 2004.

[124] G. Facheris and K. G. F. Janssens, "Cyclic mechanical behavior of 316L: Uniaxial LCF and strain-controlled ratcheting tests," *Nucl. Eng. Des.*, vol. 257, no. 0, pp. 100–108, 2013.

[125] H. Mughrabi, "Dislocation wall and cell structures and long-range internal stresses in deformed metal crystals," *Acta Metall.*, vol. 31, no. 9, pp. 1367–1379, Sep. 1983.

Chapter 3 – Experimental Techniques

3.1 Introduction

The investigations carried out on the steels demanded several series of mechanical tests, with appropriate apparatuses and devices, as well as the use of different techniques for surveying the microstructure and study its evolution. This chapter, then, describes the experimental set-up and provides a brief scientific background of the techniques employed.

The first part is dedicated to the tests concerning macroscopic mechanical properties of the materials. Mechanical tests for determining tensile strength, ductility, creep-rupture life and anelastic response in creep transients are detailed in terms of Standards, specimen design, machine specifications, devices for recording the strain and data analysis procedures.

In later section, the use of diffraction techniques is covered, with particular emphasis on neutron diffraction for the measurement of lattice strains and intergranular stresses. Finally, the last section concerns microstructural assessment techniques based on image data from which evolution of the internal state of the materials is analysed. These include optical and electron microscopy and complementary methods of the microscopes.

3.2 Uniaxial tensile test

The uniaxial tensile tests, carried out at room temperature and high temperature (650°C), were aimed at the characterisation of the tensile properties of the ODS steels studied. Conducted under the guidance of the ASTM E8M Standard [1], these tests were divided in two experimental set ups, one for room temperature and the other one for high temperature.

For room temperature tensile tests, a flat specimen design was chosen, following dimensions and proportions recommended in the ASTM E8M, as illustrated in Figure 3.1:

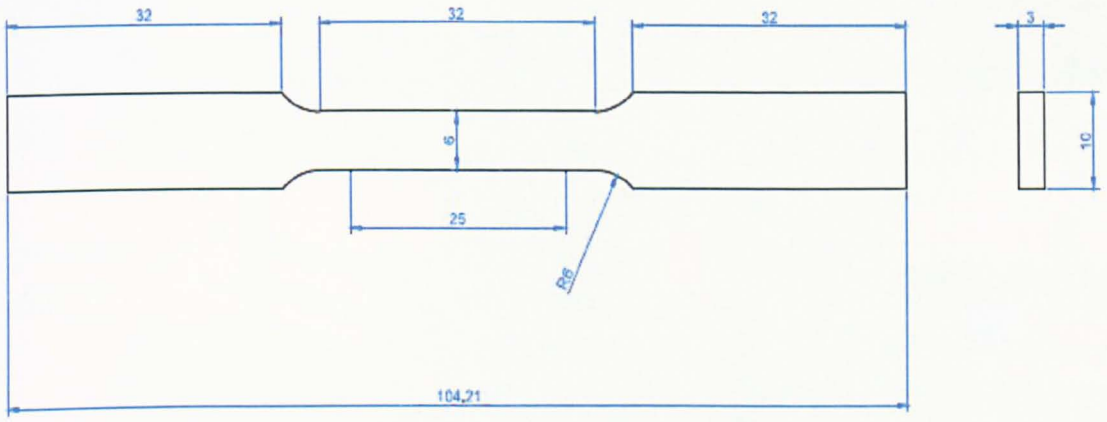

Figure 3.1 - Room temperature tensile specimen geometry (drawing). Dimensions in mm.

An Instron 5969 test rig with 50 kN load capacity was used for carrying out the tests at a strain rate of 4 $\times 10^{-4}$ s^{-1}, which is equivalent to a displacement rate of 10^{-2} mm/s, given the gauge length of 25 mm of the specimens. Parameters for the tensile test execution were controlled through built-in Instron Bluehill software, and the strains were measured by an Instron 2620-601 extensometer, mounted onto the specimen gauge length and interfaced with the machine and the software. This extensometer has a gauge length of 12.5 mm and a maximum travel of ±2.5 mm, and is appropriate for flat specimens, given the flat knife-edges, which can be pressed against the gauge length of the sample and kept firm in position by passing springs around the specimen and connecting them to the knife-edges, as shown in Figure 3.2.

Prior to the tensile tests, calibration of the extensometer was conducted, using the Instron calibrator unit in order to ensure accuracy of the strain measurements. With the elongation of the specimen, as the test proceeds, the legs of the extensometer move apart, thus transmitting mechanical displacement to the strain gauge housed in the extensometer body. It is the conversion of this displacement into an electrical signal, by the extensometer strain gauge, that allows real time monitoring of the strains.

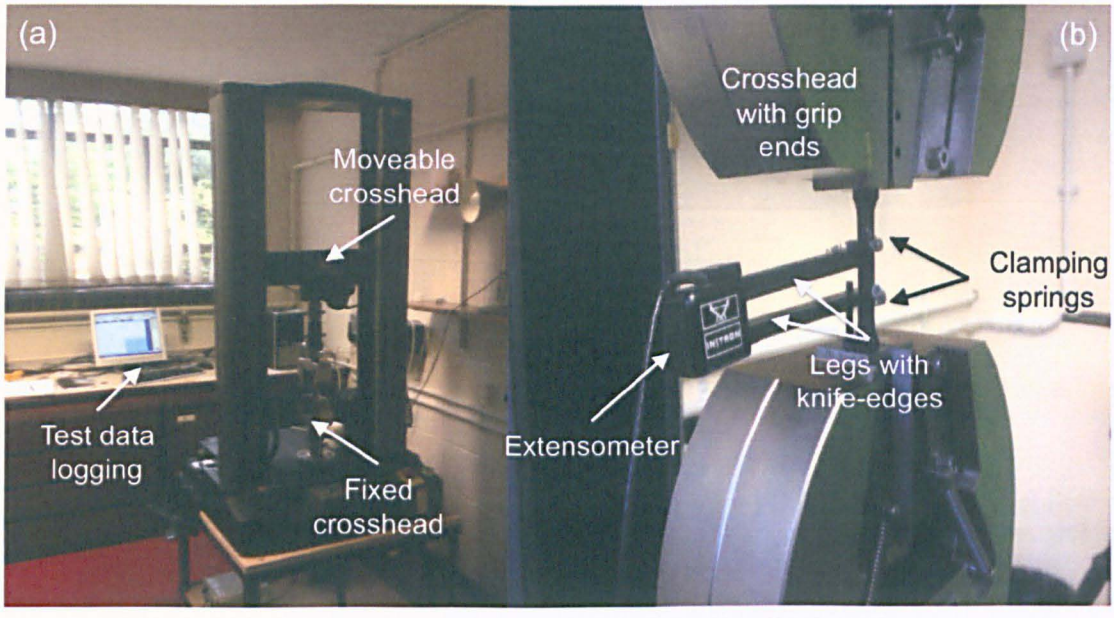

Figure 3.2 - Pictures of (a) Instron test machine and data logging system and (b) detail of experimental set-up, showing the extensometer fixed onto the specimen.

The high temperature tensile tests were performed using round samples of 4 mm gauge diameter and 20 mm gauge length, also designed according to ASTM E8M. The dimensions of the sample, corresponding to the sub-sized round specimen geometry in the Standard, can be seen in Figure 3.3. Ideally, flat specimens would be preferable, given that they can be machined with less waste of material and, therefore, produce a larger number of samples. However, since the equipment used in the room temperature tensile tests does not contain high temperature apparatus, specimens for high temperature tests had to be redesigned for the appropriate rig.

For the high-temperature tests, an Instron 8862 slow strain-rate machine, with 100 kN load cell and a screw electromechanical actuator, was used in displacement control mode. Likewise, parameters were monitored via Bluehill software.

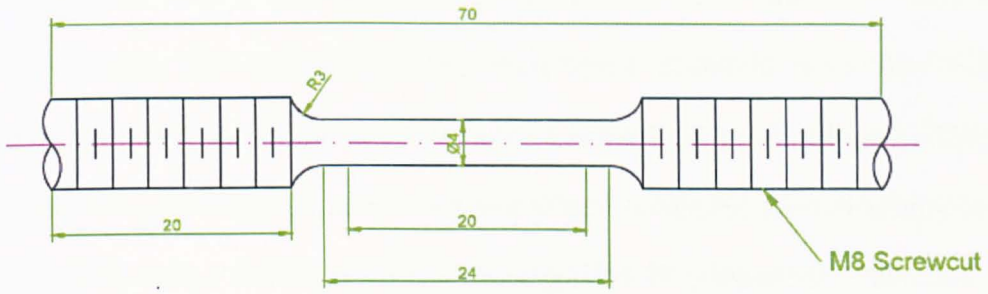

Figure 3.3 - Round specimen design for high temperature tensile tests. Dimensions in mm.

A high temperature extensometer model Instron 2632-054, attached to the specimen via two ceramic cords holding the quartz (or alumina) rods steadily in position, and also interfaced with the machine, measured the strains, developed under a strain rate of 5×10^{-4} s^{-1}; that is, a displacement rate of 0.01 mm/s, and supplied them to the Bluehill control software.

The Instron 8862 machine uses a split construction furnace for achieving the desired temperature of 650°C. Two thermocouples type N were attached to the specimen as figure 3.4 shows:

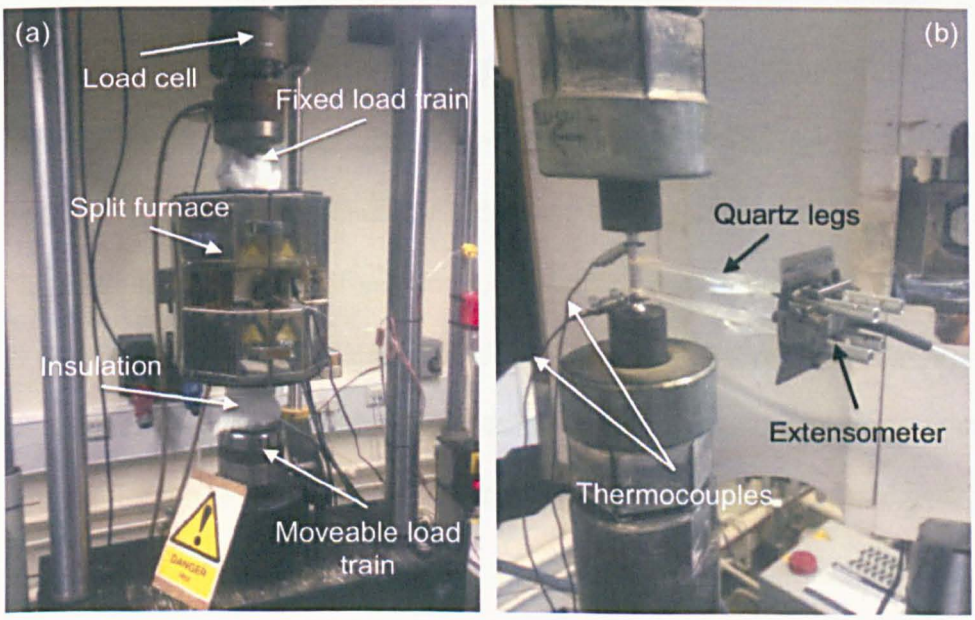

Figure 3.4 - Instron 8862 machine (a) and experimental assembly (b).

In order to obtain uniform temperature along the specimen, a Eurotherm 3216 controller was used, in which temperature adjustments allow the creation of three independent heating zones in the furnace (top, middle and bottom), by radiation and convection heat transfer processes. The temperatures read by the N-type thermocouples, firmly attached to the sample by bracing wires and clamps, were used to determine the desired 650°C within a variation of ±1°C.

Time, crosshead extension, strain (from the extensometer) and applied load, were continuously recorded and exported as raw data for analysis and calculations of ductility (determined by the elongation of the sample), yield stress and ultimate tensile strength.

3.3 Uniaxial creep tests

Constant load uniaxial creep tests are based on applying loads and recording the produced strains. These tests were carried out by loading the specimen at a constant temperature of 650°C, aiming to observe the creep ductility; the creep-rupture life, assessed by the total time to fracture, and the anelastic response following the removal of the load at some point in secondary creep stage.

The series of creep tests were based on the recommendations in Standard BS EN ISO 204: 2009 [2]. Thus, temperatures were kept within ±2°C of the intended value, so that stability during the test could be maintained. Since creep is a temperature-dependent phenomenon, it is important to minimize the variations. Before the onset of each test, regardless of the purpose, the specimens were held at the test temperature for at least 30 minutes under zero load, so that homogeneity and stability of readings could be achieved. Similarly to the high temperature tensile tests, N-type thermocouples were attached to the gauge length of the specimens for continuous monitoring of the temperatures, which were recorded at regular intervals using a PicoLog reader and software.

In the case of ODS steels, scaling down the samples to sub-sizes was necessary to overcome the shortage of material and maximise the number of specimens. The series of

creep transient tests on the 316H specimens employed cylindrical samples whose dimensions were provided by the ASTM E8M Standard for regular size creep specimens. Its drawing can be found in the Appendix 1. These tests make use of the same devices and experimental set up as the high temperature tensile tests, except for the loading conditions and the control mode, which has extension replaced by load in the case of creep tests. Also, after the tests, the split furnace was opened and specimens were quickly cooled to ambient temperature, while still under load, in an effort to preserve the microstructure.

Both ODS steels investigated, the ODS 316L and the MA956 ferritic steel, were subjected to creep-rupture tests, for characterisation of their creep properties, as well as for comparison of their behaviour with that of conventional alloys. In the case of MA956, the tests were also aimed at determining potential effects caused by anelasticity, induced by the load transients, on the creep-rupture life. Similar investigations could not be reproduced for the ODS 316L due to insufficient material.

For the ODS 316L, a bespoke solution was adopted, in order to overcome the limitations imposed by the shortage of material, which would admit the fabrication of only one regular size creep sample, considering all the tests of the experimental programme. Miniaturized creep specimens were designed following ECCC Recommendations, part III, issue 4 [3]. They were machined with a gauge diameter of 3.8 mm and 19 mm gauge length. Full dimensions can be seen in Appendix 1, which shows all creep specimen designs used. This approach was adopted following Mälzer et al. [4], who used flat dog-bone-type mini specimens for studying creep behaviour of a single-crystal nickel superalloy and reported successful correspondence of recorded strains and properties, with regards to conventional size samples, for creep-rupture tests. Creep-rupture specimens of MA956 had their geometry based on the design proposed by British Standard BS EN ISO 204: 2009 [2]. Although similar, in terms of shape, to the ODS 316L specimens, the MA956 samples were regular size, with 8 mm gauge diameter and 50 mm gauge length. This design has tear ridges machined between the gauge length and the shoulders, onto

which the extensometer frame can be fixed, thus allowing changes in gauge length to be measured from the relative movement of the frame arms [5]. This method is reported to yield the most satisfactory means of achieving accuracy on the measurements [6, 7].

All the creep-rupture samples were tested using a constant load creep rig based on dead-weight design and a lever arm capable of increasing the load ratio by 10:1. Figure 3.5 shows a schematic with the subsystems of the rig. Calibrated disks of known weight are placed on the load pan, which is connected to a hanger. This hanger is attached to the 10:1 levering system, which, in turn, connects to the driving subsystem of the machine. All these connections, as well as the fulcrum of the lever arm, use knife-edges, in order to minimize bending stresses [5]. The driving subsystem comprises pull-rods containing universal coupling joints, for flexibility of connections, and an electric motor as driving unit. The specimen is fixed to the load train by means of the threads and is deformed under the load applied by the weights on the load pan. The creep frames are fitted with a limit switch, which is triggered by changes in the specimen gauge length, prompting the motor to drive the pull rods of the load train up or down for maintaining the lever arm horizontal and, thus, keeping the effective ratio unchanged.

These creep frames are also equipped with furnaces, capable of sliding upwards or downwards along the load train, for correct positioning and for accessing the specimen. Each furnace supplies heat independently to the bottom, middle and top zones, according to the set point adjustments on the Eurotherm 3200 controllers.

In these creep tests, strain was constantly monitored and recorded at regular intervals, starting with readings being taken every two minutes and, then, once secondary creep was reached, time intervals of 5 minutes. In most creep frames of similar construction, Linear Variable Displacement Transformers (LVDT's) are employed, which means that displacement is the variable monitored and measured, so that obtaining of the strain values requires conversion.

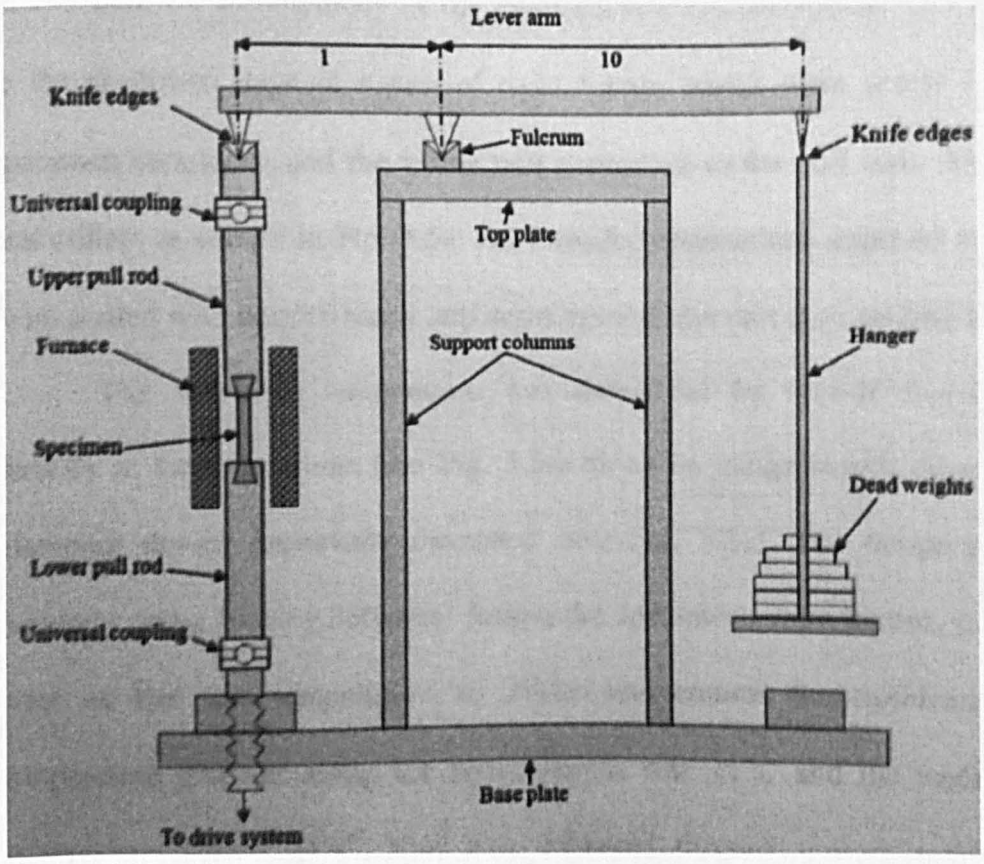

Figure 3.5 - Schematic of a constant load creep frame.

The LVDT reads displacement based on the principle of electromagnetic induction. It consists of a primary coil and two secondary coils symmetrically spaced and wrapped around a core in an insulated bobbin, as shown in figure 3.6. The primary coil is excited by an alternating current, thus creating an alternating magnetic field, which induces voltages in the secondary coils. These induced voltages depend on the position of the core. When it is centred, the voltages in the secondary coils are equal, but with opposite signs, resulting in a zero net output voltage. Within certain limits, the deformation of the gauge length of the specimen to which the LVDT is attached causes the core to move from the centre, in which case an output voltage is developed in the secondary coils, being linearly proportional to the displacement.

For each creep specimen, two LVDT's were used. They had a maximum travel of 5 mm and a displacement resolution of 1μm. The LVDT's were calibrated before each test with

an Instron device, for improvement of accuracy, and connected to a Solatron box, which is a conditioning unit for calculating the displacement from the voltage.

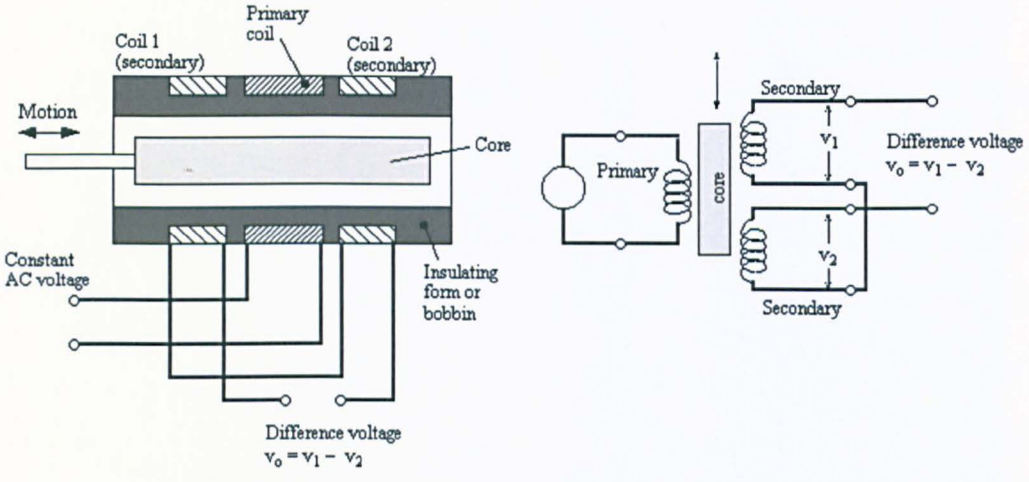

Figure 3.6 - Section view of the LVDT and corresponding circuit diagram [8].

The experimental assembly ensured that the LVDT's were put in connection with the specimen by means of a pair of rigid frames that were clamped to the tear ridges machined on the shoulders of the specimens (Appendix 1). The whole unit, then, was fixed to the pull rods by nose caps and collets, as figure 3.7 illustrates.

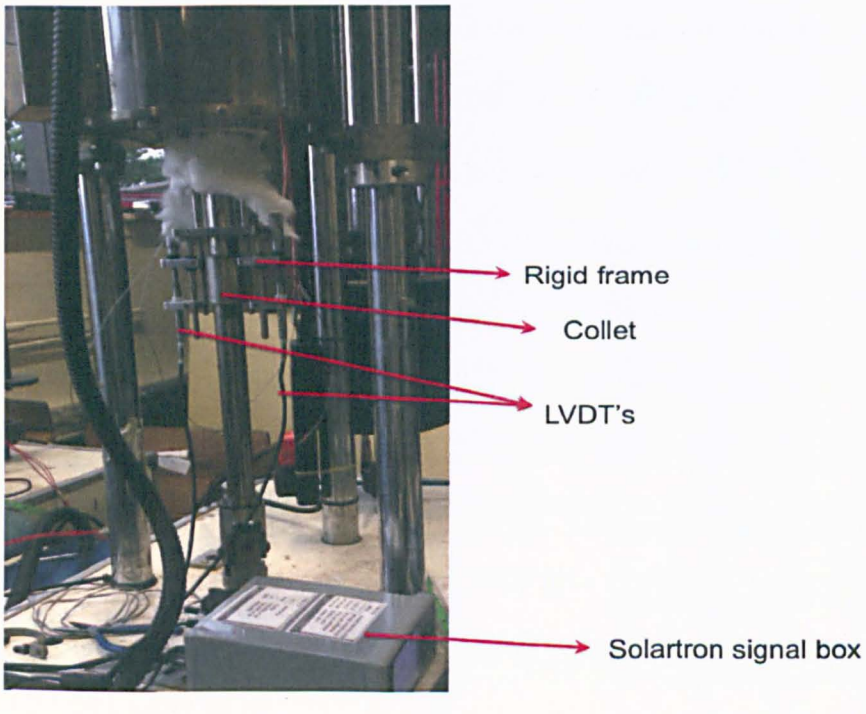

Figure 3.7 - Set-up of the LVDT's frame on the load train of the machine.

In-house software was used to monitor and record the raw data from the test, comprised by output voltage, the correspondent displacement, obtained as the average of the two LVDT's connected to each test specimen, and the elapsed time. These data were employed to compute the total creep strain and the time to rupture. Since three different stress levels were used in the creep-rupture tests for the ODS 316L, it was possible to use a parametric representation, namely, the Larson-Miller parameter (LMP), in order to estimate the behaviour of the alloy under longer creep conditions, for which a test is impractical. Although the use of these parameters for extrapolation requires caution, due to the fact that they do not take into account changes in the microstructure of the alloy that may arise from longer exposure to high temperatures [7], they are a reasonable means of having a preliminary idea of the relative creep performances of materials under long-term creep.

3.4 Hardness Measurements

Hardness is defined as the resistance offered by a material to localized plastic deformation. While it provides useful information on the material's properties, it does not constitute an intrinsic property in itself. The tests are based on the application of a force, onto the surface of a material, by a small indenter at controlled conditions of load and rate of penetration [9]. The depth or geometry of the resulting indentation is measured and converted into a number, according to a scale related to the technique used. The softer the material, the larger (or deeper) the mark produced, resulting in a lower hardness index number. These tests, although providing relative information, are widely deployed, given the ease and simplicity of execution and its relatively non-destructive character: preparation of sample involves only the conventional grinding and polishing required for any other microstructural survey; and no fracture or excessive deformation is imposed [10].

The hardness measured in the current investigations made use of the Vickers technique of testing, based on a square-shaped diamond pyramid indenter presenting 136° between

the indenter facets. The measurements were carried out following guidelines from ASTM E384 [11], using a Struers Duramin A300 Vickers machine, with 5 kgf of force applied for 10 seconds. The spacing between consecutive indentations was, at least, three times the dimensions of the diagonals, as advocated by ASTM E384, resulting in an adopted value of 0.75 mm for the indenter spacing. In terms of the physical parameters involved, the Vickers hardness number is given by [9, 10]:

$$HV = \frac{2P\,sin\left(\xi/2\right)}{d_1^2} = \frac{1.854P}{d_1^2} \qquad \text{(Eq. 3.1)}$$

where P is the applied load in kgf, ξ is the angle between the indenter's punching facets (136° in the case of Vickers micro hardness) and d_1 is the average length, in mm, of the indentation diagonals, determined from microscopic measurements.

Hardness measurements were performed on all materials investigated in the experimental programme. In the case of the 316H, this technique was used as a preliminary assessment of the relative hardening/softening of the steel at each condition investigated, starting with the as-received and following interruptions at the steady-state creep stage, the anelastic recovery stage and the reloading stage. In the case of the ODS steels, Vickers hardness provided primary appraisals on the effects of high temperature exposure on their microstructures, either due to heat treatment, in the case of the MA956 steel, or due to the diffusion bonding process to which the ODS 316L was subjected, as explained in Chapter 5.

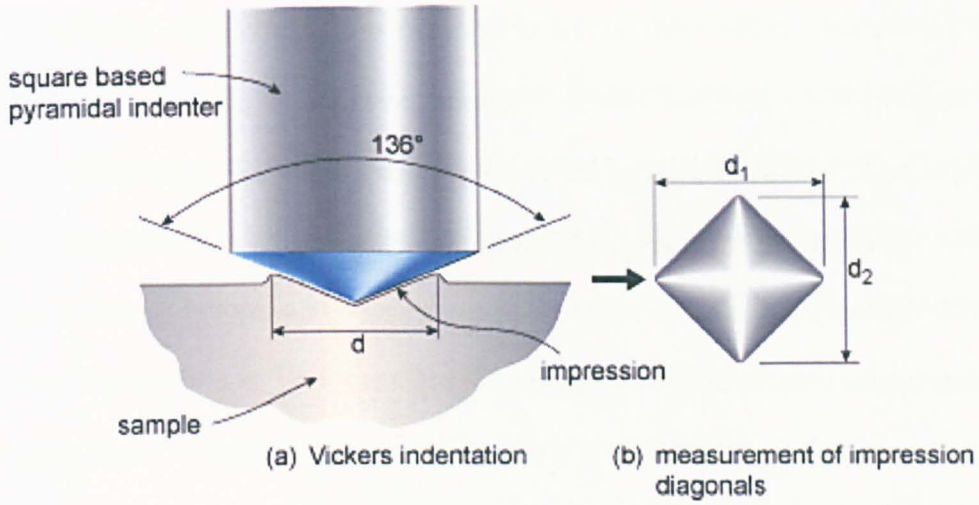

Figure 3.8 - Schematic of indenter (a) and measurement of diagonals (b) in Vickers hardness test [12].

3.5 Mechano-acoustic test for Young's modulus

Young's modulus is a property of the material quantifying its stiffness, that is, the resistance the material offers against being elastically strained under a certain stress. In basic physical mechanisms, it is related to how easily atoms can be displaced from their equilibrium positions when the lattice is stretched by the applied stress. The magnitude of the Young's modulus of ferritic and austenitic steels is reported to decrease linearly with increasing temperature up to a certain level, after which the drop is more pronounced, although the temperature levels at which the drop starts differs from one steel to the other [13].

While it is common practice to measure the Young's modulus from tensile tests, by evaluating the slope of the elastic portion of the stress vs. strain curve, there are cases where alternative procedures are desirable: for example, when the material's tensile curve do not show a linear proportionality between stress and strain, even though they are still in the elastic region of a test, which is the case of rubber; or due to inaccuracies of measurement, bias or external disturbance. One such alternative is the mechano-acoustic technique, based on the natural frequencies of response of the material to a step excitation, caused by hitting the sample with a small rigid hammer.

Being preferable to the conventional determination of the Young's modulus, since it yields more reliable results, the mechano-acoustic technique relies on specific frequencies of the specimen, which are determined by its geometry, mass and mechanical properties. Given the relevance of these parameters, well-defined specimen geometry and accurately measured physical properties are required, as advocated by the ASTM E1876-09 Standard for dynamic measurement of Young's modulus [14].

Mechano-acoustic measurements of Young's modulus were made on both ODS steels, the ODS 316L and the MA956. Following recommended procedures and suggestions of the standard, but, also, being careful not to waste material, given the limited amount available in some cases, the rectangular bar shape was adopted. The arbitrarily defined dimensions were, first, entered into an Excel spread sheet containing the expression, reproduced below in equation 3.2, for the calculation of Young's modulus from the flexural vibration modes of a rectangular bar, as defined by the ASTM C1259; for an initial estimation of the fundamental resonant frequency of the material:

$$E = 0.9465.\left(\frac{m.f_f^2}{w}\right).\left(\frac{L}{t_t}\right)^3.T_1$$

(Eq. 3.2)

where E is the Young's modulus, for which an approximate value is used (in this case, since both materials are stainless steels, 200 GPa was a reasonable approximation), m is the mass of bar, in grams; w is the width of the bar, in mm; L, the length of the bar, and t_t, its thickness, are also in mm; f_f is the fundamental flexural frequency of the sample, in Hz and, T_1 is an ASTM C1259 correction factor for the calculation of the flexural mode that accounts for the finite thickness of the sample, errors in Poisson's ratio, etc. [15]. This step is important, since there is a limitation associated with the fact that the frequencies should not exceed approximately 18 kHz, the maximum frequency the measurement system is capable of detecting.

The rectangular bar sample of ODS 316L was cut with 30 mm x 5 mm x 3 mm as nominal dimensions, and the MA956, for which the specimen could be machined with larger dimensions (due to its larger batch), presented a rectangular bar with 40 mm x 14 mm x 4.85 mm. These dimensions were checked to produce reasonable resonant frequencies (that is, below 18 kHz). A high-precision scale (±0.0001) was used to measure the mass of the specimens. Their densities, for the purpose of data input to the test analysis software, were determined using Archimedes principle, which consists in immersing them in water and calculating the density from the weight of the displaced liquid. This was done by attaching a thin wire around the specimen, being careful to minimize the portion of wire submerged and slightly reducing the surface tension of the water with a drop of surfactant. A high-precision scale was used to measure the weight of the displaced water. This technique leads to more accurate results, since it is capable of addressing the deviations from the nominal values as well as the microscopic surface irregularities, which affect the volume of material. After these data were entered into the RFDA-MF software, its internal routines calculated the distance between the tensioned cords of the cradle that provide the support points on which the specimens rest (nodes) and the distance between the first node and one extreme of the sample. Then, the experimental procedure is reduced to hitting the specimen with a small hammer, while a microphone records the resulting natural frequencies of vibration and transfers the data to the software. Figure 3.9a shows the experimental apparatus for the technique, while figure 3.9b depicts the RFDA-MF software interface, with plots of the signal in time and frequency domains and the calculated value of Young's modulus, which produces uncertainties as low as less than 1%:

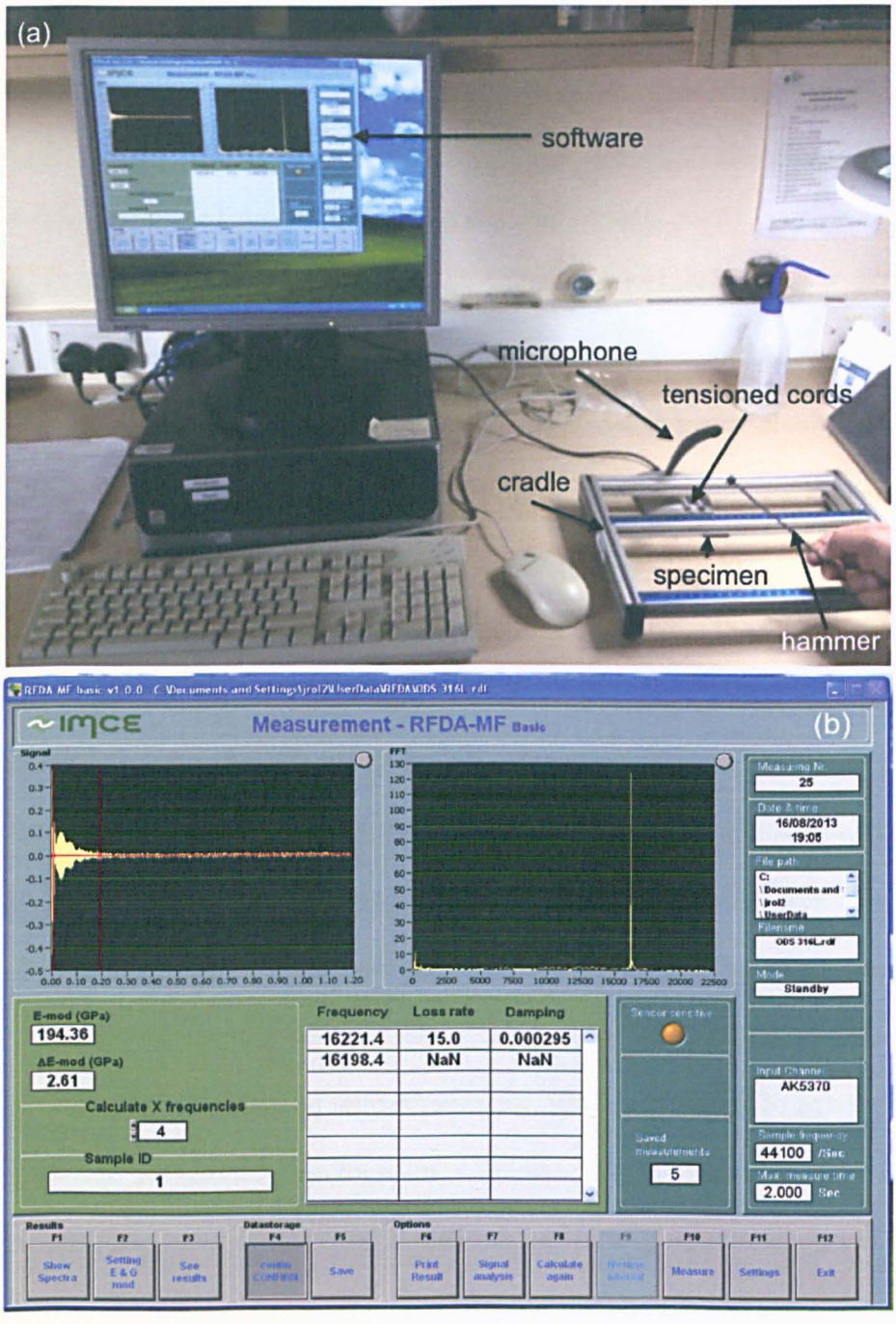

Figure 3.9 - Experimental set-up (a) and software interface (b) for the mechano-acoustic test.

The RFDA-MF software takes the signal in time domain and, executing a Fast Fourier Transform (FFT) upon the data, plots the amplitudes against the frequency. The peaks correspond to natural (resonance) frequencies of the material, and the dimensions and physical properties provided will be used to calculate the Young's modulus.

3.6 Diffraction and Scattering

When electromagnetic radiation, in the form of waves, is incident on a crystalline material presenting a periodic atomic arrangement, the three-dimensional nature of the interaction will cause atoms to scatter the incident beam in all directions. When the scattering occurs elastically, that is, the energy of the parallel incident beam is preserved, and the scattered beams mutually reinforce each other, it is termed diffraction [16]. For diffraction to take place, it is necessary that the wavelength of the incident beam present the same order of magnitude as the entities that will serve as obstacles and with which the beam will interact. The conditions for a crystalline material to diffract an incident beam are mathematically described by Bragg's law, which relates the mutual reinforcement of scattered beams with the difference in their path length. This latter, in turn, is related to the interplanar spacing d. From Bragg's law, expressed by equation 3.3, the d spacings can be determined, provided that the wavelength, λ, of the incident beam and the incidence angle θ are known [9]:

$$\lambda = 2d \sin \theta \qquad \text{(Eq. 3.3)}$$

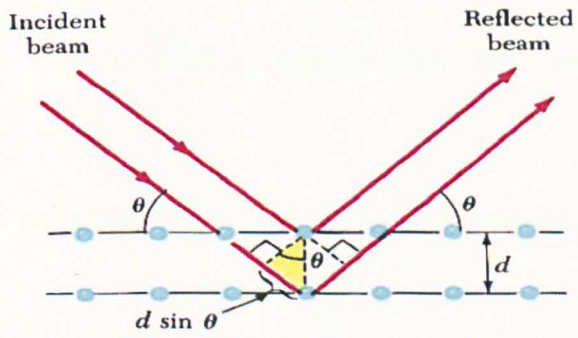

Figure 3.10 - Schematic of diffraction – adapted from [9].

3.6.1 Neutron Diffraction

The usefulness of the phenomenon described above lies on the fact that it can be used to detect changes in the d spacings, from which intergranular elastic strains can be calculated and used to determine the internal stresses. From these data, it is possible to assess the

elastic anisotropy of a polycrystalline material, associated with the differences in stiffness and tendency to yield, among the differently oriented grains [17].

Due to their capability of penetrating many centimetres in the bulk of a material, and wavelengths that are comparable to the atomic interplanar spacing of many crystalline materials, neutrons are widely used for measuring internal stresses. Other advantages include their electrical neutrality, which ensures they will not interact with electrons of an atom, but with the nuclei instead, thus preserving the chemical state of the material; and the fact that neutrons behave as waves under the conditions of their deployment in diffraction [17, 18], which allows the use of DeBroglie's principle of wave-particle duality to derive the relation between their velocities and wavelengths. From Planck's equation, the energy E_f of oscillation of a physical component – either wave or particle – is related to the frequency f, as expressed by $E_f = hf$, where h is Planck's constant. But, also, from the relation between energy and mass of accelerated particles, Einstein's equation, $E_f = m.c^2$; rewriting this equation in terms of the linear momentum of a photon, p, and equating this equation and Planck's, comes:

$$m.c.c = hf \ \therefore p = \frac{hf}{c}$$

(Eq. 3.4)

But, for electromagnetic waves, it is known that $c = \lambda.f$; replacing this in equation 3.4:

$$p = \frac{hf}{\lambda f} \therefore p = \frac{h}{\lambda}$$

(Eq. 3.5)

DeBroglie established that the relation expressed in equation 3.5 is general, being valid for photons and particles alike. The linear momentum of a neutron in motion is $p = mv$, where m is the mass of the neutrons. Replacing it in equation 3.5 and rearranging for the wavelength:

$$\lambda = \frac{h}{mv}$$

(Eq. 3.6)

Substituting 3.6 into 3.3:

$$\frac{h}{mv} = 2d \sin\theta$$

(Eq. 3.7)

The length of the path travelled by the neutrons, associated with the time of flight from the source to the detector can be used in equation 3.7 in order to establish relations between elementary parameters:

$$\frac{ht}{mL} = 2d \sin\theta$$

(Eq. 3.8)

From the above equation, it is possible to see that, keeping a constant diffraction angle, the interplanar spacings of different lattice planes can be simultaneously obtained from the elapsed time taken by a parallel beam of neutrons to travel from the source to the detector, which will correspond to different neutron wavelengths, each associated with a particular family of crystal planes [19]. This is exactly the principle of a time-of-flight neutron diffraction instrument. Provided that a reference stress-free interplanar spacing d_0 is measured, the strain can be calculated as:

$$\varepsilon = \frac{d - d_0}{d_0}$$

(Eq. 3.9)

Time-of-flight neutron diffractometers are associated with spallation neutron sources. In these, neutrons are produced in pulsed beams. The process starts with high-energy protons (order of hundreds of MeV) being accelerated in a synchrotron ring, before being delivered to a heavy atomic number target material, such as Ta, Pb, U or W [18, 20]. The collisions cause the nuclei to become unstable and, as a result, neutrons are produced, with a range of

different energies, varying from a few to hundreds of MeV. In these conditions, in which they are called *fast neutrons*, they are unsuitable for diffraction. These neutrons, then, are made to pass through a "moderator", in order to have their energies reduced to the order of magnitude of meV [20]. This is accomplished by placing the moderator, a substance made of light atoms such as liquid methane, water or graphite, among others, around the target. By successive collisions, neutrons are slowed down to the desired distribution of wavelengths, which, then, will be directed (via collimators) to the sample to be measured. A schematic of the basic components of a time-of-flight diffractometer is shown in figure 3.11:

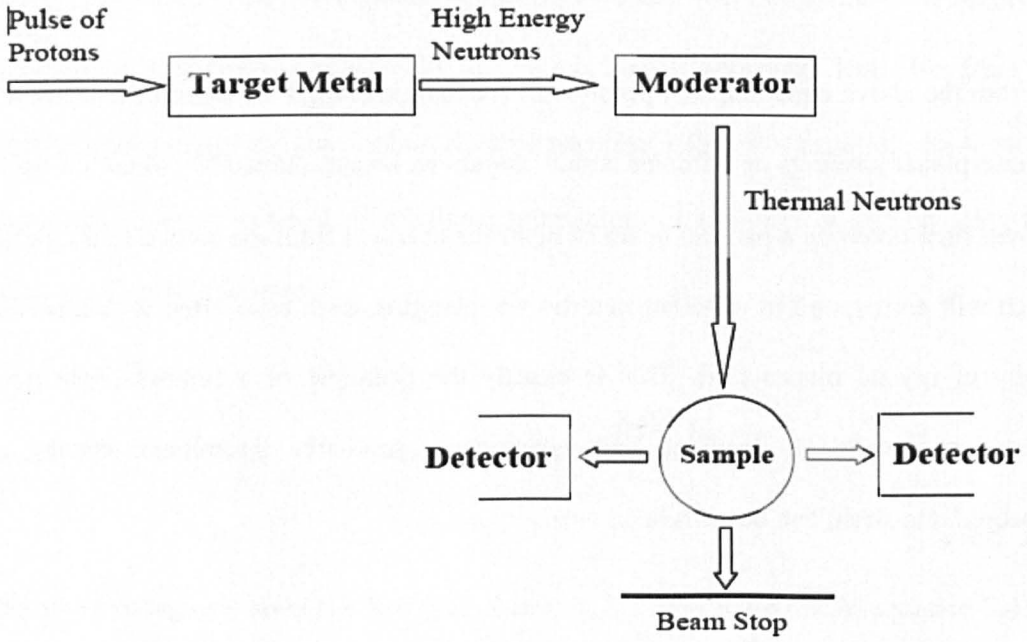

Figure 3.11 - Schematic of a spallation neutron source diffractometer [18].

The two neutron diffraction experiments of the programme were carried out using the ENGIN-X time-of-flight diffractometer at the ISIS Neutron Source, Rutherford Appleton Laboratory, Oxfordshire, UK. This instrument uses protons of 800 MeV to produce neutrons from a tantalum target, with energies ranging from 1 to 800 MeV, which are moderated in liquid methane [16]. Detector banks are placed at 90° from the incident

neutron beam, as shown in the schematic of figure 3.11, and each bank is formed by 135 elements distributed in three horizontal rows spanning an angular range of 15° [18, 20]. In order to obtain the diffraction spectrum, the intensities of the peaks from all detection elements are summed. Then, it is possible to perform either the single-peak fitting, for each grain orientation, or the Pawley (or Rietveld) analysis for the average lattice strain [20, 30].

The alternative way in which neutrons can be produced relates to a reactor source. In this case, a steady state nuclear fission reactor continuously produces neutrons. Modern reactors use an assembly of uranium alloy plates enriched in ^{235}U as the core [16]. Similarly to spallation sources, the neutrons produced are fast neutrons, which are forced to pass through moderators, in order to be slowed down. The beams emitted by the reactor are also polychromatic, with the range of wavelengths being defined by the temperature of thermalization. In this case, in order to be used in diffraction experiments, the beam is made monochromatic, by means of a crystal inserted in the beam tube, which will select a particular wavelength by Bragg scattering; or by using a chopper-like mechanical selector. Experiments with this type of neutron source usually are carried out by using the θ-2θ condition, according to which sample and detector are both rotated, so that Bragg condition is satisfied. The variation of intensity *versus* 2θ (angle of diffraction) is plotted, and, from each angular position, a d-spacing is determined using equation 3.3.

3.7 Microscopy and Microstructural Survey

A routine way of observing the microstructures of materials is by means of microscopy techniques. They are available in several modalities, using sources of different wavelengths; therefore, different resolution capabilities can be achieved according to how deep in the microstructure investigations need to probe. The main microscopy techniques deployed in the present studies are Optical microscopy, Scanning Electron Microscopy (SEM) and Transmission Electron Microscopy (TEM and their complementary resources,

such as X-ray Energy Dispersive Spectroscopy. The next sections are dedicated to some brief explanations of their principles and scope of use.

3.7.1 Optical Micoscopy (OM)

Optical microscopy is, almost always, the primary tool deployed in microstructural assessments under low magnifications. Also known as light microscopy, this technique uses visible light as the incident radiation and a system of lenses for magnifying the images from samples. The resolution of microscopes, that is, their capacity to distinguish, in the image, two points of the sample as separate entities, is given from diffraction theory [21]:

$$d_1 = \frac{0.61\lambda}{\mu . \sin \alpha_0}$$

(Eq. 3.10)

where λ is the wavelength of the radiation used, μ is the refractive index of the medium where sample and objective lens are inserted; α_0 is the semi-angle subtended at the specimen by the microscope objective aperture; and, finally, d_1 represents how far apart two spots must be in order to be resolved. In a light microscope, it is possible to minimize d_1 (that is, improve resolution) by using light of wavelength towards the blue end of the sprectrum (such as green, to which the human eye is more sensitive), thus decreasing λ to approximately 400 nm; by using a large aperture, which may increase $sin\ \alpha$ towards 1; and by using an oil immersion objective lens, with higher refractive index. However, given that it is not practical to have the denominator of equation 3.10 much greater than 1.6, since $sin\ \alpha$ must be less than unity and even exotic materials are usually limited to refractive indexes of the order of 1.7, the resolution of the instrument usually sits about 200 nm [22]. Moreover, given that the human eye detects details only to 0.2 mm [21], optical microscopes should be used to magnify the smallest details that can be resolved only up to this limit, considering that any further magnification will just make the details bigger, but will not provide any extra insight.

For research in materials science, optical microscopy plays an important role, being the tool with which preliminary observation of the microstructure is carried out. With proper preparation, which involves grinding, polishing and etching, contrast between different regions stemming from variations in topography or reflectivity is obtained, allowing distinction between phases, as well as the observation of surface irregularities such as grain boundaries, precipitates, twinning lines, slip bands, etc., which appear dark as their reflected light is not collected by the objective.

In the present study, a Leica DMI 5000M reflection microscope fitted with a Leica DFC280 digital camera was used for observation and capture of images, processed through the Leica Application Suite software. This instrument has an inverted configuration, as shown in figure 3.12, with the specimen table placed on top of the objective lenses and light source. Due to this, only the surface to be examined needs to be flattened (in fact, the mounting procedure automatically leaves only the surface of interest exposed). The microstructural surveys were conducted in bright field mode (BF) and different magnifications. Grain size measurement was carried out using the GrainExpert feature of the Leica Application Suite software, which has the ASTM E112 intercept measurement method embedded. When selected, it draws a pattern of five randomly oriented lines onto the micrograph and determines the grain size from the number of times the lines intercept grain boundaries. Manual corrections for misidentified boundaries are possible in the GrainExpert feature, and were carried out in order to ignore twins and scratches.

Figure 3.12 - Leica DMI 5000M microscope; the specimen is placed on the table, below which the objective lenses and the light source are placed (not visible).

3.7.1.1 Sample preparation

Because the principle of OM is based on reflection of the light, a mirror-like surface finish is required for adequate observation. This surface condition is achieved by carefully conducting the preparation, which involves:

- **Sectioning** the bulk material and/or deformed specimens, in order to extract samples. This was accomplished by using wire EDM cutting, in some cases, and high-speed circular saw in others;

- **Mounting** the samples, in order to protect them from accidental damage as well as for ease of handling; they were hot-mounted in phenolic thermosetting resin, which is electrically conductive and, as such, allowed examination under the scanning electro microscope. The mounting procedure was carried out at a maximum temperature of 150°C, under 2 bar of pressure, with time settings of 10 minutes for heating and 5 minutes for cooling of each sample.

- **Grinding** the mounted samples to remove the damage introduced while sectioning the sample. Conducted on a Buehler semiautomatic grinding machine with increasingly finer silicon carbide grinding paper, as indicated in table 3.1, the grinding procedure has the

advantage of being able to be applied to several samples simultaneously. Similar conditions of load (2.2 lbf per sample), applied for 2 minutes, were imposed on the samples twice for each paper. A counter-rotation of 150 rpm was kept between the grinding plate and the sample holder, with water being constantly poured for the purposes of cooling and lubrication. After the use of each grinding paper, the samples were thoroughly rinsed in tap water, in order to remove grinding particles that might have remained on their surface. This is done to avoid contamination of finer papers with particles from previous coarser ones, given that each grinding stage removes the scratches left by the previous paper on the surface of the specimens.

Table 3.1- Grinding papers used under 2.2 lbf / 2 min (x 2) on the samples.

Grinding paper	Grit size [μm]
P120	78
P240	68
P500	30
P800	22
P1200	14
P2500	8.5
SiC 4000	5

- **Polishing** the ground samples; this stage was executed in two steps, one aimed at removing the scratches and damages produced during the finest grinding stage; and the other aimed at producing a smooth surface finish. For this task, a Struers TegraForce-5 automatic polishing machine was used, with napped cotton cloths (MD-Short and MD-Nap) impregnated with abrasive diamond particles and a high viscosity propylene glycol oily lubricant (RedLube). Polishing conditions are summarised in table 3.2. The machine

was set to operate at 120 rpm, again with counter-rotation between the sample holder and the polishing plate. Four drops of diamond particle suspension and two drops of lubricant per minute were used as injection rates. After each polishing step, samples were once more thoroughly rinsed in soapy water, bathed in isopropanol and dried in hot air, before surface conditions were checked under a low magnification, to ensure good sample quality.

Table 3.2 - Polishing conditions used.

Napped Cloth	Particle size [μm]	Applied load/sample	Time [min]
MD-Short	6	10 N	5 min
MD-Nap	1	15 N	5 min

- **Etching** as the final preparation procedure for OM survey, used to reveal microstructural features by selective chemical attack. The etchant will not only attack high-energy regions, such as grain boundaries, precipitates and others, but it also removes the highly deformed thin superficial layer induced by grinding and polishing. For all the alloys investigated, the austenitic stainless steels 316H and ODS 316L and the ferritic ODS steel MA956, electrochemical etching deploying 60% nitric acid as electrolyte under 2V potential applied for less than 15 seconds yielded very good results. This was also the case for Inconel 718 Nickel-based superalloy, used in a pilot diffusion bonding study applied on the ODS 316L and described in chapter 5.

3.7.2 Scanning Electron Microscopy (SEM)

The necessity for more detailed observations, associated with the limitations of the optical microscopes, requires the use of electron microscopes. The same DeBroglie's principle of the duality wave-particle mentioned earlier predicts wave behaviour for electrons, which present two desirable properties for microscopy: a much-reduced wavelength, ranging between 0.001 nm and 0.01 nm, thus differing from visible light by a

factor of some thousands [21, 22]. This allows much higher resolution, since this latter is proportional to the wavelength of the beam, as can be inferred from equation 3.10; and the fact, still in comparison with light, that electrons carry a charge, with the implications that the lenses of these microscopes are electromagnetic fields and that it is possible to use deflector coils to scan a beam of electrons back and forth across the specimen. That is exactly the principle of the SEM. In order to understand in more details, a schematic of the instrument is provided in Figure 3.13:

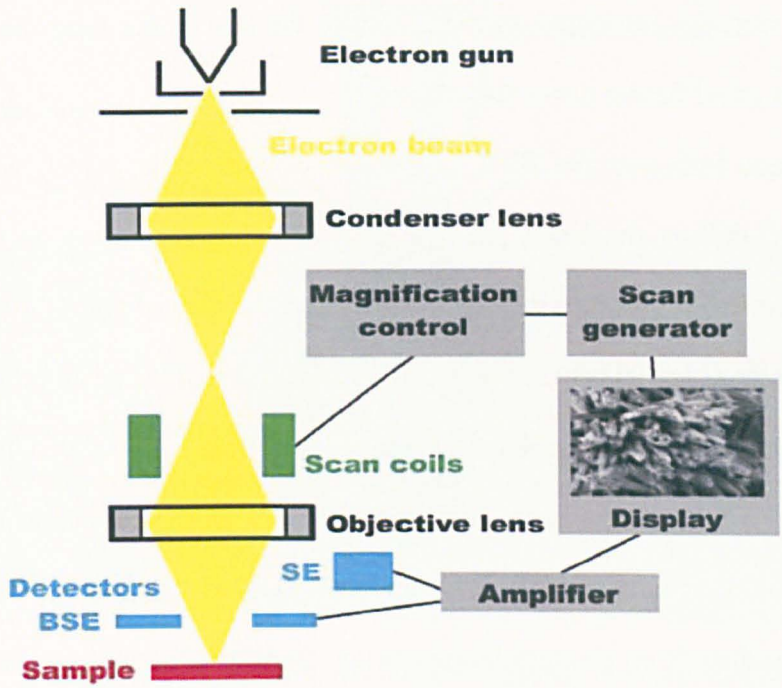

Figure 3.13 - Schematic of a Scanning Electron Microscope [23].

Electrons for the beam are generated by the electron gun, which can be either a thermionic emission gun or a field emission gun (FEG). In the first case, a tungsten filament is heated by the passage of an electric current, while being kept at a high negative potential with respect to the anode. At the high temperature achieved, about 2800 K, the wire emits electrons, which are rapidly accelerated towards the anode across a potential difference of some kilovolts [21]. This beam of high-energy electrons leaves the gun through a central hole of the anode and is directed to the sample down the instrument

column. In a FEG instrument, the generation of electrons takes place by applying an extremely intense electric field to the filament. In order to create an electrical field that must exceed 10^9 V/m, the tip of the filament is made extremely sharp, with a diameter close to 0.1 μm, and the vacuum generated in the column must be some orders of magnitude lower than the levels required for thermionic emission.

As the electrons travel down, the beam tends to become wider, as shown in the schematic (Fig. 3.13). In order to focus and guide the passage of the electrons, condenser lenses (sometimes two pairs) are deployed. They focus the electrons into a tighter beam and, together with the condenser aperture, control the size of the beam as well as how many electrons travel further down the column.

An important device in the SEM is the set of scan coils, which are effectively responsible for shifting the beam position, thus allowing its motion on the specimen surface. This control is accomplished by the placement of a set of plates around the beam and by varying the potential between them, so that deflection of the beam occurs.

The last stage before the beam hits the sample is provided by the objective lenses, whose purpose is to focus the beam on the desired spot on the surface of the sample, a necessary step for obtaining good, in-focus imaging. Similarly to the condenser lenses, the objective lenses also fit an aperture located below them, but, in this case, the aperture is primarily dedicated to control the contrast of the image.

The interactions of electrons with atoms of the specimen occur over a volume inside the sample, called the interaction volume. Essentially, this volume is determined by the atomic number of the specimen, with higher atomic number elements presenting smaller interaction volumes, due to their higher capacity of absorbing electrons; by the accelerating voltage being used, given that higher voltages produce beams of higher energies, which penetrate further into the sample, thus creating larger volumes; and by the angle of incidence of the electron beam with regards to the normal to the surface of the specimen, for which a greater angle from the normal causes the volume to decrease. The interaction

volume bears an adverse relation with the resolution, with larger volumes reducing the spatial resolution. Therefore, every parameter altering the volume, as described above, will also affect the resolution. For example, this latter can be improved by using lower voltages, for which the electron penetration in the material would be reduced. However, the quality of the image would also experience a reduction, since less signal would be able to escape the sample and reach the detector, due to the lower energies. Figure 3.14 depicts the interaction volume along with some of the secondary effects arising from it. The relevance of these effects is fundamental, as explained next:

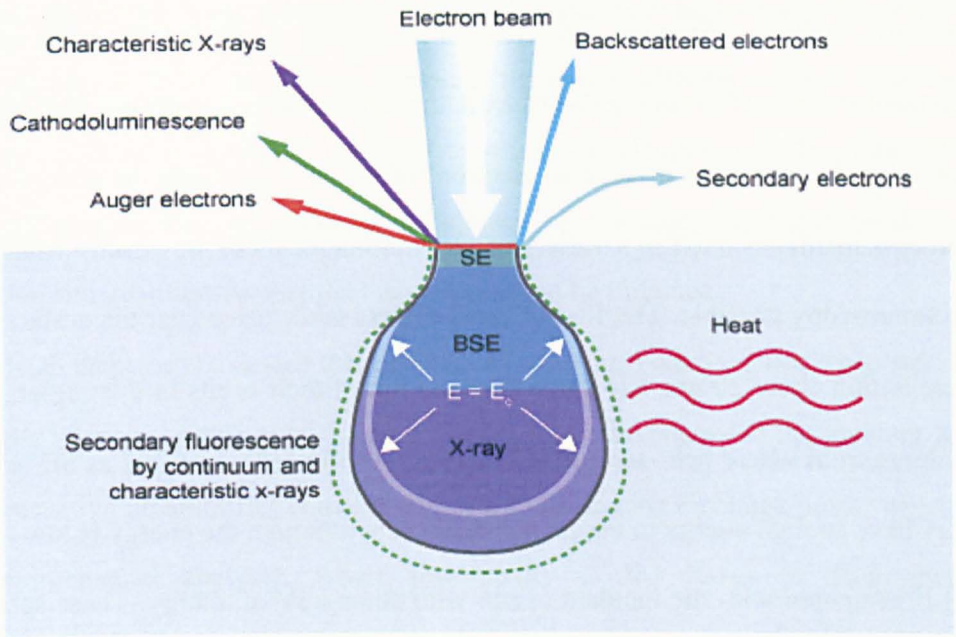

Figure 3.14 - Schematic of electron-substrate interactions [24].

For an incoming electron of the beam that hits the sample, there are four possibilities: it may pass straight through the specimen, that is, be transmitted. This happens only if the sample is very thin (some hundreds of nanometres) and is the basis of another electron microscopy technique, Transmission Electron Microscopy (TEM). The second possibility is that the electron may pass close to the nucleus of the sample atoms, experiencing either a slight deflection or an almost complete reversal of its path, but preserving its energy in the process. This is elastic scattering. The third possibility is interaction between the incident electron from the beam and an orbital electron of the sample's atoms. In this case, mutual

repulsion takes place and part of the energy of the incoming electron is lost to the orbital electron. Both electrons move on, and a vacant electron site is left in one of the atom's shells. This is inelastic scattering. An electron that suffers a succession of inelastic interactions will lose all its energy and, eventually, be absorbed by the specimen [21]. It is reasonable, then, to expect thicker samples to absorb more effectively the electrons.

The final possibility, which is the most likely, provided that the specimen is thicker than ~20 nm, is that an incident electron is both elastically and inelastically scattered several times, either coming to rest or reaching the other side of the specimen. As said above, each time inelastic collision happens, an electron is knocked out of its orbit and the correspondent atom is left in an excited state. Although the various ways in which the atom can relax from the excitation involve an electron filling the orbital gap, the energy emitted in the process manifests itself in a variety of ways. Some of these are exactly what makes electron microscopy possible. The first of these effects takes place near the surface of the specimen, within about 20 nm. Electrons knocked out of their orbits in this region, which is the volume from where near-surface information is collected, identified as SE in Figure 3.14, may have enough energy to escape the specimen, although the energy is low (around 100 eV) if compared with the incident beam, with some keV of energy. These secondary electrons (SEs) are used for topographical imaging in the SEM. Since it is necessary to use very small apertures, in order to avoid spherical aberration, the depth of field obtained in SEM is larger than in OM [21, 23], and allows observation of topographic features without losing focus.

In the present work, a FEG SEM Zeiss Supra 55VP, operated at 5 keV and with 30 μm objective aperture, was used for SE imaging, in microstructural surveys of etched (or polished) samples and fractographic studies of ruptured specimens. In the case of untested materials, samples were subjected to the same preparation procedure outlined in sub-section 3.7.1.1, although previous preparation is not really required, in the case of conductive materials. The only exceptions were the diffusion-bonded samples, as

explained in chapter 5, which were polished to OP-S particle suspension, given that microstructural examination was not the primary goal.

3.7.2.1 X-ray Energy Dispersive Spectroscopy (EDS)

Being one complementary resource of the electron microscopes (both SEM and TEM), EDS is an analytical technique for elemental or chemical characterisation of materials. It harnesses another secondary effect of electron-matter interactions, the characteristic X-rays. These are produced when an electron fills the vacant electron site in one of the orbitals of an excited atom, which has its state changed from high-energy (excited) to low-energy (stable), with the subsequent release of the energy difference. One of the ways this energy is given out is in the form of X-rays, whose wavelength depends on the difference of energy between the two states of the atom [21]. By analysing the emitted X-rays, a qualitative and quantitative chemical description can be obtained.

The EDS detector is a device that operates by creating a charge pulse when struck by an X-ray, the intensity of this pulse being proportional to the energy of the incident X-ray. A charge-sensitive preamplifier converts the charge pulse into a voltage pulse, which is sent to a multichannel analyser, where the energy of the X-ray is determined from measurements of the received voltage pulse. Then, the energy data for each X-ray is further processed through software, for evaluation of the spectrum and elemental composition of the target area [24]. It is relevant to say that, although a very useful tool for chemical characterisation, the technique fails to provide reliable information on light elements (carbon and below), since the windows in front of the detectors will absorb low-energy X-rays [25]. Besides, different elements may have overlapping peaks in the spectrum; so, a previous knowledge of the composition of the material may be necessary for a correct appraisal on its composition.

The SEM used in the present studied has an EDS X-Max 50 mm^2 detector, while the EDS system attached to the TEM is an EDAX Genesis. The measurements were carried

out in spot mode, on microstructural features, precipitates and nanoparticles. In the case of the SEM EDS, an accelerating voltage of 20 keV was used, with the same objective aperture of 30 μm, while the working distance of 8.5 mm was maintained. AZTec software was deployed for analysis of the EDS spectra.

3.7.2.2 Electron Backscatter Diffraction (EBSD)

EBSD is a relatively recent technique aimed at the analysis of near-surface crystallographic orientations, from where relevant information on general microstructural constitution and accumulated deformation in a given material can be obtained. It is another complementary resource of a SEM, based on a modification of the standard usage of the instrument. It relies on the backscattered electrons, that is, those from the incident beam which interact with the nuclei of the atoms, experiencing strong reversal in the direction of travel, but preserving almost entirely the energy of the primary electrons of the beam.

The proportion of backscattered electrons (BSEs) varies with the atomic number of the specimen's elements, which allows for composition contrast mapping, with higher atomic numbers appearing brighter than the lower number elements. Also, the elastic scattering of the BSEs provides information on crystal orientation. As seen in Figure 3.14, the sampling volume (within the interaction volume) of BSEs is relatively large, given the high energies of these electrons. A significant proportion of the electrons of the beam are incident on several crystallographic planes of a crystalline sample, at angles that satisfy Bragg's criterion for each of the corresponding interplanar distances, as expressed by Equation 3.3; so they are coherently diffracted and backscattered from the specimen. In order to maximise the number of BSEs, the sample is tilted 70° from the horizontal and held at this position, so that a diffraction pattern of sufficient intensity is generated [31].

Because scattering occurs for all lattice planes within the interaction volume, two cones of diffracted electrons are developed around the normal to each set of crystallographic planes, as Figure 3.15 illustrates:

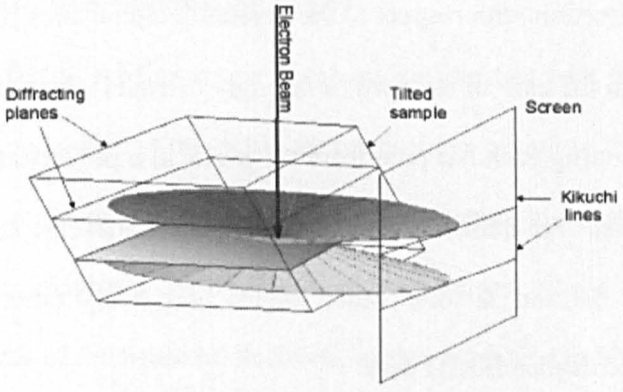

Figure 3.15 - Diffraction cones and their projections on a flat screen [26].

The projection of the edges of these cones on a flat phosphor screen, thus, is a set of two near parallel lines, called Kikuchi bands. Since the cones are symmetric, the lines represent the (hkl) and (-h-k-l) planes. Once all bands have been detected, they are indexed, following a comparison between the measured values of intensity, width and angles, and the theoretical calculated values for all diffracting planes in a crystal of known structure [27]. The correct indexing, then, depends on previous knowledge of the crystal structure of the material. The whole process is automated and computer-controlled, by means of software in charge of both the SEM operation and the data acquisition procedures. Analysis of the acquired data is carried out by data processing software and can be done offline, away from the SEM. Since the software stores specimen coordinates and crystal orientations, it is possible to build a two-dimensional map of the orientation of grains on the surface of a polycrystalline material, just by focussing the beam on each sampling point on the area of interest and selecting the reference crystal system on the software, for comparing the orientation of each point to the reference orientation.

With this technique, useful microstructural information and ways to represent it can be readily obtainable. Orientation distribution, grain size, texture measurements and even quantitative assessment of strain can be obtained and conveniently visualized in orientation maps, which are colour-coded micrographs depicting the distribution of crystallographic orientations within grains; as well as in Inverse Pole Figures, which plot the transverse,

normal or rolling direction with respect to the crystallographic axes [27, 28]. The IPFs are particularly useful in the case of textured or strongly oriented materials, for which purpose the Pole Figures, plotting each *hkl* pole from all grains in a polycrystalline material onto a stereogram whose axes are defined by the same rolling, transverse and normal directions, are an alternative. Schmid factors, Euler angles and many other parameters can be extracted from the processed EBSD data.

In the course of the investigation, EBSD was primarily used on the microstructural characterisation of the MA956 ferritic ODS steel, for which optical microscopy could not provide satisfactory examinations. For this endeavour, the same preparation procedures described in sub-section 3.7.1.1 were applied on the MA956 specimens, except for the etching step, which was replaced by a final polishing stage with colloidal silica suspension OP-S. This suspension consists of silicon oxide particles of sub-micron size range (<0.1 μm) in an alkaline medium. It removes the damaged layer of material, developed in previous stages, by means of simultaneous mechanical and chemical actions due to the particle's abrasive effects and the slight etching effect of the alkaline medium. This step is fundamental for good pattern generation. A NordlysF EBSD detector fitted in the Zeiss Supra 55VP SEM was used for the measurements, carried out under an accelerating voltage of 20 keV, with a working distance (WD) of 15±0.1 mm and an objective aperture of 120 μm, the maximum achievable in this instrument, in order to increase the intensity of the diffracted electron cones. The dynamic focus condition was used, under a magnification of x200, given the large grains of the material. Orientation maps based on the *bcc* iron crystal structure were obtained for the MA956 in its as-received condition as well as after the annealing heat treatment. Each map was created over an area of 2560 μm x 1920 μm, using a 5 μm step-size in a square grid, with 25% overlapping between adjacent areas. The processing of the data was carried out using HKL Fast Acquisition software, from which IPF maps, IPF figures, Pole Figures and other relevant information were obtained.

3.7.3 Transmission Electron Microscopy (TEM)

The Transmission Electron Microscope has many similarities with the SEM, but allows microstructural characterisation at much higher resolutions, owing to the high accelerating voltages used, of the order of hundreds of keV, which means much shorter wavelengths, and a system of electromagnetic lenses, the condenser lenses, whose primary function is controlling the diameter of the beam of electrons, as it is supposed to hit the specimen [21], a necessary step since the area that must be illuminated depends on the magnification at which it is viewed. In order to avoid unnecessary illumination of the specimen out of the areas of interest, the beam is condensed to illuminate an area only a little larger than the desired field of view, thus maximising the brightness.

Figure 3.16 shows a schematic of the instrument. Although, in several aspects, it bears similar features and components as to the SEM, the working principle differs significantly. The top of the instrument houses the electron gun, which can be, again, either thermionic emission or FEG. The most common TEM guns are capable of accelerating the electrons to 200 keV or even higher. Below the gun, condenser lenses, usually a pair, focus the beam into the desired diameter, for the purpose of increasing the brightness of the area under investigation in the final image.

Below the condenser lenses lies the specimen chamber, where the specimen holder is inserted. These parts involve very sophisticated devices. The chamber contains an airlock, in order to minimize the volume to be evacuated by the vacuum pumps. Translation mechanisms provide means for smoothly moving the specimen in the horizontal plane, allowing it to be examined in different areas. Sample tilting at an angle of up to 45° is possible with some holders, allowing the electron beam to strike the specimen at different angles.

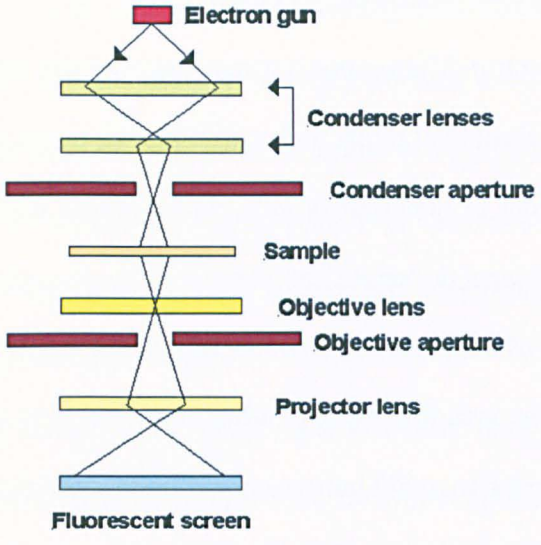

Figure 3.16 - Schematic of the TEM instrument.

With regards to positioning, a useful tool is found in the double-tilt holders, which allow tilting in two directions, thus providing conditions for accurate alignment of the foil for the purpose of recording specific diffraction conditions, such as two-beam.

Immediately below the position where the specimen is inserted lies the objective lens, considered the heart of the instrument, for this lens is responsible for the image formation. By fine-tuning of the current passing through the objective lens, the image is focused on a plane. As seen from the schematic, this lens, similar to the condenser lenses, also boasts a set of apertures, which are pinholes of different sizes. However, if the condenser apertures are used to define the area of illumination, the objective aperture has more specific and relevant roles: it defines the angular aperture α and, therefore, the ultimate resolution of the instrument. On top of that, the use of the objective aperture also improves the contrast in the image, as explained later. Normally, a trade-off has to be reached, since a larger aperture will reduce the resolution due to spherical aberration, but a smaller aperture also limits the resolution, due to the diffraction effect, in which a parallel beam is transformed into a series of cones by the opening, thus making a spot appear as a series of cones, whose projections are the circles called Airy's rings [21, 22]. In the image plane, there is another aperture holder, the selected area aperture set, with three or four pinholes, by which

different sized areas of the field of view can be selected for obtaining electron diffraction patterns.

Finally, the image produced by the objective lens is enlarged to the desired magnification by two or three sets of projector lenses, depending on the microscope. The projected image can be seen, by the operator, on a fluorescent screen, through a glass window. Also, photographic records can be taken by simply lifting the screen and allowing the electrons to hit a CCD camera below.

3.7.3.1 Image formation in the TEM

Image formation in TEM arises from two major mechanisms of contrast generation. Both rely on the effects introduced by the objective aperture, without which the image formed would be almost uniformly grey. These mechanisms are scattering contrast and diffraction contrast. Strictly, diffraction is a particular case of scattering, occurring when the electrons emerging from the sample are in phase with the incident electrons. This is the coherent scattering, in opposition to the general case in which electrons, after interacting with the specimen, are no longer in phase (termed incoherent scattering) [22]. Although they act simultaneously, diffraction contrast occurs more appreciably in crystalline materials, especially in metals. It is based on the fact that the brightness of the whole image critically depends on the angle between the electron beam and the sample, making it possible to obtain a completely "dark" image or a completely "white" one of the same crystal, simply by tilting the specimen [29]. This stems from Bragg's Law: if a flat crystalline sample is oriented in such a way as to favour diffraction from a certain set of lattice planes, the majority of electrons will leave the specimen at an angle 2θ with regards to the incident beam. With the objective aperture in position, these electrons will be stopped and prevented from contributing to the image, which will appear dark. If, however, the specimen is tilted away from the Bragg condition, even slightly, no diffraction will take place from the considered lattice planes anymore, and the beam will pass through the

objective aperture, creating an uniformly bright image. Although real samples are not flat, due to the fact that they are thinned down to the extent to which they may become buckled, the principles described apply. Lattice planes will not be all at the same angle to the incident beam, with certain parts of the specimen obeying the Bragg condition, therefore appearing dark; and other parts lying away from the Bragg angle, shown as bright areas. This effect leads to the formation of extinction (or bending) contours, which are dark lines on the image of the foil, as shown schematically in figure 3.17a and in a TEM micrograph in Figure 3.17b.

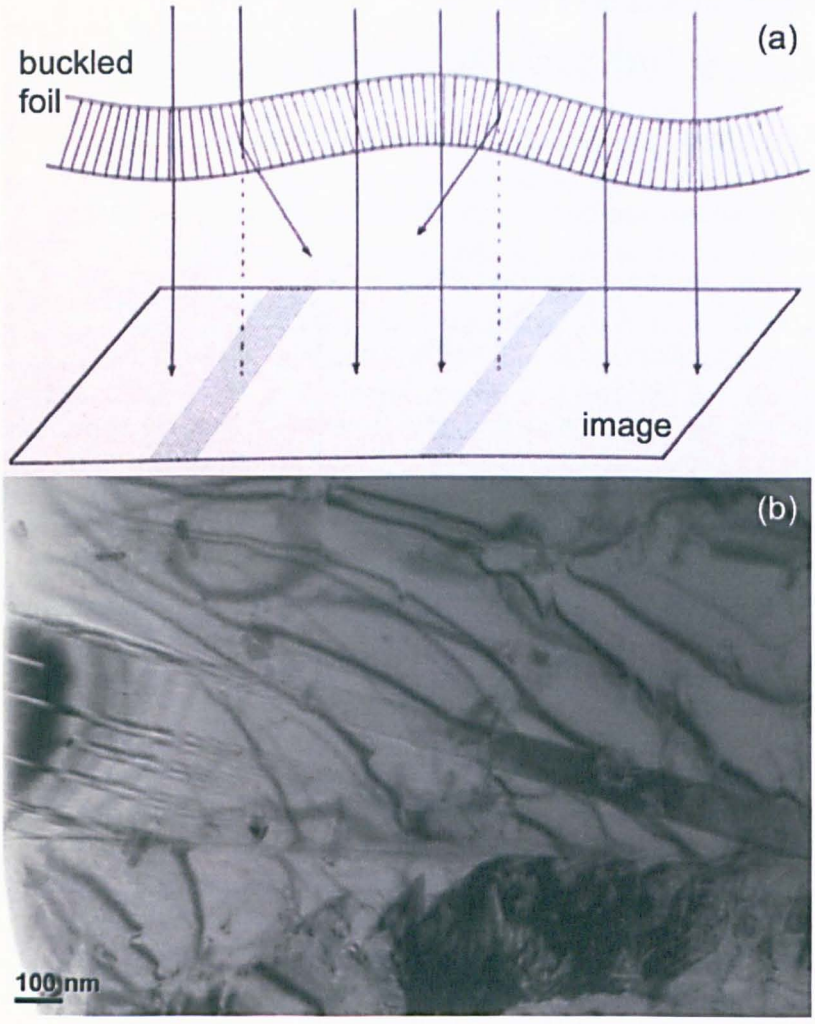

Figure 3.17 - Schematic of the formation of extinction contours, showing the dark areas where diffraction occurs (a) –adapted from [21]; and a TEM micrograph depicting several extinction contours in 316H steel (b).

Although the extinction contours are not particularly useful, it is relevant to know what they are, since they are present in almost every image of a crystalline specimen. On top of that, the contrast effect just described is the same for defects of the crystal structure, such as dislocations, grain boundaries and twins. These defects will either bend the lattice planes locally, the case of dislocations, or cause interference between the diffracted electrons from two overlapping crystals, thus giving rise to fringes, as in the case of grain boundaries, twin boundaries and stacking faults [21].

The other mechanism, scattering contrast, is related to the amount of electron scattering that occurs as the incident beam travels across a certain region of the specimen. It is reasonable to expect, then, more pronounced scatter from a thicker part of the specimen, which will appear darker than a thinner one. Similarly, an area containing heavy elements scatters more than a region of the same thickness bearing lighter elements.

Given that the TEM specimen is a foil with a thickness of just few hundreds of nanometres (usually, less than 200 nm) and is examined under very high magnifications (several thousands), only one grain is usually studied at a time. The limited sampling area of a specimen requires proper preparation, so that more visual information can be extracted from the same foil, and the representativeness of the microstructure is statistically improved.

Another relevant aspect related to imaging defects and features of the crystal structure is associated with the conditions for their visibility. The presence of a dislocation in a crystal causes a lattice distortion, represented by an atomic displacement field **R**(r,ϕ), written in polar coordinates for convenience. Hirth and Lothe [32] showed that the displacement field for a dislocation in an isotropic solid could be expressed by:

$$\boldsymbol{R} = \frac{1}{2\pi}\left(b\phi + \frac{1}{4(1-\nu)}\{b_e + b \times u(2(1-2\nu)\ln r + \cos 2\phi)\}\right)$$

(Eq. 3.11)

where b is the Burgers vector considered at a point in a stretch of the mixed-character dislocation, b_e is the edge component of the Burgers vector, u is the dislocation line unit vector and v is the Poisson's ratio. The descriptions of electron diffraction by crystalline solids establish that the amplitude of the diffracted beam has a direct dependence on the displacement field and on the diffracting vector, related to each other by the contrast provided by **g.R** [22, 29]. Since equation 3.11 is written for the general case of a mixed-character dislocation, there are two specific cases for analysis, the pure screw dislocation and the pure edge one. The simpler case is the screw dislocation, for which there's no edge component ($b_e = 0$) and b is parallel to u ($b \times u = 0$). Equation 3.11, then, is reduced to

$$R = b\frac{\phi}{2\pi}$$

(Eq. 3.12)

This means that, at an angular position ϕ, measured from the dislocation position, the displacement field is proportional to the Burgers vector, so that the visibility of dislocations is expressed in terms of the **g.b** contrast. Because this product causes contrast, a criterion for imaging screw dislocations can be envisaged. When **g.b** = 0, there won't be any contrast, due to the diffracting plane being parallel to the displacement field **R**. This is the condition set as the invisibility criterion [22].

For the edge dislocation, $b = b_e$, so that the **g.R** product presents two vector terms, a **g.b** and a **g.b×u**. This latter term arises from the fact that an edge dislocation causes its glide plane to buckle.

Theoretically, the identification of a Burgers vector of a dislocation would be a simple matter of identifying two noncoplanar reflections, $\mathbf{g}_1$ and $\mathbf{g}_2$, for which **g.b** = 0; then, their cross product would yield a vector parallel to b [33]. In practice, there are some difficulties in the application of these criteria. First, because dislocations are reported to go out of contrast when **g.b** < 1/3 [22]; also, even if **g.b** = 0, the dislocation may not necessarily be invisible, provided that **g.b×u** $\neq$ 0. Moreover, screw dislocations at the surface of the

material can still be imaged, given the different structure conditions of the surface with regards to those of the bulk material [22], allowing screw dislocations to relax, therefore presenting contrast, even when **g.b** and **g.b×u** are zero.

Some initiatives may be used to overcome the invisibility influence, thus obtaining a statistically more accurate quantification. Norfleet et al. [34] suggested using STEM to provide simultaneous imaging of all dislocations in a foil coinciding with a trace plane. In conventional TEM, these criteria play an important role, since the extent to which they are used will represent the statistical accuracy of quantifications.

3.7.3.2 TEM sample preparation

In order to produce samples suitable for examination under the TEM, a careful preparation procedure was adopted, as follows.

1. Sectioning of 0.3 mm thick slices from the as-received material or the deformed samples. This stage was carried out using the Struers Accutom-50 slow-speed saw.

2. Grinding; this step was performed using a Gatan 623 disc grinder. The slices were mounted to a specimen holder by means of a low melting point glue, with this holder being inserted into the grinder and having its exposure height adjusted, depending on how much material is to be removed. The slices were sequentially passed onto a 40 μm, 15 μm and 5 μm grit SiC paper, lubricated with distilled water. Both sides of the slices were ground until a thickness of about 100 μm was achieved. Grinding beyond this stage was avoided, since the slice could start bending excessively, distorting the original dislocation structure.

3. Punching; carried out with a Gatan puncher model-659, this step cuts 3 mm diameter discs from the slices. This is the appropriate size of the foil to sit on the TEM specimen holders.

4. Electropolishing; this step is the most crucial in the preparation of the foil, since it is here that the discs are thinned down to just a few hundreds of nanometres. This was achieved on a Metalthin Mk4 jet electropolishing machine. In this technique, the sample

disc is constantly bombarded on both sides with jets of an electrolyte, which, in this case, was a solution of 5% perchloric acid in methanol, while it is held as the anode of the electrolytic cell. The process was carried out under an applied potential difference of 20 V, with liquid nitrogen being constantly pumped through the electrolytic cell in order to ensure the temperature was kept at –50±5°C. Figure 3.18 shows the whole apparatus for the jet electropolishing process. Each TEM foil was electropolished up to the point where a hole was created. A photo-detector system, triggered by the light that reaches the detector though the hole in the specimens, automatically switches off the jets. Once this stage was reached, the foils were cleaned using laboratory grade methanol. Provided that the polishing was smooth, the regions of the foil around the hole are thin enough for observation in the TEM.

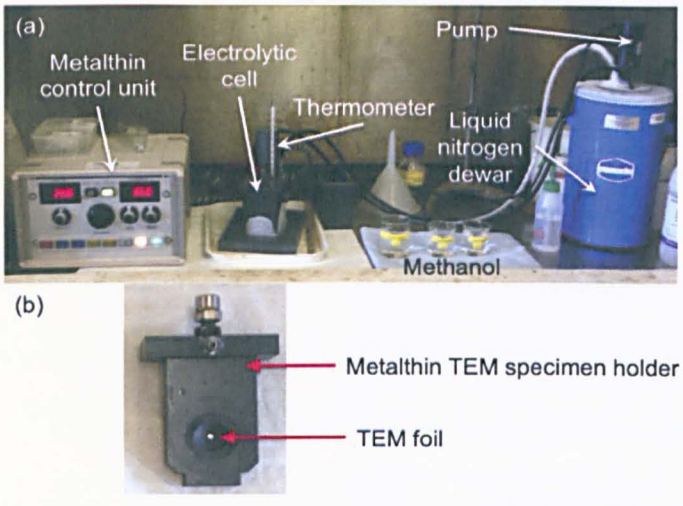

Figure 3.18 - Experimental apparatus for jet electropolishing (a) and corresponding 3 mm disc holder (b).

In the present study, all examinations were conducted on a JEOL JEM 2100 transmission electron microscope, which has a LaB_6 (lanthanum hexaboride crystal) thermionic emitter, and has a theoretical point resolution of 0.25 nm and a magnification range between 1500-1200000X. The instrument was operated at 200 keV, in bright field (BF) mode. Micrographs were acquired using a Gatan Orius SC1000 digital camera, mounted in alignment with the TEM optics, below the viewing screen.

Both quantitative and qualitative analysis were carried out, in an effort to characterise the dislocation structures and study their evolution along different stages of the creep transient test curve, in the case of 316H stainless steel; as well as to obtain visual data for analysis of the interactions between dislocations and nanoparticles, in the case of the ODS steels, the austenitic 316L and the ferritic MA956. For each sample, measurements were performed on, at least, four different locations, with different imaging vectors (g-vectors), by making use of a double-tilt holder. For each image, the corresponding diffraction pattern (DP) was recorded.

Additionally, the high-resolution (HRTEM) mode was deployed to study orientation relations between oxide nanoparticles and the matrix, in the case of the ODS steels. For every image, the corresponding Fast-Fourier Transform (FFT), which is the analogous of the DP in HRTEM, was obtained.

3.8 Summary

Uniaxial tensile tests are useful in determining the basic mechanical properties of a material. Their principles and relevance for the characterisation of the investigated steels are explained.

Creep testing apparatuses and devices are described, for understanding of how the tests were carried out, and how their relevant parameters were monitored and obtained.

The principles of the mechano-acoustic technique for measurement of Young's modulus were explained.

A comprehensive review on the basic principles of diffraction, with particular emphasis to neutron diffraction and its relevance for the measurement of intergranular stresses, is provided.

The fundamental concepts of optical microscopy and its relevance for the preliminary microstructural investigations are explained, along with the description of the methodology of sample preparation and examination.

The operating principles of electron microscopes (SEM, TEM) are described, in terms of the electron beam-specimen interactions, for better understanding of the information obtained in the investigations.

3.9 References

[1] "ASTM E8M Standard Test Methods for Tension Testing of Metallic Materials." ASTM International, 2011.

[2] "BS EN ISO 204:2009 Metallic materials - Uniaxial creep testing in tension - Method of test." 2009.

[3] E.-V. 3-P. I.-I. 4 Recommendations, "Data Acceptability Criteria and Data Generation: Recommendations for Creep Testing of Post Exposed (Ex-service) Materials." 2005.

[4] G. Mälzer, R. W. Hayes, T. Mack, and G. Eggeler, "Miniature Specimen Assessment of Creep of the Single-Crystal Superalloy LEK 94 in the 1000 °C Temperature Range," *Metall. Mater. Trans. A*, vol. 38, no. 2, pp. 314–327, 2007.

[5] R. W. Evans and B. Wilshire, *Creep of Metals and Alloys*. The Institute of Metals, 1985.

[6] R. W. Evans, J. Preston, B. Wilshire, and E. A. Little, "Creep transients in a nuclear-grade ODS ferritic steel," *J. Nucl. Mater.*, vol. 195, pp. 24–28, 1992.

[7] S. G. Hernández and A. N. Conejo, "Creep properties of 1.25Cr-1Mo-0.25V steels for turbine casings," *Rev. Esc. Minas*, vol. 58, no. 2, pp. 165–173, 2005.

[8] "IAM - What is a Linear Variable Displacement Transformer (LVDT)?" [Online]. Available: http://www.iamechatronics.com/notes/process-measurement/191-what-is-a-linear-variable-differential-transformer. [Accessed: 30-Jun-2015].

[9] W. D. Callister, *Materials Science and Engineering: An Introduction*, 5th Editio. John Wiley & Sons, 2000.

[10] G. E. Dieter, *Mechanical Metallurgy*. McGraw-Hill, 1986.

[11] A. International, "ASTM E384 - Standard Test Method for Knoop and Vickers Hardness of Materials." 2011.

[12] TWI, "Hardness Testing part I," *Technical Knowledge*. [Online]. Available: http://www.twi-global.com/technical-knowledge/job-knowledge/hardness-testing-part-1-074/. [Accessed: 09-Jul-2015].

[13] American Iron and Steel Institute, *High-Temperature Characteristics Of Stainless Steels*, A Designer. Nickel Development Institute.

[14] A. International, "ASTM E1876-09 - Standard Test Method for Dynamic Young's Modulus, Shear Modulus and Poisson's Ratio by Impulse Excitation of Vibration." ASTM International, 2009.

[15] "ASTM C1259 - Standard Test Method for Dynamic Young's Modulus, Shear Modulus and Poisson's Ratio of Advanced Ceramics by Impulse Excitation of Vibration." ASTM International, 2015.

[16] M. E. Fitzpatrick and A. Lodini, "Analysis of residual stress by diffraction using neutron and synchrotron radiation," *The use of neutrons for material characterization* . Taylor & Francis, London, pp. 3–27, 2003.

[17] P. J. Withers and H. K. D. H. Bhadeshia, "Residual stress. Part 1–measurement techniques," *Mater. Sci. Technol.*, vol. 17, no. April, pp. 355–365, 2001.

[18] A. Rao, "Creep and Anelastic Deformation in Austenitic Steels," The Open University, 2010.

[19] T. Holden, "Effect of texture on residual stress measurement," in *Analysis of Residual Stress by Diffraction using Neutron and Synchrotron Radiation*, M. Fitzpatrick and A. Lodini, Eds. Taylor & Francis, 2003, pp. 97–113.

[20] M. W. Johnson and M. R. Daymond, "Neutron Pulsed source instrumentation," in *Analysis of Residual Stress by Diffraction using Neutron and Synchrotron Radiation*, M. E. Fitzpatrick and A. Lodini, Eds. Taylor & Francis, 2003, pp. 146–169.

[21] P. J. Goodhew, J. Humphreys, and R. Beanland, *Electron Microscopy and Analysis*. CRC Press, 2000.

[22] D. B. Williams and C. B. Carter, *Transmission Electron Microscopy: A Textbook for Materials Science*, 1st ed. Springer, 1996.

[23] "ETH Zürich - Electron Microscopy," 2015. [Online]. Available: http://www.microscopy.ethz.ch/sem.htm. [Accessed: 08-Aug-2015].

[24] A. L. and T. Council, "My Scope - training for advanced research," *Electron-matter interactions*, 2011. [Online]. Available: http://li155-94.members.linode.com/myscope/sem/background/concepts/interactions.php. [Accessed: 10-Aug-2015].

[25] J. Goldstein, D. Newbury, C. Lyman, P. Echlin, E. Lifshin, L. Sawyer, and J. Michael, *Scanning Electron Microscopy and X-ray Microanalysis*, Third Edit. Springer, 2007.

[26] University of Strathclyde, "Semiconductor spectroscopy and devices," 2012. [Online]. Available: http://ssd.phys.strath.ac.uk/index.php/Electron_backscatter_diffraction_(EBSD). [Accessed: 12-Aug-2015].

[27] D. N. Githinji, "Characterisation of Plastic and Creep Strains from Lattice Orientation Measurements," PhD Thesis, The Open University, 2013.

[28] U. of Cambridge, "DoITPoMS - Crystallographic Texture," *Teaching and Learning Packages*, 2004. [Online]. Available: http://www.doitpoms.ac.uk/tlplib/crystallographic_texture/printall.php. [Accessed: 08-Jan-2015].

[29] B. Fultz and J. Howe, *Transmission Electron Microscopy and Diffractometry of Materials*, 4th ed. Springer, 2012.

[30] M. R. Daymond and P. J. Bouchard, "Elastoplastic Deformation of 316 Stainless Steel Under Tensile Loading at Elevated Temperatures," *Metall. Mater. Trans. A*, vol. 37, no. June, pp. 1863–1873, 2006.

[31] R. A. Schwarzer, D. P. Field, B. L. Adams, M. Kumar, and A. J. Schwartz, "Present State of Electron Backscatter Diffraction and Prospective Developments," in *Electron Backscatter Diffraction in Materials Science*, D. P. Field, B. L. Adams, M. Kumar, and A. J. Schwartz, Eds. Springer, 2009, pp. 1–19.

[32] J.P. Hirth, J. Lothe, *Theory of Dislocations*. McGraw-Hill, 1968

[33] S.S. Ruvimov and K. Scheerschmidt, "Burgers Vector Determination in TEM by Using the Dislocation Parity Analysis," *Phys. Status Solidi A*, vol. 141, pp. 269–284, 1994

[34] D. M. Norfleet, D. M. Dimiduk, S. J. Polasik, M. D. Uchic, and M. J. Mills, "Dislocation structures and their relationship to strength in deformed nickel microcrystals," *Acta Mater.*, vol. 56, no. 13, pp. 2988–3001, Aug. 2008.

Chapter 4 – 316H Creep and Anelasticity in Partial Unloading Stage

4.1 Introduction

This chapter describes the experimental investigations carried out for the 316H austenitic stainless steel. The material was supplied in the form of bars, this referred to as the as-received condition throughout the document. The investigations were a continuation of a previous work [15], aimed at the study of basic mechanisms for the anelastic behaviour of the 316H steel. Although the experimental approach adopted here was the same, the fundamental points of view on the physical phenomena and the relative role of the basic entities of plastic deformation (the dislocations) are different. The multi-technique approach was taken further, in order to set qualitative analysis and quantitative measurements of the basic physical mechanisms influencing the time-dependent plastic deformation of the material. This latter is described in terms of its processing historic, chemical composition and microstructural evolution, following a series of tests deliberately interrupted at certain stages of the creep life, carried out in conditions of partial unloading.

4.2 Initial Study and Characterization of the 316H steel

Power Metal Suppliers, a company that sources stainless steels for power plants, provided the steel used in this investigation, in the form of bars of 12.5 mm diameter and 3 m length. These bars were solution annealed at 1100°C for 90 minutes and water quenched, before being cold-drawn to their final shape. The chemical composition provided by the suppliers is shown in Table 4.1, along with the limits defined by the ASTM 240 Standard for this steel.

Table 4.1 - Nominal chemical composition of the as-received 316H austenitic stainless steel bars.

		C	Mn	Si	P	S	Cr	Ni	Mo
Chemical composition (%)		0.08	0.63	0.29	0.04	0.05	17.26	10.17	2.12
Composition limits – ASTM 240	**Min (%)**	0.04	-	-	-	-	16	10	2
	Max (%)	0.10	2	0.75	0.045	0.03	18	14	3

Initial microstructural survey was carried out using a Leica DMI 5000M optical microscope, after careful preparation of the samples, following the procedures described in subsection 3.7.1.1. Longitudinal and cross-section samples were extracted from the bar, prepared and examined. Figure 4.1 shows the microstructure in the cross-sectional (perpendicular to the bar axis) and longitudinal (parallel to the bar axis) directions after the electrochemical etching with 60% nitric acid, necessary for revealing the grain boundaries with good contrast.

One of the aims of the initial survey was to characterise the average grain size, given its influence on the creep behaviour of the material. This was done based on the ASTM E112 linear intercept method [1], embedded in the GrainExpert subroutine of the Leica Application Software. For each micrograph taken at a known magnification, this resource superimposes straight lines of a determined length (L) onto the image and counts the total number of intersections (N) between these lines and the visible grain boundaries. The grain size, then, is expressed in terms of the mean linear intercept value (MLI), defined as $MLI = L_t / N$, where L_t is the total length of all the lines drawn on a micrograph, and the average is determined. The result reported for the cross-sectional direction represents the intercepts taken place over 2895 grains, scattered across single micrographs of several areas of survey from five samples. The longitudinal direction had a minimum of 950 grains

examined in two panoramic pictures produced from single images of adjacent areas of the sample, placed side-by-side using the stitching feature of the Leica Application Software. The grains were found to be larger in the longitudinal direction, as seen in Table 4.2 below.

Table 4.2 - Averages of grain size measurements for the 316H steel.

Sample direction	Grain size [μm]	Uncertainty [μm]
Cross-sectional	79	12
Longitudinal	101	5

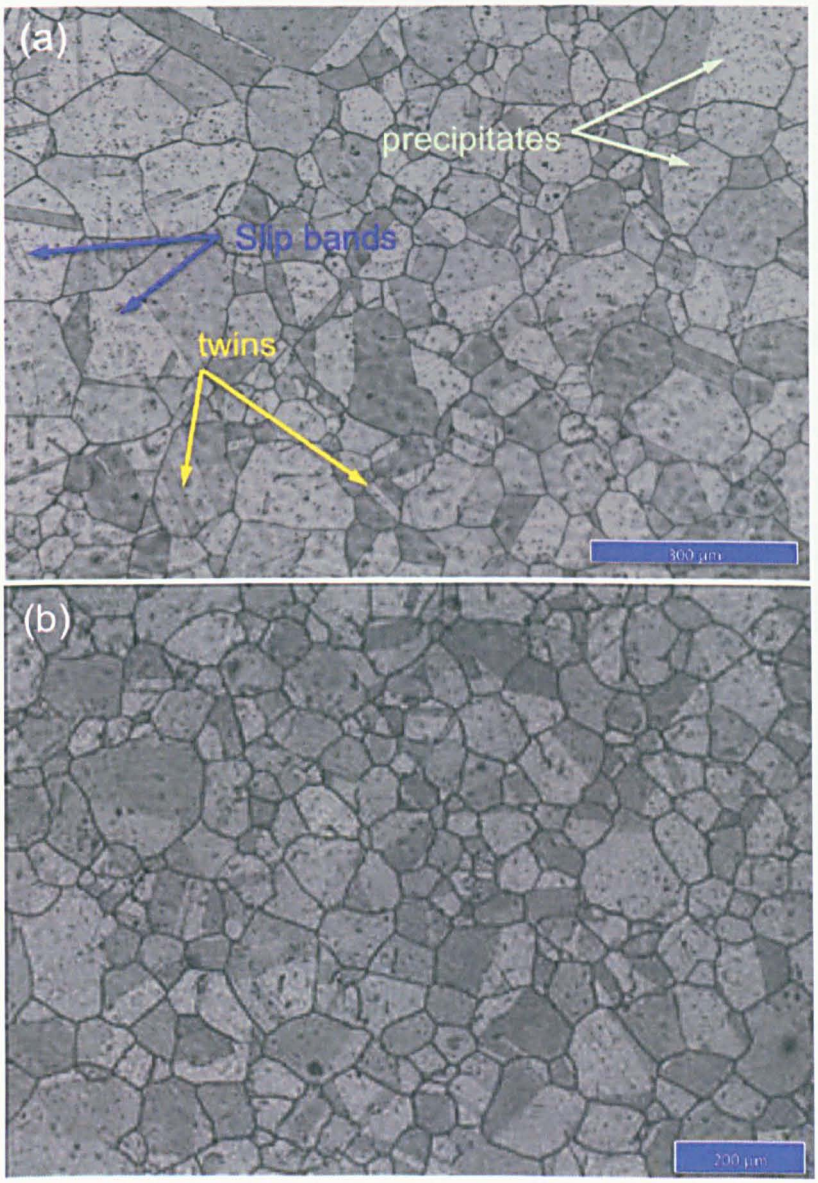

Figure 4.1 - Optical micrographs of 316H steel in the cross-sectional direction (a) and longitudinal direction (b). Slip bands and twin boundaries are highlighted in (a), and were present through all the microstructure.

As seen in Figure 4.1, slip bands were evident in some grains, indicating that plastic deformation had occurred, possibly induced by the cold drawing process. Also highlighted in the same figure are the twinning lines, which form in austenitic steels during annealing treatment [2, 3].

4.3 TEM characterization of the untested (as-received) material

From the as-received bars, slices were extracted so that TEM foils could be prepared. These slices were cut perpendicular to the longitudinal axis of the bars and prepared for examination according to the procedures described in subsection 3.7.3.2. This study was performed using a JEOL JEM 2100 Transmission Electron Microscope, under conditions given in Chapter 3. Qualitative and quantitative analyses were developed, in order to establish a reference condition for the microstructure of crept specimens.

TEM characterisation indicated an initial dislocation density of 1.1×10^{14} m^{-2} (determined using the method describe in section 4.3.1), a reasonably high value, which suggests considerable work hardening of the material. Qualitative TEM analysis showed that, in most of the micrographs depicting the as-received microstructure, many stacking faults, as well as heterogeneous dislocation arrangements such as tangles and walls, could be observed, as illustrated in Figure 4.2a. These latter support the idea of significant plastic deformation, in agreement with the slip bands detected in the optical microscopy survey. However, transitions to matrix areas with lower dislocation density were also observed (as seen ahead, in Fig. 4.20b), implying that recovery processes, including annihilation, might also have occurred, as would be expected for a hot worked (or cold worked and heat treated) microstructure.

Another interesting aspect revealed was the extensive precipitation, especially intragranular, as seen in Figure 4.2b. The intragranular precipitates appeared to be faceted, exhibiting a variety of shapes, in opposition to the round morphology commonly found in over-aged austenitic steel [4, 5]. Their distribution was found to be fairly even throughout

the matrix, although their size was found to be relatively small, bearing, on average, less than 20 nm. These precipitates were assumed to be $M_{23}C_6$ carbides, given the high contents of carbon in the 316H steel composition.

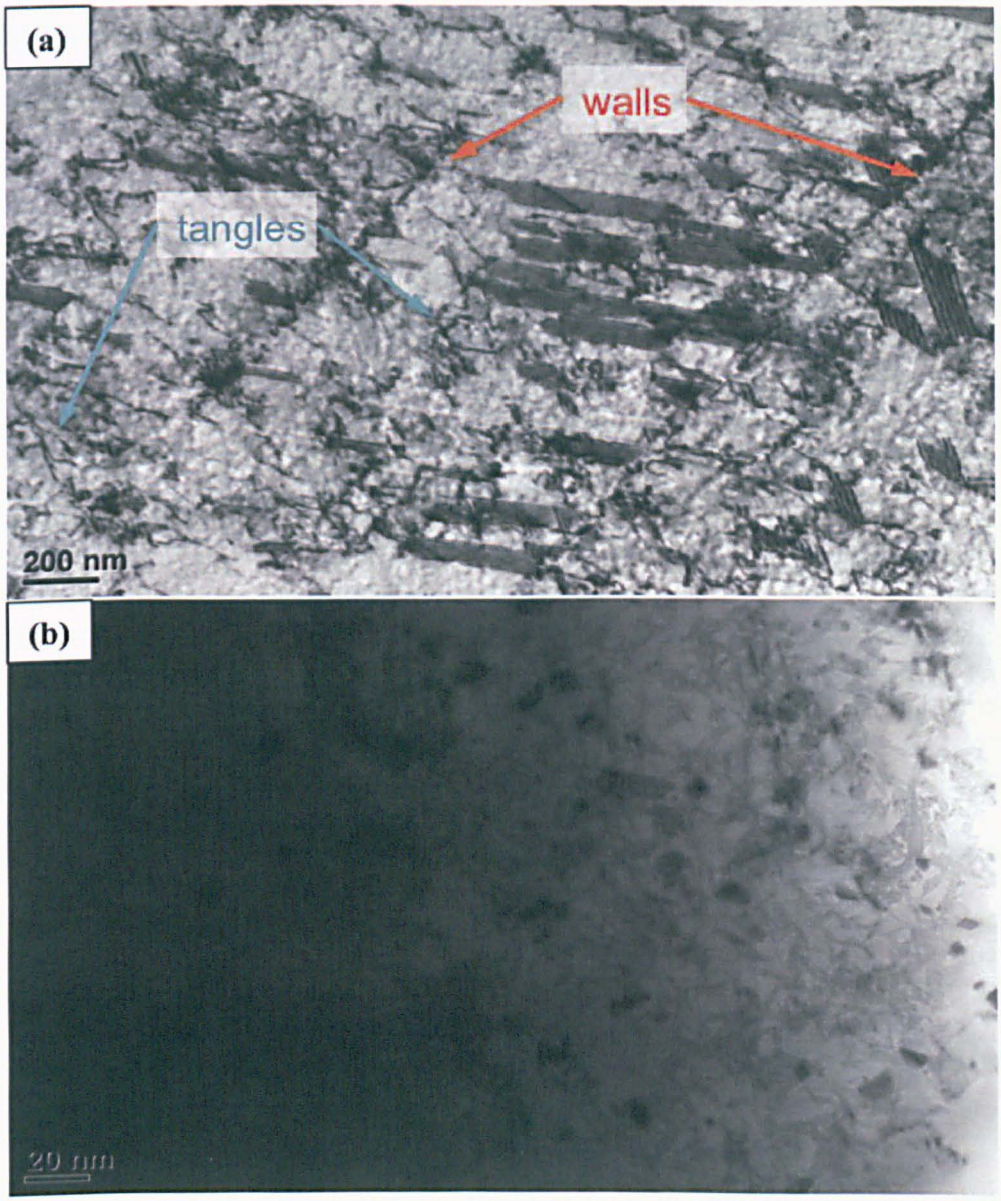

Figure 4.2 (a) Stacking fault ribbons, dislocation tangles and walls and (b) area populated by fine precipitates scattered through the matrix.

4.3.1 Dislocation density measurements

As explained in Chapter 2, strain hardening of crystalline materials is related to plastic strain build up in and around the grains. Therefore, a very effective way to ascertain the

relative changes in the microstructure, in terms of hardening or softening, is the characterisation of dislocation densities.

The dislocation density, understood as the total length of dislocation lines per unit volume of material [6, 8, 9], was calculated using an intersection method, which is based on the superposition of a number of randomly oriented lines on the TEM micrograph, with the dislocation density, ρ, expressed as [7]:

$$\rho = \frac{2N}{L_t t} \qquad \text{(Eq. 4.1)}$$

where N is the total number of intersections between dislocations and the drawn straight lines, L_t is the sum of the lengths of all test lines and t is the foil thickness at the region of interest. By examining particular slip planes parallel to the foil surface and using STEM to eliminate the condition of dislocation invisibility, Norfleet and co-authors [6] found little difference between the presented method and one based on manual tracing of the total dislocation line length within the foil image, which is a much more tedious method. The assessment was carried out by overlaying a pattern of seven lines, drawn using the ImageJ software, to each TEM micrograph, in order to cover most of the imaged foil area and to keep consistency. For the total number of TEM foils of each specimen condition, at least 35 interceptions on each micrograph were counted. Although this number seems low, in most cases, the total number of interceptions was well above this baseline. Besides, it is important to notice that the counting is conditioned to the magnification used, to the specimen condition and to the area of the foil under investigation. Therefore, a significant variability is not unusual. Yet, given the number of images of each area (under different **g-vectors**), and the number of areas and foils investigated, the total interceptions per sample was not lower than 1680. Data for the sampling and counting in this method, as well as a critical view on its drawbacks, are presented in the Appendix 4.

As for the imaging of dislocations, at least four different areas were examined in each foil, in order to maximize the number of grains and of defects surveyed [10]. A two-beam condition was sought for every image, and the same area was observed at different tilt angles, that is, using different g-vectors, in order to check for dislocations that might not have been readily visible in those reflections for which $\mathbf{g}.\mathbf{b} = 0$. It is convenient to recall that the g-vector represents a vector in the reciprocal lattice space (observed in the diffraction pattern of a TEM image) associated to the (*hkl*) plane, being perpendicular to it in real space and presenting magnitude inversely proportional to the interplanar spacing d_{hkl} [11]. From each specimen, either in the as-received condition or subject to creep transient testing, at least three foils were examined. The thicknesses of the foils were estimated using the projection method [7], based on the length w of a projected defect, such as a grain boundary or dislocation, the tilt angle of its high-contrast imaging, δ, and the angle γ between its plane and the zone axis, as schematically depicted in Figure 4.3.

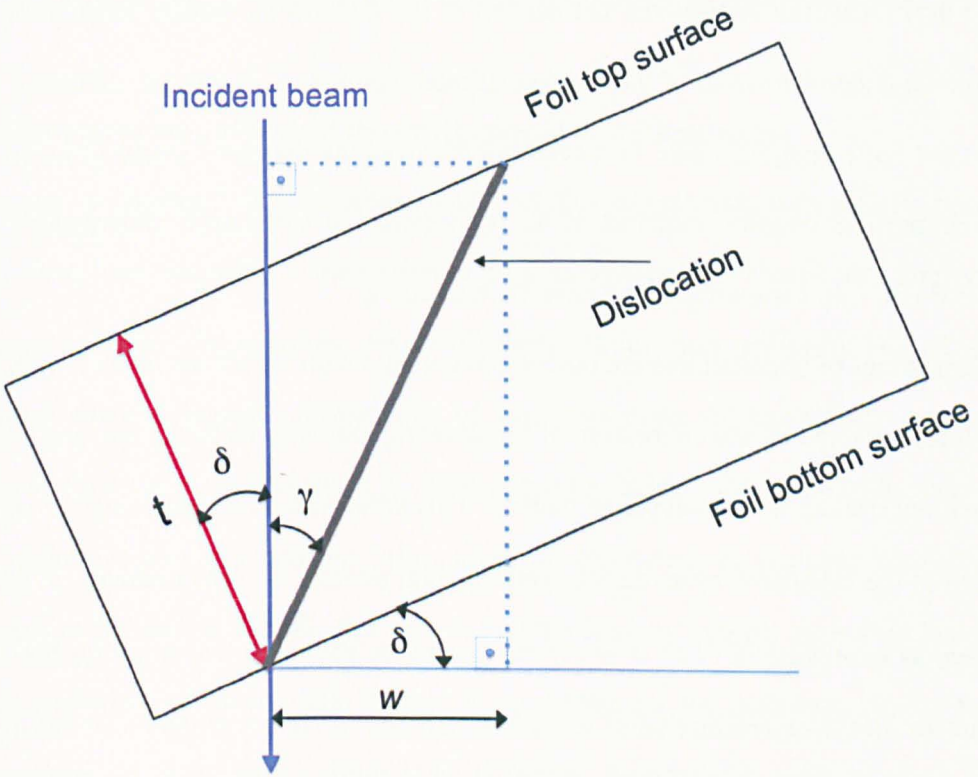

Figure 4.3 - Schematic diagram showing the geometry of the foil and necessary parameters for estimation of its thickness from the projected width of a defect.

By indexing the diffraction pattern (DP) corresponding to each region surveyed, the indices of the plane containing the defect and of the zone axis were determined, following procedures given by Fultz and Howe [11]. From the geometry above, and by projecting the dislocation line length, it can be demonstrated that the thickness, t, can be expressed as:

$$t = w\,(\cot\gamma - \tan\delta)cos\,\delta \qquad \text{(Eq. 4.2)}$$

Attention is drawn to the cosine term in the above equation, representing the correction for obtaining the thickness of the foil at zero tilt, in opposition to the distance travelled by the beam through the material, measured along its direction of incidence. Details on this method can be found in Williams and Carter [7]. Although reasonable results were attained, with estimated thicknesses ranging between 115 nm and 335 nm, uncertainties are high. Some of their components arise from the systematic errors associated with the determination of the angles between the zone axis and the plane of the defect, which can be as high as 18% of the values, and are carried to the dislocation density calculation [11]; and from an underestimation of the number of interceptions, N, due to the difficulty of the bright-field (BF) imaging mode in discerning dislocations that are closely grouped, such that their profiles overlap. Norfleet et al. [6] reported a systematic underestimation of nearly 30% in N, in comparison with dark-field imaging.

Other sources of uncertainties are random, associated with variations in the length of the drawn lines, affected by the calibration of the drawing tool with the scale bar, and with the statistical uncertainty in the calculated density. This latter was estimated using the standard deviation of the calculated mean density and the total number of measurements, n, for each specimen, as expressed in $u(\rho) = \sigma_{std}/\sqrt{n}$. A similar approach was done for the drawn line patterns for the determination of $u(L)$. The standard-deviation of the mean density was used, given that each micrograph was taken at different magnification; therefore, the lengths of the drawn lines and the number of interceptions differs greatly from one

micrograph to another of the same foil. The overall uncertainty, then, was determined by applying the expression for combined uncertainties.

It is relevant to point out that other methods for estimating t exist, including X-ray spectrometry, electron energy loss spectroscopy (EELS) and convergent beam electron diffraction (CBED) [7, 12]. However, advantages and drawbacks are relative and, overall, none is superior to the other. For example, CBED is credited as the most accurate method of thickness determination, with errors as low as ±5%, but requires an undistorted and relatively flat foil region for investigation [6]. EELS, on the other hand, can be applied on any foil condition, but errors amount to ±20% [7]. Other methods exist, based on parameters not readily obtainable or on extra features of the microscope, usually found on more sophisticated TEMs. Also, care must be exercised when determining the foil thickness, since it is valid for the region of interest only. Due to the nature of the thinning process, the foil presents a wedged profile after the electropolishing procedure, rather than uniform thickness, which means that this latter is continuously varying across the sample.

4.4 Preliminary creep transient tests with partial unloading stages

As seen in Chapter 2, it has become usual practice to associate the anelastic behaviour of polycrystalline materials to the existence of a back stress, developed as a consequence of intergranular and intragranular levels of plastic strain incompatibility [13]. The most significant methodological consequence of the association of anelasticity to the back stresses has been the popularization of stress-dip tests. Indeed, the shape of the curve after stress reduction provides relevant information on the extent of anelastic recovery. It is important to be aware, though, that this technique may be subject to errors. Due to the natural scattering of creep data, accuracy in measuring the anelastic strains may be compromised, as observed by Blum [14]. However, emphasis is given here not to their absolute magnitudes, but to the form of the curves during unloading stages and their impact on the secondary strain after reloading.

Under these considerations, the 316H samples used in the preliminary creep tests were crept for 24 hours at 650 ± 1 °C under a constant stress of 180 MPa, to ensure that the secondary creep stage was reached, and, then, each was partially unloaded to a stress level in the range 20 MPa to 150 MPa. The exact stresses to which the specimens were partially unloaded are summarized in Table 4.3 below.

Table 4.3 - Summary of test conditions for the preliminary creep transient tests.

Creep test ID	Stress regime [MPa]	Stage duration (loading/unloading) [hours]	Number of transient cycles
CTP 1	180 / 20	24 /12	2
CTP 2	180 / 45	24 /12	2
CTP 3	180 / 70	24 /12	2
CTP 4	180 / 90	24 /12	2
CTP 5	180 / 105	24 /12	2
CTP 6	180 / 120	24 /12	2
CTP 7	180 / 150	24 /12	2
CTP 8	180 / 45	24 /12	4

These stress values were chosen following a suggestion, in recent work by Rao [15] with 316H, that the back stress level might be approximately 45 MPa. In order to keep consistency with this work, the samples were crept under the same applied stress of 180 MPa and different stress levels were used for the partial unloading stage. For each test, two transient cycles were completed; a loading period of 24 hours under 180 MPa followed by an unloading period of 12 hours at one of the previously mentioned stress levels comprising one cycle. The only exception was test number 8, which comprised four cycles of 180/45 MPa. This was to check the extent of anelastic recovery, its impact on the

secondary creep rate and any variations in anelasticity from one cycle to the other. Figures 4.4 and 4.5 illustrate the evolution of shapes of the anelastic portions of the creep curve. From these creep tests, the secondary strain rate was calculated before and after the first unloading transient. The observed reductions are found in Table 4.4.

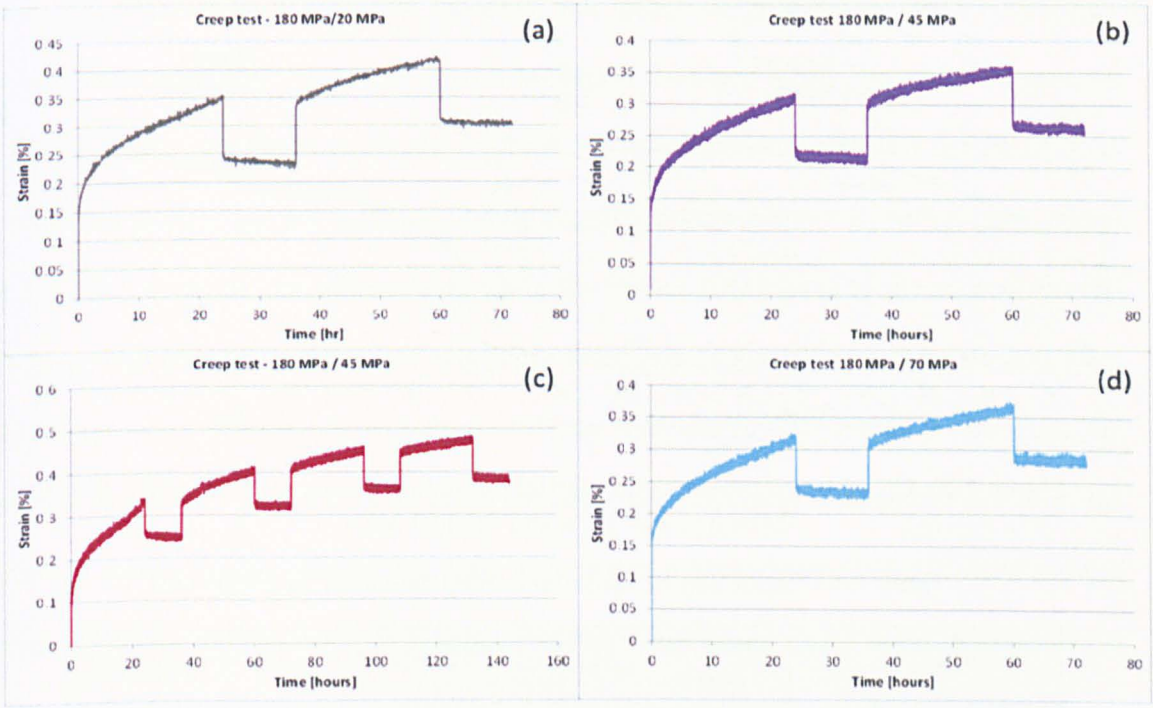

Figure 4.4 - Creep transient tests with partial unloading stages at (a) 20 MPa, (b) 45 MPa, (c) 45 MPa (4 transients); and (d) 70 MPa.

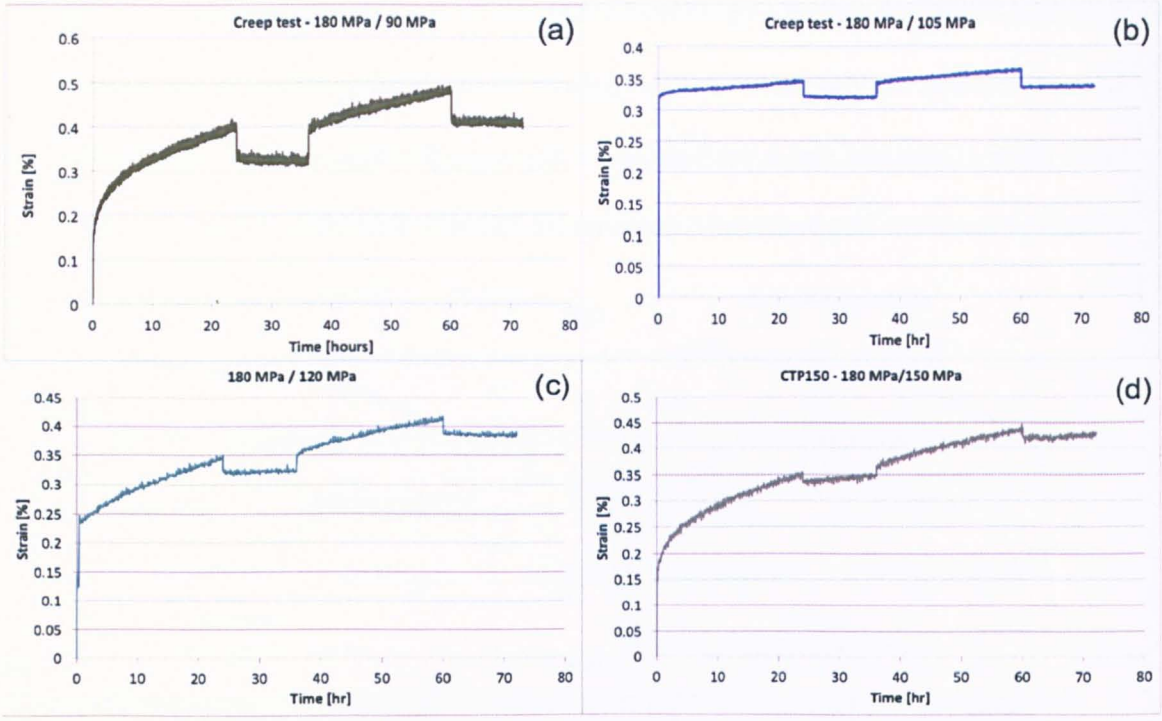

Figure 4.5 - Creep transient tests with partial unloading stages at (a) 90 MPa, (b) 105 MPa, (c) 120 MPa and (d) 150 MPa.

Table 4.4 - Reduction in secondary creep-rate after first transient.

Test ID	Stress level [MPa]	Strain-rate [1/s]		% Reduction
		before	after	
CTP 1	20	1.38E-08	8.68E-09	37
CTP 2	45	1.11E-08	5.93E-09	47
CTP 3	70	1.12E-08	6.02E-09	46
CTP 4	90	1.41E-08	8.29E-09	41
CTP 5	105	2.11E-09	2.00E-09	6
CTP 6	120	9.96E-09	6.53E-09	34
CTP 7	150	1.19E-08	7.05E-09	41
CTP 8	45	1.81E-08	8.67E-09	52

A pronounced level of scatter is observed in some of the data for the strain-rate prior to the unloading. While all test parameters were kept within controlled limits, slippage of the extensometer during initial application of the load may have affected the initial portion of the curves and the reference strain level at the onset of the test, as seen in Figures 4.5b and c. Yet, the strain levels recorded at the transition to the unloading stage were maintained within a reasonable range around approximately 0.35%.

Two features are relevant in the interpretation of the results: the shape of the anelastic portion of the curve, and the variations in the percentage of reduction in the secondary

strain-rate observed when the material is reloaded at the end of the creep transient. As the applied stress during the partial unloading stage increases from 20 MPa to 105 MPa, the anelastic curve tends to be flatter, showing a more horizontal slope. The stress level of 105 MPa seems to be a turning point, after which the creep curve following stress reduction does not show signs of anelastic recovery, but rather, of progressive creep with a new steady-state condition. This can be seen in figures 4.5c and 4.5d. The lower stress level (120 MPa) test condition shown in figure 4.5c, in comparison with test condition 4.5d, causes the slope of the curve to just slightly depart from the horizontal, with a strain rate of 8.3×10^{-10} s^{-1} at the unloading stage, while the higher stress level of the subsequent test (figure 4.5d) causes a steeper new secondary creep rate (2.8×10^{-9} s^{-1}), three times higher. This first set of tests seems to indicate that the differences after partially unloading the sample are related to a change in the dominant creep regime as well as to the role of the internal (back) stresses, since those tests unloaded to a stress lower than 105 MPa showed measurable anelastic recovery, while the tests that experienced a low stress reduction were still creeping. While the total back stress level may remain unknown, the fact that anelastic recovery is observed in partial unloading stresses of up to 90 MPa and that creep deformation was found to continue with stress reductions to 120 MPa and up, it seems natural to assume that the transition lies in-between these levels.

When the data from Table 4.4 are incorporated to the analysis, the above considerations seem to be supported by the fact that the test at 105 MPa unloading stress shows only 6% reduction in the creep rate following reloading; that is, no creep deformation is seen in the unloading stage and only little anelastic recovery seems to be present, probably associated with the sudden drop in stress. Tests in which the material was unloaded to 90 MPa or less presented an opposite trend to what would be expected. Small reductions in the steady-state creep rate would be expected for the samples that experienced large stress dips (because they would have, in principle, recovered more, therefore, upon reloading, the new strain-rate could be close to the initial one), with progressively larger reductions in the

creep rate as the unloading stress increased. Instead, they appeared to have had approximately the same amount of recovery in the partial unloading stage, as it can be seen when comparing the reductions in creep rate after reloading to 180 MPa for CTP 3 (70 MPa) and CTP 4 (90 MPa) with those from CTPs 1 (20 MPa) and 2 (45 MPa). This suggests that the amount of anelastic recovery was the same, regardless of the partial unloading level, and that these tests underwent a change in creep regime when unloaded. The stress level, in these cases, was not enough to maintain dislocation-based processes [16], being responsible for the activation of diffusion-controlled mechanisms on unloading, which granted conditions for anelasticity to occur, driven by the back stresses.

Results for CTP 6 (reduction to 120 MPa) and CTP 7 (reduction to 150 MPa) were in agreement with intuition, according to which a larger reduction in secondary creep rate after reloading to 180 MPa would be expected for the specimen previously unloaded to the higher stress level, given that, at the unloading stage, higher creep-rate would be associated with the higher applied stress. When these test conditions are checked in an appropriate deformation map, such as the one shown in fig.4.6 for a 316H stainless steel with 100 μm grain size, it is possible to see that the most likely dominant deformation mechanism during unloading is still dislocation-based, meaning that the applied stresses are still capable of causing glide [3, 14, 17].

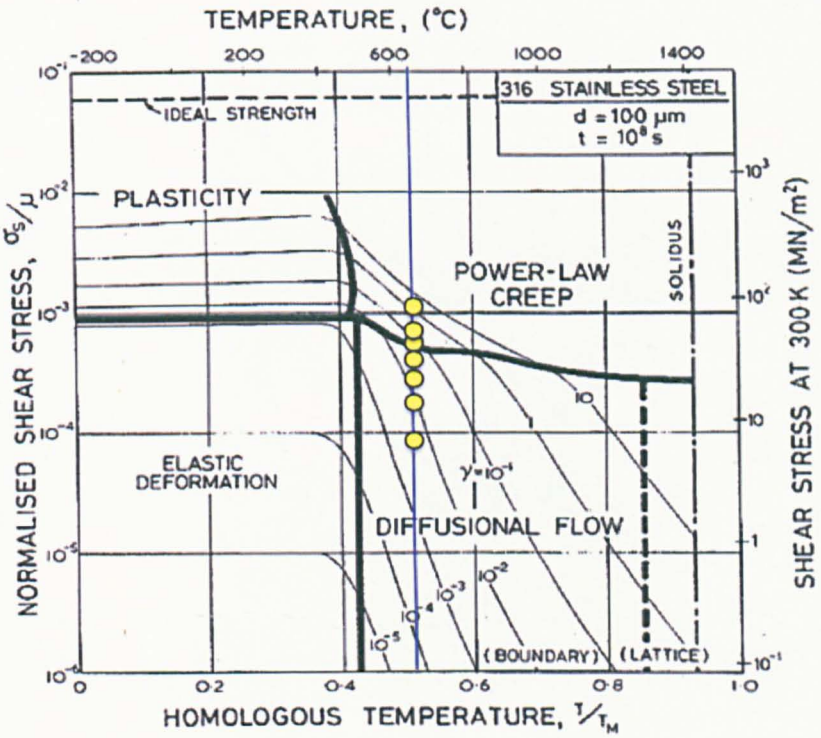

Figure 4.6 - Deformation mechanism map for 316H stainless steel with an average grain size of 100 μm.

4.5 *In situ* Neutron Diffraction creep test

As a first step of a multi-technique approach for studying anelasticity, an *in situ* creep transient experiment was devised and carried out at the ISIS neutron source, Rutherford-Appleton Laboratory, UK, using the ENGIN-X neutron diffractometer. Load was applied by the hydraulic stress rig available at ENGIN-X, with the temperature maintained at 650°C ± 1°C by a radiant furnace. The macroscopic creep strains were measured by a strain gauge and the temperature was monitored by a thermocouple, both attached to the specimen gauge length. For the neutron measurements, a gauge volume of 3mm x 3mm x 3mm was defined at the mid-length of the specimen. The stress rig is positioned at 45° relative to the collimated neutron beam, as shown schematically in figure 4.7, so that one of the detector banks measures the axial strains while the other measures the radial components [18].

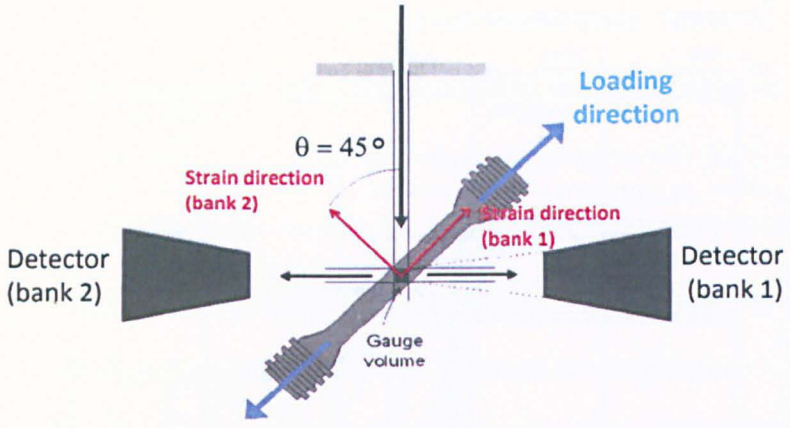

Figure 4.7 - Schematic of the *in situ* creep test set up.

A round 316H specimen, similar to the ones used in the uniaxial creep tests, described in Chapter 3, was subjected to the same load/partial unload regime of 180 MPa/45 MPa, while the evolution of internal strains was monitored by continuous neutron diffraction measurements of the inter-planar distances in differently oriented grain families. Figure 4.8 illustrates the experimental set-up corresponding to the schematic of figure 4.7, with the apparatus used.

Initially, the material was crept for 48 hours, to ensure statistical robustness of the determined values of the intergranular stresses developed during secondary creep and their stabilization, given the natural dispersion of neutron data from bulk specimens (scatter in the datasets of different grain families), so that any change could be more easily observed. The secondary creep rate, calculated as $1.19 \times 10^{-8}\ s^{-1}$, was comparable to the ones found in the previous tests, crept for 24 hours. The specimen was then partially unloaded for 12 hours to complete one cycle.

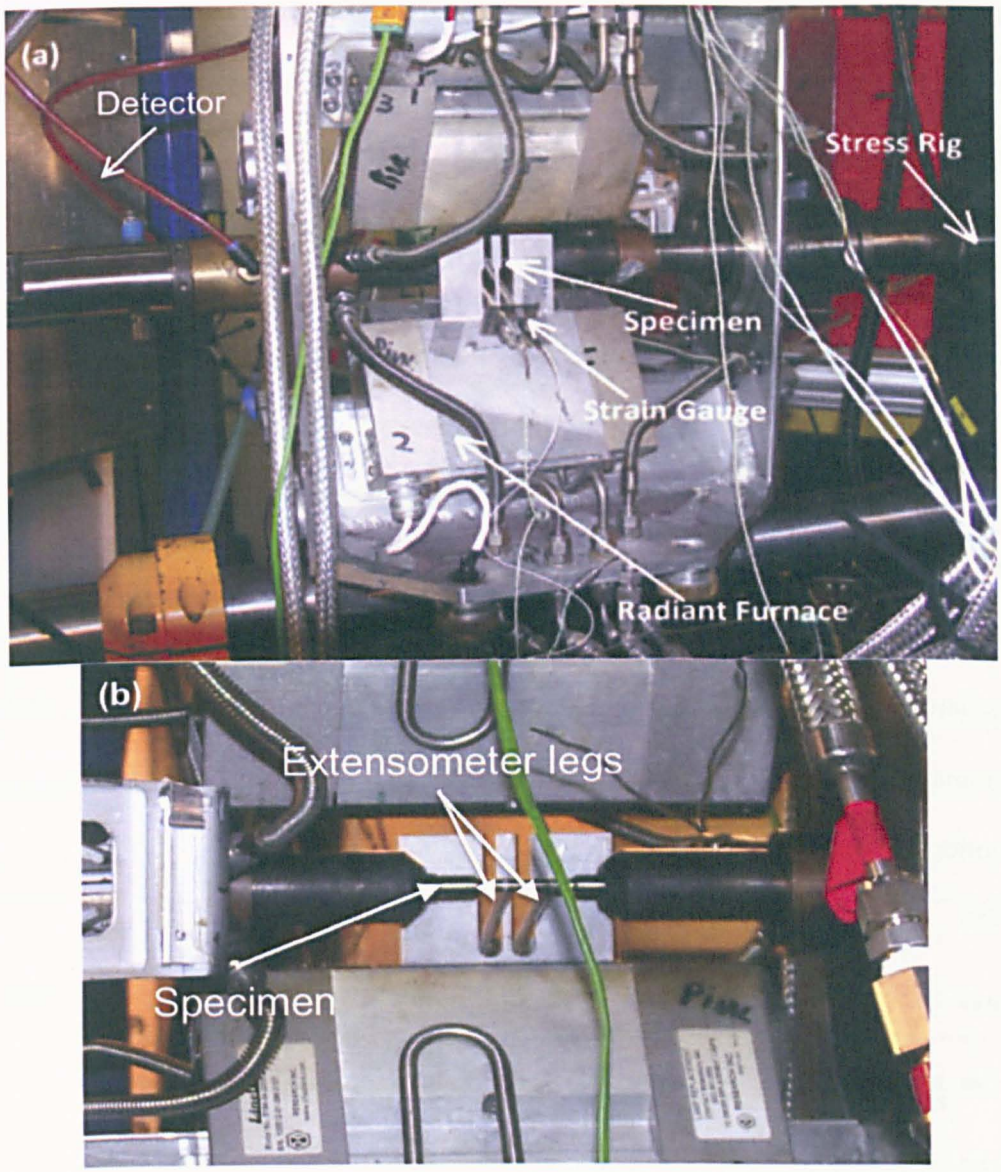

Figure 4.8 - (a) Apparatus of the neutron diffraction experiment and (b) detail of the mounting of the extensometer onto the 316H specimen.

Measurements of the interplanar spacing of differently oriented grain families (with regards to the loading direction) were taken every 16 minutes, as well as the average lattice strain, in order to calculate the evolution of the stresses borne by these grains along the creep transient test. Since the changes in interplanar spacing are determined with regards to a reference condition, as expressed in equation 3.9 (reproduced in eq. 4.3 below for convenience), the first step taken concerned obtaining a strain-free lattice parameter.

$$\varepsilon = \frac{d - d_0}{d_0}$$

(Eq. 4.3)

This was done by gradually heating up the unstressed specimen from room temperature to 650°C, while continuously measuring the d-spacings. Once the readings at 650°C stabilized, the corresponding values were taken as a reference. Then, load was gradually applied over 50 seconds, to the intended stress of 180 MPa. Figure 4.9 shows the elastic microstrains from single-peak fitting analysis, along with the Rietveld analysis for the average lattice strain. All results presented refer to the axial direction, that is, parallel to the longitudinal axis of the specimen. The gaps observed in Figures 4.9 to 4.12 are due to interruption of the neutron beam.

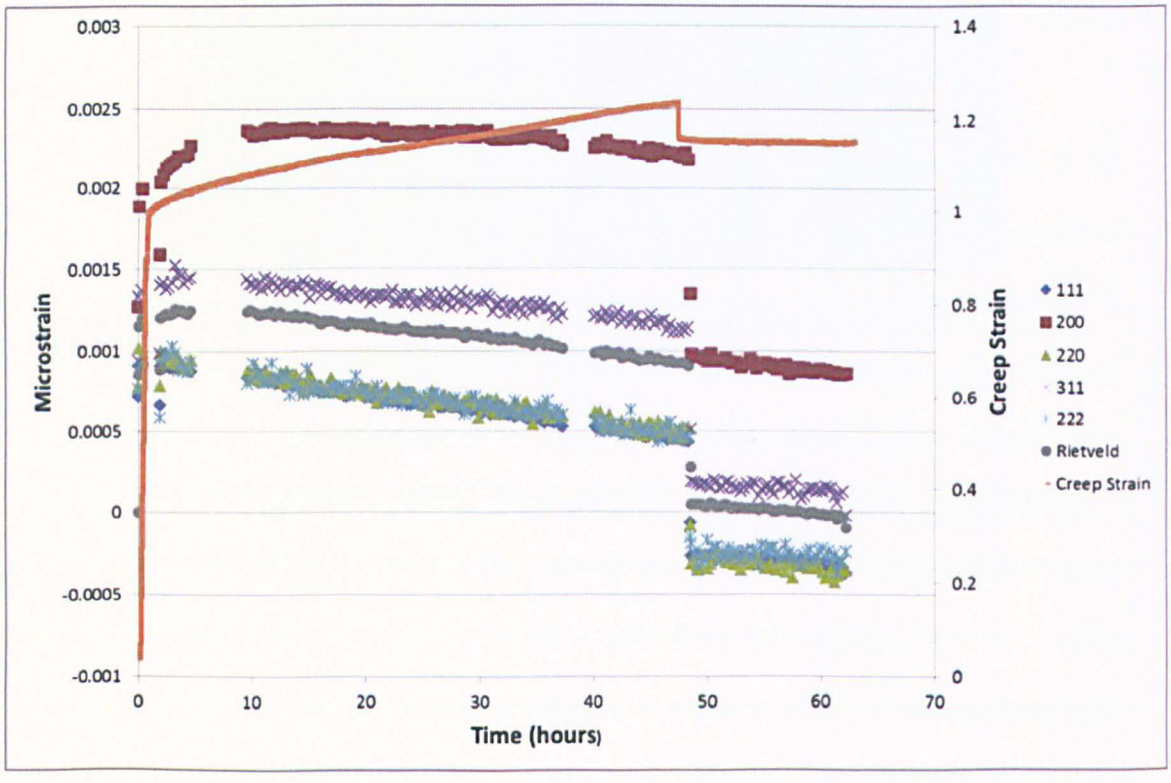

Figure 4.9 - Evolution of intergranular strains (microstrains) in the main low-index lattice planes along the *in situ* creep test.

Although these results already start to evidence the anisotropy of the material at the grain scale, it is necessary to subtract the instantaneous elastic strains observed when load is applied or removed. This is done so that the resulting dataset presents just the inelastic components of the strains, as shown in figure 4.10:

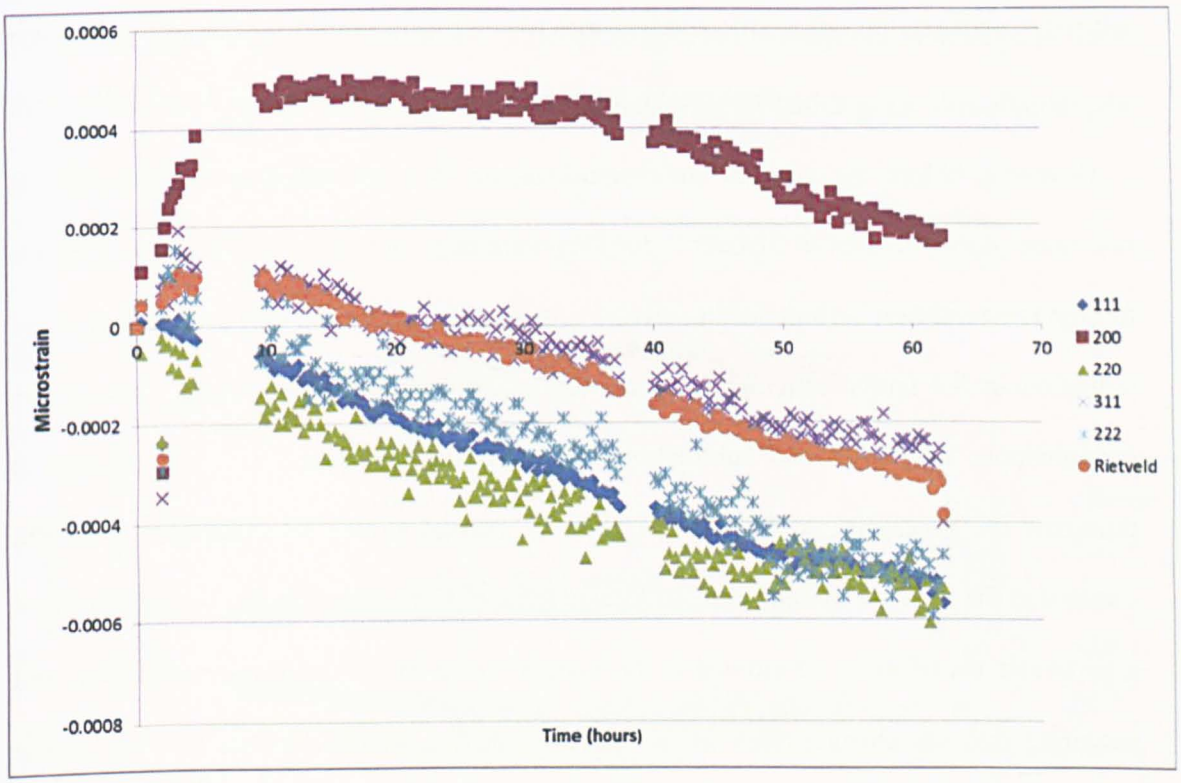

Figure 4.10 - Plot of microstrains considering inelastic effects only.

With this dataset, the elastic anisotropy of the families of grains could be quantified using Hooke's law, by calculating the ratio between the drop in stress – 135 MPa – and the virtually instantaneous drop in strain, noticed for each plane. The results are the diffraction elastic moduli, presented in Table 4.5, in GPa, and compared with values published in literature. The relevance of the elastic constants lies in the fact that, with them, an estimate of the intergranular internal stresses can be made, by using the generalized Hooke's law:

Table 4.5 - Calculated elastic diffraction moduli and their comparison to the literature.

E {111}	E {200}	E {220}	E {311}	E_{Riet}	Condition
193	113	162	142	157	Calculated
180	100	165	130	140	Literature

Uncertainties in the diffraction Young's moduli varied between 1 GPa (for the {111} family) and 7 GPa (found for the {311}). It is easy to notice that the calculated values were, mostly, higher than the ones reported in the literature. This may be attributed to the values of microstrains selected for the calculation of the drop in strain, which present a small oscillation as the stress is reduced to 45 MPa. The differences represented an error of 4%, though, still being suited for the calculation of the microstresses.

However, before the stresses are determined, another correction to the data plot is necessary. As mentioned in Chapter 2, for long-term exposure of the 316H austenitic steels to high temperatures, carbide formation and precipitation occur and will cause a continued reduction in the lattice spacing, since carbon atoms come out of solution. Due to this phenomenon, separation and subtraction of the strains associated with the changes it promotes are necessary, so that the analysis of internal strains are computing only the changes in the interplanar spacings due to load effects. The correction involves selection of a particular set of data, considered to be least affected by the intergranular strains, and assuming that the changes seen in the correspondent crystal planes are due to carbide precipitation. By making the strains constant in the selected dataset and applying the difference to each of the other planes, the relative changes between each plane and the reference one provide the strains due to loading/unloading. From figure 4.10, the Rietveld and the {311} are the datasets presenting the smallest variations in the microstrains. Considering this, the Rietveld plot was made to be constant and relative differences to all other planes were determined. Figure 4.11 shows the results. An alternative approach would be to use the {311} family of grains as a reference, as in [19], which would yield a similar outcome.

The first interesting feature is the anisotropic inelastic response, manifested as tensile microstrains for the creep-resistant grain families (200 and 311) and compressive internal strains for creep ductile planes (111 and 220). In other words, the internal tensile stresses in (200) and (311) families, accumulated during the loading stage, indicate little creep

strain. Similarly, the compressive intergranular stresses in the remaining grain families – (111) and (220) – indicate large creep deformations. This is in perfect agreement with the results found by Rao [15] and by Saleh and co-workers [20], who observed similar distribution of intergranular stresses to the ones shown in Figure 4.12, in a full unloading creep experiment; and similar responses, in terms of anisotropy and deformation, from the same grain families in a cyclic loading experiment, respectively.

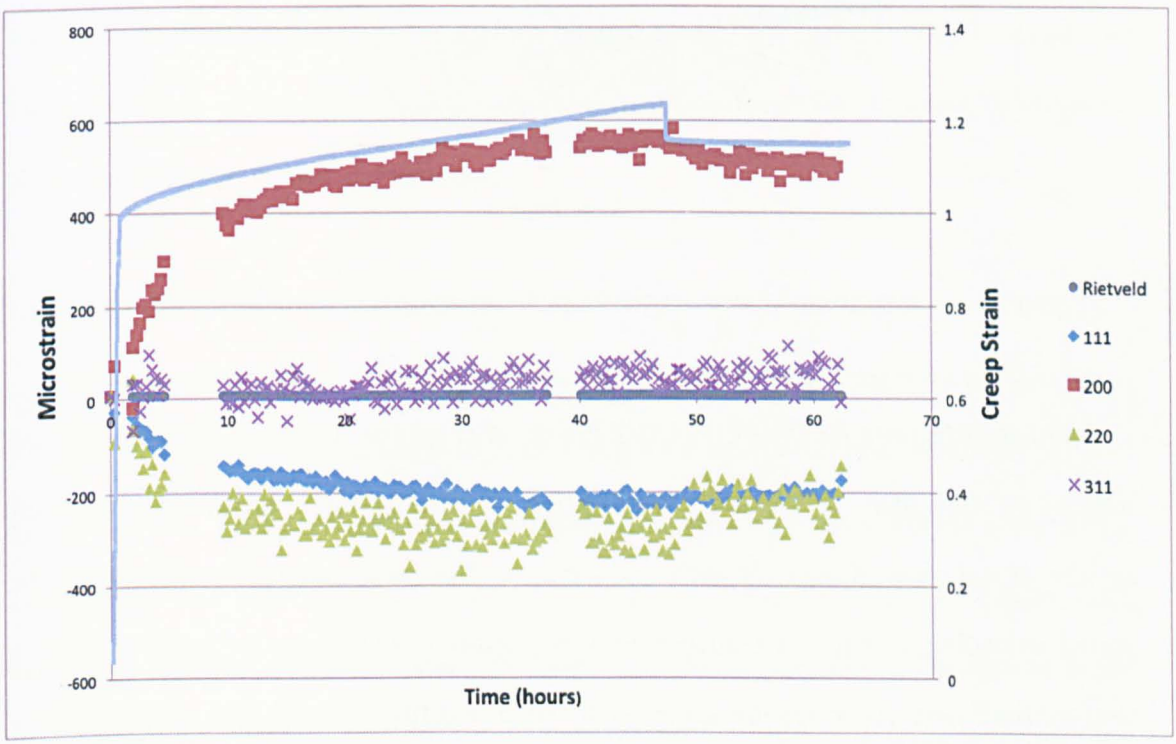

Figure 4.11 - Internal strains after correction of carbon concentration.

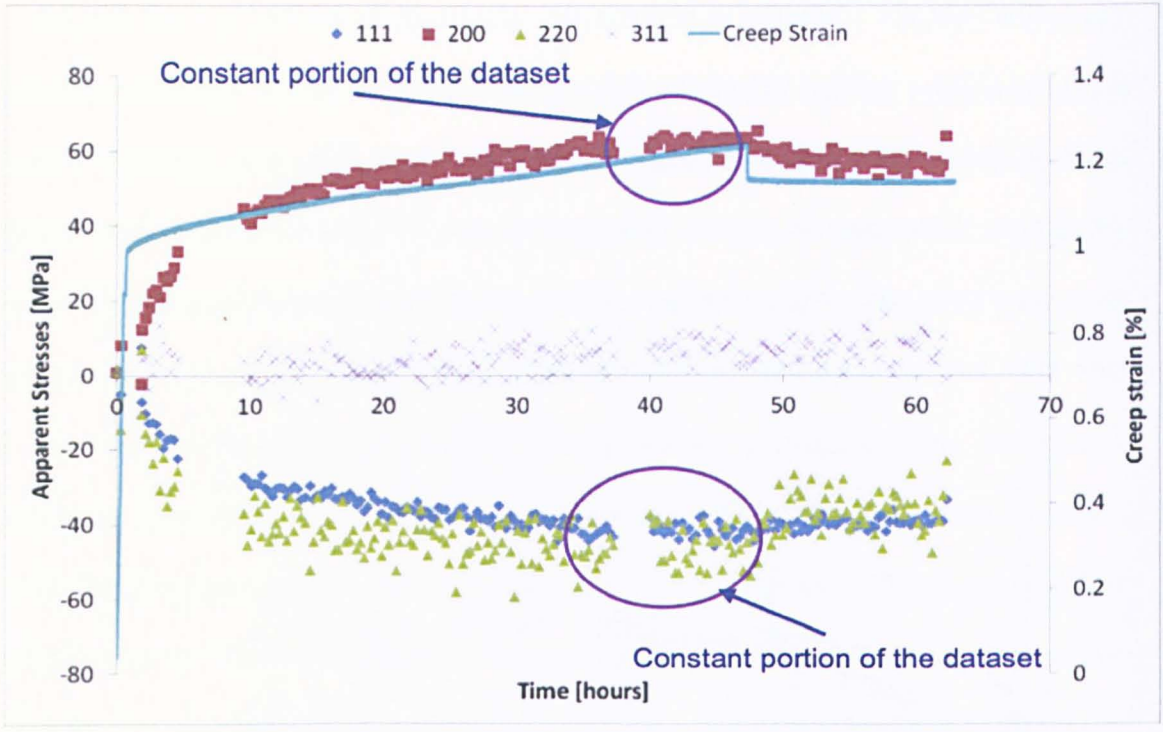

Figure 4.12 - Intergranular stresses developed corresponding to the strains in Fig. 4.11.

Another interesting feature of the curve is that, after approximately 35 hours of test, the internal stresses seem to approach stabilization, as seen in the approximately constant portion of the mass of data for each grain family. The same trend is observed after the partial unloading, in which a reduction in intergranular strains seems to be followed by a new constant state. Although the scatter in the neutron diffraction data makes it difficult to clearly identify, a tendency of stabilization of the intergranular stresses can be observed, as indicated by the circles in Figure 4.12 (especially the {111} and {200} families, for which less scatter occurred) and by the data in the partial unloading stage, which is also in agreement with [15]. Further evidence from the intragranular investigations seem to support the idea of stabilization of intergranular events in secondary creep: while the generation and motion of dislocations begin with pile-ups being formed in the active slip system and with stacking faults, promoting work-hardening and the development of intergranular stresses, cross-slip may rearrange some of these defects into heterogeneous structures, as illustrated by Figures 4.13 and 4.14, and explained in the next session.

In the case of creep-compliant families, the magnitude of stabilized stresses appears to be around 45 MPa in secondary stage and no less than 40 MPa during unloading stage, considering the {111} family. Data for {220} have more pronounced scatter, which makes analysis difficult. The magnitudes of stresses for these creep-compliant families are comparable to the ones found in the full unloading *in situ* experiment carried out by Rao [15], who reported the same stresses around 50 MPa, which is an indication that the partial unloading stress did not have any influence on the development of the internal stresses in these grains, which result from the loading regime (under the applied creep stress of 180 MPa).This analysis became complete with the investigations carried out using TEM for the study of intragranular mechanisms.

4.6 Creep test series for TEM studies

In order to complement the neutron diffraction results, TEM studies were performed on a group of specimens from a series of eight creep tests also performed under 180 MPa/45 MPa at 650 ± 1 °C, each deliberately interrupted at a different point along the creep curve. The first test was interrupted in the secondary stage of creep, after 47.5 hours under load, that is, half an hour before the unloading step would have taken place. The second to the sixth tests were interrupted at different points during the unloading stage, varying from some minutes after unloading to after the maximum time given for anelastic recovery in these tests, that is, 12 hours. The last two tests were interrupted after reloading of the sample. All these creep tests were assigned with an identification number, as shown in Table 4.6, which indicates the total time of each test until interruption:

Table 4.6 – Total hours of test up to interruption.

Specimen ID	1	2	3	4	5	6	7	8
Interruption time (hours)	47.5	48	48.5	50	56	60	60	60.5

Vickers hardness tests were performed on the cross-section of one half of each specimen, after sectioning on the gauge length, under a load of 5 kgf, using a Struers Duramin A-300 hardness machine, as described in Chapter 3. Eight indentations were produced on each specimen. From these same specimens, 3 or 4 slices were extracted and prepared for TEM examination using the JEOL JEM 2100 instrument. The investigative procedure followed the same guidelines described in subsection 4.3.1. Differences between the dislocation densities, and structures resulting from the different tests were used to estimate the back and effective stresses, in an attempt to relate them to the observed changes in the anelastic response.

As explained in Chapter 2 regarding the plasticity of the 316H steel, due to its low stacking fault energy, there are similarities between creep and other forms of plastic strain, in terms of mechanisms and dislocation arrangements. This is because, at the onset of plastic strain, dislocations will move in one active slip system and will either form pile-ups or stacking faults, given that cross-slip over long domains is limited. A creep test under similar conditions of applied stress (180 MPa) and temperature (650°C), interrupted after 4 hours, provided evidence that planar slip (that is, the mode of dislocation motion that promotes the formation of stacking faults and pile-ups) is the predominant mechanism during primary creep, in which work hardening is taking place. Figure 4.13 shows the predominance of pile-ups and stacking faults near boundaries, as the low stacking fault energy of the material has impeded cross-slip. During this stage, since in the majority of

grains, only one slip system is active, the dislocation pile-ups at the grain boundaries build up intergranular stresses.

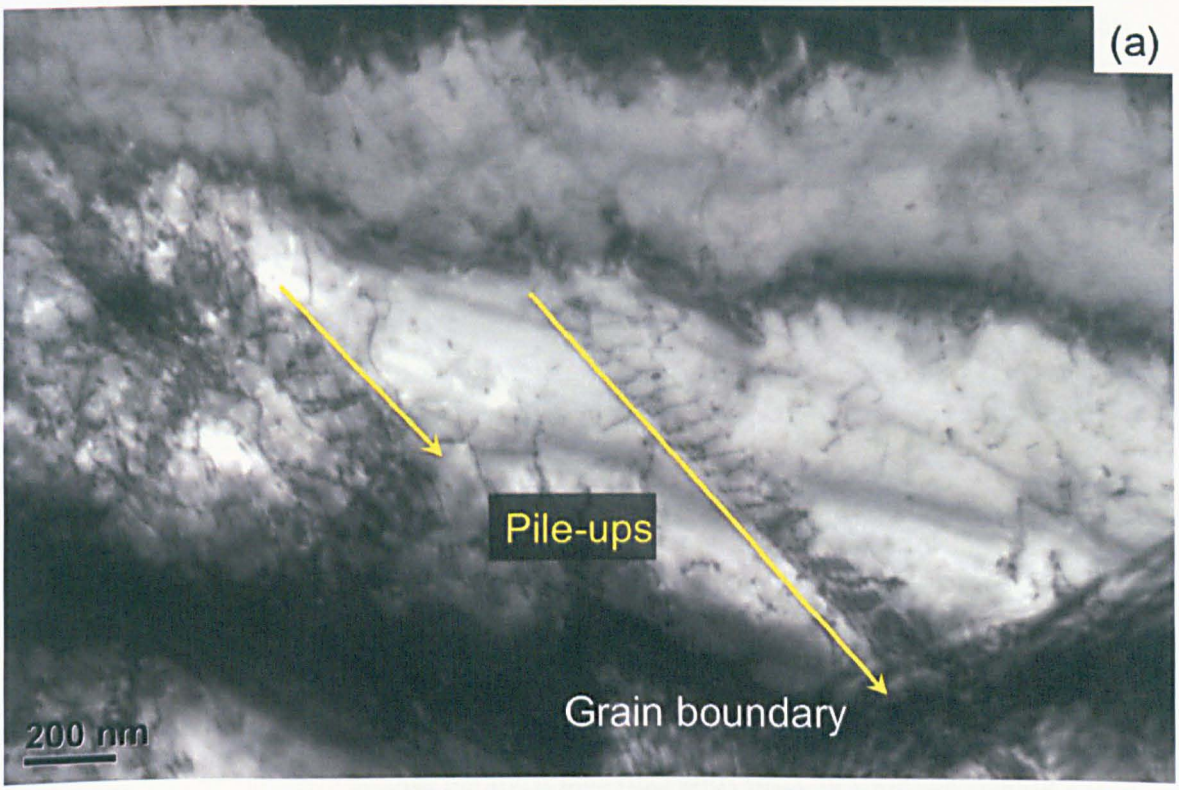

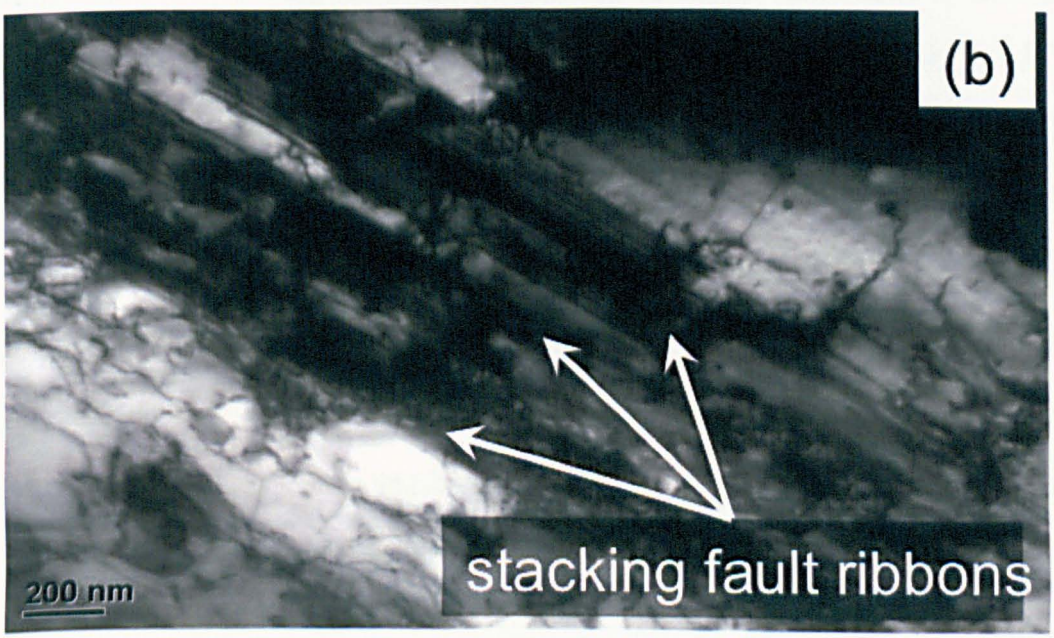

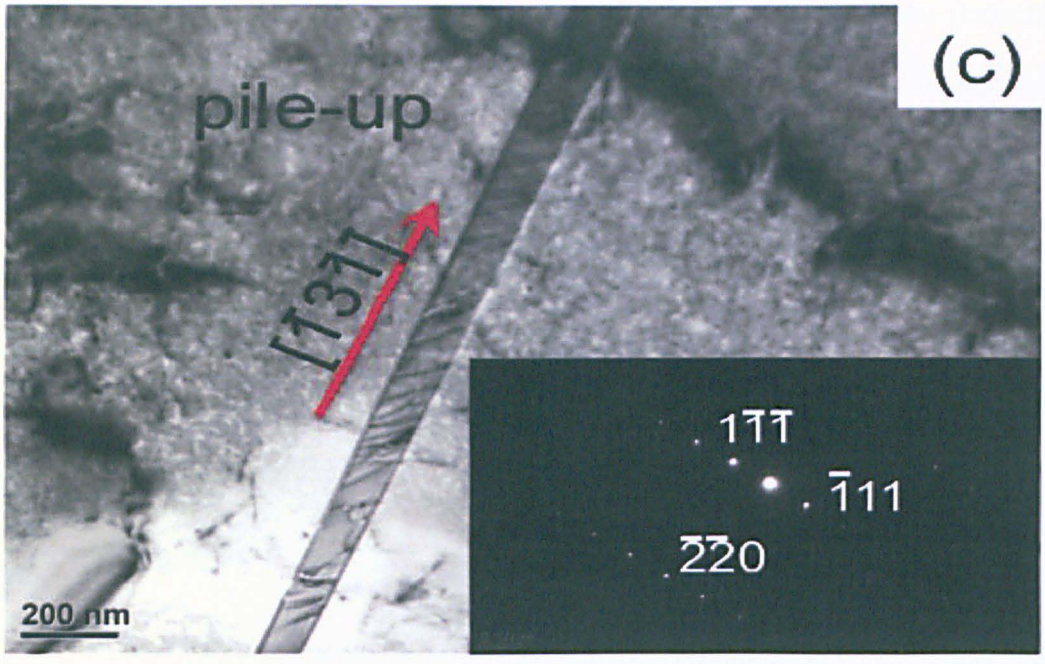

Figure 4.13 - TEM micrographs from the creep test interrupted in the primary stage, showing dislocation pile-ups stretching towards a grain boundary (a), stacking fault ribbons (b) and a pile-up following the specified direction (c).

These dislocation structures arising from planar slip were found in 88% (8 images out of 9) of the grains examined in TEM foils extracted from the sample crept in the primary stage, while 44% (5 images out of 11) of the grains examined in foils of the as-received condition showed these arrangements. In terms of distribution of the defects per total foil area examined, only one instance of dislocation pile-up was found, along with 13 stacking faults, in 43 μm² of examined foil area for the as-received material. The total for the sample crept in primary stage was 10 pile-ups and 24 stacking faults in 36 μm². When counting the stacking faults, were considered only the ribbons whose length was higher than the equilibrium separation of partials, given by $d_{eq} \approx \mu {b_p}^2 / (4\pi\gamma_E)$ [10], where b_P = 0.1458 nm is the magnitude of the Burgers vector of the partial dislocation (b_p = $a_0/6[211]$), μ is the shear modulus of the 316H steel (μ = 78 GPa) and γ_E is its stacking fault energy (adopted as 30 mJ/m²).

The onset of the secondary creep stage is characterized by the occurrence of multiple slip and cross slip, arising from the necessity of keeping cohesion and compatibility

between the grains experiencing elastic and plastic anisotropic deformation. This transition from primary to secondary creep is similar to the transition between stages I and II of tensile deformation, reported in other studies on *f.c.c.* crystals [21, 22], given that it marks the onset of long-range recovery. The processes of climb of edge dislocations and the recombination of partials into perfect dislocations, capable of cross slipping into another plane allow rearrangement of stacking faults and pile-ups, previously restricted to planar motion, into dislocation structures such as junctions, tangles, walls and, ultimately, cells (depending on the strain level reached). As a result of the development of these structures, the interiors of the grains become mechanically heterogeneous, with harder zones, where dislocations build-up in junctions, tangles and walls, and softer matrix areas ("channels"), where dislocation annihilation has occurred. The number density of planar slip structures decreases from primary to secondary creep, as they are replaced by heterogeneous dislocation arrangements. However, since secondary creep is characterized by an interplay between the generation and motion of dislocations and recovery processes, it is suggested that the number of stacking faults and pile-ups stabilises after some time in secondary creep, even though the material is still hardening, as suggested by the plateau in intergranular stresses indicated in Figure 4.12. The variations in the calculated magnitudes of back stresses (presented later) seem to indicate that, simultaneously, the intragranular stresses start to increase, as a result of the build-up of heterogeneous structures within the grains. Figure 4.14 shows TEM micrographs for the creep test interrupted in secondary stage (test ID 1), in which it is possible to see dislocations entangled around precipitates and determining channel regions in the matrix.

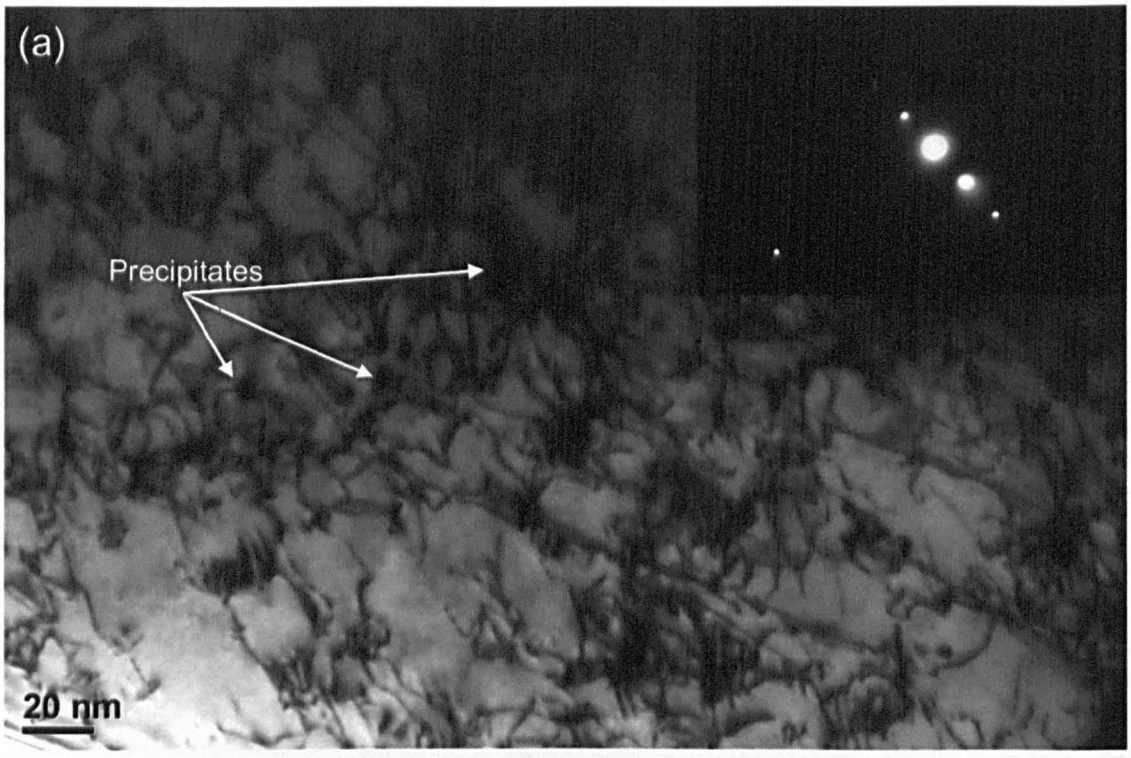
(a)
Precipitates
20 nm


(b)
20 nm

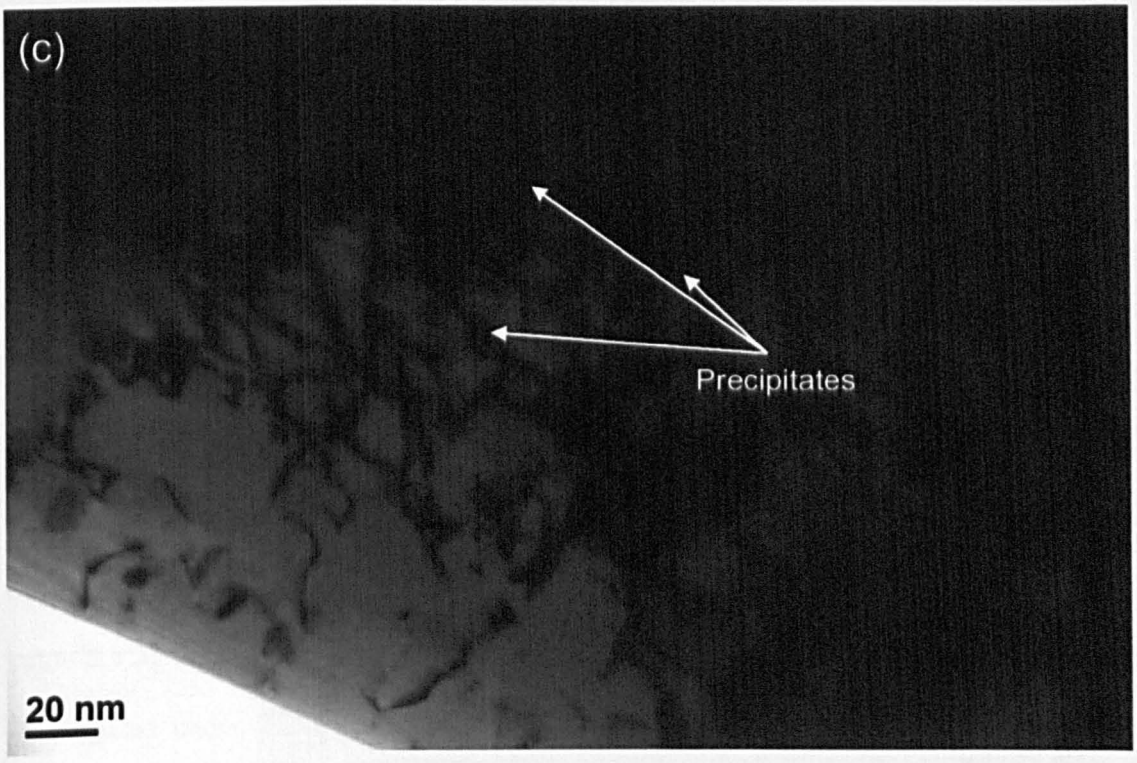

Figure 4.14 – Specimen ID 1 TEM images; (a) Dislocations tangled on precipitates all over the micrograph; same in (b), where the image of a different location was taken in a different zone axis. In (c), a third area, close to the hole. In all three cases, matrix areas with fewer dislocations (channels) surround the entanglements.

The calculated dislocation densities and the mean Vickers hardnesses of the gauge lengths of the test specimens interrupted at different points in the secondary creep stage up to reloading after the first transient are presented in Figure 4.15. Good agreement is found between the datasets, despite the scatter in the results. Upon unloading, the dislocation density, which reached about 8 x 10^{14} m^{-2} by the end of secondary stage, decreased one order of magnitude, as shown by points for test ID's 1 and 2 in the same figure. The estimated densities, when compared with those from previous work in 316H stainless steel, are found to be on a reasonable baseline. The orders of magnitude, ranging between 10^{13} m^{-2} to 10^{14} m^{-2}, were slightly higher than those reported by Rao [15], who worked with a solution annealed 316H. Also, as seen in Figure 4.15, although the upper bound uncertainties are higher, the lower bound uncertainties are significant. These latter result from the possibility of an overestimation, associated with some dislocations that may not

have been out of contrast when the diffracting conditions (g-vectors) changed and, therefore, may have been counted more than once in a determined area.

In the unloading stage, when anelasticity takes place, there is no significant hardening. Even if plastic deformation is going on by diffusion, the process is very slow and does not lead to measurable differences in the dislocation densities in such a short time. Since the applied stress is no longer capable of maintaining progressive dislocation motion, recovery (by climb and cross-slip) is dominant. The material softens, as shown by the decreases in the measured Vickers hardness and dislocation density. Since both the effective stress and the back stress depend on the dislocation density, they too are reduced.

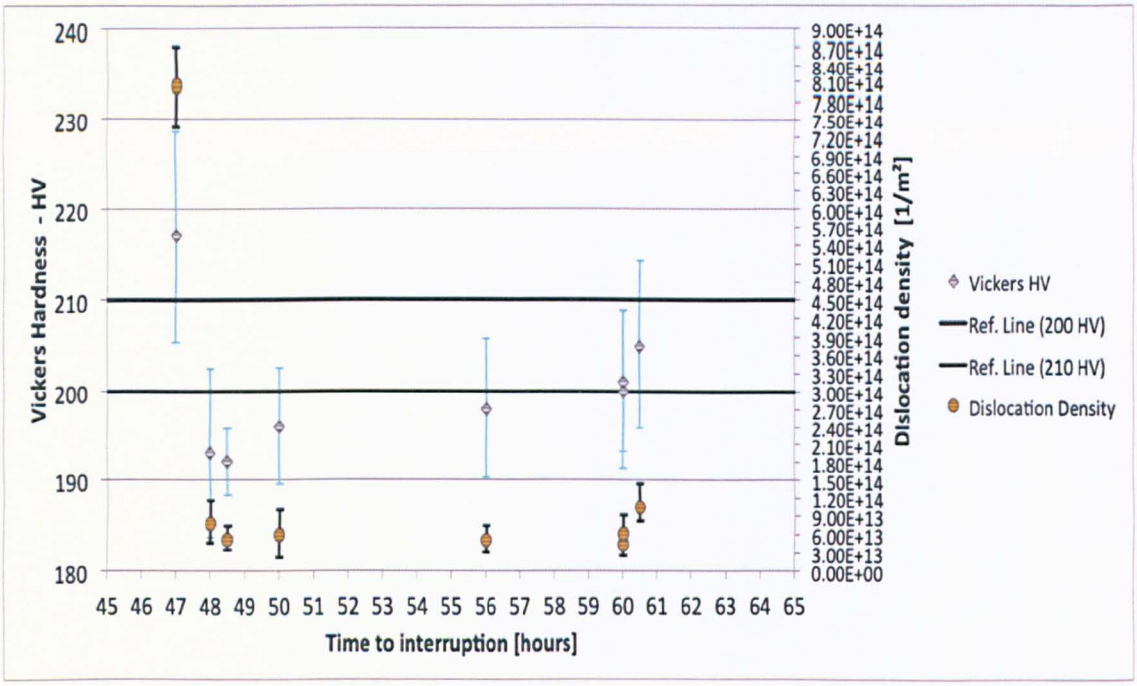

Figure 4.15 - Vickers microhardness and total dislocation density for each of the interrupted tests.

Anelastic recovery of previous plastic deformation seems to be more related to the intragranular component of back stresses, since the neutron diffraction measurements indicated only a small reduction in the intergranular stress magnitudes, although both components play a role. At the beginning of the unloading stage, back stresses are high, so

anelasticity progresses at a high rate. As recovery takes place, the back stresses reduce, but this happens differently for the intergranular and the intragranular components.

The intergranular stress component, already stabilized during secondary creep, shows only a slight decrease. This may be linked to the fact that it is associated with pile-ups and stacking faults: some pile-ups may start to relax when the external load is removed, but stacking faults remain largely unaltered, as seen in the TEM micrographs of Figures 4.17 to 4.21. Impeded from cross slipping at grain boundaries, possibly due to Suzuki clouds of solute atoms, they still contribute to maintaining the intergranular component. The occurrence of these defects decreases on unloading, but only fluctuates around a constant value during anelasticity, as shown in Figure 4.16, which depicts the proportion of grains investigated under TEM containing each group of dislocation arrangements, organized following Feaugas' work [21]. This parameter is used in the calculation of the intragranular back stresses, as shown further ahead. Since faulted regions were observed to exist in large number in grains of 316H, the intergranular stresses experience only a minor reduction.

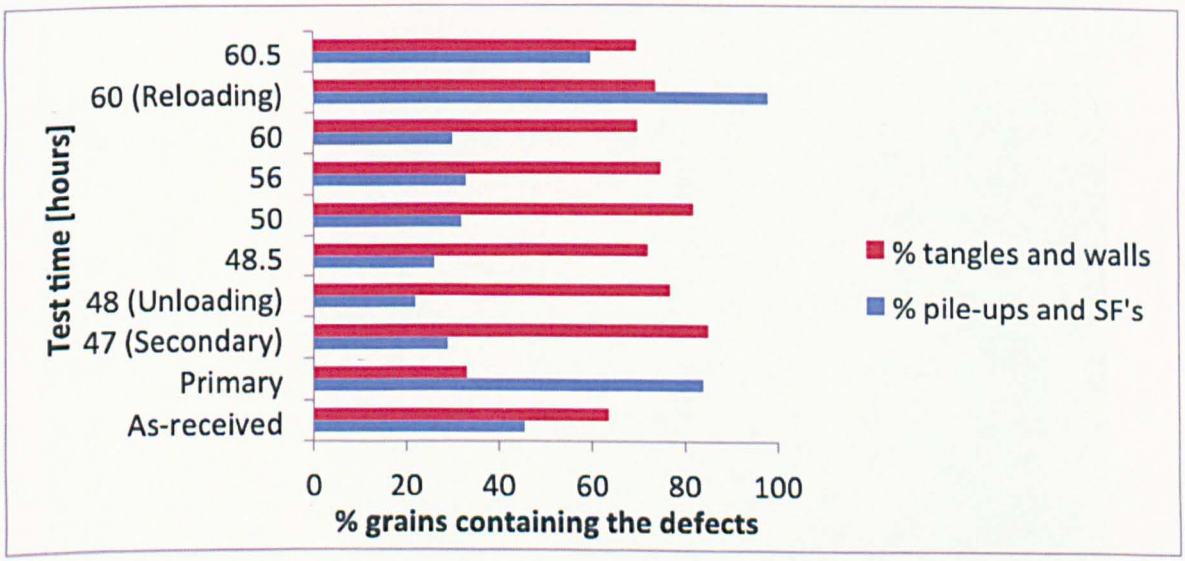

Figure 4.16 – Proportion of grains that display planar slip arrangements (pile-ups and stacking faults) and of heterogeneous structures (tangles and walls) in each interrupted test and in the as-received 316H.

The intragranular back stress decreases for two reasons, following the composite model proposed by Mughrabi [13], which is based on the existence of hard zones inside grains, associated with heterogeneous dislocation structures (in this case, tangles around precipitates, some walls and junctions), and soft zones ("channels"), which is the matrix itself with lower density of free dislocation density, it follows that:

- The channel dislocation density decreases due to motion through free matrix areas, leading to annihilation.

- The hard zones dislocation density also decreases, but not because of dissolution of walls and tangles (in fact, a reverse applied load would be required for this); it occurs due to the cessation of creation of hard zones (that is, the number density of hard zones and their dislocation densities tend to become constant) and to the annihilation of geometrically necessary mobile dislocations attracted to these hard zones.

As time at the unloading stage progresses, the difference between channel and hard zone densities becomes gradually smaller. The following figures show the microstructural features, in terms of dislocations, of each condition along the anelastic recovery stage in which the test was interrupted.

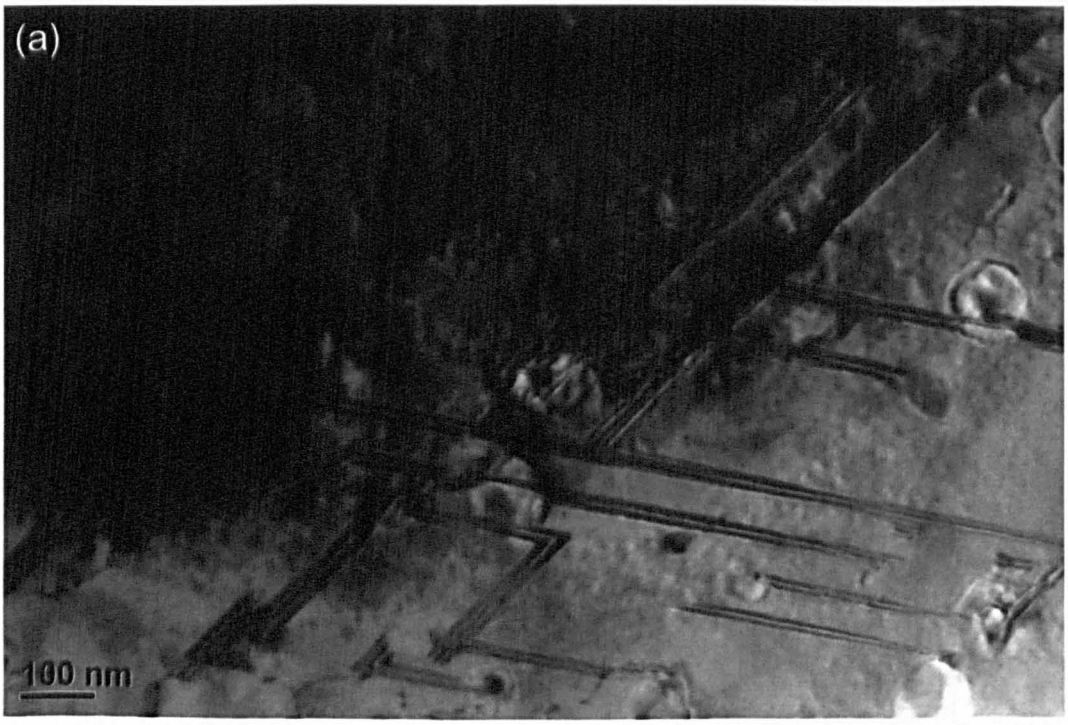

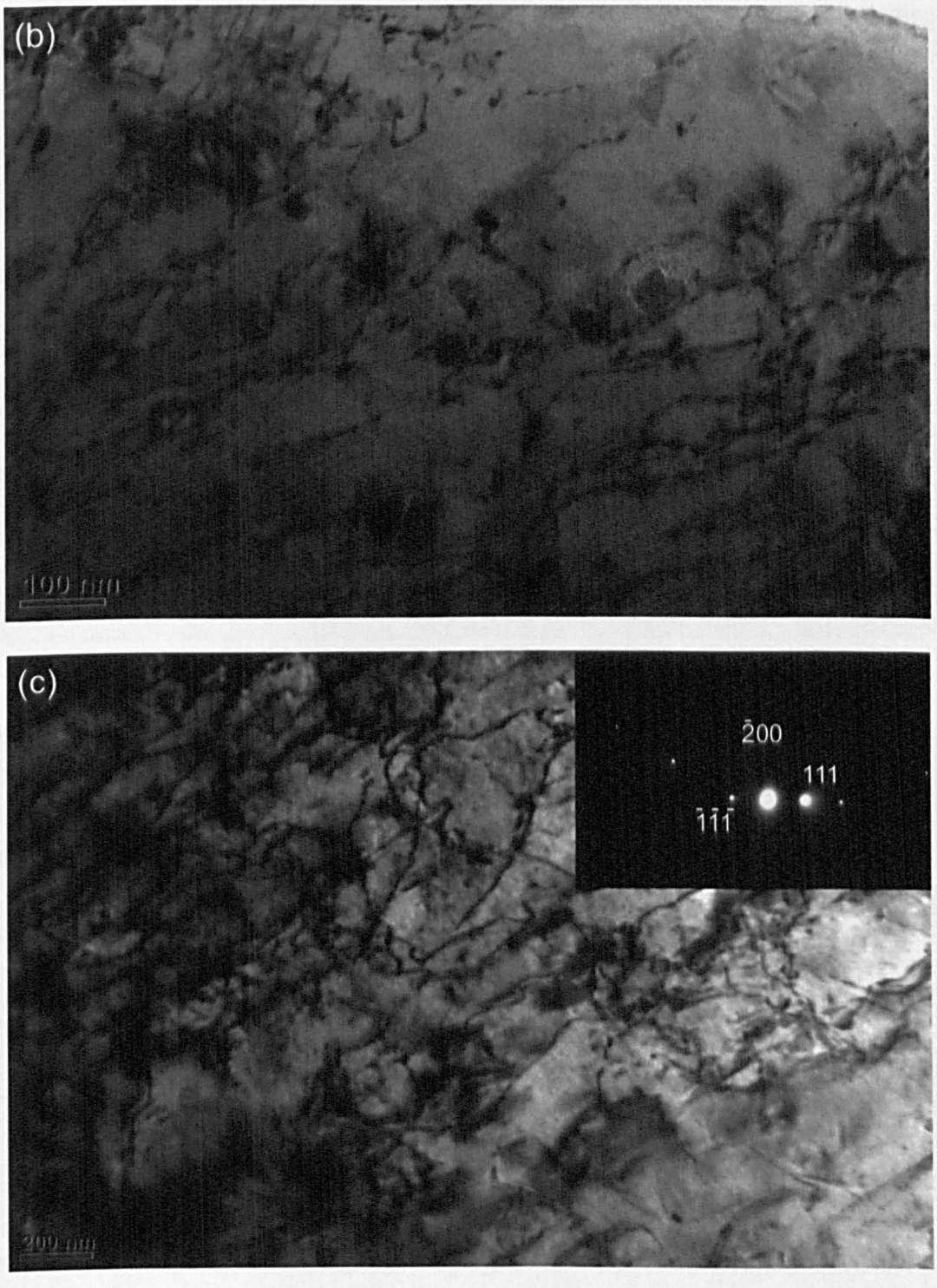

Figure 4.17 - TEM micrographs from test ID 2, the first test interrupted after unloading. In (a), some SFs forming locks; micrograph (b) shows some unaffected tangles surrounded by channel areas of matrix. And (c) shows tangles and a transition area to the matrix, where lower dislocation densities were observed (under different g-vectors).

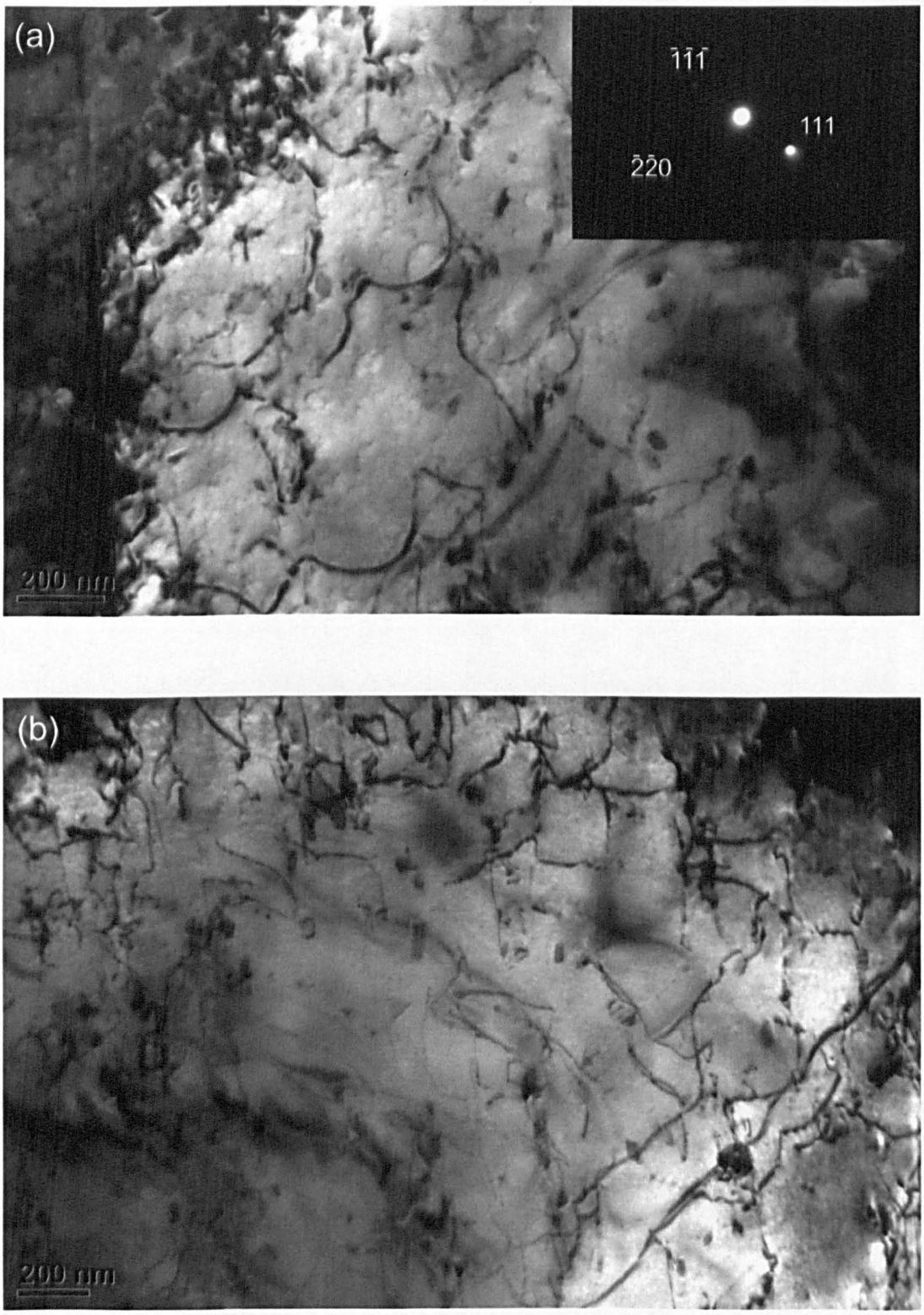

Figure 4.18 - TEM micrographs from ID 3, 30 minutes after unloading. Image (a) shows an area with free dislocations pinned and bowed by precipitates, and practically no tangles. In (b), another area shows entanglements around precipitates and matrix channels with fewer dislocations, going into poor contrast.

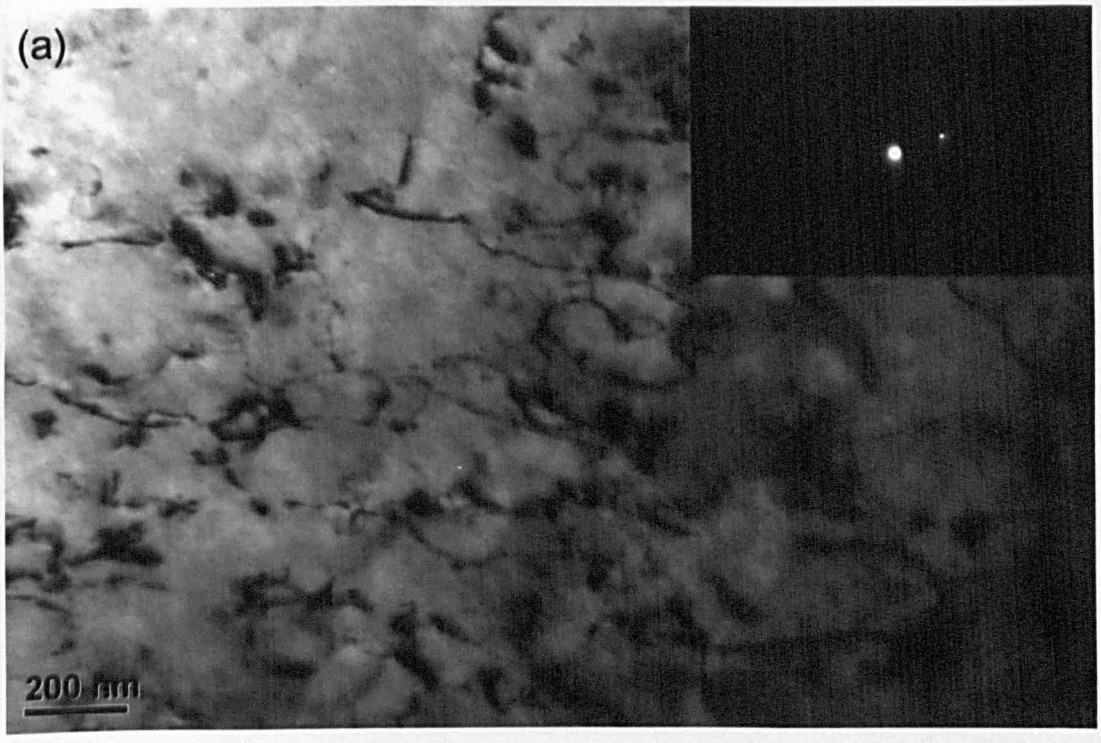
(a)
200 nm


(b)
100 nm

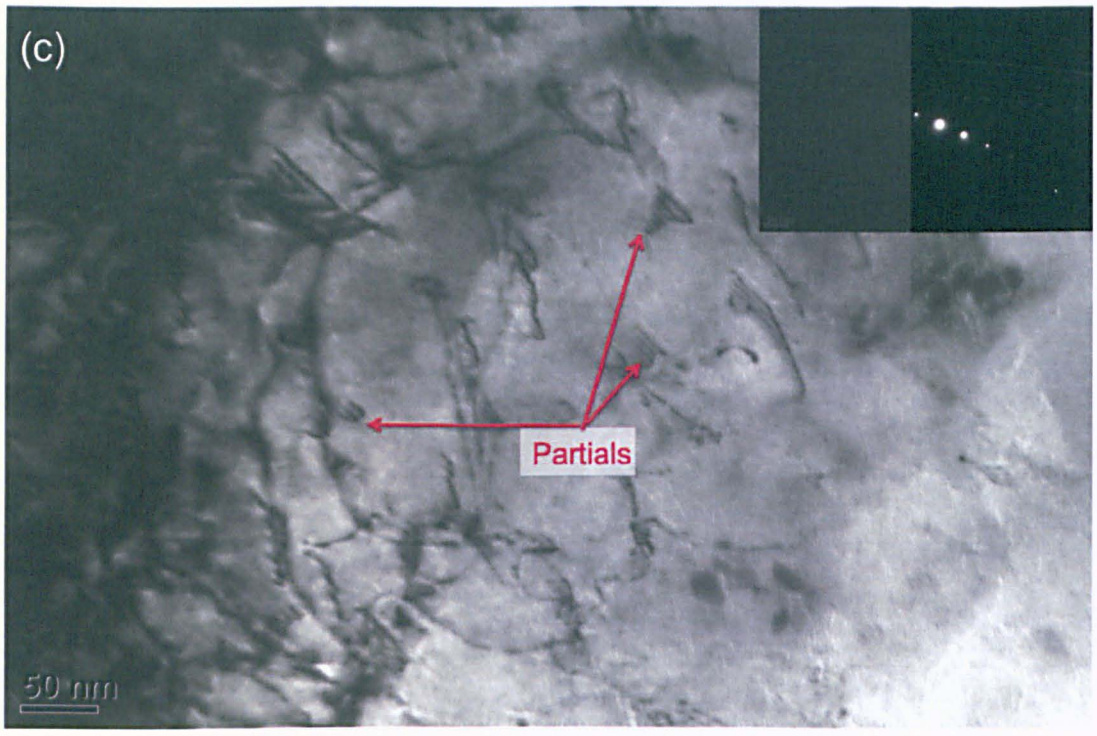

Figure 4.19 - TEM micrographs from ID 4 specimen, whose test was interrupted 2 hours after unloading. In fig. 4.19a, taken in good two-beam condition, it is possible to see tangles around precipitates and junctions preserved. Image (b) shows some tangles and stacking faults (SFs) preserved, surrounded by channel areas; (c) shows some partial dislocations (small SFs), a few tangles and a lower free dislocation density matrix area.

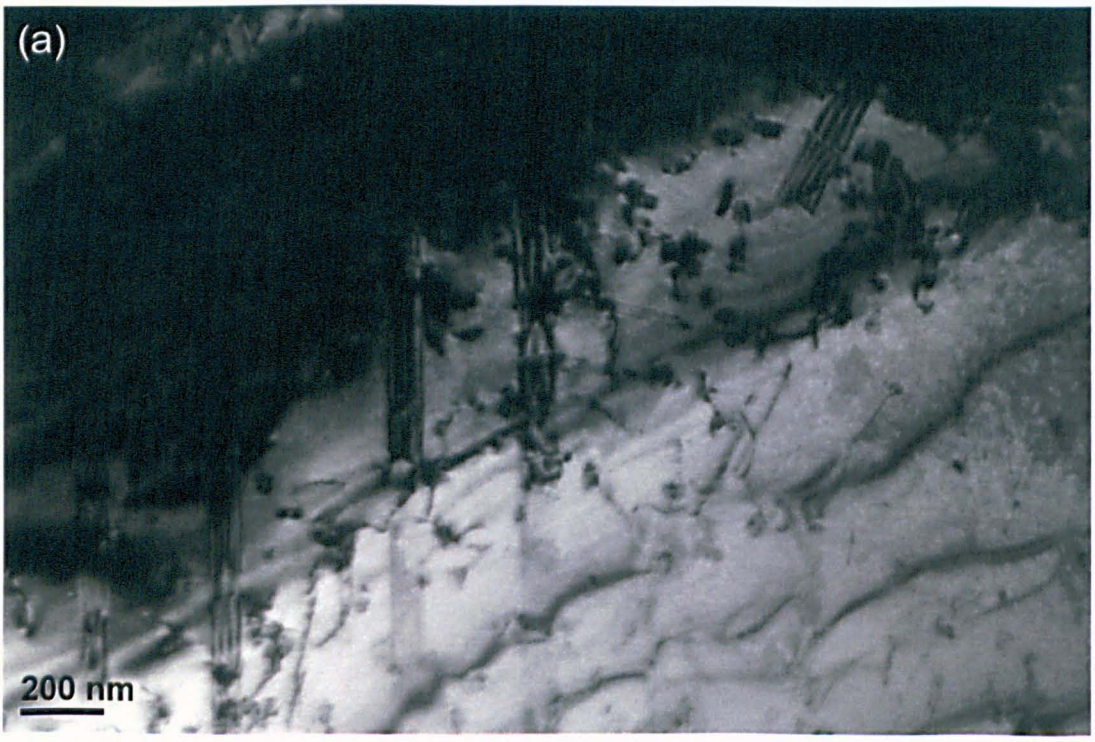

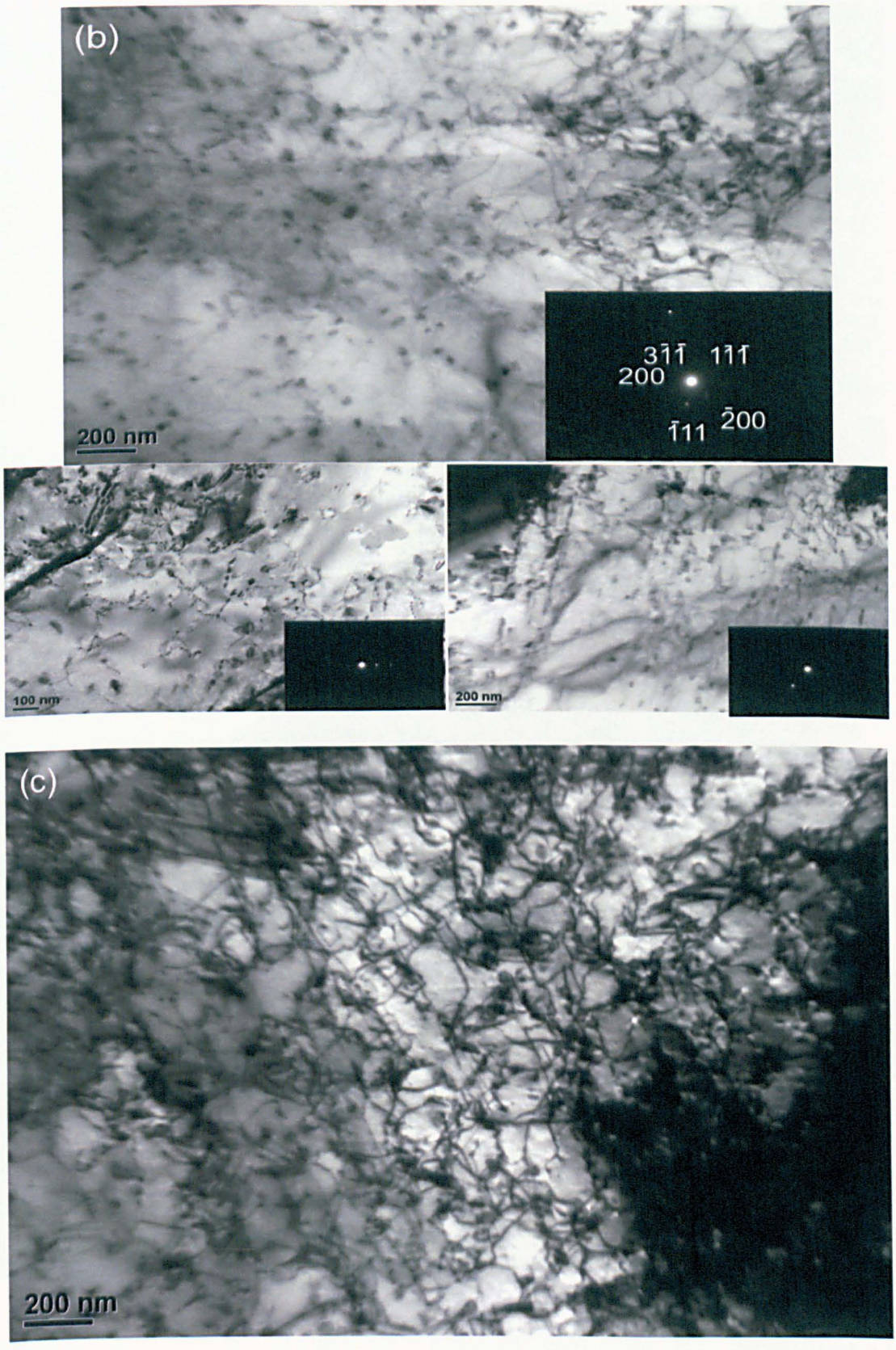

Figure 4.20 - Micrographs from ID 5 (8 hours following the unloading). In (a), unaltered SFs stretched towards a grain boundary; (b) depicts some tangles around a heavily precipitated area. In the poor contrast area, lower dislocation density was found and no tangles were observed in other two-beam conditions (two of them are shown). And (c) shows an area full of tangles, already starting to evolve to walls, also unaltered by the anelastic recovery.


(a)
111
$\bar{1}\bar{1}\bar{1}$
511
100 nm

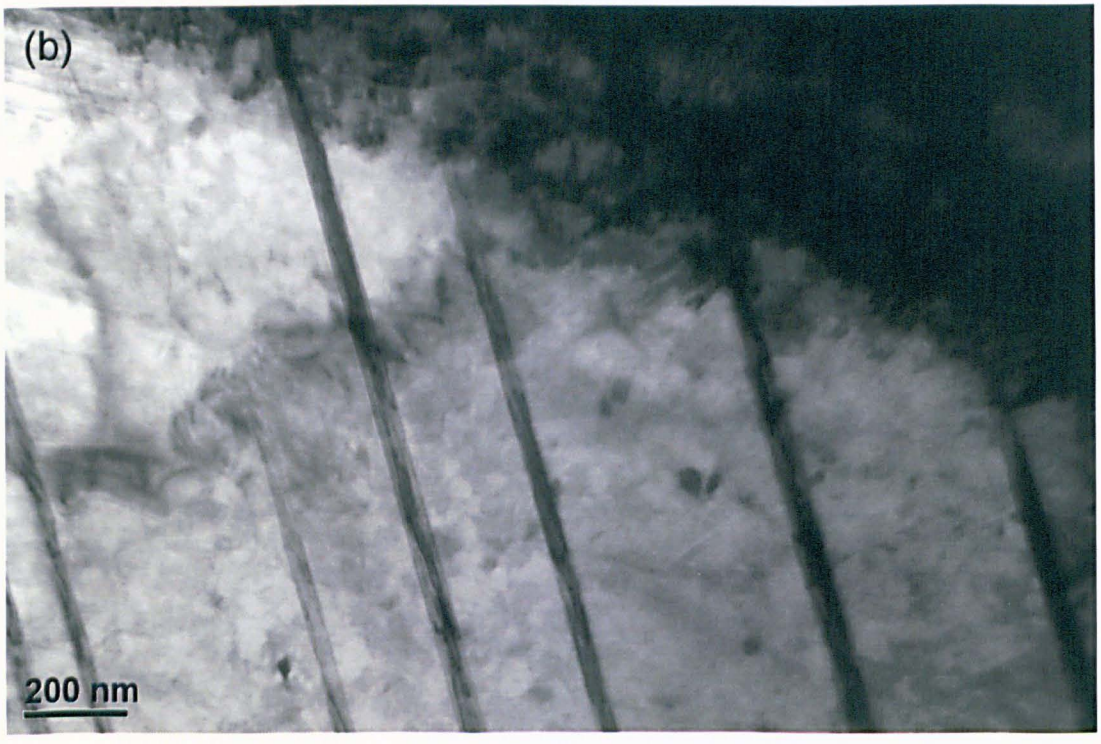
(b)
200 nm

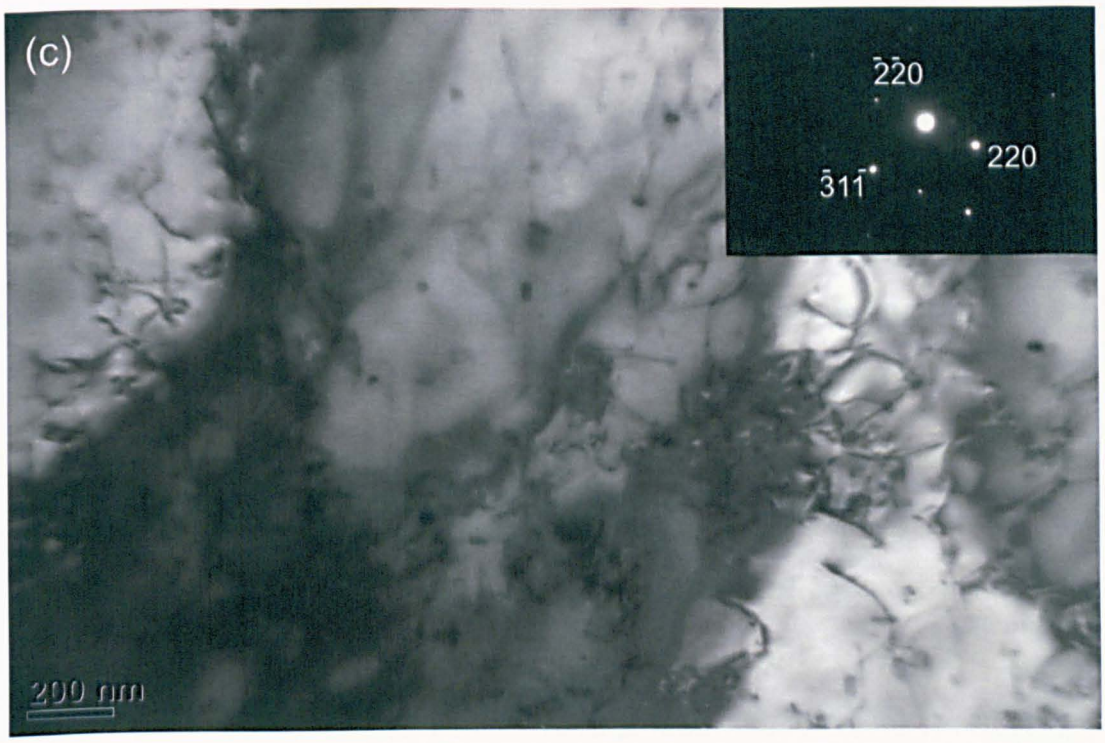

Figure 4.21 - TEM micrographs of ID 6 specimen, 12 hours into the unloading stage. As seen in (a) and (c), in all creep-compliant planes, tangles were preserved. Similarly, some stacking faults (b) could not be constricted for cross slip and remained unaltered. The poor contrast areas show low density of dislocations, which are free in the matrix.

Given that anelastic recovery takes place, as time at the unloading stage progresses, the difference between channel and hard zone densities are reduced, and more matrix areas are found to present lower dislocation densities, as Figures 4.20 and 4.21 show. This has the consequence of imposing less perceptible differences between the microstructural features of a test interrupted along the anelastic curve and the subsequent one. Although differences may be qualitatively difficult to detect, quantitative measurements of several TEM micrographs provided the base for the endeavour. Following notation used by Feaugas [21] for the intragranular back stresses:

$$X_{intra} = M f_G f_w \alpha \mu b \left(\sqrt{\rho_w} - \sqrt{\rho_c}\right) \qquad \text{(Eq. 4.4)}$$

where X_{intra} is the intragranular component of back stress, M is the Taylor hardening factor ($M = 3.06$); f_G is the fraction of grains with heterogeneous dislocation structures (tangles around precipitates, junctions and walls), measured by counting the number of micrographs showing these defects, from the total taken for each specimen (this counting

is direct, considering that each TEM micrograph represents a grain, given the high magnifications used) and represented in Figure 4.16; f_w is the fraction of hard zones inside grains, estimated in ImageJ by creating a binary image and checking the percentage of dark areas representing the dislocation arrangements, against the matrix background; α is a constant measuring the strength of the dislocation elastic interactions ($\alpha = 0.025$ for planar slip, that is, the slip regime in primary creep, and $\alpha = 0.4$ for cross-slip/multiple slip dominance, following the values obtained in [21]); $\mu = 78$ GPa is the shear modulus of the 316H, $b = 0.25251$ nm is the magnitude of the Burgers vector in *fcc* crystal structure ($b = a_0/2[110]$), and ρ_w and ρ_c the dislocation densities of hard zones and channel areas, respectively. Data for the intragranular back stress evolution calculation are presented in Table 4.7:

Table 4.7 – Summary of the effective stress and the intragranular back stress evolutions.

Stage of test	Time [hours]	ρ [cm^{-2}]	σ_{ef} [MPa]	ρ_w [cm^{-2}]	ρ_c [cm^{-2}]	f_G [%]	f_w [%]	X_{intra} [MPa]
Secondary	47.5	8.1×10^{10}	490	6×10^{10}	2.1×10^{10}	85	36.3	75.1
Unloading	48	7.8×10^{9}	245	6×10^{9}	1.86×10^{9}	77	40.4	26.7
	48.5	5.2×10^{9}	237	3.7×10^{9}	1.5×10^{9}	72	41.1	15.7
	50	5.9×10^{9}	254	3.9×10^{9}	2×10^{9}	82	41.2	13.6
	56	5×10^{9}	235	3.6×10^{9}	1.4×10^{9}	75	36.8	14.9
	60	4.3×10^{9}	232	3×10^{9}	1.3×10^{9}	70	28.4	8.7
Reloading	60	6.1×10^{9}	149	4.9×10^{9}	1.3×10^{9}	74	45.3	1.7
	60.5	1.1×10^{10}	153	7.1×10^{9}	3×10^{9}	70	42.8	1.2

It is easy to see that, as both channel and hard zone dislocation densities decrease, the driving force behind anelasticity (that is, the intragranular back stress component X_{intra}) also decreases. Thus, gradually, the anelastic recovery stabilizes, tending to approach a constant slope, which corresponds to the saturation point after a certain amount of time. Those dislocations stationed in stable positions in junctions, tangled around precipitates or existing as partials and stacking faults won't annihilate, remaining in their respective

configurations, as shown in figures 4.17 to 4.21. These phenomena were also observed by Farla and co-workers [8].

As expected, in all of these eight tests, the dislocation density in hard zones was found to be higher than that of the channel, which is in agreement with works [20, 23] supporting the idea that spreading of cross-slip throughout the grains increases slip irreversibility, and, thus, favours progressive deformation. This seems appropriate in the case of creep, since the material is still hardening in the secondary stage, that is, dislocation density is increasing.

The fraction of hard zones, f_w, indicates how much of an area in the matrix is occupied by dislocation arrangements. This parameter plays a crucial role in the model, since it is used to set the threshold between the channel and hard zone dislocations. The image manipulation software allows adjustment of the sensitivity of the binary image, created from the micrograph, to contrast. Therefore, precipitates and poorly contrasted areas will not be distinguished from the matrix and, subsequently, will not be taken into account when determining the fraction of hard zones. Moreover, it is possible to manually correct the binary images, thus eliminating undesirable darkened features, such as the bending contours and free dislocations (those away from the dislocation arrangements), but errors are also present. These procedures were adopted for determining f_w and, then, a reversion of the binary image was carried out, in order to show the free dislocations in the matrix, upon which the interception method of counting was reapplied, in order to estimate ρ_c, since this is easier than counting dislocations in arrangements. The difference between ρ and ρ_c provided ρ_w.

Although f_w was kept practically constant through the unloading stage, at its end, there was a considerable decrease, as shown in Table 4.7, before the reloading of the material could restore the fraction to its previous levels. It is important to notice, though, that the predominant arrangements in the grains vary along primary, secondary, unloading and reloading stages, as summarized by Figure 4.16.

4.7 Overall analysis

4.7.1 Anelasticity under different stress levels

It is interesting to note that, with increasing stress level at the unloading stage, the faster anelasticity reached a constant level, that is, the faster it appeared to transit from a constant slope to a flat line at the unloading portion of the curve. This, however, does not seem to determine the amount of recovery achieved, given that the steady-state creep rate measured after reloading did not follow a similar trend: it is natural to expect a higher reduction in secondary creep-rate for the test with lower unloading stress levels, while the higher stress levels would yield less reduction. Surprisingly, this was not what was observed. It is relevant, though, to acknowledge that, while reduction in secondary creep rate after reloading was calculated from the datasets of the steady-state regime, such a quantitative approach on the anelastic response was not carried out, for the scatter in creep data collection may render calculations subject to some errors, due to the poor accuracy to resolve strains [24]. However, the tendencies towards stabilization are undeniable, especially when considering the results of the TEM investigations, which show little variations in dislocation profiles during the anelastic stage.

Another important aspect stemming from the results is that the total back stress level was found to be higher than expected: for the test conditions imposed, it lies somewhere between, approximately, 90 and 125 MPa, representing a significant percentage of the applied stress, between 50% and 67%. Although it is hard to accurately estimate the stresses, the sum of the intergranular stress component for the deforming grain families (from neutron diffraction) with the intragranular component (from the quantitative TEM estimation) provides the range of magnitude. This is in good proximity to estimates done by Wilshire and co-workers, who reported back stress levels of 52% of the applied stress [25]. It must be emphasised, though, that the back stresses are dynamic and dependent on the applied stresses, as it can be seen in data presented in Table 4.7.

It is also timely to see that an analysis of the plots shown in figs. 4.4 and 4.5 reveals different levels of deformation for the specimens, even though the same stress was applied to them. This may be attributable to variations in the microstructure, as it was previously seen that the material has a bimodal distribution of grain sizes, as well as to fluctuations in the applied stress or temperature. In any case, the strain levels on primary creep, on transition to secondary creep and along this stage were well within the expected range for the conditions imposed [15, 26, 27].

4.7.2 Intergranular back stresses as measured by neutron diffraction

The idea of stabilization of intergranular stresses in two different stages seems reasonable when the apparent stress data from neutron diffraction, particularly those related to creep-compliant families, are checked and compared with the quantitative data for grains with dislocation arrangements presented in Figure 4.16. The first stabilization occurred only after some hours in secondary creep. This is reasonable to expect, since, in terms of microstructural events, a steady-state condition may require considerable time to be achieved, due to the need for converting part of pile-ups and partial dislocations accumulated during primary creep into planar heterogeneous arrangements. The second stabilization, found at the unloading stage, matches the approximately constant (within reasonable limits of variation) percentages of planar slip defects observed along the unloading stage and can be ascribed to the fact that defects such as stacking faults and pile-ups stretched towards boundaries do not come undone by simply unloading the material.

Another point favourable to the constant intergranular stress comes from the change in the creep-controlling mechanism. Under the partial unloading stresses, which do not suffice to maintain dislocation-based deformation, the creep rates become too small to cause any sensible difference in the considered timescale [28]. This will, therefore, reflect in the intergranular stresses, which tend to become constant. The material behaves as if it was fully unloaded, given that anelastic recovery takes place in a similar fashion. Indeed,

the similarities of behaviours between this partially unloaded test (45 MPa) and the full unloading test carried out by Rao [15], as well as the pattern of anelastic response from the different stress levels of unloading (first group of creep tests), seem to indicate that the conclusions for intergranular internal stresses are valid for any stress level, provided that this stress level does not cause dislocation-based creep deformation.

4.7.3 Intragranular back stress from quantitative TEM analysis

The most relevant results for understanding the role of back stresses as the driving force behind anelasticity are the ones dealing with the intragranular component, which showed more pronounced variation along the sequence of interrupted tests than the intergranular counterpart. The quantitative calculations yielded reasonable values for the intragranular back stress, whose variability provided support to the idea of a dynamic driving force, as the work carried out by Pahutová and collaborators seemed to suggest [29]. However, the values of the stresses should not be regarded as absolute, since there are many sources of uncertainties, not only arising from the dislocation density calculations, but, also, from the fractions of hard zones in grains and of grains bearing heterogeneous structures, which are statistical in nature and, thus, prone to uncertainties as well.

Difficulties associated with discerning dislocations occupying stable positions in tangles and walls from those revolving around these structures but free to move through the channel areas (and interact with dislocations of opposite sign for annihilation) exist, particularly for the case of strongly deformed regions. Bent foils also complicate the analysis, hence the need for examination using different g-vectors. This was observed in several of the micrographs shown in figures 4.17 to 4.21, but another example can be found below, in figure 4.22, a TEM micrograph extracted from ID 6 test, interrupted exactly after 60 hours of test, that is, right before being reloaded to the initial 180 MPa. It shows some tangles around precipitates, some transitions to walls and an upper region of poor contrast, where the bent foil triggers different diffraction conditions.

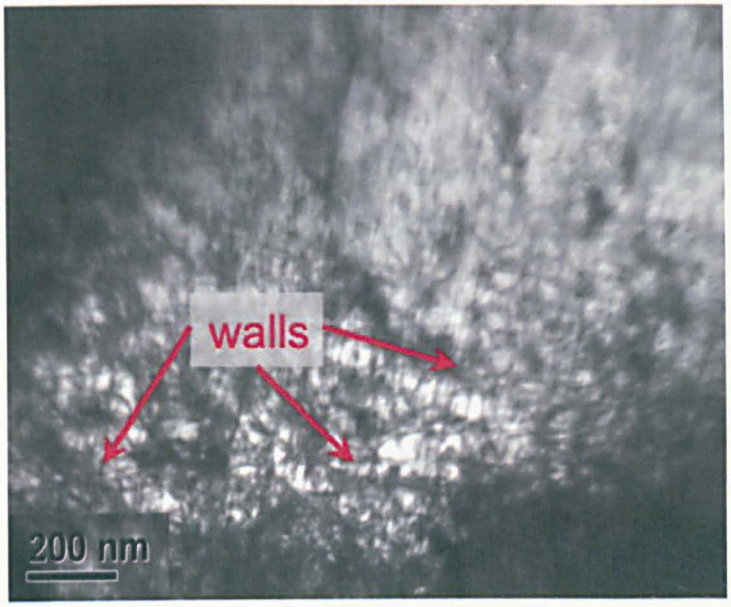

Figure 4.22 - TEM image from ID 6 showing the difficulties to the analysis imposed by the poor contrast.

In terms of proportions, table 4.7 showed an increase in the fraction of hard zones upon transition from secondary creep to the anelastic stage. Although at first glance this may seem a surprise, it must be noticed that this may well be within the error of the method, due to undesired darkened features (such as bending contours or dark matrix areas). But, as recovery went on along the anelastic stage, the fraction of hard zones decreased, as expected.

Another relevant aspect worthy of mention is the apparent increase in the back stress, from test ID 4 to test ID 5. Although the latter test was carried out for longer hours, after which one would expect a lower value of the back stress, it is important to remember that the intragranular back stresses are based on the difference between the hard zone and the channel dislocations. It is possible that the amount of free dislocations increased, by the time at which test ID 4 was interrupted, before recovery mechanisms initiated their motion towards annihilation, and, then, as the difference between the dislocation densities became smaller, a lower value of stress was calculated for this test sample.

In terms of visual information provided by the TEM micrographs, it is easy to see that the microstructure of the 316H shows precipitation of carbides either formed during

manufacturing, pre-test temperature stabilisation or during creep deformation. Dislocations interact with the precipitates, getting pinned, bowing out, circumventing them or originating dipoles, which are dislocation arrangements present in crystals deforming under low work-hardening rates resulting from dislocations of opposite signs being generated in parallel planes [30] (thus representing an intermediate state between planar slip and multiple slip), and loops [17]. An interesting phenomenon observed in the present work is the fact that precipitates seemed to serve as sites for the formation of entanglements. All these events are seen in figure 4.23, taken from test ID 6 sample (interrupted after 12 hours of anelastic recovery). It may be speculated that pinning and bowing of dislocations on precipitates contribute to the back stresses, as suggested by Morris [23] and Rao [15], but the significance of this contribution is questionable compared with structures based on heterogeneity of distribution of dislocations coupled together by the resulting internal stress fields, which are long-range in nature.

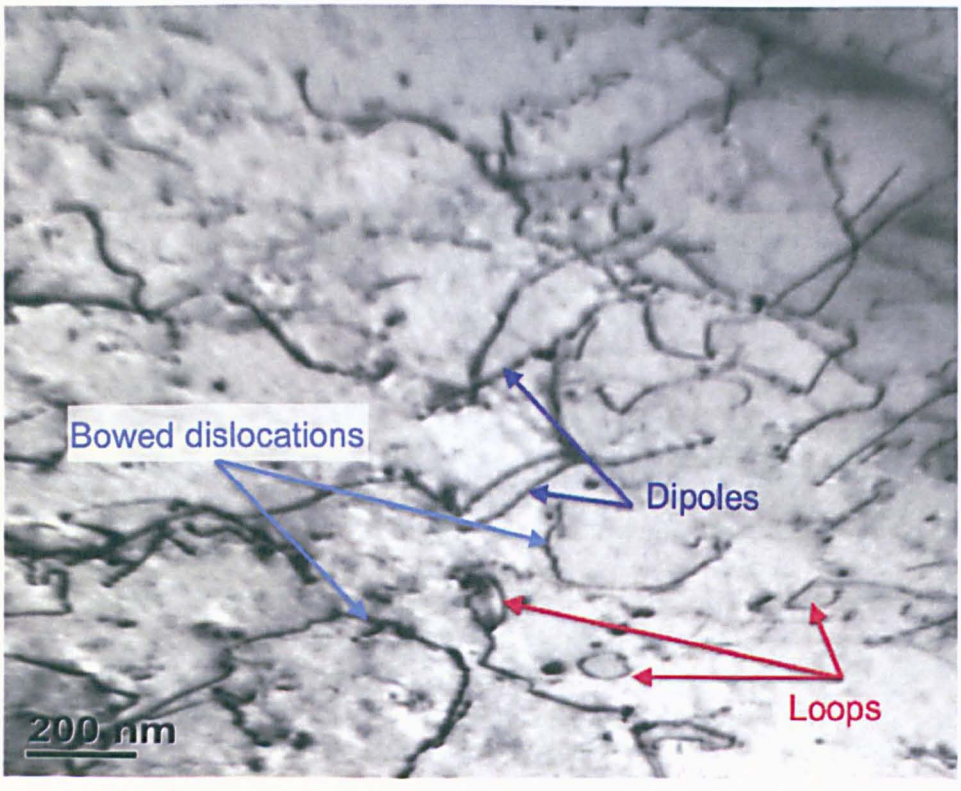

Figure 4.23 - Dislocations pinned, bowed, forming tangles, loops and dipoles around obstacles in the matrix.

It is timely to comment, here, the nature of heterogeneous arrangements observed during deformation, which did not include dislocation cells and roughly presented some initial wall configurations. This is expected, since the investigation was concentrated on the early secondary stage. Cells represent a later arrangement of dislocations, associated with higher energy inputs (either higher temperatures or higher strain levels), and are not developed at early stages of creep deformation, where tangles and some walls predominate.

4.7.4 Ratchetting and anelasticity – role of back stresses

As seen, the back stresses are caused by deformation events taking place in and near grain boundaries, and inside grains. The back stresses appear as a manifestation of plastic strain mismatches between differently oriented grains – intergranular back stresses – with regards to the loading direction, and, then, as a result of the formation of heterogeneous dislocation structures (tangles, walls, eventually cells, although not in the present work) inside the grains, as deformation in creep goes on by means of climb and cross-slip processes, which allows multiple slip systems to be active simultaneously. So, the driving force for the occurrence of anelastic recovery is the back stress generated during deformation. Its dynamic nature is evidence of the important role of the back stress on the understanding of basic mechanisms behind anelasticity of previously plastically deformed materials during creep.

At this point, it is easy to see why anelasticity saturates as the number of unloading transients increases [15, 31, 32]: after reloading the specimen at the end of the first unloading transient, the material will experience another primary creep, but, this time, a shorter one, due to the fact that the stacking faults and some of the pile-ups from deformation prior to the unloading cycle are still there, as well as the tangles and walls within grains. It is also easy to notice that, because the heterogeneous structures and some stacking faults were not undone by annihilation during anelastic recovery, the damage is

permanent and, upon reloading, the sample undergoes more deformation, this being the idea behind the concept of ratchetting [24, 33]. Due to this, deformation proceeds slower, as glissile dislocations are, once more, confined to planar slip, before cross-slip and climb are active again, in order to maintain cohesion between grains. An analysis of Figure 4.16, in which the percentage of grains with planar slip defects is seen to surge upon reloading the specimen, along with the micrographs of Figures 4.24 and 4.25 below, serves as evidence. This marks the onset of another secondary creep stage, with a reduced steady-state rate, corresponding to a new point of balance between hardening and recovery, due to the obstacles (the junctions, tangles and walls) imposed to the active dislocations on their motion. As a consequence of limited possibilities, due to an initially single active slip system, the dislocations generated upon reloading the sample will either remain in the channel areas (free matrix) or be attracted towards the very same dislocation structures that serve as obstacles to their motion. Since the straining is proceeding at a pace slower than before the unloading, hardening won't be as pronounced as before, so the back stresses built up won't present as high a magnitude as before. With less driving force, anelasticity will proceed less intensely in the next unloading stage, in which stabilization will be reached earlier. This sequence of events goes on with the number of transients up to a point in stress-transient creep where unloading the specimen will not trigger any measurable effect, with anelasticity becoming negligible, having no influence on the material recovery capability.

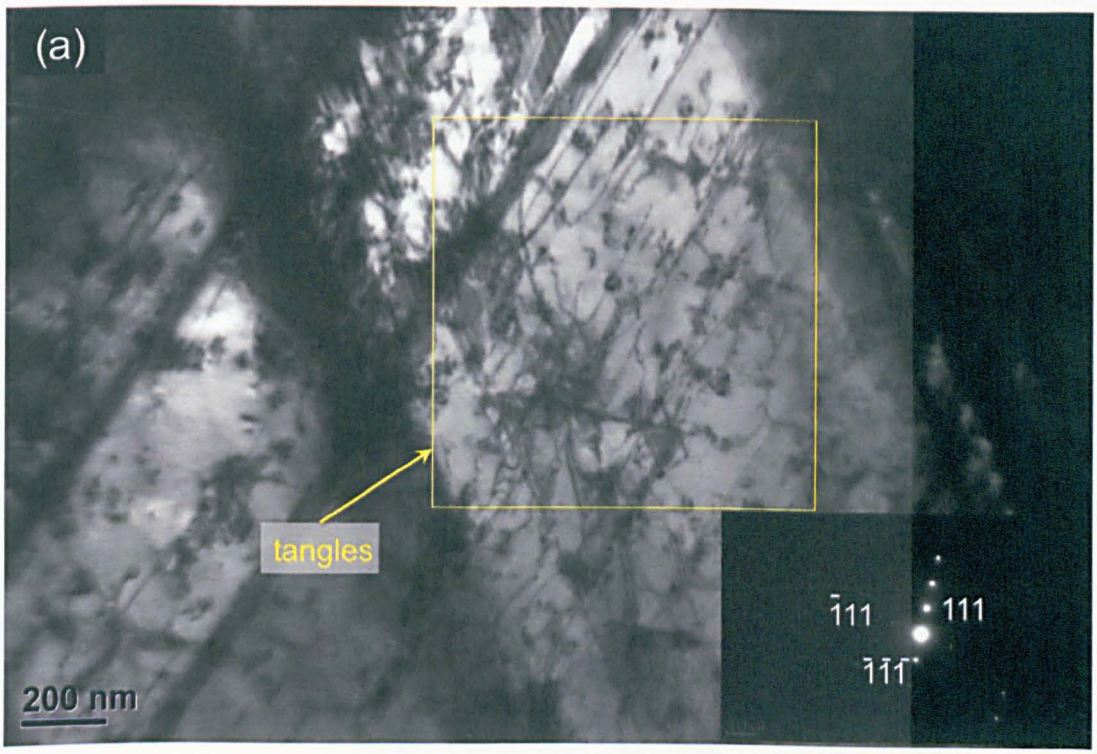
(a)
tangles
200 nm
$\bar{1}11$
111
$1\bar{1}1$

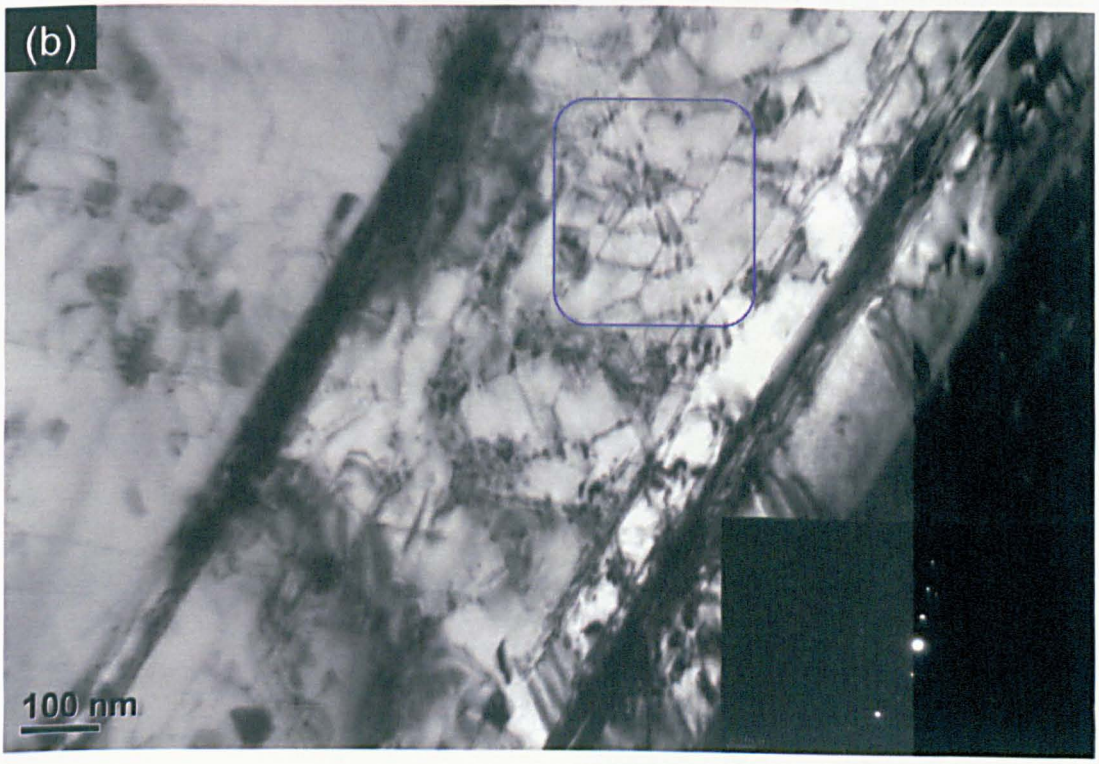
(b)
100 nm

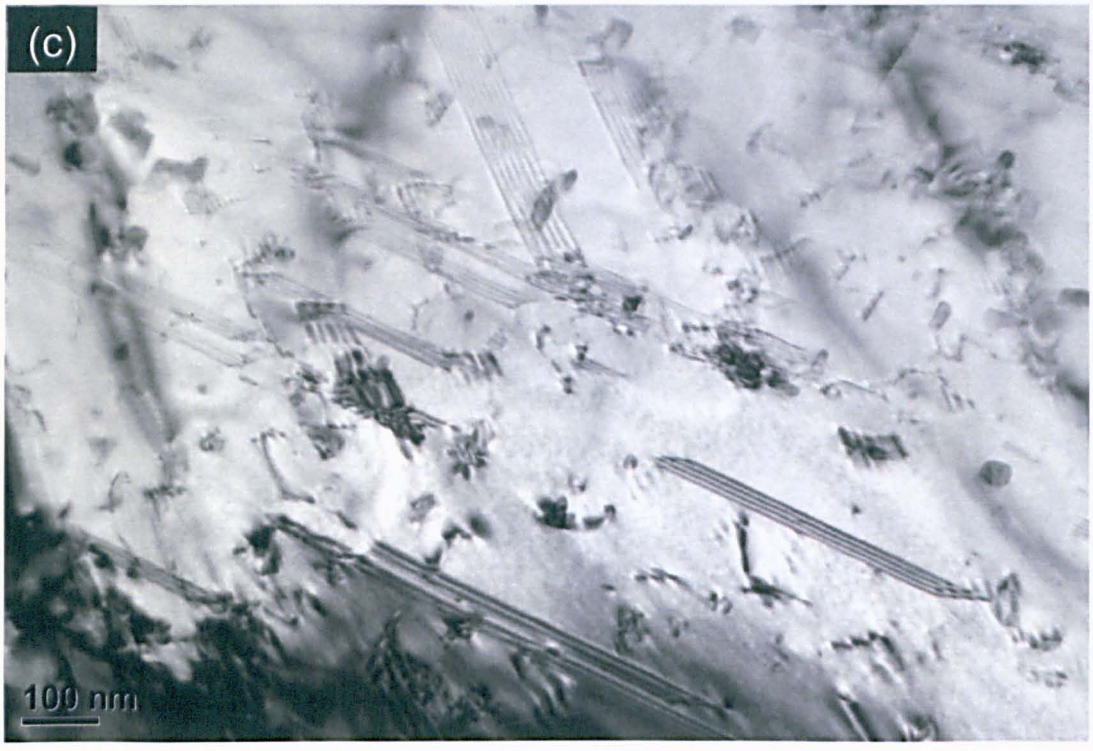

Figure 4.24 - TEM micrographs from test 7 specimen, interrupted immediately after reloading to 180 MPa. In (a) and (b) stacking faults predominate once more. While (a) shows also tangles, (b) depicts a pile-up in formation, highlighted in the blue rectangle. Image (c) shows that free dislocations in the channels start increasing, in comparison with previous micrographs from the unloading stage.

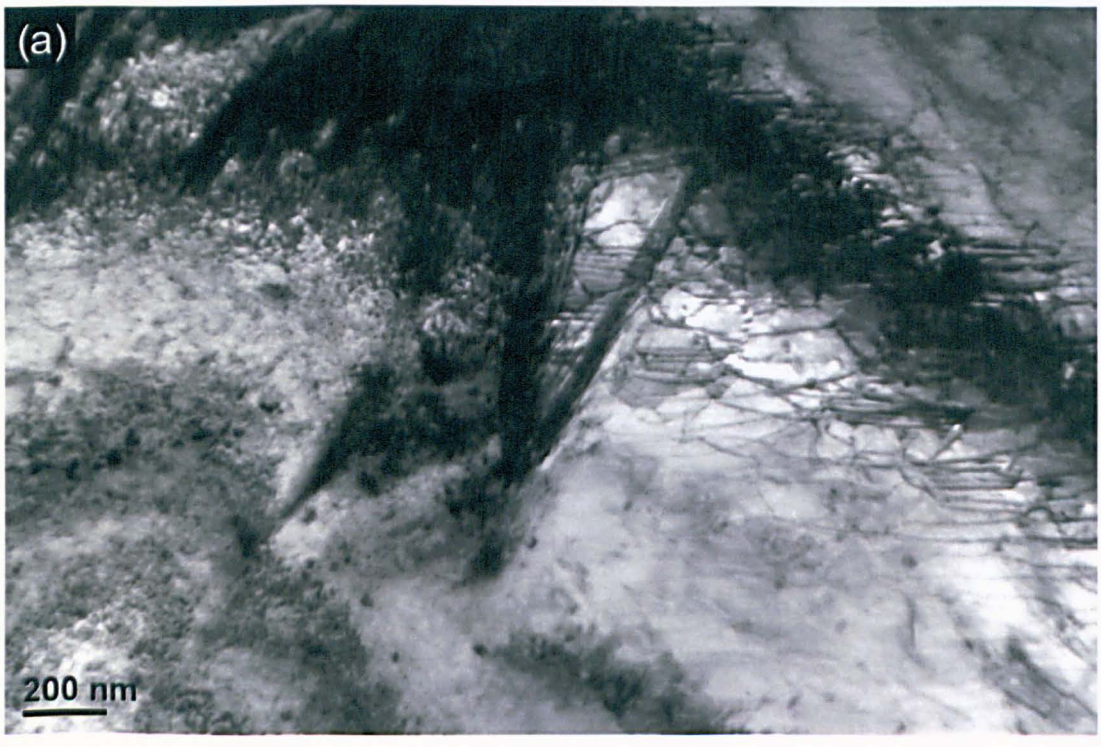

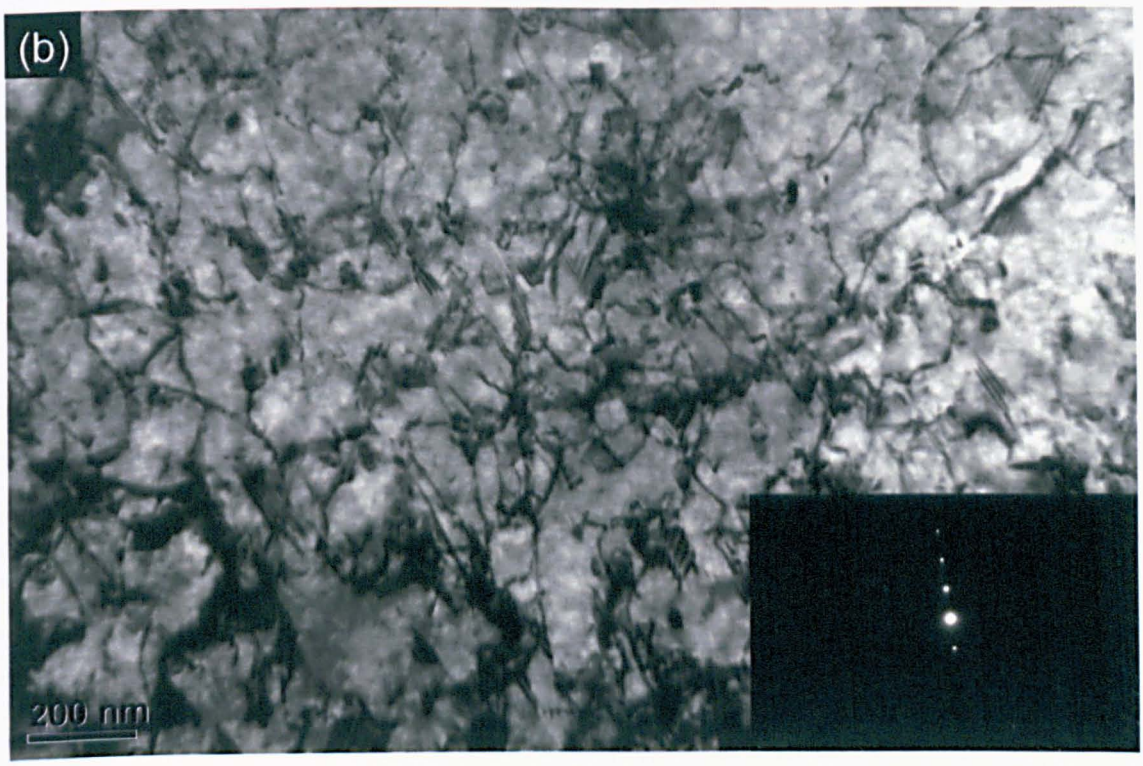

Figure 4.25 - TEM micrographs from test 8, interrupted 30 minutes after reloading the sample. Image (a) illustrates a grain boundary and a lower density of stacking faults stretching onto it. Cross-slip allows the rearrangement of some SFs in tangles, which can be observed around the boundary; (b) shows a matrix area where partial dislocations are also recombining to create tangles. These images seem to indicate that 30 minutes after reloading, the material is already entering secondary creep stage again.

4.7.5 Importance of back and effective stresses

In agreement with what was said about the effective stress in Chapter 2, it can be seen, from the studies presented, that its magnitude provides relevant information: lower values of effective stress mean few long-range interactions, that is, a dislocation has a more unhindered local path for glide, whereas higher magnitudes represent intense long-range interactions with other dislocation stress fields, that is, more energy is required locally for the dislocation to move.

As for the back stresses, it is possible to affirm that the study of the evolution of their magnitude may be essential in surveying how much potential for recovery the material has when subjected to transient creep deformation, since they are a long-range class of stresses.

Under the guidance of the above considerations, it can be envisaged what would be expected to happen if the 316H was unloaded to the exact stress level corresponding to the total back stress. Although it is reasonable to expect the dislocation density of the secondary creep stage (and, subsequently, the effective stress) to be maintained, with negligible changes, since stabilization following the unloading would be instantaneous, it is debatable whether such a condition is achievable, due to the seemingly dynamic nature of the back stresses, which would be altered as the immediate elasto-plastic recovery (the dip observed in the creep curve when stress is removed) takes place. Even if, immediately after the unloading, the applied stress could be equal to the back stress, the instantaneous drop in strain would alter the internal state of the material and, with this, the back stress. Moreover, the small changes observed in the intergranular back stresses (from neutron diffraction), in comparison with the intragranular component, indicates that the macroscopic back stresses and, as a consequence, the anelastic response, are preferably associated to the intragranular back stress. Gaudin and Feaugas [17] reported the predominant role played by this same component for the case of cyclic creep deformation of 316L.

A consequence of the current study, which encompasses the secondary creep stage, the unloading stage and the reloading stage, is the notion that the long-range internal stresses will always be present in the polycrystalline material, either in the loaded or unloaded condition. This is in full agreement with the consequences of the model developed by Mughrabi [13]. Even if the magnitude of the intragranular back stresses is near zero, the generation and emission of dislocations in grain boundaries and plastic strain mismatches between neighbouring grains provide measurable and significant component of back stresses.

4.8 Summary

Creep transient tests in which partial unloading stages were carried out to assess the effects on the anelastic strain response. It was found that as long as the drop in stress is sufficient to prevent dislocation-based creep, the anelastic response will be comparable to that of a fully unloaded specimen.

The tests with different partial unloading stress levels indicated the total back stress developed to be around 105 MPa. Unloading below or above this value results in significant anelasticity and progressive creep, respectively.

In situ Neutron diffraction experiment, conducted with partial unloading stages at 45 MPa, showed the intergranular stresses became constant in two moments throughout the creep test: after approximately 40 hours and after a few hours at the unloading stage. The magnitude of stresses in grain deforming families ({111} and {220}) showed a maximum between 40 MPa and 50 MPa at the constant portion of the curve shown in Figure 4.12.

Quantitative TEM studies were carried out for determining dislocation densities of tests deliberately interrupted in the secondary creep stage, the unloading stage and after reloading.

Qualitative TEM studies were performed to identify the dislocation features and their arrangements.

A model for calculating intragranular back stress, based on heterogeneity of dislocation distribution ("soft" and "hard" zones inside grains), was implemented and used to interpret the driving force behind anelastic behaviour.

4.9 References

[1] ASTM, "Metal Test Methods and Analytical Procedures ," *ASTM E 112 - Standard Test Methods for Determining Average Grain Size*, vol. 03.01. ASTM International, 2006.

[2] W. Blum, J. Kratochvi, R. Sedla, and A. P. Hardening, "Subgrain Formation during Deformation : Physical Origin and Consequences," *Metall. Mater. Trans. A*, vol. 32A, pp. 1–9, 2001.

[3] G. E. Dieter, *Mechanical Metallurgy*. McGraw-Hill, 1986.

[4] P. R. Rios and A. F. Padilha, "Precipitation from Austenite," in *Encyclopaedia of Materials*, Elsevier Science, 2001, pp. 7836–7841.

[5] E. H. Lee and L. K. Mansur, "Fe-15Ni-13Cr austenitic stainless steels for fission and fusion reactor applications. II. Effects of minor elements on precipitate phase stability during thermal aging," *J. Nucl. Mater.*, vol. 278, pp. 11–19, 2000.

[6] D. M. Norfleet, D. M. Dimiduk, S. J. Polasik, M. D. Uchic, and M. J. Mills, "Dislocation structures and their relationship to strength in deformed nickel microcrystals," *Acta Mater.*, vol. 56, no. 13, pp. 2988–3001, Aug. 2008.

[7] D. B. Williams and C. B. Carter, *Transmission Electron Microscopy: A Textbook for Materials Science*, 1st ed. Springer, 1996.

[8] R. J. M. Farla, H. Kokkonen, J. D. Fitz Gerald, A. Barnhoorn, U. H. Faul, and I. Jackson, "Dislocation recovery in fine-grained polycrystalline olivine," *Phys. Chem. Miner.*, vol. 38, no. 5, pp. 363–377, Dec. 2010.

[9] S. Karato, *Deformation of earth minerals: an introduction to the rheology of solid earth*. Cambridge University Press, 2012.

[10] D. Hull and D. J. Bacon, *Introduction to dislocations*, 5th Editio. Butterworth-Heinemann, 2007.

[11] B. Fultz and J. Howe, *Transmission Electron Microscopy and Diffractometry of Materials*, 4th ed. Springer, 2012.

[12] M. Klimiankou, R. Lindau, and A. Möslang, "Energy-filtered TEM imaging and EELS study of ODS particles and argon-filled cavities in ferritic-martensitic steels.," *Micron*, vol. 36, no. 1, pp. 1–8, Jan. 2005.

[13] H. Mughrabi, "Dislocation wall and cell structures and long-range internal stresses in deformed metal crystals," *Acta Metall.*, vol. 31, no. 9, pp. 1367–1379, Sep. 1983.

[14] W. Blum, "Creep of crystalline materials: experimental basis, mechanisms and models," *Mater. Sci. Eng. A*, vol. 319–321, pp. 8–15, 2001.

[15] A. Rao, "Creep and Anelastic Deformation in Austenitic Steels," The Open University, 2010.

[16] R. Raj and M. F. Ashby, "On grain boundary sliding and diffusional creep," *Metall. Trans.*, vol. 2, pp. 1113–1127, 1971.

[17] C. Gaudin and X. Feaugas, "Cyclic creep process in AISI 316L stainless steel in terms of dislocation patterns and internal stresses," *Acta Mater.*, vol. 52, no. 10, pp. 3097–3110, Jun. 2004.

[18] M. W. Johnson and M. R. Daymond, "Neutron Pulsed source instrumentation," in *Analysis of Residual Stress by Diffraction using Neutron and Synchrotron Radiation*, M. E. Fitzpatrick and A. Lodini, Eds. Taylor & Francis, 2003, pp. 146–169.

[19] M. R. Daymond and P. J. Bouchard, "Elastoplastic Deformation of 316 Stainless Steel Under Tensile Loading at Elevated Temperatures," *Metall. Mater. Trans. A*, vol. 37, no. June, pp. 1863–1873, 2006.

[20] A. A. Saleh, E. V. Pereloma, B. Clausen, D. W. Brown, C. N. Tomé, and A. A. Gazder, "On the evolution and modelling of lattice strains during the cyclic loading of TWIP steel," *Acta Mater.*, vol. 61, no. 14, pp. 5247–5262, Aug. 2013.

[21] X. Feaugas, "On the origin of the tensile flow stress in the stainless steel AISI 316L at 300 K: back stress and effective stress," *Acta Mater.*, vol. 47, no. 13, pp. 3617–3632, Oct. 1999.

[22] P. Landau, R. Z. Shneck, G. Makov, and A. Venkert, "In-situ TEM study of dislocation patterning during deformation in single crystal aluminium," *J. Phys. Conf. Ser.*, vol. 241, pp. 1–4, 2010.

[23] D. G. Morris, "Anelasticity and creep transients in an austenitic steel," *J. Mater. Sci.*, vol. 13, pp. 1849–1854, 1978.

[24] W. Blum and A. Finkel, "New technique for evaluating long range internal back stresses," *Acta Metall.*, vol. 30, no. 8, pp. 1705–1715, Aug. 1982.

[25] J. Hausselt and W. Blum, "Dynamic recovery during and after steady state deformation of Al-11wt%Zn," *Acta Metall.*, vol. 24, no. 11, pp. 1027–1039, Nov. 1976.

[26] D. G. Morris, "Creep in Type 316 Stainless Steel," *Acta Metall.*, vol. 26, pp. 1143–1151, 1978.

[27] G. Gremaud, "Theory of plasticity and anelasticity due to dislocation creep through a multi-scale hierarchy of obstacles," *Mater. Sci. Eng. A*, vol. 521–522, pp. 12–17, Sep. 2009.

[28] P. Lee and R. Raj, "Colossal anelasticity in polycrystals deforming under conditions of diffusional creep," *Acta Mater.*, vol. 58, no. 2, pp. 702–708, Jan. 2010.

[29] M. Pahutová, J. Čadek, and V. Černý, "Transients in the creep of a 16Cr-12Ni-2.5Mo austenitic steel II: Structure," *Mater. Sci. Eng.*, vol. 62, no. 1, pp. 33–40, Jan. 1984.

[30] P. Hazzledine, "Dislocation Multipoles," *J. Phys. Colloq.*, vol. 27, no. C3, pp. 210–218, 1966.

[31] D. G. Morris and D. R. Harries, "The cyclic creep behaviour of Type 316 stainless steel," *J. Mater. Sci.*, vol. 13, pp. 985–996, 1978.

[32] J. Malaplate, F. Mompiou, J. L. Béchade, T. Van Den Berghe, and M. Ratti, "Creep behavior of ODS materials: A study of dislocations/precipitates interactions," *J. Nucl. Mater.*, vol. 417, no. 1–3, pp. 205–208, 2011.

[33] G. Facheris and K. G. F. Janssens, "Cyclic mechanical behavior of 316L: Uniaxial LCF and strain-controlled ratcheting tests," *Nucl. Eng. Des.*, vol. 257, no. 0, pp. 100–108, 2013.

Chapter 5 – ODS 316L Creep Behaviour Investigations

5.1 Introduction

This chapter reports the outcome of investigations carried out on the austenitic ODS 316L steel, with emphasis on the creep behaviour. The material is a non-commercial grade of nanostructured steel and was fabricated and provided by the University of Science Technology Beijing, China. The limited availability of material required bespoke testing methods, and only creep-rupture tests could be conducted. Complementing the tests and, in an attempt to increase the number of samples for experimentation, a pilot study of diffusion bonding between ODS 316L and Inconel 718 was conducted and is described herein.

5.2 Characterisation of the as-received ODS 316L

The ODS 316L was fabricated via mechanical alloying of 316L pre-alloyed powder, Ti and yttria powders (with a purity higher than 99.9%), via ball milling at 300 rpm for 30 hours, with a ball-to-powder ratio of 5:1. The as-milled powders were degassed and consolidated by hot isostatic pressing (HIP) under 100 MPa of pressure, applied in two stages: the first was carried out at 1100°C for 2 hours and the second, at 1150°C for 1 hour. As complementary steps for improvement of ductility, impaired by the presence of pores and trapped gas in the steel [1], hot forging was applied, also in two stages: at 1150°C and, then, at 970°C, both with a 3:1 forging ratio. This step was followed by a final heat treatment, carried out at 1150°C for 0.5 hour. Figure 5.1 illustrates the as-received batch, provided in the shape of two rods with 13 mm diameter and 100 mm length, and a block with a shape of half a cylinder, with 100 mm diameter and 12 mm thickness.

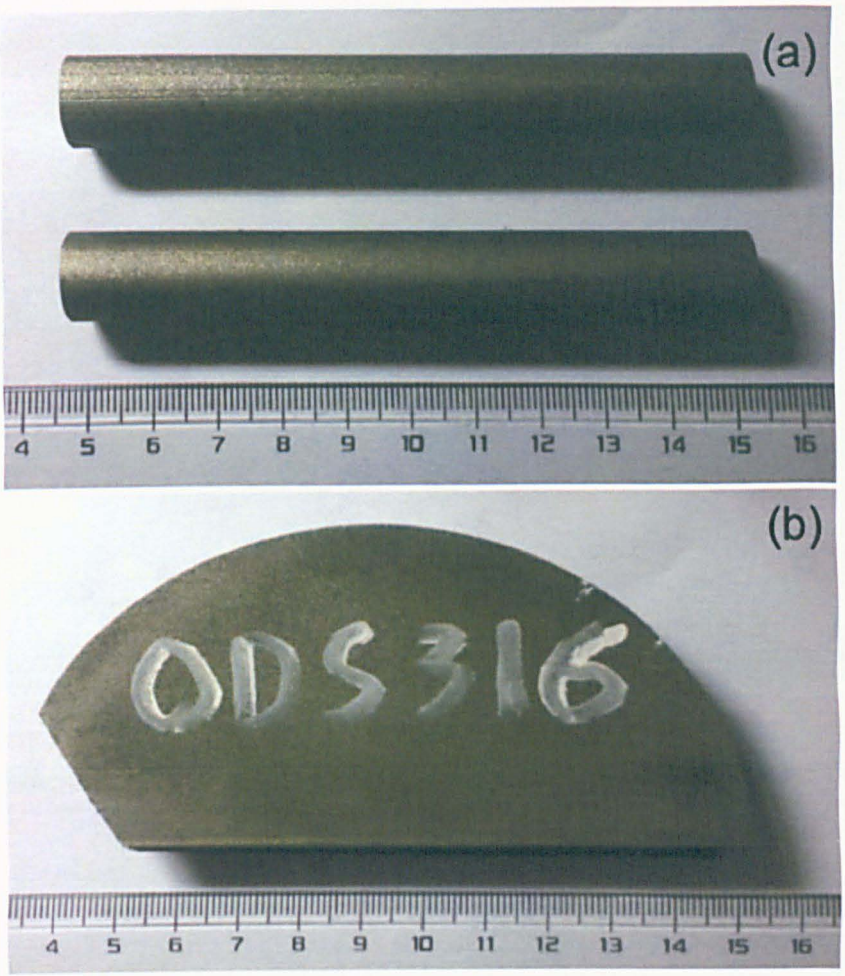

Figure 5.1 - The as-received batch of ODs 316L steel: two rods (a) and the block (b).

The composition of the ODS 316L is provided in table 5.1 below. Characterization of the material was done by optical microscopy and TEM, for which the preparation followed the procedures described in Chapter 3.

Table 5.1 - Composition of the ODS 316L steel (in % wt.) provided by the manufacturer.

Fe	*Cr*	*Ni*	*Si*	*Ti*	Y_2O_3	Al	Mo	C	N
Bal.	16.8	13.2	0.72	0.3	0.35	0.3	2.49	0.008	0.2

The optical microscopy surveys were concentrated on grain morphology and size, again measured using the ASTM E112 intersection method, embedded in the Leica Application

Software, used in tandem with the Leica DMI 5000M microscope, as described in chapter 3. One sample was cut from the bar and another from the block. Nine different areas, in total, were observed in these two samples for the purpose of grain size measurement. It is appropriate to mention here that no significant difference was found in the grain sizes of the bar and the block, whose average was found to be around 25 μm, as table 5.2 summarizes:

Table 5.2 - Average grain size of the ODS 316L samples.

Sample	**Average grain size [μm]**
Rod	25.2 ± 6.1
Block	26.4 ± 3.3

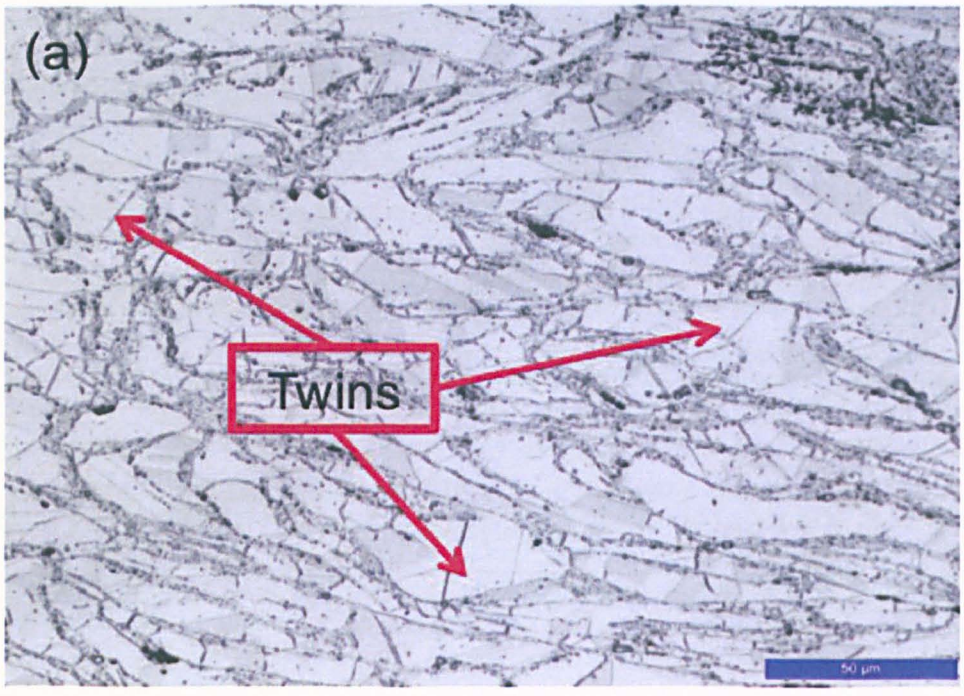

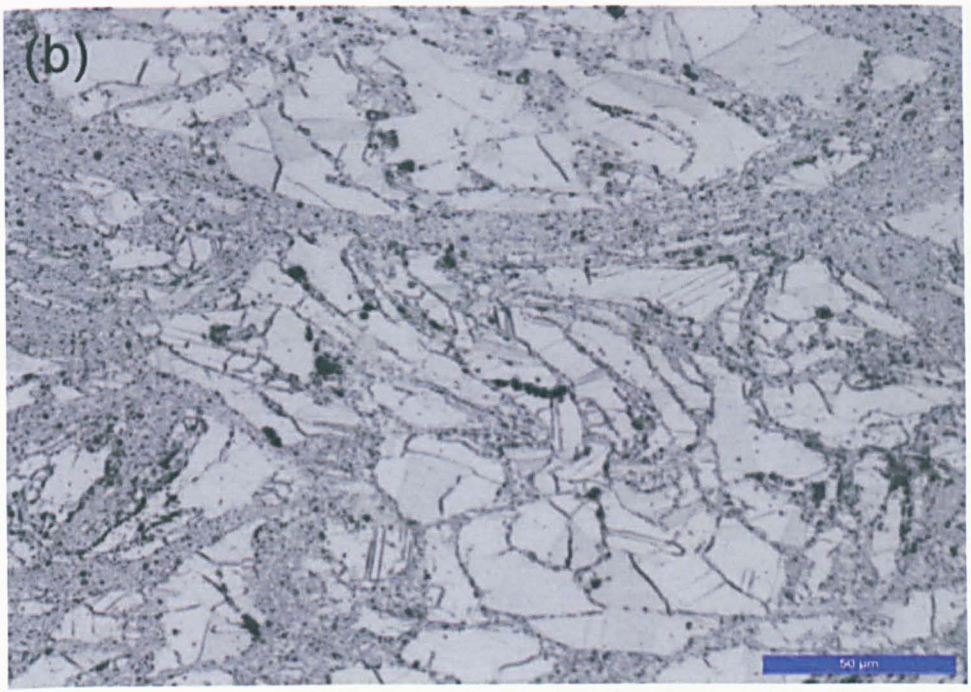

Figure 5.2 - Optical micrographs showing the irregular morphology of the ODS 316L. In (a), from the rod, twin bands are evident, while (b), from the block, shows the scale bar for an idea of the average size.

The microstructure of the ODS 316L is shown in Figure 5.2. Some features expected for austenitic steels, such as twins, are readily detectable. However, as an unusual feature, grains exhibit a rather irregular and wavy morphology. It may be speculated that this feature results from the powder metallurgy processes, due to the violent deformations undergone by the material during mechanical alloying, in comparison with conventional metallurgy. This morphology was observed throughout the material, regardless of the direction examined.

Quantitative and qualitative analysis were also conducted in the TEM. Dislocation density of the as-received condition was estimated as around 1.2×10^{10} cm^{-2}, using the same method described in Chapter 4 (section 4.3.1). Areas of higher dislocation densities were alternated with matrix areas with much lower density of dislocations, and this is indicative of a partially annealed microstructure. Predominant dislocation arrangements were stacking faults, pile-ups, some multipoles and tangles, suggesting some considerable deformation as well as the onset of recovery through more than one active slip system,

given the number density of multipoles found in the images [2]. Figure 5.3 illustrates the TEM characterization images of the as received ODS 316L.

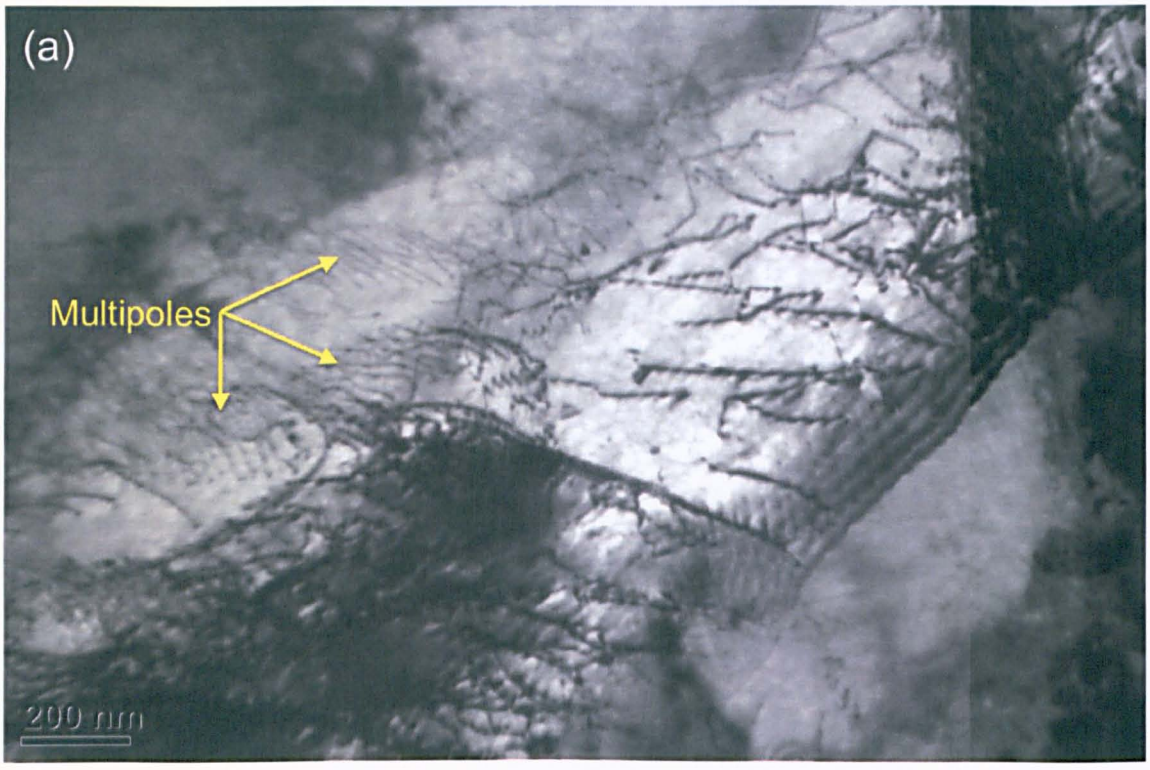

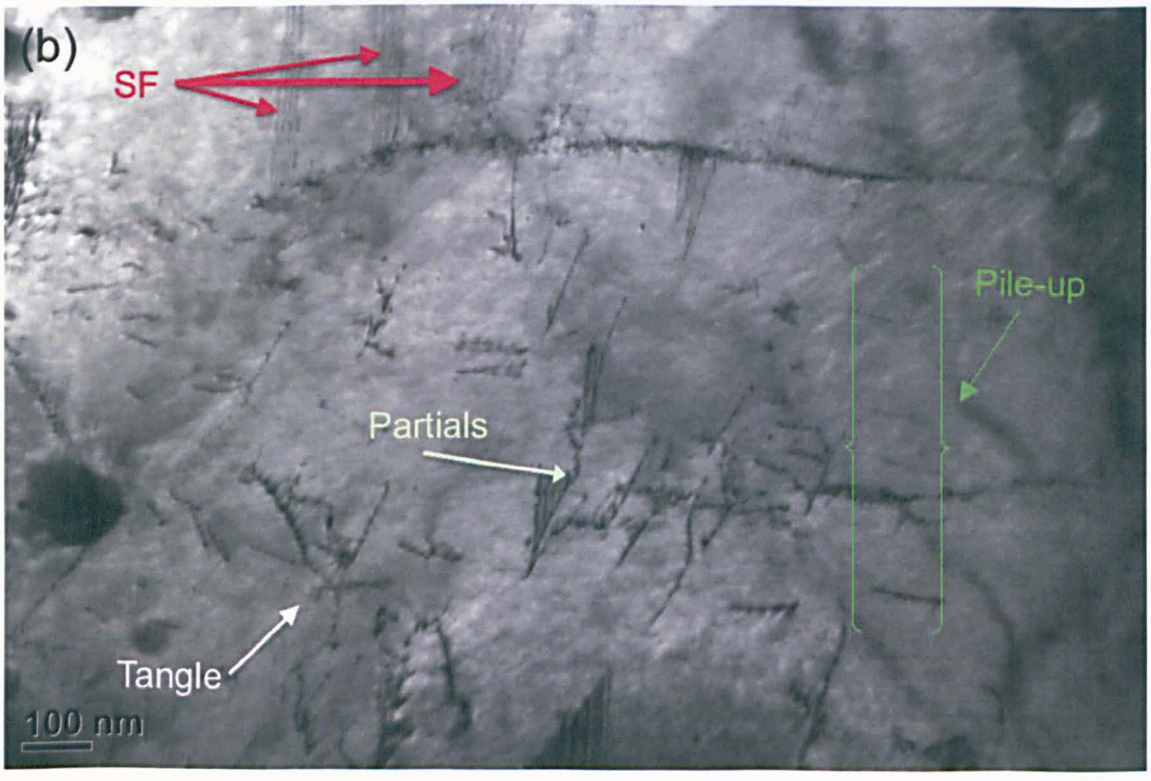

Figure 5.3 - TEM micrographs of the as received ODS 316L; (a) shows what seems to be multipoles; (b) matrix areas with lower population of dislocations, where some stacking faults (SF), small pile-ups and partial dislocations, and a small tangle. And (c) shows a small grain with some multipoles and tangles formed near grain boundaries.

5.3 Oxide particle size and distribution

5.3.1 TEM particle imaging and size distribution

TEM was used to characterize the nanometric oxide particle distribution, along with EDS, in order to determine the chemical composition of the oxide particles. The micrographs were, again, analysed in the ImageJ environment. The process for determining the particle size can be automated, by a procedure of creation of binary images similar to the one described in the previous chapter. However, due to the frequently observed faint contrast between the oxides and the matrix, a manual approach was carried out. After calibrating a micrograph with its scale bar, the measurements were set to compute the area of the marked features. Then, circles were drawn on each particle

investigated and the diameter (which is effectively the entity representing the size) was calculated from the area. The method is illustrated in the Appendix 7.

The micrographs showed that the oxide particles were relatively well distributed across the austenitic matrix, but their size range was very broad: smaller particles were in the range 10-50 nm, but larger particles, between 50 and 100 nm were also observed. TEM images in Figure 5.4 illustrate some of the nanoparticles. A histogram of size distribution is plotted in Figure 5.5. EDS analysis indicated that particles from both ranges were complex Y-Ti-O oxides. Some larger particles, also analysed by EDS, were found to be Y-Ti-O and Y-Al-O oxides, and, predominantly, TiN particles, sometimes distinguishable by their different geometry. Particles whose size was smaller than 10 nm were observed to be present but less frequently. It is possible, though, these observations are affected by a difficulty in imaging very small particles, due to the extremely reduced size and feeble contrast with the matrix background.

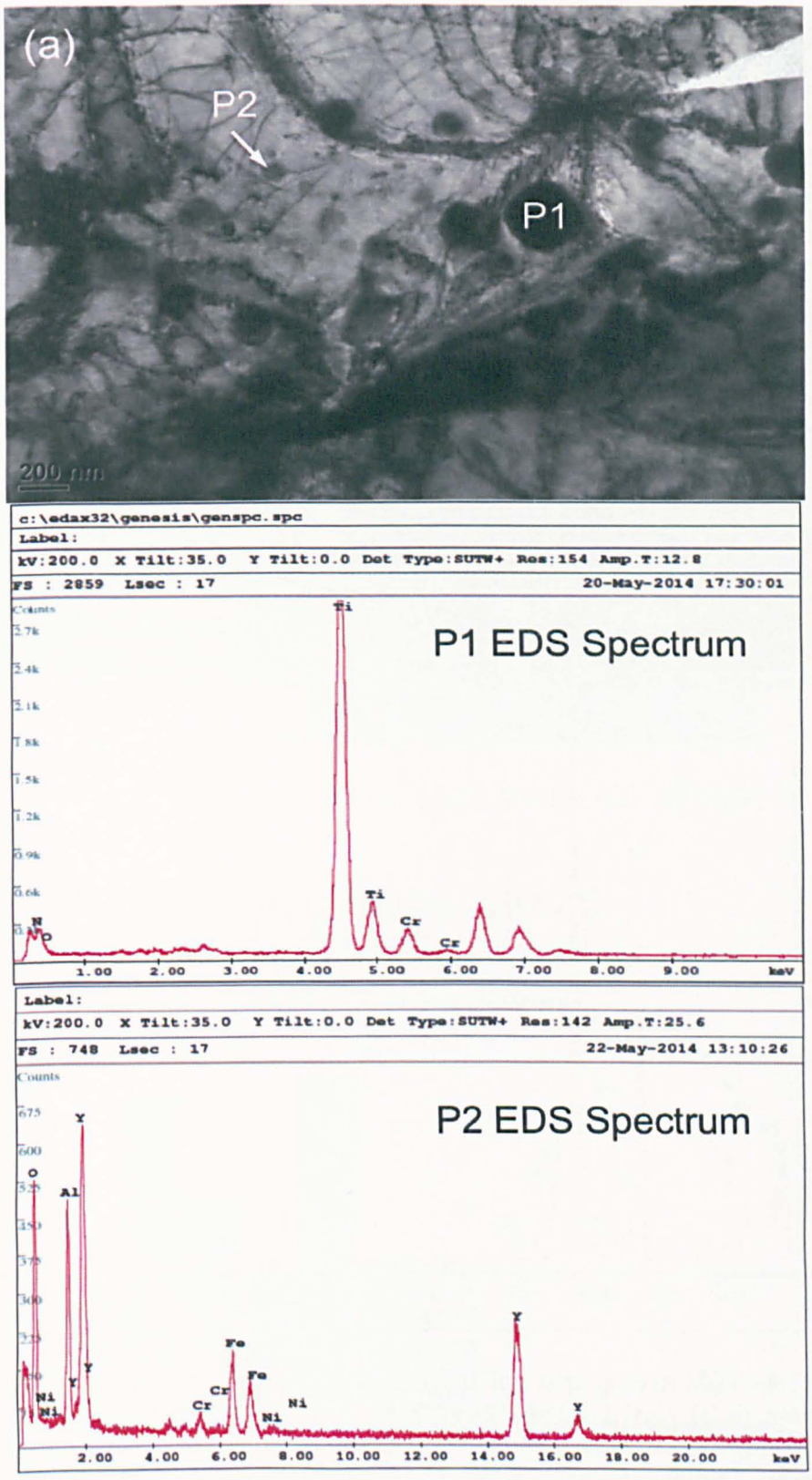
(a)
P2
P1
200 nm
c:\edax32\genesis\genspc.spc
Label:
kV:200.0 X Tilt:35.0 Y Tilt:0.0 Det Type:SUTW+ Res:154 Amp.T:12.8
FS : 2859 Lsec : 17
20-May-2014 17:30:01
Counts
P1 EDS Spectrum
Ti
Ti
Cr
Cr
N
O
1.00 2.00 3.00 4.00 5.00 6.00 7.00 8.00 9.00 keV
Label:
kV:200.0 X Tilt:35.0 Y Tilt:0.0 Det Type:SUTW+ Res:142 Amp.T:25.6
FS : 748 Lsec : 17
22-May-2014 13:10:26
Counts
P2 EDS Spectrum
Y
O
Al
Y
Y
Ni
Ni
Cr
Cr
Fe
Fe
Ni
Ni
Y
Y
2.00 4.00 6.00 8.00 10.00 12.00 14.00 16.00 18.00 20.00 keV

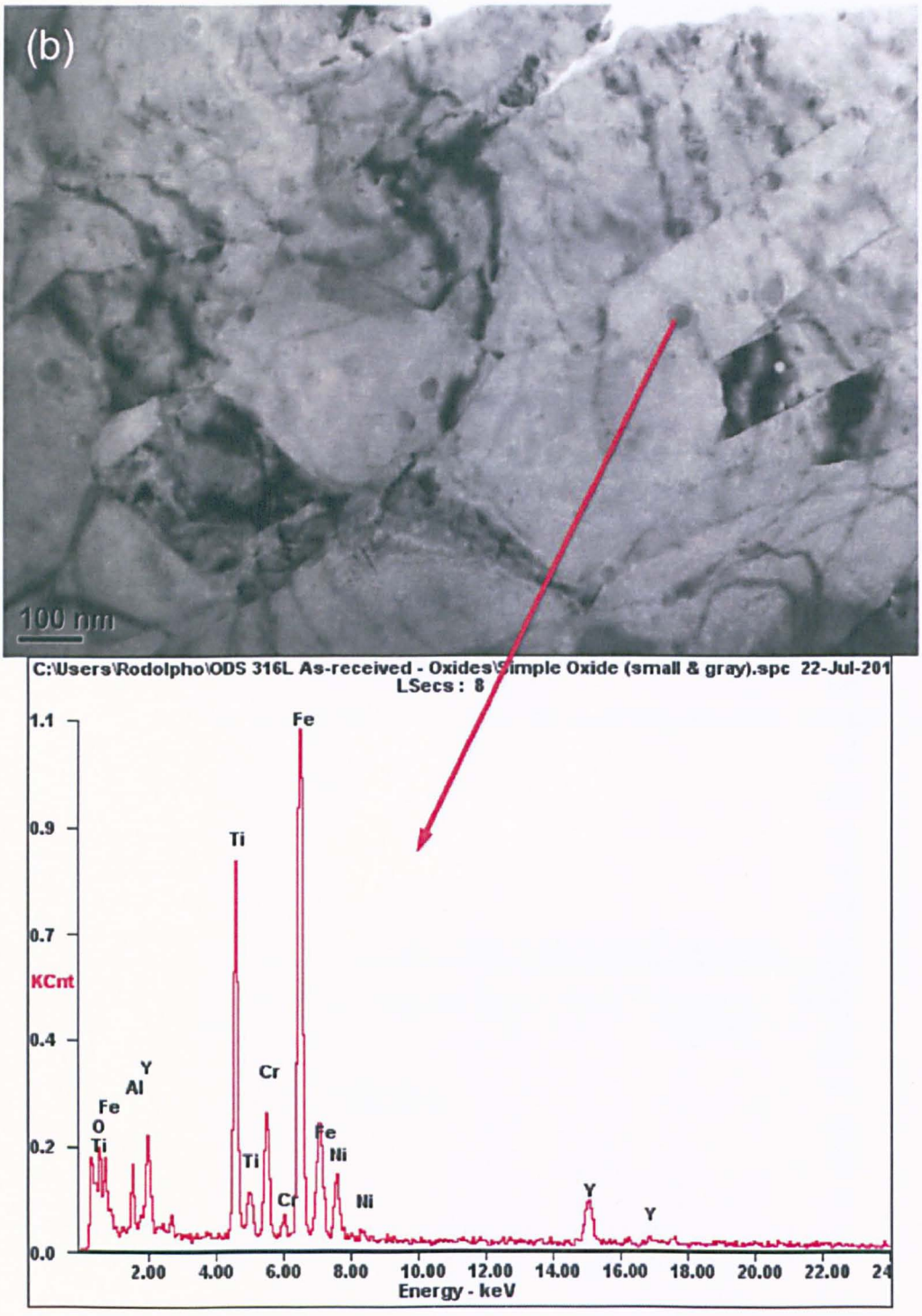

Figure 5.4 - TEM micrographs (ODS 316L as-received) and EDS of selected particles in the image. In (a), particle P1 was identified as being, most likely, TiN, while smaller particles were observed to be complex Y-Al-O oxides, given the pronounced peaks for these elements. Micrograph (b) shows an area with smaller particles, identified as Y-Ti-O oxides. The EDS spectrum detected elements from the background, given the small size of the particles.

Regarding the size distribution, the oxide particles can be considered relatively big, in comparison to other ODS steels, but presenting a desired size distribution, in the light of the literature, as seen in Chapter 2, which considers some tens of nanometres as the optimum size for them. Given the high population of particles whose size is larger than 50 nm, the average size was determined to be 68 nm. For the calculation, 268 particles in 17 different micrographs, from three foils, were measured.

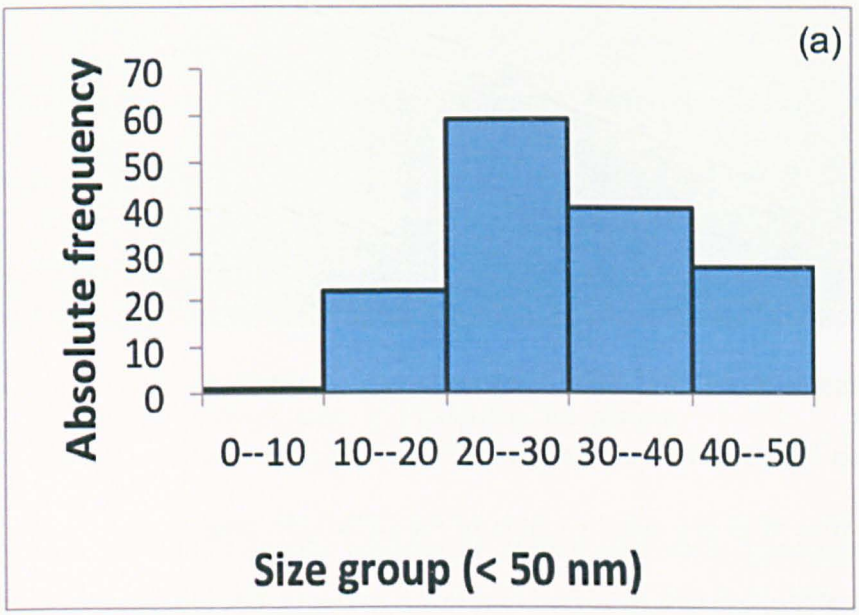

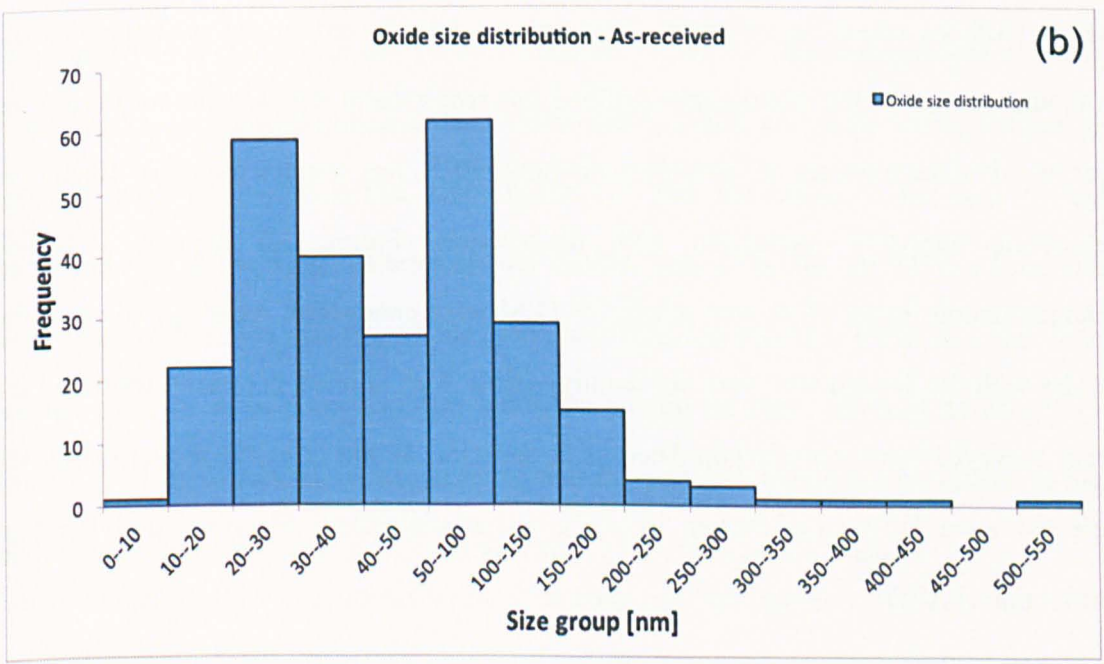

Figure 5.5 - Particle size distributions of (a) Y-Ti-O oxides with size <50nm and (b) all particles, including nitrides and carbides larger than 50 nm in as-received ODS 316L.

5.3.2 HRTEM Study of Y-Ti-O oxides

In order to study possible orientation correlations between particles and matrix, as well as the lattice coherency relationships, some High Resolution Transmission Electron Microscopy (HRTEM) studies were conducted on the same foils prepared from the as-received material. The relevance of such studies lies on the contribution given to further understanding the effectiveness of the particles in pinning dislocations and boundaries, with the consequence of improving modelling and theory at the nanometric scale [3].

Following studies concerned with the determination of crystallographic orientation relationships between oxide particles and a RAF/M steel matrix [3–5], and a recent study concerned with providing detailed information on the coherency of nanometric Y-Ti-O particles less than 10 nm with the austenitic matrix of an ODS steel [6], a conventional and high resolution TEM combined approach was devised to investigate the lattice configuration between the oxide particles, whose size was seen to be bigger than those reported by Mao et al. [6], and the matrix of the ODS 316L steel.

The first step consisted in identifying target areas of the foil, in conventional TEM, where particles could be observed. Two areas were selected in the investigated foil. Although several of the micrographs fulfilled this requirement, the selection of those used was based on the presence of particles in the range 10-50 nm, deemed the most effective in promoting attractive interaction with dislocations. Figure 5.6 depicts a typical microstructural image of an area where HRTEM were conducted. Although some of the oxides with the desired size were not readily visible – or, at least, not easily spotted – the areas surveyed were densely populated with particles. While in conventional mode, the Selected Area Diffraction Pattern (SADP), sometimes called Selected Area Electron Diffraction (SAED), was recorded and used to define the zone axis with which the matrix was observed. This is also shown in figure 5.6, from which the indexing of the spots determined a zone axis of $[11\bar{2}]_M$. This was found to be the zone axis of the other image as well.

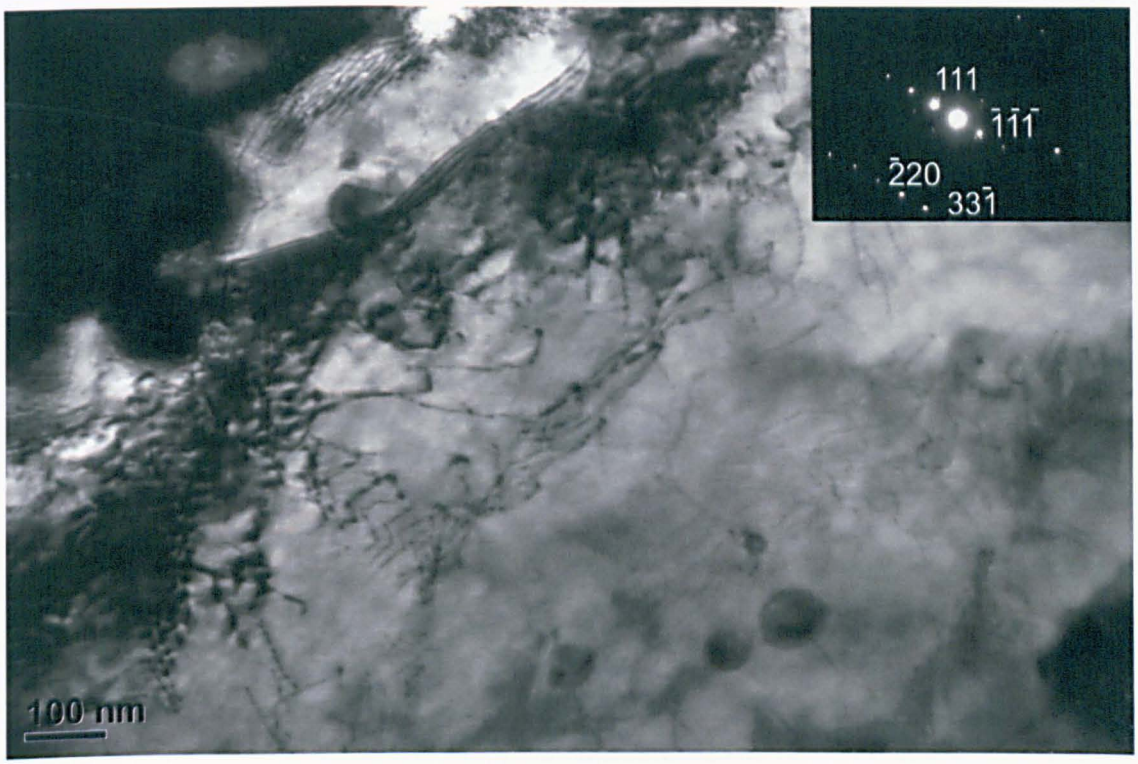

Figure 5.6 - TEM micrograph of the as-received ODS 316L showing one of the analysed areas and its diffraction pattern.

Upon switching to HRTEM mode, particles of interest were tracked and EDS was used to qualitatively verify their chemical composition, that is, to determine whether the particle belonged to the Y-Ti-O or to the Y-Al-O complex. Figure 5.7 illustrates an area of survey from fig. 5.6 in high-resolution mode, where some oxides and their lattice fringes are easily seen. It is easy to notice, from figure 5.7, that the matrix is not seen in high resolution, that is, the fringe patterns are not visible. This is because the TEM micrographs were taken with a zone axis favourable to the particles. The matrix is either in a high index orientation or in an inappropriate low index orientation for observation of its fringes [3]. Since any of these conditions would mean that the particles would not be visible in high resolution, images in a zone axis favourable to the matrix were not taken.

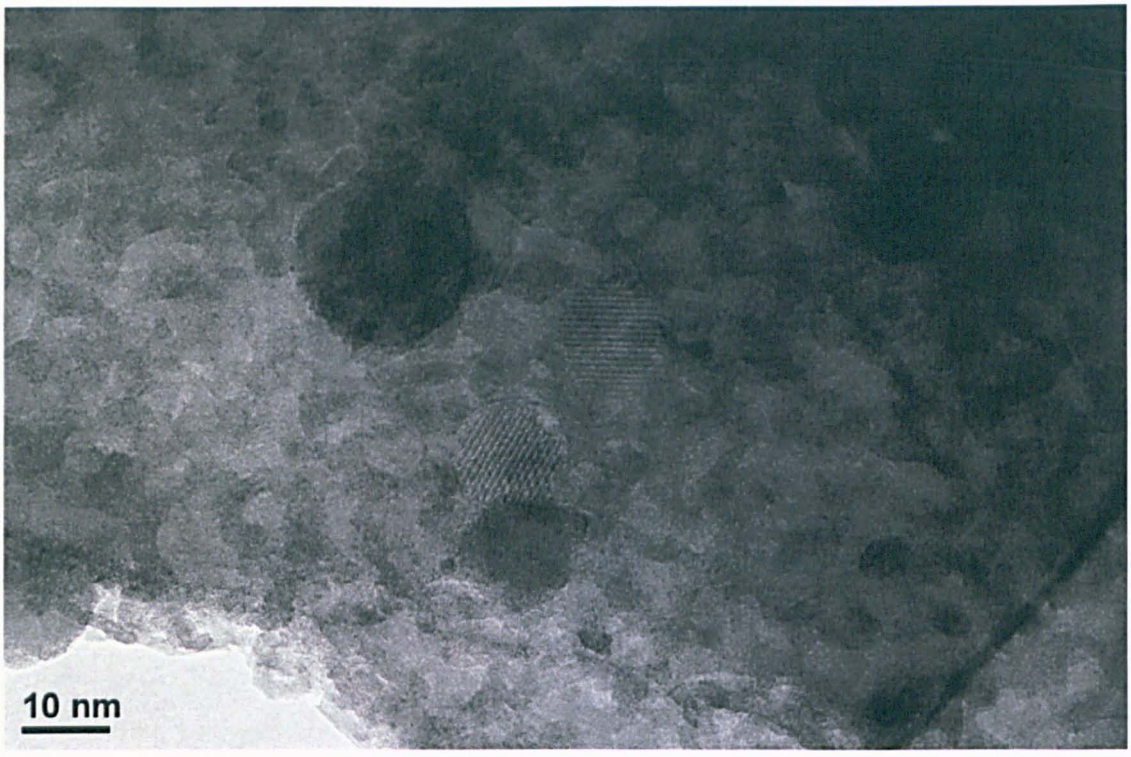

Figure 5.7 - HRTEM image of the ODS 316L, showing some particles with visible phase-contrast lattice fringes.

Oxides such as the ones observed in figure 5.7 were identified, by EDS analysis, as belonging to the Y-Ti-O complex oxide system. According to [4], there are six different Y-Ti-O compositions, each with its own stoichiometric proportions and crystal structure. Further literature survey indicated that three of these are stable forms of oxides, namely, $Y_2Ti_2O_7$, with a cubic *bcc* crystal structure whose lattice parameter was measured as 1.01 nm [6], Y_2TiO_5, orthorhombic, with lattice parameters (a = 1.04 nm, b = 0.37 nm and c = 1.13 nm) [7]; and orthorhombic $YTiO_3$, with almost all lattice constants smaller than the previous ones (a = 0.57 nm, b = 0.76 nm and c = 0.53 nm) [8]. In order to rule out the possibilities, the interplanar distances, d_{hkl}, measured in the HRTEM analysis were checked against each of the lattices, with the appropriate equation relating the interplanar spacing to the lattice constants. For all particles analysed, there was excellent agreement between the measured interplanar distances and some of the low index allowed reflections from bcc with a lattice of 1.01 nm. This result suggests that the particles analysed were $Y_2Ti_2O_7$,

which is in agreement with the findings of the works by Klimiankou et al. [3], Lindau et al. [5] and Mao et al. [6]. Apparently, $Y_2Ti_2O_7$ is the most common form of the Y-Ti-O oxide.

For the purpose of orientation correlation, parallelism was determined between particle and matrix in one direction, defined by the zone axis, and at least one plane, from which lattice misfits were quantified using the expression in equation 5.1 below [6]:

$$\delta = \frac{2\left(d_{Matrix(hkl)} - d_{Y_2Ti_2O_7(h'k'l')}\right)}{d_{Matrix(hkl)} + d_{Y_2Ti_2O_7(h'k'l')}} \quad \text{(Eq. 5.1)}$$

where d_{hkl} represents the interplanar spacing of the plane (hkl) of the matrix or of the particle.

Each particle studied was individually imaged and analysed by its Fast Fourier Transform (FFT), from which the interplanar distances were automatically determined by the image processing software ImageJ and used to determine the indices that could satisfy the relation between those distances and the lattice parameter. Once in possession of the indices, the zone axis for each particle was calculated and compared with the zone axis of the austenitic matrix, for establishment of the direction orientation correlation. The plane parallelism was determined from spots of coincident location in the SADP of the matrix TEM image and FFTs of the HRTEM particle images. Figures 5.8 to 5.10 summarize the orientation relations found.

- Particle 1

For the particle shown in Fig. 5.8 (and other similar, found in the micrographs), the parallelism was determined as $[11\bar{2}]_{Matrix} || [\bar{1}10]_{Y-Ti-O}$ with correspondent plane spots being $(\bar{1}11)_{Matrix} || (440)_{Y-Ti-O}$ and $(33\bar{1})_{Matrix} || (\bar{8}8\bar{8})_{Y-Ti-O}$. The lattice misfits between parallel planes were found to be 14.26% and 11.57%, respectively. This means that, for every 7 planes $(\bar{1}11)$ and approximately every 9 planes $(33\bar{1})$ of the matrix, a misfit dislocation should be formed, so that the misfit strain between matrix and particle is

released. This results in a distance of 1.45 nm between consecutive misfit dislocations in the case of the $(\bar{1}11)$ planes and of 0.71 nm in the case of $(33\bar{1})$ planes. The particle size being around 15 nm, these misfit dislocations can, indeed, be formed. Considering this possibility and the magnitude of the misfits, the idea of semi-coherency of particles similar to this one is reasonable.

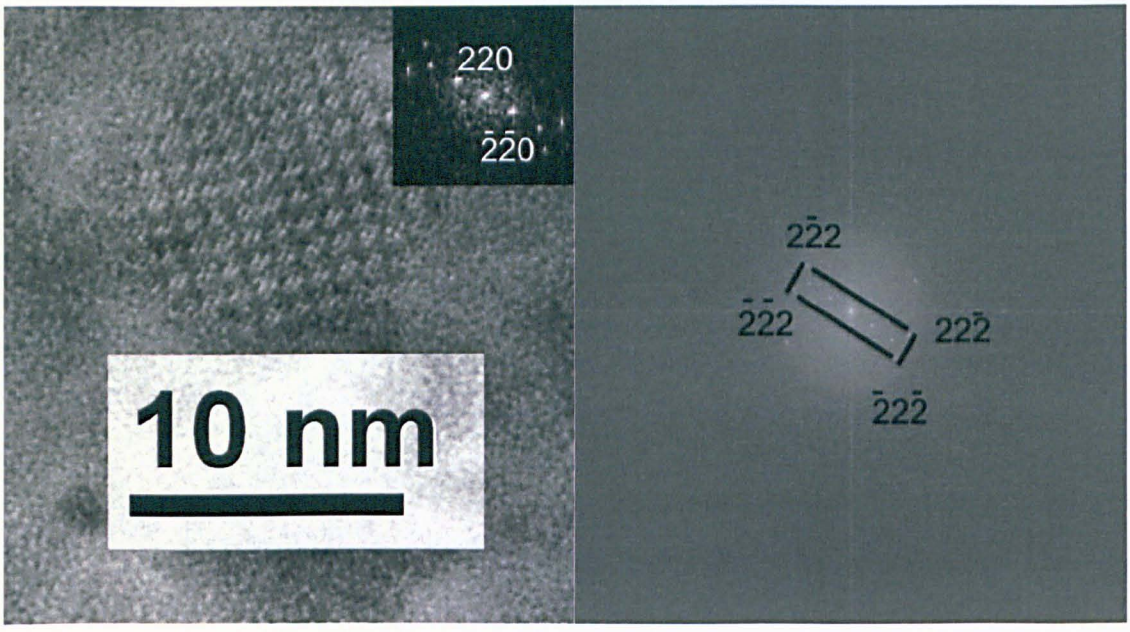

Figure 5.8 - Oxide with approximately 15 nm diameter in HRTEM image. The live FFT shows the (220) reflections, while the side image is the same FFT, but showing the (222) reflections.

- Particle 2

A second type of oxide particle was imaged and is shown in Figure 5.9. It represents larger oxides (approximately 40 nm), still bearing $Y_2Ti_2O_7$ composition. The orientation relationship for such oxides were expressed by parallelism between the $[11\bar{2}]_{Matrix}$ and $[00\bar{1}]_{Y-Ti-O}$ directions, and between the $(\bar{3}\bar{3}1)_{Matrix}$ and $(800)_{Y-Ti-O}$ planes; as well as between the $(444)_{Matrix}$ and the $(880)_{Y-Ti-O}$ – that is, between the (111) of the matrix and the (220) of the oxide. The lattice misfits increased to 42.68% and 53.68% respectively. In these conditions, misfit dislocations would be introduced approximately every 2 planes in both cases, which makes the particle incoherent with the matrix.

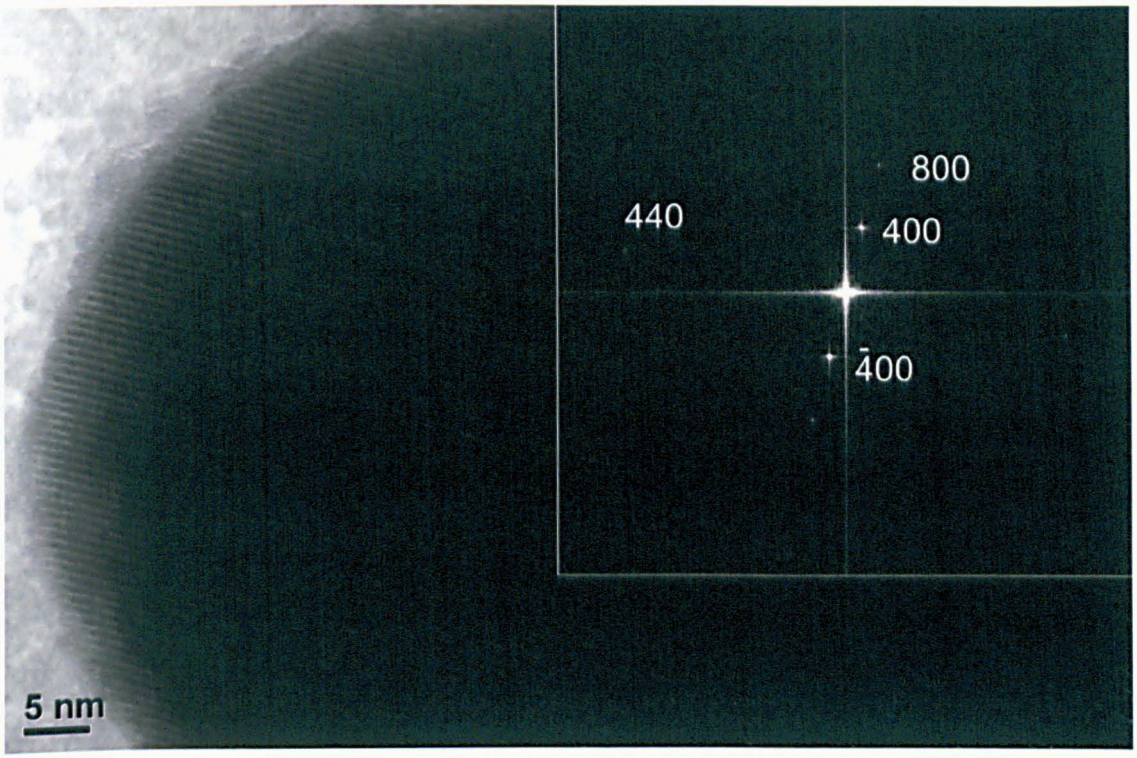

Figure 5.9 - Large oxide found to be incoherent with the matrix.

- Particle 3

Shown in figure 5.10, particles with this configuration presented an intermediate condition, reaching larger sizes than the first, but being considerably smaller than the previous type. Parallel planes were found to be $(33\bar{1})_{Matrix} \parallel (800)_{Y-Ti-O}$ and $(11\bar{1})_{Matrix} \parallel (222)_{Y-Ti-O}$, with parallel zone axes $[11\bar{2}]_{Matrix}$ and $[0\bar{1}1]_{Y-Ti-O}$.

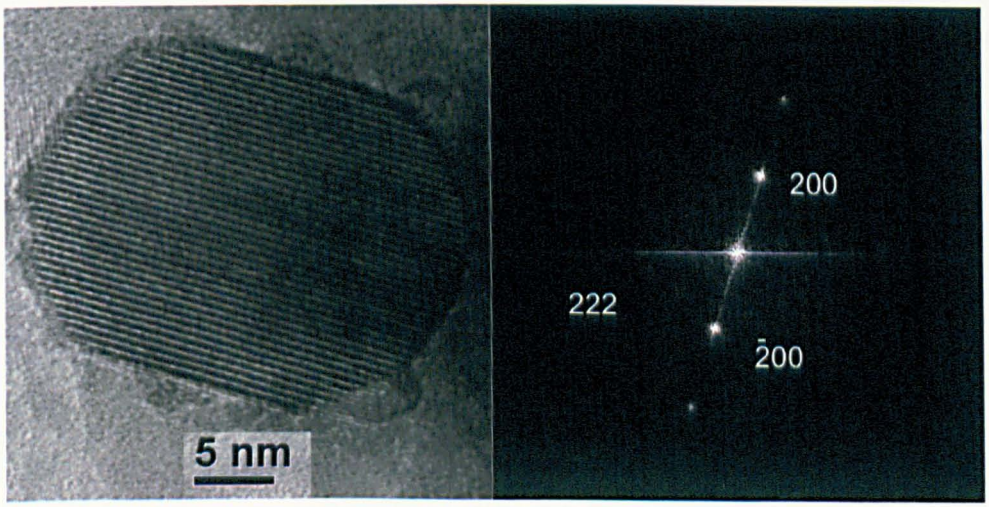

Figure 5.10 - HRTEM image of an oxide deviating from the round shape and its corresponding FFT.

From these values, the calculated misfits amounted to 42.68% for the first set of parallel planes and 34.41% for the other. Again, the level of misfit is high, yielding 2 and 3 dislocation misfits for every $(33\bar{1})$ and every $(11\bar{1})$ planes of the matrix. Again, these particles, with diameter of a few tens of nanometres, were found to be incoherent.

Other particles of the matrix areas analysed followed one of the three categories previously described. It is easy to notice that the smaller particles analysed tend to be semi-coherent with the matrix. As they grow, the orientation changes, as well as the coherency condition. These results are consistent with the idea that particles that are not too small (that is, > 20 nm) tend to be more incoherent, thus becoming non-shearable. This agrees with the observations by Arzt [9] that dislocations can cut through very small oxides (less than 10 nm), given their coherency with the matrix, as described by Mao and co-workers [6] for an austenitic ODS steel, being larger oxides preferable, for their stronger pinning effect, as explained in Chapter 2.

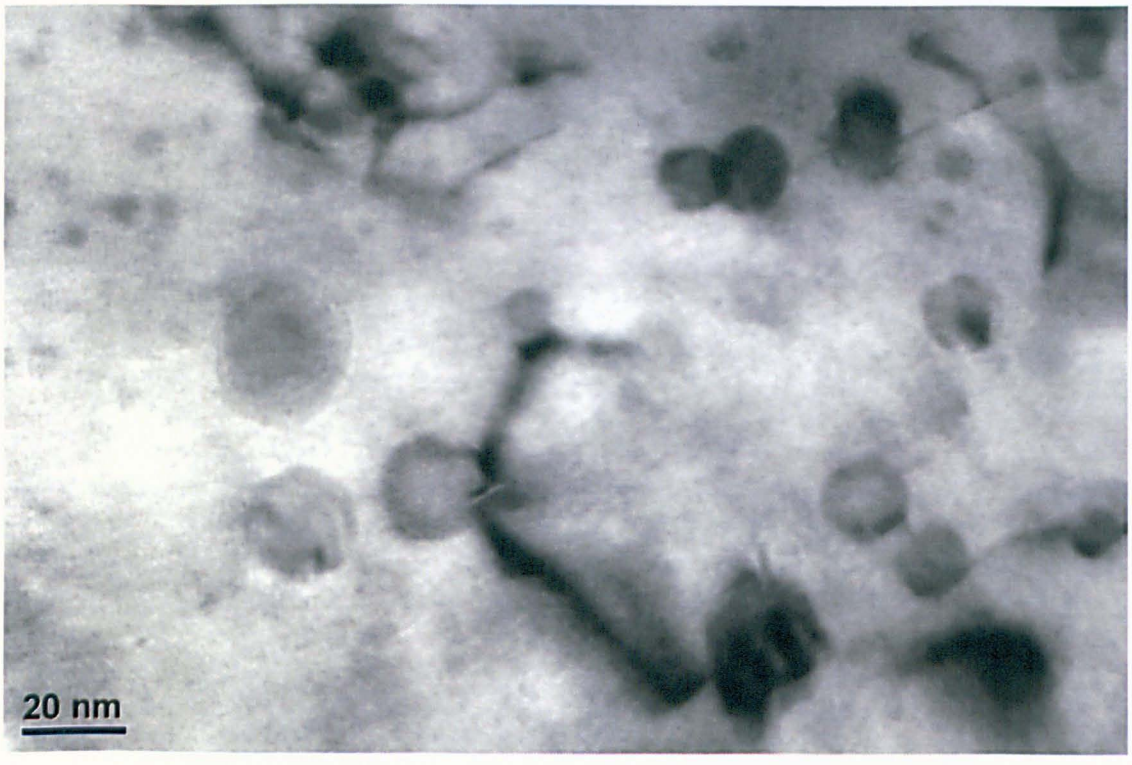

Figure 5.11 - Dislocation line being pinned by particles of various sizes; as-received ODS 316L.

With regards to pinning, limited evidence of attractive interaction between dislocations and oxides was found in the as-received material, probably due to the size distribution, which includes a significant population of very large oxides (>100 nm). Figure 5.11 is an HRTEM micrograph illustrating the pinning of dislocations by oxide particles in such a way that suggests attractive interaction. In this image, it is possible to see particles ranging from a few nanometres to some tens of nanometres in size.

5.4 Tensile properties of the ODS 316L steel

The first mechanical property investigated was the tensile behaviour, at room temperature and at 650°C. Three tests were conducted at each of these temperatures. Flat 6.25 mm wide and 3 mm thick specimens, with a gauge length of 25 mm and designed according to ASTM E8M Standard (shown in Chapter 3) were used in the room temperature tensile tests. These were carried out in an Instron 5969 test rig at 4×10^{-4} s^{-1} strain rate. Room temperature was constantly monitored and remained at 23.5°C. The high temperature tests were performed at 5×10^{-4} s^{-1} using round samples of 4 mm gauge diameter and 20 mm gauge length, under controlled temperature level (650°C ± 1°C), using an Instron 8862 test machine, as shown also in Chapter 3.

Prior to the tensile tests, the room temperature Young's modulus of the material was determined, using the mechano-acoustic technique described in the experimental methods chapter. The natural frequencies of response to a step excitation were determined from six measurements on a rectangular bar specimen of 5 mm x 3 mm x 30 mm. Results from all measurements differed from each other within 0.5%, averaging 194 GPa.

5.4.1 Room temperature tensile tests

Figure 5.12 shows the room temperature tensile test curves for the ODS 316L. The mechanical properties are summarized in table 5.3, in which a comparison with the same

properties of a conventional 316L with 0.10% nitrogen, known for refining the microstructure of austenitic steels and improve their mechanical response [10], is made.

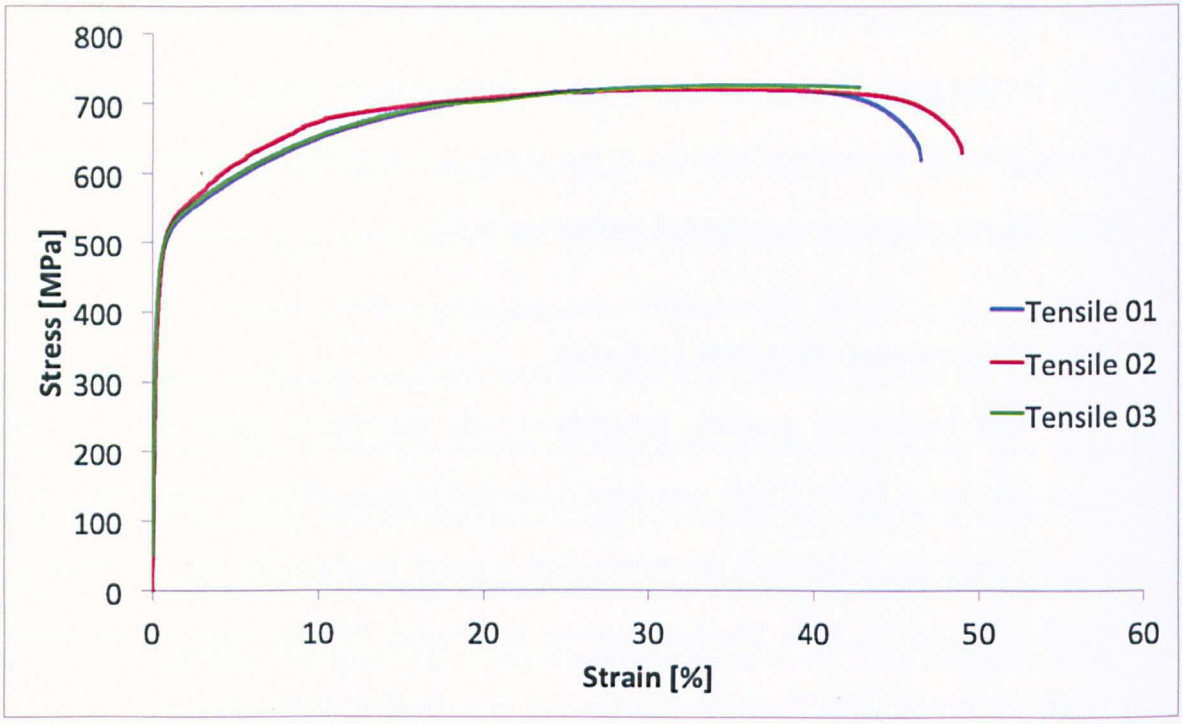

Figure 5.12 - Room temperature engineering stress-strain curves for the ODS 316L steel.

Table 5.3 - Room temperature tensile data summary. Data for the 316L(N) extracted from [10].

Material / Property	Conventional 316L(N)	ODS 316L
E [GPa]	193	194
Yield Stress (0.2%) [MPa]	306	458
Ultimate Strength [MPa]	601	723
Ductility % (elongation)	67	46

As indicated in table 5.3 above, the ODS 316L revealed much higher strength than a conventional 316L. Ductility, in terms of elongation to failure, was found to be remarkably high for an ODS steel, reaching almost 50%, but inferior to the ductile behaviour of the

conventional 316L, which presented almost 70% elongation. Figure 5.13 shows SEM fractographic analysis of the ODS 316L room temperature tensile surfaces.

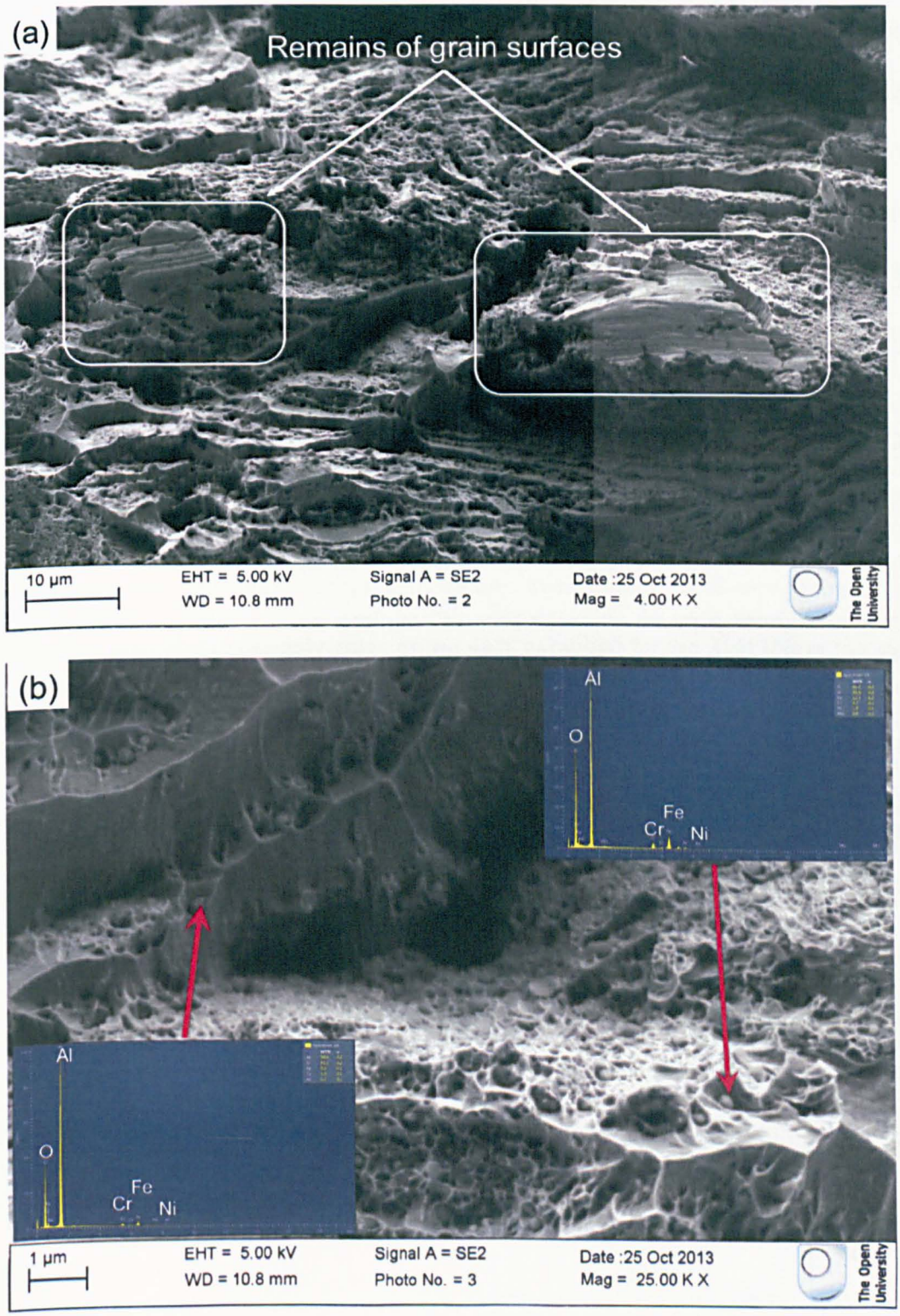

Figure 5.13 - SEM fractography of room temperature tensile test specimens. In (a), remains of grain surfaces are highlighted, while (b) has some highly dimpled surfaces. The tensile test axis is perpendicular to the images.

As Figures 5.13 (a) and (b) indicate, the surfaces of the tensile test specimens were extensively dimpled, which is expected from materials with high levels of ductility. The micrographs also reveal remains of grains that appear to have been cut by crack propagation, as in the case of transgranular mode of fracture. Yet, it appears that, in some regions, intergranular crack propagation may have been predominant, as the faceted linear parallel features at the right top and bottom parts of Figure 5.13a show. The higher magnification of Fig. 5.13b provides evidences of some particles in the dimples. EDS analysis indicated that these particles are, most likely, undissolved alumina (Al_2O_3), as seen in the inserts of Figure 5.13b.

5.4.2 High temperature tensile tests

The properties of the ODS 316L steel, again in comparison with the conventional 316L are presented in table 5.4. Young's modulus at 650°C for the conventional 316L was taken from the High-temperature characteristics of stainless steels handbook n° 9004, of the American Iron and Steel Institute [11] and its value showed good agreement with the modulus calculated from the slope of the elastic portion of the tensile curves. Figure 5.14 is a plot of the tensile test curves at 650°C.

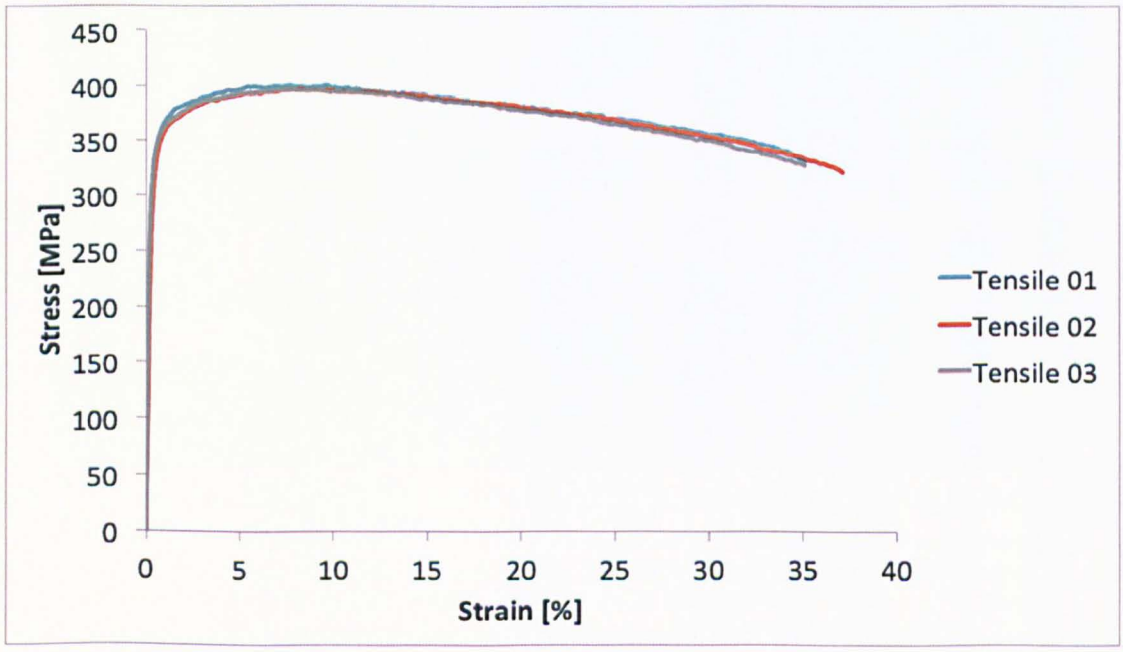

Figure 5.14 - High temperature (650°C) tensile test curves for the ODS 316L.

Table 5.4 - Tensile properties of the ODS 316L at 650°C. Data for the 316L(N) extracted from [10].

Material / Property	Conventional 316L(N)	ODS 316L
E [GPa]	145	145
Yield Stress (0.2%) [MPa]	148	305
Ultimate Strength [MPa]	421	399
Ductility % (elongation)	45	36

As expected, given that ODS materials reflect the mechanical behaviour of their base alloy, high temperature strength of the material decreased. Yield strength of the ODS 316L was found to be more than twice that of the conventional 316L with 0.10%N. However, the ultimate tensile strength exhibited a larger decrease at 650°C, when compared to the UTS of the conventional 316L. Contrary to expectations, the ductility of the ODS 316L at 650°C was lower than that at room temperature, even though 36% elongation is still significantly high and reasonably close to the 45% exhibited by the 316L(N) at the same temperature. Although lower ductility has been reported also for the conventional 316L, higher ductility is reasonably expected in the high temperature response, where recovery mechanisms and more slip systems are active. The fractographic analysis, presented in Figure 5.15, also showed features that are typical of ductile materials, such as dimples throughout the extent of the surfaces and irregular contours of torn grains. These features indicate a predominantly ductile mode of fracture. Similarly to the case for the room temperature specimens, some remains of grains can be seen, as in Figure.5.15b, which indicate the occurrence of transgranular crack propagation.

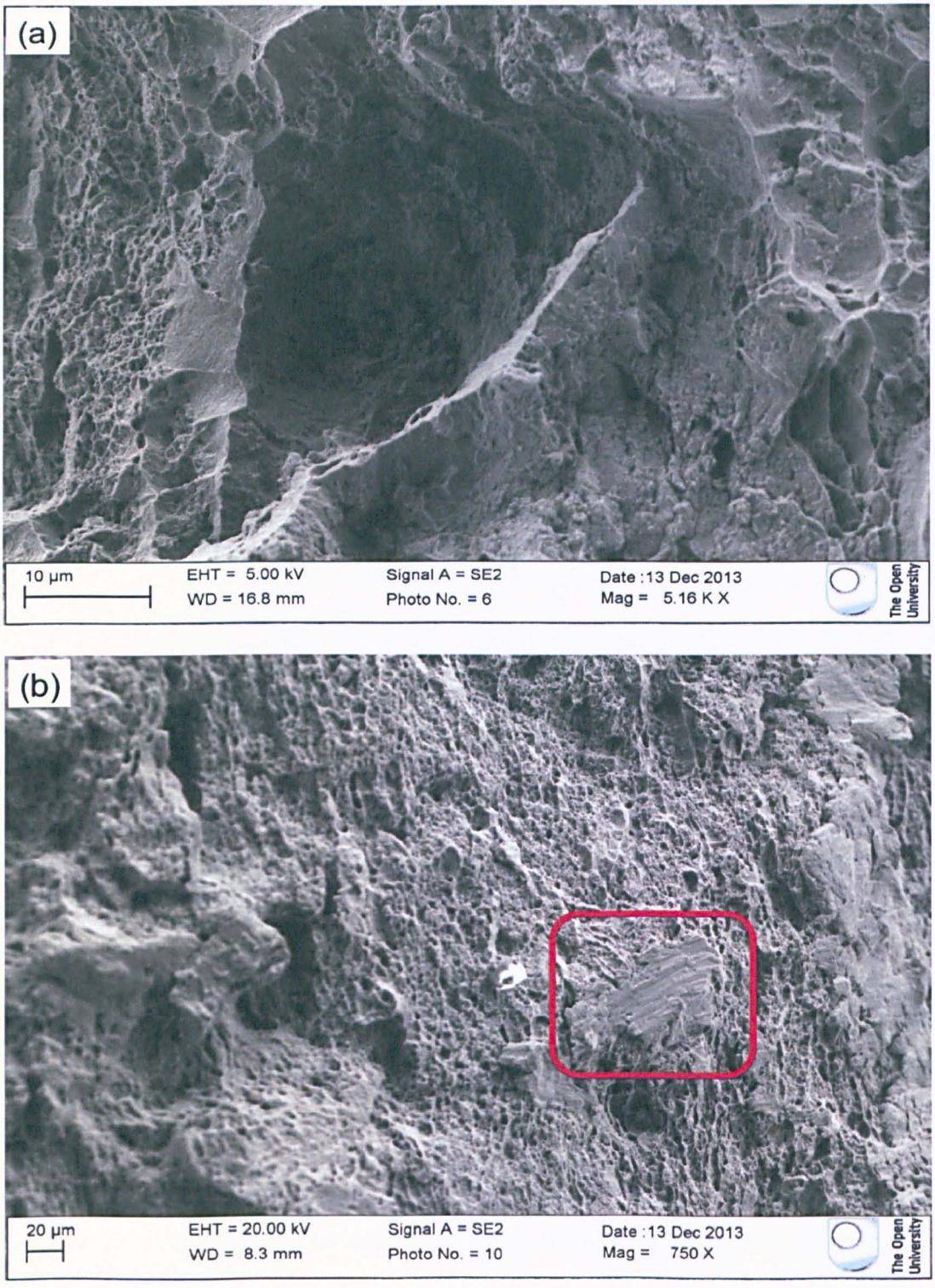

Figure 5.15 - SEM fractography of high temperature tensile test specimens. Dimples are observed all across the surface in (a). Image (b) also shows dimpled areas, but emphasis is given to the riven grain surface (remains of grains), highlighted in the red square. Tensile axis is normal to the surface of the image.

5.4.3 Qualitative TEM study of tensile test specimens

While the SEM fractography provided evidence that the ODS 316L behaved in a predominantly ductile manner in both room and high temperature tensile tests, showing many similar features, the TEM studies concentrated on the differences, in terms of dislocation arrangements. Only a qualitative analysis was executed, based on interpretation of the TEM micrographs taken from the tested specimens. For this endeavour, three foils were extracted from each test condition, all of them from the gauge length of the specimens, normal to the loading direction.

Figure 5.16 illustrates the dislocation structures found in foils from the room temperature tensile test specimens. Through these images, it is possible to notice that there is a predominance of stacking faults in the grains. It may be suggested that these partial dislocations are forming locks, since they seem impeded from cross slipping. Although recombination of partials would be expected with the progress of deformation, given the need for alleviation of strain energy around grain boundaries and other obstacles, this result is not entirely surprising. Being at room temperature, which is relatively low, the energy available for non-conservative processes (such as climb) is also very low, so that dislocations cannot easily rearrange themselves (in this case, partials cannot recombine into a perfect dislocation). Moreover, and perhaps the most significant reason, this is not a conventional steel, due to the presence of the oxides. Therefore, the nanoparticles may be playing a leading role on the hindrance of the extended dislocations (the ones of the stacking faults), by effectively interacting with them.

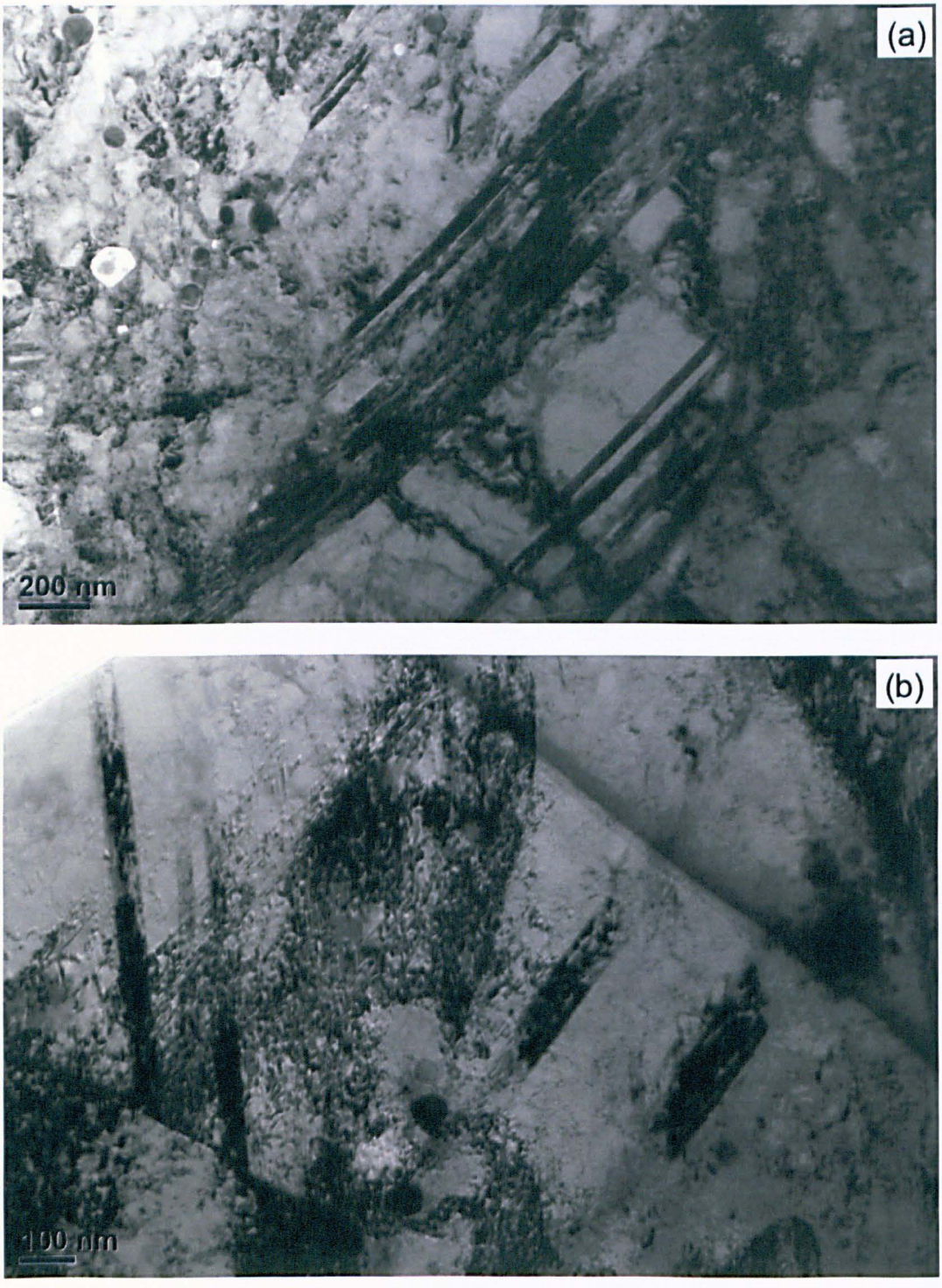

Figure 5.16 - (a) and (b) are TEM images from ODS 316L room temperature tensile specimens.

It is important to mention that stacking faults in abundance were present in almost all the areas of the foils investigated. While the aspects of figure 5.16 (a) and (b) are similar, it

is possible to see that the stacking faults in image (b) are in close proximity with oxide particles, which may be exerting the pinning effect on the partials of these defects.

The configuration changes dramatically for the high-temperature tensile specimens TEM micrographs. The 650°C (923 K), representing more than $0.4T_m$, allows climb and cross slip to occur. Due to this, the population of stacking faults is almost entirely converted into heterogeneous dislocation arrangements. Because of the high level of plastic strain imparted to the material, it is possible to see areas with entanglements, areas where tangles are evolving to walls, as well as dislocation cells being formed. Figure 5.17 illustrates the predominance of these arrangements.

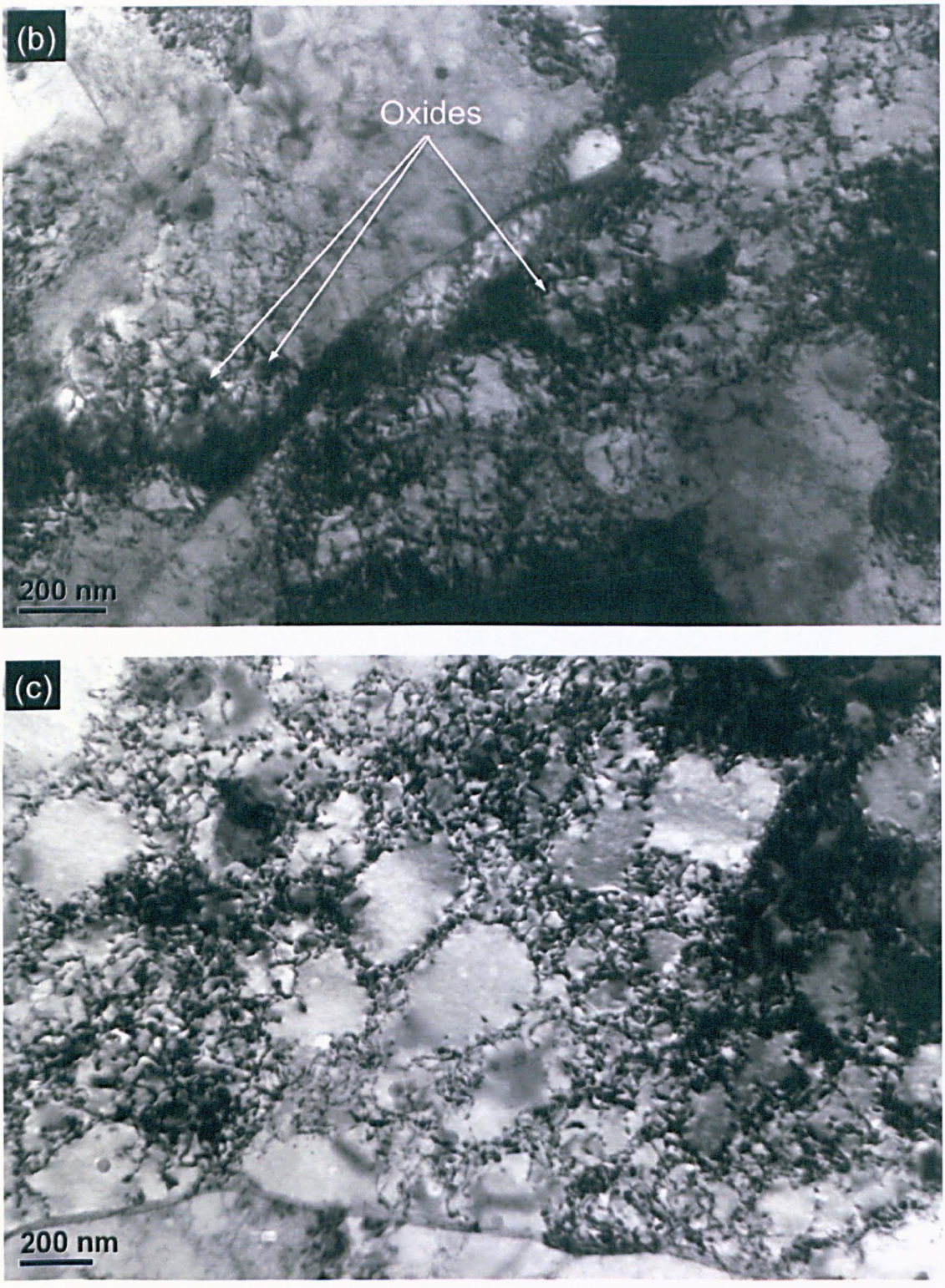

Figure 5.17 - Dislocation arrangements in high temperature tensile strained specimens of the ODS 316L. In (a), tangles are seen on both sides of the boundaries of a small grain, inside it as well as in the neighbouring grain. In (b), tangles start to organize themselves in walls, close to oxides, while (c) illustrates dislocation cells formed extensively throughout the area, indicating advanced stage of deformation in this region.

5.5 Creep-rupture tests of ODS 316L

Due to the interest in assessing the suitability of ODS austenitic steels for high temperature applications in advanced nuclear power plants, the material was tested for determining its response to creep deformation in creep-rupture tests. These were carried out also at 650°C under three different stress levels, 140 MPa, 175 MPa and 200 MPa, chosen so that the behaviour of the ODS 316L could be compared to the conventional 316L(N) steel showing increased creep strength as studied by Mathew and colleagues [12].

Given the limited availability of material, miniaturized specimens with 3.8 mm gauge diameter and 19 mm gauge length, as described in Chapter 3 and illustrated in Figure 5.18 below, were used. Further details on the sample can be seen in the Appendix 1. Creep-rupture data were plotted and compared to the creep performance of conventional 316L steel. Larson-Miller Parameters were calculated for the extrapolation of data for longer service hours.

Figure 5.18 - Miniaturized creep specimen design adopted for the ODS 316L steel.

The curves from the creep-rupture tests of the ODS 316L are shown in figure 5.19. Rupture time under 140 MPa of stress was determined to be 1461 hours, while the material failed after 411 hours under 175 MPa and after 239 hours under 200 MPa. The most outstanding feature observed was the predominance of the tertiary creep stage: in all tests,

tertiary creep accounted for more than 50% of the rupture life of the material. These results are contrary to the trend reported for ferritic-martensitic ODS steels, which usually show creep curves with no tertiary stage [13–16], or, depending on composition and microstructural history, have anomalies in their creep response, as reported by Evans and co-workers [17]; in all cases, steady-state creep was the most pronounced stage.

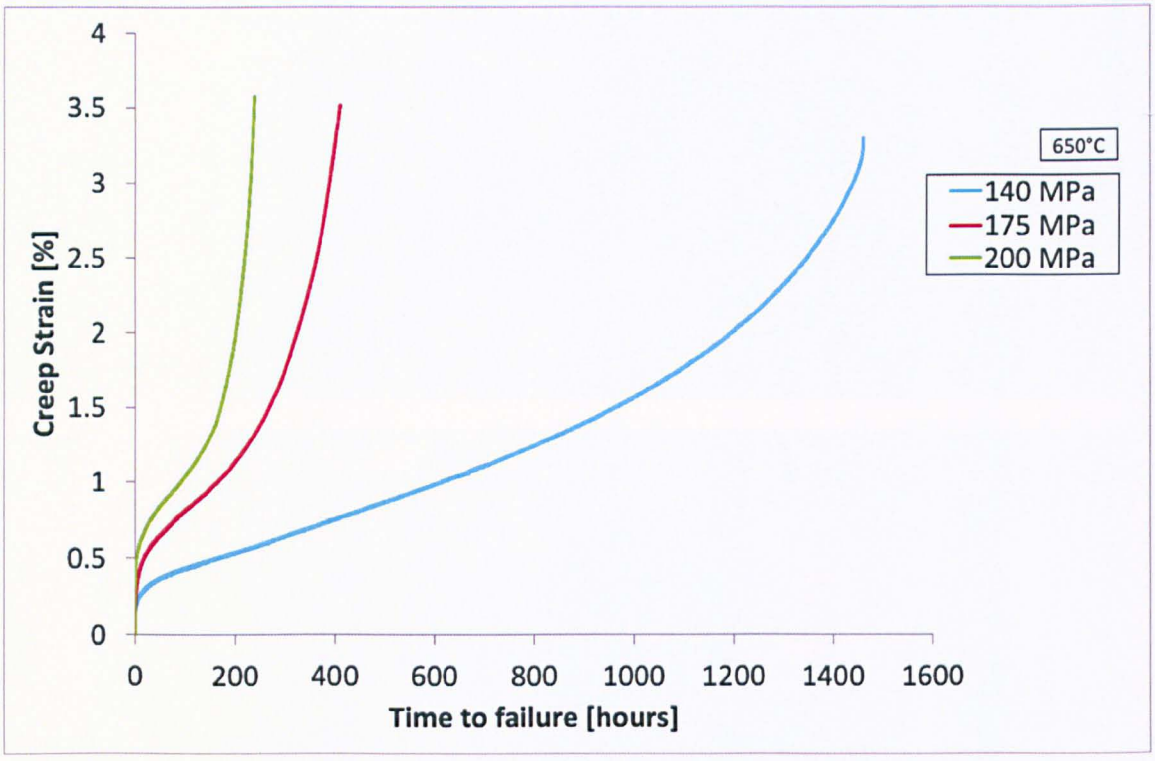

Figure 5.19 - Creep-rupture test curves of the ODS 316L.

In order to more properly evaluate the performance of the material when creep tested, the data extracted from the creep-rupture tests were checked against the curve with minimum stresses demanded for different rupture times, by the RCC MR code, for a 316L steel with 0.07 wt.% nitrogen [12]. The same data were used to determine the Larson-Miller Parameters (LMPs), in order to estimate, based on extrapolation, the maximum stress level expected to be applied on ODS 316L if this material had to last 10,000 hours. The LMPs were calculated according to equation 5.2 [13, 28]:

$$LMP = T(\log t_r + C) \qquad \text{(Eq. 5.2)}$$

where T is the temperature of the tests, in Kelvin; t_r is the time to rupture, in hours, and C is a material-dependent constant, usually taken as 20, in the case of steels. Figure 5.20 brings the comparison between the ODS 316L performance and the RCC MR minimum requirement for 316L steel to be considered suitable for nuclear applications, as well as a prediction, based on the LMP, for 10,000 hours of operation.

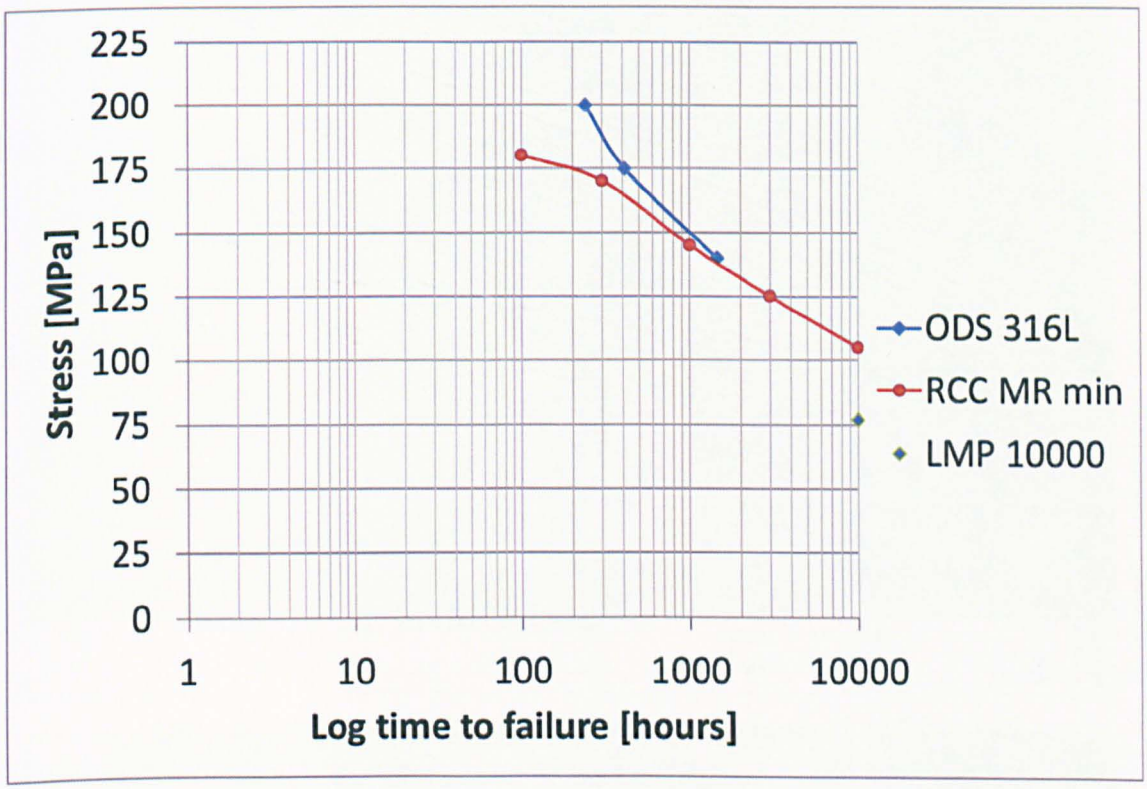

Figure 5.20 - Plot of stress vs. log of time to failure; the isolated point is the extrapolation for 10,000 h based on Larson-Miller parameter.

As seen from Fig. 5.20, although compliant with the code for the tested stress levels, since all experimental points were found to be above the RCC MR curve, it is likely, from the trend of the ODS steel curve, that the compliance is not maintained, as rupture times increase. The extrapolation indicated a rupture life of 10,000 hours for the ODS 316L under a stress of 77 MPa, significantly below the minimum stress according to the code.

Another interesting aspect stemming from Figure 5.19 regards the creep ductility of the material, which was very moderate, since the maximum ductility found at rupture of the ODS 316L was around 3.5%. The recorded maximum creep strain in each test (140 MPa,

175 MPa and 200 MPa) is shown in Figure 5.21. Although lower strains have been reported, such as for the dual-phase ferritic-martensitic 9Cr ODS steel investigated by Sakasegawa and co-workers [18], which failed with less than 1.5% strain after approximately 1500 hours under 180 MPa, several works recorded strains of 16% to 20% under similar stress levels, and longer rupture lives [14, 17, 19]. This simple comparison seems to suggest creep weakness for the ODS 316L.

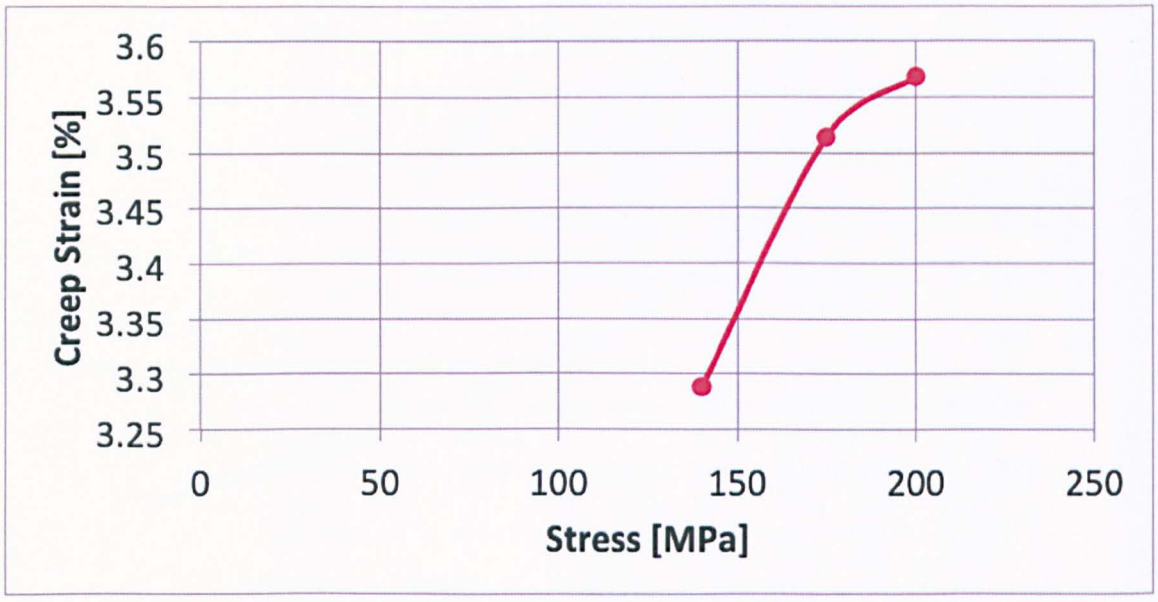

Figure 5.21 - Variation of the maximum strain to rupture in each creep test.

The stress exponent n was calculated from the steady-state creep rate of the tests, by means of a log-log plot of creep rate vs. stress, and found to be around 4. This is within the range 3-7, usually reported for polycrystalline metals and alloys, when dislocation-based mechanisms are predominant.

5.5.1 SEM Fractography and TEM studies of crept specimens

The creep-rupture test specimens, when subject to analysis of their fracture surfaces, revealed a slightly different fractography than the samples from tensile tests, as Figure 5.22 depicts. Although it was dull and porous, with the presence of dimples, these were sparser across the surface, which presented some deep cracks. The topographic aspect of the

fracture surface provides support to the idea that cracks were predominantly intergranular, the boundaries being the more favourable path, presumably due to the presence of larger particles, which may have provided the de-cohesion site. The same intergranular ductile fracture mode was seen in an Fe-14CrWTi steel by Steckmeyer et al. [14].

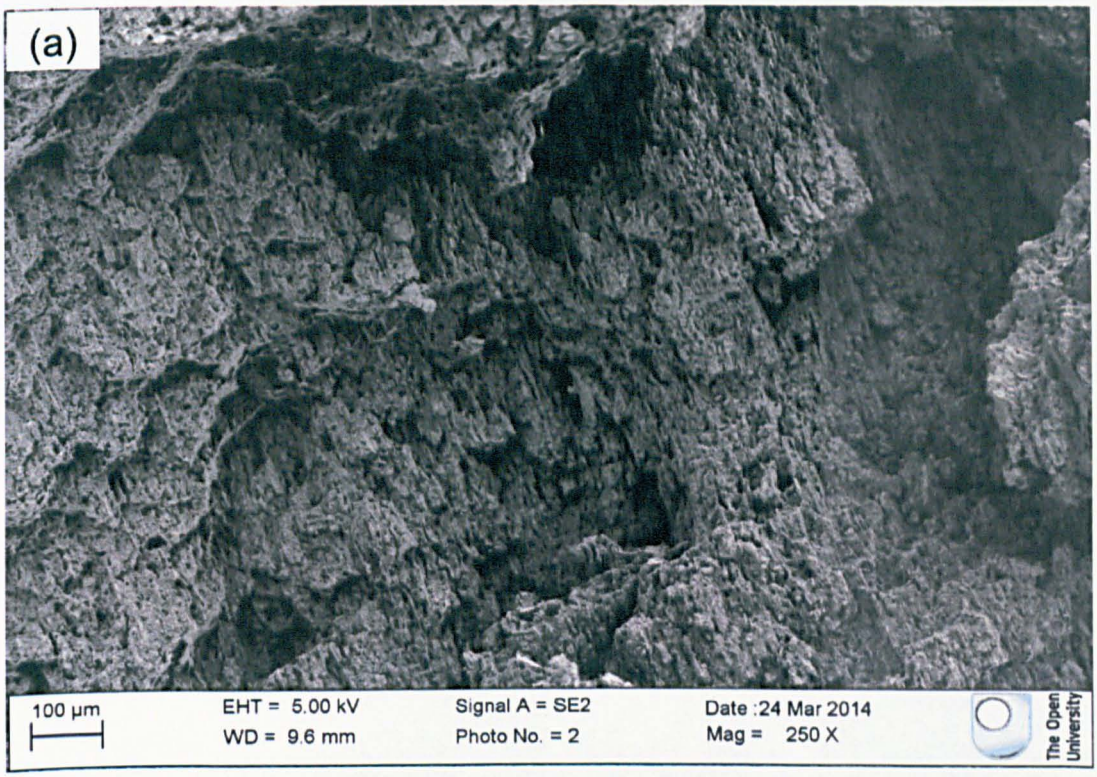

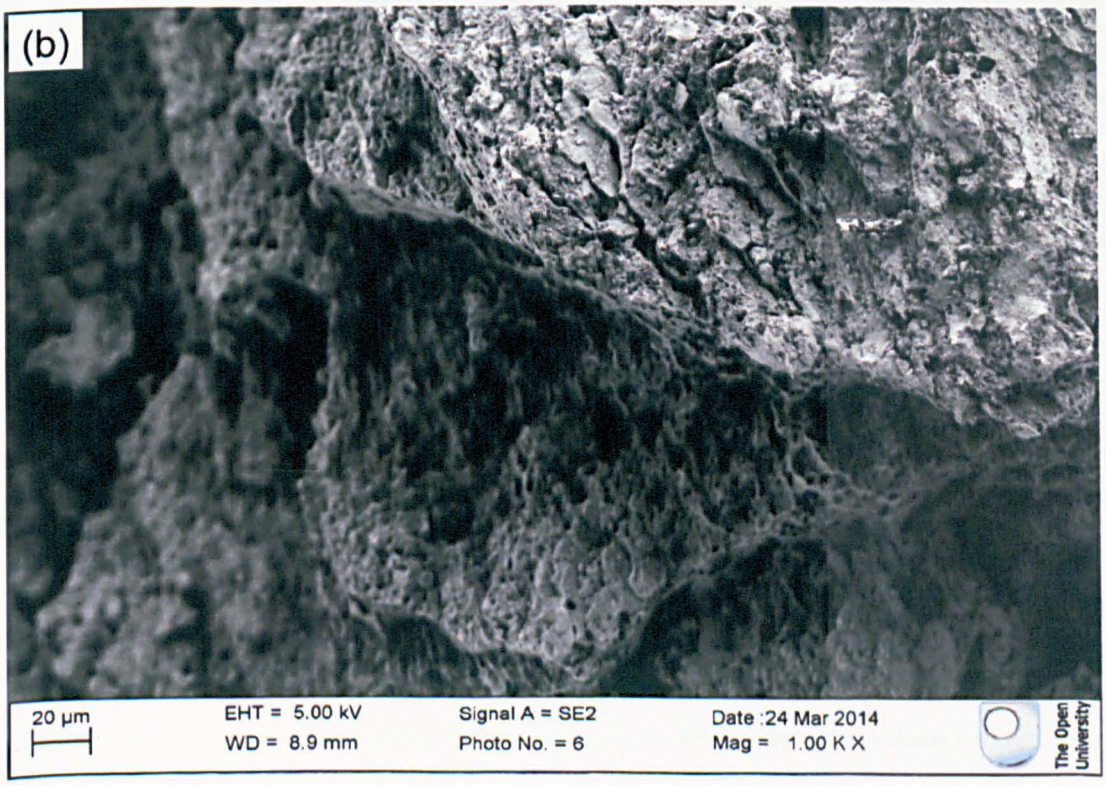

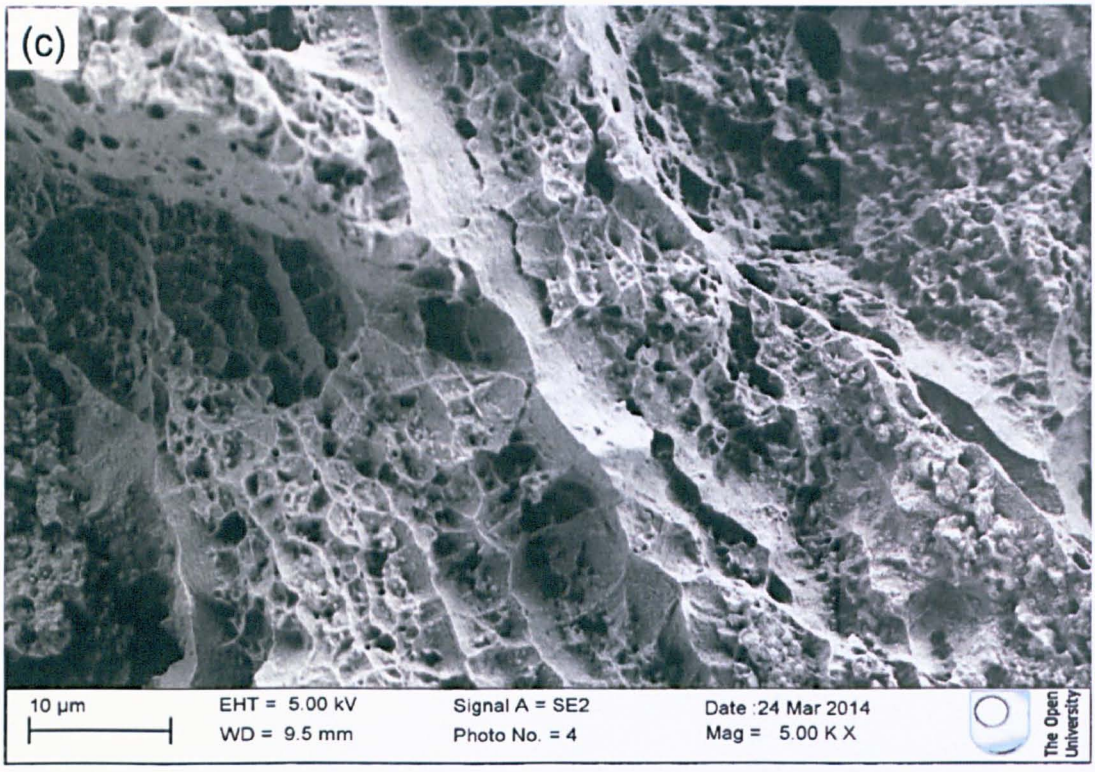

Figure 5.22 - SEM fractographic images of the ODS 316L specimen crept under 175 MPa. The surface shows deep cracks and cleaved topography, as in (a) and (b); the surface in (c) suggests intergranular ductile fracture.

Complementary TEM studies were carried out in order to assess qualitatively and quantitatively the differences between the crept and the as-received conditions. Four foils were extracted from the cross-section of the as-received rods and three foils were cut from the gauge length of the specimen CR-02 (crept under 175 MPa) for examination. The dislocation density, measured with the same method described in Chapter 4, did not reveal any detectable change above the attainable precision, remaining at the 1.2×10^{10} cm^{-2} magnitude. This is reasonable, considering that the material, in all tests, failed after only approximately 3.5% strain.

In terms of dislocation arrangements, the micrographs were consistent with the idea that plastic deformation occurred, but not as extensively as would be expected, judging from the extent of the tertiary creep stage. Figure 5.23 shows the main features found, which were predominantly tangles, walls at early stages of formation from tangles, and free matrix dislocations, including some that developed interactions with oxides. Stacking

faults and pile-ups were practically absent, indicating significant creep deformation. However, differently than the high temperature tensile specimens, the crept ones did not show any advanced stages of walls nor cells, despite the prolonged exposure to the high temperature deformation process, which encompassed tertiary creep. This is another result seen as an evidence of premature failure. It might be expected that, prior to failure, the material showed evolution of the dislocation arrangements from tangles to walls, cells and, ultimately, subgrains, as strain is increased. Instead, the micrographs reveal only part of the expected features.

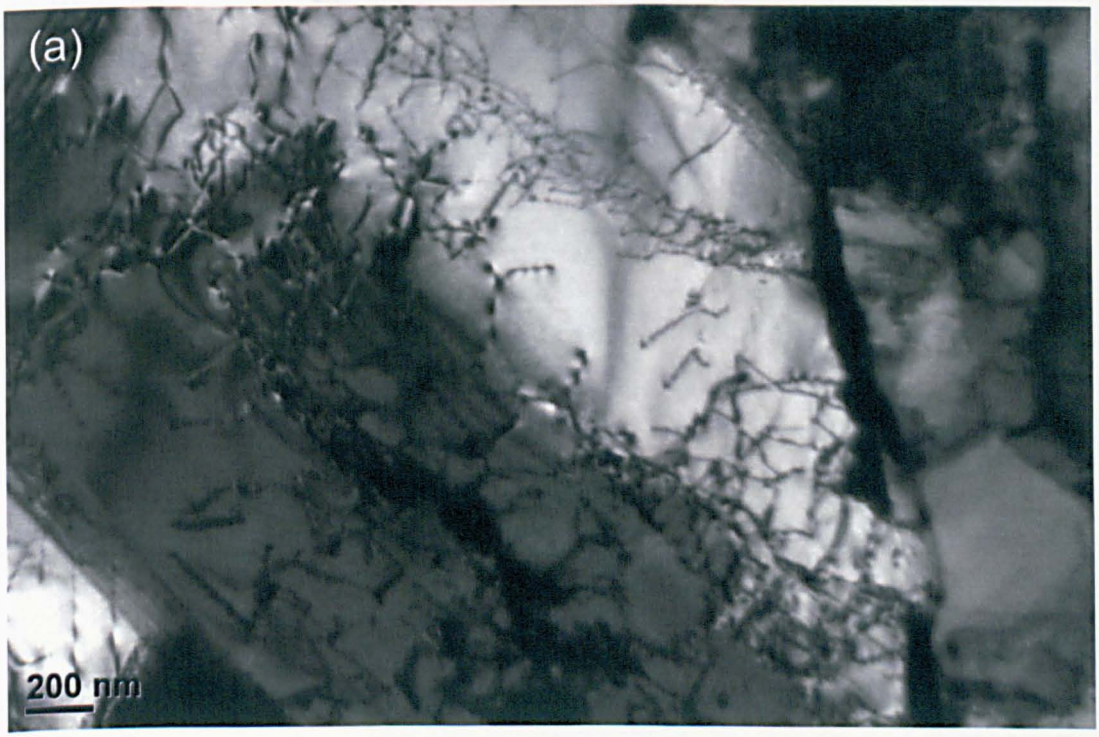

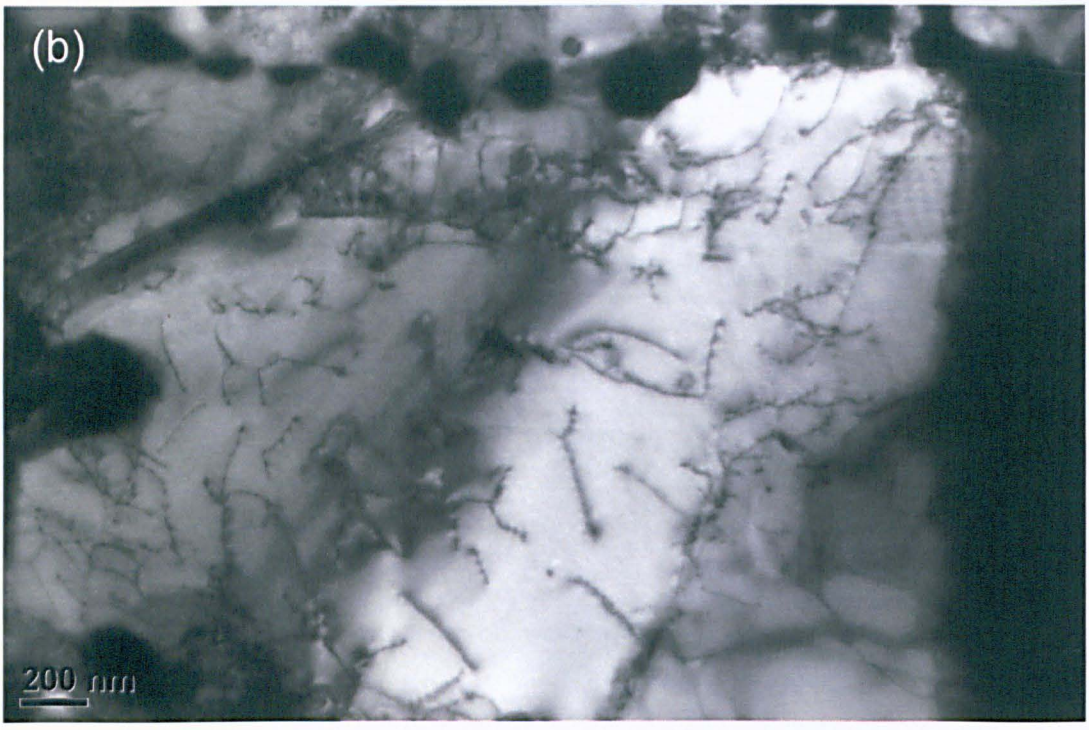
(b)
200 nm

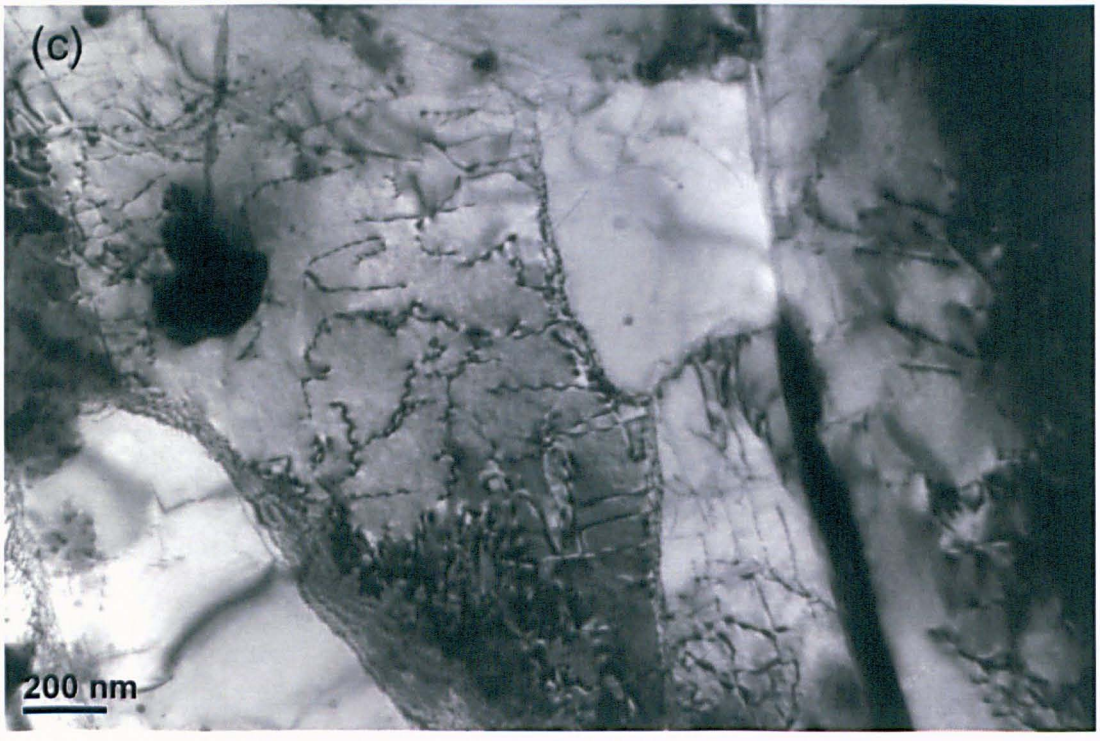
(c)
200 nm

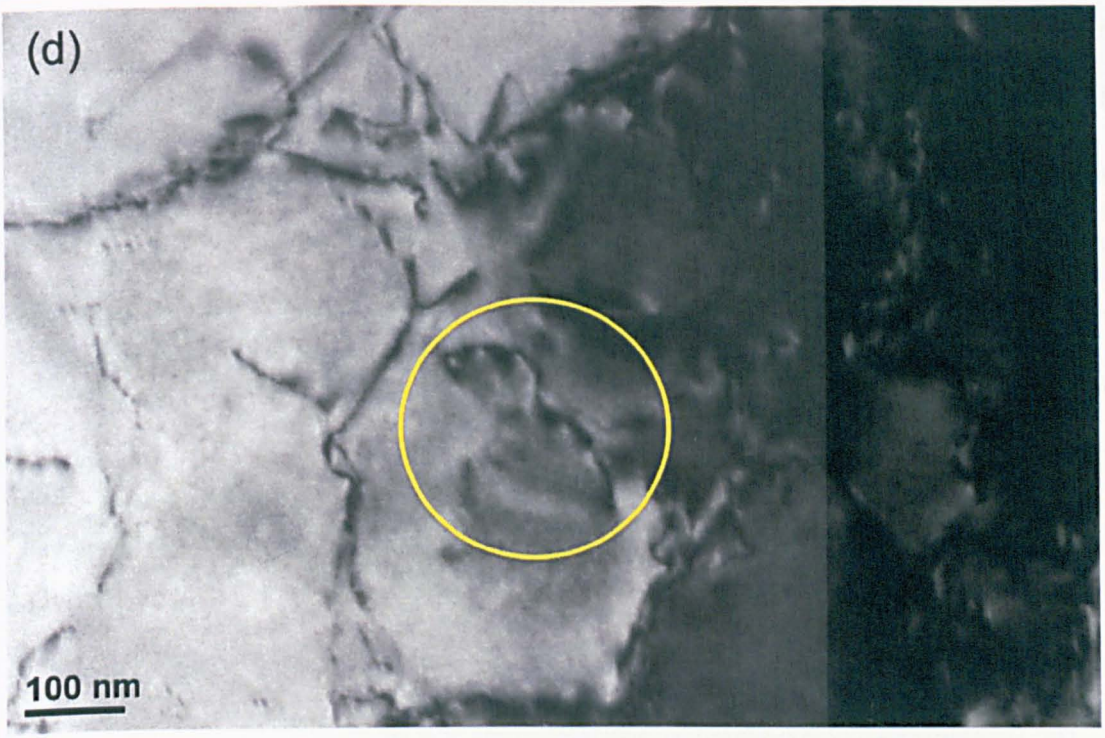

Figure 5.23 - TEM micrographs of the crept specimens. In (a), the predominance of tangles is evidenced, although some bowed dislocations seem to be bent on obstacles, probably small oxides. In (b), tangles that seem to have evolved from accommodation of piled-up dislocations; large particles and a small pile-up are seen on the top areas of the micrograph. (c) Areas of poor contrast alternate with images of dislocations forming tangles. Finally, (d) shows one of the limited evidences of attractive interaction between dislocations and small oxides.

5.6 Pilot study of ODS 316L Diffusion Bonding

The reduced availability of material in the ODS 316L batch, rather than being a limitation, proved to be an opportunity for opening a parallel line of investigation of the ODS steels, concerned with joining processes. Although the initial motivation was simply to increase the number of samples available for testing the ODS 316L properties, it evolved to a pilot study on the feasibility of diffusion bonding of these steels. This joining process is regarded as one of the most suitable for ODS steels, since it does not produce a molten puddle, therefore averting the disruption of the oxide particle distribution [20, 21].

Solid-state diffusion bonding was incorporated to the research as a procedure aimed at the production of hybrid specimens, whose parts would be manufactured in different

materials: the gauge length of samples (or a fraction of it) would be comprised of the ODS 316L; while other parts, such as the grips, shoulders (and even part of the gauge length) would be made of a stronger alloy. Nickel-based superalloys were chosen as the suitable materials to be diffusion bonded to the ODS 316L. Given the well known high temperature strength of these nickel-based alloys, much higher than that of any steel, and the stress level used in the tests, no deformation was expected to occur in the superalloy parts of the specimens. Therefore, provided that the diffusion bonding was well executed, having a solid bond line as result, the strains from mechanical tests were expected to be confined to the ODS 316L regions, in such a way that the hybrid specimens would behave as conventional ones, entirely machined from the steel.

The first step in this endeavour was to choose the nickel superalloy to be used in these studies. After considerations on availability of material, chemical composition, mechanical properties and use in diffusion bonding, the Inconel 718 alloy was selected. Chemical composition ranges of this material are provided in table 5.5. Subsequent EDS upon a ground and polished (following the same procedures described in Chapter 3 for optical microscopy samples) piece of the alloy cut from the as-received plate of Inconel 718 was done and the analysis indicated percentages of the elements within the specified range. The EDS chart can b seen in the Appendix 5.

Table 5.5 - Chemical composition of the Inconel 718 nickel-based alloy [22].

Ni (+Co)	Cr	Fe	Nb (+Ta)	Mo	Ti	Al	C	Si	Mn
50-55	17-21	Bal.	4.75 - 5.5	2.8-3.3	0.65 - 1.15	0.2-0.8	0.08 max.	0.35 max	0.35 max

Grain morphology and size measurements were carried out for the Inconel 718, following the same procedure as for the ODS 316L described earlier. Six different areas of the nickel superalloy OM sample were analysed (summing up to 4.8 mm^2), with a total of

1057 grains, and their average yielded a gran size of 106 ± 12 μm. Grains were found to be large, but equiaxed, as shown in Figure 5.24.

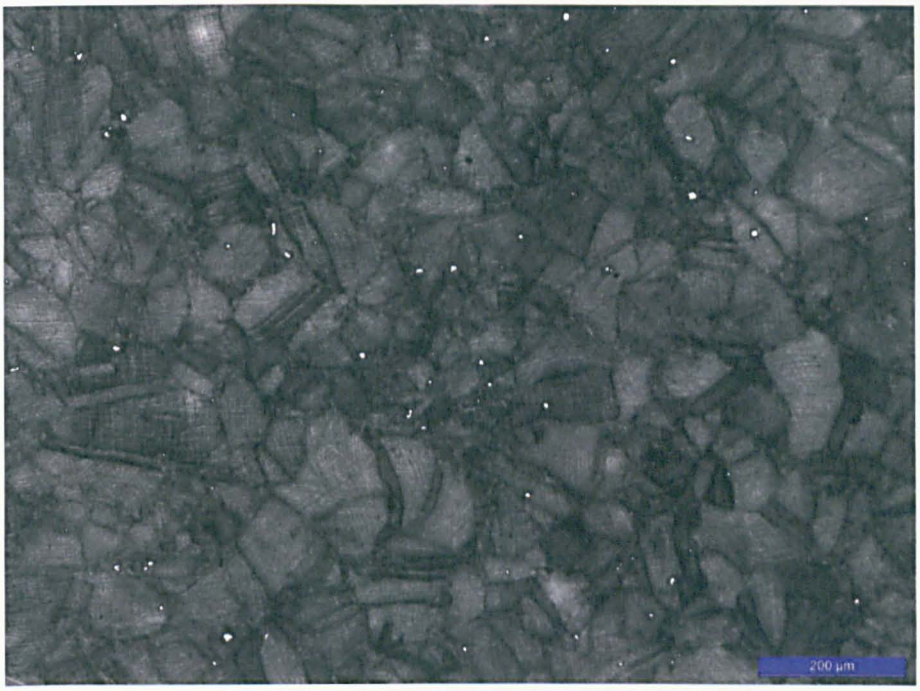

Figure 5.24 - Optical micrograph with the grain morphology of the Inconel 718.

The following step consisted in executing some trials of diffusion bonding, in order to find a suitable combination of input parameters, namely, temperature and time, in order to produce a solid bond. Too low temperature or time causes the bond to be weak. Too high temperature or too much time under the bonding process will cause the species in diffusion to penetrate largely each other structures, thus altering the properties of the original materials. The appropriate choice of parameters avoids both undesirable scenarios. After a few trials at different temperatures, ranging from 1100°C to 1250°C, and times, going from 30 minutes to 1 hour, it was seen that the most desirable combination of parameters was found for diffusion bonding carried out at 1200°C for 1 hour.

In order to achieve this conclusion, discs of 8 mm diameter by 5 mm thickness of both materials were bonded, using the diffusion-bonding machine available at the Open University, shown in figure 5.25. A heating rate of 200°C/min was used for reaching the

desired temperature level, from where the bonding time started to be counted. Experts in diffusion bonding at The Open University conducted this part of the work.

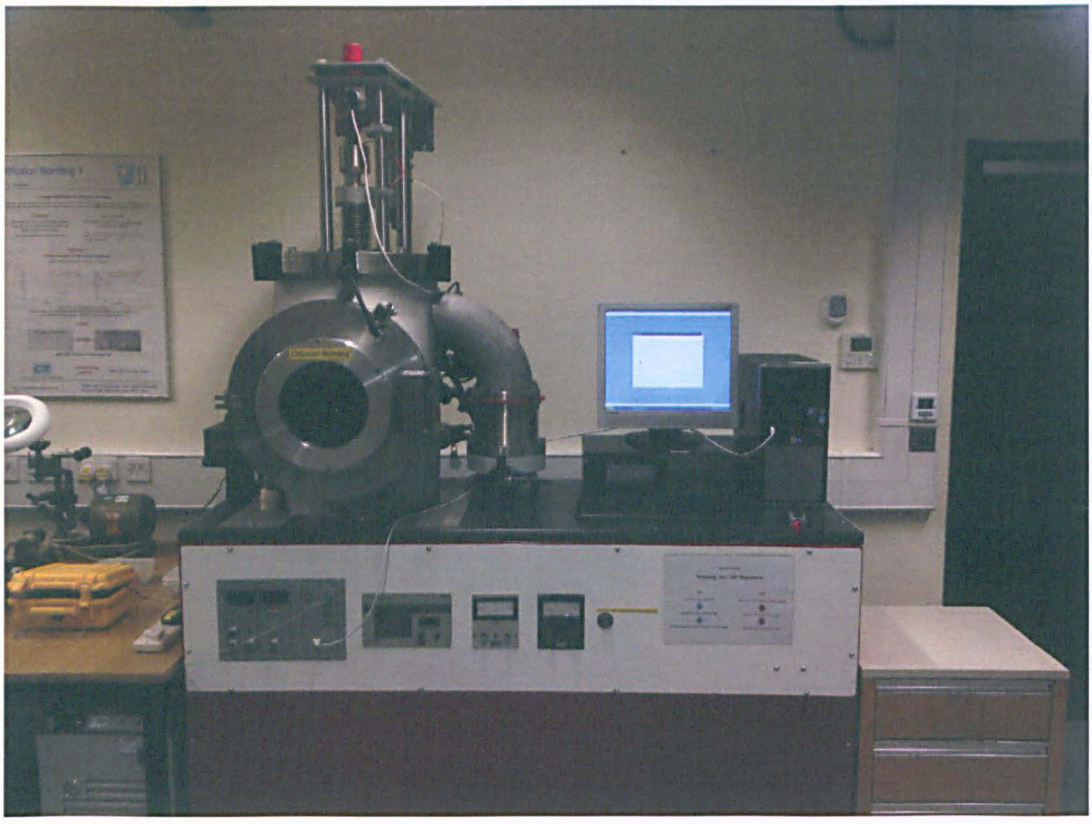

Figure 5.25 - Diffusion bonding machine at the Open University.

Thin slices (less than 1 mm) were cut from the discs along their longitudinal plane and put for examination of the microstructure and some manual-bending test. This latter is a simple bending test serving as a primary assessment of the quality of the bond. All the slices extracted resisted well the efforts of cutting and, when subjected to bending load, their bond lines remained intact. The deflexion was well supported by the slices as if they were wholly comprised by a single material. Figure 5.26 depicts one of the slices after bending. Its visual aspect is smooth, being hard to distinguish, at naked eye, one material from the other, or to locate the bond line between the surfaces.

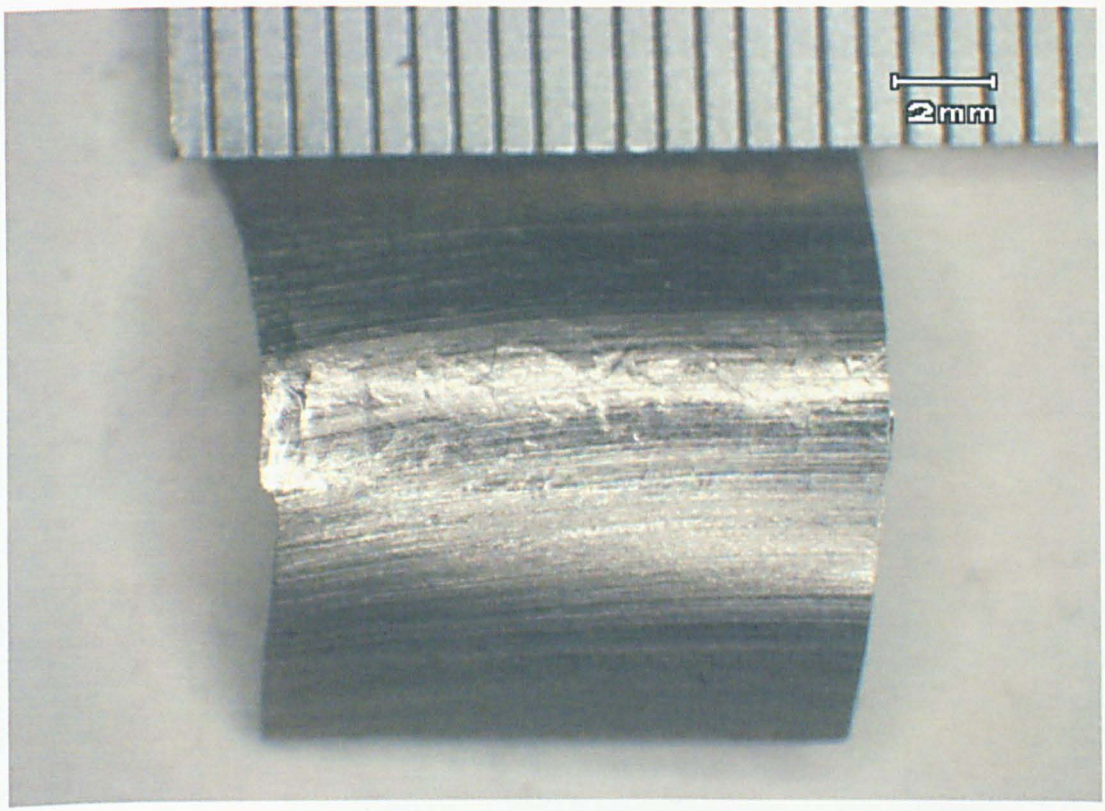

Figure 5.26 - Slice after bending test. There's no clear distinction between the ODS 316L and the Inconel 718.

In terms of the microstructure, optical microscopy revealed clean areas on both sides of the bond line, as shown in figure 5.27a, indicating a well-preserved microstructure for both materials. Samples were ground and polished to the OP-S level (as described in chapter 3). It is interesting to notice that, close to the surfaces, nickel appeared to have grown over the steel microstructure, further penetrating it, as depicted by fig. 5.27b. This is reasonable, since induction heating was used. In these circumstances, although the temperature is set to be uniform and constant, a "skin" effect is observed, in which the surface of the samples is more heated than its interior, causing higher diffusion rates at these locations. Also, from these results, it seems that the diffusion of nickel into the microstructure of the steel is processed at faster rates than those of the iron into the nickel superalloy.

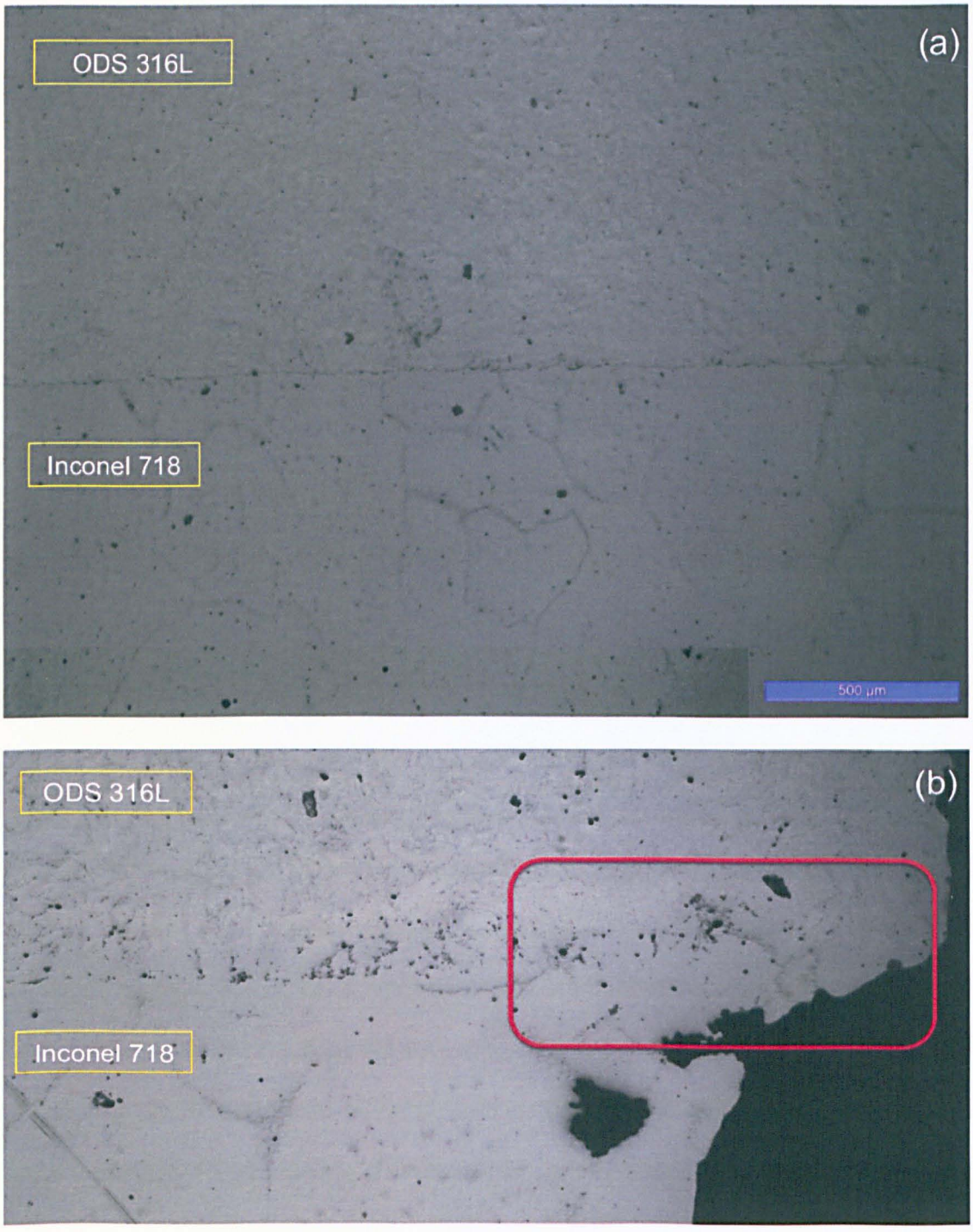

Figure 5.27 - Optical micrograph of a polished diffusion-bonded sample. In (a), the polishing procedure reveals the bond line and the clean microstructures surrounding it. In (b), the region near the surface (right edge) in which the bond line is pushed into the ODS 316L microstructure by the "skin" effect.

In an effort to characterise the microstructure of the as-diffusion-bonded materials, a study of elemental distribution close to the bond line was carried out by SEM/EDS. Quantitative EDS surveys were conducted on points along 10 µm from the bond line on

each of its sides, in steps of 2 μm. A schematic of the sample, of the extraction of slices and of the measurements is provided in Figure 5.28. Results for three different locations down the bond line (which is the zero of the scale) are shown in Figure 5.29. The elemental distribution suggests that nickel diffused more into the microstructure of the steel, than iron into the superalloy lattice. Given its interfacial nature, the bond line exhibited higher concentration of oxide forming elements, chiefly aluminium, titanium and oxygen, but, to lesser extent, some evidences of yttrium were found.

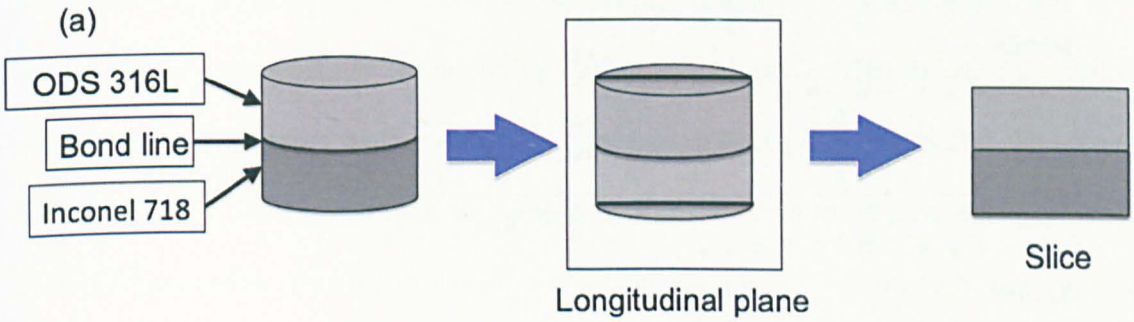

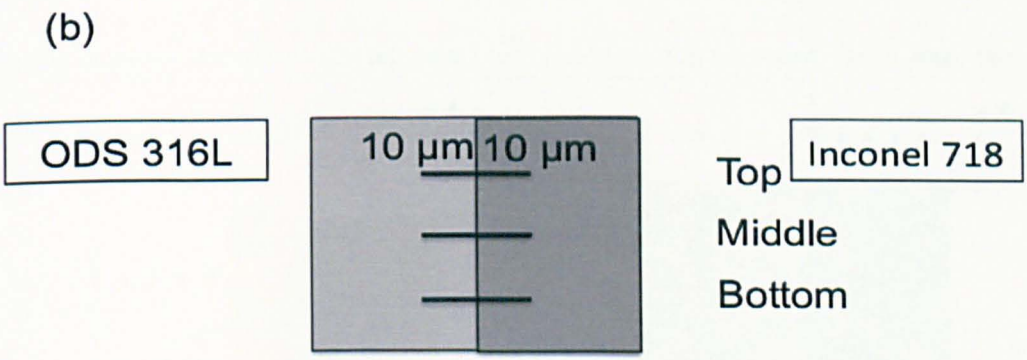

Figure 5.28 - Schematic of the bonded discs and the longitudinal cut for extracting the slices (a); and a sketch of the SEM line scans, along 10 μm on each side of the bond line, where the horizontal lines represent positions (top, middle and bottom) in which the bond line was scanned (b). Figure out of scale.

The results from the microstructural survey of the successful diffusion bonding of the discs, combined with the bond strength observed in the manual-bending tests, prompted this line of investigation to provide longer samples for diffusion bonding, aimed at the fabrication of the hybrid specimens. For this purpose, instead of discs, a sandwich sample

was devised, consisting of two Inconel 718 cylinders of 13 mm diameter and 35 mm length and a disc of ODS 316L with same diameter and 5 mm thickness.

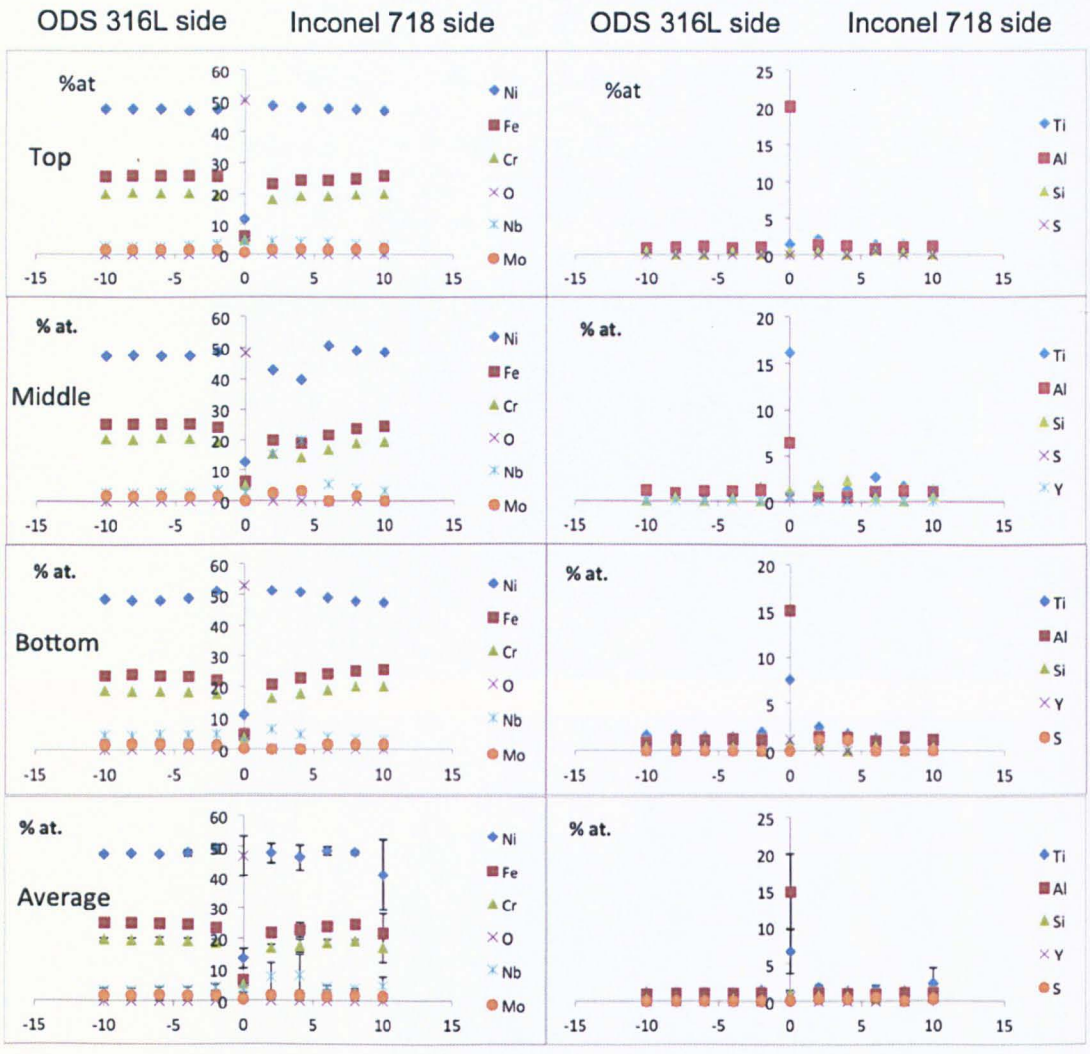

Figure 5.29 - Element distribution in atom percentage (%at.) from the bond line (zero) to 10 μm.

Given that the parts to be diffusion-bonded were cut from the batches by EDM, preparation for the joining process involved cleaning the surfaces that would be put in contact, in order to remove the layer left by the EDM cut, which is porous and contains lots of debris. This is done by applying grinding with wet emery paper. Another advantage of this procedure is the reduction of surface roughness, which improves the quality of the bond interface, in terms of cleanliness and mechanical properties, as reported by Sittel and co-workers for the Charpy impact properties of diffusion-bonded ODS steel PM2000 [21].

Also, given the length of the Inconel 718 cylinders, the lateral surfaces were ground with emery paper so that the dirty EDM cutting layer could be removed. Although these latter are not involved in the bonding, the high temperatures and high levels of vacuum cause the layer, if left onto these surfaces, to evaporate and accumulate in the turbopump of the machine, potentially causing damage [20].

Following the preparation, the parts to be diffusion-bonded were properly aligned and assembled onto the machine load train. Figure 5.30 illustrates the experimental setup. A thermocouple type K was spot welded to the sample. A coil with an appropriate size was wrapped around the specimen for providing the induction heating. The choice of the coil is crucial for the success of the bonding. An inadequate size of coil means that the spirals won't be equally distributed along the sample, so that non-uniform heating occurs. Again, the input parameters were set to 1200°C for a bonding time of 1 hour. Both heating and cooling rates were fixed at 200°C/min. Load was, similarly to the trials, left to vary freely. Since the material creeps at this elevated temperature with constant strain-rate, the load gradually decreases throughout the bonding time.

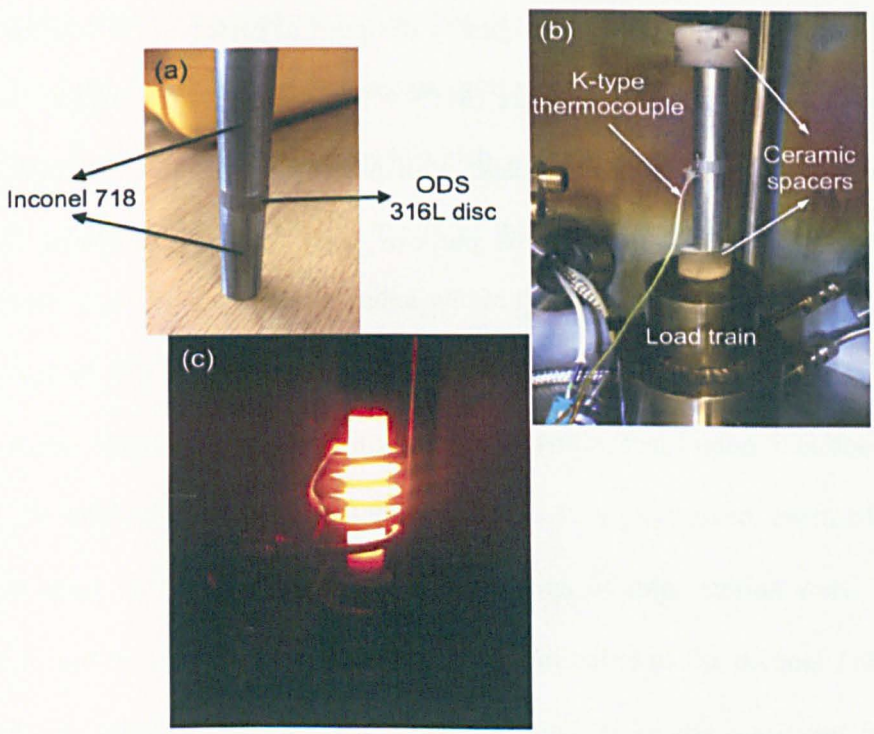

Figure 5.30 - Setup for diffusion bonding. The alignment between the cylinders and the disc is shown in (a); the vacuum chamber interior in (b) and the bonding in progress (c).

From this batch of diffusion-bonded sample, specimens for mechanical testing were machined, following the idea that the central part of their gauge lengths would correspond to the ODS 316L slice and the remaining parts, to the Inconel 718. Room temperature tensile specimens were designed following BS EN 10002-5 1992 Standard [23], modified for suiting the mini-tensile test rig available at the Open University. A creep specimen was also prepared from the same standard. Further details on the tests are provided in the following sections.

5.6.1 Room temperature tensile test of the hybrid specimen

Room temperature tensile specimens were designed following BS EN 10002-5 1992. The dimensions were scaled down in order to produce mini-tensile test specimens with 12 mm gauge length and a gauge section of 3 mm by 1 mm. Overall length totalled 44 mm. Details of the specimen design are presented in appendix I. In order to carry out the tests, an MTI/Fullam tester machine with maximum load capacity of 4.5 kN and fitted with two moveable crossheads driven by a worm gear system actuated by a direct current motor was used. Figure 5.31 illustrates the rig, originally designed to perform *in situ* tensile straining tests inside the SEM. Specific software (MTS – Material testing Software) was used to control the machine and record the data. A displacement rate of 0.096 mm min^{-1} was adopted for the tensile straining, whose purpose was to take the sample to rupture and evaluate the location where it occurred.

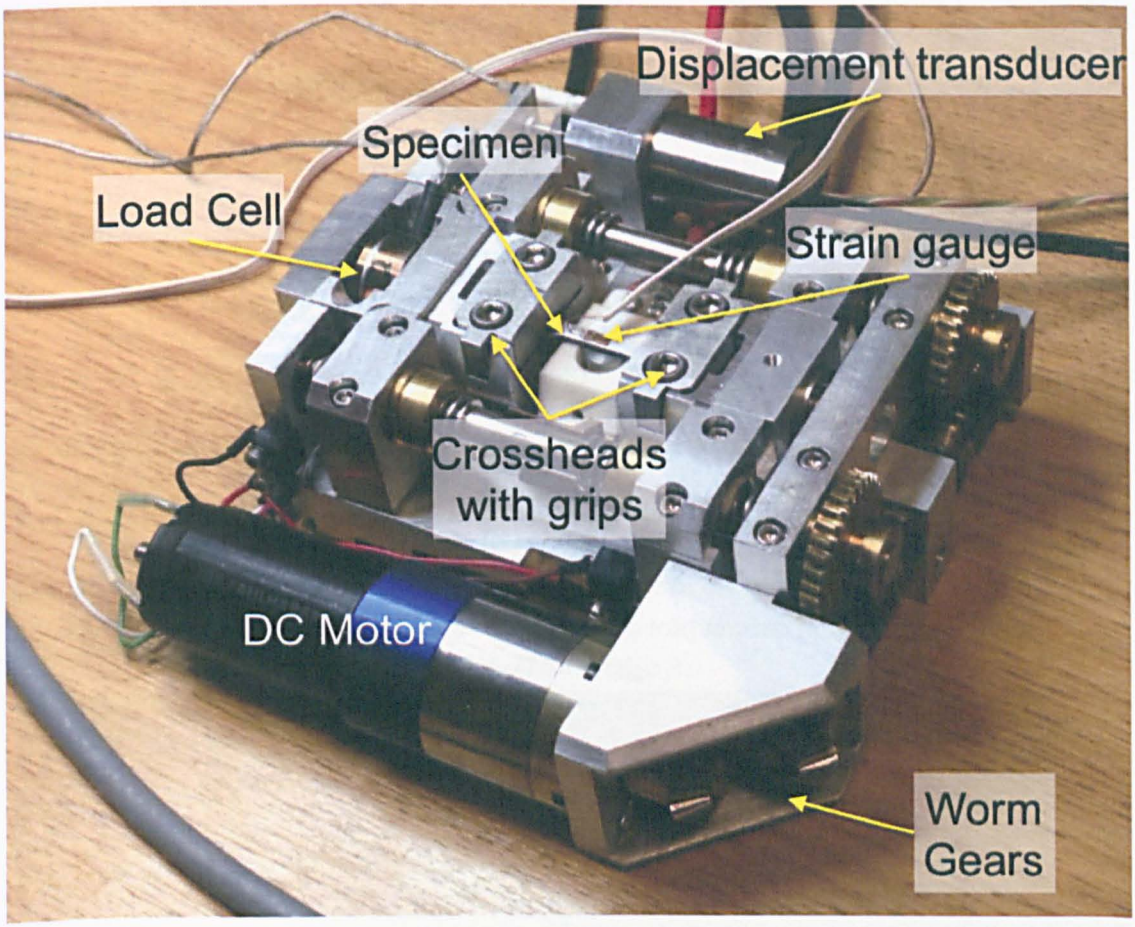

Figure 5.31 - MTI /Fullam mini-tensile test rig with hybrid specimen and strain gauge mounted.

Both samples tested presented very close results once again. Figure 5.32 depicts one of the curves obtained during the test (the second plot was practically overlapped). The stress was calculated from the readings of load, which were divided by the rectangular cross-sectional area of the sample. The aftermaths of the room temperature tensile tests were very surprising, since both specimens failed within the Inconel 718 part, under an ultimate tensile strength of 498 MPa and 503 MPa. The bond interface and the ODS 316L segment of the specimens remained intact. It is important to mention that Figure 5.32 does not show the plot of the whole dataset from the tensile tests. As they progressed, eventually reached an overflow stage in the software, in which readings of microstrains were beyond its capacity of recording. Although readings of the total ductility of the Inconel 718 could not be obtained, the primary goal of the test was fulfilled, since the important information concerned only at what location of the specimen failure would occur.

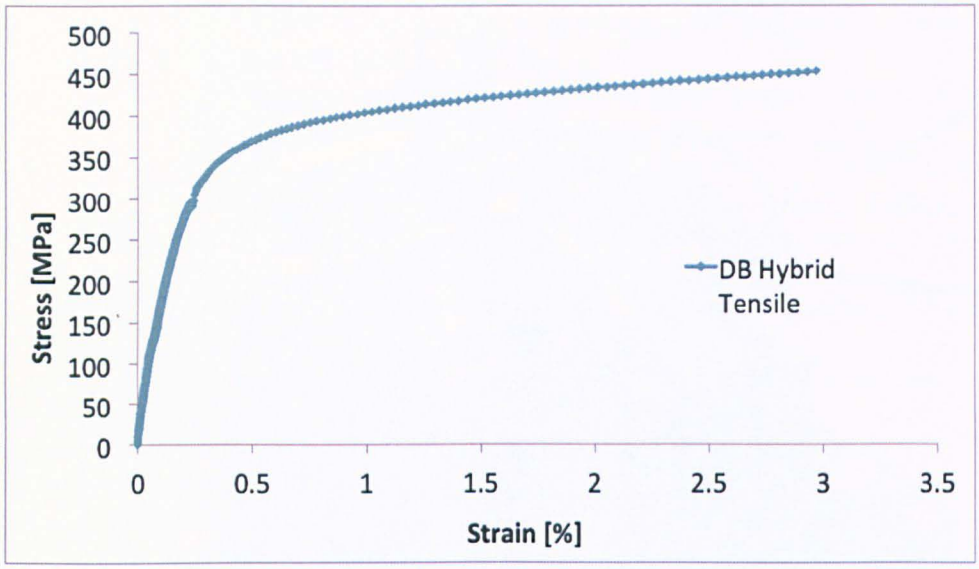

Figure 5.32 - Partial dataset plot of tensile curve of the hybrid diffusion-bonded specimen.

Some fractography was carried out in the tensile specimens, despite the fact that the cause of the failure was related to the Inconel 718 microstructure, which is not of primary concern in these studies. The SEM fractographic analysis, combined with EDS, confirmed the failure in the nickel alloy part, as shown in Figure 5.33.

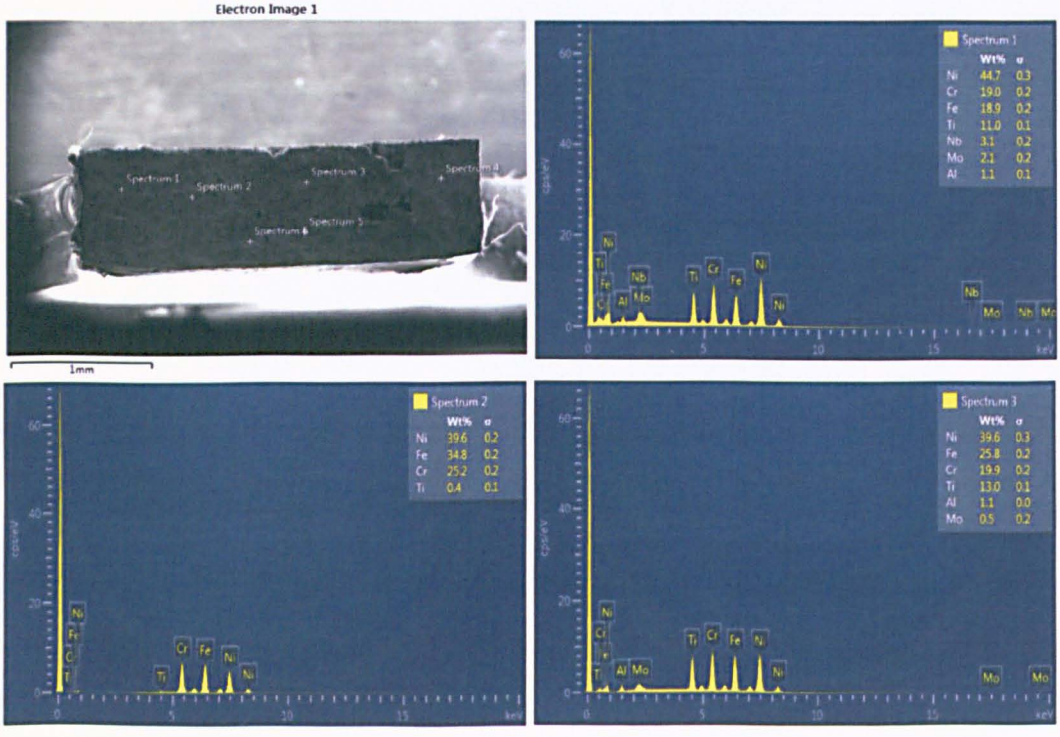

Figure 5.33 - Fracture surface of the room temperature hybrid tensile test specimen 1 and some of the EDS profiles taken, each identified by the correspondent spot number.

A short appraisal is done for the surface, which is consistent with the results obtained in the tensile test data. Even though the exact level of ductility could not be determined, it could be inferred, from a measurement on the juxtaposed fracture halves of the specimen and strain calculations involving the measured value (45.58 mm) and the initial total length of the sample (44.01 mm), that it amounted to approximately 3.6%. The fractographic studies are in agreement with this idea of limited ductility, which, although present, was not that much substantial, given the little dimpled aspect of the fracture surfaces. As Figure 5.34 suggests, a mixed mode of fracture might have taken place. The low density of dimples and the dull, porous aspect of the surface are evident from this micrograph.

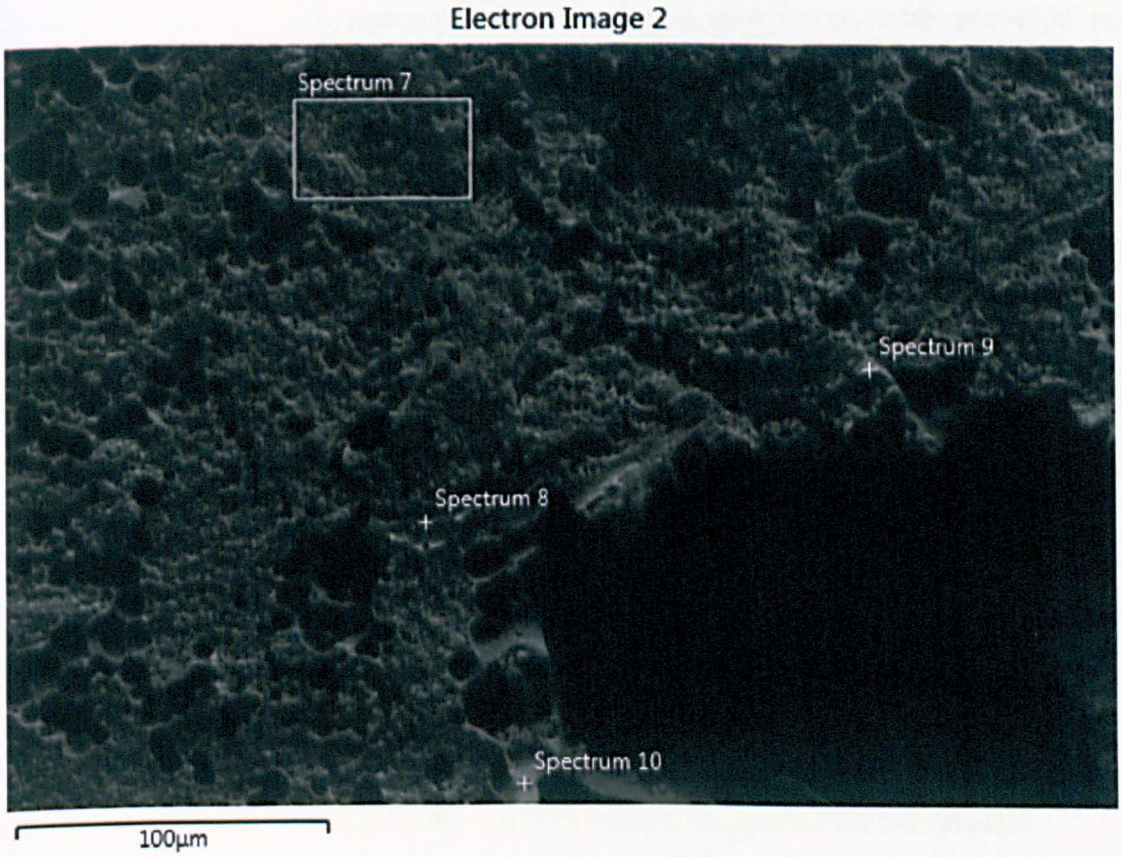

Figure 5.34 - Fracture surface of Inconel 718 from a failed tensile test specimen. There are dimples, but they are not extensively present onto the surface.

5.6.2 Creep-rupture test of the hybrid specimen

Simultaneously to the machining of the room temperature tensile test specimen, a hybrid creep-rupture test sample was also produced. Its dimensions were also scaled from the BS EN 10002-5 1992 Standard; however, it had to be adapted to fit more adequately a special creep test rig. The specimen was also machined with 12 mm gauge length and overall length of 44 mm, but bearing 1.5 mm by 1.5 mm gauge cross-section. Details can be seen in the drawing provided in the appendix I of this thesis.

Creep-rupture testing was carried out by Dr. Hon Tong Pang, in the Department of Materials Science and Metallurgy, University of Cambridge, using appropriate apparatus for high-temperature creep tests in miniaturized specimens, shown in Figure 5.35. A thermocouple was spot-welded to the ODS 316L part of the gauge length.

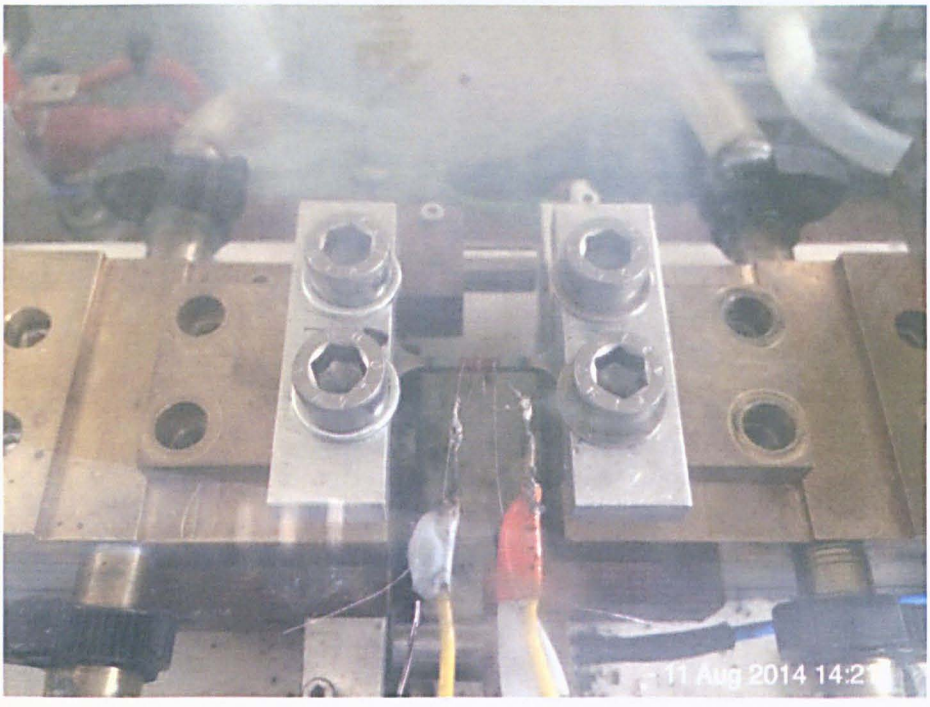

Figure 5.35 - Experimental setup for the creep test of the hybrid specimen.

The test conditions of one of the creep-rupture tests conducted on regular mini-creep specimen, fully machined from ODS 316L, were replicated for the test of the hybrid sample. It was crept under 200 MPa at 650°C, with this temperature level maintained at ±1°C. Another remarkable result was achieved, in terms of bond quality assessment, since

the failure occurred within the ODS 316L segment in the gauge length, but far away from the bond lines, as depicted by Figure 5.36:

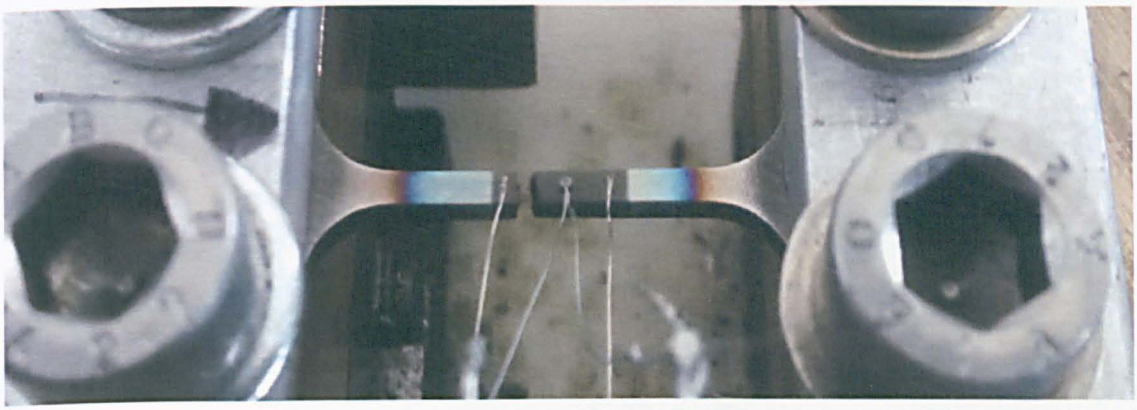

Figure 5.36 - Hybrid creep-rupture specimen. Failure occurred well inside the ODS 316L steel segment.

Despite the good result in terms of the quality of the bond interfaces, the creep performance, once again, presented undesirable features. The material exhibited a pronounced tertiary creep stage, as seen from the creep curve shown in Figure 5.37, but rupture occurred after just over 72 hours. It can also be observed that the loss of strength was accompanied by a remarkable increase in ductility, reaching almost 11% total strain. This represents roughly three times the ductility of the conventional ODS 316L samples.

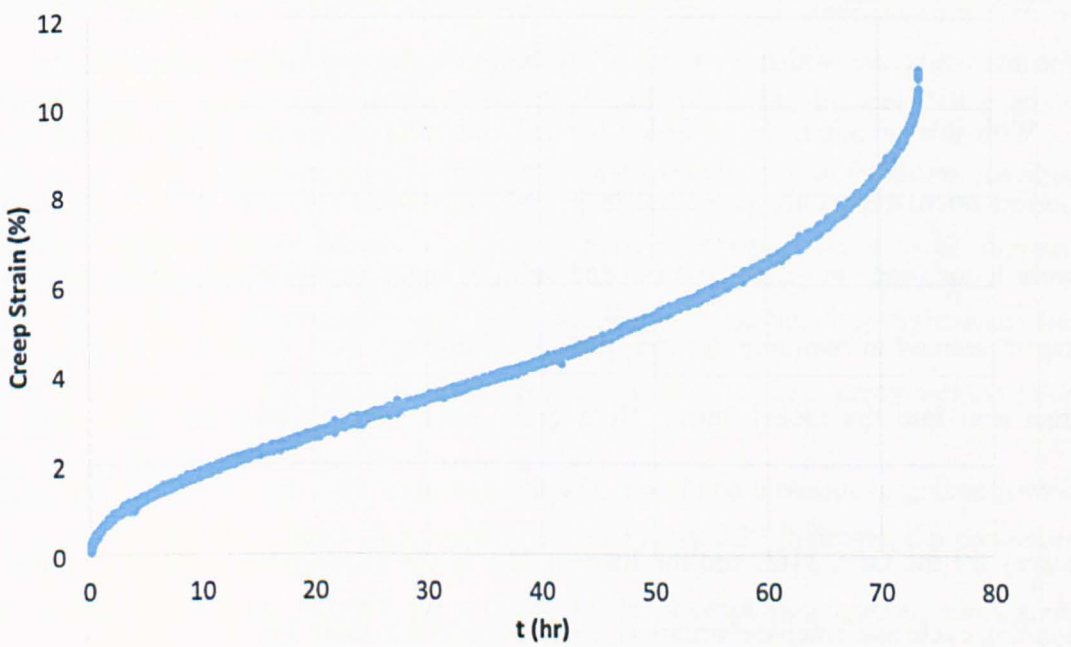

Figure 5.37 - Creep-rupture test curve for the hybrid specimen.

The trade-off between ductility and creep strength gave support to the idea that the observed behaviour was connected to changes in the microstructure of both materials after diffusion bonding. It is reasonable to speculate that the microstructural changes were a consequence of the bonding process, since the creep test temperature level is much lower and, perhaps, insufficient to cause major changes in the grain sizes and aspects. In order to ascertain these statements, optical microscopy (OM) was once more deployed for determining the grain sizes of both materials and establishing a comparison with the as-received condition. Moreover, a preliminary Vickers microhardness survey checked and compared the ODS 316L portion of the hybrid specimen gauge length with the gauge length of the ODS 316L miniaturized creep specimen tested in the same condition. Examination consisted in 21 indentations for each specimen, whose averages yielded 228 ± 5 HV for the full ODS 316L specimen and 196 ± 7 for the ODS 316L part of the hybrid specimen.

As attested by the microhardness, the observed difference in creep properties between the specimens, according to which the fully machined ODS 316L sample lasted 239 hours while the hybrid specimen only resisted 73 hours under the same conditions, is a consequence of different mechanical properties. Ultimately, this difference is associated to the microstructure, which is a result of the thermomechanical history of the material.

With this in mind, the diffusion-bonded and crept specimens were examined under optical microscopy once more and their grain sizes were measured. The bond interfaces were found, once more, to be clean and solid, without any apparent pores or defects. Its aspect seemed to reinforce the idea that nickel diffuses more easily into the steel matrix than iron into the nickel lattice. Both grain sizes were significantly larger than their corresponding as-received condition. The average grain sizes from five different areas of survey for the ODS 316L and the Inconel 718, in the as-received condition and after the bonding cycle and creep deformation, are summarized in table 5.6.

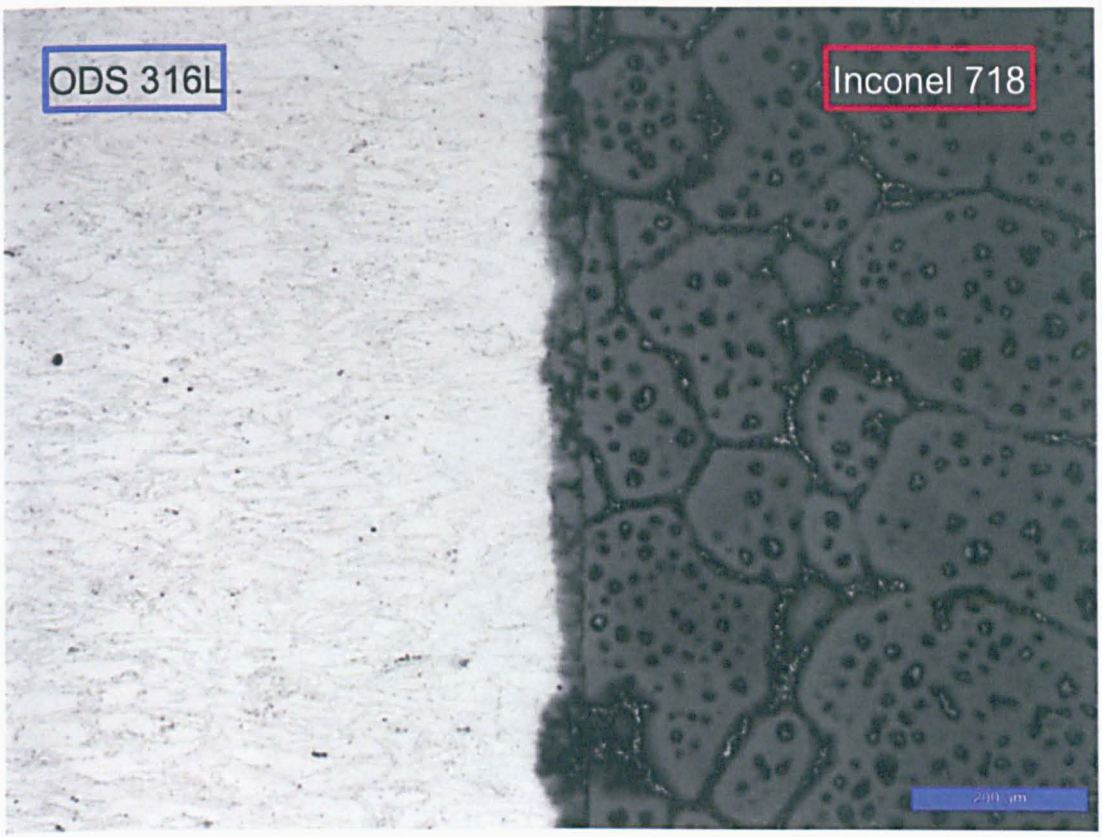

Figure 5.38 - Optical micrograph of the bond line of the failed crept specimen.

Table 5.6 – Average grain size summary for both materials.

Material	Grain size before DB (μm)	Grain size after DB & creep (μm)
ODS 316L	25.4 ± 3.3	29.2 ± 3.3
Inconel 718	106.3 ± 11.8	422.3 ± 13.1

The ODS 316L grains experienced a slight growth, while the Inconel 718 crystals achieved a four times increase with the high temperature bonding cycle exposure. Another interesting feature is found in the Inconel 718 part, with what seems to be δ-phase precipitates inside the grains and along grain boundaries. The bonding cycle takes the material to a level above the *solvus* temperature, so that, upon cooling, precipitation of this orthorhombic Ni_3Nb phase is expected to occur [24].

Finally, a fractographic study was carried out. As Figure 5.39 indicates, the premature failure is thought to have occurred via a mixed mode of crack propagation: some areas presented considerable ductility, while others failed in a brittle manner. The presence of

whole grain contours and absence of torn grain surfaces is an indication of intergranular crack propagation. This is a reasonable result for a material that exhibited almost 11% of creep ductility.

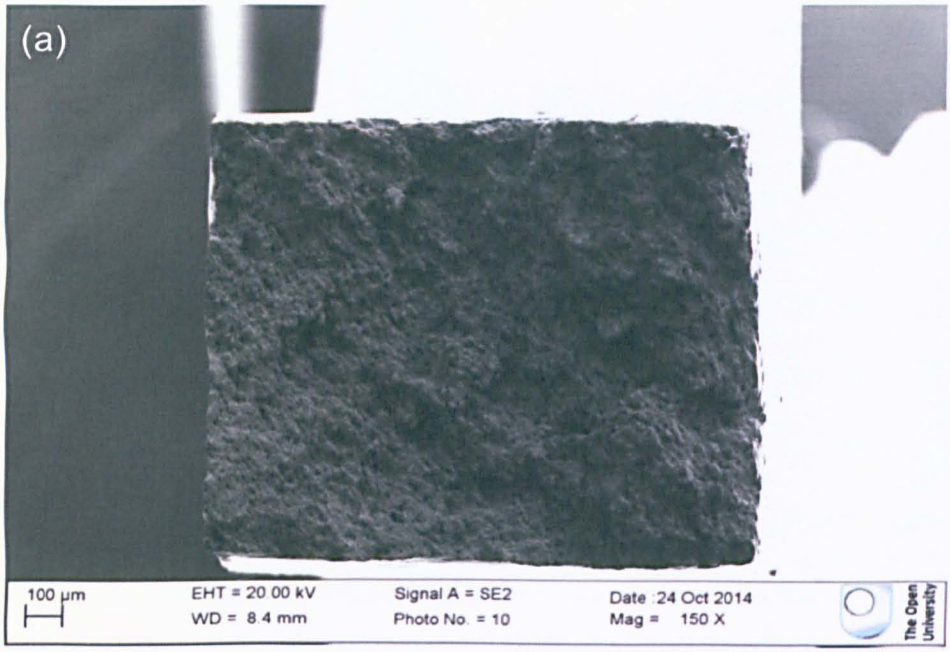

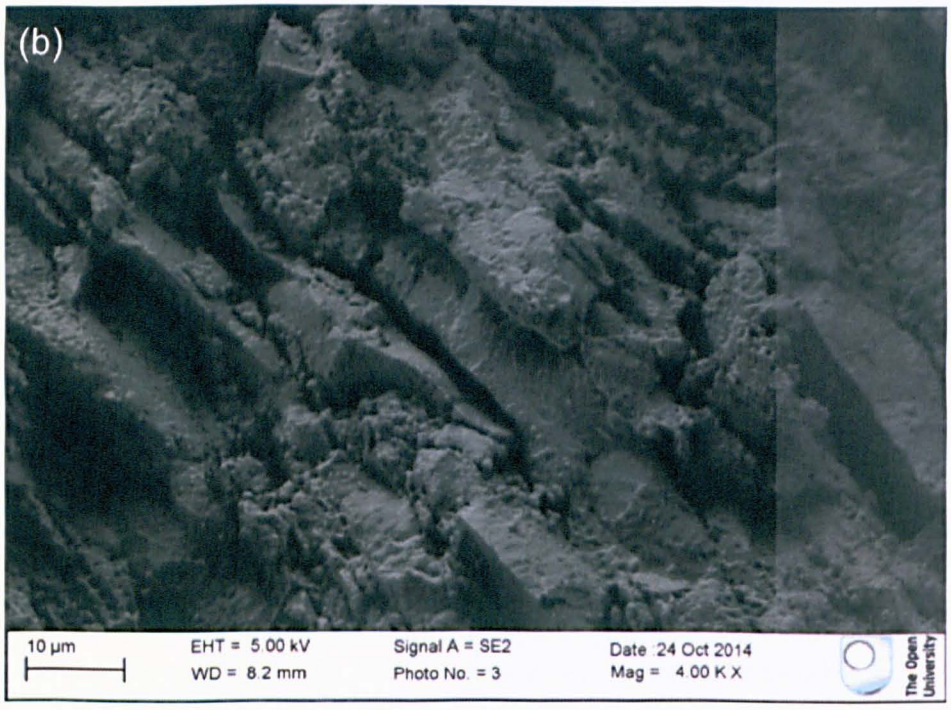

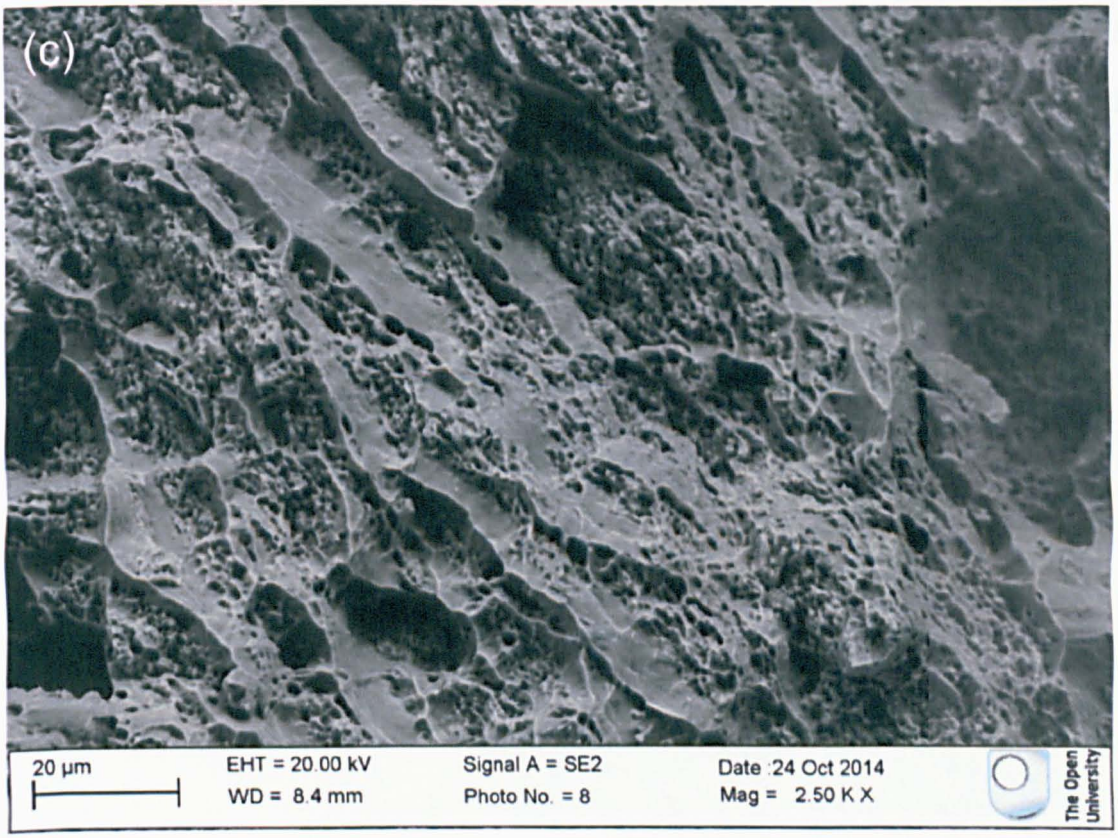

Figure 5.39 - SEM fractography of the crept hybrid specimen (failed in the ODS 316L portion). Image (a) is the low magnification general aspect, showing cracks on a topographic surface. In (b), the cleavage, smooth surface with some cracks is evidence of a brittle way of fracture in this portion of the sample. And (c) shows dimpled surface surrounding some preserved grains, indicating a more ductile portion of material failing intergranularly.

All these investigations pointed to the necessity of a post-diffusion bonding thermomechanical treatment (TMT), aimed at retrieving the initial microstructure of the ODS 316L, or even improving it. This corresponded to the final experimental approach of this pilot study and is described next.

5.6.3 Complementary TMT for diffusion bonding of ODS 316L steel

A plan was devised to promote refinement of the microstructure and achieve a condition of homogenized grains, particularly for the ODS 316L, which is the material of interest. The plan consisted of introducing some deformation to the microstructure, in order to create discontinuity sites where nucleation of new grains could take place, during the

subsequent heat treatment step. This latter was carried out by heating up the diffusion-bonded materials to the estimated recrystallization temperature of the ODS 316L, keeping them at this level for a determined time and cooling them outside the furnace (air-cooled), in order to increase the cooling rate and prevent significant diffusion, thus avoiding grain growth.

Slices of approximately 0.75 mm thickness were cut from the diffusion-bonded discs (the first bonded sample) and subject to a TMT comprised of cold rolling as the work-hardening stage and an annealing treatment carried out at 1150°C for 0.5 hour, followed by air-cooling. The parameters for the heat treatment were chosen based on the high temperatures associated with the recrystallization of ODS steels, as reported in Chapter 2, and on the values used by Wang et al. [1] on an ODS 310 austenitic steel. Table 5.7 lists the deformation levels imposed on each slice cold-rolled. These percentages were based on the works of Abou Zahra and Schroeder [25], and Engelberg et al. [26], in an attempt to achieve the lowest imposed deformation possible that was still higher than the critical level for recrystallization.

Table 5.7 – Conditions for cold rolling of slices cut from the diffusion-bonded ODS 316L/Inconel 718 discs.

Slice	Intended deformation %	Initial thickness [mm]	Intended final thickness [mm]	Measured final thickness [mm]	Imposed deformation %
Slice 1	5	0.664	0.631	0.628	5.4
Slice 2	13	0.786	0.684	0.678	13.7
Slice 3	25	0.782	0.587	0.582	25.6

Before the cold rolling was applied, the initial thickness of the slice was measured with an electronic micrometer 0–25 mm measuring range and ±0.001 mm of precision. Table 5.7 lists the resulting average of three measurements from each slice. Slices 1 and 3 presented a strongly uniform thickness along its extensions, but slice 2 showed significant non-uniformity, showing some variations in its thickness. For the rolling procedure, given

the small dimensions of the slices, a manual cold rolling device was used. In order to achieve the intended levels of deformation, the opening between the cylinders was adjusted based on the final intended thickness. Figure 5.40 illustrates the device in operation.

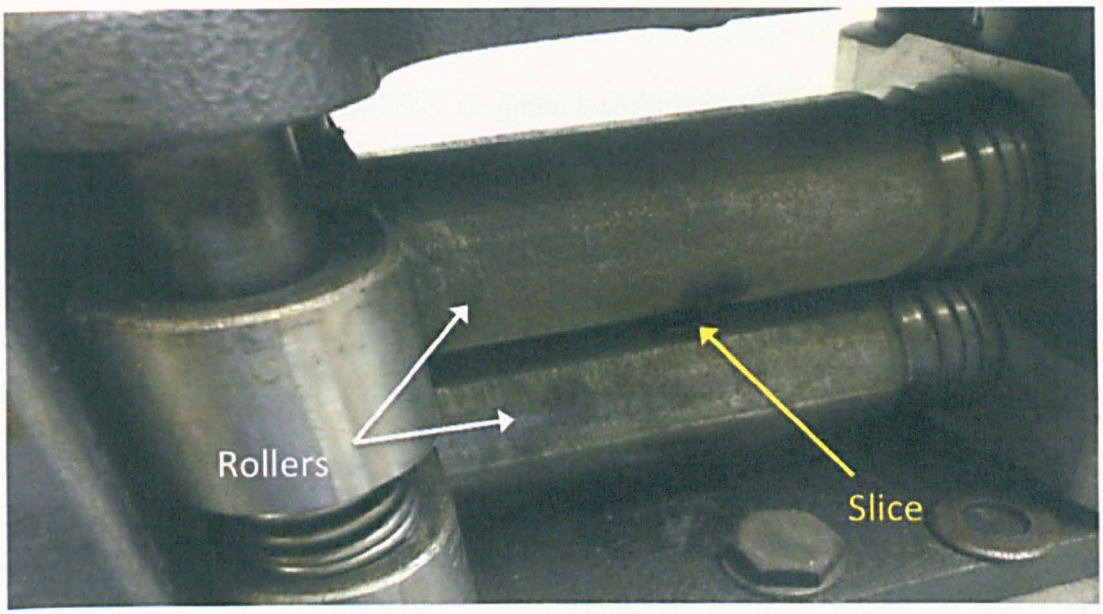

Figure 5.40 – Cold rolling device manually operated and a slice being deformed.

The obtained thicknesses after rolling are listed in table 5.7. The normalization heat treatment was the subsequent step. This annealing was carried out in a vacuum furnace and an N-type thermocouple ensured the temperature at 1150°C. The slices were, then, removed from the furnace and left to cool in ambient air. Each slice, including the as-diffusion-bonded, which was used as control for comparisons, was ground, polished and etched (as described in Chapter 3) for investigations on the optical microscope Leica DMI 5000. Grain size measurement was carried out on five different areas of each material in each slice. Table 5.8 summarizes the results.

Table 5.8 – Grain size measurement for each slice.

Material / Slice	As diffusion-bonded	Slice 1 (5%)	Slice 2 (13%)	Slice 3 (25%)
ODS 316L	29.2 ± 5.0	26.2 ± 4.7	27.1 ± 7.4	19.8 ± 2.1
Inconel 718	422.3 ± 13.1	452.7 ± 41.5	439.8 ± 17.3	609.1 ± 68.7

As observed, the values were consistent with what was expected. Slices 1 and 2 failed to produce a refined ODS 316L microstructure. A deformation of 5% did not trigger enough recrystallization so as to cause significant change in the grain size of the ODS 316L. In the case of the second condition, it was observed that the correspondent slice (Slice 2) did not present uniform thickness along its extension, so, deformation may also not have occurred uniformly. Signs of deformation were more evident than those of slice 1, but the microstructure presented variations, depending on the area surveyed: some were predominantly recrystallized, others were predominantly populated with coarse grains, as shown in Figure 5.41. All micrographs shown were taken under the same magnification. In both cases, the grain size measured was very close to the as diffusion-bonded condition and within the range of uncertainty.

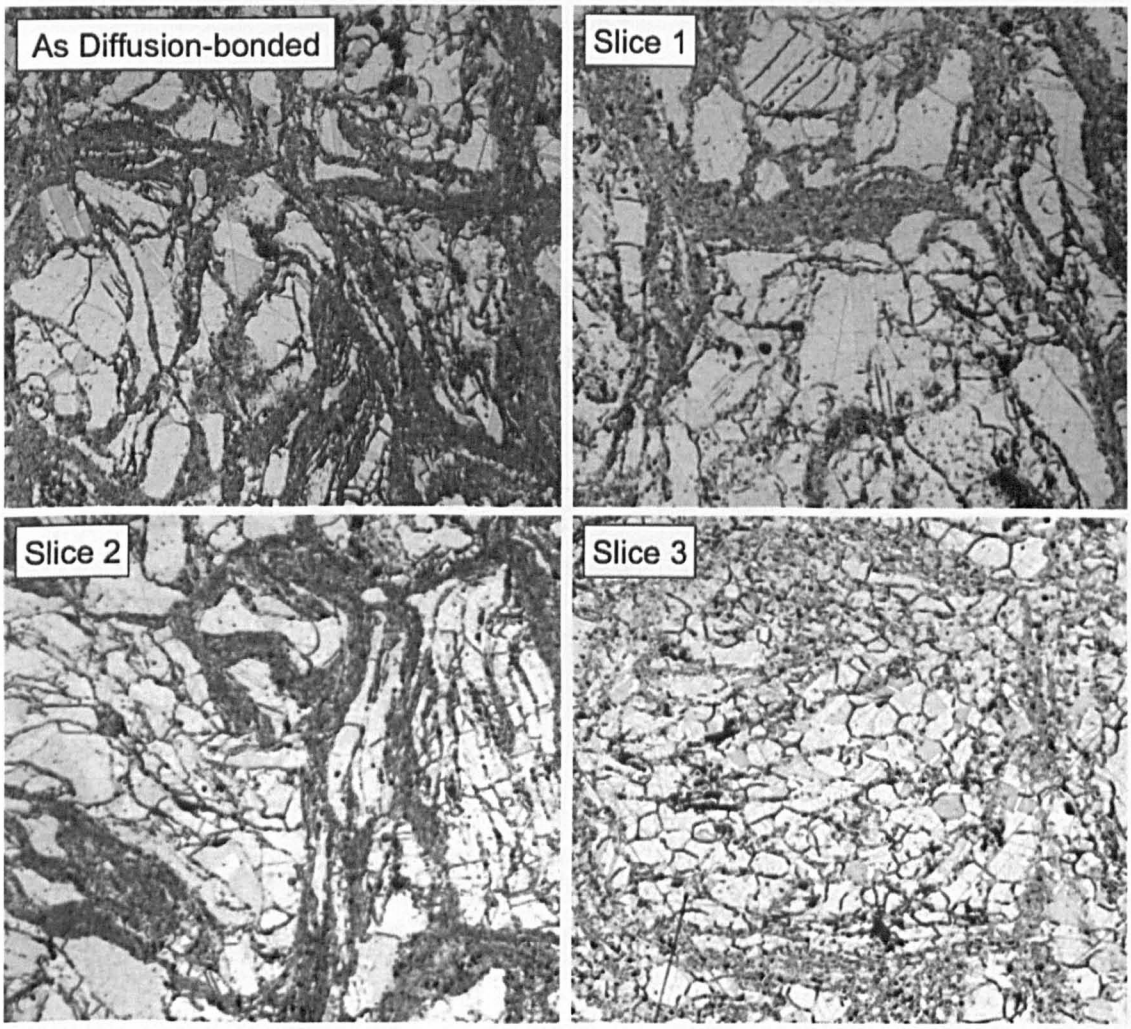

Figure 5.41 – Optical micrograph of the ODS 316L with various plastic strain levels, as shown in Table 5.8.

Slice 3 presented a very satisfactory result, being capable of refining the microstructure almost completely. Recrystallized grains were homogeneously distributed all across the ODS 316L structure. This indicates that 25% cold deformation in the TMT might be a very effective way to restore the properties of the material that might have been lost with the high-temperature exposures. From the various conditions, this level of deformation is above the critical plastic strain for recrystallization and was considered successful for the intended purpose of refining the microstructure.

Although not being the main concern in this study, the changes in the Inconel 718 are worth an appraisal. In most of the cases, its grains experienced just a slight growth. This can probably be attributed to a less pronounced work-hardening of the nickel superalloy when cold-rolled, due to its superior strength, which may have induced fewer defects and, thus, provided fewer sites for recrystallization. As a consequence, only a slight grain growth was observed. The exception was slice 3, in which larger grains were observed. As no clear reason could be discerned for such change, it is likely that the observed grain size was already present in the Inconel 718 batch, as a natural variation of the material, before any treatment was done. A more detailed study on the Inconel, involving optical microscopy and EBSD could provide further insight on the matter.

5.6.4 Effects of the thermal cycles on the oxide particles

Although the TMT previously described showed that a certain combination of parameters was effective in refining the microstructure, it must be borne in mind that the material of interest is an ODS steel. Equally important to the grain refinement are the possible effects that the exposure to these high-temperature events might have caused on the nanometric particles. As explained in Chapter 2, these oxides are known for being insoluble at high temperatures, even close to the melting point of the steel [27], and very stable. However, the temperatures envisaged for the diffusion bonding process and the recrystallization heat treatment are high enough to cause high diffusion rates. In these

conditions, it is necessary to evaluate whether changes may also have occurred for the particle size distribution. In observation of these considerations, TEM studies, aimed at obtaining the particle size distribution, were carried out for the as diffusion-bonded slice and for slice 3, in order to check for possible differences in comparison to the oxide size distribution of the as-received ODS 316L (Fig. 5.5).

TEM foils were extracted from the as diffusion-bonded slice and slice 3, and prepared for observation as described in Chapter 3. A total of 278 particles were measured for the TMT ODS 316L (counted in three foils from slice 3, from 15 images), while 301 particles were checked in the as diffusion-bonded material, in 19 different micrographs taken from three foils also. Figures 5.42 and 5.43 depict the size distribution.

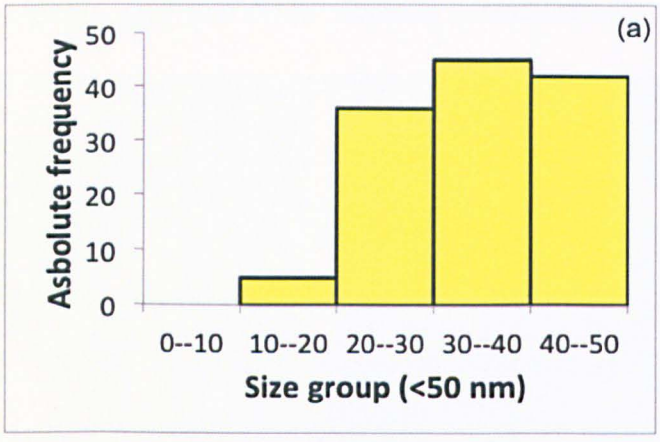

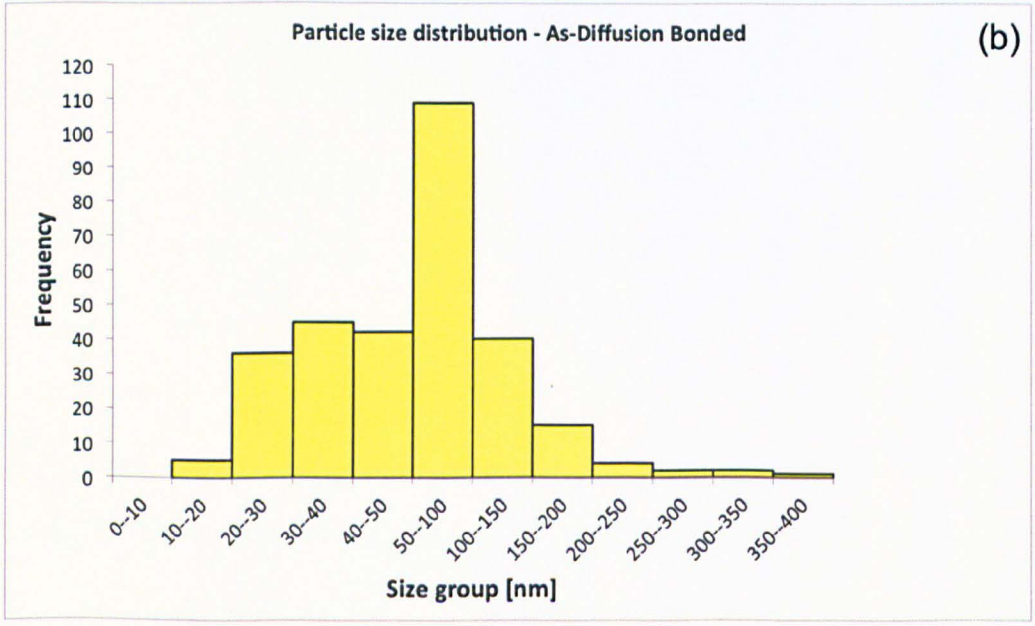

Figure 5.42 - Particle size distribution for the as diffusion-bonded ODS 316L. Image (a) depicts the oxides and (b) general particles (oxides, nitrides, carbides).

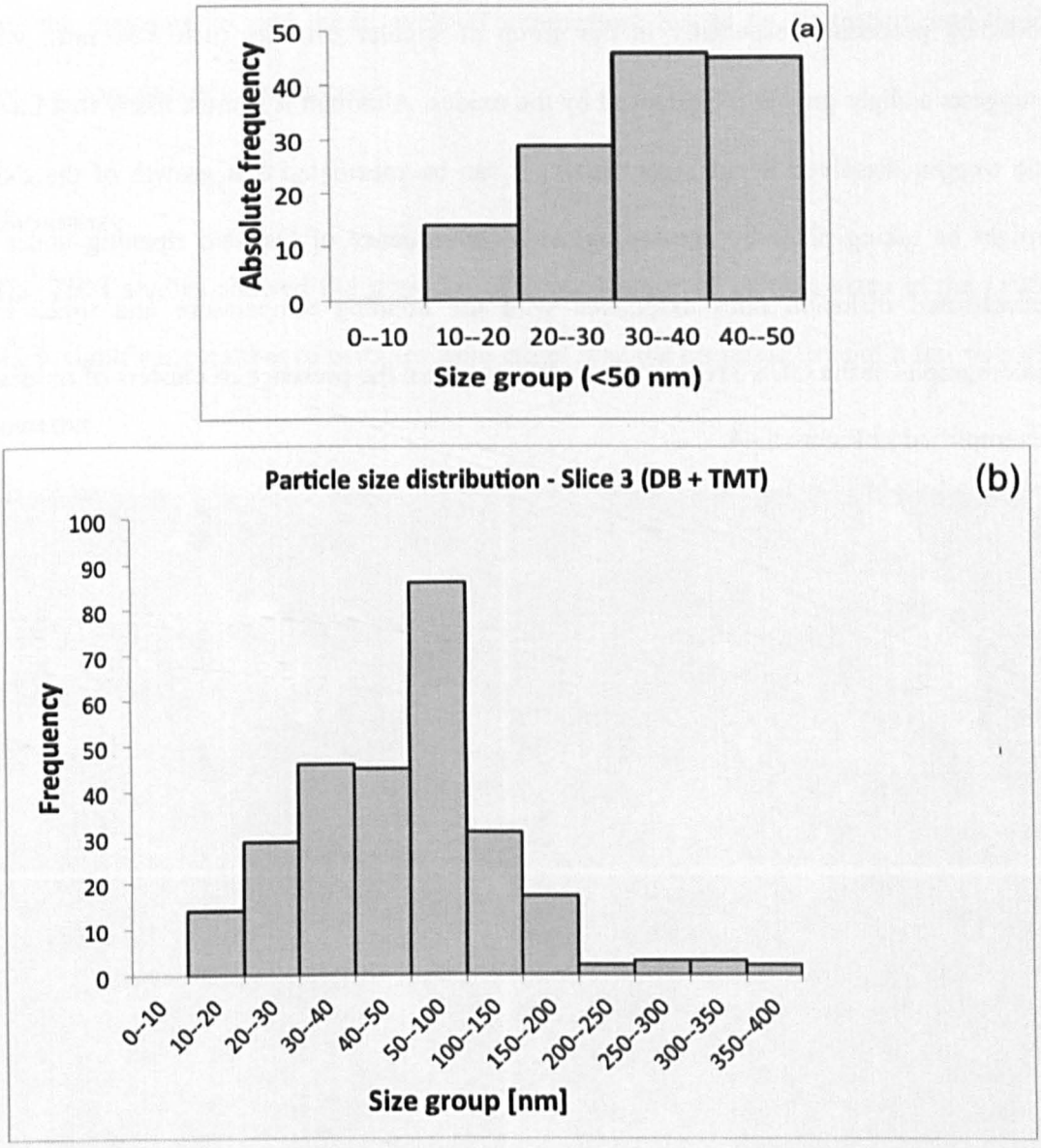

Figure 5.43 - Particle size distribution for the TMT treated ODS 316L. Image (a) depicts the oxides < 50 nm, while (b) general particles (oxides, nitrides, etc.).

Once again, area measurements were taken in the ImageJ environment, from which the diameter was calculated, as shown in the Appendix 7. The separation in size groups was done so that Figures 5.42 and 5.43 could be compared to one another, but also, compared to Figure 5.5. It is easy to see that no significant statistical difference was found between the as diffusion-bonded sample and the TMT treated one. However, differences in the size groups become evident when Figure 5.42 is checked against Figure 5.5. There seems to have been a shift in frequency towards larger particles after the material was subject to the

bonding procedure, especially in the group of smaller particles (size <50 nm), which suggests a slight growth experienced by the oxides. Although it is most likely that there is no oxygen dissolved in the steel matrix, it can be speculated that growth of the oxides might be taking place by coarsening, as a consequence of Ostwald ripening under the accelerated diffusion rates associated with the bonding temperature and time. TEM micrographs of the ODS 316L in all conditions reveal the presence of clusters of oxides, as exemplified in Figure 5.44.

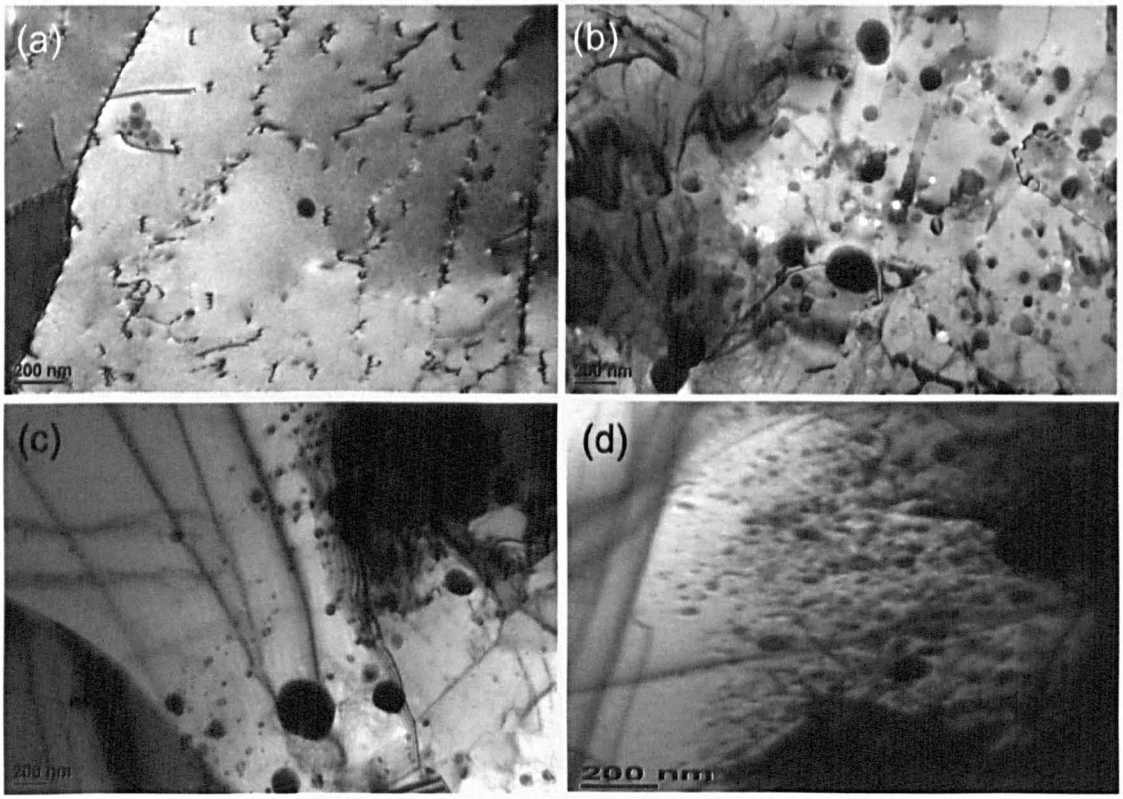

Figure 5.44 - TEM micrographs from both conditions – (a) and (c) as diffusion-bonded, and (b) and (d) TMT treated, showing possible signs of coalescence. In (a), oxides are clustered close to a pinned dislocation. (c) shows an area populated by large oxides (either present in the as-received steel or resulting from a coarsening after the bonding cycle; and (d) shows an area where several small oxides seem to be clustering for forming larger particles.

So, even though the TMT was successful in its goals, this study shows that the oxides need to be taken into consideration, as the exposure to a very high temperature for a significant period of time may cause changes to their size distribution. In this case, it does not seem to be significant, but if the intended particle size must be limited to a certain

range, the exposure to such high levels of temperature has to be controlled, and their influence, continuously investigated.

5.7 Summary

The TEM studies showed the presence of a wide range of particle sizes in the ODS 316L. A significant number of particles were larger than the desirable limit of a few tens of nanometres.

Oxide particles in the ODS 316L steel were found to be $Y_2Ti_2O_7$. HRTEM studies were carried out and determined orientation relationships of the oxides with the matrix, as well as their coherency condition.

Results from room and high temperature tensile tests of the ODS 316L are presented and compared with those of conventional 316L steel. ODS 316L presented higher yield stress and ultimate tensile strength at room temperature; higher YS and lower UTS at high temperature, and lower ductility than the conventional 316L.

Creep-rupture tests were conducted at 650°C under three different stress levels, 140 MPa, 175 MPa and 200 MPa. Creep lives complied with the minima demanded by the RCC MR code for the stresses analysed, but were outlived by the conventional 316L.

Creep ductility was found to be very low, with all tests of the as-received material failing with a total strain lower than 4%.

Hybrid specimens for creep and tensile tests were produced by bonding the ODS 316L with Inconel 718 superalloy.

Room temperature hybrid tensile specimen failed in the Inconel 718 material. Creep-rupture hybrid specimen failed in the ODS 316L. In both cases, the bond line was intact.

The diffusion bonding cycle raised the creep ductility of the ODS 316L to 11%, while decreased the life from 239 hours to 73 hours under 200 MPa.

A thermo-mechanical treatment was carried out to refine the microstructure after diffusion bonding, aiming at regaining (or improving) the creep strength of the ODS 316L.

Oxide particles have coarsened in the austenitic matrix as a result of the exposition to high temperatures, thus raising the particle size.

5.8 References

[1] M. Wang, Z. Zhou, H. Sun, H. Hu, and S. Li, "Effects of plastic deformations on microstructure and mechanical properties of ODS-310 austenitic steel," *J. Nucl. Mater.*, vol. 430, no. 1–3, pp. 259–263, Nov. 2012.

[2] P. Hazzledine, "Dislocation Multipoles," *J. Phys. Colloq.*, vol. 27, no. C3, pp. 210–218, 1966.

[3] M. Klimiankou, R. Lindau, and A. Möslang, "HRTEM Study of yttrium oxide particles in ODS steels for fusion reactor application," *J. Cryst. Growth*, vol. 249, no. 1–2, pp. 381–387, Feb. 2003.

[4] M. Klimiankou, R. Lindau, and A. Möslang, "TEM characterization of structure and composition of nanosized ODS particles in reduced activation ferritic–martensitic steels," *J. Nucl. Mater.*, vol. 329–333, pp. 347–351, Aug. 2004.

[5] R. Lindau, A. Möslang, M. Schirra, P. Schlossmacher, and M. Klimenkov, "Mechanical and microstructural properties of a hipped RAFM ODS-steel," *J. Nucl. Mater.*, vol. 307–311, P, no. 0, pp. 769–772, 2002.

[6] X. Mao, K. H. Oh, S. H. Kang, T. K. Kim, and J. Jang, "On the coherency of Y2Ti2O7 particles with austenitic matrix of oxide dispersed strengthened steel," *Acta Mater.*, vol. 89, pp. 141–152, 2015.

[7] Y. Jiang, J. R. Smith, and G. R. Odette, "Prediction of structural, electronic and elastic properties of Y2Ti2O7 and Y2TiO5," *Acta Mater.*, vol. 58, no. 5, pp. 1536–1543, 2010.

[8] S. C. Chae, Y. J. Chang, S. S. A. Seo, T. W. Noh, D.-W. Kim, and C. U. Jung, "Epitaxial growth and the magnetic properties of orthorhombic YTiO3 thin films," *Appl. Phys. Lett.*, vol. 89, 2006.

[9] E. Arzt, "Creep of Oxide-dispersion Strengthened Alloys," *Encyclopedia of Materials: Science and Technology*. Elsevier, pp. 1800–1806, 2001.

[10] D. W. Kim, "Influence of nitrogen-induced grain refinement on mechanical properties of nitrogen alloyed type 316LN stainless steel," *J. Nucl. Mater.*, vol. 420, no. 1–3, pp. 473–478, 2012.

[11] American Iron and Steel Institute, *High-Temperature Characteristics Of Stainless Steels*, A Designer. Nickel Development Institute.

[12] M. D. Mathew, K. Laha, and V. Ganesan, "Improving creep strength of 316L stainless steel by alloying with nitrogen," *Mater. Sci. Eng. A*, vol. 535, pp. 76–83, 2012.

[13] R. L. Klueh, P. J. Maziasz, I. S. Kim, L. Heatherly, D. T. Hoelzer, N. Hashimoto, E. A. Kenik, and K. Miyahara, "Tensile and Creep Properties of an Oxide Dispersion-Strengthened Ferritic Steel," *J. Nucl. Mater.*, vol. 307–311, pp. 773–777, 2002.

[14] A. Steckmeyer, V. H. Rodrigo, J. M. Gentzbittel, V. Rabeau, and B. Fournier, "Tensile anisotropy and creep properties of a Fe–14CrWTi ODS ferritic steel," *J. Nucl. Mater.*, vol. 426, no. 1–3, pp. 182–188, 2012.

[15] J. Malaplate, F. Mompiou, J. L. Béchade, T. Van Den Berghe, and M. Ratti, "Creep behavior of ODS materials: A study of dislocations/precipitates interactions," *J. Nucl. Mater.*, vol. 417, no. 1–3, pp. 205–208, 2011.

[16] A. Alamo, V. Lambard, X. Averty, and M. H. Mathon, "Assessment of ODS-14%Cr ferritic alloy for high temperature applications," *J. Nucl. Mater.*, vol. 329–333, pp. 333–337, 2004.

[17] R. W. Evans, J. A. Preston, B. Wilshire, and E. A. Little, "Creep and creep fracture of an oxide-dispersion-strengthened 13% chromium ferritic steel," *Mater. Sci. Eng. A*, vol. A167, pp. 65–72, 1993.

[18] H. Sakasegawa, S. Ukai, M. Tamura, S. Ohtsuka, H. Tanigawa, H. Ogiwara, A. Kohyama, and M. Fujiwara, "Creep constitutive equation of dual phase 9Cr-ODS steel," *J. Nucl. Mater.*, vol. 373, no. 1–3, pp. 82–89, 2008.

[19] C. Zakine, C. Prioul, and D. François, "Creep behaviour of ODS steels," *Mater. Sci. Eng. A*, vol. 219, no. 1–2, pp. 102–108, 1996.

[20] S. Noh, B. Kim, R. Kasada, and A. Kimura, "Diffusion bonding between ODS ferritic steel and F82H steel for fusion applications," *J. Nucl. Mater.*, vol. 426, no. 1–3, pp. 208–213, 2012.

[21] W. Sittel, W. W. Basuki, and J. Aktaa, "Diffusion bonding of the oxide dispersion strengthened steel PM2000," *J. Nucl. Mater.*, vol. 443, no. 1–3, pp. 78–83, 2013.

[22] S. Metals, "High performance alloys." [Online]. Available: http://www.specialmetals.com/assets/documents/alloys/inconel/inconel-alloy-718.pdf. [Accessed: 06-Feb-2014].

[23] "BS EN 10002-5 1992 Standard." 1992.

[24] S. Azadian, L.-Y. Wei, and R. Warren, "Delta phase precipitation in Inconel 718," *Mater. Charact.*, vol. 53, no. 1, pp. 7–16, 2004.

[25] A. A. Abou Zahra and H. Schroeder, "The dependence of the creep properties of din 1.4970 austenitic stainless steel at 973 K on different thermomechanical pre-treatments," *J. Nucl. Mater.*, vol. 107, no. 1, pp. 97–103, May 1982.

[26] D. L. Engelberg, R. C. Newman, and T. J. Marrow, "Effect of thermomechanical process history on grain boundary control in an austenitic stainless steel," *Scr. Mater.*, vol. 59, no. 5, pp. 554–557, Sep. 2008.

[27] F. V Lenel, *Powder Metallurgy Principles and Applications*. Metal Powder Industries Federation, 1980.

Chapter 6 – MA956 Creep and Anelasticity Studies

6.1 Introduction

This chapter is dedicated to the studies carried out on the commercial grade ferritic ODS steel MA956. The following pages describe the approach adopted for assessing the physical mechanisms acting when such an ODS steel is subject to creep transients. A series of creep tests with full unloading stages was devised. Again, a multi-technique approach was adopted, but the chapter concerns only the first part of the study, comprised of the mechanical tests and the neutron diffraction study of internal stresses (and strains) developed by each grain family under creep transient condition. The complementary studies are suggested in the Future Work section of the conclusive chapter.

6.2 Characterisation of the as received MA956

Due to the limited availability of the ODS 316L steel, and given the relevance of ferritic steels as base alloys for ODS, studies aimed at the anelastic response to creep transients were assigned to be performed on the MA956, previously described as a commercial grade of ferritic ODS steel. Special Metals provided the received batches, the first of which consisting of a hot-extruded bar with 16 mm diameter by 390 mm length, and the second consisting of two bars with same diameter and 1750 mm length. Images of the as received material are provided in Figure 6.1. Chemical composition was provided by the manufacturer, based on X-Ray Fluorescence technique and special inert gas fusion/thermal conductivity analyser LECO TC436AR and, for light elements such as N, O and C, LECO CS444 analyser. Data provided from these methods, in % weight of elements, are shown in Table 6.1.

Table 6.9 - Chemical composition of the MA956, according to Special Metals.

Cr	Al	Ti	Yttria	C	N	Mn	Si
19.4	4.8	0.38	0.51	0.015	0.022	0.10	0.04
Ni	**Cu**	**S**	**P**	**Co**	**O**	**Fe**	
0.05	0.02	0.008	0.005	<0.01	0.23	Bal.	

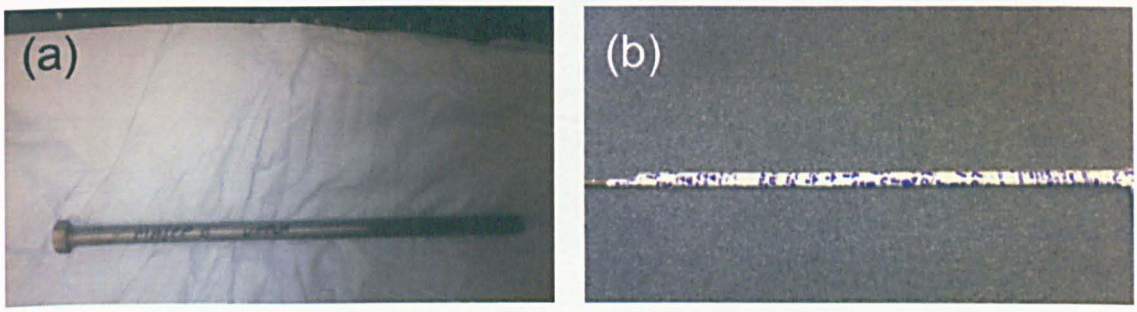

Figure 6.1 - Batches of MA956 supplied by Special Metals; (a) short bar (390 mm) and (b) long bars (1750 mm). The right-hand side end of the bar in (a) is slightly tapered.

Characterization of the as received condition followed, by means of optical and electron microscopy, and the mechano-acoustic technique for determining the elastic properties (Young's modulus constant) at room temperature. Samples were extracted from both long bars in the cross-section (perpendicular to the bar axis) and longitudinal (along the bar axis) directions. The preparation for microscopy involved grinding with SiC paper and polishing with diamond particles up to OP-S suspension, in order to achieve the polished surface finish required for EBSD (clean, but a bit matte, in opposition to the mirror-like quality usually sought for optical microscopy).

As expected, in agreement with the literature [1–3], the microscopy survey revealed elongated grains, columnar in shape and strongly oriented along the longitudinal axis of the bars, centimetres in length and several millimetres width. Only a qualitative observation of the microstructure in optical microscopy was possible, given that the large grain size, peculiar morphology and low boundary visibility made the estimation of average size impractical. Figure 6.2 exemplifies, by means of a micrograph showing variegated shades of grey as different grains, with weak contours of the grain boundaries.

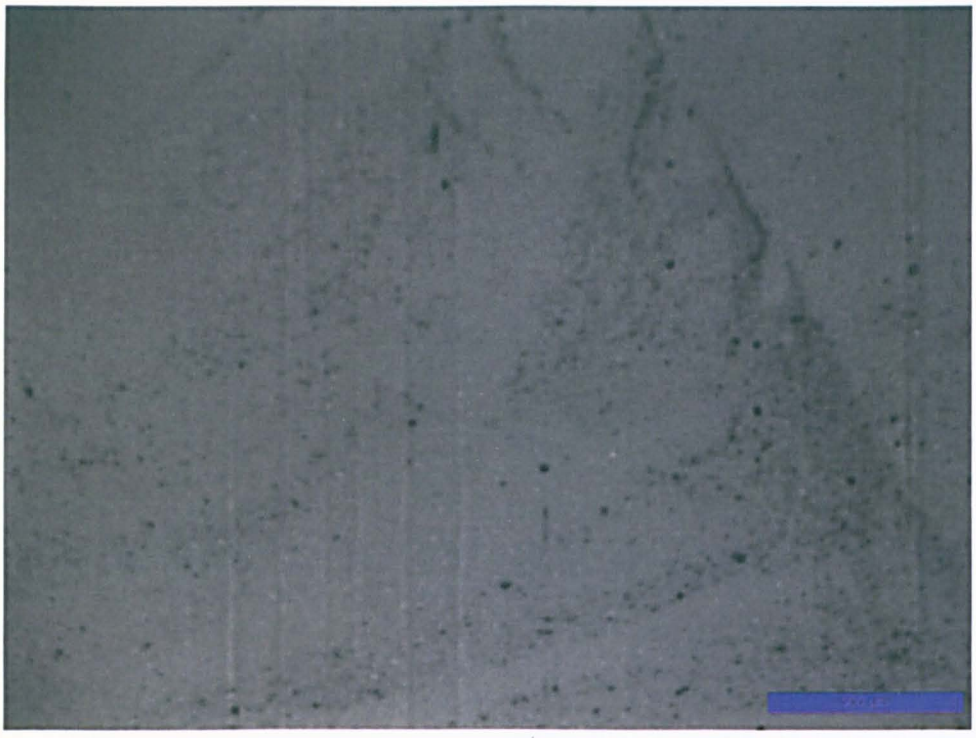

Figure 6.2 - Optical micrograph of a longitudinal sample of the as-received MA956, showing, in poor conditions of visibility, the columnar grains, in shades of grey, stretching along the extrusion direction (vertical).

SEM/EBSD analysis provided more convenient ways to observe the microstructure. Both cross-sectional and longitudinal samples were EBSD-scanned, using step sizes of 5 μm and 20 μm, respectively. The results are shown in Figures 6.3 and 6.4. It can be seen that the columnar grains, elongated along the extrusion direction, present a strong preferential orientation, mainly characterised by the {100}<110> system, also known as α-fibre, and the {111}<110> system, the γ-fibre. In Figure 6.3a, three EBSD maps of consecutive areas of the MA956 microstructure are seen and colour-coded by the IPF contouring, where these fibres are evident and confirmed by the Inverse Pole Figures (IPF) shown in 6.3b. This characterisation study revealed a microstructure in exact agreement with what would be expected from the literature.

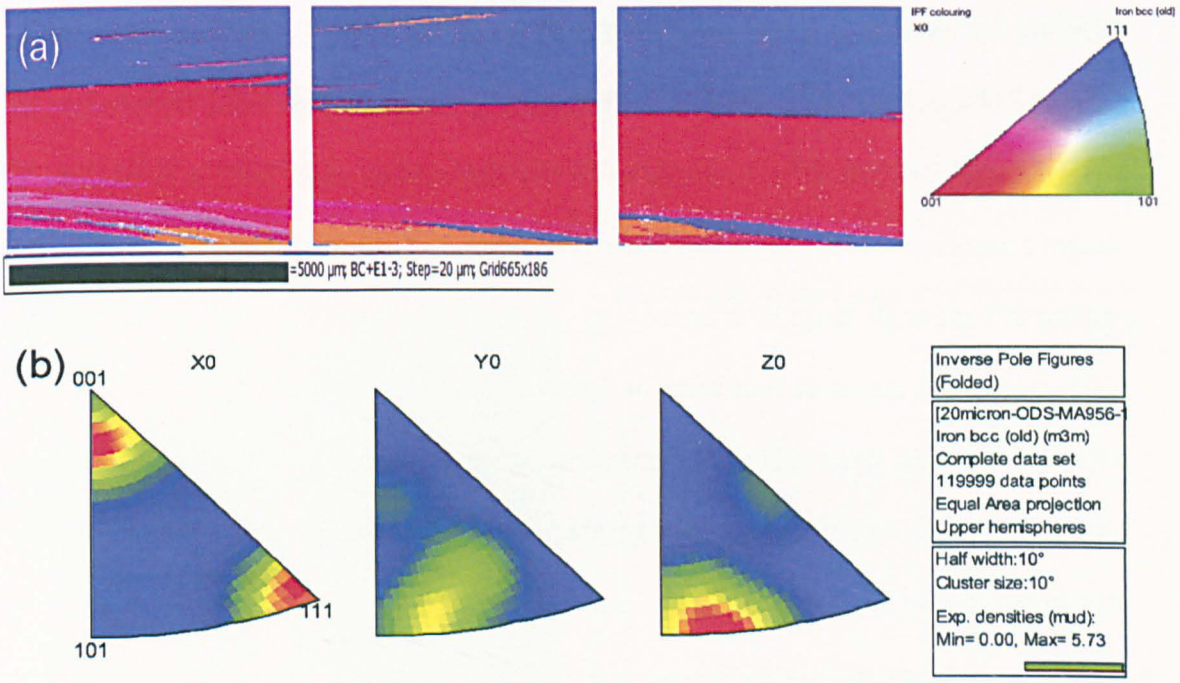

Figure 6.3 - EBSD analysis of MA956 grains in the longitudinal direction. In (a), colour-code IPF maps of consecutive areas and, in (b), their correspondent Inverse Pole Figures showing the pronounced grain orientation, especially in the rolling direction.

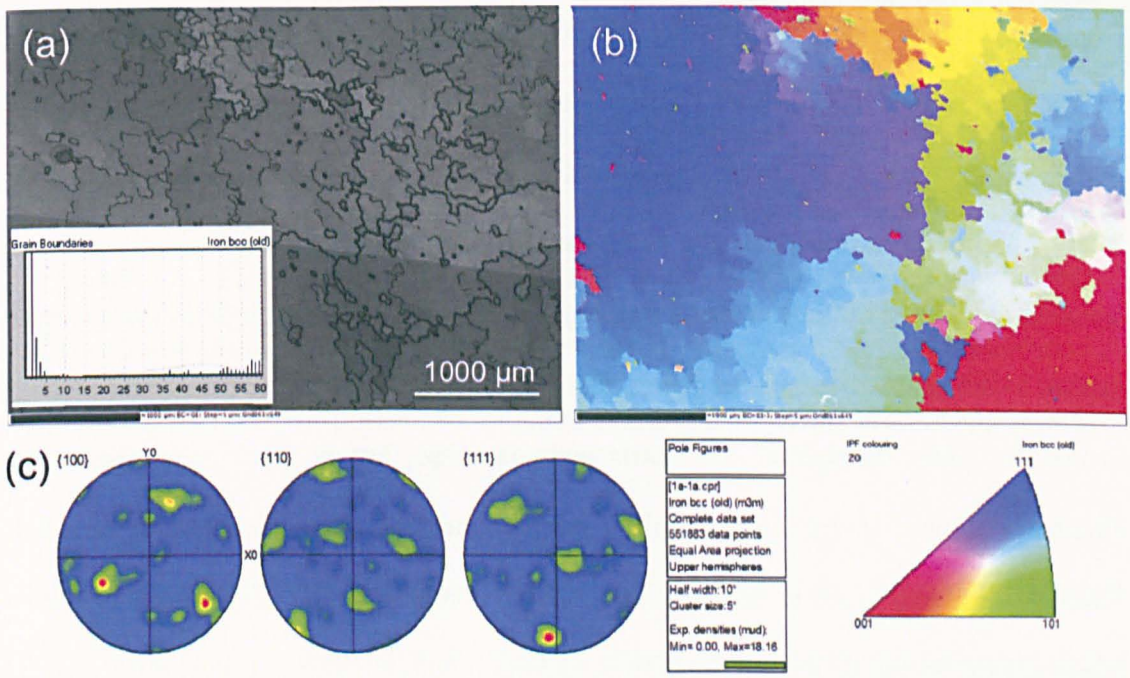

Figure 6.4 – EBSD analysis of the MA956 grains observed in cross-section. Image (a) shows the grain morphology, which is colour-coded in (b) with the IPF map; (c) shows the Pole Figures, representing a distribution of orientations.

As for the cross-sectional sample, the EBSD results showed a distinct aspect, revealing the morphology of the section area of the columnar grains. Although some orientations are preferred, they are not so pronounced as in the longitudinal case. Still, it is possible to discern a dominant {111}<110> component (in blue). A distribution function, based on the fraction of high-angle grain boundaries, was obtained from the EBSD and used to estimate the average grain size over four areas of 3750 μm^2, which was found to be 376 ± 48 μm. Although the grain size could not be quantified for the longitudinal direction, it is easy to see that the grains are elongated over several millimetres length scale, generating a very high aspect ratio.

6.3 Oxide particle size distribution

In a similar fashion to the study previously developed for the ODS 316L steel, TEM was also deployed for imaging the nanometric oxides, thus providing a means for determining the size distribution. Three foils were prepared under the procedure described in Chapter 3 and subject to conventional imaging in bright field mode in the JEOL 2100 TEM instrument, and to EDS analysis aimed at the chemical composition of the oxides. A total of 450 particles were counted and measured from 8 different micrographs, obtained by varying the area of the foil under investigation as well as the tilt angle of the specimen holder, in order to be statistically representative. A relatively homogeneous distribution of nanoscale oxides throughout the matrix was observed, but in some micrographs, the alignment of these oxides seems to follow grain boundaries, along the extrusion direction. These oxides were found to belong to the Y-Al-O complex. Some micrographs of the as-received MA956 can be seen in Figure 6.5, illustrating these findings. Figure 6.6 shows the histogram for size distribution of the oxides, whose average was calculated as 34 ±7 nm, a value pertaining to the desired range, according to some researchers, for ensuring effectiveness in pinning dislocations [4].

An interesting aspect of the microstructure was the apparent absence of carbides, nitrides or other types of precipitates different than the oxides. This is not surprising, given the negligible amounts of carbon and nitrogen reported in the composition. This was confirmed by the neutron diffraction experiment, described later.

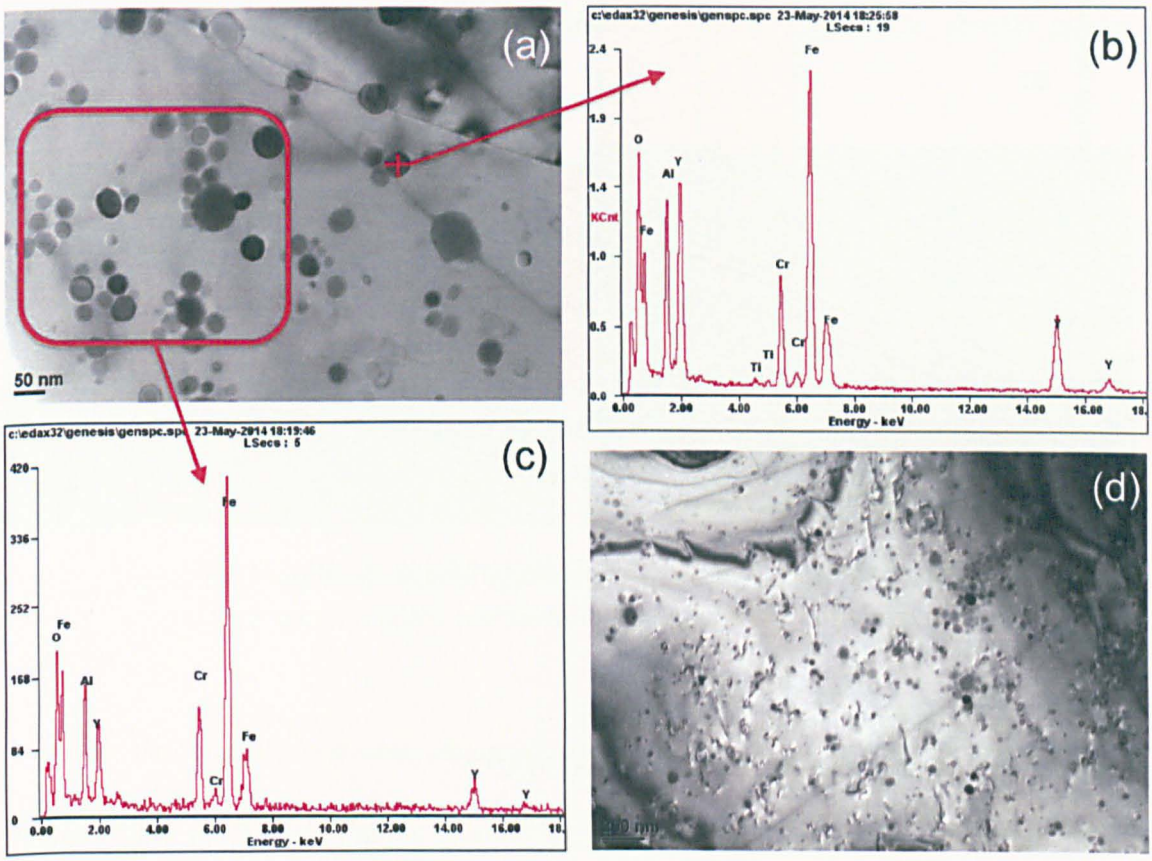

Figure 6.5 - TEM images depicting the oxide particles. Micrograph (a) shows some particles and clusters that appear to follow the boundary (top right thin line). An EDS scan of the particle identified by the cross is shown in (b), indicating a Y-Al-O composition, while (c) is an area scan, where more elements from the background are identified along with the Y-Al-O particles; (d) shows another micrograph in which particles appear to be pinning dislocations.

Some interactions between dislocations and oxide particles were observed. As figure 6.5d portrays, there are few matrix dislocations pinned by the nanometric oxides in such a way that suggests attractive interaction, that is, some dislocations would have by-passed the particle, but the attraction exerted by the particle hinders the dislocation line on its departure side, as suggested by Rösler and Arzt [5] and discussed previously in the literature review chapter.

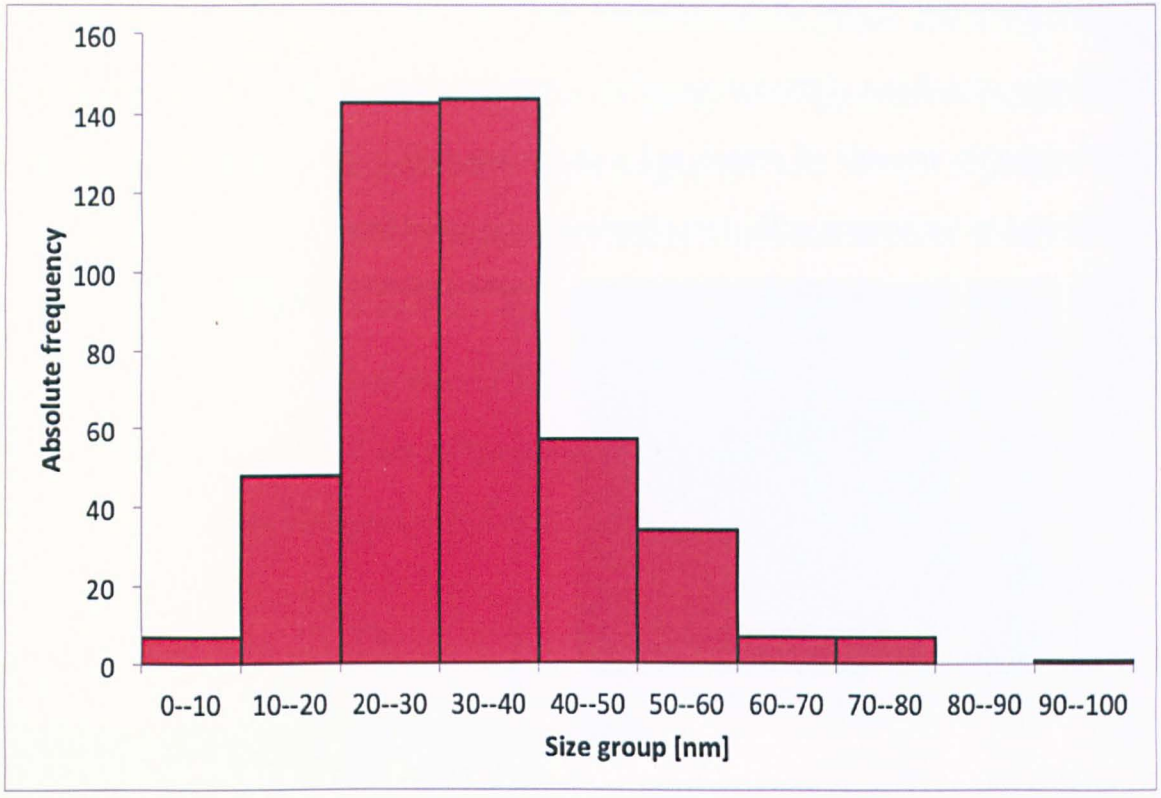

Figure 6.6 - Oxide size distribution of the as received MA956.

6.4 Stress-relief annealing of the as received MA956

The complete fabrication history of this commercial grade ferritic ODS steel, besides the process described in Chapter 2, in which the consolidation process (in this case, hot extrusion) is followed by a complementary heat treatment, presents an additional step. In order to produce bars with a neat surface finish, the material rods are subjected to bar-peeling, a machining operation responsible for removing the external layers of the bars, where cracks and skins might be present, by means of radial cutting [6]. The operation (portrayed in Figure 6.7a) induces residual stresses, which might be intensified if the bars undergo pressing after the peeling, in order to be shaped as straight rods.

A high level of residual stresses was observed, since the bars and the specimens bent while being cut, though those stresses were not quantified. These difficulties, associated with the very brittle character of the extracted specimens, which were used in some preliminary room temperature tensile tests, were taken as evidence of the unsuitability of

the MA956 for work in the as-received condition. Tests failed prematurely and no consistency for its tensile behaviour was observed. The only common feature of these samples, each failing at a different stress level, was the brittle aspect of the fracture surfaces, detectable even by the naked eye. As Figure 6.7b shows, the shiny, reflective and smooth surface, without any dimples, is indicative of negligible (or absent) plastic deformation.

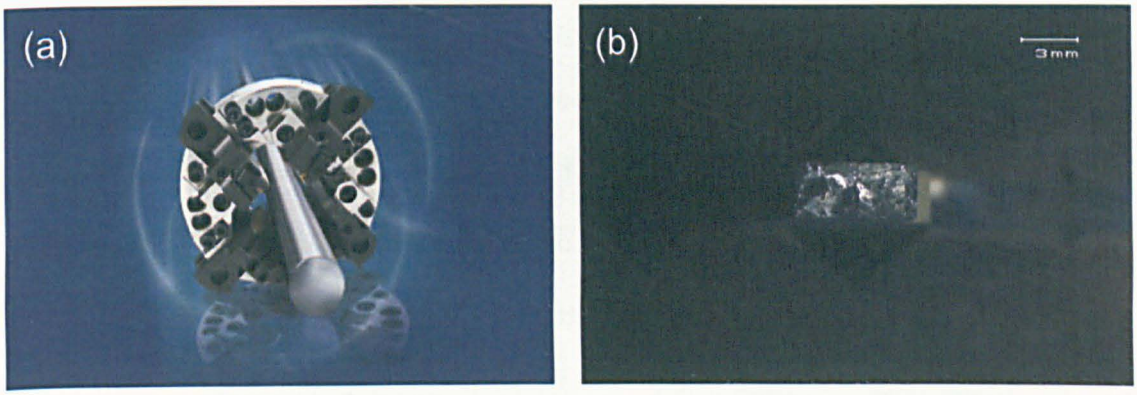

Figure 6.7 - An illustration of the bar-peeling process [24] (a) and the optical micrograph of a failed specimen in the as received condition (b).

Under the light of these observations, it was necessary to apply heat treatment on the MA956 steel; in order to relieve the residual stresses induced by the bar-peeling and to eliminate some of the cold-worked behaviour of the steel induced by the bar-peeling, in particular, the brittleness, making it suitable for further testing and investigation.

An essential condition for the heat treatment is that the microstructure is not altered, or at least, not drastically. From previous experience and, also, from the literature, it is well known that ferrite grains may grow easily to millimetre size under heat treatments at recrystallization temperatures [7, 8]. However, for this case, growth was not expected to happen significantly, for two reasons: first, because the mechanically alloyed MA956 already presents columnar grains several centimetres long and hundreds of micrometres wide. Second, because the yttria content is expected to provide further resistance to grain growth, as acknowledged as one of the advantages of the presence of dispersoids.

Following recommendations of the manufacturer of the steel, and considering the recrystallization temperatures of the MA956, found in previous work by Bhadeshia [9], another heat treatment was carried out at 1285°C for one hour on almost all the material available (only a few pieces of leftovers were kept in the as-received state), a temperature suitable for a subcritical annealing, since it is situated above $0.9T_m$. In this range of temperatures, recrystallization may occur; but, since the microstructure of the MA956 is stable, the treatment only promotes stress relief. Given that no phase transformation was expected for such a short time interval of exposure to this temperature, cooling was carried out inside the oven. Previous studies on the MA956 suggested that the only expected phase change at this temperature is the formation of the chromium-rich α'-phase, which takes more than 100 hours at isothermal treatment to be formed and is not easily distinguishable from the ferritic phase [10, 11].

Subsequent to the annealing, a second study of characterisation was carried out, to check for stability of the microstructure. The same techniques (EBSD and TEM) and procedures were carried out, for establishing comparisons between the as received condition and the annealed one. No difference was found in the microstructure, still presenting the same features as the recrystallized state of the MA956, that is, the α- and γ-fibre textures of the column-like grains, earlier represented in Figures 6.3 and 6.4, and featured in Figures 6.8 and 6.9. As for the oxide size distribution, a statistical analysis via a hypothesis test on the data for the two conditions of the material (as-received and heat-treated) revealed the existence of a significant difference between them. While an inspection on Figures 6.6 and 6.10 allows the conclusion of a slight growth experienced, this idea is confirmed by the hypothesis testing.

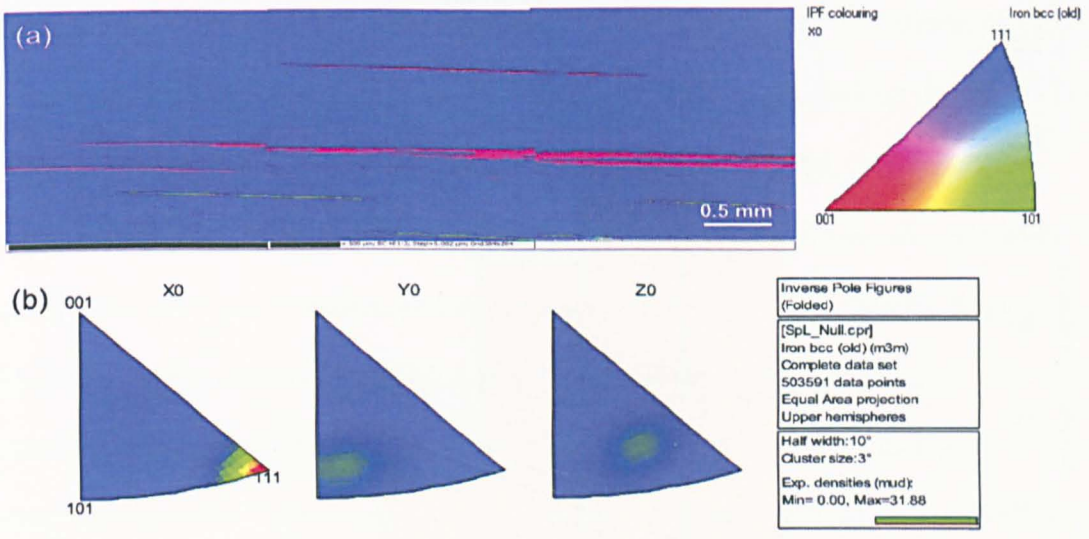

Figure 6.8 - EBSD map (stitched consecutive areas) showing the predominance of the same texture in longitudinal direction (a) and correspondent IPF figures (b) for the annealed MA956. The predominance of one of the fibres depends on the area surveyed.

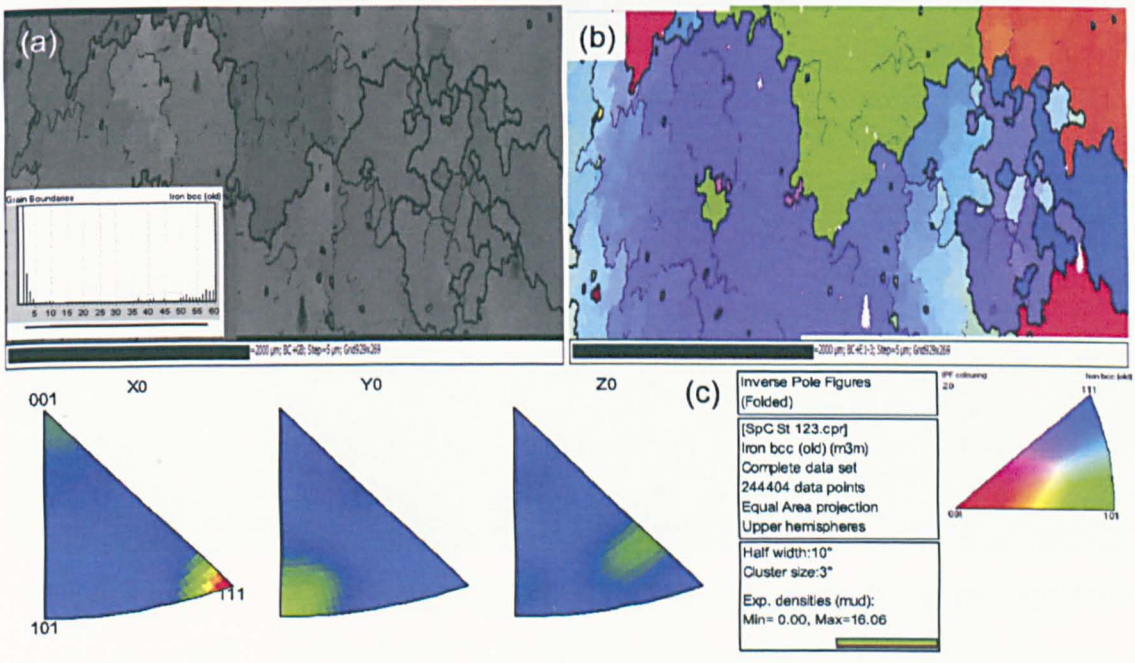

Figure 6.9 - EBSD map of heat-treated cross-sectional MA956 showing the grain morphology (a), presenting an orientation variation similar to that of the as received; (b) is the colour-coded grains with the IPF map, and (c) the IPF figures corresponding to the micrograph.

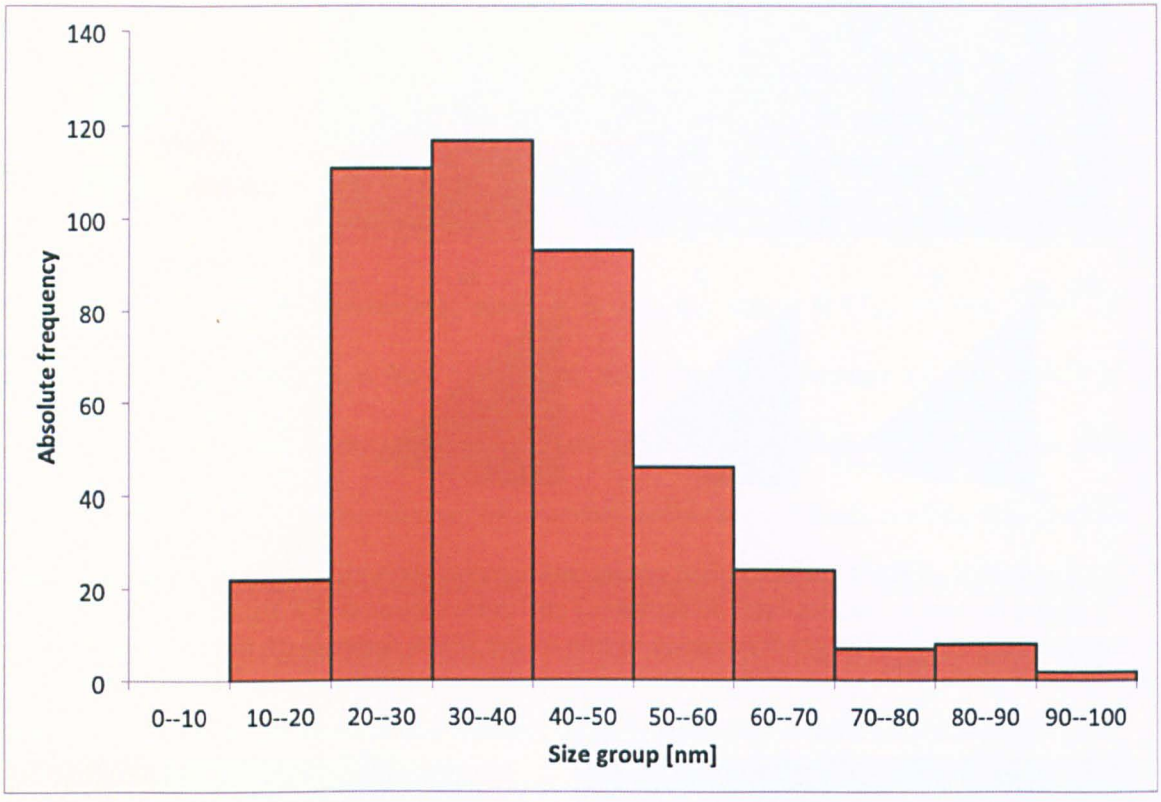

Figure 6.10 - Oxide size distribution for the heat-treated (1285°C / 1 hour) MA956.

For this distribution, 437 particles from 9 micrographs obtained from three foils were analysed and had their average diameter amounting to 41±8 nm. Although this result seems to overlap the uncertainty range for the as received average (previously reported as 34±7 nn), a hypothesis test aimed at comparing the two conditions was necessary. For this endeavour, a heteroscedastic t-test (that is, a test designed with the assumption of unequal variances) was carried out with a significance probability of 5%, that is, 95% confidence, having the null hypothesis stating that no significant difference exists between the oxide size distribution in the as-received material and in the heat-treated one. Given that the test value was calculated as 5.08, much higher than the critical value of 1.96 of the probability, the null hypothesis was rejected. The test provided support to the idea that growth of the particles has occurred under the thermal cycle of the heat treatment. This is in contrast with previous works which reported stability of the oxides in harsh conditions, such as in diffusion bonding of a ferritic ODS steel carried out at 1200°C by Noh and co-workers

[12]; and irradiation creep at temperatures up to 773 K, investigated by Chen et al. [13]. It is relevant to mention, though that the oxides, in these cases, belong to the Y-Ti-O complex, whereas the Y-Al-O oxides are predominant in the MA956.

No quantitative study of dislocations was carried out. However, evidences of interactions between dislocations and oxides were still found in TEM images. Even though the oxides might have experienced a slight growth, they were observed to effectively promote pinning of dislocations on their "departure" side, as shown in Figure 6.11, an effect that appears to have accrued from the mechanical strains suffered during fabrication.

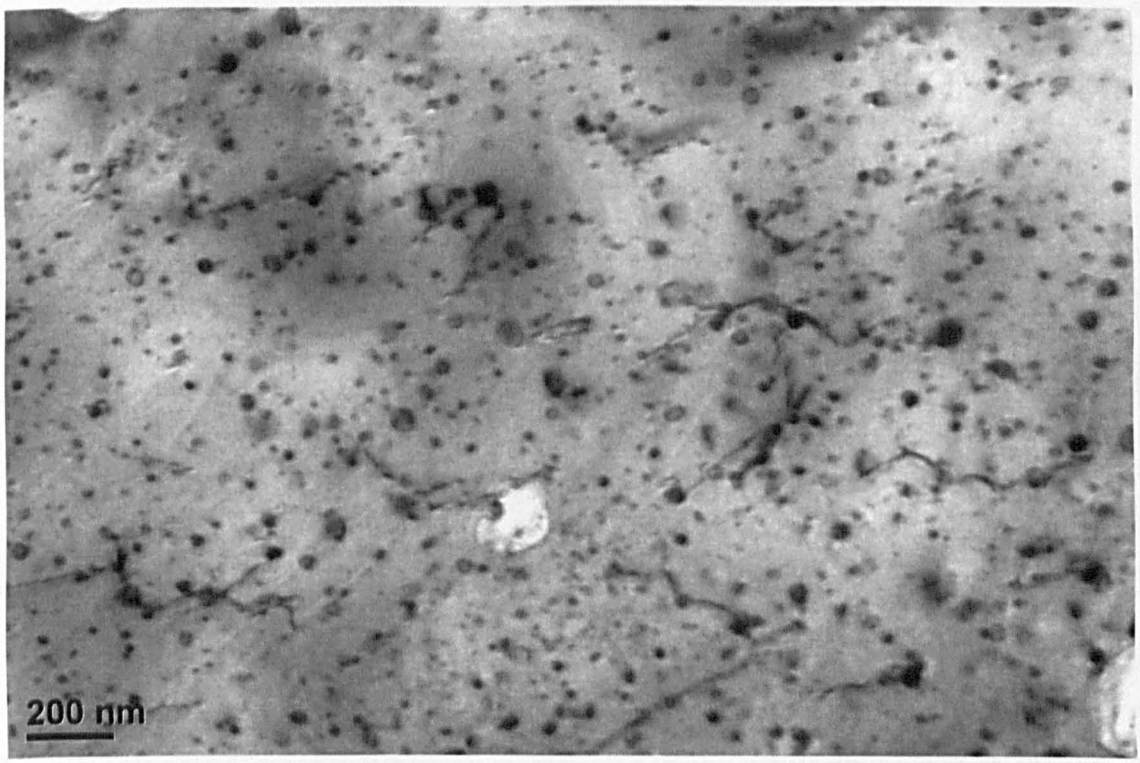

Figure 6.11 – Oxides of the heat-treated MA956 pinning dislocations on their "departure" side (ahead of the oxides), as expected for ODS steels.

6.5 Tensile properties of the MA956 steel

Mechanical tests and subsequent investigations were carried out for the heat-treated steel. The tensile behaviour of the MA956 was measured in an effort to determine the appropriate stress level for the creep transient tests. The tensile curves at room temperature

and at 650°C were obtained. The mechano-acoustic technique was once more used to obtain the Young's modulus of the material at room temperature, prior to the tensile tests.

The mechano-acoustic specimen design was a strip with nominal dimensions 14 mm x 5 mm x 40 mm. The specimen used was machined from the MA956 batch, parallel to the longitudinal axis, presenting dimensions 14.0 mm x 4.88 mm x 40.11 mm. The density of the material, measured via the Archimedes principle, was found to be 7.24 ± 0.03 g/cm^3. Six measurements of the flexural mode of vibration in the mechano-acoustic test were carried out and found to be very close to one another, for which the average was calculated as 231.2 ± 0.4 GPa. This value is consistent with the literature, allowing for the variation found in the Young's modulus, due to the predominance of one fibre system or the other [10]. Magnitudes as low as 149 GPa are found for predominant α-fibre ({100}<110>), while the predominance of γ-fibre ({111}<110>) was reported to increase the elastic modulus to 270 GPa. It is reasonable, then, to expect that different proportions of fibre texture may result in an intermediate value, as observed. A picture of the mechano-acoustic specimen being tested is provided in Figure 6.12.

Figure 6.12 - MA956 stripe being tested for Young's modulus.

6.5.1 Room temperature tensile tests

Flat tensile specimens with the same design as the ones used for the ODS 316L were adopted and tested in the Instron 5969 test rig under a strain-rate of 4×10^{-4} s^{-1}. Although the annealing treatment rendered the material suitable for the investigations, some problems still persisted. The sample design, bearing a gauge cross section of 6 mm x 3 mm and 25 mm gauge length, was found not to be the most appropriate to characterise the mechanical response of the bulk material. Results varied from sample to sample and more than one tensile behaviour was found. While some specimens failed in a completely brittle way, with less than 2% elongation, others presented considerable ductility, which, in some cases, reached 15%. Table 6.2 summarizes the data from eight tensile tests carried out. A plot of the curves is provided in Figure 6.13.

Table 6.10 - Data from room temperature tensile tests of the MA956.

Test	E [GPa]	Yield Stress [MPa]	UTS [MPa]	Ductility [%]
Tensile 1	161	603	642	1.6
Tensile 2	205	694	715	4.1
Tensile 3	211	641	648	1.2
Tensile 4	250	655	709	16
Tensile 5	158	516	537	1.3
Tensile 6	272	683	730	15
Tensile 7	151	513	553	2.7
Tensile 8	265	697	721	5.5

As seen in the above table, different calculated Young's moduli, from the elastic portion of the curves, as well as distinct ultimate tensile stress levels were associated with the different behaviour in deformation as well. This seems to suggest strong dependence of the properties on the predominant fibre in each specimen. This latter was already reported to exert effect on the ductile-to-brittle transition temperature (DBTT) of the MA956 [11]. Chao and co-workers observed the {100} fibre texture of the MA956 to be more favourable for embrittlement than the {111} fibre, or the weak {110} fibre in the

unrecrystallized steel [14]. So, the results found may well be a consequence of the predominance of certain fibre textures in each of the tested specimens.

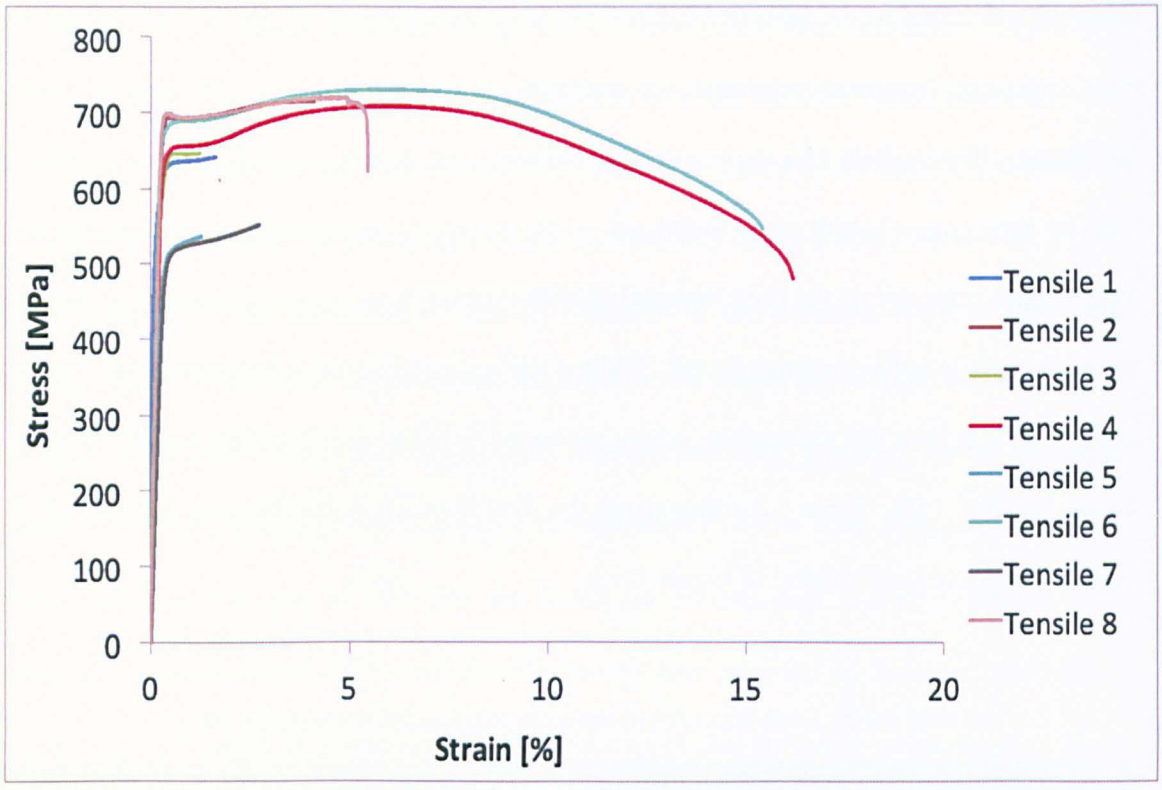

Figure 6.13 - Plot of all tensile test curves at room temperature, for comparison.

Although no consistency could be found for the room temperature tensile properties, it can be seen that there is a tendency to follow. Tests bearing the lowest levels of total ductility were also the ones that presented the Young's modulus at the same baseline level found for a predominant {100}<110>-fibre system. The same observation can be said about the tests with the highest values of Young's modulus, which were also the ones with the most significant levels of ductility, a result that corroborates the influence of texture on the DBTT of the alloy and, as a consequence, its mechanical behaviour.

An interesting common aspect, though, that can be drawn from these tests, is that the yield stress and the ultimate tensile strength (UTS) levels at room temperature were very high, exceeding 500 MPa in all cases. Another relevant observation lies with the fact that the yield stress, in all the tests, was very close to the ultimate tensile stress, causing the

material to behave close to what would be expected from an ideal perfectly plastic alloy, that is, showing no signs of work hardening after exceeding the yield stress. Figure 6.14 shows optical fractographic images, from a preliminary study. It is easy to see the features of a predominantly brittle mode of fracture, such as the shiny and multifaceted cleavage surfaces, without any dimples, and presenting some cracks. This was observed even for number 4 tensile test specimen, for which significant ductility was found. The difference between specimen 4 and the others was simply the occurrence of necking for this latter, as deformation proceeded.

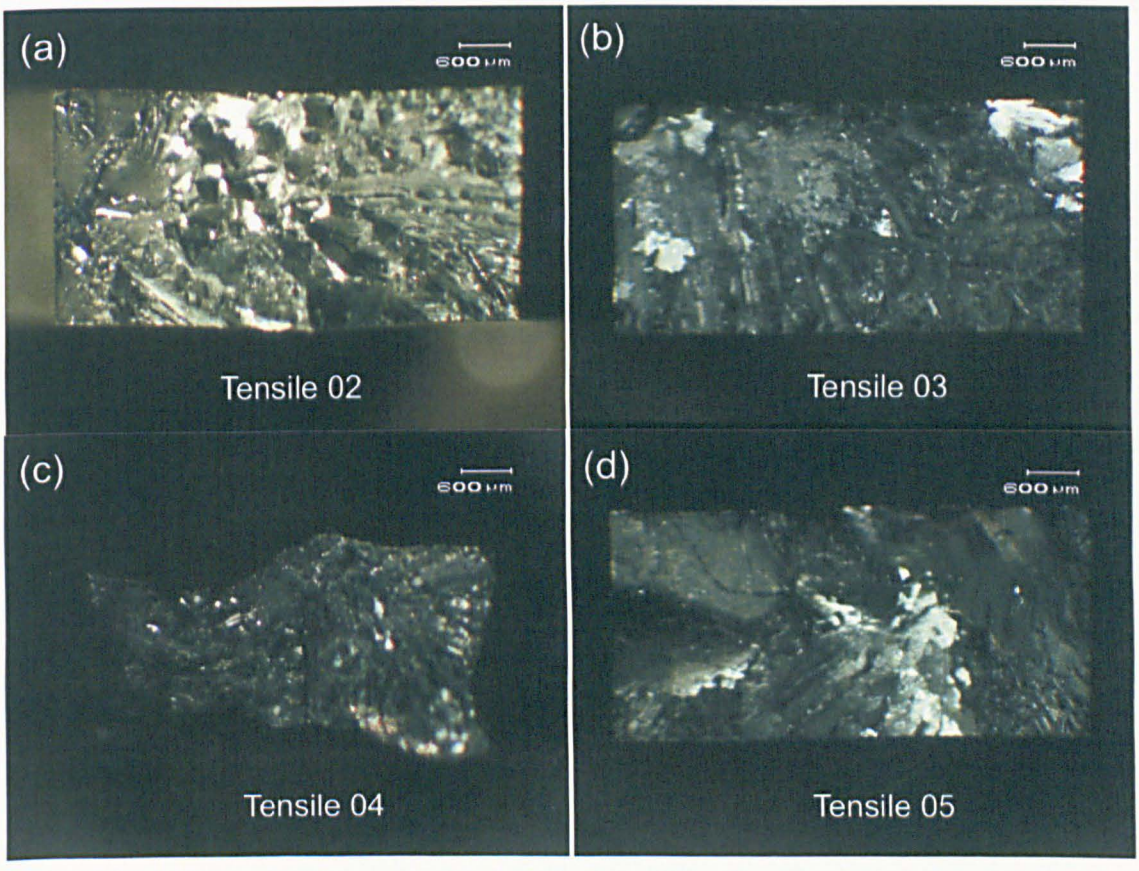

Figure 6.14 - Micrographs of the fracture surfaces of some of the MA956 room temperature tensile test specimens. In all of them, regardless of the level of ductility, features of the brittle mode of fracture predominate.

6.5.2 High temperature tensile tests

The tensile response of the material at high temperature was evaluated from tests carried out at 650°C. At this temperature, the likelihood of brittle behaviour is very low, regardless

of the predominant fibre texture. Although the DBTT of steels is controlled by many microstructural and compositional factors [7, 15], the temperature level of the test is way above DBTT's reported for ferritic ODS steels, including the commercial graded ones, expected to be in the range 200°C – 400°C, due to its high content of chromium [7]. Besides, this temperature of the test exceeds the range where dynamic strain ageing (DSA) is reported to be more prominent in the MA956, helping the material to be less brittle [16]. Due to the expected ductile behaviour at this temperature, the specimen design was kept the same as previously used for the ODS 316L, that is, 4 mm gauge diameter and 20 mm gauge length. The Instron 8862 machine was used to carry out the tests at a controlled displacement rate of 0.01 mm/s, resulting in a strain-rate of 5×10^{-4} s^{-1}. Four tests were performed and their results were kept within reasonable limits of scatter. The average ductility was calculated from the tests as 17%, and the average ultimate tensile strength at 650°C amounted to 272 MPa. Figure 6.15 is a plot of the high temperature tensile curves.

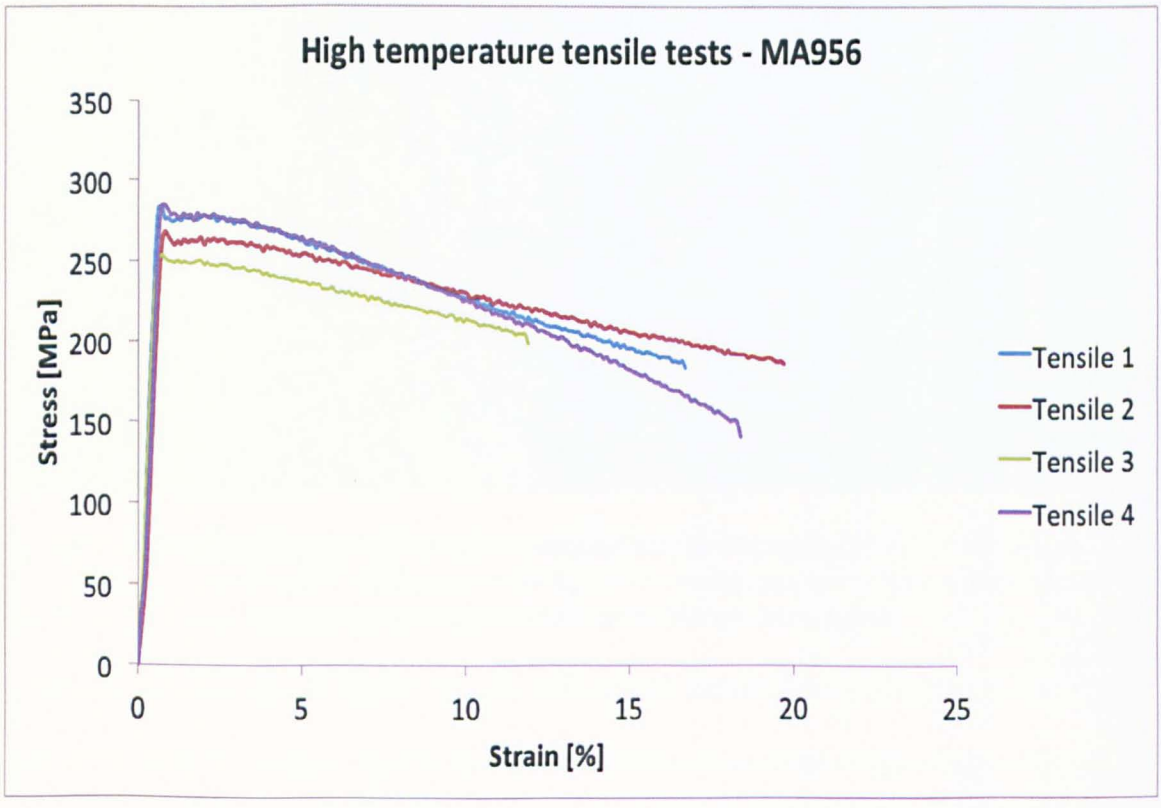

Figure 6.15 - High temperature tensile test curves for the MA956.

An interesting feature visible when plotting the stress vs. strain curve is the serrated aspect of all the curves. Although this feature is usually associated with dynamic strain ageing, such a phenomenon is not to be expected at this temperature level [16]. The remarkable loss of strength observed at 650°C, manifested in the low UTS value (in comparison with the UTS at room temperature), seems to corroborate the idea of a not pronounced DSA. Instead, based on the microstructure and on the most accepted models for explaining deformation in ODS steels [22], the observed profile of the curves may well be associated with two operating mechanisms of deformation: the attractive interaction exerted by the nanometric oxides would try to hinder the motion of dislocations, but, due to the high temperatures, thermal detachment of dislocations allows them to resume their motion [16, 22, 23], until they get pinned by the next particles on the way (and so on), thus generating the serrated profile.

Although the total ductility has also increased, reaching 20% strain in one test, it is more likely that a mixed mode of fracture might have caused the failure. Also, one of the tests showed reduced ductility, possibly resulting from the fibre system present. No fractography was carried out, but the shape of the tensile curves, with the continuously decreasing portion of the plastic deformation suggests loss of strength. This latter may well be associated with the growth of voids formed during the processing of the alloy and trapped at grain boundary interfaces, as suggested by Abd El-Azim [16], which would promote intergranular fracture; and with the nucleation and growth of voids at the particle/matrix interfaces, which would lead to the ductile dimple fracture.

6.6 Creep transient tests

The core of the experimental programme on the MA956 was dedicated to study how a coarse-grained ferritic steel with nanodispersoids would behave in conditions of creep transient deformation. The fundamental area of interest was, once more, the anelastic behaviour of the alloy, which, if present, would be triggered in the transient part of the

creep straining, following the removal of the applied load. In order to examine this behaviour, a series of creep tests with full unloading stages was performed, to be followed by investigative techniques aimed at observing the phenomena and the relative changes in the microstructure.

The first series of creep transient tests were carried out on a round specimen with 6 mm gauge diameter and 30 mm gauge length, under 150 MPa at 650°C. Similarly to the approach adopted for the 316H steel, at a certain point in secondary creep, the external load was removed, but this time, completely. The material was kept unloaded for a time interval of 0.5 hour in the first test set and 4 hours in the second test set. Two tests were carried out for each test set, using the Instron 8862 rig (slow strain-rate machine) and two transient cycles were carried out in each test. Conditions of the test sets are summarized in Table 6.3.

Table 6.11 - Creep transient test conditions of the first series.

Test ID	Stress regime	Time under load	Time unloaded	Number of transient stages
1	150 MPa/0 MPa	48 hours	0.5 hour	2
2	150 MPa/0 MPa	48 hours	4 hours	2

Due to the large number of data points in the test, causing a natural scatter in the creep datasets associated with the clouds of close points, the representation of the unloading stage was separated, as shown in Figure 6.16. There was no change in strain during any of the dwells. This can be observed from Figure 6.16. Even with the scattering of the data points, the average strain, represented by the black line, was the same at all time intervals during unloading. These findings seemed to indicate no anelastic recovery for the MA956. Because of the scattering, estimations of the secondary creep rate before and after the first transient were deemed unreliable. Longer creep tests were, then, envisaged, to verify the absence of anelasticity.

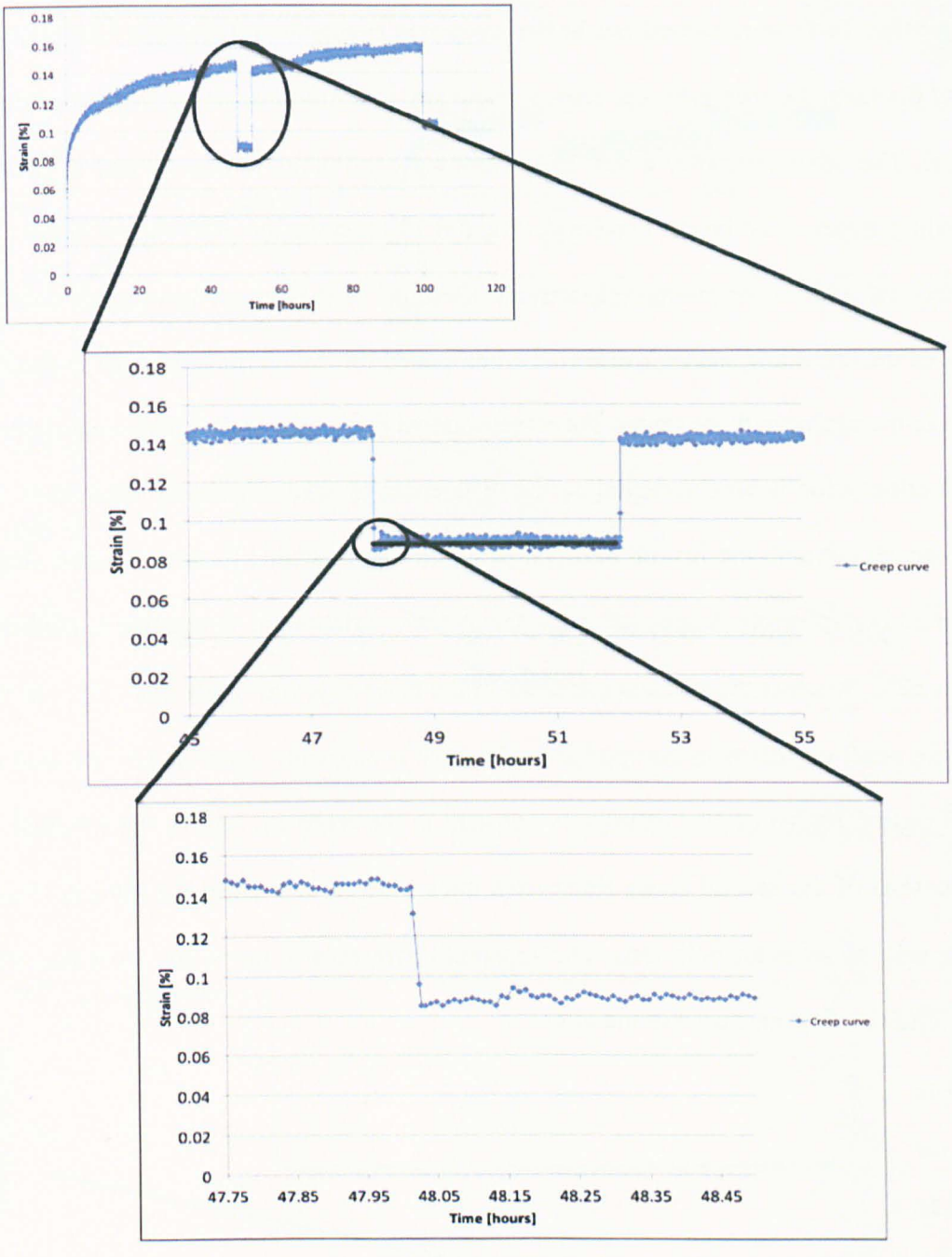

Figure 6.16 - Creep transient curve and amplified details of the first unloading stage, where the black horizontal line represents the average strain at this transient, which was found to be constant, indicating no anelasticity. The third part in the figure shows the early moments at unloading. Oscillations were found to be within the limits of scatter observed along the whole test curve.

The second series of creep tests were aimed at providing confirmation for the observed response of the MA956 to creep transient. A different specimen design, based on the BS EN ISO 204: 2009 Standard [17], with 8 mm diameter and 50 mm gauge length (described in Chapter 3 and detailed in the Appendix 1), was adopted, in order to fit the creep rig and

accessories. Tests were carried out in the creep rigs available at The Open University. In one of the tests, the specimen was crept without any interruptions, acting as the experiment control. The other test, after a few days creeping continuously, was subject to periodic unloading stages of 24 hours. Figures 6.17 and 6.18 illustrate the plots for the control test and the test with interruptions, respectively. Because of the scattering in creep data, the shape of the unloading stages is distorted when scaled for the plotting. In order to properly evaluate the strains in these stages, the correspondent part of the creep curve was zoomed.

An observation is timely, regarding the differences in scatter in the different tests. The tests carried out with the Instron 8862 (slow strain-rate machine) presented higher degree of variability, possibly associated with the higher variation in temperature, controlled within ±2°C, whereas the precision attained in the creep rigs was lower than ±1°C; as well as to the small variations in the applied load, which is constantly corrected by the load cell in the Instron rig, while it is effectively constant in the creep rig (due to the weights). As for the tests of the second series (long-term ones showed in Figures 6.17 and 6.18), the scatter was the same for both tests. The apparent differences in the scatter were due to the scale of the vertical axis used in the plots.

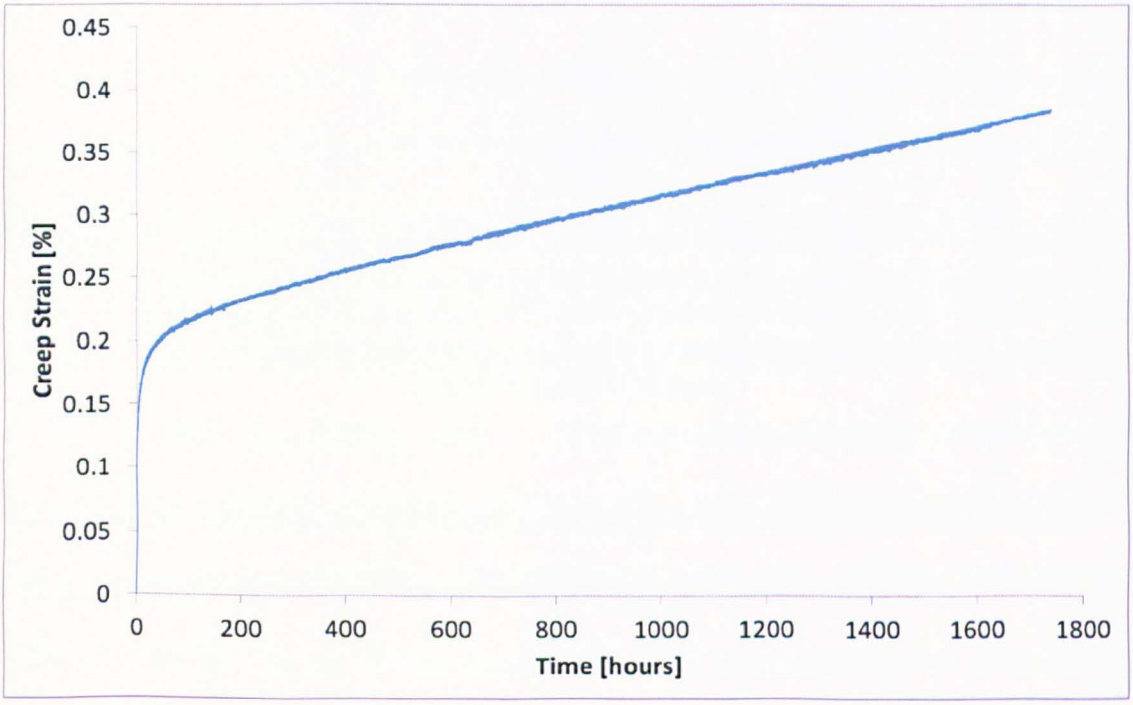

Figure 6.17 - Creep curve of the control test (no load removals).

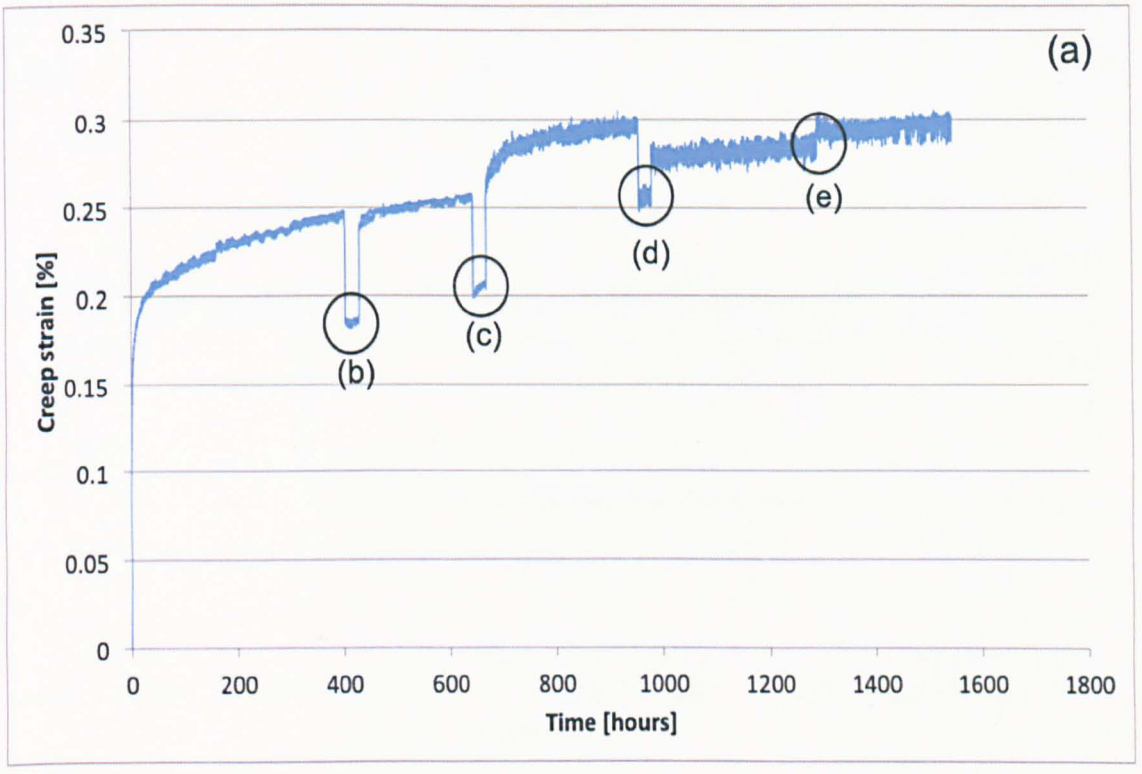
(a)
Creep strain [%]
Time [hours]
0.35
0.3
0.25
0.2
0.15
0.1
0.05
0
0
200
400
600
800
1000
1200
1400
1600
1800
(b)
(c)
(d)
(e)

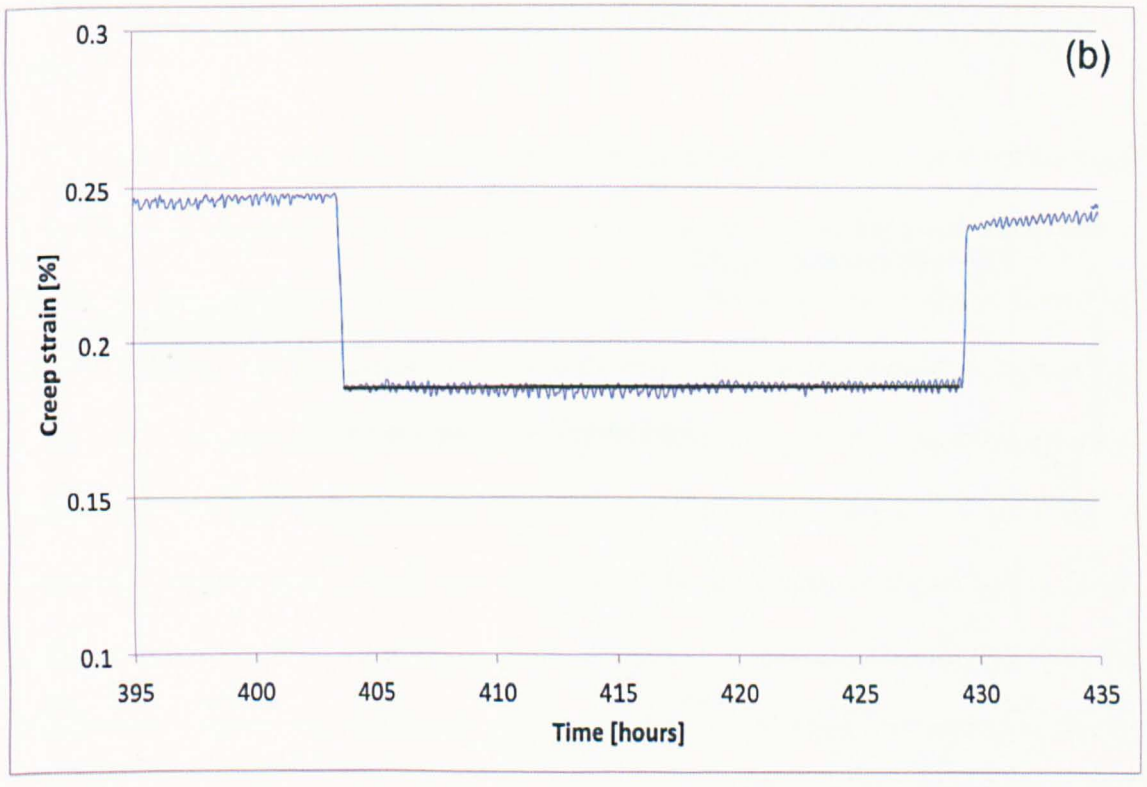
(b)
Creep strain [%]
Time [hours]
0.3
0.25
0.2
0.15
0.1
395
400
405
410
415
420
425
430
435

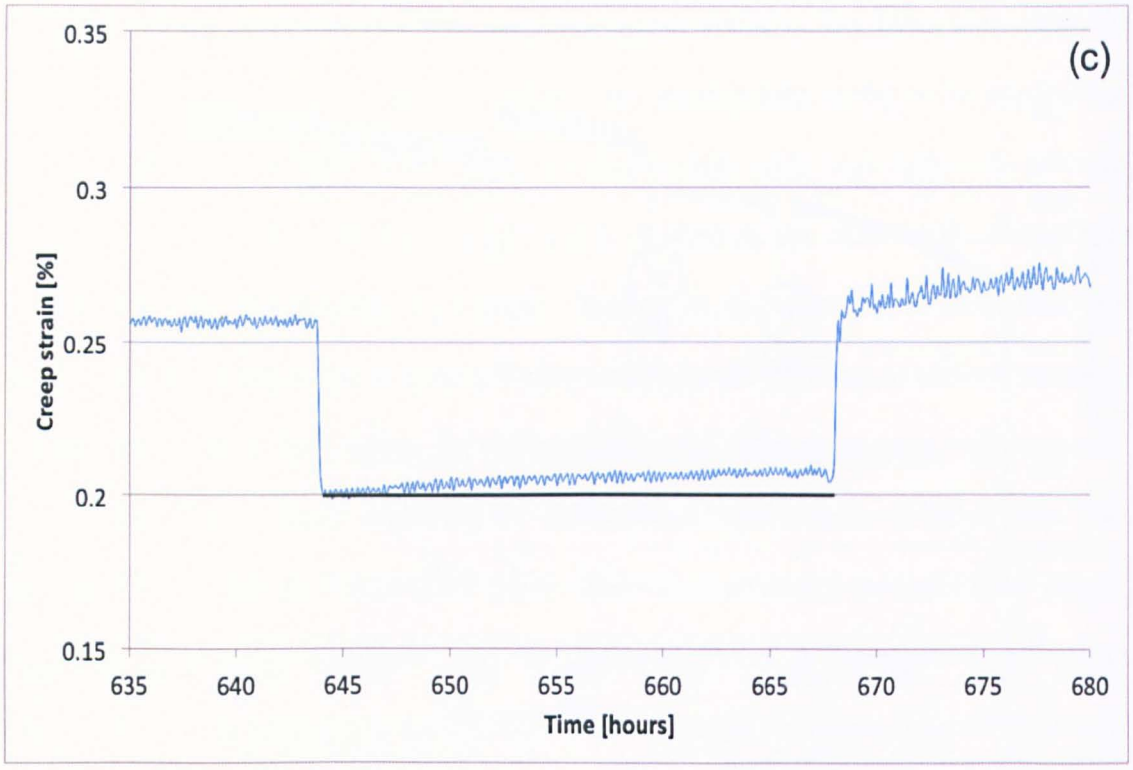
(c)
0.35
0.3
0.25
0.2
0.15
Creep strain [%]
635
640
645
650
655
660
665
670
675
680
Time [hours]

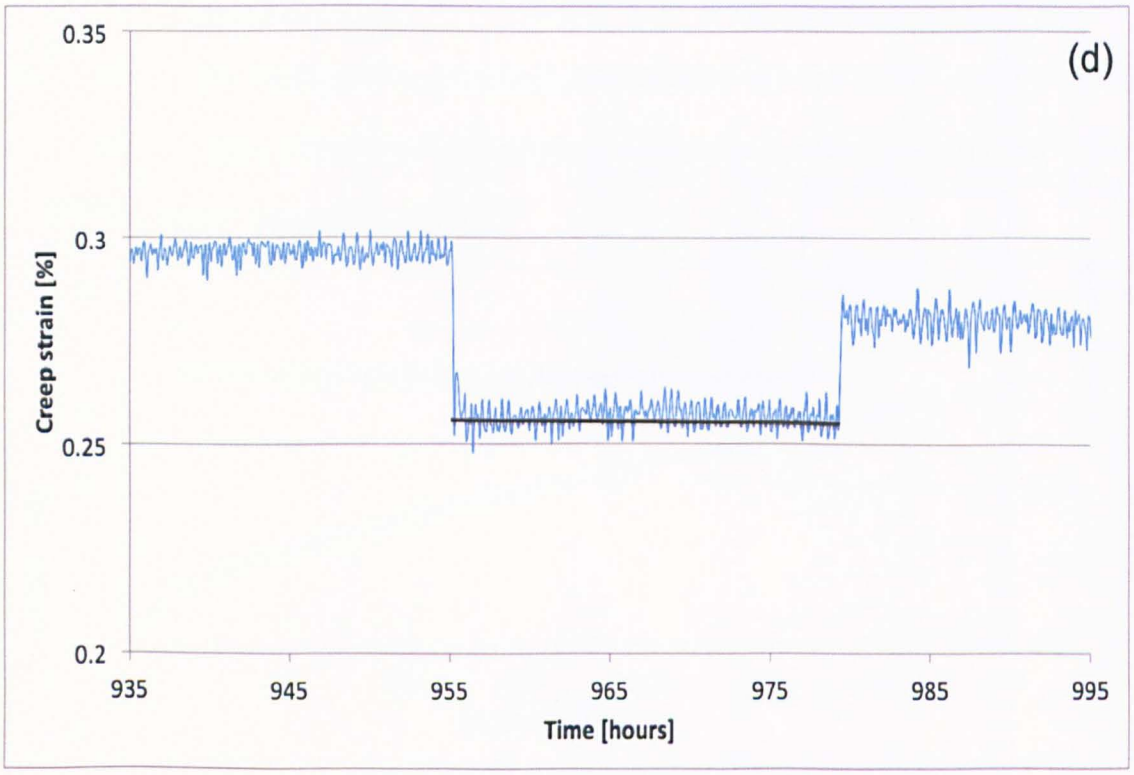
(d)
0.35
0.3
0.25
0.2
Creep strain [%]
935
945
955
965
975
985
995
Time [hours]

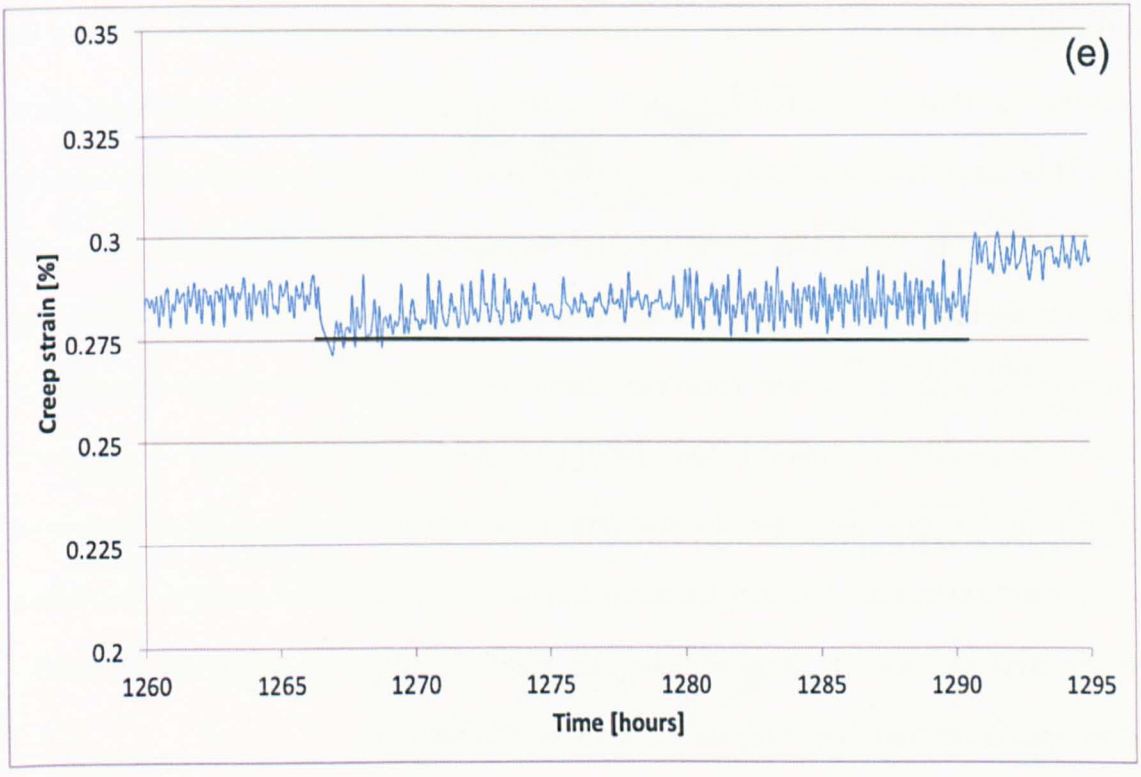

Figure 6.18 - Creep curve for the transient test (a), with zoomed plots for the first unloading stage (b), the second unloading transient (c), the third unloading transient (d) and the last unloading stage (e) before the end of the test.

It is interesting to notice the absence of anelastic recovery once more, in a similar trend as to what was observed in the first series of tests. The first unloading stage was found to exhibit the same strain level throughout. After the instantaneous drop in strain, associated with the load removal, no further recovery of the creep strain was observed, as seen in Fig. 6.18b. This was seen again in the third unloading transient (Fig. 6.18d). An anomalous and unexpected response was detected in the second transient. Instead of recovery, a progressive strain seems to have been observed at the unloading, as shown in Fig. 6.18c. Although this is, at first, a surprising result, given that, apparently, the driving force for deformation is absent, the progressive straining was interpreted as a first indication that the internal (intergranular) stresses might be resulting from resistance to creep deformation, rather than from deformation itself. In other words, predominant families of grain orientations in the specimen (with regards to the loading direction) seem to be resisting creep deformation, thus being compressed by the few grains in some favourable

orientations effectively deforming, so that tensile residual intergranular stresses might be developing while the material is under load. The progressive strains on unloading, then, would be a manifestation of the predominance of these internal stresses with tensile nature.

As seen from Fig. 6.18e, the same progressive strain was presented and caused the curve to deviate from the initial reported value recorded immediately following unloading, represented by the black line. However, after a short period of time (approximately 10 hours), the oscillations appear to have found a saturation point, stabilizing in a horizontal profile. In this particular stage, the load removal seemed not to have such a pronounced effect on the material, given that the strain drop at unloading was substantially lower than in the previous ones. The level of noise also makes it difficult to distinguish the strains developed under load from those developed after load removal.

In order to see whether the absence of anelastic recovery had an impact on creep deformation, the secondary strain rates after each unloading were determined, in order to be compared to the initial secondary strain rate (before the load removals). The secondary strain rate of the creep control test was found to be 2.5×10^{-10} s^{-1}, a very close value to the initial secondary strain rate of the creep transient test. Results for this are presented in Table 6.4 and plotted in Figure 6.19 (the R^2 factor of the linear fit being in the range 0.8 – 0.85).

Table 6.12 - Secondary strain rates from the long-term creep transient tests.

Stage	Strain rate [1/hr]	Strain rate [1/s]
Initial	9.00E-07	2.50E-10
After 1st unloading	5.00E-07	1.39E-10
After 2nd unloading	5.00E-07	1.39E-10
After 3rd unloading	3.00E-07	8.33E-11
After 4th unloading	3.00E-07	8.33E-11

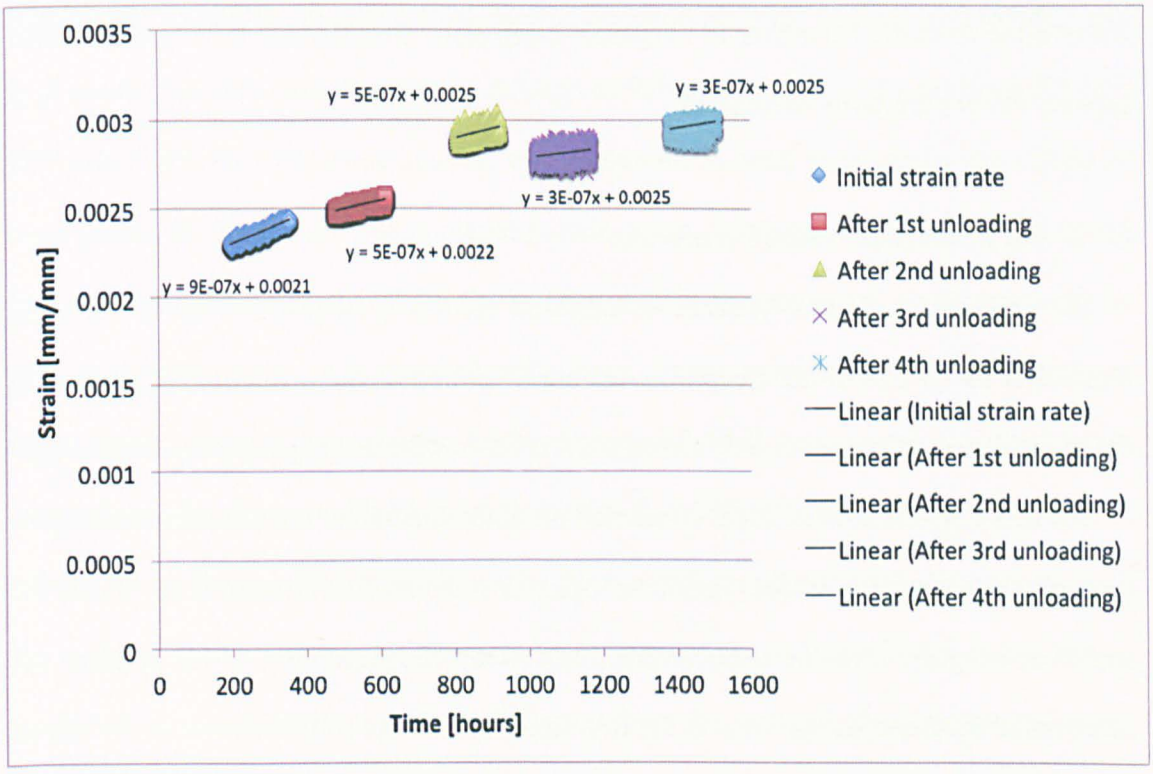

Figure 6.19 - Plot of the strain rate linear fit for each stage in Table 6.4.

The results showed that reductions in the secondary creep rate were alternated with maintenance of a constant value, as the unloading stages were being added. While it would be expected that the secondary strain-rate would remain unaltered, given that no anelastic recovery was reported, the explanation for these findings may reside in the microstructure of the ODS steel. It is not clear, judging from all the tests, whether another primary creep occurs after reloading, but it may be speculated, from the behaviour in the transient stages, that the reductions in the secondary strain rate are related to the effectiveness of the oxides in pinning dislocations, while the constancies observed would be associated to the resistance of grains in suffering creep deformation under load, meaning that work hardening is not actively taking place inside grains, either due to pinning or to unfavourable directions of the main possible slip systems. The study of these evidences is the subject of the next section.

It is relevant to mention that, although deforming continuously for a prolonged period of time, the tests of this second series were not taken to rupture. The purpose was to

observe the anelastic behaviour in long-term creep tests. Besides, due to time constraints, rupture was not primarily considered.

6.7 *In situ* neutron diffraction creep test

The previously observed absence of anelastic recovery, associated with the changes induced in the profile of the creep transient curve, prompted the investigation to examine the MA956 steel microstructure. Neutron diffraction was the technique chosen for the task.

The first step of the experiment concerned the determination of the appropriate d_0 lattice spacing, the stress-free lattice parameter used as reference, with regards to which the strains developed during the creep transient test would be measured. For this purpose, the same round specimen design used in the first series of test was held horizontally, by one of its threaded ends, on the Instron hydraulic test rig, in a similar fashion as the assembly for the creep test, except for the absence of applied load, since the opposite end of the specimen was free (cantilever configuration), as depicted in Figure 6.20:

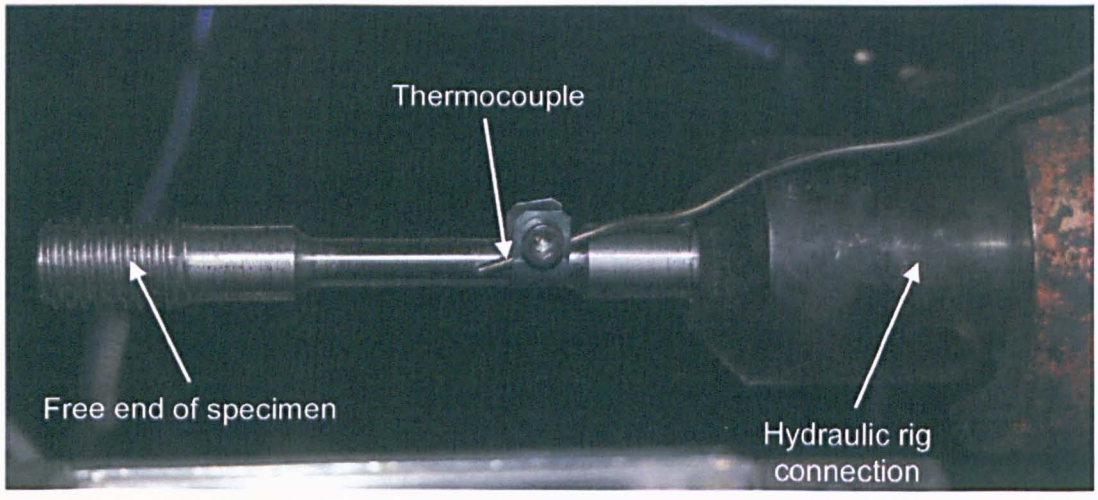

Figure 6.20 – Specimen configuration during first experiment.

The specimen was then heated up to 650°C, the temperature at which the creep test was carried out, using the radiative furnace coupled to the hydraulic rig. Neutrons continuously measured the d_0 spacings, from room temperature to 600°C, in steps of 100°C, and, then,

from 600°C to 650°C. Once the final desired temperature level was reached (650°C) and kept steady, the specimen was rotated in steps of 90° and, at each of the rotations (0°, 90°, 180° and 270°), the interplanar spacing was measured, in order to minimize the effects of large grains, strong texture and potential pseudo-strain problems. Large grains and strong texture promote similar contributions, as they reduce the statistical significance of the probed microstructure. In a material with large grains, a lower number of grains are investigated, whereas a strongly textured material will not sample random grain orientations. For these problems, measurements in different directions may reduce their effects. As for the pseudo-strains, they arise from partial immersion of the gauge volume in the material to be studied. As a consequence, part of the information is either lost or incorrectly associated with the signal diffracted from the material, thus introducing errors in the calculated strains. In order to mitigate this occurrence, the collimators were carefully positioned and set to produce a gauge volume of 4mm x 4mm x 4 mm in the specimen (whose diameter was 6 mm). Special attention is recommended when adjusting the collimators, in order to avoid deterioration of the shape of the gauge volume or a misplacing that could result in a partial immersion.

The average of the described rotations was taken and compared with each individual rotation measurement, to check for representativeness. Moreover, microstrain variations were determined using the lattice spacing of each rotation with regards to the calculated average, which was used as a strain-free lattice parameter. These microstrains also had their average determined, in order to assess how acceptable the strain free lattice parameters determined via average of rotations would be. Figures 6.21a and b illustrate the evolution of the average lattice stress-free parameter, a_0, with temperature, from room temperature, measured as 22°C, to 650°. The black spot on the plot for each detection bank represents the calculated average of four rotations at 650°C. As expected, the lattice spacings are increasing continuously with temperature:

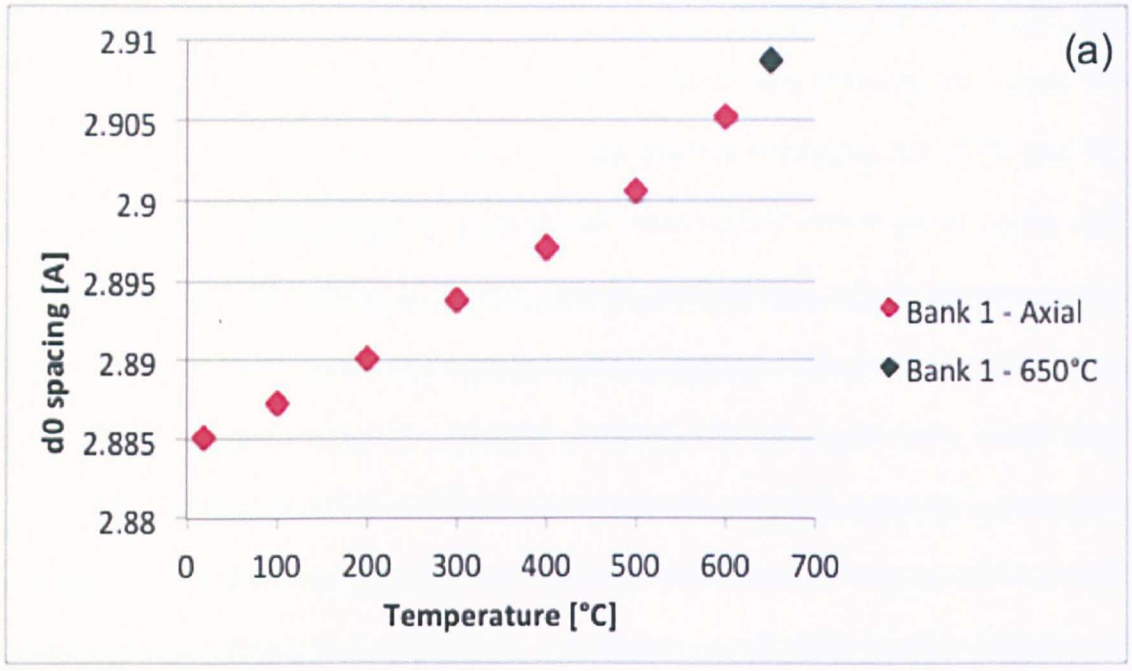

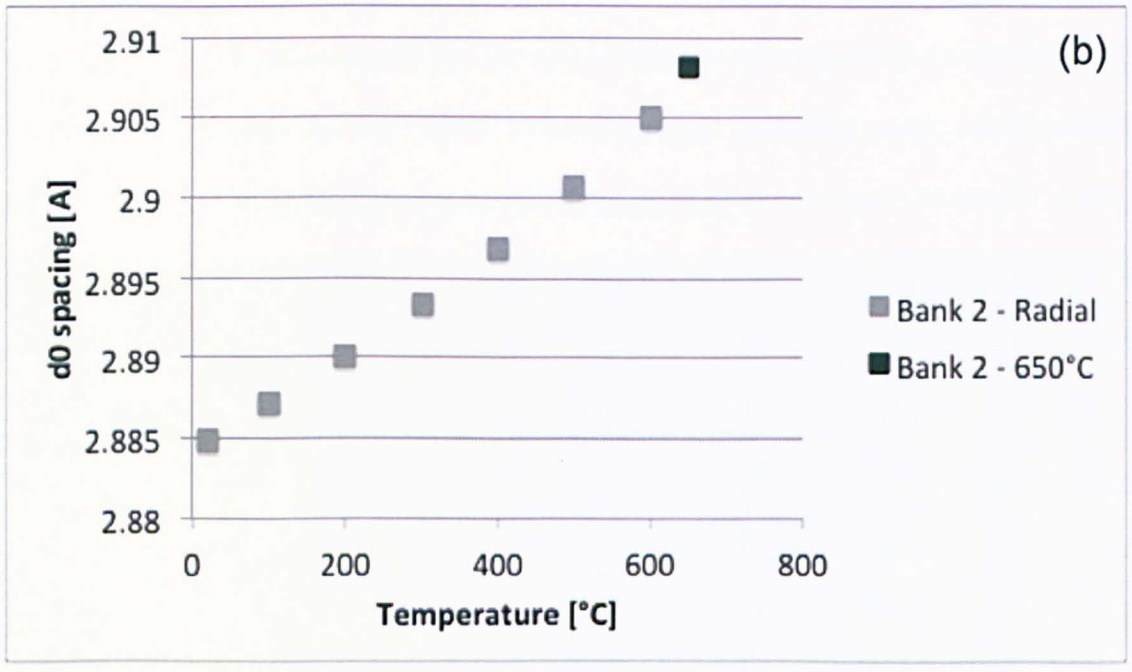

Figure 6.21 - Evolution of lattice spacings with temperature for (a) Bank 1 - axial strains and (b) Bank 2 – radial strains.

Figures 6.22a and 6.22b show the variations in the apparent microstrains resulting from the differences in the average lattice parameter from each of the considered rotations to the calculated average of the four rotations. The averages of the apparent microstrains shown in these figures were determined, yielding the values of -2.78×10^{-11} and -5.55×10^{-11},

which are practically zero. The use of the average lattice parameter, then, is justified on the basis that its use minimizes the value of the reference microstrain.

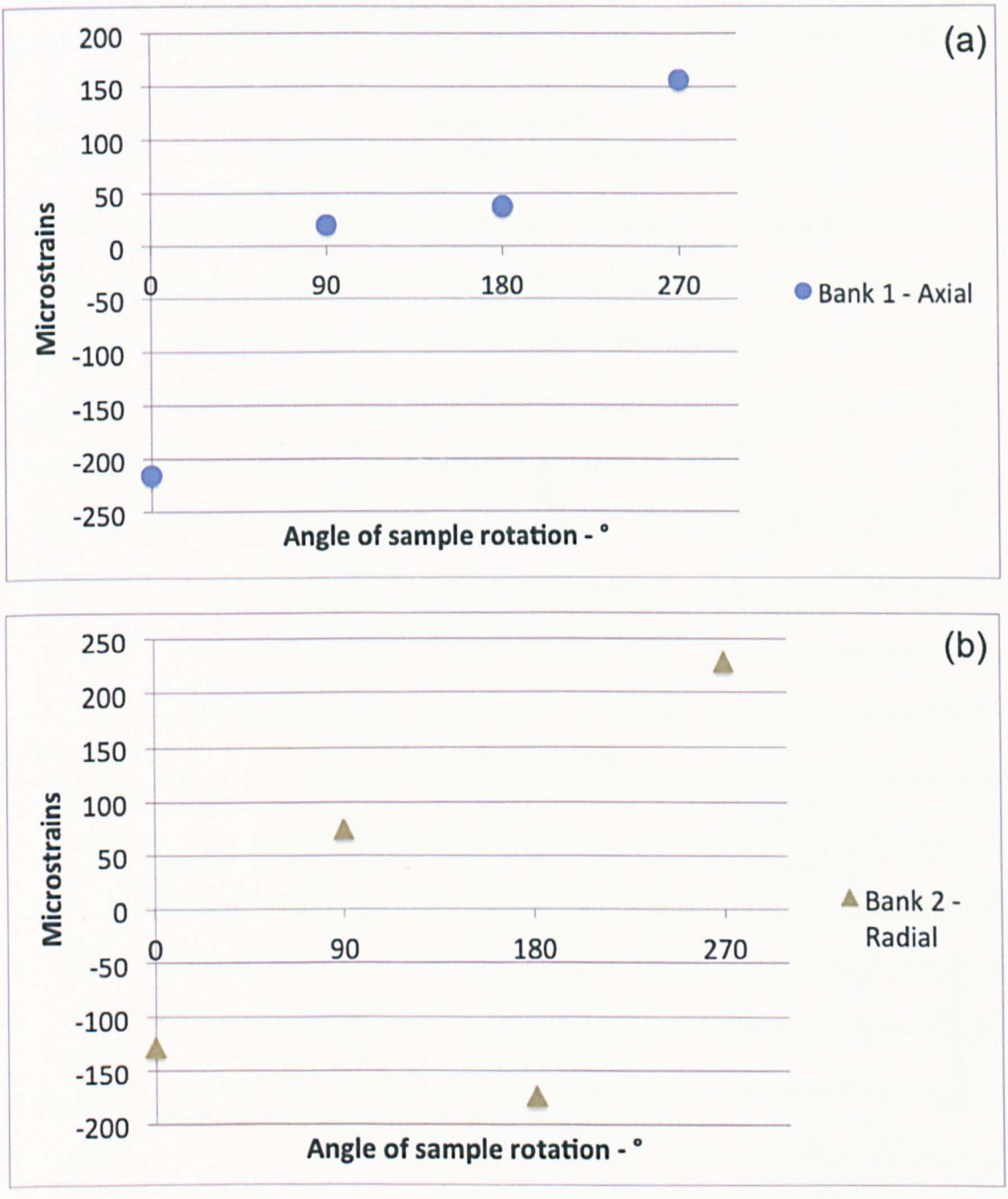

Figure 6.22 - Microstrains calculated for each rotation using the corresponding lattice parameter and, as reference, the average of the four rotations (a) axial and (b) radial.

A similar procedure was adopted for the single-peak analysis, in which each grain family of some low index orientations of the bcc structure had their variations in microstrains assessed and the average of the microstrains arising from the four rotations

was calculated. These values also present the same order of magnitude of the average lattice parameter. Table 6.5 summarizes the average microstrain for each grain family. Figures 6.23a and b show the variations according to the family orientation.

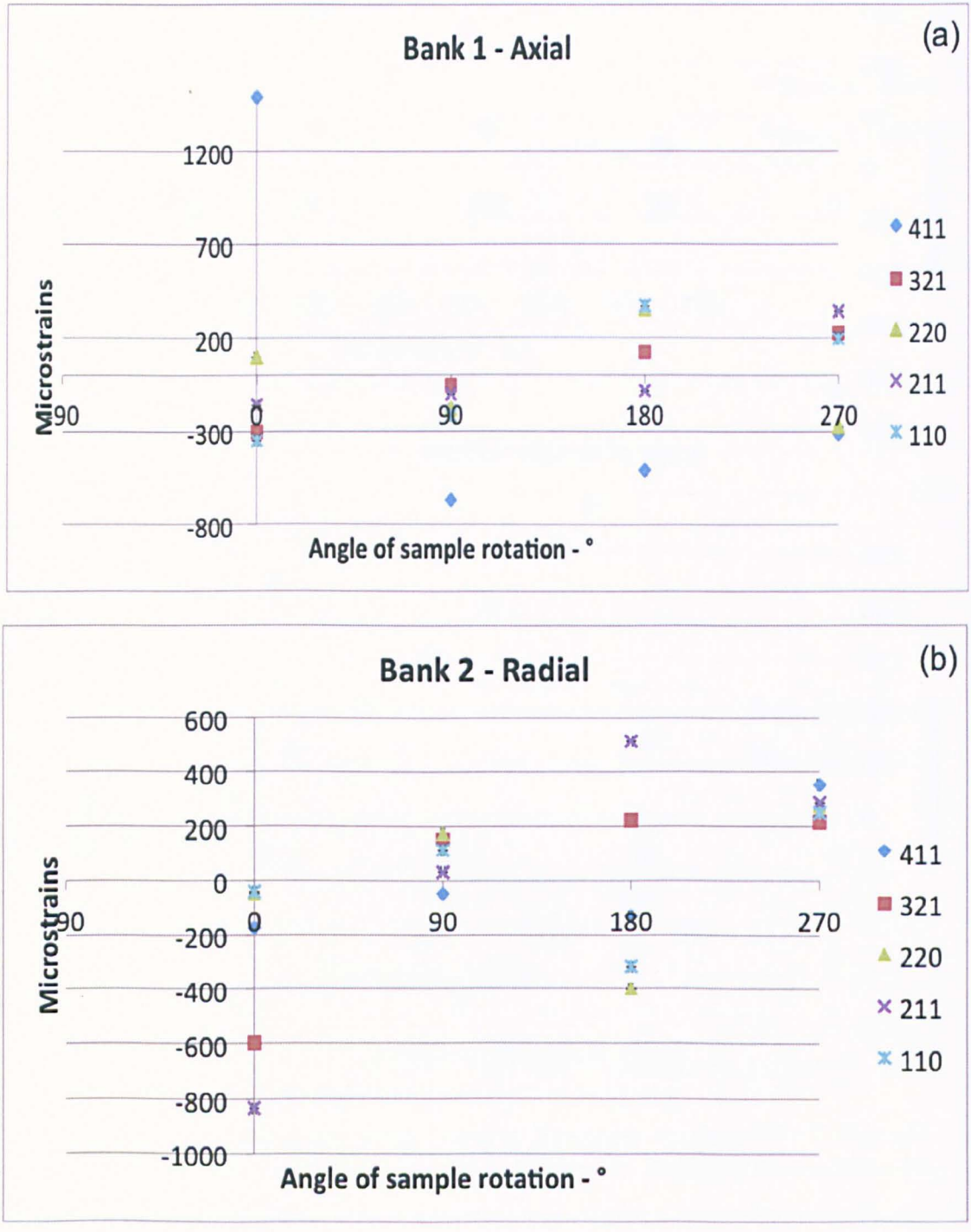

Figure 6.23 - Microstrains in each family orientation calculated from the lattice at a particular rotation and the average of the four rotations (a) axial and (b) radial.

Table 6.13 – Microstrains determined as the average four rotations in each grain family.

Bank/Family	{411}	{321}	{220}	{211}	{110}
Bank 1 - Axial	2.78×10^{-11}	8.33×10^{-11}	2.77×10^{-11}	5.55×10^{-11}	1.11×10^{-11}
Bank 2 - Radial	-8.33×10^{-11}	2.77×10^{-11}	2.77×10^{-11}	2.78×10^{-11}	-1.39×10^{-10}

Given that, in all cases, the value of the average of the lattice parameters of the four rotations was close to the individual value of each of these four readings, and that the average microstrain calculated from the differences between each rotation and its respective average yielded a negligible value, close to zero, the average of the four values of strain-free lattice spacings was adopted as a reference for calculation of lattice and interplanar spacings during creep deformation in the second experiment.

The principal experimental investigation consisted of an *in situ* creep test, carried out at 650°C, under an applied stress of 150 MPa upon the MA956 specimen (the same from the previously measured d_0 experiment), which was extracted with its axis parallel to the extrusion direction (the longitudinal axis of the bars). This specimen was crept for 24h, in order to make sure the secondary creep stage was reached, then fully unloaded and kept in this condition for 8 hours, a reasonable time interval to observe anelastic recovery, if present. At the end of these hours, which marked the first load transient, the specimen was reloaded to 150 MPa and further crept, for a second similar period. The evolution of internal strains in differently oriented grain families (crystallographic orientation defined with regards to the longitudinal direction, which is coincident with the loading direction) was determined by neutron diffraction measurements, taken at regular intervals of approximately 30 minutes. After approximately 64 hours of testing, at the end of a second cycle of 24 hours of creep deformation and another 8 hours of unloading stage, the test was finalized.

The test apparatus was similar to the one used in the first experiment and in the *in situ* creep experiment for the 316H steel. The specimen was inserted into the Instron hydraulic stress rig by connecting its threaded ends to the machine load train and the whole set was

positioned at 45° to the neutron beam. A schematic of the assembly, as well as the experimental set up, is shown in Figures 6.24 (a) and (b). An N-type thermocouple registered temperature within ±2°C and an Instron 2632-054 extensometer (12.5 mm gauge length and 0.0001 % accuracy) recorded the creep strains. The clamping of the devices is shown in Figure 6.25.

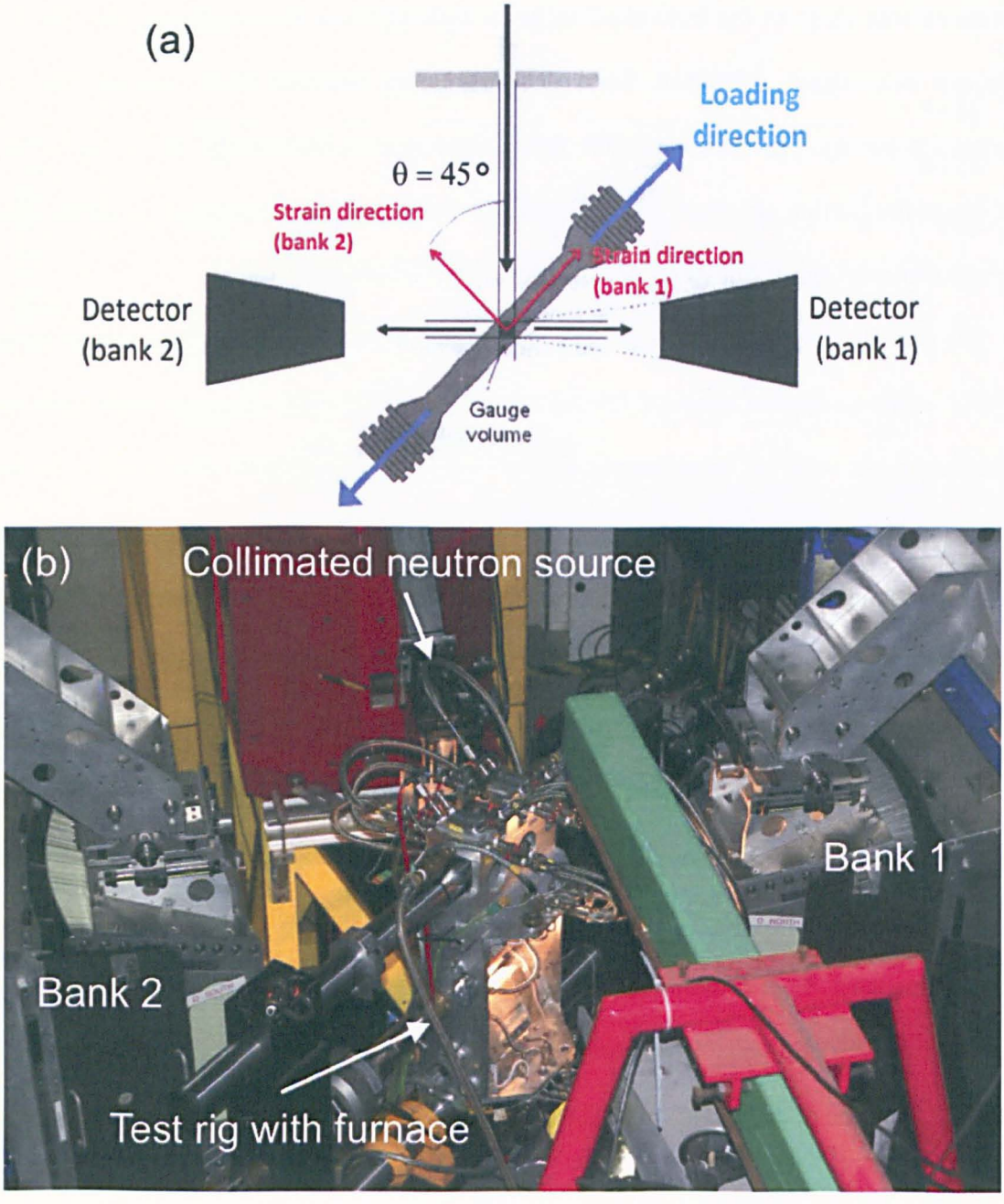

Figure 6.24 - Schematic of the neutron diffraction measurements (a) and correspondent setup (b).

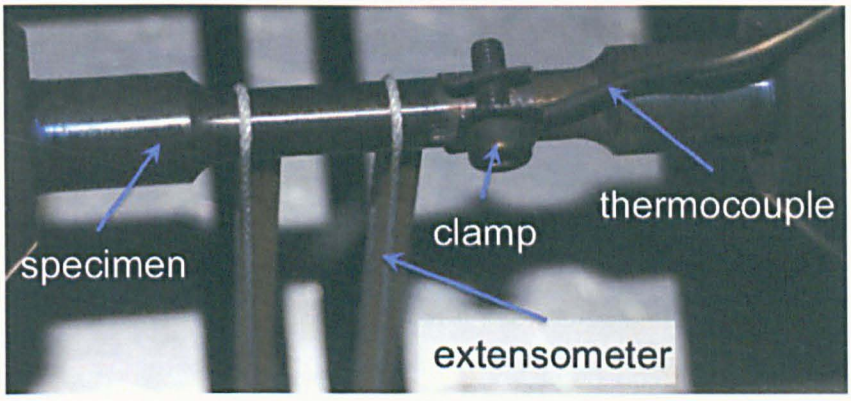

Figure 6.25 - Clamping of the extensometers and thermocouple onto the specimen.

Neutron diffraction measurements were carried out using, again, Rietveld analysis, for the average lattice deformation, and single-peak fitting, for each grain orientation considered. Due to the nature of the microstructure, it was difficult to keep track of the same intended peaks on the time-of-flight spectrum. However, four reflections of the *bcc* structure, namely, the {321}, {222}, {211} and {110} were continuously monitored throughout the test. Attention was concentrated on the axial direction, along which the columnar grains are elongated. The results presented next are for this direction. Measured microstrains along the creep test are presented in Figure 6.26.

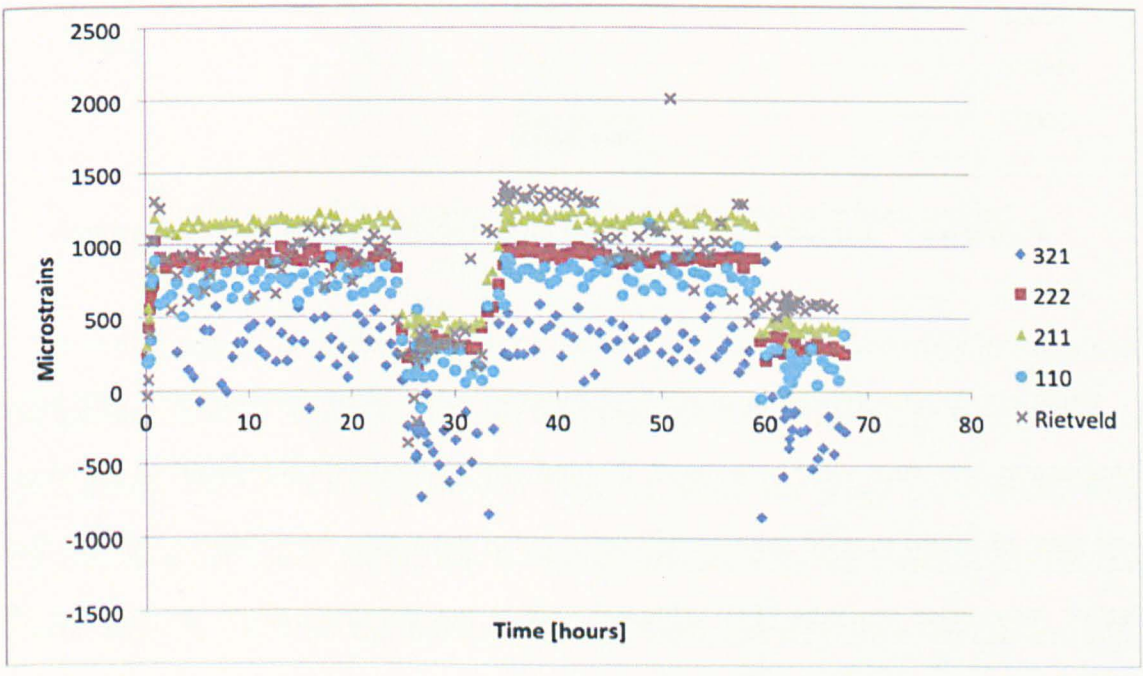

Figure 6.26 – Microstrains along the axial direction for each grain family (and average lattice) under creep.

Although a trend of resistance to creep deformation is suggested by the predominantly tensile data plots, some corrections are needed, in order to eliminate the effects of the virtually instantaneous elastic strains when load is suddenly removed from the specimen or applied on it. Four such corrections were made: two related to the instantaneous increase in strain experienced by the material when it is firstly loaded and when load is reapplied after the first transient; and other two related to the dip in strain when 150 MPa of stress is removed, at the unloading operation. With these step implemented, the above plot evolves to the one presented in Figure 6.27 below.

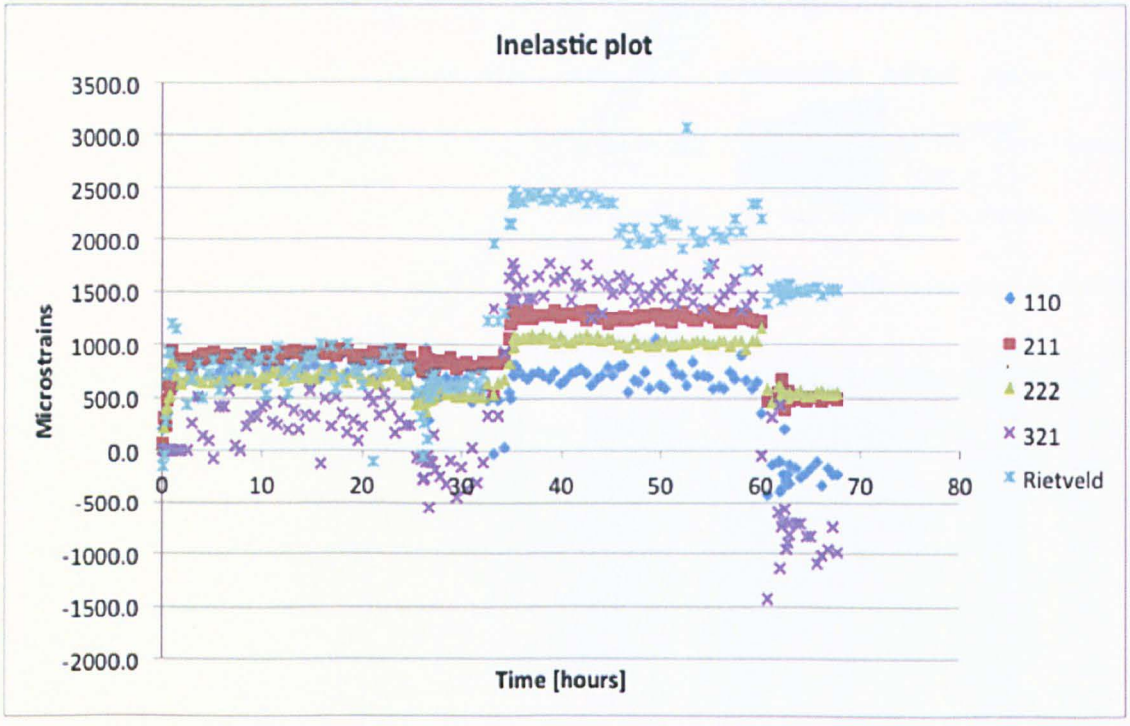

Figure 6.27 – Datasets after removal of the instantaneous strains on loading and unloading of the sample.

Other corrections, related to possible changes in solute atom concentration, with high temperature exposure, were considered. If significant precipitation is induced, as the creep test goes on, atoms in solid solution will come out of the matrix, by diffusion, reducing the lattice interplanar spacings [18]. Although this is not expected, given the absence of significant amounts of precipitation-forming elements in the MA956 composition, the procedure was done by selecting a grain family from the dataset already corrected by the

subtraction of elastic strains, assuming that that the changes observed in the crystal plane spacings are due to changes in solute atom concentration only. For this investigation, the {222} was selected, since it was the dataset that presented least variation, as seen in Figure 6.27.

The {222} dataset was set as a constant baseline, so that the relative differences between this and each of the remaining grain family datasets could be determined, so that the new microstrains represent only the effects of application or removal of load. Figure 6.28 shows the resulting plot after all the corrections.

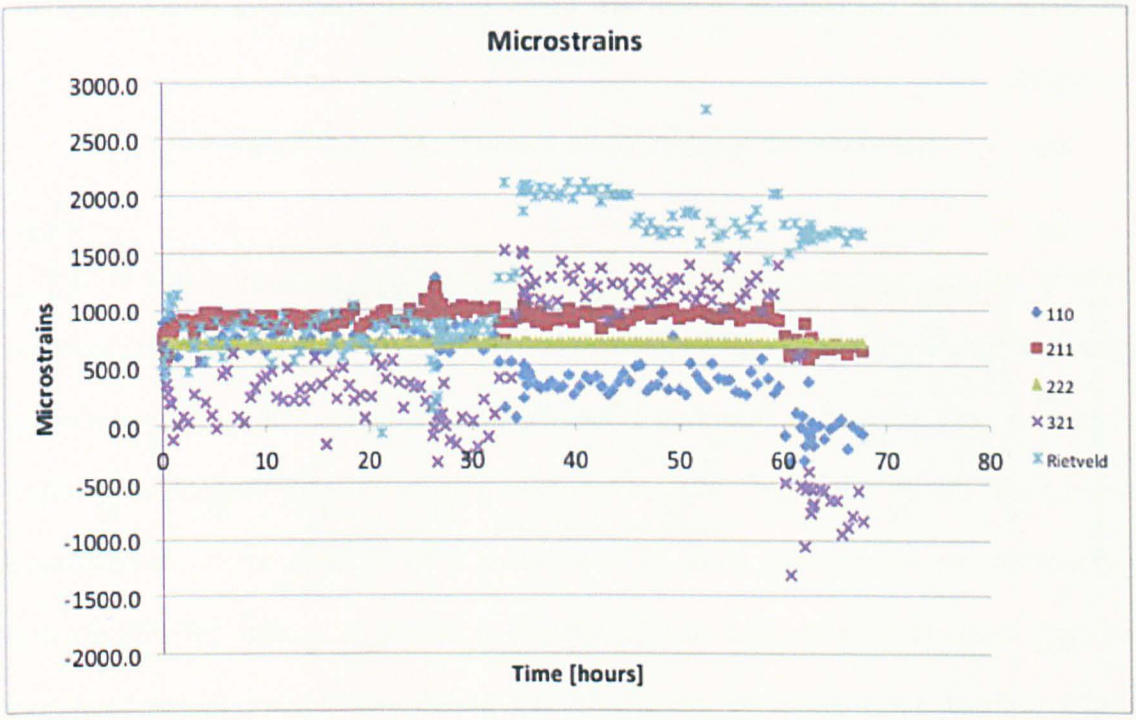

Figure 6.28 – Microstrains after all the corrections have been applied.

From the original microstrains, without any correction, the sudden drops in stress and the loading/reloading steps could be used to estimate the diffraction elastic moduli of each grain family. The results are presented in Table 6.6, which also brings a comparison with the correspondent values for the elastic moduli obtained from the literature for the *bcc* crystal structure [19]. With the diffraction elastic moduli and the microstrain datasets from Figure 6.28, the intergranular stresses between differently oriented grains could finally be calculated and plotted, as in Figure 6.29.

Table 6.14 - Comparison between the calculated elastic constants and those from literature [19].

Diffraction Elastic Moduli - GPa				
E {hkl}	E {321}	E {222}	E {211}	E {110}
Calculated	200.5	325.4	228.3	205.6
From literature	210.5	272.7	210.5	210.5

The percentage difference between the values in table 2 were 4.7%, 19%, 8.5% and 2.3%, respectively, for the {321}, {222}, {211} and {110} families. The high value for the {222} is understandable, since the strains in this dataset present less variation and, as a consequence, the calculations, which are based in differences, have their uncertainty increased.

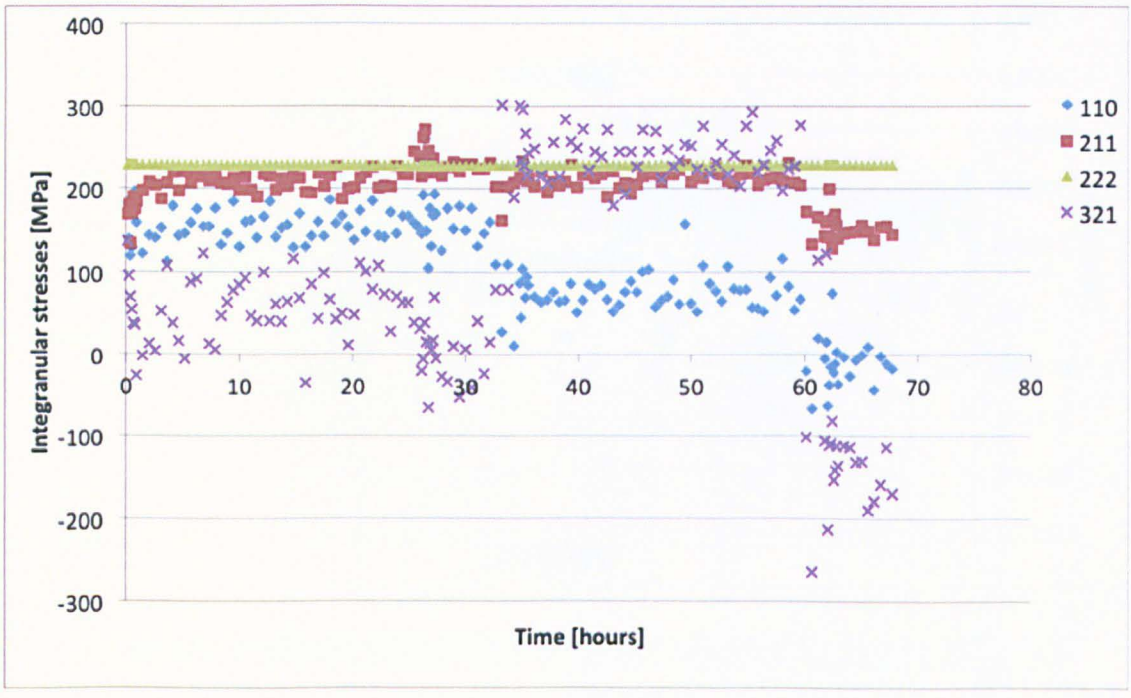

Figure 6.29 - Intergranular stresses calculated from the microstrains plotted in Figure 6.28, for each grain orientation considered.

Simultaneously to the neutron measurements, macroscopic creep strains were recorded and plotted, as seen in Figure 6.30. The total creep strains were very low and the shape of the curve at the unloading stage suggests absence of anelastic recovery, since a flat portion characterizes it.

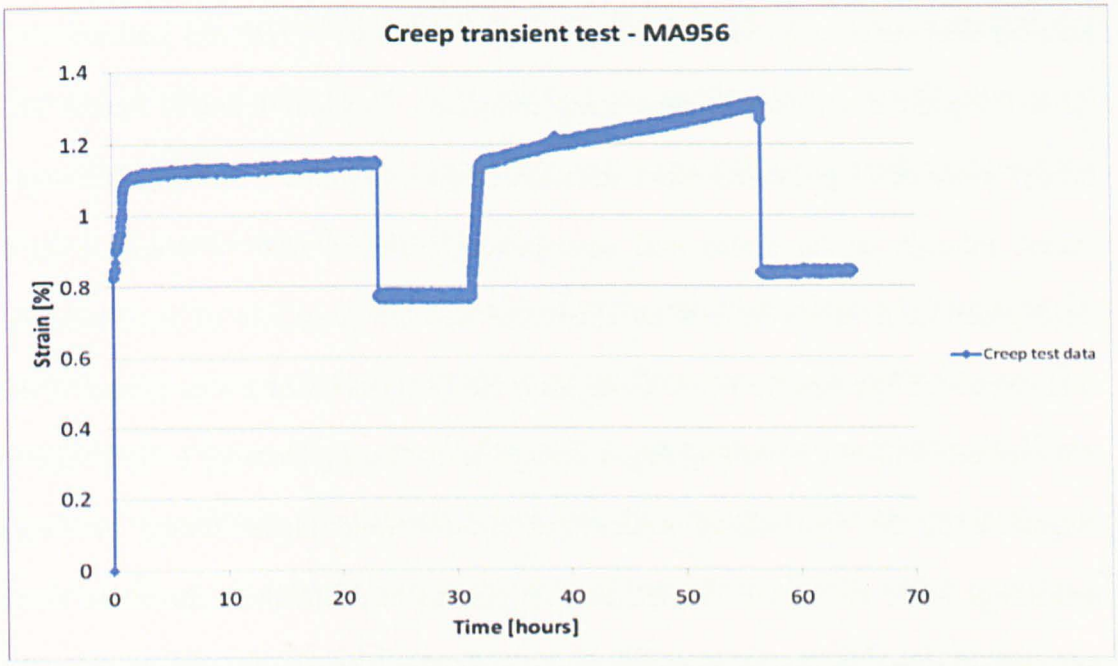

Figure 6.30 – Macroscopic creep strains of the *in situ* test.

This *in situ* experiment presented several noteworthy features regarding the MA956 behaviour under creep transient conditions. To start with, the predominantly tensile nature of the intergranular datasets provides an interesting indication that, overall, the material is fulfilling its intended role, by resisting creep deformation. While this should be a general characteristics of the class of ODS steels, most of these materials do not show creep strength [25–28]. Indeed, as shown in Figures 6.26 to 6.28, most of the grain families developed tensile microstrains during the experiment, including some families where plastic deformation was expected to occur, such as {110} and {211}, which are traditionally the active systems for plastic strain in *bcc* structure, even though its degree of anisotropy is not pronounced, due to the fact that *bcc* is not a close-packed structure [20].

For the MA956 ferritic steel, the average lattice straining was tensile during the test, a behaviour also exhibited by some grain families, namely the {222} and {211}.

As seen in Figure 6.29, intergranular stresses in the {110} were gradually less tensile with time, and only at the second unloading stage were compressive intergranular stresses developed. This seems to suggest that grains in this orientation were, initially, strongly

resisting creep deformation and, as time passed, the resistance offered was gradually lower, up to the point where they became creep compliant. This was followed by the {321} family, which developed compressive stresses of higher magnitudes during both unloading stages, although tensile strains (and correspondent stresses) were observed during the loading period. It seems there is an alternation between resistance to deformation and compliance for this family. When under load, the {321}-oriented grains appear to resist deformation; while the unloading stages induced an increasing tendency to deform, as the magnitude of the compressive strains and stresses were higher during the second unloading. While this may be associated with pinning of dislocations during the loading periods alternated with the non-conservative recovery process of climb during the unloading stages, further studies are required to elucidate this behaviour, for which no reasonable explanation could be inferred from the investigations carried out.

Another point that deserves consideration, believed to be a consequence of the intergranular behaviour described above, is the small macroscopic strain variation, resulting in low creep rates. The cause for this behaviour might be associated with the basic physical mechanisms behind ODS steel deformation; it can be speculated that the relatively homogeneous distribution of nanoparticles may be effectively pinning the dislocations, so that the test stress level is not capable of ensuring significant detachment of dislocations from the oxides. These low strains found when deforming ODS steels are strong indicators of the possibility of detachment-controlled-creep, for which these results would be expected.

Once more, anelastic recovery was seen to be absent, in agreement with the previous creep tests on the MA956. The strain readings during the unloading stage were constant, as seen from the flat plateau formed by the data. This behaviour can be associated to the creep deformation explained above: since little deformation is taking place during creep, with most dislocations hindered in those planes expected to be part of active slip systems; and, moreover, considering detachment as an active creep regime, which is a reasonable

assumption for ODS steels [5, 21–23], the potential for anelastic recovery is very low, due to reduced driving forces for it. It is relevant to mention that anelastic strains are macroscopic just like creep strains, so an extensometer can easily detect and measure them, when they are presented by the material.

A relevant point worth considering is related to the procedure adopted in data analysis, according to which corrections for change in solute atom concentrations are applied. This phenomenon may not be taking place in this case. A comparison between Figures 6.27 and 6.28 serves as evidence. The datasets before and after this correction are practically the same for most of the datasets (except the one deliberately modified), which provides a strong argument for the idea that precipitation in this steel is negligible (or, at least, not intense).

Finally, it is timely to acknowledge the facts that impose limitations on the scope of the analysis. If on one side, the neutron diffraction *in situ* experiment sheds new light onto the creep transient behaviour of the MA956, providing answers to the absence of anelastic response, on the other side, it showed the necessity of further investigations for a complete explanation, based on visual information regarding the deformation processes taking place inside grains, which would involve observing how dislocations interact with the microstructural features of the steel. Furthermore, there is a considerable amount of scatter in the dataset. Although the data were meaningful in the context of the whole investigation of the MA956, further similar tests and repetition of some of the experimentation are needed, in order to confirm the reported pattern of intergranular behaviour.

6.8 Summary

Microstructural examinations revealed columnar grains, elongated in the extrusion direction, with pronounced fibre texture for the MA956. Fine Y-Al-O oxides were distributed throughout the matrix, with an average size of 34 nm.

Room temperature tensile tests showed a predominantly brittle material, with a large variation in the yield and ultimate strengths, as well as in the Young's modulus. These different levels seem to suggest the influence of different predominant fibre textures.

High temperature tensile tests showed that, at 650°C, the behaviour of the MA956 steel is completely different, with significant levels of ductility and a remarkable loss of strength.

Creep transient tests showed anelastic recovery to be absent in all tested samples.

The *in situ* neutron diffraction measurements of intergranular stresses during a creep transient experiment indicated that most of the grains of the MA956 are resisting creep deformation during most of the test, given the predominantly tensile nature of those stresses.

6.9 References

[1] A. Czyrska-Filemonowicz, M. Wróbel, B. Dubiel, and P. J. Ennis, "Transmission Electron Micriscopy study of dislocation-dispersoid interaction in deformed Incoloy MA956," *Scr. Metall. Mater.*, vol. 32, no. 3, pp. 331–335, 1995.

[2] A. Wasilkowska, M. Bartsch, U. Messerschmidt, R. Herzog, and A. Czyrska-Filemonowicz, "Creep mechanisms of ferritic oxide dispersion strengthened alloys," *J. Mater. Process. Technol.*, vol. 133, no. 1–2, pp. 218–224, Feb. 2003.

[3] E. L. Dubiel, M. Wróbel, P. J. Ennis, and A. Czyrska-Filemonowicz, "Microstructure of Incoloy MA956 after low and high temperature deformation," *Scr. Mater.*, vol. 37, no. 8, pp. 1215–1220, 1997.

[4] K. Wolski, F. Thévenot, and J. Le Coze, "Effect of nanometric oxide dispersion on creep resistance of ODS-FeAl prepared by mechanical alloying," *Intermet. A*, vol. 4, pp. 299–307, 1996.

[5] J. Rösler and E. Arzt, "A new model-based creep equation for dispersion strengthened materials," *Acta Metall. Mater.*, vol. 38, no. 4, pp. 671–683, 1990.

[6] S. Metals, "High performance alloys." [Online]. Available: http://www.specialmetals.com/assets/documents/alloys/inconel/inconel-alloy-718.pdf. [Accessed: 06-Feb-2014].

[7] R. L. Klueh and D. R. Harries, *High-Chromium Ferritic and Martensitic Steels for Nuclear Applications*. American Society for Testing and Materials, 2001.

[8] J. R. O. Leo (2014) *Heat Treatment of ferritic ODS steel MA956.* Unpublished research, The Open University

[9] H. K. D. H. Bhadeshia, "Recrystallization of practical mechanically alloyed Iron-base and Nickel-base Superalloys," *Mater. Sci. Eng. A*, vol. 223, pp. 64–77, 1997.

[10] W. Betz, R. Brunetaud, D. Coutsouradis, H. Fischmeister, T. B. Gibbons, I. Kvernes, Y. Lindblom, J. B. Marriott, and D. B. Meadowcroft, Eds., *High Temperature Alloys for Gas Turbines and Other Applications*. D. Reidel Publishing Company, 1986.

[11] J. Chao, J. L. González-Carrasco, and C. Capdevilla, "Influence of Annealing at 1100°C and 475°C on the Mechanical Properties at Room Temperature of an Iron Base ODS Alloy," *ISIJ Int.*, vol. 47, pp. 1214–1220, 2007.

[12] S. Noh, R. Kasada, and A. Kimura, "Solid-state diffusion bonding of high-Cr ODS ferritic steel," *Acta Mater.*, vol. 59, no. 8, pp. 3196–3204, 2011.

[13] J. Chen, P. Jung, M. A. Pouchon, T. Rebac, and W. Hoffelner, "Irradiation creep and precipitation in a ferritic ODS steel under helium implantation," *J. Nucl. Mater.*, vol. 373, no. 1–3, pp. 22–27, 2008.

[14] J. Chao and J. L. González-Carrasco, "Influence of cooling rate on room temperature tensile behaviour of thermally oxidised MA956," *Mater. Sci. Technol.*, vol. 14, no. 5, pp. 440–444, 1998.

[15] Z. Oksiuta, P. Mueller, P. Spätig, and N. Baluc, "Effect of thermo-mechanical treatments on the microstructure and mechanical properties of an ODS ferritic steel," *J. Nucl. Mater.*, vol. 412, no. 2, pp. 221–226, 2011.

[16] M. E. Abd El-Azim, "Effect of dynamic strain ageing on the deformation behavior of Incoloy alloy MA956," *Mech. Mater.*, vol. 25, no. 4, pp. 255–261, May 1997.

[17] "BS EN ISO 204:2009 Metallic materials - Uniaxial creep testing in tension - Method of test." 2009.

[18] M. R. Daymond and P. J. Bouchard, "Elastoplastic Deformation of 316 Stainless Steel Under Tensile Loading at Elevated Temperatures," *Metall. Mater. Trans. A*, vol. 37, no. June, pp. 1863–1873, 2006.

[19] M. T. Hutchings, P. J. Withers, T. M. Holden, and T. Lorentzen, *Introduction to the Characterization of Residual Stress by Neutron Diffraction.* CRC Press, 2005.

[20] G. E. Dieter, *Mechanical Metallurgy*. McGraw-Hill, 1986.

[21] C. Zakine, C. Prioul, and D. François, "Creep behaviour of ODS steels," *Mater. Sci. Eng. A*, vol. 219, no. 1–2, pp. 102–108, 1996.

[22] E. Arzt, "Creep of Oxide-dispersion Strengthened," *Encyclopedia of Materials: Science and Technology*. Elsevier, pp. 1800–1806, 2001.

[23] J. Malaplate, F. Mompiou, J. L. Béchade, T. Van Den Berghe, and M. Ratti, "Creep behavior of ODS materials: A study of dislocations/precipitates interactions," *J. Nucl. Mater.*, vol. 417, no. 1–3, pp. 205–208, 2011.

[24] B. Magazine, "Bar peeling is heavy-duty machining in every respect," 2012. [Online]. Available: http://www.boehlerit-magazine.com/en/drehschaelen-ist-schwerzerspanung-in-jeder-hinsicht/. [Accessed: 31-Jul-2015].

[25] A. Steckmeyer, V. H. Rodrigo, J. M. Gentzbittel, V. Rabeau, and B. Fournier, "Tensile anisotropy and creep properties of a Fe–14CrWTi ODS ferritic steel," *J. Nucl. Mater.*, vol. 426, no. 1–3, pp. 182–188, 2012.

[26] A. Zeybek, S. P. Barroso, K. B. Chong, L. Edwards, and M. E. Fitzpatrick, "Incorporation of Y2O3 Particles into 410L Stainless Steel by a Powder Metallurgy Route," *J. Mater. Eng. Perform.*, vol. 23, no. 6, pp. 2120–2130, Apr. 2014.

[27] A. Alamo, V. Lambard, X. Averty, and M. H. Mathon, "Assessment of ODS-14%Cr ferritic alloy for high temperature applications," *J. Nucl. Mater.*, vol. 329–333, pp. 333–337, 2004.

[28] R. W. Evans, J. A. Preston, B. Wilshire, and E. A. Little, "Creep and creep fracture of an oxide-dispersion-strengthened 13% chromium ferritic steel," *Mater. Sci. Eng. A*, vol. A167, pp. 65–72, 1993.

Chapter 7 – Discussions

7.1 Introduction

Although each of the previous chapters has discussions embedded in the presentation of results, this chapter collates the overall points, focussing on comparisons, differences of behaviour for the investigated materials and details that have emerged from the investigations.

7.2 Anelasticity in 316H and MA956 steels

The multi-technique approach adopted for the investigations on anelasticity, although not completed for the MA956 steel, provided a means for comparison between the materials, from where inferences on the behaviour could be made. 316H and MA956 have completely different responses to creep transients, determined not only by their microstructures, but also, by the transformations allowed by their chemical compositions during the prolonged exposure to the high temperatures in creep.

For the 316H, it has been previously reported that creep deformation induces changes in the state of precipitates [1]. This had a very important consequence to the development of internal stresses throughout creep transient deformation. In the present study, the model of back and internal stresses suggested by Ahlquist and Nix [3] as viable to be applied in creep deformation with a drop in stress and developed by Mughrabi [2] was successfully adapted to correlate the anelastic response to the development of intergranular and intragranular stresses associated, ultimately, with the changes in dislocation arrangements in the grains. After being successfully deployed to explain tensile deformation of the Type-316 steel [4] and its cyclic straining behaviour [5, 6], the model conveniently described (from the phenomenological point of view), for the first time, anelasticity resulting from heterogeneous dislocation structures formed and grown around precipitates. It is not a really surprising result, since its origins are in the heterogeneity of dislocation distribution.

But it is relevant, in the sense that it has shown to be suitable in the representation of physical mechanisms behind the creep transient deformation.

Another fundamental point of the model concerns the information capable of being provided: it helped in backing up the idea that the introduction of anelasticity will decrease creep ductility, thus increasing creep-rupture life; but it went beyond, to provide quantitative information on the potential of recovery of the material. The capability of describing the dynamic nature of the back stresses as the driving force for the anelastic recovery also provided a sensible explanation for the saturation of anelasticity, as the number of transient cycles increases.

However, it is also important to acknowledge the limitations of the scope with which the model was applied. The study was very successful in providing estimations of the variations of intergranular and intragranular back stresses for the 316 grade of stainless steel, even though the model is subject to several sources of uncertainty, and is most likely to describe well the behaviour of alloys with low stacking fault energies. Materials with a high SFE's, such as aluminium, are capable of being much readily plastically deformed, which would result in a different intergranular response as well as in more elaborated intragranular arrangements, such as cells and subgrains, for which TEM quantifications would be more difficult. In every case, an adaptation might be required, in order to take into account microstructural features and transformations. For example, if the steel was crept at 550°C, precipitate formation would be different, and the description of mechanisms would have to be adapted for this condition. Also, the tests worked, once more, with events concentrated on the secondary creep stage, the most relevant for creep deformation. A description of anelastic effects in primary and tertiary stages of the 316H is still not addressed and modelling this would also require adaptation, in order to make use of the predominant influences and mechanisms in these stages.

As for the experimental approach, an accurate estimation of the stresses requires accurate measurement of the dislocation densities; therefore, the intercept method should have been applied to a more complete representation of the dislocation network in each TEM field of view, obtained by overlapping images in each TEM field of view to form a composite tracing. Only then, the images should be subjected to the procedures for counting the intersections. Likewise, the use of STEM could provide another means of improving the accuracy of the statistical analysis, as seen in Norfleet et al. [18]. With the use of a highly convergent electron beam, it is possible to mitigate the problem of dislocation invisibility and even eliminate the need for creating an assembly of different overlapped images taken with different reflections. This procedure would be more labour-intensive, but more accurate than the method used in this work.

A fourth point that should be emphasised, still regarding the scope of the model, is that, naturally, it is valid for dislocation-based processes. The back and effective stresses, as well as the measurable intergranular stress evolution, stem from plastic deformation processes associated with dislocation generation and motion. However, anelasticity is also known to occur in conditions of diffusion-based creep, as modelled by Lee and Raj [7] for polycrystalline materials. While it is recognisable that creep tests in these conditions may be very long, which is impractical for most research programmes, a full understanding of anelastic response would have to experimentally address this regime as well.

Finally, it is relevant to say that, in the adopted model, creep-ductility reduction and creep-life extension are intertwined. The reduction in creep ductility was explained to be related to mobile dislocations generated on reloading being caught by the heterogeneous structures (junctions, tangles and, depending on the deformation level, walls), which prevents them from resuming their motion. With less mobile dislocations, the creep rates find a reduced balance between generation and motion of dislocation, meaning a reduced creep rate. As for the creep-rupture life, the change in dislocation pile-ups observed in deforming grain families, as the anelastic recovery takes place, will alleviate the straining

mechanisms on grain boundaries, manifested by the slight decrease observed in the intergranular stresses measured with neutron diffraction. This, along with the reduced creep rate promoted by the dislocation arrangements, will delay the onset of mechanisms related to the mechanical and metallurgical instabilities of tertiary creep, associated with cavitation at stressed grain boundaries, and with the conversion of tangles and walls into cells and subgrains inside grains, which, eventually, may lead to recrystallization, as usually reported for polycrystals in the tertiary stage.

As for the MA956, it is likely that it represents the anelastic behaviour of other ODS steels, that is, showing no anelastic recovery at all. The *in situ* neutron diffraction experiment was the key experiment of the anelastic response investigation on the MA956, from which substantial information on this behaviour was extracted. Because TEM investigations were not possible to be accomplished, due to time constraints, visual evidence of the pinning effect caused by the oxides on dislocations could not be obtained, so, the causes for the resistance of the MA956 to creep deformation (and, therefore, for the absence of anelasticity) could only be theorised, with basis on the well-established effects of the nanometric oxides.

The first point to be discussed on the MA956's behaviour is the reduction in the secondary creep rate after unloading, which is an unexpected result for the MA956, since no anelastic recovery seemed to take place. After two of the four unloading stages during the transient test of the long-term creep experiments, described in Chapter 6, the creep rate was observed to decrease, even though the preceding unloading stage showed no signs of anelastic recovery. Strangely enough, after those unloading stages in which progressive straining was reported, no apparent change occurred in the strain rate of the subsequent secondary creep stage. But, unlike the 316H steel, in which TEM micrographs provided evidence of the predominance of dislocation structures associated with primary creep, the reduction in secondary creep rate does not seem to be associated with the presence of another primary creep stage following reloading. Due to the lack of visual support, and

based on the evidence arising from the neutron diffraction investigations, it seems unlikely that a primary creep stage is succeeding the unloading stages, given that, mostly, the grains are resisting creep deformation. Because of this, it is plausible, then, to think that the reductions may be a consequence of an attractive interaction between the nanoparticles and the generated dislocations on reloading the sample, as well as the previously existing dislocations. The particles may be effectively pinning the dislocations and acting as sinks where annihilation takes place. As for those creep rates whose magnitudes were maintained, following unloading stages in which signs of forward strain were reported, the interpretation is related to resistance of the microstructure against creep deformation. Tensile intergranular stresses are developed during creep, which promote the slightly forward strain throughout the unloading stage. But these unloading stages in which forward straining is observed are preceded by secondary creep stages in which a reduction in the strain rate is reported. In these latter, the resistance of the material to creep deformation is even higher, leading to higher internal stresses, which, in turn, drive a small forward straining process during unloading. As a consequence, a small part of the internal stresses is relieved, restoring the internal resistance to the level of the preceding secondary stage. The reapplication of load to the same previous level (150 MPa) will restore the previous condition of generation and motion of dislocations, so the same balance between strain and recovery is ensured, meaning that the secondary strain rate value remains unaltered. The alternation between no anelasticity at all and slight forward creep in successive unloading stages appears to corroborate this. However, further tests, with longer duration and higher number of unloading stages, are necessary to confirm this behaviour.

Two other points related to the MA956 were found in the *in situ* creep test. First, in any of the in-house creep tests conducted, the specimen experienced transition from primary to secondary stage somewhere between 0.1% and 0.2% strain. In the case of the *in situ* neutron diffraction creep specimen, the initial strain on loading took the strain level to 0.8% approximately, and the transition to secondary creep took place at a level superior to

1% strain, with all the tests carried out under the same condition. This, again, is most likely related to the predominance of different fibre textures in different specimens, for which mechanical properties may vary, as described for the room temperature tensile tests (and, also, to a lesser extent, to the high temperature tensile tests). This possibility became preponderant after ruling out variations in the experimental conditions exceeding the specified ranges (since a tight and careful control was exerted on the temperature and load conditions), as well as differences in the rate of load application onto the specimen, since the stress was gradually increased in steps of 25 MPa to the desired level (150 MPa) in all tests.

The second point concerns an apparent increase in the strain rate after the unloading stage. This is shown in Figure 7.1, and the calculated strain rates are listed in Table 7.1. While no anomalies or fluctuations were found in the stress or temperature dataset, this could be associated with a change in the predominant deforming grain family of the material (as seen in Chapter 6, the {110} family became less creep-resistant with time and, eventually, reached a creep-compliant condition), causing a sudden increase in the strain rate as a consequence of more favourable slip systems becoming active (or in which oxide particles are not so efficient).

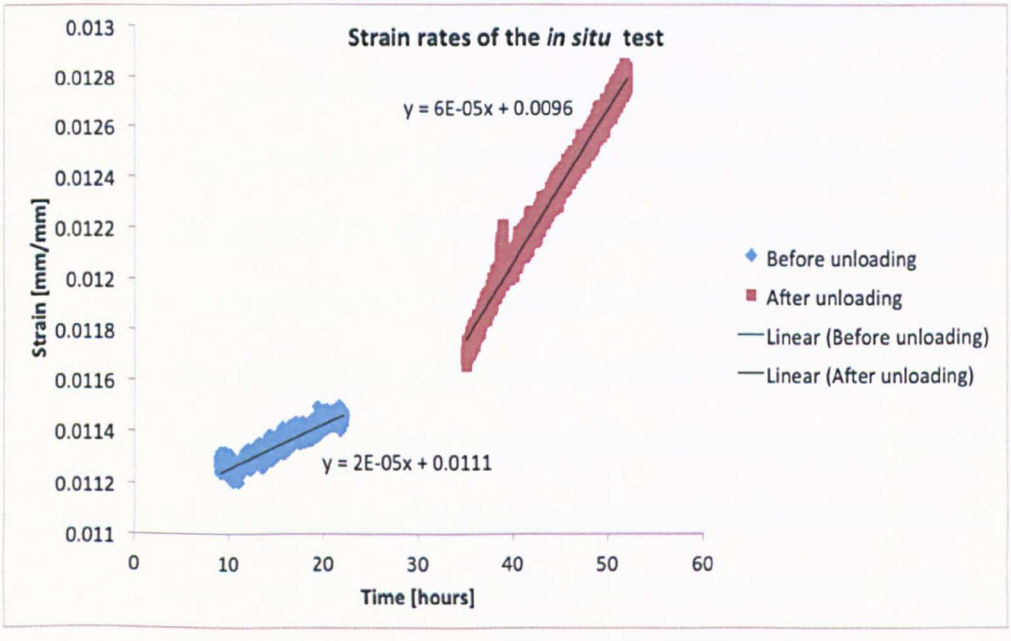

Figure 7.1 - Plot of the strain rates before and after unloading of the *in situ* test.

Table 7.15 - Strain rates from the in situ creep test.

Strain rates	[1/hr]	[1/s]
Before unloading	2.00E-05	5.56E-09
After unloading	6.00E-05	1.67E-08

It is relevant to mention that all the linear fittings carried out, including those in Chapter 6, had a R^2 factor above 0.8.

The MA956 was found to be a strong material, capable of resisting continued creep exposure for a long period of time, exceeding two months, as the control test (the one with no unloading stages) of the long-term creep test series described in Chapter 6 suggests. In terms of its overall performance, it has a tendency to be brittle at room temperature, but it seems that its response to any external mechanical condition is related to the microstructure in a very peculiar way: not only does it exhibit strong anisotropy, as described by Turba and co-workers [8], who studied the creep resistance, ductile-to-brittle transition temperature (DBTT) and fracture energies of the MA956 in the longitudinal direction (parallel to the extrusion axis) and in the transverse direction, finding completely different properties; but also, the mechanical properties vary within the same direction, depending on the predominant fibre texture. In the studies of the present experimental programme, only the longitudinal direction was investigated, but the mechanical properties seemed to have been conditioned by the preferential orientation of the grains. Although the most representative study of this behaviour was the room temperature tensile test, where several different levels of ductility, Young's modulus, yield stress and ultimate tensile stress were recorded, all the other mechanical properties seem to represent an average between the extremes defined by the α- and γ-fibre systems of texture, as seen from the creep tests carried out and from the literature [8]. It is relevant to acknowledge that, with grains as long as several millimetres, the varied brittle behaviour may also be associated with transverse grain boundaries being present for some samples with a particular fibre

system and, thus, favouring embrittlement in certain points along the gauge length of the specimens. But the comparison between the work developed for the MA956 and the results from the literature seem to favour explanations based on the fibre textures properly speaking, given that this behaviour is very analogous to single crystal materials (for example, a single crystal pure iron), whose properties in one direction are completely different than in another. Further studies using EBSD mapping of all the samples could be used to clarify the relevance of the predominant fibre texture, in a more detailed way, for the general mechanical behaviour of this steel, including the same tests carried out in this programme, such as tensile, as well as fatigue, fracture toughness, among others.

Also, it is relevant to mention that a more refined understanding of the absent anelastic behaviour would be achieved by carrying out TEM investigations, as originally proposed in the multi-technique approach concentrated on the anelastic studies. But, at least, the characterization of the material under TEM provided visual and statistical data regarding the nanometric oxide particles, with their apparent distribution and sizes reported to be within the desirable range for optimal pinning properties; and this has to be (and was) taken into account when deliberating on certain phenomena observed, which, at first light, seemed unusual or unexpected.

If an appraisal could be given, at this moment, as for the suitability of the MA956 for advanced nuclear power plant applications, it would certainly acknowledge that the material has its merits and is a potentially adequate material for the harsh environment, as seen from its desirable creep strength, reported in this study, and high temperature oxidation resistance. However, more studies aimed at elucidating some properties (anisotropy, influence of fibre-texture on the mechanical response, irradiation behaviour, etc.) would be recommended for an increased understanding of its behaviour and creation of databases. In a similar way to what was done in the case of 316H, a systematic TEM study would surely contribute, in this regard, for comprehension of the creep properties; particularly if aimed at the interactions of the oxide particles with dislocations, using the

most regarded creep model for ODS steels, proposed by Rösler and Arzt [9] and reported to find good agreement with experimental data from coarse-grained ODS steels [10], which is the case for this material. This could be a potential advantage that the MA956 carries in comparison with other ferritic ODS steels, such as MA957, PM2000 and several non-commercial grades. Its stable microstructure is a bonus for high temperature applications, given that the recrystallized morphology is not altered even at temperatures which are close to the melting point. However, studies of further effects of prolonged exposure to very high temperatures are also necessary, in order to understand their influence on the oxide particles and its consequences, which may affect the effectiveness of pinning dislocations and the stability of the grain morphology, as well as possible phase transformations induced by these temperatures.

7.3 ODS 316L mechanical behaviour

With regards to the austenitic ODS steel investigated in the PhD programme, some interesting facts were noticed, as for its mechanical performance. Tensile tests showed a promising material, capable of withstanding higher mechanical loads than conventional 316L steels and exhibiting very desirable ductility levels at both room and high temperatures. However, the same exceptional behaviour was not observed in creep. Although positive points were found, such as the compliance with the minima demanded by the RCC MR criterion for performance at the stress levels used in the tests and a very extensive tertiary creep regime, indicating a creep ductile behaviour that could serve as an alert for imminent failure, the drawbacks of the creep performance are a matter of concern. Failure was achieved earlier than would be expected based on the tensile tests, and a comparison with conventional austenitic 316L material tested at the same temperature and under the same stress levels revealed a much weaker material. Mathew and co-workers [11] investigated 316L steels bearing different contents of nitrogen, an element found to improve the creep properties of these austenitic steels. Even the material with the lowest

content of nitrogen presented superior creep properties. For example, while the ODS 316L failed after 1461 hours under 140 MPa, the 316L (with lowest nitrogen content – 0.08 wt. %) endured almost 3000 hours. Similarly, failure under 175 MPa occurred at 411 hours of test in the case of the ODS 316L, but the same conventional 316L crept for approximately 800 hours. Only the tests at 200 MPa were the exception, with ODS 316L enduring longer total hours of creep (239 hours) than the 316L, which failed after a little more than 100 hours. However, just a slight increase in the nitrogen content of the conventional 316L steel (to 0.12 wt. %) was enough to take the creep properties to a new baseline, far superior to the performance of the ODS 316L. While it could be speculated that increasing the nitrogen contents of the ODS version of the steel could produce the same effect, a simple check on the chemical composition provided in table 5.1 of Chapter 5 shows that the material already has a high content of nitrogen (0.2 wt.%), which may even be responsible for strengthening the steel, along with the nanometric oxides and the carbides. Therefore, other means of eliminating the apparent weaknesses should be envisaged that do not involve the composition, which appears to have been tailored to maximize the performance.

It is well established and widely acknowledged that the powder metallurgy routes for fabrication of ODS steels, even if very carefully controlled, cannot get rid of the porosity and voids entrapped in the consolidated microstructure. The same fabrication procedures may yield ODS materials with different properties because of process variability [12]. But there are ways to minimize the presence of defects. A relatively effective way of doing this is subjecting the material to thermomechanical treatments (TMTs), in which plastic deformation is introduced to the material, as reported in Chapter 2 [13, 14]. As reported in Chapter 5, good improvements can be achieved, such as in the case of the TMT applied after the diffusion bonding cycle, which raised the creep ductility of the ODS 316L from 3% to nearly 11%. Even though the observed loss of strength was, in this case, associated with the growth of grains, it is not implausible to consider that the strength would not have

been much higher if the grains had not grown. In essence, TMTs are a helpful tool, convenient and easy to apply, but have a limit. In order to effectively improve the properties of these austenitic ODS steels, more efficient ways of eliminating the porosity and entrapped gas should be devised and acted upon during fabrication, especially from the powder state.

Still regarding the creep properties, from the tests described in Chapter 5, a stress exponent n of 3.88 was calculated. This value rules out detachment (of dislocations from oxide particles) as a dominant creep mechanism in the tests. It is possible that the chosen stress levels were high enough to cause conventional dislocation-based processes, such as glide and/or climb. But this is also an indication that, during creep deformation under these mechanical loads, the oxides are not exerting a strong pinning influence on the dislocations. For such interactions, the expected magnitudes of the stress exponent would be much higher (n = 20, at least, or 50). Likewise, during the diffusion bonding cycle, the oxides were not effective at preventing grain growth by pinning grain boundaries. Given that TEM studies offered a very broad range of sizes for the particles, ranging from only a few nanometres to hundreds, possibilities are that the inhomogeneity in the size distribution, with a predominance of large oxides, is facilitating thermally assisted detachment of dislocations from oxide particles, made possible by climb. This thermally assisted detachment is not immediate (or effective) if the particle presents sizes within the optimal range of a few tens of nanometres, for which the pinning effect is strong. Therefore, care must also be taken as for the parameters of fabrication that determine the size of the oxide particles in the ODS steel, for the sake of improvement of its performance, especially under elevated temperature exposure.

A final observation with regards to the creep studies of the ODS 316L is related to the use of Larson-Miller Parameters (LMP). Although very useful, these numerical values associated with functions of the relevant creep variables (time, temperature, stress and strain) provide only an estimate of the variable of interest, which, in this case, was the

stress associated with a particular value of rupture time. The fact that materials may undergo phase transformation when exposed to creep introduces inaccuracies in the prediction. Although it does not invalidate the extrapolation procedures on which these parameters are based, it is always good practice to have in mind that their outputs provide just a preliminary indication of the creep tendency of the material and that their actual creep response may significantly differ from the prediction. Several other models exist, such as Dorn and Manson-Haferd [15], which are also based on extrapolation. The same care should be taken when using them, and, although the LMP is simpler and requires variables readily obtainable from the creep curves, none is superior to the others.

7.4 Microstructural properties of the ODS 316L

Because the microstructure was investigated in all operations executed on the ODS 316L, it is timely to purvey some appraisals on the findings regarding the microstructural observations. First, the HRTEM studies carried out for characterisation of the particles offered valuable insights as for the possible orientation relationships between the nanometric oxide particles and the matrix. However, unfortunately, these studies do not answer the question of "dissolution vs. amorphization", as the possible crystallographic orientations might have suggested. In fact, no technique currently available is capable of providing a definitive answer. The most likely mechanisms may reside somewhere in between, comprised by dissolution of a small part of the yttria, up to the limit of solubility in the steel matrix, and amorphization of the remainder of the yttria content, as reviewed in Chapter 2. This is a very likely scenario, since the introduction of oxides beyond the limit of solubility is made possible by the mechanical alloying procedure. Still, the HRTEM studies were relevant, by giving an idea of the change in the crystallographic orientation with the size (or the growth) of the oxides. Although individual particles cannot be tracked in the steel for an assessment of the changes in orientation as the material is subject to any thermal or mechanical event that may alter the basic microstructural features, it was

inferred, based on the concepts of coherency, that, if a particle is experiencing growth, it is also experiencing rearrangement in its orientation relationship with the surrounding matrix. This is a requirement of the loss of coherency. For small particles (less than 10 nm), the orientation is such that there is almost perfect match between lattice planes of the particles and the matrix. As the particle grows, it becomes semi-coherent (or incoherent), and therefore, mismatches are generated at the interfaces; this is accomplished by assuming a different orientation relationship. It must be mentioned that these oxides are very stable. Still, it is plausible that a slight growth may occur if the material is exposed to very high temperatures, in which diffusion rates are expected to be high, leading to coarsening of the oxides, as shown in the particle size distributions of the previous chapters dedicated to ODS steels. Further investigations involving such high levels of temperature (those of heat treatment or diffusion bonding) are required to confirm this as a tendency of the austenitic ODS steels and of the ODS steels in general, since the growth was reported for both ODS steels exposed to very high temperatures (1200°C – 1300°C) in this research programme.

Finally, although the results of the thermomechanical treatment (TMT) applied to the diffusion-bonded slices were successful at refining the microstructure, they are just preliminary and can also be improved by more appropriate selection of parameters of the TMTs or by introducing severe plastic deformation to the samples. A current way of enhancing mechanical properties, particularly creep resistance, is found in the application of cyclic thermomechanical treatments comprising repetitive plastic deformation processes, aimed at increasing the fraction of the so-called special boundaries, as reported by Szabo [16] for austenitic stainless steels. Therefore, TMT's could be tailored to promote the presence of these special boundaries, characterized by the Coincident Site Lattices, which are those presenting a fraction of atoms in the grain boundary plane belonging to both lattices separated by the boundary. Because these special boundaries establish a geometric connection between the adjacent lattices and present lower surface energies than random boundaries, they are capable of improving the strength of the interfaces, imposing

higher resistance against damages prone to propagation along them [16, 17]. This approach could represent a further degree of strengthening to the ODS 316L, being worth investigating.

7.5 References

[1] A. Rao, "Creep and Anelastic Deformation in Austenitic Steels," The Open University, 2010.

[2] H. Mughrabi, "Dislocation wall and cell structures and long-range internal stresses in deformed metal crystals," *Acta Metall.*, vol. 31, no. 9, pp. 1367–1379, Sep. 1983.

[3] C. N. Ahlquist and W. D. Nix, "The measurement of internal stresses during creep of al and Al-Mg alloys," *Acta Metall.*, vol. 19, no. 4, pp. 373–385, Apr. 1971.

[4] X. Feaugas, "On the origin of the tensile flow stress in the stainless steel AISI 316L at 300 K: back stress and effective stress," *Acta Mater.*, vol. 47, no. 13, pp. 3617–3632, Oct. 1999.

[5] C. Gaudin and X. Feaugas, "Cyclic creep process in AISI 316L stainless steel in terms of dislocation patterns and internal stresses," *Acta Mater.*, vol. 52, no. 10, pp. 3097–3110, Jun. 2004.

[6] X. Feaugas and C. Gaudin, "Ratchetting process in the stainless steel AISI 316L at 300 K: an experimental investigation," *Int. J. Plast.*, vol. 20, no. 4–5, pp. 643–662, Apr. 2004.

[7] P. Lee and R. Raj, "Colossal anelasticity in polycrystals deforming under conditions of diffusional creep," *Acta Mater.*, vol. 58, no. 2, pp. 702–708, Jan. 2010.

[8] K. Turba, R. C. Hurst, and P. Hähner, "Anisotropic mechanical properties of the MA956 ODS steel characterized by the small punch testing technique," *J. Nucl. Mater.*, vol. 428, no. 1–3, pp. 76–81, Sep. 2012.

[9] J. Rösler and E. Arzt, "A new model-based creep equation for dispersion strengthened materials," *Acta Metall. Mater.*, vol. 38, no. 4, pp. 671–683, 1990.

[10] C. Zakine, C. Prioul, and D. François, "Creep behaviour of ODS steels," *Mater. Sci. Eng. A*, vol. 219, no. 1–2, pp. 102–108, 1996.

[11] M. D. Mathew, K. Laha, and V. Ganesan, "Improving creep strength of 316L stainless steel by alloying with nitrogen," *Mater. Sci. Eng. A*, vol. 535, no. 0, pp. 76–83, 2012.

[12] J. Pearce, "Fusion Materials Development at ORNL," *ASTM Standardization News*, 2010. [Online]. Available: http://www.astm.org/SNEWS/JF_2010/pearce_jf10.html.

[13] M. Wang, Z. Zhou, H. Sun, H. Hu, and S. Li, "Effects of plastic deformations on microstructure and mechanical properties of ODS-310 austenitic steel," *J. Nucl. Mater.*, vol. 430, no. 1–3, pp. 259–263, Nov. 2012.

[14] M. Wang, Z. Zhou, H. Sun, H. Hu, and S. Li, "Microstructural observation and tensile properties of ODS-304 austenitic steel," *Mater. Sci. Eng. A*, vol. 559, pp. 287–292, Jan. 2013.

[15] M. E. Kassner and M. T. Pérez-Prado, *Fundamentals Of Creep In Metals and Alloys*, Second Edi. Elsevier, 2009.

[16] P. J. Szabo, "Effect of partial recrystallization on the grain size and grain boundary structure of austenitic steel," *Mater. Charact.*, vol. 66, pp. 99–103, Apr. 2012.

[17] D. L. Engelberg, R. C. Newman, and T. J. Marrow, "Effect of thermomechanical process history on grain boundary control in an austenitic stainless steel," *Scr. Mater.*, vol. 59, no. 5, pp. 554–557, Sep. 2008.

[18] D. M. Norfleet, D. M. Dimiduk, S. J. Polasik, M. D. Uchic, and M. J. Mills, "Dislocation structures and their relationship to strength in deformed nickel microcrystals," *Acta Mater.*, vol. 56, no. 13, pp. 2988–3001, Aug. 2008.

Chapter 8 – Conclusions and Future Work Suggestions

8.1 Introduction

This chapter is dedicated to the final considerations and briefly summarizes the main findings, key points and ideas elaborated around the activities developed throughout the research programme. Suggestions for further investigations, as well as for new lines of research that may depart from the work carried out, are also provided, based on the ideas discussed in the previous chapter.

8.2 Conclusions

This thesis describes experiments for investigating high-temperature deformation, with specific emphasis to creep behaviour, of conventional and ODS steels aimed at advanced

nuclear power plant applications. Herein, the results for characterisation of the alloys, the tests and procedures executed, and the investigative approaches were presented, in an effort to understand straining mechanisms triggered by creep and creep transient deformation processes, the response these mechanisms produce, in terms of the performance of the material, and their suitability to the operational demands expected in advanced nuclear reactors.

- For the 316H stainless steel

➢ Anelastic response, representing the time-dependent plastic strain recovery, was found to exist for the partially unloaded steel under creep transients, provided that the stress applied during the unloading stage is no longer capable of maintaining dislocation-based creep processes.

➢ The effects of partial stress removal, in these cases, appeared to produce the same effects on creep response of 316H as full stress removal, given that, in all tests carried out, the secondary creep rate after reloading was lower than the rate prior to unloading. Even though a similar reduction in the secondary creep rate was observed also for the tests unloaded to stress levels that were high enough to cause dislocation creep, this reduction is not associated with the anelastic effects, but simply with a new secondary creep balance condition between the generation (and motion) of dislocations and recovery processes, under the new imposed stress.

➢ A model for the intragranular back stresses, based on heterogeneous dislocation structures within the grains of a polycrystalline material, was successfully adapted to describe the evolution of the driving force for anelasticity, in terms of early heterogeneous arrangements of dislocations (tangles and walls in formation) around precipitates. This model, based on quantitative and qualitative TEM investigations, was vital for understanding the basic mechanisms behind deformation and recovery in creep transients, but this was made possible by a combined approach of different

techniques, which provided insights as for the role of the microstructural features on the response of the 316H steel.

- Although the total (internal) back stress level can be envisaged as a sum of intergranular and intragranular components, both arising from dislocation events in grain boundaries and inside grains, anelasticity appears to be more sensitive to the intragranular back stress, whose dynamic nature indicates a measure of the material's potential for recovery (back stresses were seen to gradually develop during the loading periods and to gradually decrease along the unloading stage). These back stresses drive the recovery events associated with dislocations and their arrangements, once the material is unloaded.

- For the ODS 316L

- The characterisation of the nanoparticles showed a very broad distribution of particle size, ranging from very small diameters (10 nm or less) to hundreds of nanometres.
- The size distribution was very inhomogeneous and the presence of large particles (> 50 nm), whose diameter exceeded the ideal range of sizes, may have contributed to decrease the effectiveness of the pinning capacity of the oxides during creep, thus allowing climb-assisted detachment of the dislocations. This result suggests the need for a controlled fabrication process, in order to promote refinement of the oxide sizes obtained in the final compact.
- The tensile properties of the ODS 316L reached a desirable baseline at both room and high temperature. However, the creep behaviour fell short of the expectancy, and the inhomogeneous size distribution of the particles seems to be directly

associated with that. While ductility was a hallmark of the material, as observed in the fact that over 50% of its creep-rupture life was spent in the tertiary creep stage, the absolute magnitudes of the strains at rupture, between 3.3% and 3.6%, suggest this steel to lack creep strength. This idea is reinforced by a comparison established between the ODS 316L and an equivalent (in terms of composition) conventional 316L steel, that presented much higher creep-rupture lives under the same test conditions. Even though the ODS 316L was compliant with the minima demanded by the RCC MR code, improvements are necessary, in order to produce a more competitive austenitic ODS steel for long-term high temperature creep exposure.

- From the pilot study of diffusion bonding carried out with the ODS 316L, it could be inferred that the procedure seems promising for joining ODS steels. A solid bond was obtained, bearing good mechanical properties and preserving the original materials joined together.
- This study also pointed out the possibility of a slight growth of the smaller oxides (less than 50 nm) under influence of the high temperatures of the cycle (1200°C), forming clusters in the matrix. This finding is unexpected, seemingly contradicting the idea of stability of these oxides.
- A thermo-mechanical treatment (TMT) comprised of cold rolling with 25% deformation, followed by annealing at 1150°C provided an effective combination of parameters for refining the microstructure of the ODS 316L steel after diffusion bonding, without disrupting the particle size distribution. Since this was a preliminary study, improvements on the TMT parameters may strengthen the material even more, producing more refined microstructures and, subsequently, increased creep-resistance.
- Finally, a useful observation on the nature of the oxides of the ODS 316L stemmed from the HRTEM studies. The particles investigated were found to be $Y_2Ti_2O_7$

complex oxides and to bear different orientation relationships with the matrix according to their sizes.

- For the MA956 ferritic ODS steel:

➢ Creep transient tests revealed that anelastic recovery appears to be absent. In almost all the tests executed, a flat line characterised the unloading stages, indicating that the strains read at the onset of these stages and at its end (immediately before reloading) were the same.

➢ The *in situ* creep test provided the most valuable clues on the phenomena that were taking place in the MA956's microstructure, since no visual evidence (by means of electron microscopy) could be obtained. The experiment showed that families of grain orientations expected to be deforming, such as the {110}, {211} and {321}, were, actually, resisting creep deformation for most of the test.

➢ The behaviour of the grain family {321} was reported to oscillate between resistance to deformation during the loading periods and creep compliance during the unloading stages. This may be the reason for the progressive creep straining observed in some of the unloading stages of the in-house creep tests on the MA956. However, reasons why this particular family exhibits this behaviour are not understood and need to be further studied.

➢ With little or no deformation, there is no potential for anelastic strain recovery.

➢ Another remarkable feature of the MA956 microstructure is the effect that the predominance of a strong fibre texture has on its properties, particularly those at room temperature. Tensile tests at this temperature level exhibited different properties, according to indications of the predominant orientation of the grains in the specimen. The effect is not so pronounced at high temperature, likely due to the fact that, at 650°C, transition from brittle to ductile is already expected to have taken place.

- Although a strong material, the MA956 exhibited strong anisotropy not only regarding the direction (longitudinal or transversal), but also, the predominant fibre texture in the sample.
- The characterisation of the MA956 by TEM revealed a more uniform distribution of particles through the matrix and a more homogeneous oxide size distribution, with the average size reported to be within the limits considered ideal for effective pinning.
- The oxides were found as belonging to the Y-Al-O complex system, rather than to the Y-Ti-O system.
- A hypothesis testing applied to the oxide size distributions for the as-received and heat-treated MA956 in a comparative TEM study revealed that the oxides in the ferritic matrix also experienced a slight growth, when exposed to the high temperatures (1300°C) of the heat treatment cycle. This points out to the need for assuring a controlled powder metallurgy fabrication routine, in order to provide particles within a desirable range of sizes, taking into account also the possibility for growth during the fabrication of the steel. Although these oxides are stable, it seems continuous exposition to such levels of temperature may cause them to grow.
- Overall, the MA956 presents desirable high temperature performance, but further investigations and extensive tests are needed to confirm the findings as well as to clarify some issues raised, particularly those associated with the room temperature properties and some anomalous phenomena reported in the creep tests.

8.3 Future work suggestions

From all the previous chapters and discussions, the following guidelines for future works in alignment with the tasks accomplished in this programme are suggested.

- For the 316H steel

A systematic study of anelastic effects on the creep life of the 316H stainless steel triggered by transients imposed during the primary creep stage would provide further comprehension of the material's behaviour. Also, although longer creep tests would have to be envisaged, no description of anelasticity associated with tertiary creep has been provided. Although the secondary stage represents the longest and most important creep regime, the contributions of the remaining stages cannot be neglected. For studies in primary and tertiary creep, a multi-technique approach would, again, be welcome, for the establishment of the relation between the transients of stress (or temperature) and the microstructural features, such as dislocations, precipitates, cavities and boundaries. TEM, SEM, neutron diffraction, small-angle neutron scattering (SANS) and atomic force microscopy (AFM) certainly would create a comprehensive understanding of the creep transients' effects on creep life as a whole.

- For the ODS 316L

Although a tendency could have been obtained from the creep tests carried out, either on specimens entirely machined from the material or on hybrid bonded specimens, further creep tests would be desirable and welcome, to help in clarifying what creep mechanisms could be active and controlling the deformation under a range of different stress levels. Also, ways to improve the microstructure of austenitic ODS steels demand deeper investigations, covering all stages of fabrication and processing of the alloy. Studies on optimal conditions for fabrication of these steels, the effect of milling parameters, size of initial powders, consolidation processes and all complementary operations for producing a strong microstructure in the austenitic versions of ODS steels are required.

Equally important is the study of joining processes of these steels. From the pilot study presented, it is a natural step to investigate the diffusion bonding of the ODS 316L steel to another part of ODS 316L steel. Also, to extend the investigation to other types of ODS

steels, both ferritic and martensitic. Diffusion bonding seems a promising and effective way to ensure continuity of mechanical performance at the interfaces. Selection of appropriate parameters for joining, mechanical properties in tensile straining, fracture toughness and, especially, creep properties of diffusion bonded ODS steels are, certainly, topics to be explored for confirmation of the suitability of the process.

Also, incorporation of the so-called grain boundary engineering processes, aimed at manipulating the microstructure in order to introduce higher fractions of special boundaries, as described in Chapter 7, is a trend that should be considered. Given that the preliminary TMT applied on the ODS 316L yielded refinement of the structure, repetitive plastic deformation followed by heat treatments (cyclic TMT's) could be tested in an effort to enhance intergranular properties of the material against creep, corrosion and other processes taking place at grain boundaries.

- For the MA956

Because the creep transient behaviour has just been superficially surveyed, with only a few aspects of the behaviour of the MA956 being elucidated, much more experimentation is necessary to start understanding its behaviour. Similarly to what was applied to the 316H, a multi-technique programme, looking at the intergranular mechanisms (diffraction techniques, such as neutrons and X-ray), and at the intragranular mechanisms (TEM) would provide a more complete picture. In this regard, the suitability of the use of established models, based on attractive interactions between dislocations and particles could be put to test, as well as formulation (or adaptation) of appropriate models for quantification of back stresses generated by these peculiar physical mechanisms inherent to ODS materials.

Another complementary study, more general, could be envisaged to carry out extensive EBSD on MA956 samples and correlate them to the mechanical properties, in a more

systematic way, in order to confirm the role of the predominance of systems of fibre texture on the mechanical response of the material. The use of samples of larger dimensions is also desirable for the MA956, in order to statistically accommodate more grains of the material in test specimens and improve the description of the bulk behaviours.

Another possibility of deepening the understanding of the MA956 consists of HRTEM studies on the nature of the nanoparticles for providing detailed information on coherency of particles, their orientation relationship with the matrix and what properties these latter entail.

Irradiation properties of these steels are another very broad and relevant topic for understanding their behaviour and analyse their suitability for applications in advanced nuclear power plants, where irradiation damage is expected to take place.

And, finally, but no less important, joining processes of the MA956 is also crucial for applications where the interfaces have to withstand, with the same properties as the bulk material, the harsh conditions expected in advanced nuclear reactors.

APPENDIX 1: Creep specimen drawings

During the course of the investigation, creep tests were carried out in different rigs and for different purposes. This demanded the adoption of a different design for each case. Below are the detailed sketches of the created (and adopted) specimen designs.

Creep transient test specimen: adopted for the 316H and MA956

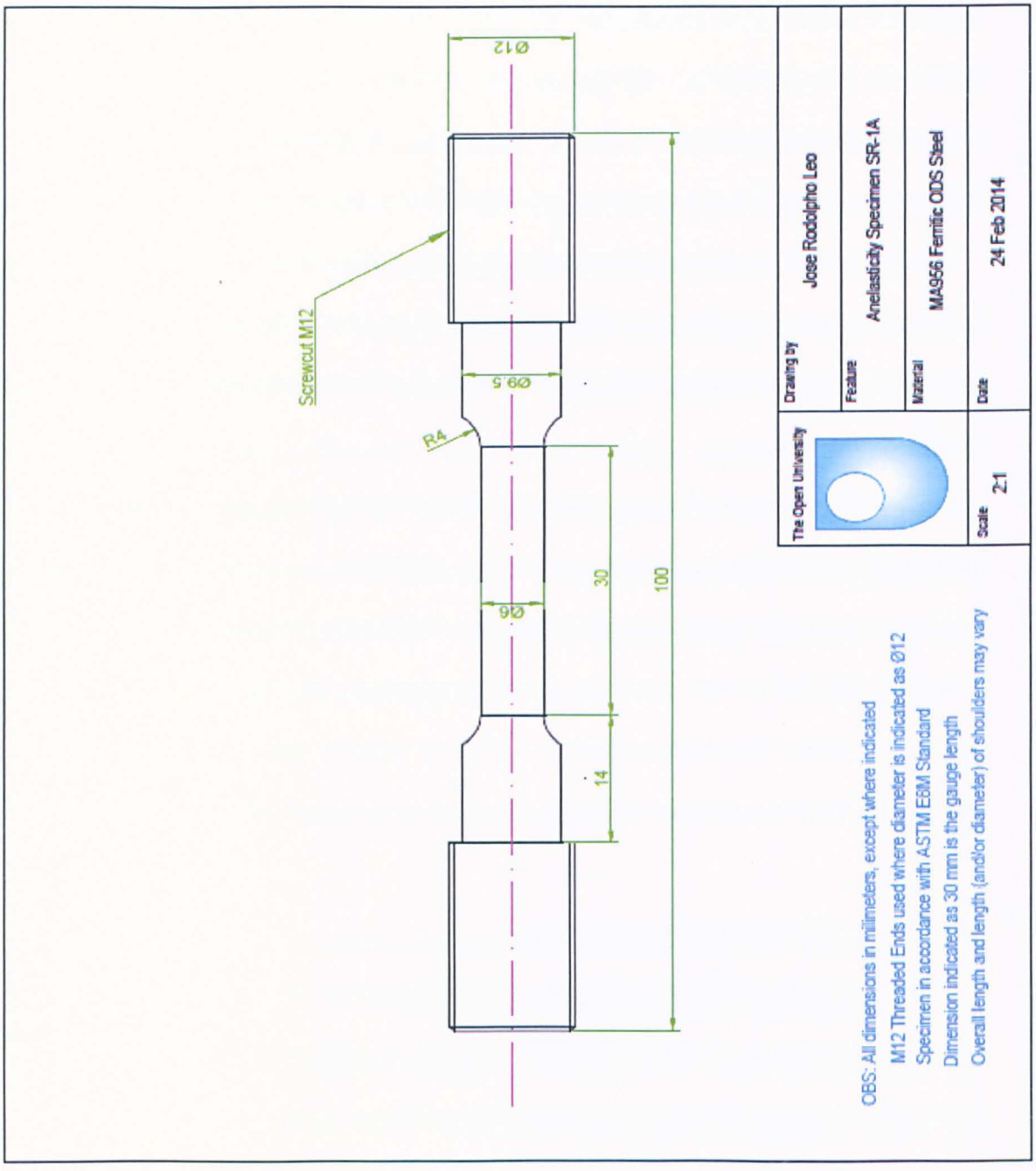

Miniaturized creep-rupture specimen: designed for the ODS 316L

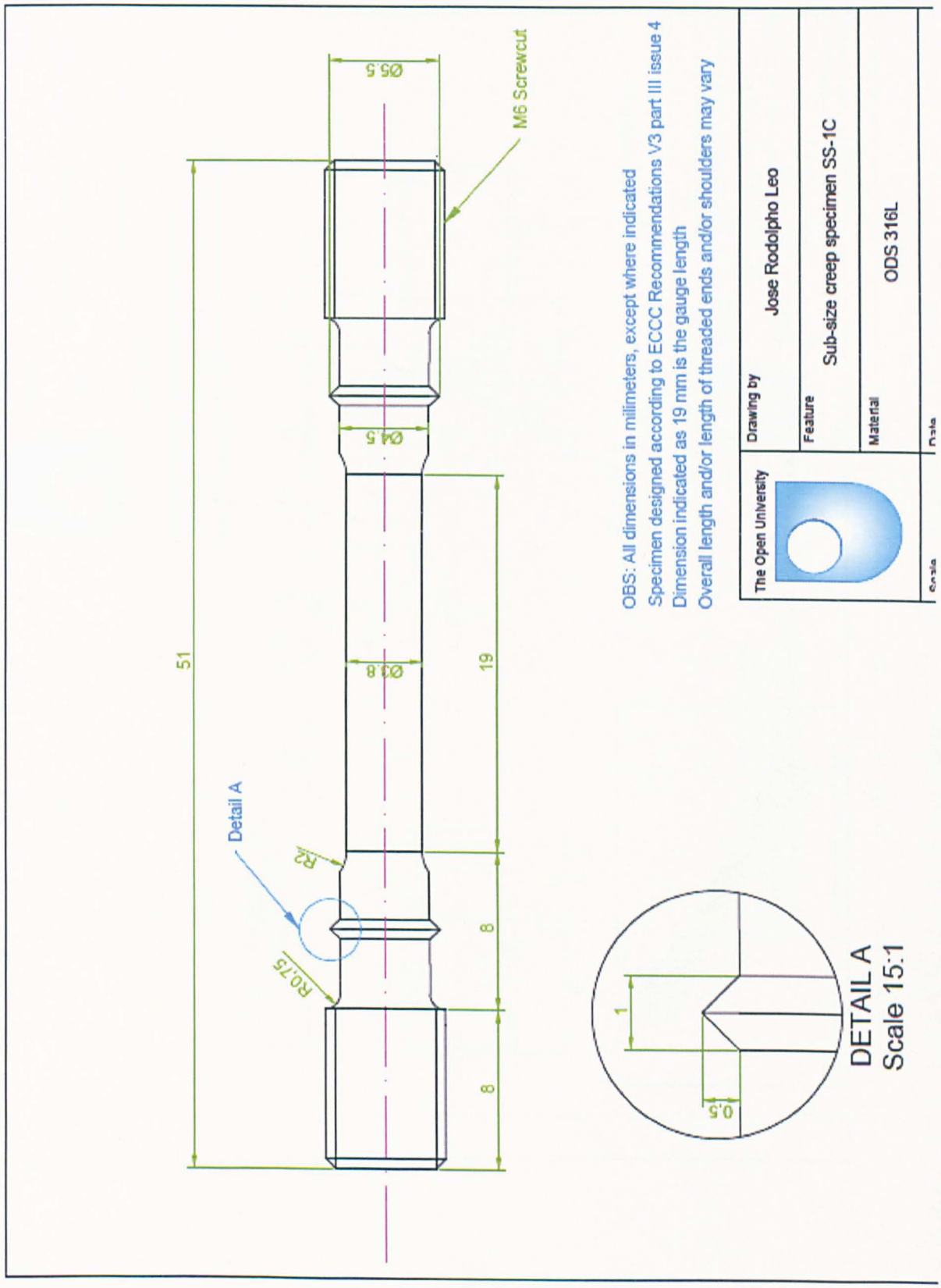

Creep-rupture specimen with tear ridges: designed for the MA956

Miniaturized creep hybrid specimen: designed for the diffusion-bonded ODS 316L / Inconel 718 sample.

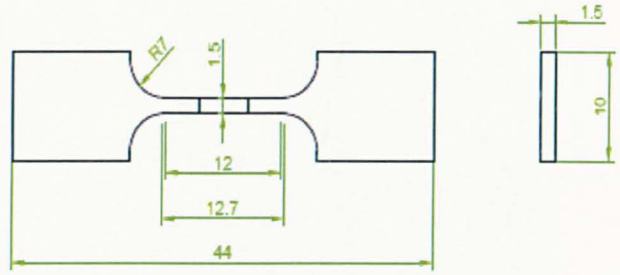

OBS: All dimensions in milimeters, except where indicated
Specimen in accordance with BS EN 10002-5 1992
Dimension indicated as 12 mm is the gauge length
Dimension indicated as 12.7 mm is the parallel length

The Open University	Drawing by: Jose Rodolpho Leo
	Feature: Mini Tensile Hybrid Specimen SH-2T
	Material: ODS 316L / Inconel 718
Scale: 2:1	Date: 12 May 2014

APPENDIX 2: MA956 chemical composition certificate

SPECIAL METALS — IncoTest

Holmer Road, Hereford, England HR4 9SL
Tel: + 44 (0)1432 382230
Fax: + 44 (0)1432 353545
Email: info@incotest.co.uk
www.incotest.co.uk
A Division of Special Metals Wiggin Limited
Registered in England at the above address under number 36721

Nadcap

CERTIFIED LABORATORY
TEST REPORT
UKAS Testing Laboratory no. 0281

0281

CUSTOMER BY E-MAIL

Customer
THE OPEN UNIVERSITY
FINANCE DIVISION
PO BOX77
WALTON HALL
MILTON KEYNES
MK7 6BT
FAO: Ping-Mui Cheung

Certificate No.	LT 0266864/01
Dated	13 02 2014
Page No.	1 of 1
Customer Order Number	PO 4842B4
Date Received	05/02/2014
Laboratory Reference Number	J080G3 1

Specification
None Quoted

Description of Samples
Bar
Number of Samples 1

HEAT TREATMENT ON TEST PIECES

CHEMICAL COMPOSITION Weight % (except where stated ppm)

	C	Si	Mn	P	S	Al	Co	Cr
2M X 16MM MA956 ABD0725	0.015	0.04	0.10	0.005	0.008	4.80	<0.01	19.4
Method of Analysis	LEC1	XRF	XRF	XRF	LEC1	XRF	XRF	XRF

	Cu	Fe	N	Ni	O	Ti	Yttria
2M X 16MM MA956 ABD0725	0.02	Balance	0.022	0.05	0.23	0.30	0.51
Method of Analysis	XRF		LEC2	XRF	LEC2	XRF	XRF

OTHER REMARKS/ENDORSEMENTS

Tested in compliance with ISO/IEC 17025.
Analysis entered using original cast data.

DETAILS OF METHOD CODES

LEC2 - LECO TC436AR ANALYSER
LEC1 - LECO CS444 ANALYSER
XRF - X-RAY FLUORESCENCE ANALYSIS

End of test results

Certified that the above mentioned specimens/parts/materials/systems have been tested/examined in accordance with the terms of the contract order applicable thereto. This Certificate does not relate to the standard or quality of manufacture of the item/material except as may be specified in test.

Signed

APPENDIX 3: Illustration of the method deployed for counting dislocations

The following is a composite showing the same investigated area of Specimen ID 3 (creep test interrupted 30 min after the unloading), under the four different **g-vectors** used for computing the dislocation densities, along with their correspondent SADP's. The TEM micrographs were taken from the ImageJ environment, and show the superimposed pattern of drawn lines.

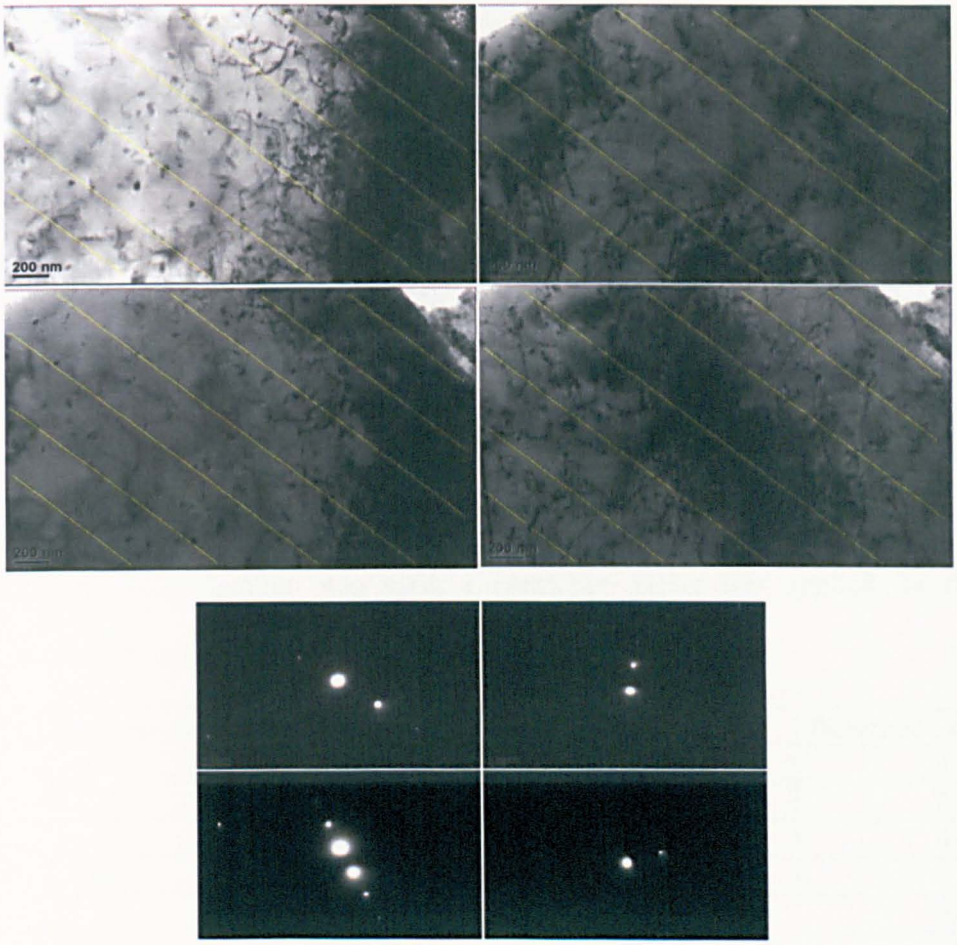

Attention must be drawn here to the fact that it is preferable to use this method with a grid of lines of different orientations, in order to avoid the possibility of having the chosen direction of parallel lines in the grid coinciding with the preferential dislocation line orientation, given that a non-random distribution of dislocation line directions is expected, as a consequence of the anisotropy of slipping systems in a grain.

It is acknowledged that, since the measurements carried out in the same area (4x) <u>are not</u> independent, despite having different **g-vectors**, large errors are expected when

conducting statistical analysis. Also, to improve the accuracy of the analysis carried out in this work, the equations used to express the uncertainties (described in Chapter 4) also should have been modified, to accompany the composite tracing and its associated lower level of uncertainties.

APPENDIX 4: Table of total interceptions per specimen ID and critique of the method used for counting

The total number of interceptions per specimen ID is listed in this table, along with the total line length and the calculated average dislocation densities. The total number of interceptions has to be understood as the result of the number of interceptions of a particular micrograph times the number of micrographs of a particular area times the number of areas investigated from the foil times the number of foils extracted from a particular specimen ID of the third group of creep tests (aimed at TEM studies).

The variations found in the total line length refer to the use of different magnifications. For example, TEM micrographs from specimen ID 1 were taken under higher magnifications. Therefore, the calibration of pixels per unit, carried out in the ImageJ environment, yielded lines of shorter lengths. For each specimen ID, the images used in the calculations were, mostly, taken under the same magnification. When an image with different magnification was used, a correction factor was applied for the setting the proportion and compensate for the magnification.

Test Specimen ID	Total Line length [nm]	Total Interceptions	Dislocation density [/m²]
1	7150	2076	8.1E+14
2	45603	3752	7.8E+13
3	48398	3304	5.2E+13
4	55586	3152	5.9E+13
5	110555	2496	5.0E+13
6	62359	2840	4.3E+13
7	43333	4080	6.2E+14
8	79509	4720	1.1E+14
As-received 316H	69687	3116	1.1E+14

It must be acknowledged that this method is not without flaws. The use of micrographs of the same area, using different g-vectors, could have led to a more accurate analysis if they were overlapped in a composite (tracing/assembly). The method used in this work could lead to high levels of uncertainties, due to overestimations (i.e. dislocations visible in more than one reflection being counted more than once) or, less likely, underestimations

(i.e. dislocations invisible in all reflections). If the overlapped assembly had been used, any double-counting and under-counting of dislocations could have been minimized, resulting in higher accuracy. This is because, in the tracing method, each dislocation would have counted only once.

APPENDIX 5: TEM images of the 316H as-received vs. TEM images of the 316H specimen interrupted during primary creep

- As-received 316H steel:

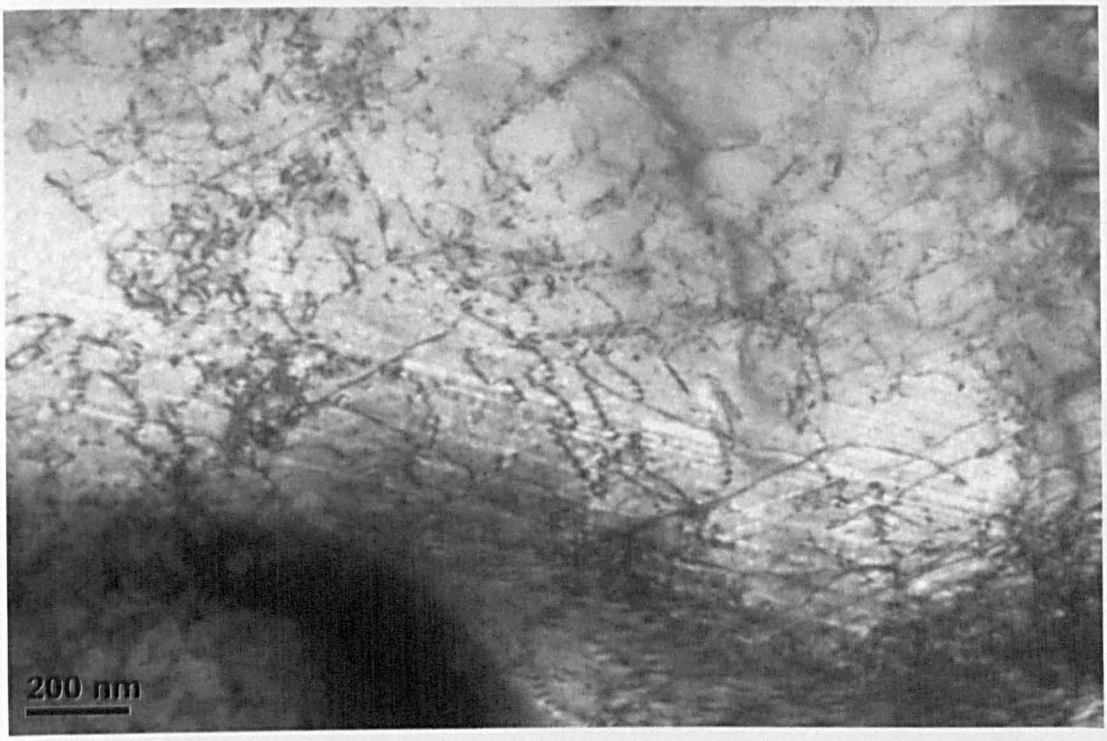

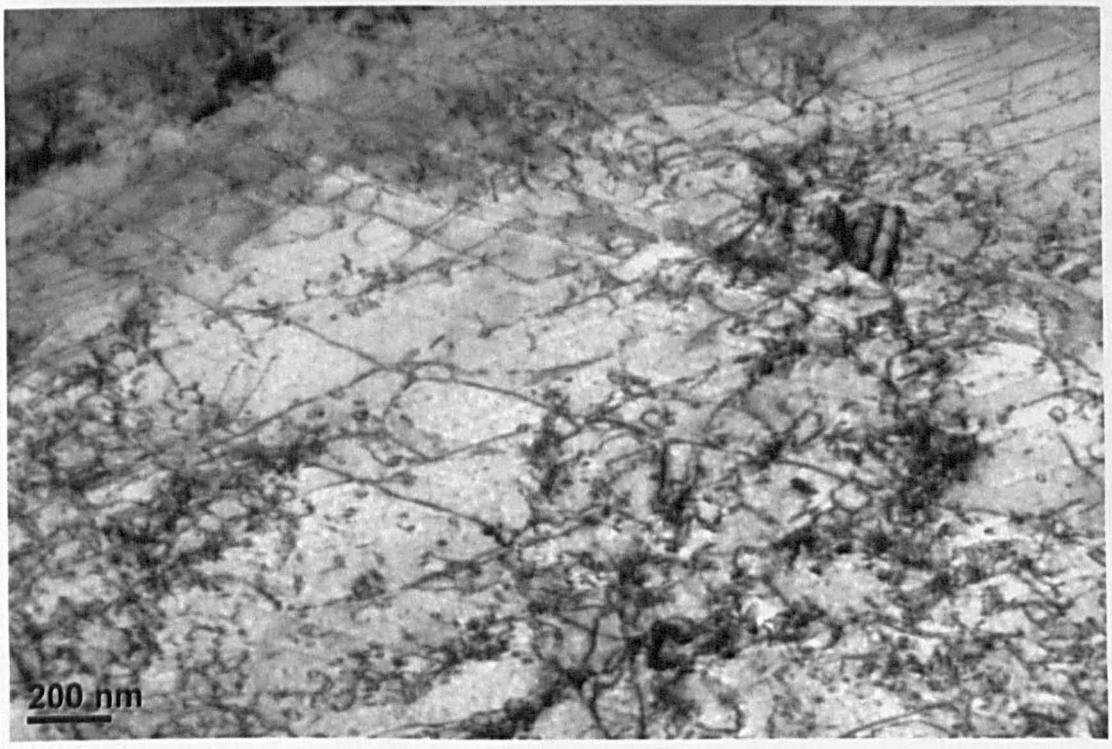

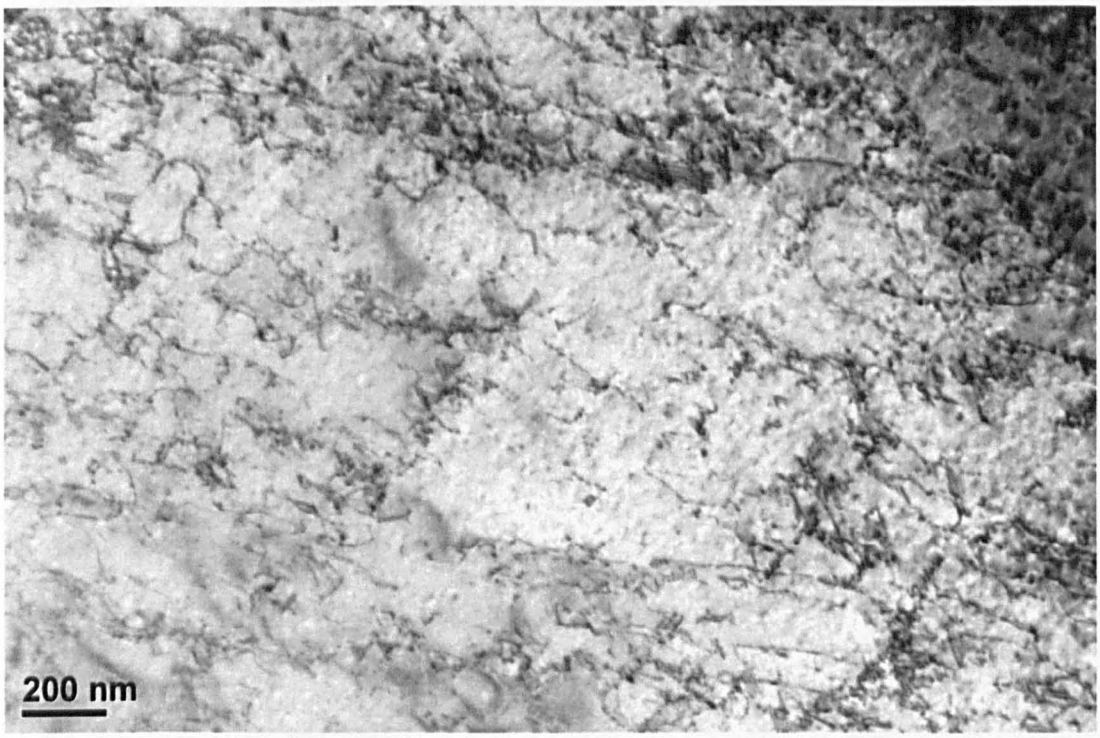

Stacking faults were observed in some of the as-received condition micrographs, as likely remnants of the plastic deformation suffered during processing. Only one instance of pile-up was recorded. There are no predominant dislocation arrangements. Matrix dislocations, dipoles, tangles are observed in the same proportion.

- Primary creep interrupted specimen

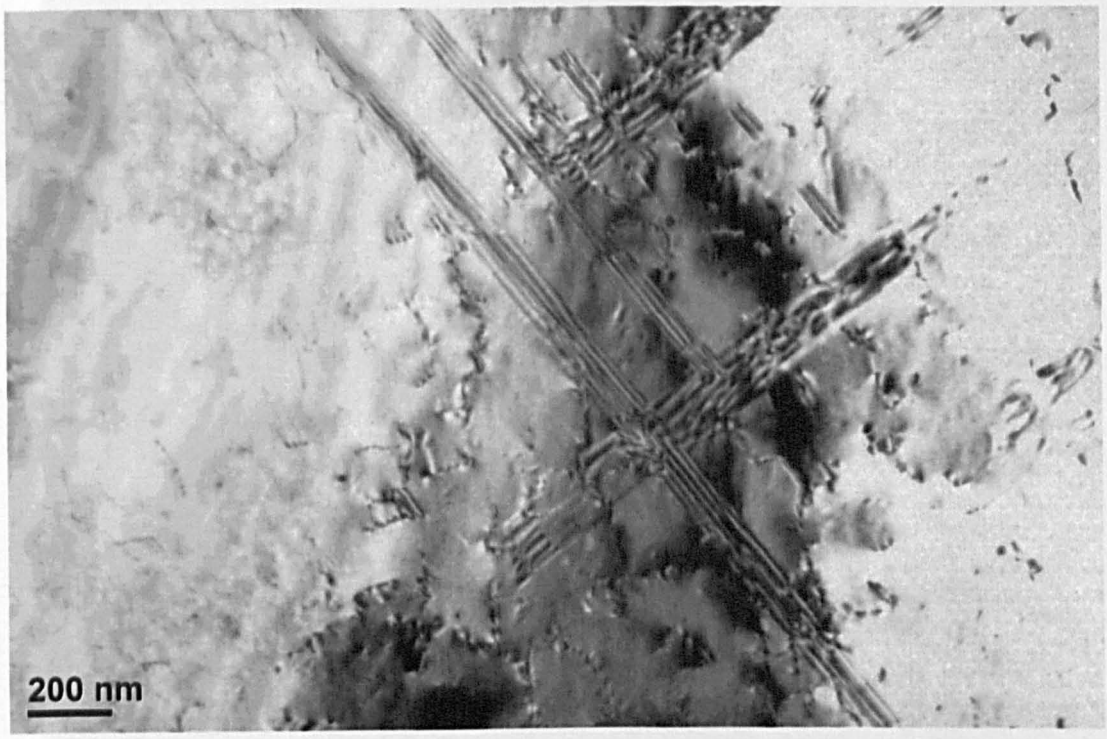

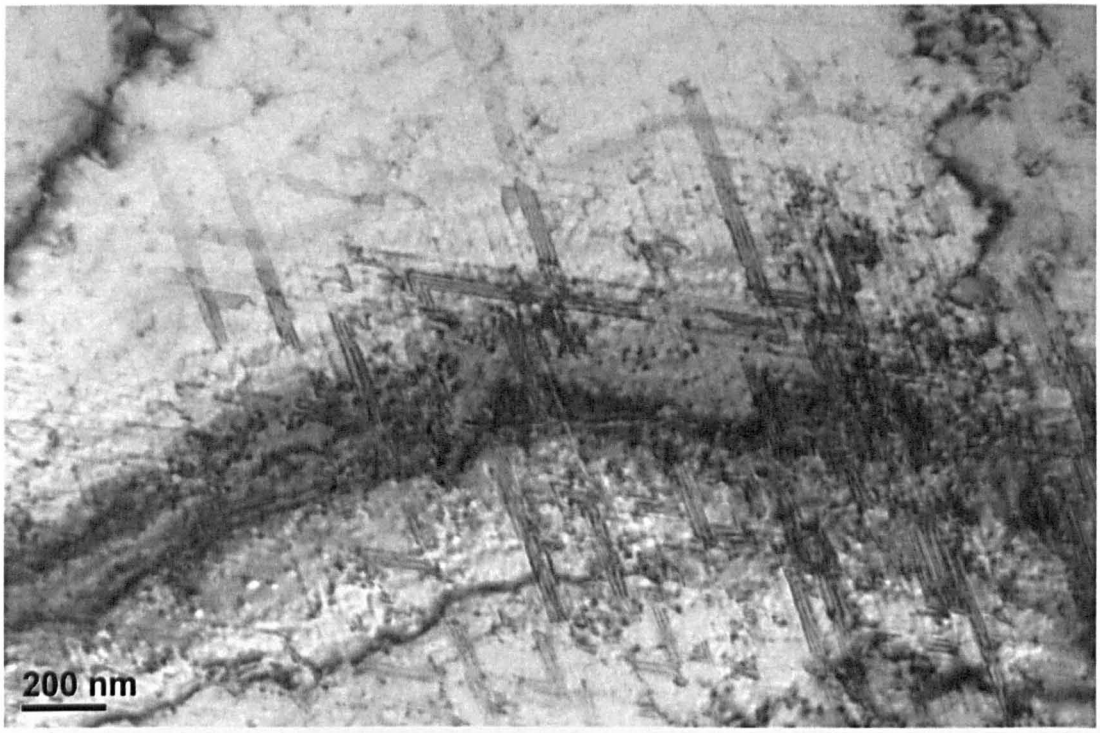

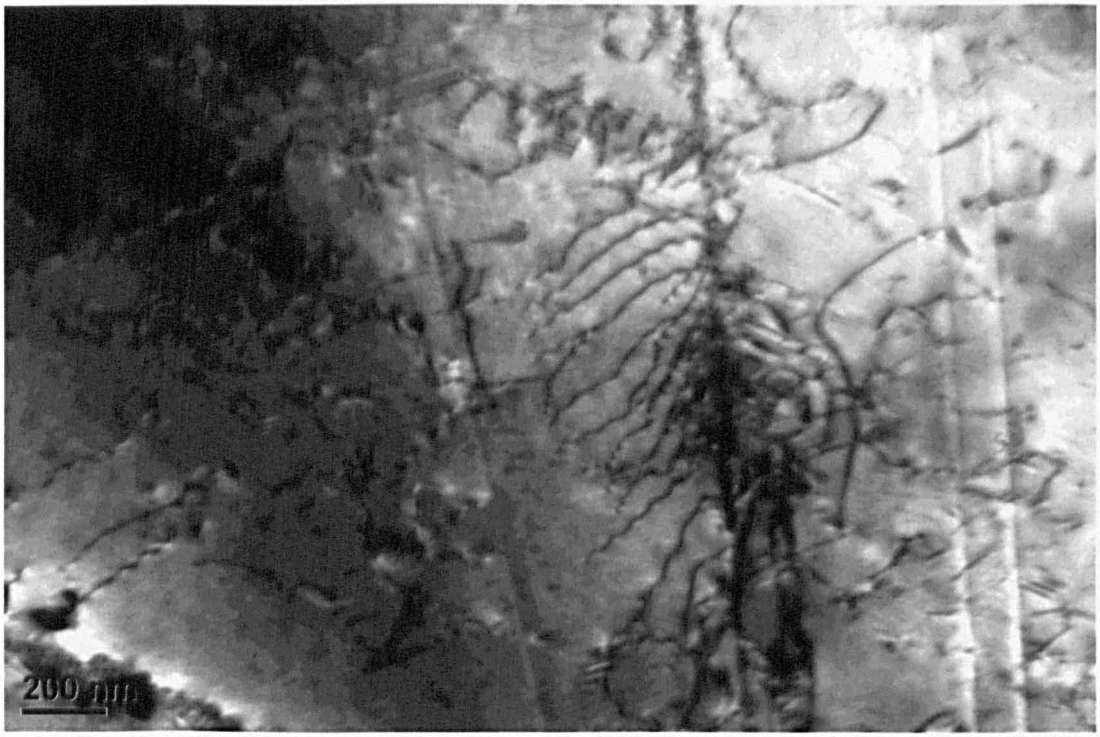

The 316H crept in primary stage only shows a different collection of micrographs, where populations of SF's are increased, examples of locks between them are observed, as well as more frequent examples of pile-ups.

APPENDIX 6: Data on crystal structures of the oxides for HRTEM

Oxide	Crystal structure	Lattice parameters [nm]		
		a	b	c
$Y_2Ti_2O_7$	Cubic (*bcc*)	1.01	–	–
Y_2TiO_5	Orthorhombic	1.04	0.37	1.13
$YTiO_3$	Orthorhombic	0.57	0.76	0.53

The following table shows the allowable reflections for the first low-order *hkl* indices of a *bcc* structure:

Reflection	$h^2+k^2+l^2$	$\sqrt{h^2+k^2+l^2}$
{110}	2	1.414213562
{200}	4	2
{211}	6	2.449489743
{220}	8	2.828427125
{310}	10	3.16227766
{222}	12	3.464101615
{123}	14	3.741657387
{400}	16	4

The table below register the interplanar distances, d_{hkl}, determined, in the ImageJ software, from the FFTs of the particles. The second column illustrates the ratio between the lattice parameter for the *bcc* crystal structure and the same d_{hkl} of the first column, related by:

$$d_{hkl} = \frac{a}{\sqrt{h+k+l}} \qquad \text{(Eq. A.1)}$$

The ratio, then, provides the term under the square root, which is compared to the last column of the allowed reflections for possible match (identification of the plane).

Particle type	measured d_{hkl}	a/d ratio	{hkl}
Particle 1	0.29	3.48	222
	0.36	2.81	220
Particle 2	0.71	1.42	110
	0.23	4.39	400
Particle 3	0.5	2.02	200
	0.29	3.48	222

Similar agreement could not be found for the expressions relating the lattice parameters to the interplanar spacings for the orthorhombic crystal structures. Therefore, they were ruled out.

APPENDIX 7: Illustration of the method for determining the oxide size

The following screenshots, taken from the ImageJ environment, illustrate the method for determining the diameter. The first step is the calibration of the pixels from the scale bar. Then, the "Oval/Elliptical Area" tool is selected and circles are drawn on the particles. From the areas, the diameter is calculated.

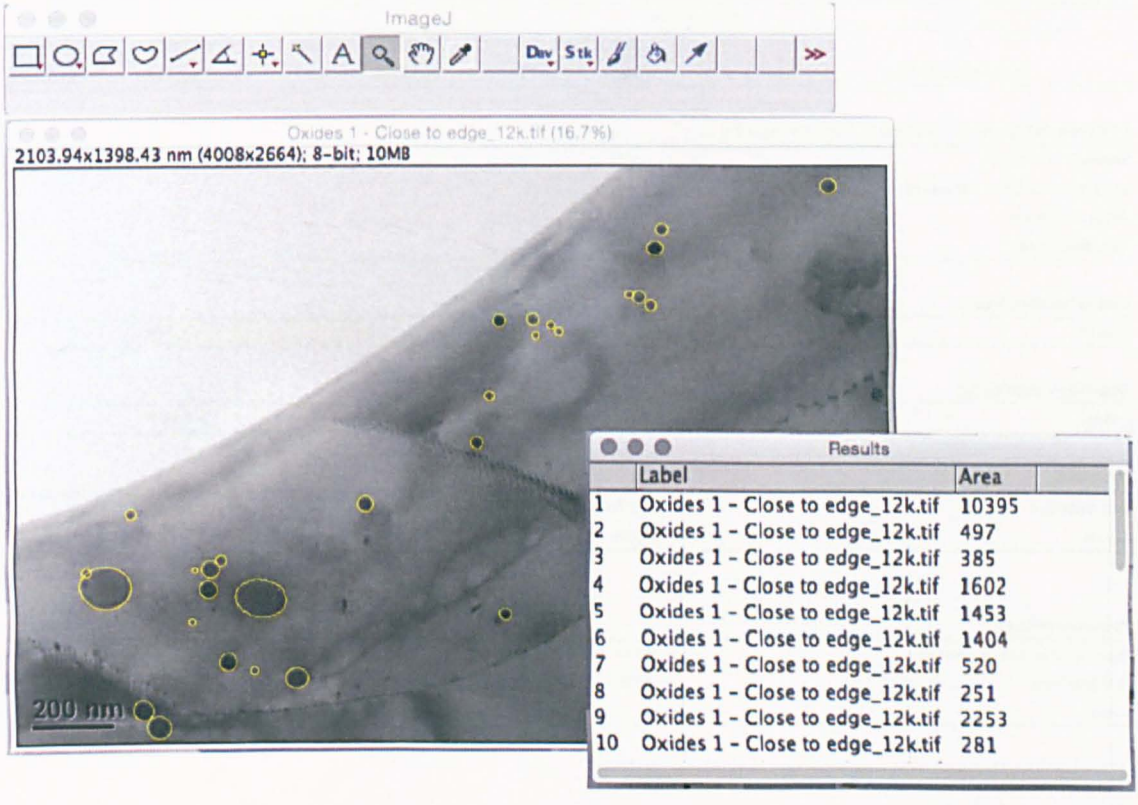

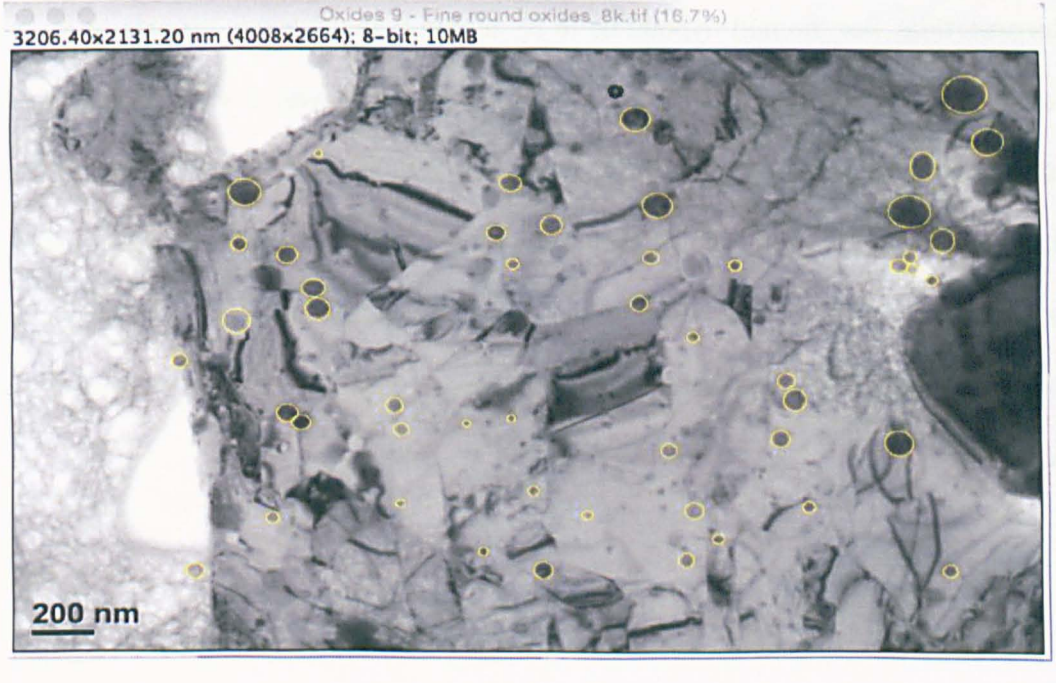

APPENDIX 8: Hypothesis test for comparison of the oxide size distributions for the as-received and heat-treated MA956 steel.

Null hypothesis: There's no significant difference between the oxide size distribution in the as-received condition and in the heat-treated one.

Compare Means

Descriptive Statistics

VAR	*Sample size*	*Mean*	*Standard Deviation*	*Variance*
44.1	449	34.20022	18.14111	329.09998
84.02448021592564	436	41.14561	22.2872	496.71933

t-test assuming unequal variances (heteroscedastic)

Degrees of Freedom	838		
Hypothesized Mean Difference	0.		
Pooled Variance	411.67576		
Test Statistics	5.07595		
Two-tailed distribution			
p-level	4.7519E-7	*Critical Value (5%)*	1.9628
One-tailed distribution			
p-level	2.37595E-7	*Critical Value (5%)*	1.64667
G-criterion			
Test Statistics	#N/A	*Critical Value (5%)*	#N/A
p-level	#N/A		
Pagurova criterion			
Ratio of variances parameter	0.39149		
Test Statistics	5.07595	*Critical Value (5%)*	0.06273
p-level	1.		

Interpretation: For the null hypothesis to be accepted, the T-test value should be lower than the critical value in the hypothesis test (carried out with a 95% confidence and assuming unequal variances). Since, by inspection, a value of 5.08 was found for the T-test, and this is significantly higher than the t-value of the two-tailed test (1.96), the null hypothesis is rejected. Therefore, there is a significant difference between both distributions, and the particle diameter (size) has grown under the thermal cycle of the heat treatment.